Journal of Fluids Engineering

Published Bimonthly by ASME

VOLUME 126 • NUMBER 2 • MARCH 2004

Special Section on Complex Fluids and Issues in Manufacturing Processes

TECHNICAL PAPERS

ADDITIONAL TECHNICAL PAPERS

(Contents continued on inside back cover)

This journal is printed on acid-free paper, which exceeds the ANSI Z39.48-1992 specification for permanence of paper and library materials. ∞™
♲ 85% recycled content, including 10% post-consumer fibers.

FLUIDS ENGINEERING DIVISION
Editor
JOSEPH KATZ (2005)
Assistant to the Editor
LAUREL MURPHY (2005)

Associate Editors
MALCOLM J. ANDREWS (2006)
S. BALACHANDAR (2005)
KENNETH S. BREUER (2006)
STEVEN L. CECCIO (2004)
GEORGES L. CHAHINE (2006)
WILLIAM W. COPENHAVER (2004)
THOMAS B. GATSKI (2006)
SIVIRAM GOGINENI (2006)
FERNANDO F. GRINSTEIN (2005)
HAMID JOHARI (2006)
JINKOOK LEE (2006)
M. VOLKAN ÖTÜGEN (2004)
MICHAEL W. PLESNIAK (2004)
DENNIS SIGINER (2005)
KYLE D. SQUIRES (2005)
YOSHINOBU TSUJIMOTO (2006)

BOARD ON COMMUNICATIONS
Chair and Vice-President
OZDEN OCHOA

OFFICERS OF THE ASME
President, **REGINALD VACHON**
Exec. Director
V. R. CARTER
Treasurer
R. E. NICKELL

PUBLISHING STAFF
Managing Director, Engineering
THOMAS G. LOUGHLIN
Director, Technical Publishing
PHILIP DI VIETRO
Managing Editor, Technical Publishing
CYNTHIA B. CLARK
Production Coordinator
CARMEN WALKER
Production Assistant
MARISOL ANDINO

Transactions of the ASME, Journal of Fluids Engineering (ISSN 0098-2202) is published bimonthly (Jan., Mar., May, July, Sept., Nov.) by The American Society of Mechanical Engineers, Three Park Avenue, New York, NY 10016. Periodicals postage paid at New York, NY and additional mailing offices. POSTMASTER: Send address changes to Transactions of the ASME, Journal of Fluids Engineering, c/o THE AMERICAN SOCIETY OF MECHANICAL ENGINEERS, 22 Law Drive, Box 2300, Fairfield, NJ 07007-2300. **CHANGES OF ADDRESS** must be received at Society headquarters seven weeks before they are to be effective. Please send old label and new address.

STATEMENT from By-Laws. The Society shall not be responsible for statements or opinions advanced in papers or ... printed in its publications (B7.1, Par. 3). **COPYRIGHT © 2004** by the American Society of Mechanical Engineers. Authorization to photocopy material for internal or personal use under those circumstances not falling within the fair use provisions of the Copyright Act, contact the Copyright Clearance Center (CCC), 222 Rosewood Drive, Danvers, MA 01923, tel: 978-750-8400, www.copyright.com. Request for special permission or bulk copying should be addressed to Reprints/Permission Department.

INDEXED by Applied Mechanics Reviews and Engineering Information, Inc. Canadian Goods & Services Tax Registration #126148048.

Downloaded 03 Jun 2010 to 171.66.16.159. Redistribution subject to ASME license or copyright; see http://www.asme.org/terms/Terms_Use.cfm

(**Contents continued**)

Journal of Fluids Engineering **Volume 126, Number 2** **MARCH 2004**

TECHNICAL BRIEFS

BOOK REVIEW

The ASME Journal of Fluids Engineering is abstracted and indexed in the following:

Applied Science & Technology Index, AMR Abstracts Database, Chemical Abstracts, Chemical Engineering and Biotechnology Abstracts (Electronic equivalent of Process and Chemical Engineering), Civil Engineering Abstracts, Computer & Information Systems Abstracts, Corrosion Abstracts, Current Contents, Ei EncompassLit, Electronics & Communications Abstracts, Engineered Materials Abstracts, Engineering Index, Environmental Engineering Abstracts, Environmental Science and Pollution Management, Excerpta Medica, Fluidex, Index to Scientific Reviews, INSPEC, International Building Services Abstracts, Mechanical & Transportation Engineering Abstracts, Mechanical Engineering Abstracts, METADEX (The electronic equivalent of Metals Abstracts and Alloys Index), Petroleum Abstracts, Process and Chemical Engineering, Referativnyi Zhurnal, Science Citation Index, SciSearch (The electronic equivalent of Science Citation Index), Shock and Vibration Digest, Solid State and Superconductivity Abstracts, Theoretical Chemical Engineering

Journal of Fluids Engineering

Guest Editorial

The papers included in this special section of the Journal of Fluids Engineering are drawn from those presented at the IMECE 2002 in New Orleans in the Symposia on the ''Rheology and Fluid Mechanics of Nonlinear Materials,'' ''Advances in Processing Science,'' and ''Electric and Magnetic Phenomena in Micro and Nano-Scale Systems'' sponsored by the Fluids Engineering and the Materials Divisions. They represent excellent examples of cross-disciplinary research as well as investigations relevant to important issues in manufacturing processes.

Symposia focused on the theme of complex and smart fluids that have been organized in every Winter Annual Meeting of the ASME starting in the very early 1990s. The focus of early Symposia emphasized electro-rheological fluids and the broader topic of non-Newtonian fluids and industrial applications. The series widened its scope and adopted a more encompassing recurring theme on the ''Rheology and Fluid Mechanics of Nonlinear Materials'' in the mid-1990s. Lately, parallel and complementary Symposia series addressing issues on the related themes of ''Electric and Magnetic Phenomena in Micro and Nano-Scale Systems,'' ''Advances in Materials Processing Science,'' and ''Flows in Manufacturing Processes'' have been organized regularly, the former two were held during IMECEs and the latter during summer meetings of the Fluids Engineering Division all initiated and led by Dennis Siginer.

These series developed as an interdivisional effort and has been sustained thanks to the support of the Fluids Engineering, Materials, and Applied Mechanics Divisions with organizing committees led by Dennis Siginer. The ongoing concurrent series of Symposia truly reflect the overlapping interests of the participants and present excellent examples of interdisciplinary research. The interests of the fluid mechanician, applied mathematician, continuum mechanician and the material scientist, as well as the industrial practitioner find a home in these series and feed on each other culminating in syntheses leading to new developments. Over the years, excellent and occasionally groundbreaking papers have been presented and published in the Proceedings of these Symposia. A prominent example which leaps to mind is the papers on suspensions by the late Yuri A. Buyevich presented at the IMECEs in the mid-1990s, and in particular the paper on fine suspensions in IMECE in Anaheim, Calif., in 1998.

Knowledge of non-Newtonian behavior is of vital importance to numerous manufacturing processes. The ''Rheology and Fluid Mechanics of Nonlinear Materials'' encompasses intriguing phenomena with enormous potential for manufacturing processes not observed in the case of materials with linear constitutive behavior. New materials are discovered constantly. Engineers are tasked with the design and manufacture of products by taking advantage of the special properties of these materials, which may undergo phase changes during the manufacturing process. Materials at the forefront of innovative technological applications rarely exhibit linear Newtonian stress—strain rate relationships, rather behaving in a very nonlinear fashion that needs to be characterized. This characterization is then used to describe their flow behavior under applied stress. Fluid flow and heat transfer phenomena may significantly affect the feasibility and the efficiency as well as the economic aspects of materials processing. Most manufacturing processes are strongly affected by the related transport phenomena. Product quality in particular and the efficiency of the process depend to a large extent on optimizing the characteristics of a given flow and/or heat transfer phenomenon pivotal to the process.

The 12 papers in this collection are loosely divided into three groups. The first five papers are more centered on fundamental issues with underlying important practical applications. The three papers in the next group present novel measurement techniques. The final four papers in this special section are directly related to manufacturing processes.

To begin the first group, Yamamoto et al. discuss new experimental results for the penetration problem of a long gas bubble through a viscoelastic fluid in a tube. This problem is relevant to the displacement of oil by a low viscous fluid in enhanced oil recovery as well as film coating on the inner wall of a tube and gas-assisted injection molding where viscous fingering may occur. They show that for values of the Weissenberg number larger than one ($We>1$) elastic normal force is the dominant factor in shaping the film thickness between the bubble and the wall, and when $We<1$ shear thinning viscosity defines the thickness. They discuss the consequences of their findings.

The petroleum industry relies on a number of polymer-based viscoelastic fluids in various operations such as well drilling and stimulation. These fluids are pumped partly through coiled tubing. The prediction of energy losses is central to the design of coiled tubing pumping operations. The drag reducing property of these fluids as well as viscoelasticity generated secondary flows in the curved geometry impact the energy losses in addition to frictional effects. The paper ''Rheological Properties and Frictional Pressure Loss of Drilling, Completion, and Stimulation Fluids in Coiled Tubing'' by Zhou and Shah explores these issues and presents interesting new experimental results, which point at the energy losses in coiled tubing to be significantly higher than straight tubing.

The addition of polymers to lubricants to produce viscoelastic ''multigrade'' oils is reported to lead to reduced bearing wear and engine friction. The mechanism associated with these effects remains unclear despite recent efforts to elucidate the physics of the phenomenon. The authors of ''Rheology of Dilute Polymer Solutions and Engine Lubricants in High Deformation Rate Extensional Flows Produced by Bubble Collapse'' experimentally investigate liquid jets formed by the collapse of bubbles under cavitation generated pressure waves. High rates of extension found in such jets are relevant to oil flows in dynamically loaded bearings, which subject the fluid to extension rates of the order of several thousand per second within a millisecond transit time. They report a mitigating effect of viscoelasticity on the cavitation damage mechanism.

Applied large electric fields generate a dramatic response in the rheological properties of electro-rheological suspensions. Development of industrial applications, including electro-rheological clutches, brakes, engine mounts in the automotive industry and robotic actuators, is at this time limited by a lack of understanding of the underlying mechanisms with the added difficulty of producing stable suspensions. Kadaksham et al. develop a novel numerical approach based on distributed Lagrange multiplier method for the direct simulation of the dynamics of electro-rheological suspensions subjected to spatially nonuniform electric fields. They show that particle collection time in a flowing electro-rheological fluid subjected to a nonuniform electric field depends on the ratio of dielectrophoretic and viscous forces as well as the relative importance of the electrostatic particle-particle interaction force, the dielectrophoretic force, and the hydrodynamic forces.

Liquid crystal technology is crucial to electronic display component manufacturing among other things. Nematic phase is the simplest phase in a liquid crystal (LC) with an orientation order but no translational order. Of particular interest are rod-like and disk-like polymer-molecule-based LCs. Most hydrodynamic theories formulated for flows of LC materials are predicated on rod-like polymer molecules. Wang, the lead author of the paper on the kinetic theory for nonhomogenous nematic liquid crystalline polymers, recently developed a kinetic theory for spheroidal liquid crystal polymers with the aim of establishing a unified theory for rod-like and disk-like LCPs. In the present paper together with his co-authors, he discusses the extension of the previously proposed unified field theory to account for the translational diffusion and the related density variations. The constitutive theory presented is applicable to flows of rod-like liquid crystal polymers at large aspect ratios and to flows of disk-like LCPs at small aspect ratios.

The three papers in the next group present novel measurement techniques. Greenwood and Bamberger describe a noninvasive technique to measure the density of a liquid or slurry through the stainless steel pipeline wall. The self-calibrating ultrasonic sensor they introduce measures the density by coupling measurements of acoustic impedance and velocity of sound. The technique and the associated self-calibrating sensor represent an exciting development, and may have a variety of applications.

Bakhtiyarov et al. present a new technique for measuring fraction solid in molten metals and alloys, as well as the results of the application of the method to a commercial aluminum alloy. The technique is based on measuring the opposing torque generated by the circulating eddy currents induced by a rotating magnetic field in a stationary solidifying metal sample or vice versa. The torque is related to the amount of solid phase in a solidifying melt. The method is an important contribution to the understanding of the solidification phenomenon in the mushy zone. Fraction solid is a pivotal parameter in optimizing metallurgical processes and in developing mathematical models of the casting process.

Ferrofluids are rapidly becoming a commercially viable example of polarizable suspensions with potentially promising applications in microfluidic pumps and actuators driven by alternating or rotating magnetic fields, in drug delivery vectors and other biomedical applications such as magnetocytolysis of localized tumors. These fluids are suspensions of magnetized colloidal particles coated with a stabilizing dispersant in a carrier fluid. For theoretical modeling, they present a challenge, in that they are characterized by body-couples and nonsymmetric viscous stresses as well as couple stresses representing the transport of microstructure angular momentum. The paper by Rosenthal et al. discusses theoretical developments and experimental observations concerning the spin-up flow and the measurement of the torque required to restrain a hollow cylinder containing the ferrofluid with the underpinning aim of clarifying an ongoing controversy in the spin-up flow of ferrofluids.

The remaining four papers in this special section are directly related to manufacturing processes. High-speed water jets proved to be feasible replacements for cutting tools, be it surgical scalpels or rock cutting. Among the myriad of applications, the capability of water jets and water/ice slurries to perfectly clean contaminated surfaces in an inexpensive and environmentally sound way is particularly noteworthy. The paper by Petrenko et al. describes a numerical study to investigate the dynamics of the water slug propelled by powder explosion in a water cannon. The slug is very much like a bullet, but moves at speeds significantly exceeding that of a bullet driven by a similar explosion, typically speeds in excess of 1.5 km/s. The computational method is based on a finite difference scheme coupled with the method of characteristics and predicts the pressure, velocity and density fields in the course of slug acceleration.

The collaborative effort of Correia et al. examines extensively the vacuum assisted resin transfer molding process (VARTM) widely used in a variety of manufacturing processes involving composite materials. A governing equation for VARTM is developed, followed by a numerical 1D/2D solution predicting the flow and time-dependent thickness of the preform by introducing models for compaction and permeability. The paper also provides a comparative study of VARTM with the conventional resin transfer molding (RTM).

Boutaous and Bourgin explore the flow of an air layer squeezed between a solid smooth substrate and a plastic film. The problem is of pivotal importance in obtaining good quality plastic film rolls, as stresses generated by trapped air pockets lead to defects. Experimental evidence points to the plastic film roughness as the governing parameter in determining the flow characteristics. The authors present experimental measurements of the plastic film roughness, a very involved concept in itself as the word roughness contains so much information, and an elegant theoretical analysis of the squeeze flow via Hele-Shaw approximation introduced by T. C. Fung in 1969 together with periodic homogenization techniques.

The last paper in this collection explores the effect of buoyancy convection on the growth of a particular type of crystal grown by the traveling solvent method (TSM) under different heating conditions. Saghir et al. use a finite-element approach to solve simultaneously the full Navier-Stokes equations together with the energy and solutal equations. The TSM is a commonly used method in industry to produce pure and homogenous simple crystals for the production of high-quality semiconductors. The modeling in this paper accounts for the heat losses by radiation. The authors present interesting results pointing to strong convection currents in the solvent detrimental to the growth uniformity of the crystal rod.

I would like to thank the authors of the papers in this special section of the Journal of Fluids Engineering for their devoted efforts in preparing and improving their manuscripts in response to the reviews. Special thanks are due to the referees who contributed their time and expertise.

Dennis A. Siginer
Associate Editor

Takehiro Yamamoto*
Department of Mechanophysics Engineering,
Graduate School of Engineering,
Osaka University,
2-1, Yamadaoka, Suita,
Osaka 565-0871
Japan
e-mail: take@mech.eng.osaka-u.ac.jp

Takanori Suga
Department of Mechanical, Materials and
Manufacturing Science,
Faculty of Engineering,
Osaka Universit,y
2-1, Yamadaoka, Suita,
Osaka 565-0871
Japan
e-mail: suga@rheol.mech.eng.osaka-u.ac.jp

Kiyoji Nakamura
Department of Mechanophysics Engineering,
Graduate School of Engineering,
Osaka University,
2-1, Yamadaoka, Suita,
Osaka 565-0871
Japan
e-mail: nakamura@mech.eng.osaka-u.ac.jp

Noriyasu Mori
Department of Mechanophysics Engineering,
Graduate School of Engineering,
Osaka University,
2-1, Yamadaoka, Suita,
Osaka 565-0871
Japan
e-mail: n.mori@mech.eng.osaka-u.ac.jp

The Gas Penetration Through Viscoelastic Fluids With Shear-Thinning Viscosity in a Tube

The penetration of a long gas bubble through a viscoelastic fluid in a tube was studied. Experiments were carried out for two Newtonian and five polymeric solutions to investigate the relation between the coating film thickness and rheological properties of the test fluids. The polymeric solutions are viscoelastic fluids having shear-thinning viscosity. A bubble of air was injected into a tube filled with a test fluid to form hydrodynamic coating on a tube wall. The film thickness was evaluated by hydrodynamic fractional coverage m. The fractional coverage was characterized using the capillary number Ca and the Weissenberg number Wi. For viscoelastic fluids, Ca and Wi were evaluated considering the shear-thinning viscosity. Two kinds of representative shear rate were used for the evaluation of Ca and Wi. The dependence of m on Ca in viscoelastic fluids was different from that of the Newtonian case. The film was thinner than that of the Newtonian case at the same Ca when Wi was small, i.e. the viscous property was dominant. The shear-thinning viscosity had a role to make the film thin. On the other hand, the film tended to be thicker than the corresponding Newtonian results at large Wi because of normal stress effect. [DOI: 10.1115/1.1669402]

Introduction

Gas penetration through a viscoelastic fluid is related to problems such as film coating on an inner wall of a tube, displacement of oil by a low viscous fluid in enhanced oil recovery, and fluid replacement in gas-assisted injection molding. In industrial application, we often encounter the gas penetration through non-Newtonian fluids. For example, gas penetration through viscoelastic fluids is observed in gas-assisted injection molding. Gas-assisted injection molding is an operative technique to manufacture products with hollow structure. In this process, compressed gas such as Nitrogen is injected into a core of polymer melt in a mold during usual injection molding process. The interface between the gas and the polymer melt moves to replace the polymer melt with the gas. Because polymer melts are viscoelastic fluids, the viscoelastic properties of polymer melts are expected to affect the interface motion.

Viscous fingering is related to a phenomenon occurring in gas-assisted injection molding. Some experimental studies have been performed using channels similar to those in real gas-assisted injection molding process. Lu et al. [1] used large flat plates with ribs to investigate gas fingering in the rib parts. Yang and Chou [2] examined the gas penetration through a polymer melt in circular tubes with dimensional variations and curved section to study shape effects on the uniformity of residual wall thickness.

As for gas penetration in a tube, there are early studies of the gas penetration through Newtonian fluids (e.g., [3–7]). It was indicated that the relation between the fractional coverage and the capillary number for Newtonian fluids was described by a master curve. In addition, Cox [6] visualized streamlines during a gas penetration. Huzyak and Koelling [8] and Gauri and Koelling [9] have studied the gas penetration through viscoelastic fluids. They used Boger fluids, a viscoelastic fluid having a constant Newtonian viscosity, to investigate the elastic effect on the coating film thickness. The dependence of the fractional coverage on the capillary number for Boger fluids is nearly identical to the Newtonian case at low capillary numbers, while the results for Boger fluids deviate from the Newtonian counterparts at high capillary numbers. They pointed out that the elastic property of the fluid thickened the coating film. Gauri and Koelling [9] also performed a PIV measurement to elucidate the velocity field near gas-bubble tips.

Many engineering polymers used in polymer processing have shear-thinning viscosity and this property has important role in flows in polymer processing [10]. Thus, it is important to clarify the effect of shear-thinning viscosity on bubble-tip behavior. Kamisli and Ryan [11] have proposed a simple model for gas-liquid dynamics in liquid displacement in circular tubes and noncircular channels based on a power-law viscosity function. Bonn and Meunier [12] and Lindner et al. [13–15] have indicated the effect of both shear thinning viscosity and normal stress on finger growth

---

*Corresponding author

Contributed by the Fluids Engineering Division for publication in the JOURNAL OF FLUIDS ENGINEERING. Manuscript received by the Fluids Engineering Division October 17, 2002; revised manuscript received June 4, 2003. Associate Editor: D. Siginer.

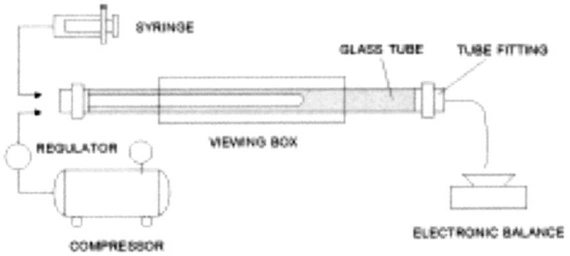

Fig. 1 Experimental setup

in a Hele-Shaw cell. The authors' group has also pointed out the effect of shear-thinning viscosity on fingering pattern in a Hele-Shaw cell [16,17]. However, the experiments of the gas penetration through viscoelastic fluids with shear-thinning viscosity are not enough and sufficient experimental data have not been obtained.

In the present study, we have analyzed the gas penetration through viscoelastic fluids having shear-thinning viscosity to elucidate the effect of the shear-thinning property on the motion of the interface between the gas and the viscoelastic fluid. We characterized the coating film thickness on a tube wall using both the capillary number and Weissenberg number; these non-dimensional groups were evaluated considering the shear-thinning effect. The present analysis shows the Weissenberg number characterizes which effect of the shear-thinning viscosity or the elastic normal force is dominant.

Experimental

Experimental Setup. Gas penetration in a glass tube was observed. Figure 1 shows the experimental setup for the gas penetration. The glass tube is 1,000 mm long and its inner diameter is 7 mm. A tube fitting was connected to each tube end. A test fluid or air was injected into the glass tube from one end of the tube. A syringe was used to fill the tube with a test fluid. Air was injected into the tube at a constant pressure ranging from 4 to 200 kPa using an air compressor (Hitachi Super Bebicon). The injection pressure was controlled with a precision regulator. A contraction part was attached to the other end to adjust the pressure gradient across the tube. The tube was covered by a viewing box filled with glycerin to reduce the refraction of light; Glycerin has similar refraction index to that of the glass. The mass outflow rate was measured with an electronic balance (A&D FA-200).

Test Fluids. We used two Newtonian and five viscoelastic fluids as test fluids. The Newtonian fluids include glycerin and 90wt% malt jelly in water. The viscoelastic fluids are 2.0, 2.5, and 3.0 wt% polyacrylamide (PAA; Sanyo Chemical Industries SANFLOC AH70P) in water, 1.0 wt% carboxymethyl cellulose (CMC; Daicel Chemical Industries CMC DAICEL 2260) in water, and the mixture of 0.95 wt% CMC and 0.08 wt% PAA in water.

Figures 2 and 3 show the shear viscosity and the first normal stress difference of the test fluids, respectively. Rheological measurements were carried out with a cone-plate type rheometer (UBM Rheosol-G2000). All the viscoelastic fluids have shear-thinning viscosity and non-zero first normal stress difference. The shear viscosity of every viscoelastic fluid shows strong shear-thinning property. We adjusted the mixing ratio of the mixture of CMC and PAA solutions so that the mixture and the 1.0 wt% CMC solution are almost the same in the shear-thinning property and are different in the elastic property. The measurements of rheological properties were carried out at 25°C, which is the same temperature condition for the gas penetration experiments. Table 1 summarizes both surface tension σ and the density ρ of the test fluids at 25°C. The surface tension was measured with a Du Nouy type tension meter.

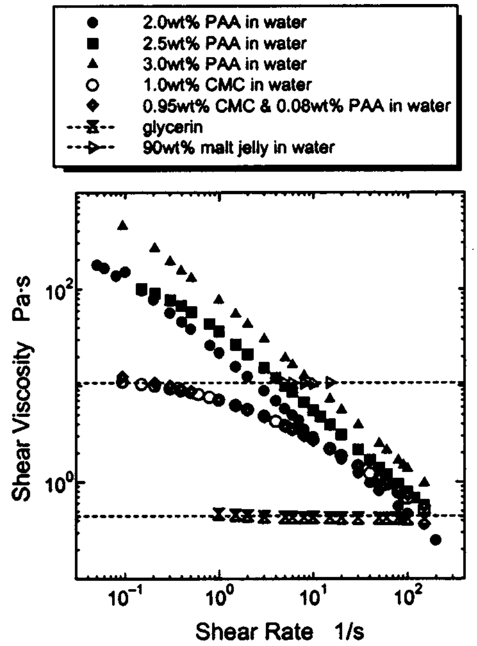

Fig. 2 The shear viscosity of test fluids at 25°C

Experimental Method. In the present experiment, the mass flow rate of test fluids expelled from the tube exit and the bubble-tip velocity were measured to estimate the coating film thickness on the inner wall of the tube. Because viscoelastic fluids have memory effect, the test fluid was left at rest for 10 minutes after filling process of the test fluid.

The film thickness was evaluated by a fractional coverage m defined by

$$m = \frac{R_0^2 - R_b^2}{R_0^2}, \tag{1}$$

where R_0 is the inner radius of the tube and R_b is the radius of a gas bubble (see Fig. 4). When the fractional coverage is constant along the tube, the balance of mass yields

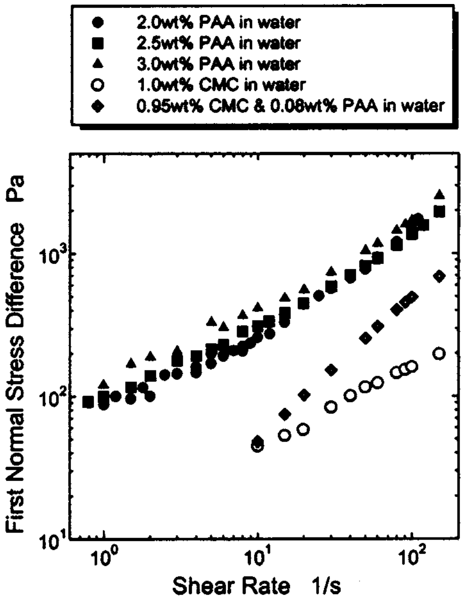

Fig. 3 The first normal stress difference of test fluids at 25°C

Table 1 Interfacial tension and density of test fluids at 25°C

Test fluids	Interfacial Tension σ mN/m	Density ρ kg/m^3
2.0 wt% PAA in water	76.5	1000
2.5 wt% PAA in water	78.1	1000
3.0 wt% PAA in water	77.7	1000
1.0 wt% CMC in water	77.0	1000
0.95 wt% CMC & 0.08 wt% PAA in water	75.8	1000
Glycerin	65.0	1264
90 wt% malt jelly in water	81.1	1355

$$m=1-\frac{w}{\rho\pi R_0^2 L}, \tag{2}$$

where w is the mass of the test fluid replaced by the gas bubble, ρ the fluid density, and L the length of the test measuring region. We measured w to obtain the film thickness according to Eq. (2).

The experimental results were characterized using the capillary number Ca and Weissenberg number Wi that are defined in the next subsection. Shear viscosity is necessary for evaluating these values. Shear viscosity of viscoelastic fluids changes with the shear rate; hence we need to obtain the bubble-tip velocity to determine a representative shear rate for the evaluation of shear viscosity. The bubble-tip velocity was measured in a test section of 200 mm long that was located from 400 to 600 mm downstream of the tube inlet. The bubble-tip velocity was estimated by measuring time that a bubble passed through the test section. Preliminary experiments had confirmed that the tip velocity in the test section was almost constant. For the evaluation of w, the mass outflow rate of the test fluid was also measured during a period of time when a bubble passed through the test section. We ran the measurements five times at each injection pressure and confirmed the reproducibility. The average mass flow rate and tip-velocity of five measurements were used for the analysis.

In addition, we carried out flow visualization experiments to observe the motion of bubble tip. The motion of the gas bubble was captured on videotape using a digital video camera (SONY DCR-TRV900). Transmitted light through tracing paper was used for a light source.

Non-Dimensional Group. We characterized the experimental results using the following non-dimensional groups: The capillary number Ca is a ratio of viscous force to interfacial force and is defined by

$$Ca=\frac{\eta(\dot{\gamma})U}{\sigma}, \tag{3}$$

where η is the viscosity and U is a representative velocity. The Weissenberg number Wi is a ratio of elastic force to viscous force and is defined by

$$Wi=\frac{\lambda(\dot{\gamma})U}{H}, \tag{4}$$

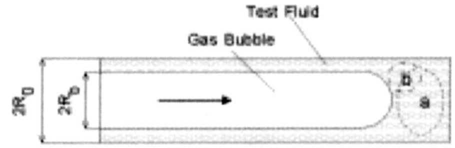

Fig. 4 Schematic of gas penetration: Areas (a) and (b) indicate schematic of regions where representative shear rates are defined

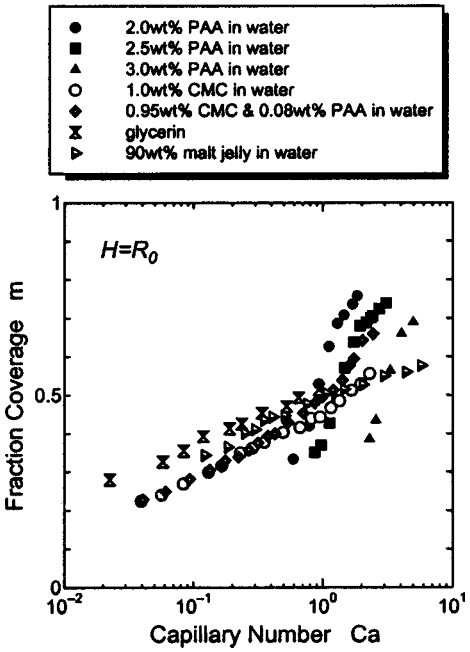

Fig. 5 Fractional coverage *m* as a function of capillary number *Ca* when $H=R_0$; case (a)

where H is a representative length and λ is a relaxation time. The Maxwell type relaxation time (5) was used for λ:

$$\lambda=\frac{N_1}{2\eta\dot{\gamma}^2}, \tag{5}$$

where N_1 is the first normal stress difference. The Reynolds number defined by $\mathrm{Re}=\rho UH/\eta$ ranges from $O(10^{-5})$ to $O(10^{-1})$ in the present experiments and hence the effect of inertia is negligible.

We need to determine a representative shear rate $\dot{\gamma}=U/H$ to evaluate $\eta(\dot{\gamma})$ and $\lambda(\dot{\gamma})$. In the present analysis, we applied the mean bubble-tip velocity as U and two definitions of H: (a) $H=R_0$ and (b) $H=R_0-R_b$ to estimate the shear rate. The shear rate evaluated using the former definition corresponds to the mean velocity gradient in front of a bubble tip; the latter case represents the mean velocity gradient near the tube wall. The schematic of regions where these shear rates are defined are illustrated in Fig. 4.

Results and Discussion

Effect of Capillary Number. Figure 5 shows the dependence of the fractional coverage m on the capillary number Ca in the case (a). The fractional coverage increases consistently with Ca. In the Newtonian case, the fractional coverage tends to approach about 0.6 at high Ca.

For the viscoelastic fluids, the effect of elastic properties has been reported in previous studies [8,9,12] and the present results agree with these studies. The fractional coverage m is larger than the corresponding Newtonian result when the bubble-tip velocity is large, i.e. at high Ca. This phenomenon agrees with the results by Huzyak and Koelling [8]. They carried out the experiments of the gas penetration through Boger fluids and reported the thickening of film at high Ca was caused by elasticity of the fluids. Because Wi also increases with increasing the bubble-tip velocity, it is large at high Ca and elastic effects strongly appear. The effect of elastic normal force can be explained as follows [12]: Normal force exists in the radial direction. The force direction is towards the centerline and the force becomes larger with increasing the

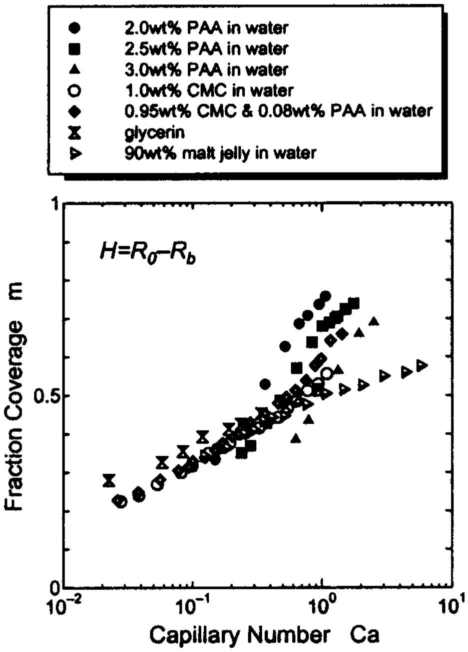

Fig. 6 Fractional coverage *m* as a function of capillary number *Ca* when $H=R_0-R_b$; case (b)

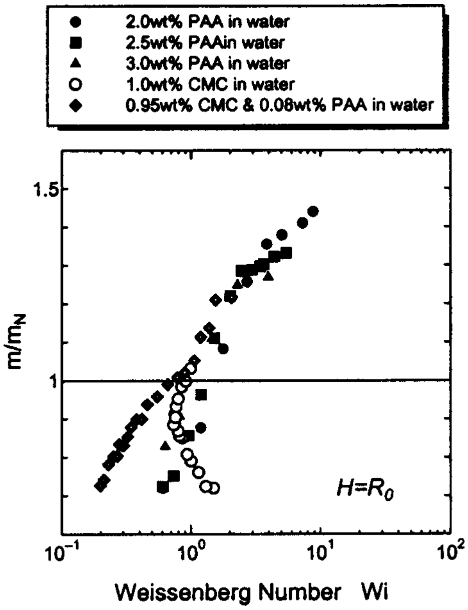

Fig. 7 Reduced fractional coverage m/m_N as a function of Weissenberg number *Wi* when $H=R_0$; case (a)

shear rate or the velocity gradient. Consequently, the film thickens and *m* increases consistently with the capillary number.

On the other hand, when the bubble-tip moves slowly, i.e., *Ca* is small; *m* is smaller than the corresponding Newtonian result. Boger fluids, however, behave nearly identically to the Newtonian fluids at low *Ca* [8]. The decrease in film thickness is probably related to the shear-thinning viscosity: Because of the shear-thinning viscosity, apparent shear viscosity decreases near the tube wall, thus the velocity of bubble-tip near the wall becomes faster than that in the corresponding Newtonian fluid. Consequently, the film thickness becomes thinner than the Newtonian case. This effect of shear-thinning viscosity obtained in the present experiment coincides with the prediction by Kamisli and Ryan [11].

Figure 6 shows the dependence of *m* on *Ca* in the case (b). Because the definition of the representative shear rate is different from that in the case (a), the plots shift in the direction of the axis of *Ca*. However, the results show qualitatively the same behavior as that shown in the case (a). The present experimental results show that the relation between *m* and *Ca* reported in the previous studies is also obtained for fluids with shear-thinning viscosity by evaluating *Ca* as a function of the shear rate.

In both cases (a) and (b), the mixture and the CMC solution behave similarly at low *Ca*, while the fractional coverage of the mixture becomes larger than that of the CMC solution at high *Ca*. The representative shear rate in the present experiments ranges from 0.1 to 45 s^{-1} in the case (a) and from 0.5 to 130 s^{-1} in the case (b). The shear viscosities of the two fluids are almost the same and the first normal stress difference N_1 of the mixture is larger than that of the 1.0 wt% CMC in water at $\dot{\gamma}>10\,\mathrm{s}^{-1}$ as shown in Figs. 2 and 3. The shear rates at which the difference in *m* of the two fluids becomes apparent are approximately 15 s^{-1} and 45 s^{-1} in the cases of (a) and (b), respectively. These shear rates is in the range that the two fluids remarkably differ in N_1. This fact indicates that the difference of the two fluids in *m* at high *Ca* originates in the difference in N_1 at high shear rate.

It is important and interesting to quantitatively evaluate the effect of the shear-thinning property, e.g. intensity of the shear-thinning and find parameters that characterizes the effect. However, this issue is unsolved in the present study because it is not easy to carry out the experiments in a wide range of *Ca* using enough test fluids having different shear-thinning viscosity; a numerical approach may be an effective alternative method.

Effect of Weissenberg Number. We next analyze the elastic/viscous effects considering the relation of the fractional coverage and the Weissenberg number. Figures 7 and 8 show the dependence of a reduced fractional coverage m/m_N on *Wi* in the cases (a) and (b), respectively. Here, m_N is the fractional coverage of Newtonian fluid at the corresponding *Ca*. Consequently, the condition $m/m_N>1$ means the coating film is thicker for a viscoelastic case than the Newtonian case; $m/m_N<1$ means the film is thinner than the Newtonian case.

In both cases (a) and (b), $m/m_N<1$ at low *Wi* and $m/m_N>1$ at high *Wi*. For the PAA solutions, the Weissenberg number at which

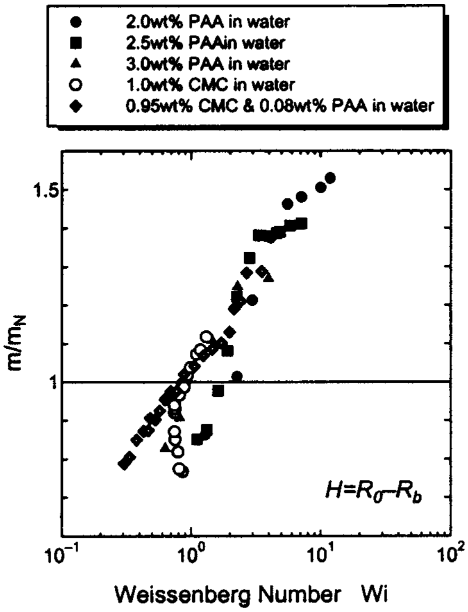

Fig. 8 Reduced fractional coverage m/m_N as a function of Weissenberg number *Wi* when $H=R_0-R_b$; case (b)

m/m_N is unity, Wi_C, is about 1.2 for the case (a) and is about 1.5 for the case (b); for the CMC solution, Wi_C is nearly equal to 1.0 for both cases (a) and (b). The results in Figs. 7 and 8 indicate that the magnitude relation of film thickness changes at $Wi \approx 1.0$: The film thickness is thin as compared to the Newtonian case owing to the shear-thinning viscosity when viscous property is dominant, i.e. at $Wi < 1$. On the other hand, the normal force effect makes the film thick when elastic property is dominant, i.e. at $Wi > 1$. We can conclude that the Weissenberg number characterizes which property of the shear-thinning viscosity and the elastic normal force mainly affects the film thickness.

We applied two definition of the Weissenberg number. In general, flow behaviors near the wall are principal in shear-dominant flows. The definition (b) may reflect this fact. However, it is not confirmed which definition is suitable for quantitatively evaluating the effect of *Wi* on the film thickness. The analysis of flow field near the bubble tip will be helpful to decide which definition of *Wi* is proper and the numerical simulation is an effective method. In addition, the CMC solution shows anomalous behavior at $Wi \approx 1$: When $m/m_N < 1$, *Wi* slightly changes near unity despite m/m_N changes comparatively largely. This fact suggests that other rheological properties affect the mechanism of bubble-tip motion. The elongational property probably affects the bubble motion because fluid element near the bubble front is stretched. The elongational viscosity of PAA solutions shows strong stretch-thickening property, while that of CMC solutions are very weak [18]. The effect of elongational viscosity was also suggested in our study of viscous fingering [16]. On the other hand, Linder et al. [15] concluded that the influence of elongational viscosity was insignificant. However, the measurement of elongational viscosity of polymer solutions is still a challenging problem and quantitative evaluation of elongational effects on the film thickness remains unsolved.

Conclusion

We have experimented the gas penetration through viscoelastic fluids in a circular tube. The experimental results indicated that viscoelastic properties affected the film thickness on the inner wall of the tube. The results showed that the Weissenberg number characterized which effect of the shear-thinning viscosity or the elastic normal force on the film thickness was dominant: The former effect appears strongly at $Wi < 1$, and the latter does at $Wi > 1$. Normal force toward the tube center occurs because of the elastic property such as normal stress difference. The force plays a role to thicken the film. This effect appears at high Weissenberg number. Because of the shear-thinning viscosity, apparent shear viscosity is low near the tube wall. Consequently, the film becomes thinner than the Newtonian case when the Weissenberg number is small and viscous effect is dominant. In addition, further study of both the flow field near the bubble-tip and the effect of elongational properties such as stretch-thickening elongational viscosity may be necessary to elucidate the mechanism of film coating of viscoelastic fluids.

References

[1] Lu, X., Chiang, H. H., Fong, L., and Zhao, J., 1999, ‘‘Study of ‘Gas Fingering’ Behavior in Gas-Assisted Injection Molding,’’ Polym. Eng. Sci., **39**, pp. 62–77.

[2] Yang, S. Y., and Chou, H. L., 2002, ‘‘Study on Residual Wall Thickness at Dimensional Transitions and Curved Sections in Gas-Assisted Molded Circular Tubes,’’ Polym. Eng. Sci., **42**, pp. 111–119.

[3] Taylor, G. I., 1961, ‘‘Deposition of a Viscous Fluid on the Wall of a Tube,’’ J. Fluid Mech., **10**, pp. 161–165.

[4] Bretherton, F. P., 1961, ‘‘The Motion of Long Bubbles in Tubes,’’ J. Fluid Mech., **10**, pp. 166–188.

[5] Cox, B. G., 1962, ‘‘On Driving a Viscous Fluid Out of a Tube,’’ J. Fluid Mech., **14**, pp. 81–96.

[6] Cox, B. G., 1964, ‘‘An Experimental Investigation of the Streamlines in Viscous Fluid Expelled From a Tube,’’ J. Fluid Mech., **20**, pp. 193–200.

[7] Schwartz, L. W., Princen, H. M., and Kiss, A. D., 1986, ‘‘On the Motion of Bubbles in Capillary Tubes,’’ J. Fluid Mech., **172**, pp. 259–275.

[8] Huzyak, P. C., and Koelling, K. W., 1997, ‘‘The Penetration of a Long Bubble Through a Viscoelastic Fluid in a Tube,’’ J. Non-Newtonian Fluid Mech., **71**, pp. 73–88.

[9] Gauri, V., and Koelling, K. W., 1999, ‘‘The Motion of Long Bubbles Through Viscoelastic Fluids in Capillary Tubes,’’ Rheol. Acta, **38**, pp. 458–470.

[10] Tanner, R. I., 2000, *Engineering Rheology*, 2nd ed., New York, Oxford University Press.

[11] Kamisli, F., and Ryan, M. E., 2001, ‘‘Gas-Assisted Non-Newtonian Fluid Displacement in Circular Tubes and Noncircular Channels,’’ Chem. Eng. Sci., **56**, pp. 4913–4928.

[12] Bonn, D., and Meunier, J., 1997, ‘‘Viscoelastic Free-Boundary Problems: Non-Newtonian Viscosity vs Normal Stress Effects,’’ Phys. Rev. Lett., **79**, pp. 2662–2665.

[13] Lindner, A., Bonn, D., and Meunier, J., 2000a, ‘‘Viscous Fingering in Complex Fluids,’’ J. Phys.: Condens. Matter, **12**, pp. A477–A782.

[14] Lindner, A., Bonn, D., and Meunier, J., 2000b, ‘‘Viscous Fingering in a Shear-Thinning Fluid,’’ Phys. Fluids, **12**, pp. 256–261.

[15] Lindner, A., Bonn, D., Poire, E. C., Amar, M. B., and Meunier, J., 2002, ‘‘Viscous Fingering in Non-Newtonian Fluids,’’ J. Fluid Mech., **469**, pp. 237–256.

[16] Yamamoto, T., Kamikawa, H., and Nakamura, K., 1996, ‘‘The Fractal Phenomenon of the Non-Newtonian Fluid in a Hele-Shaw Cell,’’ Nihon Reoroji Gakkaishi, **24**, pp. 105–109 (in Japanese).

[17] Yamamoto, T., Kamikawa, H., Tanaka, H., Nakamura, K., and Mori, N., 2001, ‘‘Viscous Fingering of Non-Newtonian Fluids in a Rectangular Hele-Shaw Cell,’’ Nihon Reoroji Gakkaishi, **29**, pp. 81–87.

[18] Koshiba, T., Mori, N., and Nakamura, K., 1996, ‘‘Measurement of Elongational Viscosity for Polymer Solutions With a Spinline Rheometer and Numerical Analysis of the Flow,’’ Trans. Japan Soc. Mech. Eng., **62**, Series B, pp. 3890–3898 (in Japanese).

Rheological Properties and Frictional Pressure Loss of Drilling, Completion, and Stimulation Fluids in Coiled Tubing

Yunxu Zhou
Graduate Research Assistant
e-mail: YunxuZhou@yahoo.com

Subhash N. Shah
Stephenson Chair Professor
e-mail: subhash@ou.edu

Mewbourne School of Petroleum and
Geological Engineering,
Well Construction Technology Center,
The University of Oklahoma,
Norman, OK 73019

The rheological properties and friction pressure losses of several common well-drilling, completion, and stimulation fluids have been investigated experimentally. These fluids include polymeric fluids—Xanthan gum, partially hydrolyzed polyacrylamide (PHPA), guar gum, and hydroxyethyl cellulose (HEC), bentonite drilling mud, oil-based drilling mud, and guar-based fracturing slurries. Rheological measurements using a Bohlin CS 50 rheometer and a model 35 Fann viscometer showed that these fluids exhibit shear thinning and thermal thinning behavior except the bentonite drilling mud whose viscosity increased as the temperature was raised. Flow experiments using a full-scale coiled tubing test facility showed that the friction pressure loss in coiled tubing is significantly higher than in straight tubing. Since the polymeric fluids displayed drag reducing property, their drag reduction behavior in straight and coiled tubings was analyzed and compared. Plots of drag reduction vs. generalized Reynolds number indicate that the drag reduction in coiled tubing was not affected by polymer concentration as much as in straight tubing. The onsets of turbulence and drag reduction in coiled tubing were significantly delayed as compared with straight tubing. The effect of solids content on the friction pressure losses in coiled tubing is also briefly discussed.

[DOI: 10.1115/1.1669033]

Introduction

Coiled Tubing (CT) has been successfully used in well drilling, completion, and stimulation operations in the petroleum industry. When pumping fluids through coiled tubing, part of the coiled tubing string is in the wellbore and, therefore, can be treated as straight tubing (ST), the other part of the coiled tubing that remained spooled on the coiled tubing reel is in coiled geometry. The hydraulics design of coiled tubing pumping operations should, therefore, include prediction of friction pressure losses in both straight and coiled tubing sections. The maximum obtainable flow rate in coiled tubing is often limited due to the relatively small tubing diameter and the extra flow resistance caused by the secondary flow in the curved flow geometry. Since the pioneering study of Dean [1,2], the flow of Newtonian fluids in coiled pipes has been studied extensively; in contrast, the flow of non-Newtonian fluids in coiled pipes has remained relatively unstudied [3]. There is a need to understand the flow behavior of the common drilling, completion, and stimulation fluids in coiled tubing and to develop correlations to predict the friction pressure losses in coiled tubing.

The rheological properties of drilling, completion, and stimulation fluids are important in determining their solids-carrying capacity and estimating their frictional losses in tubulars. The solids-carrying capability of these fluids is mainly affected by the viscosity at low shear rates. The drilling cuttings are carried out from the bottom to the surface through the wellbore annulus. In hydraulic fracturing, the sand used as proppant has to be transported by the fracturing fluids into the hydraulically-induced fractures to keep the fractures open after the pumping pressure is released. Similarly, the gravel-packing completion fluids have to be viscous enough to transport gravels to the desired locations. But, when the fluids are pumped through the tubing string where the shear rates are generally high, low viscosity and/or drag-reducing properties would be desired.

The effect of temperature on rheological properties has to be considered for the drilling, completion, and stimulation fluids. As the fluids are pumped downhole, their temperature would increase due to geothermal gradient of the formation and the effect of viscous heating. It is therefore important to understand the effect of temperature on the viscosity and the solids-suspending ability.

In this study, the rheology and the tubing flow behavior of several fluids commonly used as drilling, completion, and stimulation fluids are investigated experimentally. These fluids include polymeric fluids—Xanthan gum, partially hydrolyzed polyacrylamide (PHPA), guar gum, and hydroxyethyl cellulose (HEC), bentonite drilling mud, oil-based drilling mud, and guar-based fracturing slurries. A Bohlin CS 50 rheometer and a model 35 Fann viscometer were used to measure the viscous behavior at various shear rates and temperatures. Extensive tubing flow tests were conducted using a full-scale coiled tubing test facility to investigate the friction pressure losses of fluids in both straight and coiled tubings. The experimental results are presented and the friction characteristics of drag-reducing fluids in coiled tubing as compared with straight tubing are discussed.

Experimental

Rheological Characterization. The rheological properties of the fluid samples taken during the tubing flow tests were measured using a model 35 Fann viscometer and a Bohlin CS 50 rheometer. The former was used for viscosity measurements at ambient temperature, whereas the latter was used for elevated-temperature measurements.

Contributed by the Fluids Engineering Division for publication in the JOURNAL OF FLUIDS ENGINEERING. Manuscript received by the Fluids Engineering Division January 7, 2003; revised manuscript received June 30, 2003. Associate Editor: D. Siginer.

Table 1 Dimensions of Coiled Tubing Reels

Reel No.	CT OD (in.)	CT ID (in.)	Length (ft)	Reel Diameter (in.)	Curvature Ratio (a/R)
1	1	0.810	500	48	0.0169
2	1	0.810	1000	72	0.0113
3	1-1/2	1.188	1000	72	0.0165
4	1-1/2	1.188	2000	72	0.0165
5	1-1/2	1.188	2000	72	0.0165
6	2-3/8	2.063	1000	111	0.0185
7	2-3/8	2.063	2000	111	0.0185

The Model 35 Fann viscometer is a rotational viscometer with a rotating cylinder and a stationary bob. Fluid is contained in the annular space between the co-axial cylinders. The outer cylinder (rotor) is driven at a predetermined rotational speed and the torque arising from the fluid's viscous drag is exerted on the inner cylinder or the bob. The torque is balanced by a helically wound spring and the dial reading which indicates the spring deflection is used to calculate the torque. Fann viscometer is widely used in the petroleum industry for testing drilling, completion, and stimulation fluids. Use of Fann viscometer has been included in the recommended practices on the rheology and hydraulics of drilling and stimulation fluids by the American Petroleum Institute (API) [4,5].

The Bohlin CS 50 is also a rotational rheometer. But unlike the Fann 35, the Bohlin rheometer is a controlled stress instrument in which a shear stress is applied and the resultant shear rate is measured. It is equipped with three test cells—parallel plates, cone and plate, and concentric cylinders. To measure rheology at high temperature, a closed cell called HPC (High Pressure Cell) is used. The temperature is controlled by a circulating heating oil bath and the cooling system. The HPC is also a concentric geometry in which the torque from the motor is magnetically transferred from an outer coupling to the inner rotor (bob) inside the HPC. The operation and data acquisition is controlled by a computer. In addition to steady shear viscosity measurement, it is capable of performing viscoelastic measurement. In this study, fluid samples were tested at several temperatures from 75 to 250°F.

Flow Tests With Coiled and Straight Tubings

Experimental Setup. The coiled tubing test facility consists of several reels of coiled tubing. Table 1 shows the dimensions of these coiled tubing reels. The coiled tubing strings of the three diameters −1, 1-1/2, and 2-3/8 in., were spooled onto seven reel drums of diameters of 48, 72, and 111 in. which results in curvature ratio (a/R, where a and R are the radii of the tubing and the reel drum) values of 0.0113, 0.0165, 0.0169, and 0.0185. For comparison purposes, two 30-foot straight tubing sections were installed upstream and downstream of the reels of each tubing size. Two 30-foot annular sections, one concentric and the other eccentric, with 2-3/8 in. pipe inside 3-1/2 in., provided annular flow measurements. In addition, two 200-foot straight tubing sections of 1-1/2 and 2-3/8 in. were installed and could be easily hooked up with the coiled tubing flow loop. Two 50 bbl tanks were used for fluid mixing and storage. The pumping equipment is a triplex plunger pump which was boosted by a Galigher centrifugal pump. Honeywell differential pressure transducers were used to measure the differential pressures across the coiled tubing strings, straight as well as annular sections. A MicroMotion® flow meter was used to measure flow rate, temperature, and density of fluid. The measured data were transmitted to a remote personal computer using a Fluke Hydra system for data acquisition.

Experimental Procedure. The experimental procedure began with fluid preparation. To simulate the field conditions as closely as possible, the fluid mixing and preparation procedures recommended by the service companies (or fluid providers) were closely followed. Sometimes technical representatives from the service companies came to the test facility to witness the fluid preparation process. Care was taken to avoid lumps or ''fish eyes'' during the mixing. Various chemicals were added to control the pH and bacteria, to reduce air bubbles, or to ensure proper hydration. Some fluids such as Xanthan gum and bentonite mud may take longer (up to 24 hours) to hydrate. In those cases, fluids were prepared the day before the test for adequate hydration.

After the fluid was prepared, water was pumped through the flow loop to check the system and collect the water flow data. The test fluid (gel) was then pumped through the loop, and when the loop was completely filled with gel, it was switched to recirculation mode. In order to reduce any heating or gel degradation due to extensive shearing, the test sequence preferred was first through 2-3/8 in. tubing system, followed by test through 1-1/2 in., and finally, through the 1 in. tubing. Differential pressures across coiled tubing and straight sections were measured at various pump rates. At each pump rate, 2–3 min of steady flow was allowed to collect quality data. In the beginning and at the end of each test through each tubing size, fluid samples were taken from a sampling port in the flow loop and sent to the Bohlin rheometer and the Fann viscometer for rheological measurements.

Fluids Tested. Table 2 shows the test matrix and fluids tested. Among these fluids, Xanthan gum, guar gum, PHPA, and HEC are polymeric solutions. The solutions tested in this study were linear gels, though they are sometimes crosslinked to increase viscosity in certain field applications. They are the most commonly used water soluble polymers for well drilling, completion, and stimulation [6–8].

Xanthan gum is a biopolymer and is produced by the bacterial fermentation of microorganism Xanthamonas Campestris [9,10]. Xanthan gum solutions display exceptional shear thinning properties. Its major application in drilling fluids is as a suspending

Table 2 Test Matrix

Fluids	CT and 30 ft ST			200 ft Long Straight Sections (ST)	
	1 in.	1-1/2 in.	2-3/8 in.	1-1/2 in.	2-3/8 in.
Water	×	×	×	×	×
10, 20, 40 $\mathrm{lb_m}$/Mgal Xanthan Gum	×	×	×		
30, 40 $\mathrm{lb_m}$/Mgal Xanthan Gum				×	×
20 $\mathrm{lb_m}$/Mgal Xanthan+1 $\mathrm{lb_m}$/bbl Starch	×	×	×		
20 $\mathrm{lb_m}$/Mgal Xanthan+3% vol. Rev Dust	×	×	×		
20, 30, 40 $\mathrm{lb_m}$/Mgal Guar Gum	×	×	×	×	×
20, 40 $\mathrm{lb_m}$/Mgal PHPA	×	×	×	×	×
20, 30, 40 $\mathrm{lb_m}$/Mgal HEC	×	×	×		
8 $\mathrm{lb_m}$/bbl Bentonite+1 $\mathrm{lb_m}$/bbl MMH	×	×	×		
Oil-based Drilling Mud			×		
25, 35 $\mathrm{lb_m}$/Mgal Guar			×		×
25 and 35 $\mathrm{lb_m}$/Mgal Guar+Brady Sand			×		×

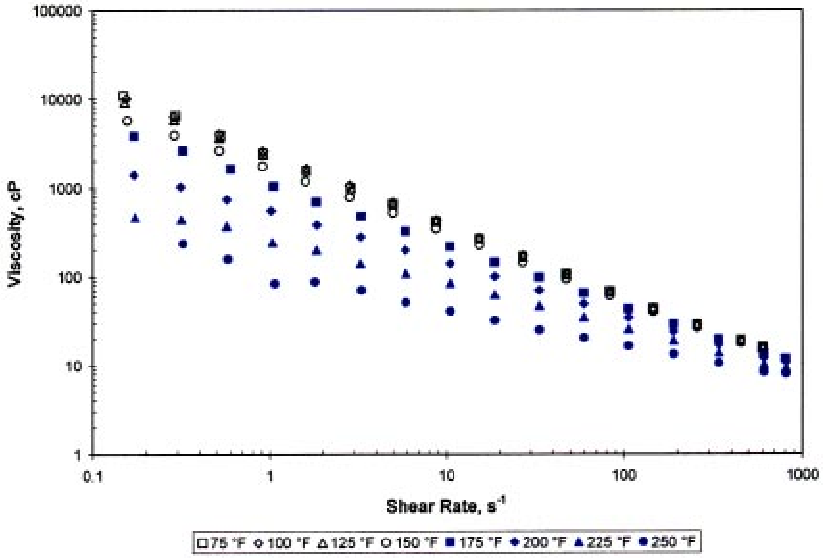

Fig. 1 Viscosity Behavior of 40 lb$_m$/Mgal Xanthan

agent due to its high viscosity at low shear rate. It also has desirable properties for completion and stimulation fluids.

Guar gum is a natural polymer and is derived from the seeds of the guar plant. Guar has been used in low solids muds and is widely used in hydraulic fracturing.

Hydroxyethyl cellulose (HEC) is also a natural polymer. It is made by chemically reacting cellulose with ethylene oxide. HEC can be used in drilling mud, but more commonly is used in completion and workover fluids. Various grades of the polymer are available. The HEC used in this study was a frac grade HEC.

Partially hydrolyzed polyacrylamide (PHPA) is a synthetic water-soluble polymer. The primary benefits of synthetic polymers over natural polymers are increased temperature stability and contamination resistance. PHPA muds have proven effective for inhibiting troublesome shale formations [11].

Bentonite is a clay to increase the viscosity of water in drilling mud. This increase in viscosity enhances the ability of the drilling fluid to carry the rock cuttings to the surface. The clay particles also form a mud cake to reduce the filtration into the formation. MMH (mixed metal hydroxide) is used to increase the formation stability and starch in drilling mud is solely to reduce filtration.

In order to study the effects of solids content on the rheology and hydraulics of drilling mud, we tested and compared 20 lb$_m$/Mgal clean Xanthan gum with 20 lb$_m$/Mgal Xanthan gum with 3% vol. Rev Dust®. Rev Dust® is a calcium montmorillonite clay used as a standard solids to simulate the drilling solids.

Since coiled tubing fracturing has been successfully used in the oil and gas industry, we investigated the flow behavior of fracturing slurries in coiled tubing by using 25 and 35 lb$_m$/Mgal guar with Brady sand at various sand concentrations.

Finally, an oil-based drilling mud was tested with 2-3/8 in. coiled and straight tubing. The oil mud is essentially a water-in-oil emulsion of about 85% oil and 15% water plus other additives. It was prepared at Baroid Drilling Fluids and shipped to the test facility for testing.

Results and Discussion

Viscosity Behavior. As examples, Figs. 1 and 2 show the viscosity behavior of 40 lb$_m$/Mgal Xanthan and PHPA measured at various temperatures using the Bohlin rheometer.

Shear Effect. In the range of shear rate investigated, all the fluids exhibit various degrees of shear-thinning effect at different temperatures. Among the four types of polymer fluids, Xanthan and PHPA are more pseudoplastic than guar and HEC. The latter two, both being natural polymers, show some similar shear-thinning behavior. Since primary interest of this study was flow behavior at shear rates representative of flow in coiled tubing which are usually high, the rheology at low shear rates (below 0.1 s^{-1}) was not investigated. The upper shear rate was limited by the rheometer and viscometer. In the shear rate range investigated, upper Newtonian and lower Newtonian regions were not observed for the polymer solutions. Only the bentonite mud seemed to show a plateau at the last 2 or 3 shear rates (about 300−800 s^{-1}). Therefore, for all these fluids, the viscosity behavior can be approximately described by power law model over certain shear rate ranges depending on the type of fluid, the temperature, and polymer concentration. It was found that as polymer concentration decreases, the fluids became less viscous and less shear-thinning.

Thermal Effect. Temperature has very different effects on the viscosity of fluids. PHPA appears to be the most thermally stable over the whole shear rate range. Xanthan gum viscosities at low shear rate range are affected by the temperature more than at high shear rate. Guar and HEC are somewhat similar—increased effect of temperature in the range of higher shear rate. The unique feature of Xanthan gum is that at different temperatures, the shear-thinning behavior can be described reasonably well by the power law model over the shear rate range investigated.

The effect of temperature on the viscosity of bentonite mud is different from that of polymer solutions. Instead of thermal thinning, the bentonite mud has increasing viscosity as the temperature increases. The behavior is more obvious in the range of low shear rate. This is because bentonite mud is a clay suspension and there are four particle association mechanisms that can control the viscosity of clay suspension: aggregation, dispersion, flocculation, and deflocculation. For the present case, increasing temperature may have enhanced dispersion or flocculation or both mechanisms so that the effective viscosity of the clay mud was increased. The practical implication is that high pump pressures would be needed to start circulation if the mud were left at the bottom of the hole and heated for sometime. Figure 3 compares the viscosity behavior of the four polymer fluids at polymer concentration of 40 lb$_m$/Mgal and at 75°F. The viscosity of bentonite mud was also plotted for comparison. Of course, the application of these fluids

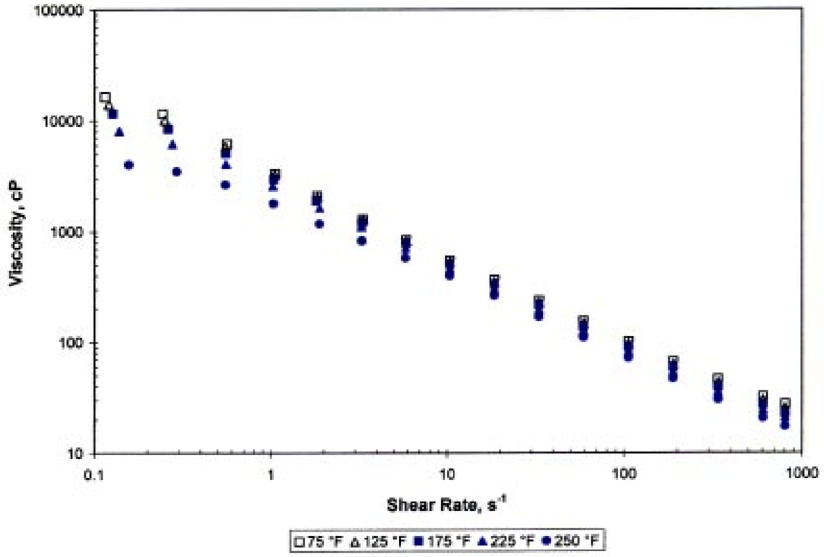

Fig. 2 Viscosity Behavior of 40 lb_m/Mgal PHPA

would not only depend on viscosity behavior but also on their cost and other considerations such as formation damage, fluid loss control, etc.

Hydraulic Behavior in Coiled and Straight Tubings

Water Test. For any coiled tubing size, water test was always conducted first to establish the baseline for comparison with other test fluids. Water tests were also required for system calibration check. Figure 4 shows the result of water test in 2-3/8 in. coiled tubing reel. Friction factor correlations of Ito [12] and Srinivasan et al. [13] for turbulent flow of Newtonian fluid in curved pipes were compared with the water data.

It was found that Ito [12] and Srinivasan et al. [13] correlations gave close results and both underestimated the water data. Note that both correlations were developed from experimental data using smooth curved pipes. If the friction factor estimated by Srinivasan et al. [13] correlation is adjusted by a factor equal to the ratio of the friction factor in straight rough pipe (such as Chen [14] correlation) to that in straight smooth pipe, then, as shown in Fig. 4, much closer agreement is obtained.

Friction Factor vs. Generalized Reynolds Number in Coiled Tubing. Figure 5 shows the plot of friction factor vs. generalized Reynolds number of 25 lb_m/Mgal guar gum in 2-3/8 in. straight and coiled tubings. This plot is typical of the polymeric fluids in coiled tubing. It is observed that the friction factor in coiled tubing is higher than in straight tubing. This is believed to be due to the secondary flow caused by the curvature of the coiled tubing. For flow in straight tubing, the friction factor is above but close to the Virk's asymptote for maximum drag reduction [15].

The friction factor in coiled tubing is significantly higher than the Virk's asymptote and did not approach it. The correlation by Srinivasan et al. [13] for Newtonian fluid is also plotted in Fig. 5. It can be seen that the friction factor for coiled tubing is significantly lower than the Srinivasan et al. [13] correlation, indicating

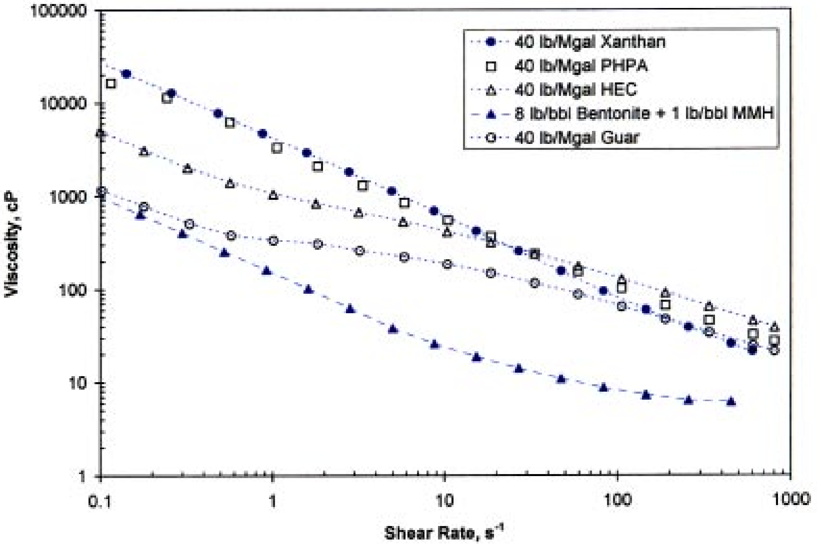

Fig. 3 Comparison of Viscosity Behavior of Fluids Tested at 75°F

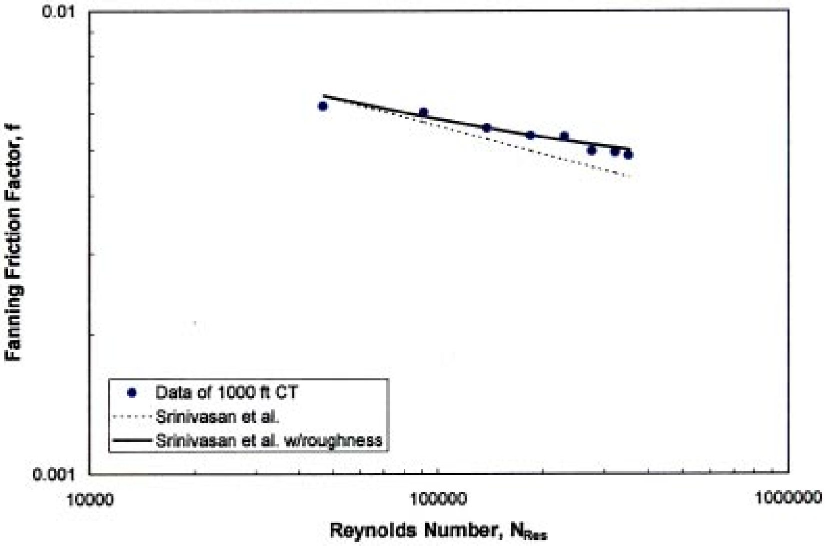

Fig. 4 Friction Factor of Water in 2-3/8 in. Coiled Tubing

that there is also drag reduction in coiled tubing. Therefore, we will try to understand the friction behavior of polymer fluids by observing their drag reduction performance.

Drag Reduction in Coiled and Straight Tubing. Figures 6 and 7 show the drag reduction behavior of guar gum in coiled tubing (CT) by plotting the friction factor data on the Prandtl-Karman coordinates. The Reynolds number used in the plots are based on the solvent (i.e., water) viscosity. The zero drag reduction line or baseline for coiled tubing is from the Srinivasan et al. correlation [13] instead of the Prandtl-Karman correlation for straight tubing as given below:

$$1/\sqrt{f} = 4.0 \log_{10} N_{\mathrm{Re}\,s} f^{1/2} - 0.4 \tag{1}$$

Note that the ordinate is the reciprocal of the square root of friction factor, i.e., $f^{(-1/2)}$. Therefore, data points above the zero drag reduction line represent positive drag reduction while the data points below the baseline represent drag increase or negative drag reduction. The intersection of the baseline with the data line represent the onset of drag reduction. The Poiseuille's law for laminar flow and the Virk's maximum drag reduction asymptote [15] are also plotted. Actually, the corresponding lines for coiled tubing should have been used. But unfortunately, such equations are not yet available and will be pursued in future study.

Figure 6 indicates that for 2-3/8 in. coiled tubing, the guar fluid exhibits negative drag reduction (more friction than water) at low flow rates. Beyond the onset of drag reduction, the data lines seem to change slopes slightly.

The polymer concentration affects the vertical position of the data lines. Higher polymer concentrations lowered the data lines. Figures 6 and 7 indicate that as the tubing diameter decreases, more data points fall above the baseline. For 1 in. tubing, all data points show drag reduction. These data points fall more or less on straight lines.

Figure 8 shows the behavior of guar fluids in 2-3/8 in. straight tubing (ST). The data were obtained from the 200-foot tubing sections. It is found that the slopes of the data lines for straight tubings are greater than those in coiled tubing. This should be understandable since for a given Reynolds number, the friction

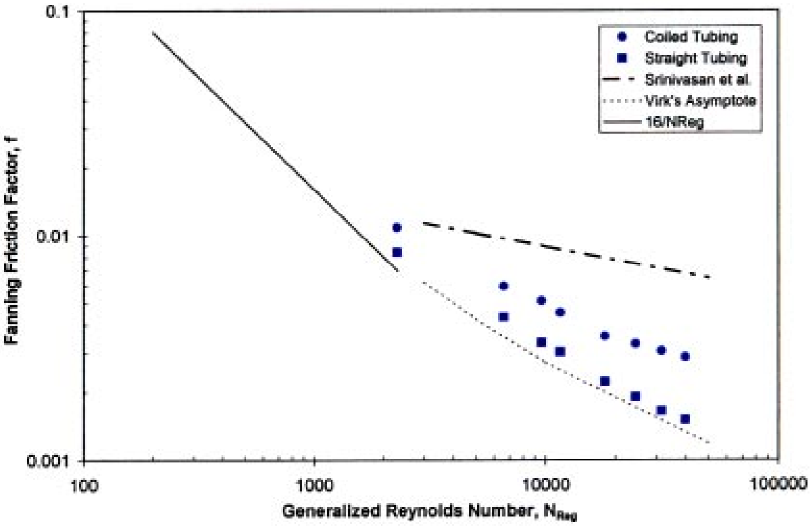

Fig. 5 Friction Behavior of 25 $\mathrm{lb_m}$/Mgal Guar Gum in 2-3/8 in. Straight and Coiled Tubings

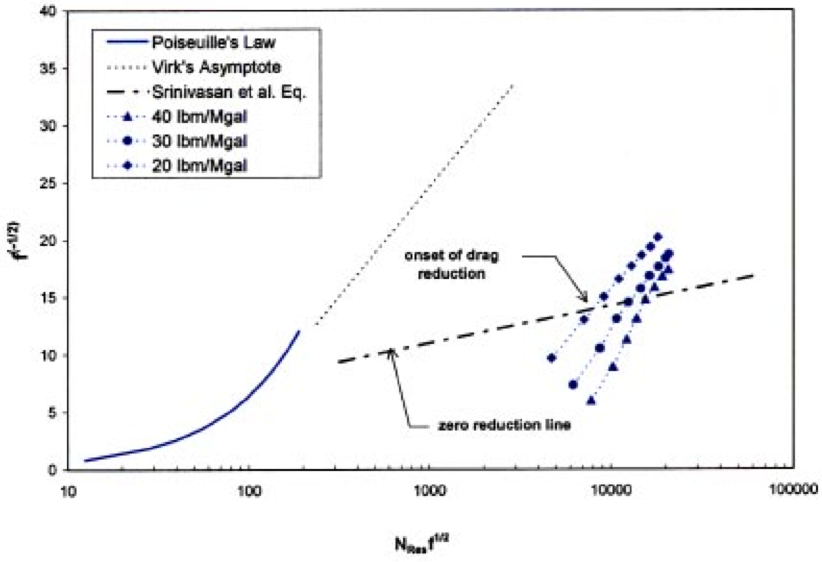

Fig. 6 Drag Reduction Behavior of Guar Gum in 2-3/8 in. Coiled Tubing

factor in straight tubing is less than in coiled tubing, and therefore, the abscissa ($N_{\mathrm{Re}\,s}f^{1/2}$) will be smaller and the ordinate [$f^{(-1/2)}$] will be larger.

Figure 8 indicates that for 20 $\mathrm{lb_m}$/Mgal guar gum, the data points are in line with the zero reduction line before the onset of drag reduction. At higher polymer concentration (30 and 40 $\mathrm{lb_m}$/Magl), there are a number of points below the baseline. Beyond the onset of the drag reduction, the slopes of the data lines seem to increase with the polymer concentration.

To further examine the drag reduction behavior in coiled tubing and straight tubing, we plotted the drag reduction versus generalized Reynolds number, as in Fig. 9 for 1-1/2 in. tubing. Here, the drag reduction, DR, is defined in a customary fashion, i.e.,

$$DR=(1-f_p/f_s)\times 100 \tag{2}$$

where f_p is the friction factor for polymer solution, f_s refers to the friction factor of the solvent, and both are evaluated at the same pump rate. These plots provide another way of understanding the effects of tubing diameter, polymer concentration, Reynolds number, and the tubing curvature (straight vs. coiled) on the drag reduction behavior of the polymer solution in straight tubing and coiled tubing.

The drag reduction behavior in all three tubing sizes was examined and it appears that the smaller tubing results in greater drag reduction for both straight and coiled tubings. For each tubing size, the polymer concentration has more significant effect on the drag reduction in straight tubing than in the coiled tubing. For straight tubing, as the concentration increases, the drag reduction also increases for the polymer concentration and flow conditions tested. For coiled tubing, the effect of polymer concentration is not as significant.

The drag reduction in straight tubing is much higher than in coiled tubing for the three polymer concentrations. At low Reynolds numbers, drag reduction in coiled tubing is much smaller than in straight tubing. As Reynolds number increases, the differ-

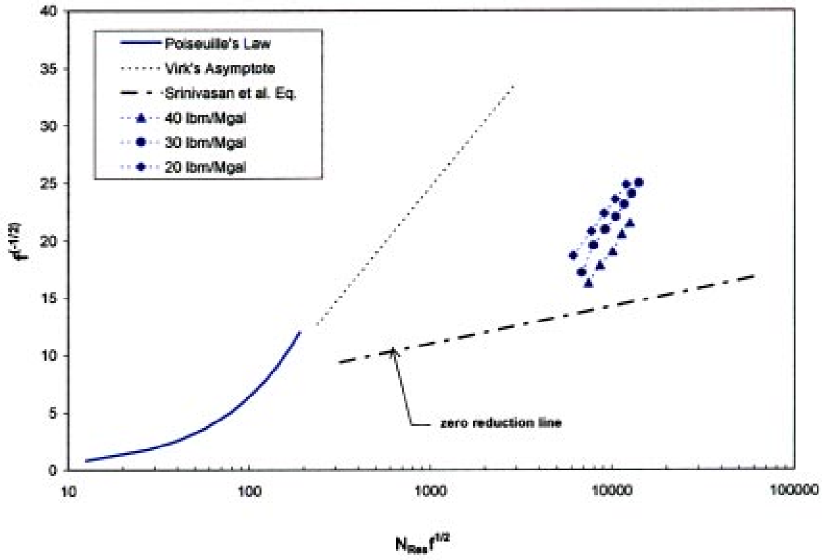

Fig. 7 Drag Reduction Behavior of Guar Gum in 1 in. Coiled Tubing

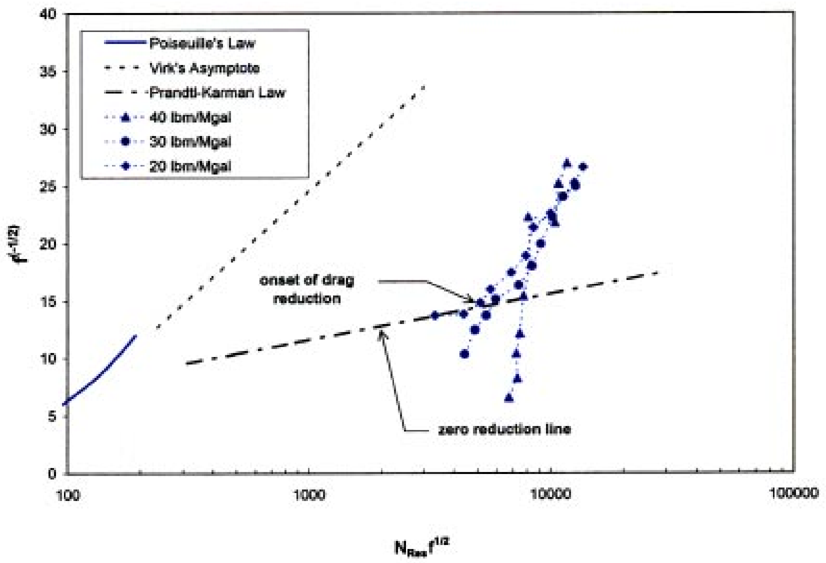

Fig. 8 Drag Reduction Behavior of Guar Gum in 2-3/8 in. Straight Tubing

ence in drag reduction between straight and coiled tubings becomes smaller. But, even at the highest Reynolds number investigated, the difference in *DR* is still about 15%.

Onset of Drag Reduction and Flow Regime Transition. In Figs. 6–8, the intersections of the data lines or their extrapolations with the Newtonian line (i.e., the zero-drag reduction line defined by the Srinivasan et al. [13] correlation) can be taken as the representative onsets of drag reduction, since beyond the "onset" conditions, the friction pressure of polymer solutions becomes lower than that of the Newtonian solvent (water in this case). The generalized Reynolds number corresponding to the zero drag reduction can also be read from plots such as the one shown in Fig. 9. For example, the generalized Reynolds numbers thus obtained for guar fluids are approximately 7500 for 2-3/8 in. coiled tubing (curvature ratio=0.0185) and 5500 for 1-1/2 in. coiled tubing (curvature ratio=0.0169), respectively. These values can be compared with the critical Reynolds number for laminar/turbulent transition for Newtonian fluid in coiled tubing. According to Ito [12]'s correlation, $N_{Rec}=20000(a/R)^{0.32}$, the corresponding critical Reynolds numbers are 5579 and 5419 for curvature ratios of 0.0185 and 0.0169 respectively. Therefore, even for Newtonian fluid, the critical Reynolds number in coiled tubing is higher than in straight tubing. This is because the turbulence is suppressed and delayed in curved pipes [16,17]. The larger the curvature ratio, the greater the Reynolds number required to maintain turbulence. Since it is widely accepted that the drag reduction of polymer solutions in pipe is associated with turbulent flow, it, therefore, may be assumed that the onset of drag reduction can be an approximate (or close) indicator of onset of turbulence. In this sense, the observed behavior of polymer solutions may imply a delayed laminar/turbulent transition for polymer solutions in coiled tubing flow.

It should be pointed out that drag reduction in coiled tubing is not well understood. Drag reduction in coiled tubing may not necessarily occur only in turbulent flow. One study [18] claimed that drag reduction could occur in laminar flow since the drag

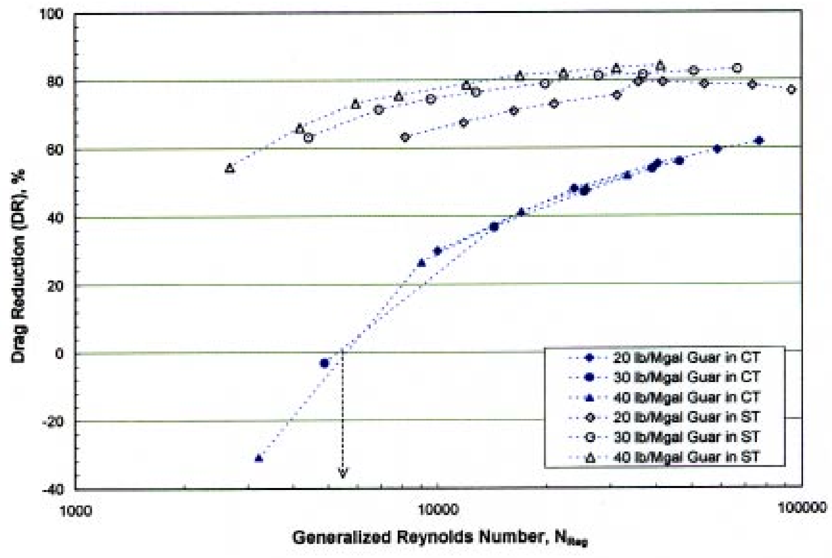

Fig. 9 Comparison of Drag Reduction between 1-1/2 in. Coiled and Straight Tubings

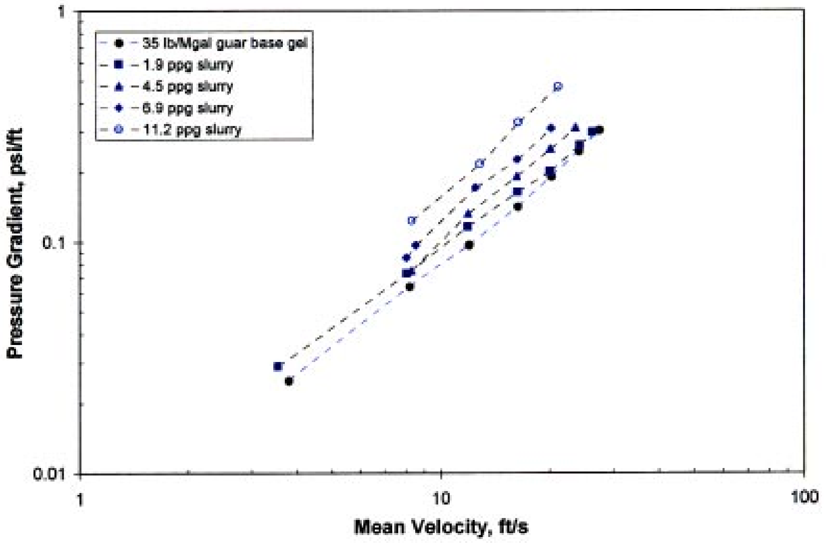

Fig. 10 Effect of Solids on Friction Losses of 35 lb_m/Mgal Guar Gum in 2-3/8 in. Coiled Tubing [19]

reducing fluids reduced the secondary flow. It should also be pointed out that the transition from laminar to turbulent in coiled tubing is very gradual, especially for concentrated polymer solutions.

Effect of Solids on Friction Factor in Coiled Tubing. Recently, coiled tubing fracturing has been successfully used in the oil and gas industry. Therefore, experiments were conducted to investigate the friction behavior of hydraulic fracturing slurries in coiled tubing. Figure 10 shows the friction pressure gradients of 35 lb_m/Mgal guar slurries in coiled tubing. The sand concentration varied from 1.9 ppg to 11.2 ppg. Figure 10 shows that the friction of slurries is increased significantly with increasing sand concentration. An empirical correlation [19] was developed to predict the friction pressure of slurries as a function of sand concentration from the friction pressure of sand-free fracturing fluid. Considering that well drilling muds often contain solids from entrained cuttings in the muds, experiments were also performed on the effect of drilling solids. As indicated in the test matrix, 3% Rev Dust was used to simulate the drilling cuttings. The experiments showed that the solids content has significant effect on the friction pressure in coiled tubing.

Summary and Conclusions

1. The drilling, completion, and stimulation fluids tested in this study exhibit shear-thinning and drag-reducing non-Newtonian behavior. The high viscosity at low shear rates is beneficial for carrying cuttings through the annulus during drilling, suspending solids when circulation is stopped, and transporting proppants in the hydraulically induced fractures in the well stimulation. The low viscosity at high shear rates, on the other hand, helps to reduce the friction pressure losses when the fluids are pumped through the tubing or drill pipe.
2. The effect of temperature on the viscosity behavior has been studied using a Bohlin rheometer. It was found that the thermal stability of fluids varies from polymer to polymer and depends also on the polymer concentration and shear rate range. PHPA appeared to be the most stable. The thermal effect of Xanthan is more significant at low shear rates than at high shear rates, while HEC and guar gum showed temperature effect over a wide range of shear rate. The bentonite mud, being a clay suspension, became more viscous when the temperature was increased.
3. The friction pressure losses of both water (Newtonian fluid) and the drilling, completion, and stimulation fluids (non-Newtonian fluids) in coiled tubing are significantly higher than in straight tubing. This is because of the secondary flow caused by the centrifugal forces in curved pipes.
4. The polymeric fluids investigated are typically drag-reducing fluids. Their drag reduction behavior in both straight and coiled tubings has been examined by plotting the friction data on the Prandtl-Karman coordinates. On these plots, the slopes of the data lines for coiled tubing are smaller than those for straight tubing. The drag reduction also depends on the type of polymer, the tubing diameter, and the polymer concentration.
5. Experimental results showed that the drag reduction (DR) in coiled tubing is lower than in straight tubing. This difference is more pronounced at low values of generalized Reynolds number. On the plots of drag reduction vs. generalized Reynolds number, the drag reduction in straight tubing increased with polymer concentration for the same value of generalized Reynolds number, whereas the DR in coiled tubing is less sensitive to the polymer concentration in the range of flow conditions investigated.

Acknowledgments

The authors wish to thank the members of the Coiled Tubing Consortium (CTC) for their continued support for the CTC project and the research team at the Well Construction Technology Center of the University of Oklahoma for their assistance during this research.

Nomenclature

a = radius of tubing
CT = coiled tubing
DR = drag reduction, Eq. (2)
f = Fanning friction factor
f_p = Fanning friction factor of polymer solution
f_s = Fanning friction factor of solvent
HEC = hydroxyethyl cellulose
lb_m = pound mass
Mgal = thousand gallons
MMH = mixed metal hydroxide
$\text{N}_{\text{Re c}}$ = critical Reynolds number
$N_{\text{Re}\,g}$ = generalized Reynolds number
$N_{\text{Re}\,s}$ = Reynolds number based on solvent viscosity
PHPA = partially hydrolyzed polyacrylamide
ppg = pound per gallon
R = radius of curvature of the coiled tubing reel

s^{-1} = reciprocal second
ST = straight tubing

SI Metric Conversion Factors

bbl×1.589 E-01 = m^3
cP×1.000* E-03 = Pa·s
ft×3.048* E-01 = m
°F (°F-32)/1.8 = °C
gal×3.785412 E-03 = m^3
in.×2.54* E-02 = m
lb_m×4.5359924 E-01 = kg
Mgal×3.785412 E+00 = m^3
psi×6.894 E+00 = kPa
ppg×1.198282 E+02 = kg/m^3

---

*Conversion factor is exact.

References

[1] Dean, W. R., 1927, ''Note on the Motion of Fluid in a Curved Pipe,'' Philos. Mag., **20**, pp. 208–223.
[2] Dean, W. R., 1928, ''The Streamline Motion of Fluid in a Curved Pipe,'' Philos. Mag., **30**, pp. 673–693.
[3] Zhou, Y., and Shah, S. N., 2002, ''Fluid Flow in Coiled Tubing: A Critical Review and Experimental Investigation,'' paper 2002-225, *the Canadian International Petroleum Conference*, June 11–13, Calgary, Canada.
[4] API, 1998, *RP 39, Recommended Practice on Measuring the Viscous Properties of a Cross-linked Water-based Fracturing Fluid*, 3rd edition, API, Dallas.
[5] API, 1995, *RP 13D, Recommended Practice on the Rheology and Hydraulics of Oil-well Drilling Fluids*, 3rd edition, API, Dallas.
[6] Darley, H. C. H., and Gray, G. R., 1988, *Composition and Properties of Drilling and Completion Fluids*, Gulf Publishing Company, Houston, Texas.
[7] Bourgoyne, A. T., Jr., Millheim, K. K., Chenevert, M. E., and Young F. S., Jr., 1991, *Applied Drilling Engineering*, Society of Petroleum Engineers, Richardson, Texas.
[8] Allen, T. O., and Roberts, A. P., 1989, *Production Operations: Well Completions, Workover, and Stimulation*, 3rd ed., Oil & Gas Consultants International, Tulsa, Oklahoma.
[9] Lipton, D., and Burnett, D. B., 1976, ''Comparisons of Polymers Used in Workover and Completion Fluids,'' paper SPE 5872, *the 46th Annual California Regional Meeting of the SPE of AIME*, Long Beach, California.
[10] Rochfort, W. E., and Middleman, S., 1987, ''Rheology of Xanthan Gum: Salt, Temperature, and Strain Effects in Oscillatory and Steady Shear Experiments,'' J. Rheol., **31**, pp. 337–369.
[11] Kadaster, A. G., Gild, G. J., Hanni, G. L., and Schmidt, D. D., 1992, ''Field Applications of PHPA Muds,'' SPEDE, September, pp. 191–199.
[12] Ito, H., 1959, ''Friction Factors for Turbulent Flow in Curved Pipes,'' J. Basic Eng., **81**(2), pp. 123–134.
[13] Srinivasan, P. S., Nandapurkar, S. S., and Holland, F. A., 1970, ''Friction Factors for Coils,'' Trans. Inst. Chem. Eng., **48**, pp. T156–T161.
[14] Chen, N. H., 1979, ''An Explicit Equation for Friction Factor in Pipe,'' Ind. Eng. Chem. Fundam., **18**, pp. 296–297.
[15] Virk, P. S., 1975, ''Drag Reduction Fundamentals,'' AIChE J., **21**, pp. 625–656.
[16] Sreenivasan, K. R., and Strykowski, P. J., 1983, ''Stabilization Effects in Flow Through Helically Coiled Pipes,'' Exp. Fluids, **1**, pp. 31–36.
[17] Webster, D. R., and Humphrey, J. A. C., 1993, ''Experimental Observations of Flow Instability in a Helical Coil,'' ASME J. Fluids Eng., **115**, pp. 436–443.
[18] Tsang, H. Y., and James, D. F., 1980, ''Reduction of Secondary Motion in Curved Tubes,'' J. Rheol., **24**, pp. 589–601.
[19] Shah, S. N., Zhou, Y., and Goel, N., 2002, ''Flow Behavior of Fracturing Slurries in Coiled Tubing,'' paper SPE 74811, *the SPE/ICoTA Coiled Tubing Conference and Exhibition*, Houston, Texas.

M. S. Barrow
S. W. J. Brown
S. Cordy
P. R. Williams*
R. L. Williams

Center for Complex Fluids Processing,
School of Engineering,
University of Wales Swansea,
Singleton Park,
Swansea SA2 8PP UK

Rheology of Dilute Polymer Solutions and Engine Lubricants in High Deformation Rate Extensional Flows Produced by Bubble Collapse

We report a study of liquid jets formed by the collapse of bubbles under cavitation-generated pressure waves. Such jets involve an extensional flow which is characterized by high rates of extension, the latter being relevant to considerations of the flow of oils within dynamically loaded journal bearings. The technique reported here is found to be sensitive to the influence of extremely small concentrations of high molecular weight polymeric additive (xanthan gum). Commercial multigrade oils are also found to exhibit significantly larger resistance to extensional flow than their Newtonian counterparts and, insofar as the multigrade oils studied here are made viscoelastic by polymer additives, and possess significant levels of resistance to extension, the results provide evidence in support of a mitigating effect of viscoelasticity on cavitation, as mooted by Berker et al. [3]. [DOI: 10.1115/1.1667889]

1 Introduction

The addition to polymers to lubricants, to produce viscoelastic ‘multigrade’ oils, is reported to lead to reduced engine friction and bearing wear [1] but the relaxation times of such oils (*ca.* 10^{-6} seconds) are usually considered to be too low to permit any measurable influence of viscoelasticity on journal-bearing characteristics [2]. One possible explanation mooted by Binding et al. [2] is that viscoelasticity may have an “extravagant” effect on the cavitation properties of the oils. Similarly, Berker et al. [3] have mooted that the role of polymer additives in reducing journal bearing wear may be associated with some “mitigating effects” of viscoelasticity on cavitation.

The precise mechanism(s) associated with any such effects are unclear. It is important to note that, whereas gas-filled bubbles expand by diffusion from the liquid (or by pressure reduction, or temperature rise), in the case of predominantly vaporous bubbles a reduction of pressure may cause an “explosive” vaporization of the liquid into the bubble. Such bubbles may grow several times larger than their initial size prior to their eventual collapse, the latter being associated with the production of extreme intracavity temperatures and pressures. The behavior of such bubbles also provides the relatively violent activity required in processes such as industrial ultrasonic cleaning but which, in some circumstances, leads to instances of cavitation damage [4]. It should also be noted that cavitation can have a stabilising (i.e., beneficial) influence on journal dynamics whereas its absence can often lead to bearing failure [5–8]. It is necessary, therefore, to consider the role of polymer additives on specific cavitation *damage* mechanisms, the principal contributors to which are the high amplitude pressure waves and high speed liquid jets arising from the dynamics of cavitation bubbles [9,10].

Although numerous studies have failed to identify any ‘extravagant’ effects of polymeric additives on cavitation bubble dynamics [11,12], it is noteworthy that such effects *are* readily identified in experiments involving extensional flow. Whereas for Newtonian liquids the extensional viscosity, η_E, equals three times the shear viscosity, η, for dilute polymer solutions η_E can exceed η_E by as much as a factor of 10^4 [13,14].

Thus it is extensional flow and its possible role in cavitation damage phenomena which we consider in the present paper but our focus is different from previous studies in this area [11,15] insofar as we are concerned with the role of viscoelasticity in instances of liquid jet formation by bubble collapse under a pressure wave. Liquid jets formed under such circumstances are widely implicated in cavitation damage [16–18] and we have established that the evolution of such jets can involve a significant component of extension [19]. Herein we seek to establish whether the extensional viscosity characteristics of multigrade oils could have a significant (possibly extravagant) influence on a cavitation damage-related mechanism.

2 Experimental

The apparatus involves a vertical cylindrical polycarbonate tube (length 100 cm., internal diameter 2.1 cm.) containing liquid (see Fig. 1). Two Kistler 603B pressure transducers are flush-mounted in mechanically isolated mountings in the tube sidewall, their outputs being fed to a 1 MHz/12-bit Microlink 4,000 transient recorder. The 603B has a 200 bar dynamic range, a risetime of ~1 μs and a natural frequency in excess of 400 kHz. The tube is pulled downwards over a distance of a few centimeters against tensioned rubber supports and released. Following the tube’s sudden arrest by a buffer, the liquid continues its upward motion thereby generating a tension pulse (Fig. 2*a*) whose amplitude, F_i, is varied by varying the tube’s impact velocity. When F_i exceeds the liquid’s effective tensile strength, cavitation occurs near the base of the liquid column [20], and the subsequent collapse and rebound of cavitation bubbles results in the development of a pressure wave (Fig. 2*b*), the amplitudes (*ca.* 150 bar) and risetimes (*ca.* 3 μs) of which are consistent with those of cavitation-induced pressures [9]. The subsequent pulses (Fig. 2*c*–*e*) are associated with the re-expansion of the bubble(s) and the reflection of *b* from the free surface of the liquid column [20].

In the present experiments, a syringe at the base of the liquid

---

*Corresponding author.

Contributed by the Fluids Engineering Division for publication in the JOURNAL OF FLUIDS ENGINEERING. Manuscript received by the Fluids Engineering Division June 3, 2003; revised manuscript received October 30, 2003. Associate Editor: D. Siginer.

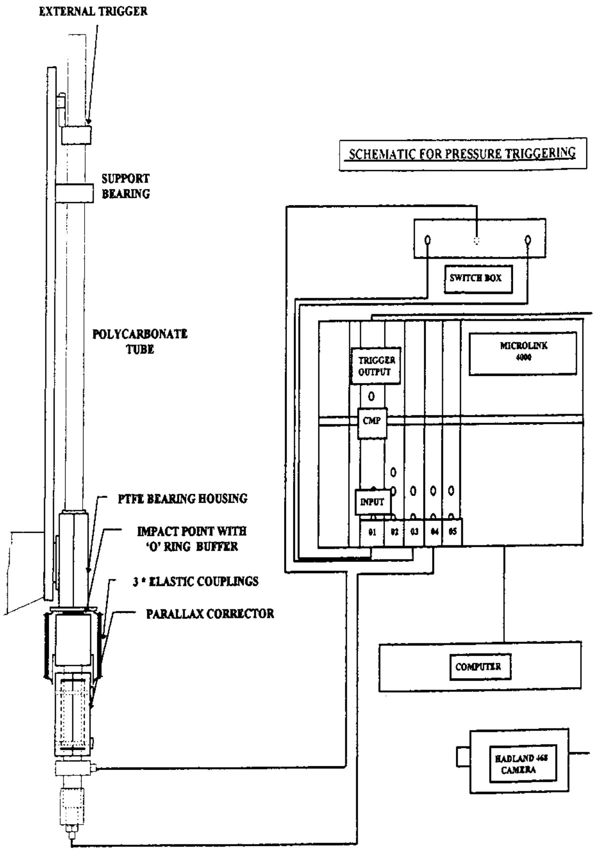

Fig. 1 Apparatus and ancillary recording equipment including high-speed camera and pressure recording system

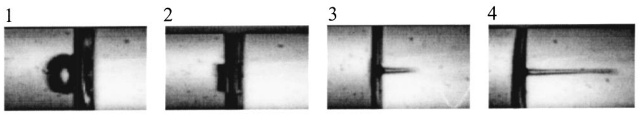

Fig. 3 Formation of liquid jet. Four (nonconsecutive) images from a sequence recorded at 2,000 f.p.s in which the tube's vertical axis appears horizontally. The liquid (a commercial 10W40 multigrade engine oil) is located to the left of the liquid-air interface which appears as the dark vertical band.

column was used to admit a metered quantity of air into the liquid, thereby forming a bubble whose size was chosen such that, having risen through the liquid, it rested immediately beneath the free surface of the liquid column, on the optical axis of a Kodak HS4540 high-speed video system capable of recording at up to 40,000 frames per second (f.p.s.). Illumination was provided by a pair of Xenon flash lamps. The output of one of the pressure transducers was fed to an electronic comparator which supplied a trigger voltage (width ~6 μs) at a specified level of pressure: this, in turn, triggered the data recorder, illumination and cameras.

We may summarize the idea exploited in the present work as follows. A pressure wave generated by cavitation at the base of the liquid column propagates upwards and drives the collapse of a gas bubble which is positioned immediately beneath the free surface. This collapse produces a liquid jet, the evolution of which is the focus of the present study.

3 Results

3.1 Formation and Development of the Jets. The process by which the liquid jet forms is illustrated in Fig. 3 in which four (non-consecutive) images from a sequence recorded at 2,000 f.p.s are shown. In this sequence, the tube's vertical axis appears horizontally as the camera axis has been rotated through 90 deg, and the liquid (a commercial 10W40 multigrade engine oil) is located

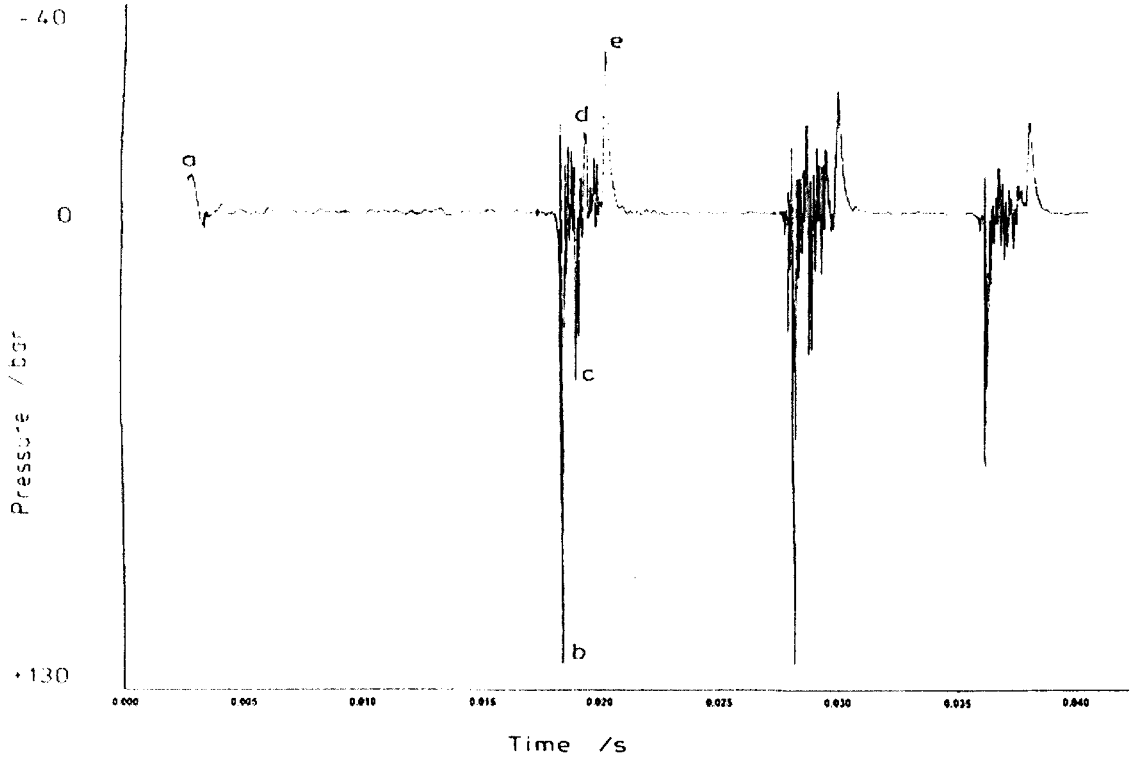

Fig. 2 (*a*) Cyclic pressure-tension record accompanying cavitation showing initial tension pulse and (*b*) high-amplitude pressure pulse to the left of the liquid-air interface which appears as the dark vertical band. The jet length, L, in the fourth frame is 2 cm. The first frame shows the gas bubble at its maximum diameter, 0.5 ms prior to the pressure wave's arrival. The second frame captures the final instant of collapse. In the third frame the velocity of the jet (with reference to its tip) is *ca.* 7 ms^{-1}. The correspondence of the pressure wave's arrival at the bubble and the ensuing collapse was verified by comparison of the video sequences and the pressure records [21].

In previous work measurements of the total jet volume as a function of time were used to confirm whether the jet volume remains constant [19], measurements of the jet's profile from the high speed video images being used to locate the boundaries of constant-volume sections in order to calculate local values of the extensional strain, ε, defined as

$$\varepsilon=\frac{L(t)-L(0)}{L(0)} \tag{1}$$

where $L(0)$ is the initial (reference) length of the jet. The extensional strain rate, $\dot{\varepsilon}$, experienced by the liquid is defined as

$$\dot{\varepsilon}=\frac{dL}{dt}\frac{1}{L(t)} \tag{2}$$

where dL/dt is the velocity of extension (with reference to the tip of the jet) and $L(t)$ is the instantaneous value of the length. Analysis of video sequences recorded in all experiments confirmed that, in each case, the liquid experiences a uniaxial extensional flow (or, more properly, a flow with a significant extensional *component*). It is emphasized that, as in the case of the pressure-driven contraction flow technique described by Binding et al. [2], the technique reported herein is intended to provide a convenient measure of resistance in a flow dominated by extension. Such a limitation is placed on *all* extensional rheometers for mobile liquids, such as those studied here [22,23].

3.2 Experiments on Dilute Aqueous Polymer Solutions. The polymer chosen for these experiments was a xanthan gum (Keltrol *F*), as used by Cheny and Walters [24] in their study of the role of fluid elasticity in the development of liquid jets. In their work, the addition of small amounts of polymer to a Newtonian solvent was found to lead to a substantial reduction in the length of the ascending vertical jet formed when a sphere is dropped into a reservoir of liquid. The reduction in jet length was tentatively ascribed to the role of extensional viscosity but Cheny and Walters [24] did not calculate the rates of deformation experienced by the fluid, or estimate the levels of extensional viscosity exhibited by the fluids. In the present work, small quantities of xanthan gum (up to 50 ppm by weight) were added to mixtures of glycerol and water, the shear viscosity of the liquids being measured using an ARES controlled-strain rheometer (Rheometric Sci., USA) fitted with a cone-and-plate geometry. All experiments reported herein were conducted within a temperature controlled environment at 23°C (±1°C).

Figure 4 shows the elongation rates (in reciprocal seconds, s^{-1}) obtained by analyzing the results of experiments on a Newtonian glycerol/water mixture and solutions of xanthan gum of the same shear viscosity as the Newtonian sample (in order that any changes in flow characteristics could be assigned to the viscoelasticity of the polymer solutions). Figure 5 shows the values of jet deceleration (expressed in g) obtained, these being average values which were calculated with respect to the velocity of the tip of the jets. The estimated uncertainty in the determination of the jet velocity was ±5%. The data in each figure represent the mean results of ten consecutive experiments, the height of the error bars indicating the standard deviation about the mean. It is important to note that the results presented in these figures were produced in experiments involving approximately the same initial gas bubble size, these bubbles being caused to collapse under incident pressure waves of approximately the same amplitudes (*ca.* 150 bar) and rise times.

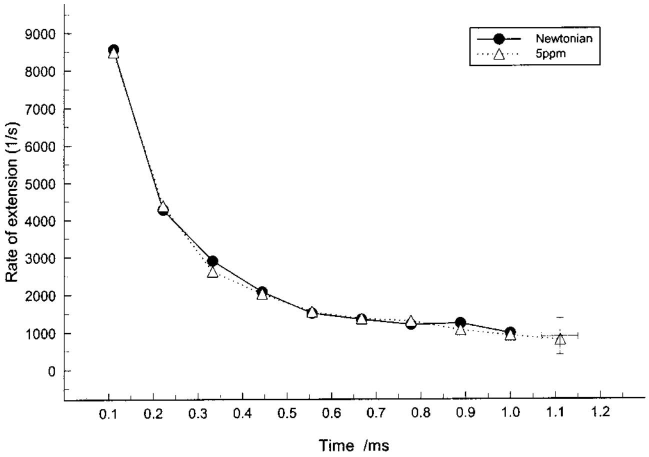

Fig. 4 Extension rate as a function of time for Newtonian glycerol/water mixture and 5wppm solution of xanthan gum

For the sake of clarity Figs. 4 and 5 show results for the Newtonian mixture and those obtained for the lowest concentration of polymer (5 wppm) only. The rates of extension $\dot{\varepsilon}$ experienced by the jets are large, being within the range *ca.* $1{,}000\ \mathrm{s}^{-1}<\dot{\varepsilon}<9{,}000\ \mathrm{s}^{-1}$ while it may be seen that the Newtonian jets experience a significantly lower deceleration throughout their evolution, the largest difference in deceleration corresponding to the highest rates of fluid extension.

3.3 Experiments Involving Multigrade Oils. The results of further experiments on commercial multigrade oils are now described. The experiments involved two different types of 15W40 and 10W40 multigrade oils, these being formulated for use in petrol- and diesel-powered engines. Samples of a 5W30 oil for use in petrol engines were also tested, along with Newtonian oil counterparts of each multigrade sample (i.e., oils without polymer additives but having the same shear viscosity as the multigrade oils).

Figures 6 and 7 show the elongation rates and jet deceleration respectively, for the 15W40 oils. Figures 8 and 9 show the corresponding data obtained in experiments on samples of the 5W30 oil and its Newtonian counterpart. Figures 10 and 11 show the corresponding data obtained in experiments on samples of the

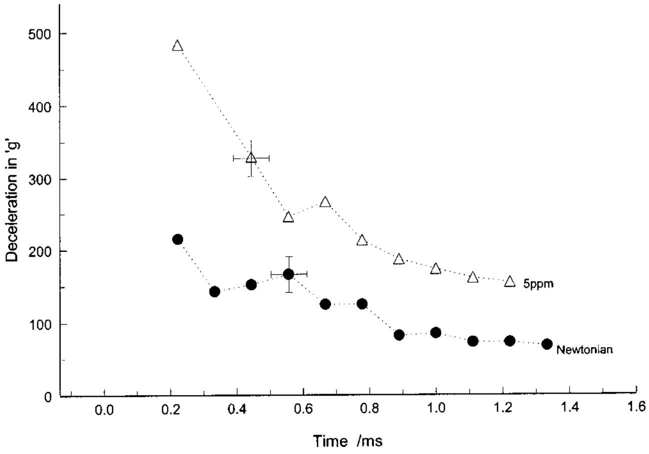

Fig. 5 Jet deceleration as a function of time for Newtonian glycerol/water mixture and 5wppm solution of xanthan gum

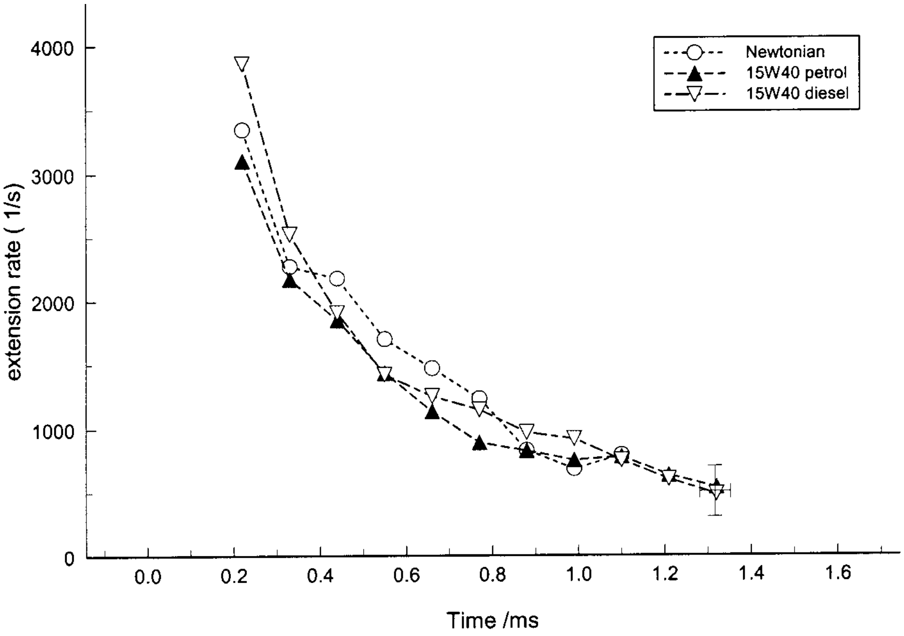

Fig. 6 Extension rate as a function of time for Newtonian and 15W40 multigrade oils

10W40 oils (for petrol and diesel engines) and their Newtonian fluid counterpart. The rates of extension experienced by the jets formed from 15W40 oils and their Newtonian counterpart lie within the range $500\ \mathrm{s}^{-1} < \dot{\varepsilon} < 4{,}000\ \mathrm{s}^{-1}$, the Newtonian jets experiencing a significantly lower deceleration throughout their evolution. The largest difference in deceleration corresponds to the highest rates of fluid extension, indicating a very substantial resistance to fluid extension. Similar results are evident in the results for the 5W30 oil and its Newtonian counterpart; and for both the 10W40 oils and their Newtonian counterpart.

Two features of the results obtained in the present experiments on multigrade oils are particularly relevant to journal bearing lubrication. Firstly, the technique produces high rates of extension, $\dot{\varepsilon}$, in a range relevant to discussions of the lubrication of engine bearings, some $500\ \mathrm{s}^{-1} < \dot{\varepsilon} < 5{,}000\ \mathrm{s}^{-1}$ [14]. Secondly, the results are pertinent to discussions of processes which subject a fluid to such high extension rates for a brief time: the typical transit time of an oil within contacts is *ca.* 1 millisecond [25], commensurate with the fluid's "residence time" of 1–2 milliseconds in the present experiments.

3.3 Estimates of Extensional Viscosity Levels. We next consider the forces associated with the extension of the jets in the present experiments. Given that uniaxial extension is equivalent to

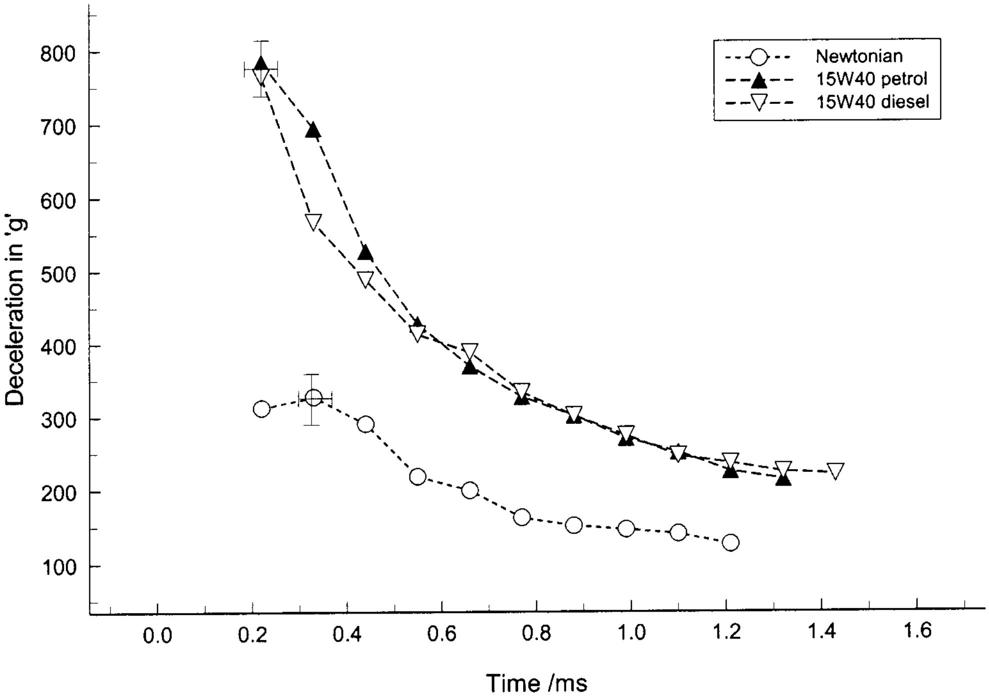

Fig. 7 Jet deceleration as a function of time for Newtonian and 15W40 multigrade oils

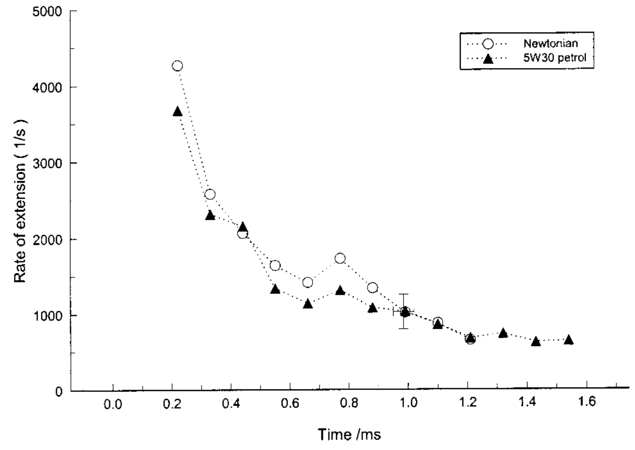

Fig. 8 Extension rate as a function of time for Newtonian and 5W30 multigrade oil

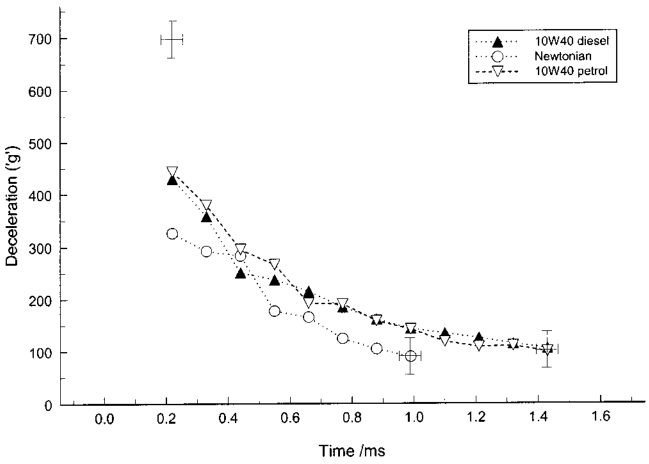

Fig. 11 Jet deceleration as a function of time for Newtonian oil and 10W40 multigrade oils

the longitudinal stretching of a homogeneous cylindrical liquid element subjected to a tensile force, F_T, then the tensile stress in the liquid, σ_E, is given by,

$$\sigma_E=\frac{F_T}{A}$$

where A is the cross-sectional area of the liquid cylinder. An appropriate measure of the liquid's (uniaxial) extensional viscosity, η_E, is then

$$\eta_E=\frac{\sigma_E}{\dot{\varepsilon}}$$

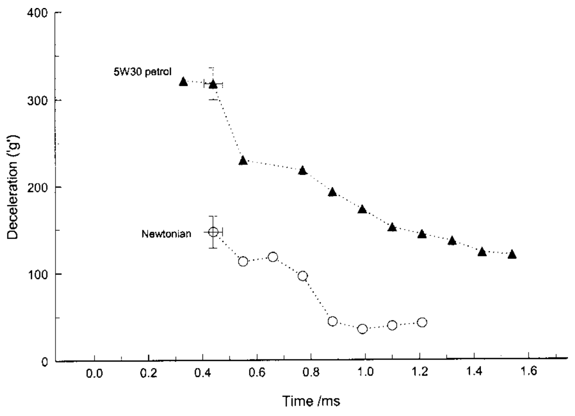

Fig. 9 Jet deceleration as a function of time for Newtonian and 5W30 multigrade oil

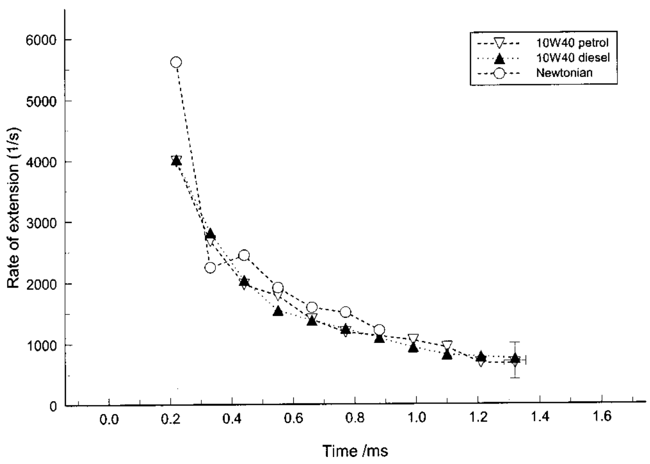

Fig. 10 Extension rate as a function of time for Newtonian oil and 10W40 multigrade oils

The average value of the tensile stress, σ_E, developed in the jet deceleration phase may be estimated using the analysis proposed by Brown and Williams [26]. This involves estimating the tensile force from a knowledge of the mass of liquid which replaces the annihilated volume of the gas bubble (based on its maximum diameter prior to collapse) and the subsequent deceleration of this mass of liquid (which forms the jet) during the jet's extension. (In view of the large values of deceleration involved in the evolution of the jets the role of gravity is discounted). From a knowledge of the jet's diameter, this force provides an estimate of the average tensile stress, σ_E, sustained by the liquid during its residence within the extensional flow, the latter being characterized by an average value of the rate of extension, $\dot{\varepsilon}$. The value of analysing extensional flow experiments on mobile fluids using such an averaged approach is well established [22]. In essence, as in previous related studies [2,23], we seek a measure of extensional viscosity *levels*. To do so, we first consider a steady simple shear flow with velocity components, referred to as fixed rectangular Cartesian coordinates, given by

$$i_1=\dot{\chi}x_2 \quad u_2=u_3=0 \tag{3}$$

where $\dot{\chi}$ is the constant shear rate. If p_{ik} is the stress tensor, the relevant stress distribution for incompressible elastic liquids can be written in the form

$$p_{12}=\dot{\chi}\eta(\dot{\chi}) \quad p_{11}-p_{22}=\nu_1(\dot{\chi}) \quad p_{22}-p_{33}=\nu_2(\dot{\chi}) \tag{4}$$

Where η is the apparent (or shear) viscosity and ν_1 and ν_2 are the first and second normal-stress differences, respectively. We next consider a *uniaxial* extension flow given by

$$\nu_1=\dot{\varepsilon}x_1 \quad \nu_2=-\frac{\dot{\varepsilon}x_2}{2} \quad \nu_3=-\frac{\dot{\varepsilon}x_3}{2} \tag{5a}$$

where $\dot{\varepsilon}$ is the constant strain rate. The associated stress distribution for an elastic liquid can be written in the form

$$p_{ik}=0, \quad i\neq k$$

$$p_{11}-p_{22}=p_{11}-p_{33}=\dot{\varepsilon}\,\eta_E(\dot{\varepsilon}) \tag{5b}$$

where η_E is the uniaxial extensional viscosity.

We argue that although a knowledge of the extensional viscosity of elastic liquids may be useful in its own right, it is helpful in the present study to make a comparison between the extensional viscosity and the corresponding shear viscosity. Since these depend on the strain rate $\dot{\varepsilon}$ and shear rate $\dot{\chi}$, respectively, the resulting Trouton ratio, T_R, given by

$$T_R = \frac{\eta_E(\dot{\varepsilon})}{\eta(\dot{\varepsilon})} \tag{6}$$

clearly depends on $\dot{\varepsilon}$ and $\dot{\chi}$ and some ambiguity of interpretation results. We address this question by reference to the so-called Generalized Newtonian Fluid (GNF) model, which characterizes a non-Newtonian *inelastic* fluid. This has equations of state of the form

$$p_{ik} = -p\,\delta_{ik} + T_{ik} \tag{7}$$

$$T_{ik} = 2\,\eta(I_2)\,d_{ik} \tag{8}$$

where (for incompressible fluids) p is an arbitrary isotropic pressure, T_{ik} is the 'extra stress' tensor, d_{ik} is the rate-of-strain tensor and I_2 is the second invariant of d_{ik}, which we choose to write in the form

$$I_2 = (2\,d_{ik}d_{ki})^{1/2} \tag{9}$$

so that in a steady simple shear flow like that represented by (3), we have

$$I_2 = \dot{\chi} \tag{10}$$

For the uniaxial extensional flow given by (5*b*), we find that

$$I_2 = \dot{\varepsilon}\sqrt{3} \tag{11}$$

and the relevant normal stress differences for the GNF model in such a flow are

$$p_{11} - p_{22} = p_{11} - p_{33} = 3\,\eta(\sqrt{3}\,\dot{\varepsilon})\,\dot{\varepsilon} \tag{12}$$

From the definition of the extensional viscosity η_E given in (4) we have

$$\eta_E = 3\,\eta(\sqrt{3}\,\dot{\varepsilon}) \tag{13}$$

and calculate the Trouton ratio according to

$$T_R = \frac{\eta_E(\dot{\varepsilon})}{\eta(\sqrt{3}\,\dot{\varepsilon})} \tag{14}$$

A value of 3 is obtained for all values of $\dot{\varepsilon}$ *if the fluid is inelastic*, departures from this value being associated with the influence of viscoelasticity. This definition of T_R provides an indication of the scale of viscoelastic influence on the extensional flow characteristics.

Based on these ideas, the foregoing analysis of the experiments (in terms of *average* values of $\dot{\varepsilon}$ and σ_E) was applied to the results of the jet experiments in order to provide estimates of T_R. The results are summarized in Figs. 12–15.

Figure 12 shows the calculated values of the Trouton ratio for a Newtonian glycerol/water mixture and solutions of xanthan gum. The broken line indicates a Trouton ratio of 3. The value of T_R for the Newtonian oil is somewhat higher than the expected value (3) for a *steady* uniaxial elongational flow but (within the uncertainty of the data indicated by the error bars) as would be expected, T_R is sensibly independent of the residence time of the fluid within the jet and hence of the accumulated level of total extensional strain, ε. In view of the difficulty of extensional flow measurements on mobile fluids, the values of T_R reported here for the Newtonian fluid provide encouraging agreement with the theoretical value [2,23]. The polymer solutions clearly show enhanced levels of resistance to extension, a significant feature of the results is the finding that the technique reveals the influence of the polymer additive on the flow characteristics at a concentration as low 5 wppm.

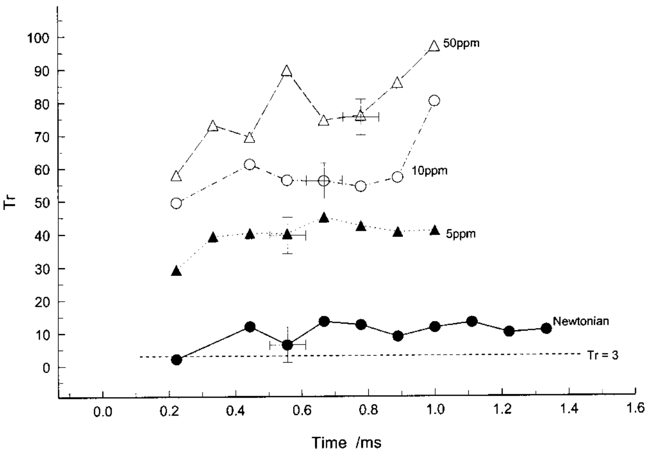

Fig. 12 Calculated values of the Trouton ratio for a Newtonian glycerol/water mixture and solutions of xanthan gum. The broken line indicates a Trouton ratio of 3.

Figure 13 shows the calculated values of T_R for the 15W40 oils and their Newtonian counterpart. The multigrade 15W40 oils (for petrol and diesel engines) clearly exhibit substantially greater resistance to extension, the values of T_R being typically an order-of-magnitude greater than those of their Newtonian counterpart.

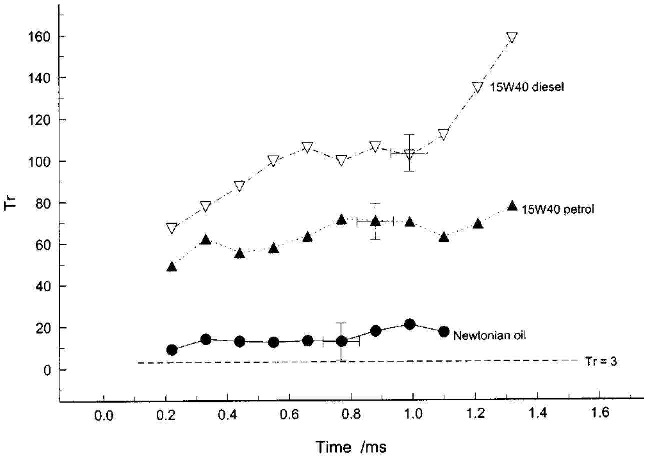

Fig. 13 Calculated values of the Trouton ratio for the 15W40 oils and their Newtonian counterpart. The broken line indicates a Trouton ratio of 3.

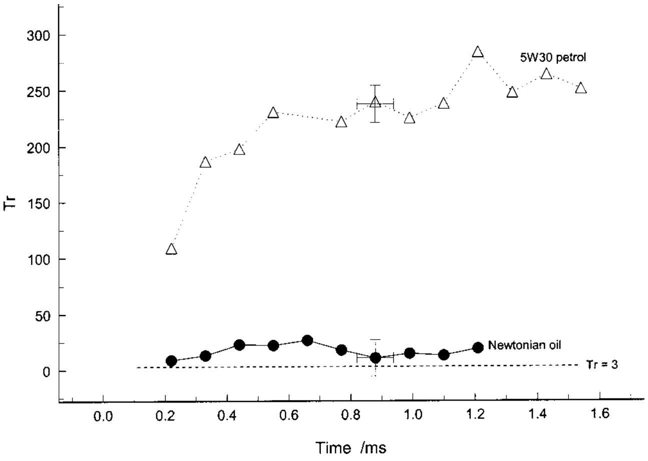

Fig. 14 Calculated values of the Trouton ratio for the 5W30 oil and its Newtonian counterpart. The broken line indicates a Trouton ratio of 3.

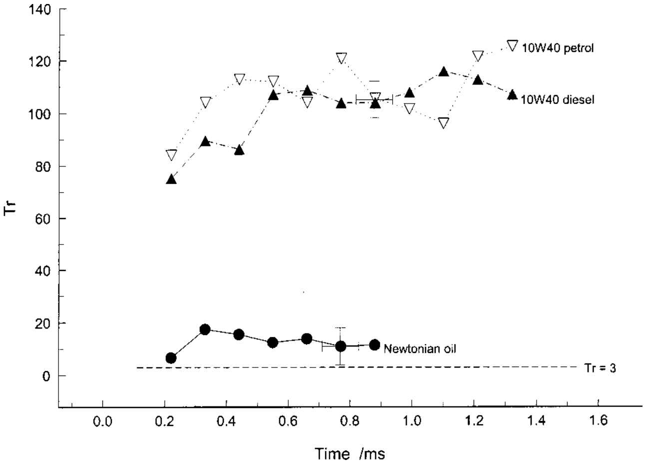

Fig. 15 Calculated values of the Trouton ratio for the 10W40 oils and their Newtonian counterpart. The broken line indicates a Trouton ratio of 3.

Although the extensional viscosity appears to be increasing as a function of time, it should be noted that the extensional rate is in fact decreasing throughout the experiment, and the interpretation of the transient response of the liquid on the basis of a single variable (i.e. strain *rate*) can be misleading. For both oils, the increase of T_R as a function of time corresponds principally to the increasing extensional strain accumulated by the fluid, in accordance with previous findings for polymer solutions [27]. It is interesting to note that the 15W40 oil formulated for use in diesel-powered engines appears significantly more elastic than its counterpart for petrol engines.

The results presented in Fig. 14 for the 5W30 oil show that this fluid also has a far higher resistance to extension than its Newtonian counterpart. As in the previous case, T_R is sensibly independent of the residence time of the fluid within the jet, unlike the 5W30 oil for which T_R increases with time despite the decline in rate of extension over this interval. The data for the 5W30 oil suggest that the value of T_R for this oil and its Newtonian counterpart would be indistinguishable for sufficiently low levels of strain.

The data presented in figure 15 reveal that, like their 5W30 and 15W40 counterparts, the two 10W40 oils also show a far higher resistance to extension than their Newtonian counterpart, with the results for the latter fluid again providing encouraging agreement with the predicted value. Unlike the 15W40 oils, there is no significant difference apparent in the behavior of the different multigrade oils and neither show as marked a dependence on time as the other oils.

4 Discussion

Our findings concerning the large deceleration experienced by the multigrade oil jets (relative to their Newtonian counterparts) are relevant to their ability to damage a solid boundary insofar as this is dictated principally by the impact velocity achieved by the jet. It follows that a mechanism which tends to ameliorate the value of jet velocity may be expected to reduce the tendency for damage to occur. To this extent, the present findings could be taken to support a mitigating effect of viscoelasticity on cavitation [3]. More properly, it supports a mitigating effect on a possible cavitation damage related mechanism. The most significant outcome of the present work is that it reveals that the rapidly decelerating jets experience high deformation rate extension flow, and that multigrade oils exhibit a high extensional viscosity when subjected to such a flow, even for short (1–2 millisecond) residence times within it.

The finding that extensional strain rates between 1,000 s^{-1} and 5,000 s^{-1} are produced in the present experiments is relevant to a previous study of the flow of multigrade oils in an extensional flow field [14]. Gupta et al. [14] attempted to relate their results to the performance of such fluids at engine operating conditions by estimating the rate of extension experienced by an oil within the main front bearing of a typical engine. Their results indicated that the fluid would experience a maximum rate of extension of *ca.* 2000 s^{-1} at an engine speed of 2,500 RPM but in practice, due to end leakage of fluid within the bearing, the actual value of the rate of extension would be somewhere between zero and this maximum value. The range of deformation rates calculated by Gupta et al. [14] coincides broadly with that produced in the present work.

A drawback of elongational viscometers which operate on a 'flow through' principle, such as that used by Gupta et al. [14] is that the deformation experienced by the liquid immediately prior to entering the extensionally dominated regime (the precursor flow) is a *shearing* flow [23]. The studies reported by Binding et al. [2] indicate that although the shear history of a multigrade oil may have negligible influence on its shear viscosity, the oil's extensional viscosity may be significantly reduced by shear. It is interesting to speculate, therefore, on the possible significance of the fact that bubble collapse (which precedes the liquid jet's formation in the present work) is itself associated with the generation of an extensional flow field [11]. In the case of spherically symmetrical bubble collapse this involves uniaxial extension [15], i.e., the same as that experienced by fluid within the jets. In the case of a liquid jet formed by the collapse of a bubble near a rigid boundary, a previous numerical study of the pathlines of particles of fluid on the bubble's surface has shown that nearly all such particles end up in the jet [28]. In such a case, the flow field associated with the collapse of the bubble may be considered to represent the precursor flow to the jet's production. The fact that the oils were subjected to a significant degree of shearing prior to extension in the work of Gupta et al. [14] may therefore provide an explanation for the significantly lower values of T_R (less than 20) reported by them for multigrade oils in the 5W30 and 10W40 categories, although it is noteworthy that, as in the present work, their results indicated that the 5W30 oil is more elastic in extension than its 10W40 counterpart.

Cheny and Walters [24] have reported studies of the role of fluid elasticity in the development of liquid jets, including those formed from commercial multigrade oils. In their work [24] the addition of small amounts of polyacrylamide to a Newtonian solvent was found to lead to an order-of-magnitude reduction in the length of the ascending vertical jet formed when a sphere is dropped into a reservoir of liquid. By analysing the evolution of the shape of jets formed from samples of a 10W40 multigrade oil during their ascending and descending phases, Cheny and Walters [24] concluded that the deformation of the fluid involved substantial elongation, but they did not calculate the rates of deformation experienced by the fluid, or estimate the levels of extensional viscosity exhibited by the fluids. While it is clearly important to bear in mind the different circumstances involved in the work described by Cheny and Walters [24] and that reported herein, the role played by elongation during the evolution of the jets in these different experiments is noteworthy (particularly in the case of non-Newtonian fluids). Given the rich diversity of fluid mechanical phenomena underlying the production of the jets in the present work, this phenomenon clearly merits further study.

5 Summary

The experimental technique used in this study provides a means of producing and recording liquid jets formed by bubble collapse under cavitation-generated pressure waves. The jets so formed from samples of commercial multigrade oils experience high rates of extension, $\dot{\varepsilon}$, in the range $500\ s^{-1} < \dot{\varepsilon} < 5{,}000\ s^{-1}$. The results are pertinent to discussions of processes which subject a fluid to such high extension rates within a brief (millisecond) transit time, the latter conditions being representative of those experienced by an oil within the dynamically loaded bearing of an engine under operating conditions. Insofar as the multigrade oils studied here are made viscoelastic by polymer additives, and evidently possess significant levels of resistance to extension, the results provide clear evidence in support of a mitigating effect of viscoelasticity on a mooted cavitation damage mechanism (i.e., liquid jet production).

Acknowledgments

This work was conducted under EPSRC Grant GR/L62160. The authors are grateful to Dr. P.M. Williams for his assistance with the construction of the apparatus.

Nomenclature

F_c = tensile strength (cavitation threshold) of liquid
T_R = Trouton ratio
η = shear viscosity
η_E = extensional viscosity
F_T = tensile force
σ_E = tensile stress
g = acceleration due to gravity
$\dot{\varepsilon}$ = rate of extension
$\dot{\chi}$ = shear rate

References

[1] Williamson, B. P., Walters, K., Bates, T. W., Coy, R. C., and Milton, M. L., 1997, ''Viscoelastic properties of multigrade oils and their effect on journal-bearing characteristics.'' J. Non-Newtonian Fluid Mech., **73**, 115–126.

[2] Binding, D. M., Couch, M. A., and Walters, K., 1999, ''The rheology of multigrade oils at elevated pressures.'' J. Non-Newtonian Fluid Mech., **87**, 155–164.

[3] Berker, A., Bouldin, M. G., Kleis, S. J., and Van Arnsdale, W. E., 1995, ''Effect of polymer on flow in journal bearings.'' J. Non-Newtonian Fluid Mech., **56**, 333–347.

[4] Williams, P. R., 2002, ''Cavitation and Bubble Dynamics.'' Chapter 5 in: Transport Processes in Bubbles, Drops and Particles, 2nd Edition. Eds. De Kee, D. & Chhabra, R. P. (Taylor & Francis, New York), ISBN 1-56032-906-8, pp. 102–127.

[5] Li, X. K., Gwynllyw, D. Rh., Davies, A. R., and Phillips, T. N., 2000, ''On the influence of lubricant properties on the dynamics of two-dimensional journal bearings.'' J. Non-Newtonian Fluid Mech., **93**, 29–59.

[6] Brindley, J., Elliott, L., and McKay, J. T., 1983, ''The role of cavitation in whirl instability in a rotor bearing.'' ASME J. Appl. Mech., **50**, 877–890.

[7] Dowson, D., and Taylor, C. M., 1979, ''Cavitation in Bearings.'' Annu. Rev. Fluid Mech., **11**, 35–66.

[8] Cameron, A., Basic Lubrication Theory. Ellis Horwood, London, 1981.

[9] Tomita, Y., and Shima, A., 1986, ''Mechanisms of impulsive pressure generation and damage pit formation by bubble collapse.'' J. Fluid Mech., **169**, 535–564.

[10] Dear, J. P., and Field, J. E., 1988, ''A study of the collapse of arrays of cavities.'' J. Fluid Mech., **190**, 409–425.

[11] Ryskin, G., 1990, ''Dynamics and sound emission of a spherical cavitation bubble in a dilute polymer solution.'' J. Fluid Mech., **218**, 239–263.

[12] Kim, C., 1994, ''Collapse of spherical bubbles in Maxwell fluids.'' J. Non-Newtonian Fluid Mech., **55**, 37–58.

[13] Jones, D. M., Walters, K., and Williams, P. R., 1987, ''On the extensional viscosity of mobile polymer solutions.'' Rheol. Acta, **26**, 20–30.

[14] Gupta, R. K., Chan, R. C., and Deysarkar, A. K., 1990, ''Flow of multigrade motor oils in an extensional flow field.'' J. Rheol., **34**, 1373–1386.

[15] Pearson, G., and Middleman, S., 1977, ''Elongational flow behavior of viscoelastic liquids: Part 1. Modelling of bubble collapse.'' AIChE J., **23**, 714–721.

[16] Plessett, M. S., and Prosperetti, A., 1977, ''Bubble Dynamics and Cavitation.'' Annu. Rev. Fluid Mech., **9**, 145–185.

[17] Brennen, C. E., 1995, *Cavitation and Bubble Dynamics*. Oxford University Press, Oxford.

[18] Fruman, D. H., 1999, ''Effects of non-Newtonian fluids on cavitation.'' In: *Advances in the Flow and Rheology of Non-Newtonian Fluids*, Part A. Eds. Siginer DA, De Kee D and Chhabra RP. Elsevier

[19] Barrow, M. S., Brown, S. W. J., and Williams, P. R., 2004, ''Extensional flow of liquid jets formed by bubble collapse under cavitation-generated pressure waves.'' *Experiments in Fluids*, in press.

[20] Williams, P. R., Williams, P. M., and Brown, S. W. J., 1997, ''Pressure waves arising from the oscillation of cavitation bubbles under dynamic stressing.'' J. Phys. D: Appl. Phys., **30**, 1197–1206.

[21] Brown, S. W. J., *PhD Thesis*, University of Wales, 1999.

[22] Jones, D. M., Walters, K., and Williams, P. R., 1987, ''On the extensional viscosity of mobile polymer solutions.'' Rheol. Acta, **26**, 20–30.

[23] James, D. F. and Walters, K., 1993, ''A critical appraisal of the available methods for the measurement of extensional properties of mobile systems.'' in *Techniques in Rheological Measurements*, A. A. Collyer (Ed.), Elsevier, London.

[24] Cheny, J.-M., and Walters, K., 1999, ''Rheological influences on the splashing experiment.'' J. Non-Newtonian Fluid Mech., **86**, 185–210.

[25] Cameron, A. Basic Lubrication Theory. Ellis Horwood, London, 1981.

[26] Brown, S. W. J., and Williams, P. R., 2000, ''The tensile behavior of elastic liquids under dynamic stressing.'' J. Non-Newtonian Fluid Mech., **90**, 1–11.

[27] Sridhar, T., Nguyen, D. A., and Fuller, G. G., 2000, ''Birefringence and stress growth in uniaxial extension of polymer solutions.'' J. Non-Newtonian Fluid Mech., **90**, 299–315.

[28] Cerone, P., and Blake, J. R., 1984, ''A note on the instantaneous streamlines, pathlines and pressure contours for a cavitation bubble near a boundary.'' J. Aust. Math. Soc. Ser. B, Appl. Math., **26**, 31–44.

Dynamics of Electrorheological Suspensions Subjected to Spatially Nonuniform Electric Fields

J. Kadaksham

P. Singh

N. Aubry

Department of Mechanical Engineering,
New Jersey Institute of Technology,
University Heights,
Newark, NJ 07102

A numerical method based on the distributed Lagrange multiplier method (DLM) is developed for the direct simulation of electrorheological (ER) liquids subjected to spatially nonuniform electric field. The flow inside particle boundaries is constrained to be rigid body motion by the distributed Lagrange multiplier method and the electrostatic forces acting on the particles are obtained using the point-dipole approximation. The numerical scheme is verified by performing a convergence study which shows that the results are independent of mesh and time step sizes. The dynamical behavior of ER suspensions subjected to nonuniform electric field depends on the solids fraction, the ratio of the domain size and particle radius, and four additional dimensionless parameters which respectively determine the importance of inertia, viscous, electrostatic particle-particle interaction and dielectrophoretic forces. For inertia less flows a parameter defined by the ratio of the dielectrophoretic and viscous forces, determines the time duration in which the particles collect near either the local maximums or local minimums of the electric field magnitude, depending on the sign of the real part of the Clausius-Mossotti factor. In a channel subjected to a given nonuniform electric field, when the applied pressure gradient is smaller than a critical value, the flow assists in the collection of particles at the electrodes, but when the pressure gradient is above this critical value the particles are swept away by the flow. [DOI: 10.1115/1.1669401]

1 Introduction

In this paper, we numerically study the dynamics of particle separation in electrorheological (ER) suspensions subjected to spatially nonuniform electric fields. The suspending fluid is assumed to be Newtonian, and the particles spherical and monodispersed. Both the particles and the fluid are assumed to be nonconducting.

It is well known that when an ER liquid is subjected to a spatially uniform electric field the particles form chains and columns that align parallel to the electric field direction [1]. The effective viscosity of the ER suspension increases dramatically because the length of these chains and columns is of the same order as the gap between the electrodes, and their distribution on the planes perpendicular to the electric field direction is approximately uniform. In spatially varying electric fields, on the other hand, the particles collect either near the local maximums or local minimums of the electric field magnitude because of an electrostatic force, called dielectrophoretic force (DEP), which depends on the gradient of the electric field, that acts on the particles [2,3]. Since in a nonuniform electric field no domain sized structures are formed, the change in the effective viscosity of the ER suspension is relatively small.

In a spatially nonuniform electric field, the particles of ER liquids are subjected to the dielectrophoretic (DEP) force as well as the electrostatic particle-particle interaction force which acts even when the electric field is uniform. The electrostatic particle-particle interactions, which lead to the formation of chains and columns, in the past have been referred to as mutual dielectrophoresis [3], as the electrostatic force on a particle arises due to the nonuniform electric field produced by the other particles.

The DEP force arises because a dielectric sphere placed in a spatially varying electric field becomes polarized and experiences a net force:

$$\mathbf{F}_{DEP} = 4\pi a^3 \varepsilon_0 \varepsilon_c \beta \mathbf{E}\cdot\nabla\mathbf{E} \tag{1}$$

where a is the particle radius, ε_c is the permittivity of the fluid, $\varepsilon_0 = 8.8542\times10^{-12}$ F/m is the permittivity of free space and $\mathbf{E}$ is the electric field, β is the real part of the complex frequency dependent Clausius-Mossotti factor $(\varepsilon_p^* - \varepsilon_c^*)/(\varepsilon_p^* + 2\varepsilon_c^*)$, i.e., $\beta(f) = \mathrm{Re}((\varepsilon_p^* - \varepsilon_c^*)/(\varepsilon_p^* + 2\varepsilon_c^*))$, ε_p^*, and ε_c^* being the complex permittivities of the particles and the fluid, and $\varepsilon^* = \varepsilon - j\sigma/f$, where σ is the conductivity, ε is the permittivity and f is the angular frequency of the applied electric field. From this expression we notice that when β is positive the direction of the dielectrophoretic force is along the gradient of the electric field magnitude and when β is negative, the force acts in the opposite direction. In our simulations, we will assume that both fluid and suspended particles are nonconductive or ideal dielectrics. Notice that in this case the Clausius-Mossotti factor is real as the conductivities of both mediums are zero. The equations used here are however applicable even for lossy dielectrics, provided the frequency of the applied AC electric field is sufficiently large such that $\varepsilon \gg \sigma/f$.

It follows that the direction of the dielectrophoretic force determines the regions in which the particles collect. For example, when β is positive, the dielectrophoretic force moves the particles into the regions where the electric field strength is locally maximum which is normally on the electrode surfaces, while when β is negative, it moves the particles into the regions where the electric field strength is locally minimum. The dielectrophoretic force, therefore, makes the particle distribution less uniform and thus, as mentioned above, can have a dramatic impact on the particle scale suspension structure. Such a force can also be used for removing particles from a suspending liquid, as well as for separating particles for which the sign of β is different. For a given particle, the

---

Contributed by the Fluids Engineering Division for publication in the JOURNAL OF FLUIDS ENGINEERING. Manuscript received by the Fluids Engineering Division March 4, 2003; revised manuscript received October 6, 2003. Associate Editor: D. Siginer.

sign of β depends on the dielectric constant of the fluid, as well as the frequency of the applied AC field. Therefore, at least in principle, any two sets of particles with different dielectric constants can be separated, provided a suitable fluid is used, such that the sign of β for them is different.

Winslow [1] was the first to experimentally study the electrorheological effects in suspensions of both nonconducting and semi-conducting particles in a media of low conductivity. He introduced the concept of ''fibrillous'' chain structure formation in the electrorheological fluid under the application of an electric field, a phenomenon that is responsible for the increase in viscosity of the suspension. Since then several models have been proposed to explain the formation of fibrillated chain structure in ER fluids. Some of the early models included the electric double layer model [4,5] and the water bridge model [6,7]. Both these models explain the chain structure formation in an ER fluid by the amount of water present in the suspension.

Marshall, Goodwin and Zukoski [8] performed experimental studies of ER fluids for a wide range of shear rates, field strengths and volume fractions and proposed a model for the dependence of the suspension viscosity of the ER fluid on the Mason number, which is the ratio of the viscous force to the electrostatic particle-particle interaction force acting on the particles. Zukoski et al. [9,10] performed elaborate experimental studies of ER fluids to quantify their rheological properties.

The polarization model, along with the point-dipole approximation, has been widely used to explain many experimental phenomena observed in ER fluids. Specifically, theoretical and numerical studies based on the polarization model have been used to study idealized ER fluids containing spherical, monodispersed and nonconducting particles in a nonconducting suspending medium [11–14]. In these studies the Stokes drag law is used to approximate the hydrodynamic force acting on the particles, which assumes that the Reynolds number is zero, and the Brownian forces acting on the particles are ignored. The latter is appropriate for suspensions containing large sized particles. The trajectories of particles are obtained by integrating Newton's second law, as is done in the molecular dynamic studies of liquids. These simulations have been used to study the steady state behavior, as well as the transient response of ER fluids, in simple shear flows [12–14,15–18]. In [16,17] the electrostatic particle-particle interaction forces among the particles were computed by accounting for the many body interactions that are ignored in the point-dipole approximation. The hydrodynamic forces acting on the particles, as well as the particle-particle and fluid-particle interactions, in the zero Reynolds number limit, were computed using the Stokesian dynamics approach [16,17]. Specifically, simulations were performed for a planar mono-layer containing 25 spherical particles subjected to simple shear flows. All these studies, however, assumed the spatial distribution of the electric field to be uniform.

Even though the accuracy of the point-dipole approximation decreases with decreasing distance between the particles, it has been used in the past studies of electrorheological fluids extensively due to its simplicity and its ability to qualitatively capture the phenomenon of particle chaining [19]. To overcome this, we are currently working on developing an alternative approach which calculates the force acting on a particle by integrating the Maxwell stress tensor on the particles surfaces [20].

Most previous experimental and theoretical studies of dielectrophoresis have focused on the separation and characterization of particles [[21–25] and references therein]. Dussaud, Khusid and Acrivos [21] studied the behavior of quiescent and flowing dilute suspensions of ER fluids subjected to spatially varying electric fields both experimentally and theoretically. In their experiments they showed that the dielectrophoretic behavior of their system is frequency dependent [26] and that, as expected, the particles with $\beta<0$ collect in the regions where the electric field strength is locally minimum. The time taken for particle collection in their experiments agreed with their theoretical analysis, in which the hydrodynamic and electrostatic particle-particle interactions, as well as the influence of particles on the fluid, were neglected.

The rest of the paper is organized as follows. In the next section we present the governing equations and the dimensionless parameters that are important in determining the rheological behavior of the ER fluids subjected to nonuniform electric fields. The numerical method is described in section 3 and the results are presented in section 4, which show that the particle collection time in a flowing ER fluid subjected to a nonuniform electric field depends on the ratio of the dielectrophoretic and viscous forces, as well as the relative importance of the electrostatic particle-particle interaction and dielectrophoretic forces, and the hydrodynamic forces.

2 Governing Equations

In this section, we describe the electrostatic forces that arise in a nonuniform electric field due to the polarization of particles and state the governing equations for both the particles and the fluid. Let us denote the domain containing a Newtonian fluid and N solid particles by Ω, the interior of the ith particle by $P_i(t)$, and the domain boundary by Γ. The governing equations for the fluid-particle system are:

$$\rho_L\left(\frac{\partial \mathbf{u}}{\partial t}+\mathbf{u}\cdot\nabla\mathbf{u}\right)=\rho_L\mathbf{g}-\nabla p+\nabla\cdot(2\eta\mathbf{D}) \quad \text{in } \Omega\backslash\overline{P(t)}$$

$$\nabla\cdot\mathbf{u}=0 \quad \text{in } \Omega\backslash\overline{P(t)} \tag{2}$$

$$\mathbf{u}=\mathbf{u}_\mathrm{L} \quad \text{on } \Gamma$$

$$\mathbf{u}=\mathbf{U}_\mathrm{i}+\boldsymbol{\omega}_\mathrm{i}\times\mathbf{r}_\mathrm{i} \quad \text{on } \partial P_i(t),\ i=1,\ldots,N \tag{3}$$

Here $\mathbf{u}$ is the fluid velocity, p is the pressure, η is the dynamic viscosity of the fluid, ρ_L is the density of the fluid, $\mathbf{D}$ is the symmetric part of the velocity gradient tensor, $\mathbf{U}_\mathrm{i}$ and $\boldsymbol{\omega}_\mathrm{i}$ are the linear and angular velocities of the ith particle, and $\mathbf{g}$ is the acceleration due to gravity. The above equations are solved using the following initial conditions $\mathbf{u}|_{t=0}=\mathbf{u}_0$, where $\mathbf{u}_0$ is the known initial value of the velocity.

The linear velocity $\mathbf{U}_\mathrm{i}$ and angular velocity $\boldsymbol{\omega}_\mathrm{i}$ of the ith particle are governed by

$$m_i\frac{d\mathbf{U}_i}{dt}=\mathbf{F}_i+\mathbf{F}_{E,i}$$

$$I_i\frac{d\boldsymbol{\omega}_i}{dt}=\mathbf{T}_i \tag{4}$$

$$\mathbf{U}_i|_{t=0}=\mathbf{U}_{i,0}$$

$$\boldsymbol{\omega}_i|_{t=0}=\boldsymbol{\omega}_{i,0} \tag{5}$$

where m_i and I_i are the mass and moment of inertia of the ith particle, $\mathbf{F}_\mathrm{i}$ and $\mathbf{T}_\mathrm{i}$ are the hydrodynamic force and torque acting on the ith particle and $\mathbf{F}_\mathrm{E,i}=\mathbf{F}_\mathrm{DEP,i}+\mathbf{F}_\mathrm{D,i}$ is the net electrostatic force acting on the ith particle. The dielectrophoretic force $\mathbf{F}_\mathrm{DEP,i}$ acting on the ith particle is given by (1) and $\mathbf{F}_\mathrm{D,i}$ is the particle-particle interaction force on the ith particle. In this study we will assume that the particle density is approximately equal to that of the fluid and thus drop the gravity term.

In a nonuniform electric field, the particle interaction force on the ith particle due to the jth particle is:

$$\mathbf{F}_{D,ij}=\frac{1}{4\pi\varepsilon_0\varepsilon_c}\frac{3}{r^5}\left(\mathbf{r}_{ij}(\mathbf{p}_i\cdot\mathbf{p}_j)+(\mathbf{r}_{ij}\cdot\mathbf{p}_i)\mathbf{p}_j+(\mathbf{r}_{ij}\cdot\mathbf{p}_j)\mathbf{p}_i-\frac{5}{r^2}\mathbf{r}_{ij}(\mathbf{p}_i\cdot\mathbf{r}_{ij})(\mathbf{p}_j\cdot\mathbf{r}_{ij})\right) \tag{6}$$

where $\mathbf{p}_\mathrm{i}$ and $\mathbf{p}_\mathrm{j}$ are the dipole moments of the ith and the jth particles given by $\mathbf{p}_\mathrm{i}=4\pi\varepsilon_0\varepsilon_c\beta a^3\mathbf{E}_\mathrm{i}$ and $\mathbf{p}_\mathrm{j}=4\pi\varepsilon_0\varepsilon_c\beta a^3\mathbf{E}_\mathrm{j}$. The net electrostatic interaction force acting on the *i*th particle is the sum of the interaction forces with all other particles of the suspension:

$$\mathbf{F}_{D,i}=\sum_{i=l,i\neq j}^{N}\mathbf{F}_{D,ij} \tag{7}$$

As mentioned above, in this work, we restrict ourselves to the case where the particles are spherical, and therefore we do not need to keep track of the particle orientation. The particle positions are obtained from

$$\frac{d\mathbf{X}_i}{dt}=\mathbf{U}_i \tag{8}$$

$$\mathbf{X}_i\big|_{t=0}=\mathbf{X}_{i,0} \tag{9}$$

where $\mathbf{X}_{i,0}$ is the position of the *i*th particle at time $t=0$. In this work, we will assume that all particles have the same density ρ_p, and since they have the same radius, they also have the same mass, *m*.

It is shown in [27] that the above equations contain the following dimensionless parameters: $\mathrm{Re}=\rho_L Ua/\eta$, $P_1=6\pi\eta a^2/mU$, $P_2=3\pi\varepsilon_0\varepsilon_c\beta^2a^3|E_0|^2/4mU^2$, $P_3=4\pi\varepsilon_0\varepsilon_c\beta a^4|E_0|^2/mU^2L$ and $h'=L/a$. Another important parameter, which does not appear directly in the above equations, is the solids fraction. We define another Reynolds number $\mathrm{Re}_L=\rho_L LU/\eta$ based on the channel width L and another parameter $P_4=P_2/P_3=3\beta L/16a$.

When the particle and fluid inertia are negligible, i.e., the particle and fluid inertia terms can be set to zero, the number of dimensionless parameters reduces to two. The dimensionless parameters in this case are the Mason number, $Ma=P_1/P_2=8\eta U/\varepsilon_0\varepsilon_c\beta^2a|E_0|^2$, and $P_5=P_3/P_1=2\varepsilon_0\varepsilon_c\beta a^2|E_0|^2/3\eta UL$.

For the pressure driven flows of ER suspension, the characteristic velocity is assumed to be the center line velocity of the parabolic flow, undisturbed by the particles, in 2-D channel of the same width, i.e., $U=(L^2/8\eta)dp/dx$, where L is the channel width and dp/dx is the applied pressure gradient. This is appropriate because for our simulations the channel width is larger than the channel height. For the cases where the imposed pressure gradient is zero, the characteristic velocity $U=2\varepsilon_0\varepsilon_c\beta a^2|E_0|^2/3\eta L$, which is obtained by assuming that the dielectrophoretic force and the viscous drag terms balance each other (see [27] for details).

3 Finite-Element Method

The computational scheme used in this paper is a generalization of the DLM finite-element scheme described in [28,29]. In this scheme, the fluid flow equations are solved on the combined fluid-solid domain, and the motion inside the particle boundaries is forced to be rigid-body motion using a distributed Lagrange multiplier. The fluid and particle equations of motion are combined into a single combined weak equation of motion, eliminating the hydrodynamic forces and torques, which helps ensure stability of time integration scheme. For the sake of simplicity, in this section, we assume that there is only one particle. The extension to the multi-particle case is straightforward.

The solution and variation are required to satisfy the strong form of the constraint of rigid body motion throughout $P(t)$. In the distributed Lagrange multiplier method, this constraint is removed from the velocity space and enforced weakly as a side constraint using a distributed Lagrange multiplier term. It was shown in [28,29] that the following weak formulation of the problem holds in the extended domain:

For a.e. $t>0$, find $\mathbf{u}\in\overline{W}_{u\Gamma}$, $p\in L_0^2(\Omega)$, $\boldsymbol{\lambda}\in\Lambda(t)$, $\mathbf{U}\in\mathbf{R}^3$, and $\boldsymbol{\omega}\in\mathbf{R}^3$, satisfying

$$\begin{aligned}&\int_\Omega\rho_L\left(\frac{d\mathbf{u}}{dt}-\mathbf{g}\right)\cdot\mathbf{v}d\mathbf{x}-\int_\Omega p\nabla\cdot\mathbf{v}d\mathbf{x}+\int_\Omega 2\eta\mathbf{D}[\mathbf{u}]:\mathbf{D}[\mathbf{v}]d\mathbf{x}\\&+\left(1-\frac{\rho_L}{\rho_d}\right)\left(M\left(\frac{d\mathbf{U}}{dt}-\mathbf{g}\right)\cdot\mathbf{V}+I\frac{d\boldsymbol{\omega}}{dt}\xi\right)-\mathbf{F}'\cdot\mathbf{V}\\&=\langle\boldsymbol{\lambda},\mathbf{v}-(\mathbf{V}+\xi\times\mathbf{r})\rangle_{P(t)}\quad\text{for all}\quad\mathbf{v}\in\overline{W}_0,\ \mathbf{V}\in\mathbf{R}^3,\\&\qquad\text{and}\quad\boldsymbol{\xi}\in\mathbf{R}^3,\end{aligned} \tag{10}$$

$$\int_\Omega q\nabla\cdot\mathbf{u}d\mathbf{x}=0\quad\text{for all}\quad q\in L^2(\Omega), \tag{11}$$

$$\langle\boldsymbol{\mu},\mathbf{u}-(\mathbf{U}+\boldsymbol{\omega}\times\mathbf{r})\rangle_{\mathrm{P(t)}}=0\quad\text{for all}\quad\boldsymbol{\mu}\in\Lambda(\mathrm{t}), \tag{12}$$

$$\mathbf{u}\big|_{\mathrm{t}=0}=\mathbf{u}_0\quad\text{in}\quad\Omega, \tag{13}$$

as well as the kinematic equations and the initial conditions for the particle linear and angular velocities. Here $\mathbf{F}'$ is the additional body force applied to the particles to limit the extent of overlap (see Eq. (19) in Glowinski et al. (1999) and $\boldsymbol{\lambda}$ is the distributed Lagrange multiplier

$$\begin{aligned}\overline{\mathrm{W}}_{\mathrm{u}\Gamma}&=\{\mathbf{v}\in\mathrm{H}^1(\Omega)^3|\mathbf{v}=\mathbf{u}_\Gamma(\mathrm{t})\quad\text{on}\quad\Gamma\},\\\overline{\mathrm{W}}_0&=\mathrm{H}_0^1(\Omega)^3,\\\mathrm{L}_0^2(\Omega)&=\left\{\mathrm{q}\in\mathrm{L}^2(\Omega)\,\middle|\,\int_\Omega\mathrm{q}d\mathbf{x}=0\right\},\end{aligned} \tag{14}$$

and $\Lambda(\mathrm{t})$ is $L^2(P(t))^3$, with $\langle\cdot,\cdot\rangle_{\mathrm{P(t)}}$ denoting the L^2 inner product over the particle, where Γ^- is the upstream part of Γ. In our simulations, since the velocity and $\boldsymbol{\mu}$ are in L^2, we will use the following inner product

$$\langle\boldsymbol{\mu},\mathbf{v}\rangle_{\mathrm{P(t)}}=\int_{\mathrm{P(t)}}(\boldsymbol{\mu}\cdot\mathbf{v})\mathrm{d}\mathbf{x}. \tag{15}$$

In order to solve the above problem numerically, we will discretize the domain using a regular tetrahedral mesh $\mathrm{T_h}$ for the velocity, where h is the mesh size, and a regular tetrahedral mesh $\mathrm{T_{2h}}$ for the pressure. The following finite dimensional spaces are defined for approximating $\overline{\mathrm{W}}_{\mathrm{u}\Gamma}$, $\overline{\mathrm{W}}_0$, $\mathrm{L}^2(\Omega)$, and $\mathrm{L}_0^2(\Omega)$:

$$\begin{aligned}\mathrm{W}_{\mathrm{u}\Gamma,\mathrm{h}}&=\{\mathbf{v}_\mathrm{h}\in\mathrm{C}^0(\overline{\Omega})^3|\mathbf{v}_\mathrm{h}|_\mathrm{T}\in\mathrm{P}_1\times\mathrm{P}_1\times\mathrm{P}_1\quad\text{for all}\quad\mathrm{T}\in\mathrm{T_h},\\&\qquad\mathbf{v}_\mathrm{h}=\mathbf{u}_{\Gamma,\mathrm{h}}\quad\text{on}\quad\Gamma\},\\\mathrm{W}_{0,\mathrm{h}}&=\{\mathbf{v}_\mathrm{h}\in\mathrm{C}^0(\overline{\Omega})^3|\mathbf{v}_\mathrm{h}|_\mathrm{T}\in\mathrm{P}_1\times\mathrm{P}_1\times\mathrm{P}_1\quad\text{for all}\quad\mathrm{T}\in\mathrm{T_h},\\&\qquad\mathbf{v}_\mathrm{h}=0\quad\text{on}\quad\Gamma\},\end{aligned} \tag{16}$$

$$\begin{aligned}\mathrm{L_h^2}&=\{\mathrm{q_h}\in\mathrm{C}^0(\overline{\Omega})|\mathrm{q_h}|_\mathrm{T}\in\mathrm{P}_1\quad\text{for all}\quad\mathrm{T}\in\mathrm{T_{2h}}\},\\\mathrm{L}_{0,\mathrm{h}}^2&=\left\{\mathrm{q_h}\in\mathrm{L_h^2}|\int_\Omega\mathrm{q_h}d\mathbf{x}=0\right\},\end{aligned} \tag{17}$$

The particle inner product terms in (10) and (12) are obtained using the discrete L^2 inner product defined in Glowinski et al. (1999). Specifically, we choose M points, $\mathbf{x}_1,\ldots,\mathbf{x}_\mathrm{M}$ that uniformly cover $\overline{\mathrm{P}}(\mathrm{t})$, and define

$$\boldsymbol{\Lambda}_\mathrm{h}(\mathrm{t})=\left\{\boldsymbol{\mu}_\mathrm{h}\,\middle|\,\boldsymbol{\mu}=\sum_{\mathrm{i}=1}^{\mathrm{M}}\boldsymbol{\mu}_{\mathrm{h,i}}\delta(\mathbf{x}-\mathbf{x}_\mathrm{i}),\quad\boldsymbol{\mu}_{\mathrm{h,l}},\ldots,\boldsymbol{\mu}_{\mathrm{h,M}}\in\mathbf{R}^3\right\}.$$

Using these finite dimensional spaces, it is straightforward to discretize equations (10–13).

3.1 Time Discretization Using the Marchuk-Yanenko Operator Splitting Scheme.

The initial value problem (10–13) is solved by using the Marchuk-Yanenko operator-splitting scheme, which allows us to decouple its three primary difficulties:

1. The incompressibility condition, and the related unknown pressure p_h,
2. The nonlinear advection term,
3. The constraint of rigid-body motion in $P_h(t)$, and the related distributed Lagrange multiplier $\boldsymbol{\lambda}_h$.

The Marchuk-Yanenko operator-splitting scheme can be applied to an initial value problem of the form

$$\frac{d\phi}{dt}+A_1(\phi)+A_2(\phi)+A_3(\phi)=f$$

where the operators A_1, A_2, and A_3 can be multi-valued. Let Δt be the time step. We use the following version of the Marchuk-Yanenko operator splitting scheme to simulate the motion of particles in an ER fluid:

Set $\mathbf{u}^0=\mathbf{u}_{0,h}$, $\mathbf{U}^0=\mathbf{U}_0$, $\mathbf{X}^0=\mathbf{X}_0$, and $\boldsymbol{\omega}^0=\boldsymbol{\omega}_0$, and calculate $\mathbf{E}$ by solving $\nabla^2\varphi=0$, subjected to the electric potential boundary conditions, and then calculating $\mathbf{E}=\nabla\varphi$.

For n=0, 1, 2, . . . assuming $\mathbf{u}^n$, $\mathbf{U}^n$, $\mathbf{X}^n$, and $\boldsymbol{\omega}^n$ are known, we find the values for the (n+1)th time step using the following steps:

STEP 1:
Find $\mathbf{u}^{n+1/4}\in W^{n+1}_{u\Gamma,h}$ and $p^{n+1/4}\in L^2_{0,h}$, by solving

$$\int_\Omega \rho_L\frac{\mathbf{u}^{n+1/4}-\mathbf{u}^n}{\Delta t}\cdot\mathbf{v}d\mathbf{x}-\int_\Omega p^{n+1/4}\nabla\cdot\mathbf{v}d\mathbf{x}$$
$$+\alpha_1\int_\Omega 2\,\eta_s\mathbf{D}[\mathbf{u}^{n+1/4}]:\mathbf{D}[\mathbf{v}]d\mathbf{x}=\mathbf{0}\quad\text{for all}\quad \mathbf{v}\in W_{0,h}, \tag{18}$$

$$\int_\Omega q\nabla\cdot\mathbf{u}^{n+1/4}d\mathbf{x}=0\quad\text{for all}\quad q\in L^2_h,$$

STEP 2:
Find $\mathbf{u}^{n+2/4}\in W^{n+1}_{u\Gamma,h}$, by solving

$$\int_\Omega \rho_L\frac{\mathbf{u}^{n+2/4}-\mathbf{u}^{n+1/4}}{\Delta t}\cdot\mathbf{v}d\mathbf{x}+\int_\Omega \rho_L(\mathbf{u}^{n+2/4}\cdot\nabla\mathbf{u}^{n+2/4})\cdot\mathbf{v}d\mathbf{x}$$
$$+\alpha_2\int_\Omega 2\,\eta_s\mathbf{D}[\mathbf{u}^{n+2/4}]:\mathbf{D}[\mathbf{v}]d\mathbf{x}=0\quad\text{for all}\quad \mathbf{v}\in W_{0,h} \tag{19}$$

STEP 3:
Compute $\mathbf{U}^{n+2/4}$ and $\mathbf{X}^{n+2/4}$ using the prediction procedure
Set $\mathbf{U}^{n,0}=\mathbf{U}^n$, $\mathbf{X}^{n,0}=\mathbf{X}^n$.
Do k=1, K
Calculate $\mathbf{F}_E(\mathbf{X}^{n,k-1})$

$$\mathbf{U}^{*n,k}=\mathbf{U}^{n,k-1}+\left(\mathbf{g}+\left(1-\frac{\rho_L}{\rho_d}\right)^{-1}M^{-1}[\mathbf{F}'(\mathbf{X}^{n,k-1})+\mathbf{F}_E(\mathbf{X}^{n,k-1})]\right)\frac{\Delta t}{K}$$
$$\mathbf{X}^{*n,k}=\mathbf{X}^{n,k-1}+\left(\frac{\mathbf{U}^{n,k-1}+\mathbf{U}^{*n,k}}{2}\right)\frac{\Delta t}{K} \tag{20}$$

$$\mathbf{U}^{n,k}=\mathbf{U}^{n,k-1}+\left(\mathbf{g}+\left(1-\frac{\rho_L}{\rho_d}\right)^{-1}M^{-1}\frac{\mathbf{F}'(\mathbf{X}^{n,k-1})+\mathbf{F}'(\mathbf{X}^{*n,k-1})+\mathbf{F}_E(\mathbf{X}^{n,k-1})+\mathbf{F}_E(\mathbf{X}^{*n,k-1})}{2}\right)\frac{\Delta t}{K}$$

$$\mathbf{X}^{n,k}=\mathbf{X}^{n,k-1}+\left(\frac{\mathbf{U}^{n,k-1}+\mathbf{U}^{n,k}}{2}\right)\frac{\Delta t}{K}$$

end do
Then set $\mathbf{U}^{n+2/4}=\mathbf{U}^{n,K}$, $\mathbf{X}^{n+2/4}=\mathbf{X}^{n,K}$.

The next step consists of finding $\mathbf{u}^{n+1}\in W^{n+1}_{u\Gamma,h}$, $\boldsymbol{\lambda}^{n+1}\in\Lambda_h((n+2/4)\Delta t)$, $\mathbf{U}^{n+1}\in\mathbf{R}^3$, and $\boldsymbol{\omega}^{n+1}\in\mathbf{R}^3$, satisfying

$$\int_\Omega \rho_L\frac{\mathbf{u}^{n+1}-\mathbf{u}^{n+2/4}}{\Delta t}\cdot\mathbf{v}d\mathbf{x}+\left(1-\frac{\rho_L}{\rho_d}\right)\left(M\frac{\mathbf{U}^{n+1}-\mathbf{U}^{n+2/4}}{\Delta t}\cdot\mathbf{V}\right.$$
$$\left.+I\frac{\boldsymbol{\omega}^{n+1}-\boldsymbol{\omega}^{n+2/4}}{\Delta t}\xi\right)$$
$$=\langle\boldsymbol{\lambda}^{n+1},\mathbf{v}-(\mathbf{V}+\xi\times\mathbf{r}^{n+2/4})\rangle_{P((n+2/4)\Delta t)}$$
$$\text{for all}\quad \mathbf{v}\in W_{0,h},\quad \mathbf{V}\in\mathbf{R}^3,\quad\text{and}\quad \xi\in\mathbf{R}^3 \tag{21}$$

where the center of the particle $P((n+2/4)\Delta t)$ is at the location $X^{n+2/4}$.

Then set $\mathbf{X}^{n+1,0}=\mathbf{X}^n$.
For k=1, K, follow the do-loop

$$\mathbf{X}^{*n+1,k}=\mathbf{X}^{n+1,k-1}+\left(\frac{\mathbf{U}^n+\mathbf{U}^{n+1}}{2}\right)\frac{\Delta t}{K} \tag{22}$$
$$\mathbf{X}^{n,k}=\mathbf{X}^{*n,k-1}+\left(1-\frac{\rho_L}{\rho_d}\right)^{-1}$$
$$\times M^{-1}\left(\frac{\mathbf{F}'(\mathbf{X}^{n+1,k-1})+\mathbf{F}'(\mathbf{X}^{*n+1,k})}{2}\right)\frac{(\Delta t)^2}{2K}$$

end do
Then set $\mathbf{X}^{n+1}=\mathbf{X}^{n+1,K}$.
Then set $p^{n+1}=p^{n+1/4}$, and go back to the first step.
Remarks:

1. The problems arising in the first and second steps are solved using the conjugate gradient algorithm described in [28].
2. In this paper, we will assume that $\alpha_1=0.5$, $\alpha_2=0.5$., K=10.
3. The third step is used to obtain the distributed Lagrange multiplier that enforces rigid body motion inside the particles. This problem is solved by using the conjugate gradient method described in [28,29]. In this step, we account for the electrostatic forces that arise due to the dielectrophoretic effect and the particle-particle interactions.

4 Results

In this section we discuss the numerical results obtained using the above algorithm for the motion of the particles of ER suspensions subjected to a spatially varying electric field. Figure 1*a* shows a typical domain used in our simulations, as well as an initial periodic arrangement of the particles and the coordinate system. The fluid velocity is assumed to be zero on the sidewalls of the domain and periodic along the *z*-direction. The electric field is also assumed to be periodic in the *z*-direction. The electrostatic and hydrodynamic forces include contributions from the periodic images of particles in the *z*-direction. The pressure gradient along the *z*-direction of the channel will be denoted by dp/dz and the *x*-, *y*- and *z*-components of the fluid velocity are referred to as *u*, *v* and *w*, respectively.

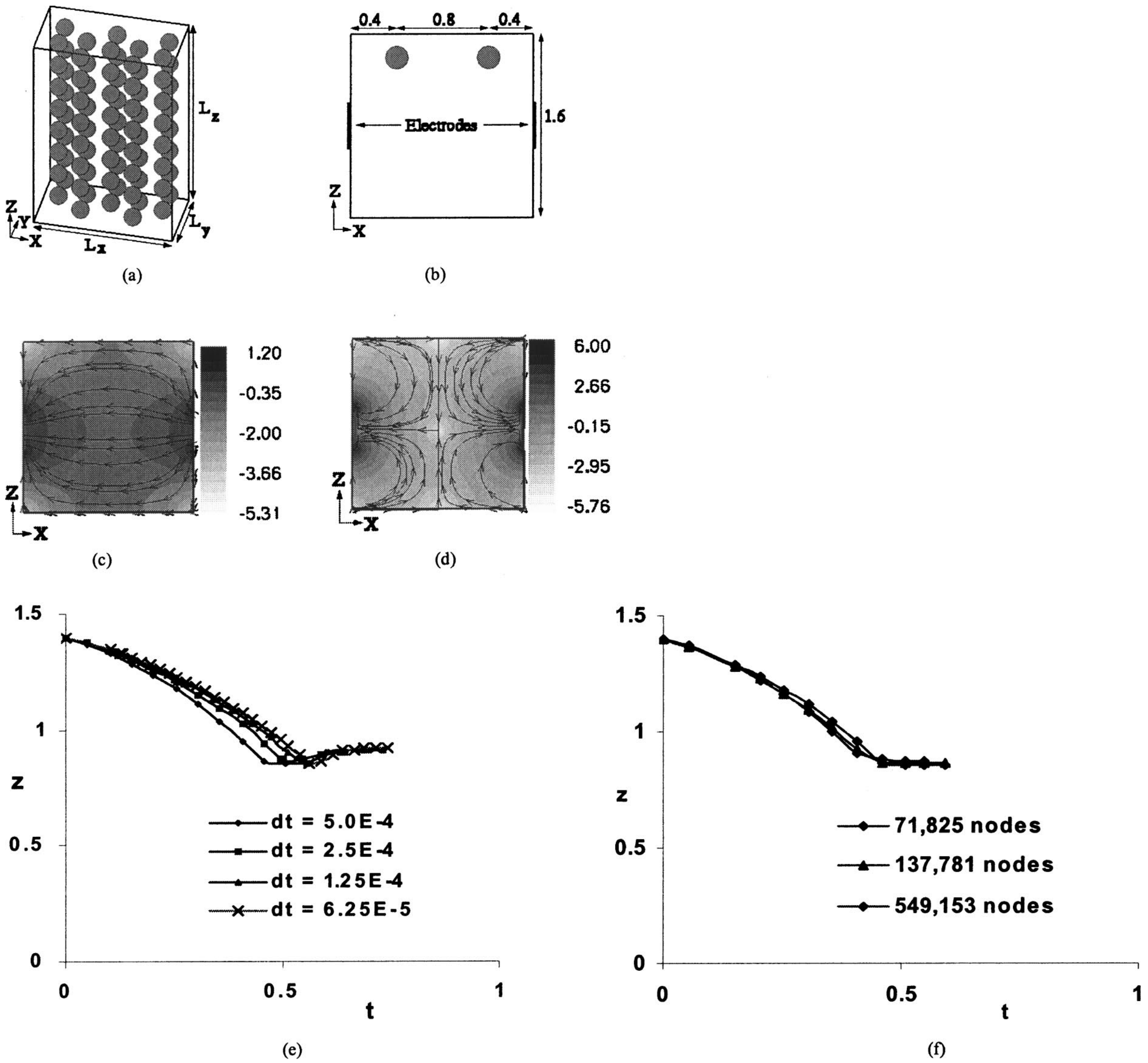

Fig. 1 (*a*) **An oblique view of a typical domain used for simulations.** (*b*) **The domain midsection normal to the y-axis is shown. Also shown are the electrode locations and the initial positions of the two particles. The potential is prescribed on the electrode surfaces and the normal derivative of the potential is assumed to be zero on the rest of the boundary. The velocity is assumed to be periodic in the** *z***-direction and zero on the other domain surfaces.** (*c*) **Isovalues of log(|E|) and the direction of E at the domain midsection are shown. The electric field is maximum on the electrode tips and does not vary with** *y*. (*d*) **Isovalues of log(|E.∇E|) and the lines of dielectrophoretic force are shown. E.∇E does not vary with** *y*. (*e*) **The** *z***-coordinate of the second particle is plotted as a function of time for four different time steps.** (*f*). **The** *z***-coordinate of the second particle plotted as a function of time for three different mesh sizes.**

The nonuniform electric field is generated by placing one or two pairs of electrodes on the domain side walls parallel to the *yz*-coordinate plane. In order to generate a nonuniform electric field the electrodes are made shorter than the side walls so that they do not cover the side walls entirely. The electrodes are so placed that they do not affect the fluid boundary conditions, by embedding them into the side walls. The generated nonuniform electric fields vary at scales comparable to the domain size since the electrodes are separated by distances which are comparable to the length of the electrodes. The width of the electrodes in the *y*-direction is equal to the domain width and hence the electric field does not vary in the *y*-direction. The fluid and particle velocities, and particle-particle interaction forces, however, vary in the *y*-direction.

Throughout this paper, we assume that the dynamic viscosity of the fluid $\eta=1.0$ Poise and the particle diameter is 0.2 mm. The fluid density is $\rho_L=1.0\,\mathrm{g/cm}^3$. The gravity is ignored, as the density of particles is quite close to that of the fluid and the particle diameter is small. The initial fluid and particle velocities are set to zero. The domain is discretized using a regular pseudo P2-P1 tetrahedral mesh, as described in the previous section.

4.1 Convergence.

To show that our results converge with mesh and time step refinements, we consider the transient motion of two particles subjected to the nonuniform electric field shown in Figs. 1*c* and *d*. The applied pressure gradient is assumed to be zero. Notice that even though the pressure gradient is zero, the fluid velocity and the electric field are assumed to be periodic in the *z*-direction, and the electrostatic particle-particle interaction force is computed by accounting for the periodicity.

The domain used in this study is 1.6 mm×0.4 mm×1.6 mm. At $t=0$, two particles with $\beta=0.297$ are placed at (0.4 mm, 0.2 mm, 1.4 mm) and (1.2 mm, 0.2 mm, 1.4 mm) respectively, as shown in Fig. 1*b*. The electric field is generated by placing two 0.4 mm wide electrodes in the domain walls parallel to the yz-coordinate plane, as shown in Fig. 1*b*. The left electrode is grounded and the electric potential for the right electrode is assumed to be 1.0. Isovalues of the electric field magnitude and the magnitude of $\mathbf{E}\cdot\nabla\mathbf{E}$ are shown in Figs. 1*c–d*. The values of dimensionless parameters are: $\mathrm{Re}=0.40$, $P_1=11.1$, $P_2=9.92$, and $P_3=11.1$. The Mason number is 1.12, P_4 is 0.892 and P_5 is 1.0. As the parameters P_2 and P_3 are approximately equal, the electrostatic particle-particle interaction and dielectrophoretic forces acting on the particles are of the same order of magnitude.

The initial positions of the two particles in this case were selected such that the magnitudes of the electrostatic particle-particle interaction force and the dielectrophoretic force are comparable. Thus, once the simulation is started, the particles move toward each other, and at the same time, each one moves towards the electrode closer to it due to the dielectrophoretic force. The particle on the left side moves towards the left electrode and the right side particle moves towards the right electrode. As the distance between the particles and the electrodes decreases, the dielectrophoretic force becomes greater than the electrostatic particle-particle interaction force. This causes the particles to move away from each other and toward the edges of the electrodes where they are collected approximately at $t=0.5$ s.

To show that our results converge when the time step size is reduced, the z-coordinate of the second particle is plotted as a function of time for four different values of the time step: 5×10^{-4} s, 2.5×10^{-4} s, 1.25×10^{-4} s, and 0.625×10^{-4} s (see Fig. 1*e*). The number of velocity nodes for all four cases is 71,825. Since the trajectories for the smallest two time steps are approximately the same, we conclude that the results converge as the time step is reduced.

In order to show that the results also converge with mesh refinement, we performed simulations for three different mesh sizes. The number of velocity nodes for the three cases are 71,825, 137,781, and 549,153, respectively. The time step used for these calculations was 5×10^{-4} s. For the three mesh refinements, the z-coordinate of the second particle is plotted as a function of time in Fig. 1*f*. As the trajectories of the particles for the two finer meshes are approximately the same, we may conclude that the results are also independent of mesh resolution.

4.2 Cases With $dp/dz=0$. In this section, we study the transient motion of 40 particles in a channel subjected to a nonuniform electric field. The pressure gradient in the z-direction for all cases in this subsection is assumed to be zero. The channel dimensions are 1.6 mm, 0.8 mm and 2.4 mm, in the x-, y- and z-directions. The nonuniform electric field is generated by placing two pairs of 0.6 mm wide electrodes in the channel walls parallel to the yz-coordinate plane, as shown in Fig. 2*a*. The direction and magnitude of the electric field and $|\mathbf{E}\cdot\nabla\mathbf{E}|$ are shown in Figs. 2*b–c*. For all results reported in this subsection, a uniform tetrahedral mesh with 208,065 nodes is used and the time step is 5×10^{-4} s. The initial particle and fluid velocities are assumed to be zero. The solids fraction is 0.0545. The values of the other parameters are $\mathrm{Re}=0.40$, $P_1=11.1$, $P_2=9.93$, $P_3=11.1$, $Ma=1.12$, $P_4=0.892$, and $P_5=1.0$. We remind the reader that the parameter $P_5=1.0$ because the characteristic particle velocity used for estimating the dimensionless parameters is obtained by balancing the viscous drag and dielectrophoretic force terms.

As explained earlier, in a nonuniform electric field, the particles are subjected to both the electrostatic particle-particle interaction and the dielectrophoretic forces, and thus their transient motion depends on the magnitudes and directions of both $\mathbf{E}$ and $\mathbf{E}\cdot\nabla\mathbf{E}$. Figure 2*b* shows that in the middle of the domain the electric field is relatively uniform and its direction is horizontal. The magnitude of $\mathbf{E}\cdot\nabla\mathbf{E}$, displayed in Fig. 2*c*, is relatively small near the domain mid plane on which it is zero at three inner points and the top. The bottom is the same as the top due to the periodic nature of the domain. Even though the dielectrophoretic force is zero at these points, the particles cannot accumulate there, since these points are the saddle points. This can also be seen in Fig. 2*b*, which shows that the electric field is not locally minimum at these points. Assuming $\beta>0$, the stable branch of the saddle point in the middle of the domain is horizontal and the unstable branch is vertical. For the two saddle points in between the electrodes the reverse is true, i.e., the stable branches are vertical and the unstable branches are horizontal. The lines of dielectrophoretic force shown in Fig. 2*c* indicate the direction of force for $\beta>0$.

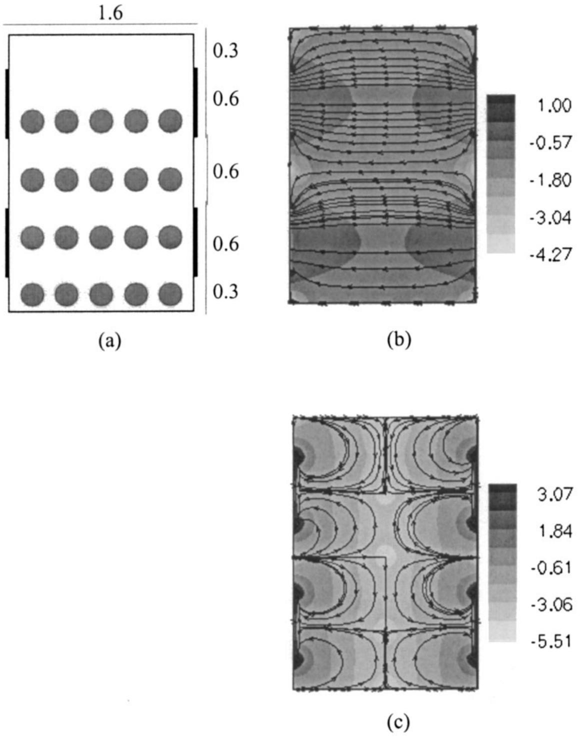

Fig. 2 (*a*) **The initial particle positions, on the midsection normal to the *y*-direction, are shown. The domain dimensions along the *x*-, *y*-, and *z*-directions are 1.6 mm, 0.8 mm, and 2.4 mm, respectively. The potential is prescribed on the electrode surfaces and the normal derivative of the potential is assumed to be zero on the rest of the boundary. The electrodes on the left are grounded, while the electrodes on the right are activated.** (*b*) **Isovalues of the log(|E|) and the direction of E on the domain midsection are shown.** (*c*) **Isovalues of log(|E.∇E|) and the lines of dielectrophoretic force are shown.**

The next two subsections describe the transient motion of the particles and their final positions for positive and negative dielectrophoresis, i.e., $\beta>0$ and $\beta<0$. As mentioned earlier, in the case where $\beta>0$, the particles collect in the regions where the magnitude of electric field is locally maximum, which is generally on the electrode edges, and for $\beta<0$ they collect in the regions where the electric field is locally minimum.

4.2.1 Positive Dielectrophoresis: β Positive. First, we study the case where $\beta=0.297$, i.e., the dielectric constant of the particle is greater than that of the suspending fluid. Initially, the particles are arranged periodically as shown in Fig. 2*a*. There are four rows of particles in the z-direction, which do not cover the entire domain uniformly. The top row is close to the top pair of electrodes, and the third and fourth rows from the top are closer to the second pair of electrodes in the lower half of the domain. The second row from the top is exactly at the center of the domain and equidistant from the lower and upper electrode pairs. There are four layers of particles in the y-direction.

After the simulations are started, the top rows of particles move toward the upper electrode edges, and the third and fourth rows of particles from the top move toward the lower electrode edges,

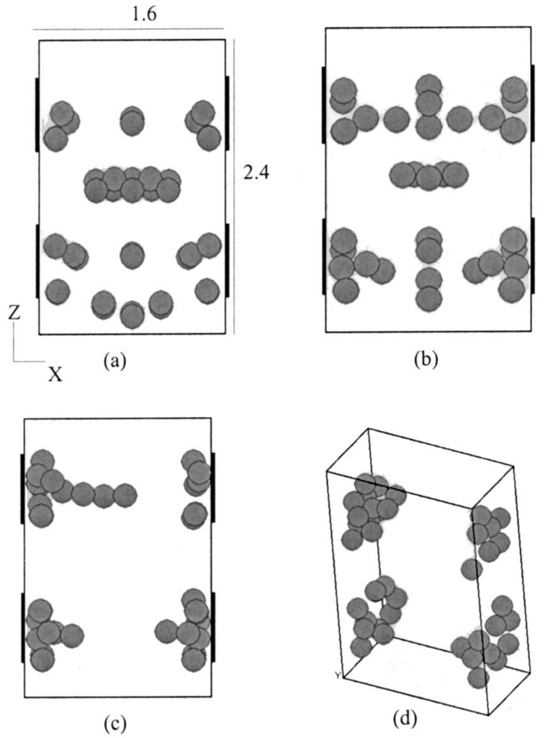

Fig. 3 The top view of the particle distribution for $\beta=+0.297$. (*a*) $t=0.20$ s. The particles get divided into three groups. Those on the left move toward the left electrodes, those on the right move toward the right electrodes and those near the center stay near the center. The particles near the domain center come together and form horizontal chains. (*b*) $t=0.7$ s. Notice that the particles near (x=0.8 mm, z=0.6 mm) and (x=0.8 mm, z=1.8 mm) form vertical chains and the horizontal chain which was at (x=0.8 mm, z=1.2 mm) moves upwards along the unstable branch of the saddle point. (*c*) t=11.0 s. The particle chain, in the upper-left part of the domain, is moving toward the electrode. (*d*) t=13.3 s.

since for these particles, the dielectrophoretic force is greater than the particle-particle interaction force. Also, notice that these rows of particles essentially break into three groups, with particles on the left moving toward the left electrodes, those on the right moving to the right electrodes and those near the middle staying in the middle (see Fig. 3*a* which shows particle positions at $t=0.20$ s). For the second row of particles from the top, since the dielectrophoretic force is small compared to the particle-particle interaction force, they first come close to each other and then move toward the middle of the domain while maintaining their horizontal positions (see Fig. 3*b*).

It is interesting to notice that the particles in different rows along the y-direction initially do not interact with each other, but form separate chains. This is a consequence of the fact that there is no electric field variation in the y-direction and thus the dielectrophoretic force in the y-direction is zero. The particle-particle interaction force in the y-direction is not zero, but for $t<0.20$ s it is small because of the symmetry of the initial particle positions.

As shown in Fig. 3*b*, at $t=0.70$ s the particles that were initially near the domain midplane form chains. The orientation of these chains is determined by the stable and unstable directions of the saddle points of the dielectrophoretic force (see Fig. 2*c*). The chains are parallel to the stable direction of the saddle point and are formed because the particles under the action of the dielectrophoretic force move toward the zeros. Consequently, the chains near the center are horizontal and those near $z=0.6$ mm and 1.8 mm are vertical. Once the chains are formed, the particles remain together in chains because of the electrostatic particle-particle interactions, but continue to move towards the local maximum of the electric field under the influence of the dielectrophoretic force (Fig. 3*c*).

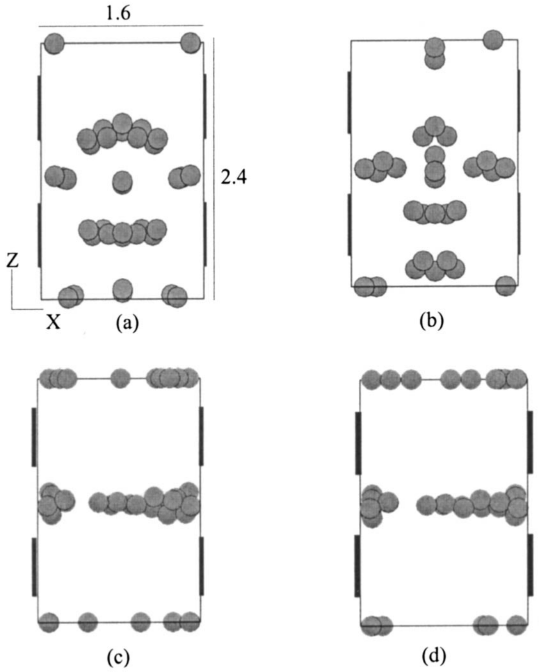

Fig. 4 The top view of the particle distribution for $\beta=-0.297$. (*a*) t=0.2 s. Since $\beta<0$, the particles collect in the regions where the electric field strength is locally minimum, i.e., on the domain walls at the center of the domain and the domain walls at the top and bottom of the domain. (*b*) t=0.85 s. The chains collect in the regions where the electric field strength is locally minimum and that the chains between the lower pair of electrodes are horizontal and those near the domain center are vertical. (*c*) $t\sim12$ s. (*d*) t=16.4 s. There is no noticeable change in the particle structure after t=12 s.

The chains near the domain mid plane experience a dielectrophoretic force which acts along the unstable branches of the saddle points and causes them to slowly move to the regions where the electric field magnitude is locally maximum, that is near the electrode tips. As more and more particles get collected, they start forming chains extending from the edges of the electrodes toward the center of the domain. The simulation was stopped at $t=\sim13.3$ s, as all forty particles are nearly collected. The particle positions at this time are shown in Fig. 3*d*.

4.2.2 Negative Dielectrophoresis: β Negative. We next describe the case where $\beta=-0.297$. All other parameters, including the domain size and the initial particle arrangement, are the same as for the case of positive dielectrophoresis described in the previous subsection.

As expected, the motion of particles in this case, even at early times, is quite different from the case where β is positive. The particles do not move toward the electrode edges, where the electric field strength is locally maximum, but instead move toward the regions where the electric field strength is locally minimum. From Fig. 2*b*, we know that the electric field strength is locally minimum on the domain walls in between the electrodes and at the top and bottom edges of the domain parallel to the xz-plane.

Once the simulations are started, the second row of particles located at the center of the domain move towards the sidewalls at the center and gets collected there around time $t=0.2$ s (see Fig. 4*a*). This is due to the action of the dielectrophoretic force which for $\beta<0$ tends to move the particles away from the domain center along the horizontal branch of the saddle point at the center, which forms the unstable branch for the particles with negative β. The direction of the dielectrophoretic force for $\beta<0$ is the opposite to that shown in Fig. 2*c*. We also recall that the directions of the stable and unstable branches of the dielectrophoretic force saddle points determine the orientation of the particle chains (see Fig. 2*c*). The chains near $z=0.6$ mm and 1.8 mm are horizontal, in contrast to the case corresponding to $\beta>0$ where the chains near these points were vertical.

The particles in the first, third and fourth rows from the top form inter-particle chains and move toward the regions where the electric field strength is locally minimum. Some of the chains move toward the top and bottom edges of the domain while the remaining migrate toward the center part of the domain, as can be seen in Fig. 4*b*. With further increase in time, all particles get collected in regions of low electric field strength at time, $t=12.0$ s (see Fig. 4*c*).

As can be observed from Fig. 4*c*, the particle chains extend from the domain wall to the middle of the domain. The particle-particle interaction force is holding the particles together in chains. With further increase in simulation time, there is no noticeable change in the suspension microstructure (see Fig. 4*d*). The reason for this being, even though the particles are being pulled toward the region of low electric field, all of them cannot accumulate there because of space constraints.

4.3 Cases With $dp/dz\neq 0$.

We next consider the case where a pressure gradient dp/dz is applied to the channel in the z-direction. All other parameters are the same as in the subsection (4.2). The particles in this case are subjected to the hydrodynamic drag force, as well as the electrostatic dielectrophoretic and particle-particle interaction forces.

The particle distribution in pressure driven flows depends on the relative magnitudes of the hydrodynamic and electrostatic forces. Obviously, when the applied pressure gradient is very small, in the sense that the electrostatic forces dominate, the motion of particles is expected to be similar to that in section 4.2. On the other hand, if the applied pressure gradient is sufficiently large, in the sense that the hydrodynamic drag force is much larger than the electrostatic forces, particles will be swept away by the flow. We will investigate the regime in which the magnitudes of the electrostatic and hydrodynamic forces are comparable.

For sufficiently small particle concentrations, the velocity profile in a channel subjected to a pressure gradient is parabolic which implies that the particles near the channel center move faster than those near the channel walls. At higher particle concentrations, the parabolic velocity profile, as well as the dependence of the drag force on the distance from the channel center, is modified. The drag acting on a particle also depends on the particle concentration and their distribution within the channel, which, as we have already seen, is not uniform, especially when the electrostatic forces are strong.

We first present the results for the case where the imposed pressure gradient is 1 dyne/cm^3 and $\beta=0.297$. The pressure driven flow is along the negative *z*-direction. There are 40 particles which are arranged periodically, as shown in Fig. 2*a*. As discussed in section 2, based on the center line velocity of the pressure driven flow, the dimensionless parameters Re, P_1, P_2, P_3, Ma, P_4, and P_5 are 0.32, 13.9, 15.5, 17.4, 0.896, 0.892, and 1.25, respectively. For all cases presented in this subsection, we can alternatively compute the characteristic velocity by balancing the dielectrophoretic force and the viscous drag on the particles, as was done in the previous subsection. But, if this is done, then the dimensionless parameters will have the same values as in section 4.2. Also notice that as P_2 and P_3 are approximately equal, the electrostatic particle-particle interaction and dielectrophoretic forces acting on a particle are of the same order of magnitude.

After the simulations are started, the pressure driven flow gains strength with time and the flow rate becomes steady at $t=\sim 0.45$ s. The hydrodynamic drag due to the flowing liquid moves the particles and particle chains in the downward direction, i.e., along the negative *z*-direction. Here again, the first, third and fourth rows of particles move toward the electrode edges whereas those in the second row form chains parallel to the *x*-direction. All particles, which are on the left and right sides of the domain, get collected near the electrode edges at $t\sim 0.45$ s (see Fig. 5*a*). For the case where the imposed pressure gradient is zero, the particle chains which are formed at the center of the domain, that is the chains formed by the second row of particles, remain parallel to the *x*-direction at all times and the particle chains near the center of the domain are collected by the top electrodes. But, in the present case, the particles near the domain center are pushed down by the pressure driven flow to the regions where they experience a larger downward dielectrophoretic force, especially those away from the domain midplane. This leads to the formation of the chains that are curved concave down, as shown in Fig. 5*b*. The chains continue to move downward with the flow and at $t\sim 0.8$ s some of the particles from the edges of the chains get separated and are collected on the lower pair of electrodes. At $t\sim 1.5$ s, the chains become convex up because of the parabolic flow, as can be seen in Fig. 5*c*.

The velocity of the particles and chains near the electrodes is smaller compared to those away from the electrodes because the fluid velocity near the walls is smaller and the electrostatic forces are stronger near the walls. In fact, the particles and chains close to the electrodes at times even move in the opposite direction of the flow. Most particles are collected near the electrode edges before $t\sim 9.0$ s. Notice that the particle collection time, in this case, is smaller than for the corresponding case with $dp/dz=0$. This, as noticed above, is a result of the fact that the flow assists in the collection of particles by pushing them out of the regions where the dielectrophoretic force is small.

We next present the cases where the pressure gradient is increased to 2 dynes/cm^3. All other parameters are kept fixed. The magnitudes of the parameters Re, P_1, P_2, P_3, Ma, P_4, and P_5 in this case are 0.64, 6.96, 3.88, 4.35, 1.79, 0.892, and 0.626, respectively. Simulations show that the particles are collected in 8.0 s, which is smaller than for the case where the pressure gradient is 1 dyne/cm^3.

Next, we discuss results for the case where the applied pressure gradient is 5 dynes/cm^3. Eighty particles for which $\beta=0.297$ are present in the suspension and are initially arranged in a periodic manner, as shown in Fig. 1*a*. All other parameters are the same as before. The parameters for this case are Re=1.6, $P_1=2.78$, $P_2=0.62$, $P_3=0.697$, $Ma=4.48$, $P_4=0.892$, and $P_5=0.25$. The solids fraction is 0.118.

From Fig. 2*c*, we know that $\mathbf{E}\cdot\nabla\mathbf{E}$ is periodic and that there are regions in the domain where the dielectrophoretic force moves the particles away from the electrodes and other regions where the force moves the particles toward the electrodes. A particle moving along a streamline, therefore, experiences a dielectrophoretic force which, in some regions, tends to move it towards the electrodes and, in the other regions, away from the electrodes.

The initial fluid velocity due to the applied pressure gradient, in this case, is obviously larger and thus the particles that are initially pulled toward the electrodes, cannot stick to the electrodes and, instead, keep moving in the downstream direction. After they enter the region where the dielectrophoretic force acts away from the electrodes, they indeed move away from the electrodes. Two such particles are shown in Figs. 5*d*–*g*. Since the electric field distribution is periodic, the escaped particles can be captured in the next period cell, at a later time, where the dielectrophoretic force acts towards the walls. This, however, increases the time needed for capturing all particles. Our simulations show that even if a particle is not captured, after every cycle its distance from the electrodes decreases, and thus the particle is eventually captured. This process for two particles, painted white, is described in Figs. 5*d*–*g*.

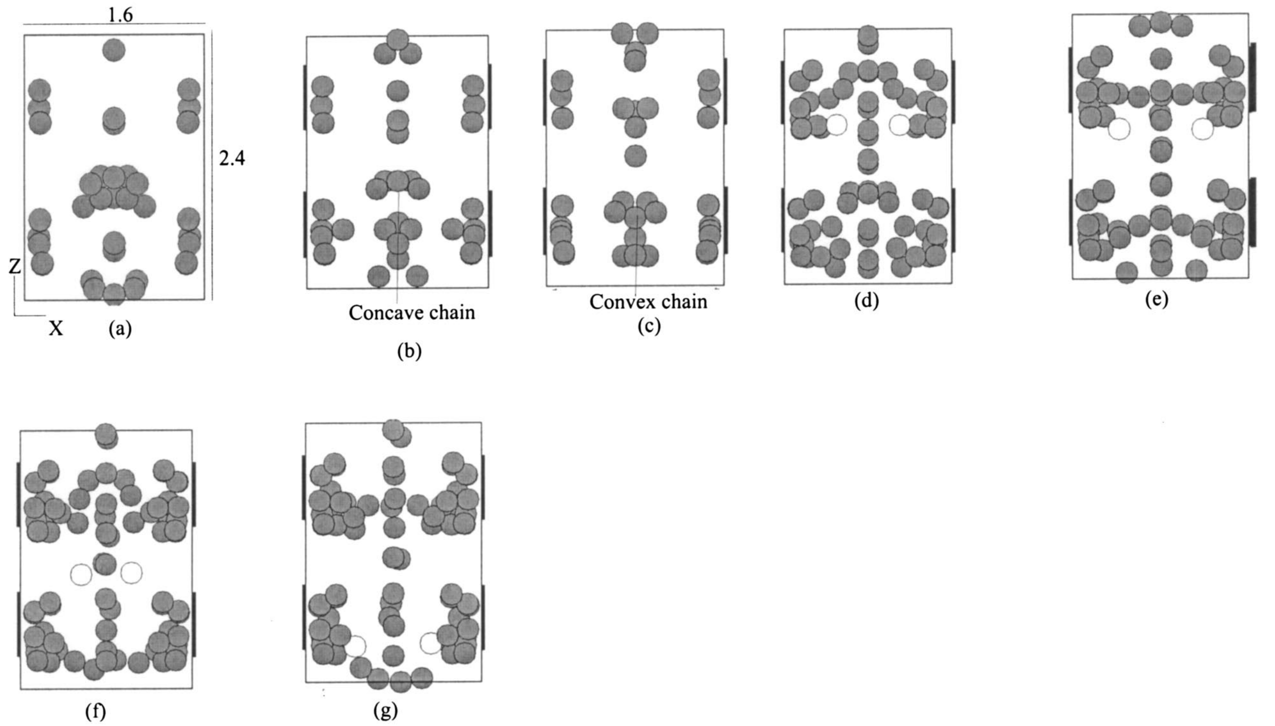

Fig. 5 The top view of the particle distribution for $\beta=0.297$. (*a*) $t=0.45$ s and dp/dz=1 dyne/cm^3. The particles collect near electrodes. (*b*) $t=0.8$ s and dp/dz=1 dyne/cm^3. Notice the curved, concave down chains near the center. (*c*) $t=1.5$ s and dp/dz =1 dyne/cm^3. Notice the curved, convex up chains. (*d*) $t=0.5$ s and dp/dz=5 dynes/cm^3. The white particles close to the electrodes were collected in the case of small or no pressure gradient flow described before. (*e*) $t=1.0$ s and dp/dz=5 dynes/cm^3. The white particles are pushed downstream by the flow. (*f*) $t=1.40$ s and $dp/dz=5$ dynes/cm^3. The white particles are moving away from the electrodes, while getting closer to each other because of interparticle attraction and the dielectrophoretic force, which in this region pushes them toward the domain center. (*d*) $t=2.0$ s and dp/dz=5 dynes/cm^3. The white particles are now captured by the lower electrodes.

Also notice that the captured particles form chains that extend from the electrodes and the chains are more obvious than in the case of zero pressure gradient $dp/dz=0$ because the captured particles experience a hydrodynamic force which pushes them downwards while the particle-particle interaction force keeps them attached, leading to more apparent chains.

We next describe the case where the pressure gradient is 10 dynes/cm^3. The parameters Re, P_1, P_2, P_3, Ma, P_4, and P_5 are 3.2, 1.39, 0.155, 0.174, 8.96, 0.892, and 0.125, respectively. The remaining parameters are the same as for the previous case. Since the hydrodynamic force in this case is stronger, the effect of the electrostatic force is felt only on the particles that are close to the electrodes. In particular, simulations show that the particles close to the electrodes decelerate when they are in the regions where the dielectrophoretic force acts against the flow direction. The dielectrophoretic force, however, is not strong enough to overcome the hydrodynamic drag and capture all the particles. The particles that are farther away from the electrodes move approximately along the undisturbed streamlines of the pressure driven flow.

5 Conclusions

This is the first direct simulation study of electrorheological suspensions subjected to spatially nonuniform electric fields. In our numerical scheme the fluid and particle equations of motion are combined into a single combined weak equation of motion, eliminating the hydrodynamic forces and torques, which helps ensure the stability of the time integration scheme. The distributed Lagrange multiplier method (DLM) [28,29] is used to constrain the flow inside particle boundaries to be rigid body motion while the electrostatic forces acting on the polarized particles are obtained using the point-dipole approximation [13]. The numerical scheme is verified by performing a convergence study which shows that the results are independent of both the mesh and time step sizes. Simulations show that the particles with $\beta>0$ collect in the regions where the magnitude of the electric field is locally maximum, whereas the particles with $\beta<0$ collect in the regions where the magnitude of the electric field is locally minimum. The dielectrophoretic effect thus can be used to separate mixtures containing two sets of particles for which the sign of β is different. For relatively small applied pressure gradients, the bulk flow induced by the applied pressure gradient assists in the collection of particles by pushing them out of the regions where the dielectrophoretic force is small. However, when the applied pressure gradient is sufficiently large, the flow prevents particles from being collected.

Acknowledgments

We gratefully acknowledge the support of the National Science Foundation KDI Grand Challenge grant (NSF/CTS-98-73236), the New Jersey Commission on Science and Technology through the New-Jersey Center for Micro-Flow Control under Award Number 01-2042-007-25, the W. M. Keck Foundation for providing support for the establishment of the NJIT Keck laboratory for Electrohydrodynamics of Suspensions and the support of the Office of Naval Research under Award Number 992294.

Nomenclature

a = radius of particle
$\mathbf{E}$ = applied electric field
E_0 = magnitude of uniform electric field
$\mathbf{F}_{\mathrm{D}}$ = particle-particle electrostatic interaction force
$\mathbf{F}_{\mathrm{DEP}}$ = Dielectrophoretic force
$\mathbf{g}$ = acceleration due to gravity
h' = ratio of domain width and particle radius
I = moment of inertia of the particle
i, j = particle indices
L = width of the domain used for computation
m = mass of the particle
Ma = mason number
p = pressure
$\mathbf{p}$ = polarization of particle
P_1 = ratio of viscous and inertia forces
P_2 = ratio of electrostatic particle-particle interaction and viscous forces
P_3 = ratio of dielectrophoretic and viscous forces
P_4 = ratio of particle-particle interaction and dielectrophoretic forces
P_5 = ratio of dielectrophoretic and viscous forces
r = distance between particles
Re = Reynolds number
Re_L = Reynolds number based on domain width
t = time
$\mathbf{U}$ = velocity of the particle
$\mathbf{u}$ = velocity of the fluid
x, y, z = coordinate axes
β = Real part of the Clausius-Mossotti factor
ε_c = dielectric constant of liquid
ε_p = dielectric constant of particle
ε_0 = permittivity of vacuum
η = dynamic viscosity of the fluid
φ = electric potential
ρ_L = density of the fluid
$\boldsymbol{\omega}$ = angular velocity of the particle

References

[1] Winslow, M. W., 1949, ''Induced Fibration of Suspensions,'' J. Appl. Phys., **20**, pp. 1137–1140.
[2] Jones, T. B., 1995, ''Electromechanics of Particles,'' Cambridge University Press, New York City, NY.
[3] Pohl, H. A., 1978, ''Dielectrophoresis,'' Cambridge University Press, Cambridge.
[4] Klass, D. L., and Martinek, T. W., 1967, ''Electroviscous Fluids. II. Electrical Properties,'' J. Appl. Phys., **38**, pp. 75–80.
[5] Uejima, H., 1972, ''Dielectric Mechanism and Rheological Properties of Electrofluids,'' Japanese Journal of Applied Physics, **11**, pp. 319–326.
[6] Stangroom, J. E., 1991, ''Basic Considerations in Flowing Electrorheological Fluids,'' J. Stat. Phys., **64**, pp. 1059–1072.
[7] Stangroom, J. E., 1996, ''Basic Observations on Electrorheological Fluids,'' J. Intell. Mater. Syst. Struct., **7**, pp. 479–483.
[8] Marshall, L., Goodwin, J. W., and Zukoski, C. F., 1989, ''Effects of Electric Fields on the Rheology of Nonaqueous Concentrated Suspensions,'' Journal of Chemical Society Faraday Transactions I, **85**, pp. 2785–2795.
[9] Gast, A. P., and Zukoski, C. F., 1990, ''Electrorheological Fluids as Colloidal Suspensions,'' Adv. Colloid Interface Sci., **30**, pp. 153–202.
[10] Zukoski, C. F., 1993, ''Material Properties and the Electrorheological Response,'' Annu. Rev. Mater. Sci., **23**, pp. 45–78.
[11] Anderson, R. A., 1994, ''Electrostatic Forces in an Ideal Spherical-Particle Electrorheological Fluid,'' Langmuir, **10**, pp. 2917–2928.
[12] Klingenberg, D. J., van Swol, S., and Zukoski, C. F., 1991, ''The Small Shear Rate Response of Electrorheological Suspensions. I. Simulation in the Point-Dipole Limit,'' J. Chem. Phys., **94**, pp. 6160–6167.
[13] Klingenberg, D. J., van Swol, S., and Zukoski, C. F., 1989, ''Simulation of Electrorheological Suspensions,'' J. Chem. Phys., **91**, pp. 7888–7895.
[14] Klingenberg, D. J., Zukoski, C. F., and Hill, J. C., 1993, ''Kinetics of Structure Formation in Electrorheological Suspensions,'' J. Appl. Phys., **73**, pp. 4644–4648.
[15] Bonnecaze, R. T., and Brady, J. F., 1992, ''Yield Stresses in Electrorheological Fluids,'' J. Rheol., **36**, pp. 73–115.
[16] Bonnecaze, R. T., and Brady, J. F., 1992, ''Dynamic Simulation of an Electrorheological Suspension,'' J. Chem. Phys., **96**, pp. 2183–2204.
[17] Brady, J. F., and Bossis, G., 1988, ''Stokesian Dynamics,'' Annu. Rev. Fluid Mech., **20**, pp. 111–157.
[18] Brady, J. F., Phillips, R. J., Lester, J. C., and Bossis, G., 1988, ''Dynamic Simulation of Hydrodynamically Interacting Suspensions,'' J. Fluid Mech., **195**, pp. 257–280.
[19] Davis, L. C., 1992, ''Polarization Forces and Conductivity Effects in Electrorheological Fluids,'' J. Appl. Phys., **72**, pp. 1334–1340.
[20] Wang, X., Wang, Xiao-Bo, and Gascoyne, P. R. C., 1997, ''General Expressions for Dielectrophoretic Force and Electrorotational Torque Derived Using the Maxwell Stress Tensor Method,'' J. Electrost., **39**, pp. 277–295.
[21] Dussaud, A. D., Khusid, B., and Acrivos, A., 2000, ''Particle Segregation in Suspensions Subject to High-Gradient ac Electric Fields,'' J. Appl. Phys., **88**, pp. 5463–5473.
[22] Green, N. G., Ramos, A., and Morgan, H., 2002, ''Numerical Solution of the Dielectrophoretic and Traveling Wave Forces for Interdigitated Electrode Arrays Using the Finite Element Method,'' J. Electrost., **56**, pp. 235–254.
[23] Heida, T., Rutten, W. L. C., and Marani, E., 2002, ''Understanding Dielectrophoretic Trapping of Neuronal Cells: Modelling Electric Field, Electrode-Liquid Interface and Fluid Flow,'' J. Phys. D, **35**, pp. 1592–1602.
[24] Jones, T. B., and Washizu, M., 1996, ''Multipolar Dielectrophoretic and Electrorotation Theory,'' J. Electrost., **37**, pp. 121–134.
[25] Ramos, A., Morgan, H., Green, N. G., and Castellanos, A., 1999, ''The Role of Electrohydrodynamic Forces in the Dielectrophoretic Manipulation and Separation of Particles,'' J. Electrost., **47**, pp. 71–81.
[26] Khusid, B., and Acrivos, A., 1996, ''Effects of Interparticle Electric Interactions on Dielectrophoresis in Colloidal Suspensions,'' Physics Review E, **54**, pp. 5428–5435.
[27] Kadaksham, J., Singh, P., and Aubry, N., ''Dynamics of Particles in Electrorheological Fluids Subjected to Dielectrophoretic Forces,'' To be submitted to J. of Fluids Eng.
[28] Glowinski, R. T., Pan, W., Hesla, T. I., and Joseph, D. D., 1998, ''A Distributed Lagrange Multiplier/Fictitious Domain Method for Particulate Flows,'' Int. J. Multiphase Flow, **25**, pp. 755–794.
[29] Singh, P., Joseph, D. D., Hesla, T. L., Glowinski, R. T., and Pan, W., 2000, ''A Distributed Lagrange Multiplier/Fictitious Domain Method for Particulate Flows,'' J. Non-Newtonian Fluid Mech., **91**, pp. 165–188.

A Kinetic Theory for Solutions of Nonhomogeneous Nematic Liquid Crystalline Polymers With Density Variations

Qi Wang
Department of Mathematics
Florida State University
Tallahassee, FL 32306-4510

M. Gregory Forest
Department of Mathematics
The University of North Carolina at Chapel Hill
Chapel Hill, NC 27599

Ruhai Zhou
Department of Mathematics
The University of North Carolina at Chapel Hill
Chapel Hill, NC 27599

The kinetic theory developed in [1] for solutions of nonhomogeneous nematic liquid crystalline polymers (LCPs) of spheroidal molecular configurations is extended to account for the translational diffusion and the related spatial density variation. The new theory augments the effect of the density variation to the intermolecular potential, Smoluchowski equation and the elastic stress. It accounts for the molecular aspect ratio as well as the finite range molecular interaction so that it is applicable to liquid crystals ranging from rodlike liquid crystals at large aspect ratios to discotic ones at small aspect ratios. It also exhibits enhanced shape effects in the viscous stress and warrants a positive entropy production, thereby, the second law of thermodynamics. Moment averaged, approximate, mesoscopic theories for complex flow simulations are obtained via closure approximations. In the limit of weak distortional elasticity, weak translational diffusion, and weak flows, the theory yields the torque balance equation of the well-known Ericksen-Leslie theory. [DOI: 10.1115/1.1669031]

1 Introduction

Nematic phase in liquid crystals (LCs) is the simplest mesophase in which an orientational order exists, but there is no translational order [2,3]. The simple mesophase can be formed by polymer molecules of a variety of molecular configurations at certain concentration or temperature, which include two drastically different configurations: rodlike and discotic liquid crystals.

Most of the hydrodynamical theories formulated for flows of liquid crystal materials are based on rodlike molecules, which include the celebrated Ericksen-Leslie (LE) theory [4], suitable to low molar weight liquid crystals, the Doi kinetic theory [5] and a variety of tensor based theories such as the Hand's theory [6] for homogeneous LCs, Beris and Edwards' (BE) theory formulated through Poisson brackets [7], and Tsuji and Rey's (TR) phenomenological theory [8], both for nonhomogeneous LCs, perceived to be applicable to high molar weight liquid crystalline polymers (LCPs). Although the LE theory was first developed for rodlike liquid crystals, it has also been applied to discotic liquid crystals [9,10]. Recently, Singh and Rey used the TR theory to model homogeneous flows of discotic liquid crystalline polymers by reversing the sign of a phenomenological "shape parameter" and showed some promising results [11]. This approach appears to be not only convenient, but also reasonable from a molecular point of view. The kinetic theory for spheroidal liquid crystal polymers developed in [1] aimed at establishing a unified theory for rodlike and disklike LCPs, thus, providing a rigorous justification for the convenient practice and relating the macroscopic parameters to the microscopic ones.

In the theory, the LCP molecules are modelled as rigid spheroids of equal size so that the theory could be used to model a series of configurations of polymeric liquid crystal molecules in the neighborhood of spheroids. This approach has been undertaken by several pioneers in the past. Isihara studied the effect of the spheroidal shape on the phase transition behavior of colloidal solutions [12]. J-L Colot et al. proposed a density functional theory for the isotropic-nematic transition of hard ellipsoids [13]. Takserman-Krozer and Ziabicki studied the behavior of polymer solutions in a velocity field by treating polymer molecules as rigid ellipsoids in dilute solutions [14]. In Helfrich's molecular theory for nematic liquid crystals, the molecules are treated as equally and rigidly oriented ellipsoids [15]. In an effort to address the relationship between the Doi kinetic theory and the Ericksen-Leslie theory, Kuzuu and Doi generalized the Doi theory for homogeneous LCPs to account for the finite aspect ratio of spheroidal molecules [16] and gave the Leslie viscosity coefficients in terms of the uniaxial order parameter and a few physical parameters in the molecular theory, including the aspect ratio of the spheroid. Baalss and Hess also treated liquid crystal molecules as spheroids in their liquid crystal theory [17]. Baalss and Hess' theory predicts the liquid crystal is always flow aligning which has since been proven to be limited since tumbling has been observed in many LC flows. On the other hand, the Kuzuu and Doi theory handles both flow aligning and tumbling at different aspect ratios and polymer concentrations.

The theory developed in [1] extends the Kuzuu and Doi theory to flowing systems of nonhomogeneous liquid crystalline polymers by considering the long range elastic interaction through an extended anisotropic intermolecular potential. It also generalizes the existing Marrucci-Greco theory to a series of spheroidal LCP configurations through a shape related parameter. However, the translational diffusion was neglected in the study for highlighting the effect of the molecular shape and the anisotropic elasticity in that paper. As we all know, however, that the spatial nonhomogeneous structure of LCPs correlates to the translational diffusion of LCP molecules. So, for completeness, a theory for flows of nonhomogeneous LCPs must account for the translational diffusion. This paper addresses the additional effect of the translational diffusion to the previous theory to explore the impact of the translational diffusion and the related density variation to the intermolecular potential, Smoluchowski equation, and the stress tensor.

It is shown in [1] that the torque balance equation of the Ericksen-Leslie theory can be recovered from the kinetic theory in the limit of weak flow and weak distortional elasticity while translation diffusion is neglected. In this paper, we will show the same torque balance equation can be derived from the theory only when

---

Contributed by the Fluids Engineering Division for publication in the JOURNAL OF FLUIDS ENGINEERING. Manuscript received by the Fluids Engineering Division December 4, 2002; revised manuscript received August 28, 2003. Associate Editor: D. Siginer.

the translational diffusion is weak. When translational diffusion competes at the same order with the rotary diffusion, the current theory yields a torque balance equation with up to fourth-order spatial derivatives, which is indeed an extension of the Ericksen-Leslie theory where only up to second derivatives are included.

The rest of the paper consists of the derivation of the intermolecular potential, the Smoluchowski equation, the elastic stress tensor, the proof of the second law of thermodynamic theory and the reduction to Ericksen-Leslie torque balance equation.

2 Kinetic Theory for LCPs of Spheroidal Molecules

We first extend the intermolecular potential developed in [1], which models the intermediate to long range molecular interaction for liquid crystalline polymers of the spheroidal configuration with finite aspect ratios, to account for the density variation in LCPs and derive one of its approximations through the gradient expansion of the number density function (defined below) [18]. Then, we extend the Smoluchowski equation in the Doi kinetic theory for rodlike LCPs to accommodate the spheroidal shape of the liquid crystalline polymer and translational diffusion, and derive a consistent stress expression using the virtual work principle [3,5]. Finally, we prove the theory satisfies the second law of thermodynamics in isothermal conditions.

2.1 Intermolecular Potential. We assume all LCP molecules are of the same spheroidal configuration and immersed in viscous solvent. With the axis of revolution of the spheroid identified with the z-axis in the Cartesian coordinate (x,y,z), the surface of the spheroid is represented by:

$$x=c\sin\alpha\cos\beta,\quad y=c\sin\alpha\sin\beta,\quad z=b\cos\alpha,$$
$$0\leqslant\alpha\leqslant\pi,\quad 0\leqslant\beta<2\pi, \tag{1}$$

where b is the length of the semi-axis in the axis of revolution (identified with $\mathbf{e}_z$ now) and c is that in the transverse direction. The aspect ratio of the spheroid is then defined as

$$r=\frac{b}{c}. \tag{2}$$

Often, we use a shape parameter defined by

$$a=\frac{r^2-1}{r^2+1} \tag{3}$$

with range $-1\leqslant a\leqslant 1$. $a=1,\ 0,\ -1$ correspond to an infinitely thin rod, a sphere and an infinitely thin disk, respectively.

Let $f(\mathbf{m},\mathbf{x},t)$ be the number density function (ndf) of the LCP molecules of the spheroidal shape in their axis of revolution $\mathbf{m}$ ($\|\mathbf{m}\|=1$) with center of mass at location $\mathbf{x}$ and time t. We assume for a nonhomogeneous spheroidal LCP system that the intermolecular potential is given by a mean field accounting for the finite range molecular interaction. Based on this, we proposed an intermolecular potential in [1]

$$V_i(\mathbf{m})=\frac{kT}{|S||dV|}\int_S\int_{dV}\int_{\|\mathbf{m}'\|=1}B(\mathbf{m},\mathbf{m}')f(\mathbf{m}',\mathbf{x}+\mathbf{s}+\mathbf{r},t)\,d\mathbf{m}'\,d\mathbf{r}\,d\mathbf{s}, \tag{4}$$

where $\nu=\int_{\|\mathbf{m}\|=1}f(\mathbf{m},\mathbf{x},t)d\mathbf{m}$ is the number density of the LCP molecule per unit volume at material point $\mathbf{x}$ and time t, the excluded volume formula is given by

$$B(\mathbf{m},\mathbf{m}')=2v+2c^2br\int_0^{\pi}\int_0^{2\pi}\frac{\sqrt{(\sin^2\alpha+r^2\cos^2\alpha)}}{(\sin^2\theta'+r^2\cos^2\theta')^2}\sin\alpha\,d\alpha\,d\beta, \tag{5}$$

in which v is the volume of the spheroidal LCP with the semi-axes (b, c) [12], S is the surface of the spheroid with the axis of revolution $\mathbf{m}$, $|S|$ is the surface area of S, $\mathbf{s}$ is the vector initiated at the origin and ended at S, dV is a sphere of radius l centered at $\mathbf{0}$,

$$\cos\theta'=\mathbf{w}\cdot\mathbf{m}',$$
$$\mathbf{w}=\cos\alpha\mathbf{m}+\sin\alpha\cos\beta\mathbf{e}_1+c\sin\alpha\sin\beta\mathbf{e}_2, \tag{6}$$

with $\mathbf{e_1}$ and $\mathbf{e_2}$ the two orthonormal vectors perpendicular to $\mathbf{m}$, $|dV|$ denotes the volume of dV, $\mathbf{r}$ is the position vector for points inside dV, k is the Boltzmann constant and T is the absolute temperature. We note that $\mathbf{w}$ is the unit normal of the tangent plane at the contacting point of the two spheroidal molecules of the axis of revolution $\mathbf{m}$ and $\mathbf{m}'$, respectively, and parameterized relative to $\mathbf{m}$.

The intermolecular potential defined by (4) is nonlocal. In particular, the excluded volume given in (5) is too complicated for a hydrodynamical theory of liquid crystals to be used for complex flow simulations. We thus seek an approximate excluded volume expression that would lead to a less complex intermolecular potential.

We seek the Legendre polynomial expansion of the excluded volume (5),

$$B(\mathbf{m},\mathbf{m}')=2v+B_0(r)-\sum_{l=1}^{\infty}B_l(r)P_{2l}(\cos\angle\mathbf{mm}'), \tag{7}$$

in which $\angle\mathbf{mm}'$ is the angle between $\mathbf{m}$ and $\mathbf{m}'$. The first two coefficients B_0 and B_1 are given in the work of Isihara [12],

$$B_0=2\pi bc^2r\left[\frac{1}{r}+\frac{r}{\sqrt{r^2-1}}\arcsin\left(\frac{\sqrt{r^2-1}}{r}\right)\right]\left[1+\frac{1}{2r\sqrt{r^2-1}}\ln\left(\frac{r+\sqrt{r^2-1}}{r-\sqrt{r^2-1}}\right)\right],$$

$$B_1=8\pi c^2brh_3(r)h_4(r),$$

$$h_3=\frac{1}{4}\left[\frac{\arcsin(\sqrt{1-r^2})}{\sqrt{1-r^2}}-\frac{3\arcsin(\sqrt{1-r^2})}{4\sqrt{1-r^{23}}}+\frac{3r}{4(1-r^2)}-\frac{r}{2}\right], \tag{8}$$

$$h_4=\frac{5}{2}\left[\frac{3}{2(1-r^2)}+1+\frac{1-r^2}{r^2}-\frac{1}{4\sqrt{1-r^2}}\times\left(1+\frac{3}{1-r^2}\right)\ln\frac{1+\sqrt{1-r^2}}{1-\sqrt{1-r^2}}\right].$$

Note that

$$\cos^2\angle\mathbf{mm}'=(\mathbf{m}\cdot\mathbf{m}')^2=\mathbf{mm}:\mathbf{m}'\mathbf{m}', \tag{9}$$

where $\mathbf{mm}$ is the outer (tensor) product of $\mathbf{m}$ with $\mathbf{m}$, "$\cdot$" denotes the contraction operation between two tensors over a pair of indices. In this paper, the number of dots in tensor operations denotes the number of pairs of indices contracted therein. If we truncate series expansion (7) at the second order, the excluded volume is approximated by

$$B(\mathbf{m},\mathbf{m}')\approx 2v+B_0(r)+\frac{B_1(r)}{2}-\frac{3}{2}B_1(r)\mathbf{mm}:\mathbf{m}'\mathbf{m}'. \tag{10}$$

With this, we arrive at an approximate intermolecular potential

$$V_i \approx kT\left(2v+B_0(r)+\frac{B_1(r)}{2}\right)\frac{1}{|dV||S|}\int_S\int_{dV}\int_{\|\mathbf{m}'\|=1} f(\mathbf{m}',\mathbf{x}+\mathbf{s}+\mathbf{r},t)\,d\mathbf{m}'\,d\mathbf{r}\,d\mathbf{s} - \frac{3}{2}kTB_1\mathbf{mm}:\left[\frac{1}{|dV\|S|}\int_S\int_{dV}\int_{\|\mathbf{m}'\|=1}\mathbf{m}'\mathbf{m}' f(\mathbf{m}',\mathbf{x}+\mathbf{s}+\mathbf{r},t)\,d\mathbf{m}'\,d\mathbf{r}\,d\mathbf{s}\right], \tag{11}$$

which extends the intermolecular potential derived in [1] to account for the spatial variation of the ndf. The Legendre polynomial approximation up to the quadratic order given in (10) turns out to be an excellent approximation to (5) for all values of r as shown in [1].

Following Marrucci and Greco's approach [18], we expand the number density function $f(\mathbf{m}',\mathbf{x}+\mathbf{s}+\mathbf{r},t)$ at $\mathbf{x}$ in its Taylor series,

$$f(\mathbf{m}',\mathbf{x}+\mathbf{s}+\mathbf{r},t)=f(\mathbf{m}',\mathbf{x},t)+\nabla f\cdot(\mathbf{s}+\mathbf{r}) + \frac{1}{2}\nabla\nabla f:(\mathbf{s}+\mathbf{r})(\mathbf{s}+\mathbf{r})+\cdots, \tag{12}$$

where ∇ is the gradient operator and the derivatives are evaluated at $(\mathbf{m}',\mathbf{x},t)$. Neglecting the terms higher than the second order, we obtain a simplified intermolecular potential for spheroidal LCPs,

$$V_{si}=AkT\left(1+\left(\frac{l^2}{10}+\frac{L_1^2}{8}\right)\Delta+\frac{L_2-L_1}{8}\mathbf{mm}:\nabla\nabla\right)\nu-\frac{3NkT}{2}\left[\mathbf{I} + \left(\frac{l^2}{10}+\frac{L_1}{8}\right)\Delta+\frac{L_2-L_1}{8}\mathbf{mm}:\nabla\nabla\right]\langle\mathbf{mm}\rangle:\mathbf{mm}, \tag{13}$$

where

$$A=\left(2v+B_0(r)+\frac{B_1(r)}{2}\right),$$

$$N=B_1(r),$$

$$D_1=1+\frac{r^2}{1-r^2}\,arcsinh\left(\frac{\sqrt{1-r^2}}{r}\right), \tag{14}$$

$$L_1=\frac{2bc}{r}-\frac{L_2}{2r^2},$$

$$L_2=\frac{2bcr}{D_1}\left[\frac{1}{1-r^2}-\frac{r^2}{2(1-r^2)}-\frac{r^4}{2(1-r^2)^{3/2}}\,arcsinh\left(\frac{1-r^2}{r}\right)\right],$$

$$\Delta=\nabla\cdot\nabla,\quad (\text{Laplacian}).$$

The bracket $\langle\ \rangle$ denotes an average over all possible molecular directions at $(\mathbf{x},t)$ with respect to the number density function f:

$$\langle(\bullet)\rangle=\int_{\|\mathbf{m}\|=1}(\bullet)f(\mathbf{m},\mathbf{x},t)\,d\mathbf{m}. \tag{15}$$

Following [1,18], we introduce two new parameters $\mathcal{L}$ and L, of the unit of length, to denote the finite range of molecular interaction:

$$\mathcal{L}=\sqrt{24\left[\frac{l^2}{10}+\frac{L_1}{8}\right]},\quad L=\sqrt{3(L_2-L_1)}. \tag{16}$$

$\mathcal{L}$ measures the strength of the long-range, isotropic elasticity while $|L|$ quantifies the anisotropic elasticity. In our definition of the intermolecular potential, we note that $\mathcal{L}$ is always positive even when the length parameter l is assigned zero in (16). Then,

$$V_{si}=AkT\left(1+\frac{\mathcal{L}^2}{24}\Delta+\frac{L^2}{24}\mathbf{mm}:\nabla\nabla\right)\nu-\frac{3NkT}{2}\left(\mathbf{I}+\frac{\mathcal{L}^2}{24}\Delta + \frac{L^2}{24}\mathbf{mm}:\nabla\nabla\right)\langle\mathbf{mm}\rangle:\mathbf{mm}. \tag{17}$$

The first term in (17) corresponds to the short and long range elastic effect caused by the spatial variation of the number density. Both A and N approach ∞ as $|a|\rightarrow 1^-$ and N equals zero at $a=0$ since $B_1(r=1)=0$. The behavior of N as a function of a indicates that the strength of the intermolecular potential weakens as $|a|$ decreases for spheroidal molecules with fixed volumes and constant polymer number density [1]. The details for the dependence of the parameters on a are given in [1]. The behavior of A and N is consistent with the approximate excluded formula derived by Colot et al. using the Gaussian overlap method [13].

Free energy and the symmetric, effective intermolecular potential. Let's denote a finite volume of the LCP material by G in R^3. The free energy for the volume of LCPs is then given by [5,16]

$$A[f]=kT\int_G\int_{\|\mathbf{m}\|=1}\left[f\ln f-f+V_Hf+\frac{1}{2kT}fV_{si}\right]d\mathbf{m}d\mathbf{x}, \tag{18}$$

where V_H is the potential for the external field. Through integration by part, the free energy can be rewritten into

$$A[f]=kT\int_G\int_{\|\mathbf{m}\|=1}\left[f\ln f-f+V_Hf+\frac{1}{2kT}fV_{ei}\right]d\mathbf{m}d\mathbf{x} + \frac{AkTL^2}{48}\left[\int_{\partial G}[(\mathbf{M}\cdot\nabla\nu-\nu\nabla\cdot\mathbf{M})\cdot\mathbf{n}_n]ds - \frac{NkTL^2}{32}\int_{\partial G}[(\mathbf{M}_4\,\vdots\,\nabla\mathbf{M})\cdot\mathbf{n}_n-(\nabla\cdot\mathbf{M}_4)\,\vdots\,\mathbf{M}\mathbf{n}_n]ds,\right. \tag{19}$$

where $\mathbf{n}_n$ is the external unit normal of ∂G, the boundary of G, and

$$V_{ei}=AkT\left[\left(1+\frac{\mathcal{L}^2}{24}\Delta+\frac{L^2}{48}\mathbf{mm}:\nabla\nabla\right)\nu+\frac{L^2}{48}\nabla\nabla:\mathbf{M}\right] - \frac{3NkT}{2}\left[\left(\mathbf{I}+\frac{\mathcal{L}^2}{24}\nabla\right)\mathbf{M}:\mathbf{mm} + \frac{L^2}{48}(\mathbf{mmmm}::\nabla\nabla\mathbf{M}+\mathbf{mm}\nabla\nabla::\mathbf{M}_4)\right],$$

$$\mathbf{M}=\langle\mathbf{mm}\rangle,\quad \mathbf{M}_4=\langle\mathbf{mmmm}\rangle, \tag{20}$$

$\mathbf{M}$ and $\mathbf{M}_4$ are the second and fourth moments of $\mathbf{m}$ with respect to the ndf f, respectively. Neglecting the contribution from the surface integrals, we conclude that the contribution of V_{ei} to the bulk free energy is equivalent to that of V_{si}. We therefore name it the effective intermolecular potential. With V_{ei}, the chemical potential is calculated as usual:

$$\mu=\frac{\delta A}{\delta f}=kT\ln f+V_{ei}+kTV_H. \tag{21}$$

We remark that the symmetrization of the intermolecular potential is essential for a well-posed hydrodynamic theory, in which the positive entropy production and therefore the second law of thermodynamics is warranted. Next, we derive the Smoluchowski equation for the ndf f consistent with the spheroidal LCPs.

2.2 Smoluchowski Equation (Kinetic Equation). For a rigid spheroidal suspension in a viscous solvent, Jeffrey calculated the velocity of its axis of revolution $\mathbf{m}$ as follows [19]:

$$\dot{\mathbf{m}}=\mathbf{\Omega}\cdot\mathbf{m}+a[\mathbf{D}\cdot\mathbf{m}-\mathbf{D}:\mathbf{mmm}], \tag{22}$$

where, $\mathbf{D}$ and $\mathbf{\Omega}$ are the rate of strain tensor and vorticity tensor, defined by

$$\mathbf{D}=\frac{1}{2}(\nabla\mathbf{v}+\nabla\mathbf{v}^T), \quad \mathbf{\Omega}=\frac{1}{2}(\nabla\mathbf{v}-\nabla\mathbf{v}^T), \tag{23}$$

respectively, $\mathbf{v}$ is the velocity vector field for the flowing LCP, $\nabla\mathbf{v}=\partial\mathbf{v}_i/\partial\mathbf{x}_j$ is the velocity gradient, and the superscript T denotes the transpose of a second-order tensor. Following the development of the Smoluchowski equation for polymer solutions by Doi and Edwards [5] with both the rotary and translational diffusion included and utilizing the result of Jeffrey's (22), we arrive at the Smoluchowski (kinetic) equation for the number density function $f(\mathbf{m},\mathbf{x},t)$ for spheroidal LCPs:

$$\frac{df}{dt}=\frac{\partial}{\partial\mathbf{x}}\cdot\left[(D_{\|}(a)\mathbf{mm}+D_{\perp}(a)(\mathbf{I}-\mathbf{mm}))\cdot\left(\frac{\partial f}{\partial\mathbf{x}}+\frac{f}{kT}\frac{\partial V}{\partial\mathbf{x}}\right)\right]$$
$$+\mathcal{R}\cdot\left[D_r(\mathbf{m},a)\left(\mathcal{R}f+\frac{1}{kT}f\mathcal{R}V\right)\right]-\mathcal{R}\cdot[\mathbf{m}\times\dot{\mathbf{m}}f], \tag{24}$$

where

$$D_r(\mathbf{m},a)=\hat{D}_r(a)\left(\frac{1}{\nu^2}\int_{\|\mathbf{m}'\|=1}\|\mathbf{m}\times\mathbf{m}'\|f(\mathbf{m}',\mathbf{x},t)d\mathbf{m}'\right)^{-2} \tag{25}$$

is the rotary diffusivity, inversely proportional to the relaxation time due to molecular rotation, $\hat{D}_r(a)$ a shape-dependent rotary diffusion constant, $D_{\|}(a)$ and $D_{\perp}(a)$ are shape-dependent, translational diffusivities characterizing the translational diffusion in the direction parallel and perpendicular to $\mathbf{m}$, respectively, V is the potential including the inter-molecular potential V_{ei} and the external potential (magnetic and/or electric field effect) V_H,

$$V=V_{ei}+\nu kTV_H, \tag{26}$$

$\partial/\partial\mathbf{x}=\nabla$ and $\mathcal{R}=\mathbf{m}\times\partial/\partial\mathbf{m}$ are the spatial and the rotational gradient operator, respectively, and $d/dt(\bullet)$ denotes the material derivative $\partial/\partial t(\cdot)+\mathbf{v}\cdot\nabla(\cdot)$. In the Smoluchowski equation, rotary convection and diffusion as well as spatial (translational) convection and diffusion are all included. Due to the presence of the translational diffusion, the number density ν may no longer be a constant.

By averaging over the configurational space of $\mathbf{m}$ with respect to the ndf f, we have the evolutionary equation for the number density ν:

$$\frac{d\nu}{dt}=D_{\perp}\Delta\nu+(D_{\|}-D_{\perp})\nabla_i\nabla_j\mathbf{M}_{ij}+(D_{\|}-D_{\perp})\nabla_k\left[A\mathbf{M}_{kl}\nabla_l\left(\nu\right.\right.$$
$$\left.+\frac{\mathcal{L}^2}{24}\Delta\nu\right)+\frac{AL^2}{48}(\mathbf{M}_{4klmn}\nabla_l\nabla_m\nabla_n\nu+\mathbf{M}_{kl}\nabla_l\nabla_m\nabla_n\mathbf{M}_{mn})$$
$$-\frac{3N}{2}\left(\mathbf{M}_{4klmn}\nabla_l\left(\mathbf{M}_{mn}+\frac{\mathcal{L}^2}{24}\Delta\mathbf{M}_{mn}\right)\right.$$
$$\left.\left.+\frac{\mathcal{L}^2}{48}(\mathbf{M}_{6klmnij}\nabla_l\nabla_m\nabla_n\mathbf{M}_{ij}+\mathbf{M}_{4klmn}\nabla_l\nabla_i\nabla_j\mathbf{M}_{4mnij})\right)\right]$$
$$+D_{\perp}\nabla_k\left[A\nu\nabla_k\left(\left(1+\frac{\mathcal{L}^2}{24}\Delta\right)\nu\right)+\frac{AL^2}{48}(\mathbf{M}_{mn}\nabla_k\nabla_m\nabla_n\nu\right.$$
$$+\nu\nabla_k\nabla_m\nabla_n\mathbf{M}_{mn})-\frac{3N}{2}\left(\mathbf{M}_{mn}\nabla_k\left(\mathbf{M}_{mn}+\frac{\mathcal{L}^2}{24}\Delta\mathbf{M}_{mn}\right)\right.$$
$$\left.\left.+\frac{L^2}{48}(\mathbf{M}_{4mnij}\nabla_k\nabla_m\nabla_n\mathbf{M}_{ij}+\mathbf{M}_{mn}\nabla_k\nabla_i\nabla_j\mathbf{M}_{4mnij})\right)\right], \tag{27}$$

where

$$\mathbf{M}_6=\langle\mathbf{mmmmmm}\rangle \tag{28}$$

is the sixth moment of $\mathbf{m}$ with respect to the ndf and indices are used wherever necessary for clarity.

Like in most kinetic theories, the mesoscopic, or average, internal orientational properties of nematic liquid crystals are defined in terms of the moments of $\mathbf{m}$ with respect to the probability density function $1/\nu f$ (normalized ndf) [5]. Often, one uses the normalized second moment $1/\nu\mathbf{M}$ or its deviatoric part $\mathbf{Q}$ (a second order, symmetric, traceless tensor $\mathbf{Q}$) known as the orientation tensor (or structure tensor):

$$\mathbf{Q}=\frac{1}{\nu}\langle\mathbf{mm}\rangle-\mathbf{I}/3. \tag{29}$$

Taking the second moment of $\mathbf{m}$ in the configurational space of $\mathbf{m}$ with respect to the ndf governed by the kinetic Eq. (24), we arrive at the mesoscale *orientation tensor equation*

$$\left\{\frac{d}{dt}\mathbf{M}-\Omega\cdot\mathbf{M}+\mathbf{M}\cdot\Omega-a[\mathbf{D}\cdot\mathbf{M}+\mathbf{M}\cdot\mathbf{D}]\right\}_{\alpha\beta}$$
$$=\left\{-2a\mathbf{D}:\mathbf{M}_4-6D_r^0\left[\mathbf{M}-\frac{\nu}{3}\mathbf{I}-\frac{1}{6kT}(\langle\mathbf{m}\times\mathcal{R}V\mathbf{m}\rangle+\langle\mathbf{mm}\times\mathcal{R}V\rangle)\right]\right.$$
$$\left.+(D_{\|}-D_{\perp})\nabla\nabla:\mathbf{M}_4+D_{\perp}\Delta\mathbf{M}\right\}_{\alpha\beta}+\frac{1}{kT}(D_{\|}-D_{\perp})\nabla_i\langle\mathbf{m}_{\alpha}\mathbf{m}_{\beta}\mathbf{m}_i\mathbf{m}_j\nabla_jV\rangle+\frac{1}{kT}D_{\perp}\nabla_i\langle\mathbf{m}_{\alpha}\mathbf{m}_{\beta}\nabla_iV\rangle$$
$$=\left\{-2a\mathbf{D}:\mathbf{M}_4-6D_r^0\left[\mathbf{M}-\frac{\nu}{3}\mathbf{I}-\frac{N}{2}\left(\left(\mathbf{I}+\frac{\mathcal{L}^2}{24}\Delta\right)\mathbf{M}\cdot\mathbf{M}+\mathbf{M}\cdot\left(\mathbf{I}+\frac{\mathcal{L}^2}{24}\Delta\right)\mathbf{M}\right)\right.\right.$$
$$+N\left(\mathbf{I}+\frac{\mathcal{L}^2}{24}\Delta\right)\mathbf{M}:\mathbf{M}_4-\frac{NL^2}{96}((\nabla\nabla\mathbf{M})\,\vdots\,\mathbf{M}_4+((\nabla\nabla\mathbf{M})\,\vdots\,\mathbf{M}_4)^T+\mathbf{M}_4\,\vdots\,\nabla\nabla\mathbf{M}+(\mathbf{M}_4\,\vdots\,\nabla\nabla\mathbf{M})^T+\mathbf{M}\nabla\nabla\,\vdots\,\mathbf{M}_4$$
$$\left.\left.+(\mathbf{M}\nabla\nabla\,\vdots\,\mathbf{M}_4)^T-4\mathbf{M}_6::\nabla\nabla\mathbf{M}-2\mathbf{M}_4\nabla\nabla::\mathbf{M}_4)+\frac{AL^2}{144}(\nabla\nabla\nu\cdot\mathbf{M}+\mathbf{M}\cdot\nabla\nabla\nu-2\nabla\nabla\nu:\mathbf{M}_4\right]\right\}_{\alpha\beta}$$
$$+(D_{\|}-D_{\perp})\nabla_i\nabla_j\mathbf{M}_{4ij\alpha\beta}+D_{\perp}\Delta\mathbf{M}_{\alpha\beta}+(D_{\|}-D_{\perp})\nabla_i\left[A\left(\mathbf{M}_{4\alpha\beta ij}\left(1+\frac{\mathcal{L}^2}{24}\Delta\right)\nabla_j\nu+\frac{L^2}{48}(\mathbf{M}_{4\alpha\beta ij}\nabla_j\nabla_k\nabla_l\mathbf{M}_{kl}+\mathbf{M}_{6\alpha\beta ijkl}\nabla_j\nabla_k\nabla_l\nu)\right)\right.$$

$$-\frac{3N}{2}\left(\mathbf{M}_{6\alpha\beta ijkl}\nabla_j\left(1+\frac{\mathcal{L}^2}{24}\Delta\right)\mathbf{M}_{kl}+\frac{L^2}{48}\mathbf{M}_{8\alpha\beta ijklmn}\nabla_j\nabla_m\nabla_n\mathbf{M}_{kl}+\mathbf{M}_{6\alpha\beta ijkl}\nabla_j\nabla_m\nabla_n\mathbf{M}_{4klmn}\right)+D_\perp\nabla_i\Bigg[A\left(\mathbf{M}_{\alpha\beta}\left(1+\frac{L^2}{24}\Delta\right)\nabla_i\nu\right.$$
$$\left.+\frac{\mathcal{L}^2}{48}(\mathbf{M}_{\alpha\beta}\nabla_i\nabla_k\nabla_l\mathbf{M}_{kl}+\mathbf{M}_{4\alpha\beta kl}\nabla_i\nabla_k\nabla_l\nu)\right)-\frac{3N}{2}\left(\mathbf{M}_{4\alpha\beta kl}\left(1+\frac{\mathcal{L}^2}{24}\Delta\right)\nabla_i\mathbf{M}_{kl}+\frac{L^2}{48}(\mathbf{M}_{6\alpha\beta klmn}\nabla_i\nabla_k\nabla_l\mathbf{M}_{mn}\right.$$
$$\left.\left.+\mathbf{M}_{4\alpha\beta kl}\nabla_i\nabla_m\nabla_n\mathbf{M}_{4klmn})\right)\Bigg]+D_r^0[\langle\mathbf{m}\times\mathcal{R}V_H\mathbf{m}\rangle+\langle\mathbf{mm}\times\mathcal{R}V_H\rangle]. \tag{30}$$

where D_r^0 is an averaged rotary diffusivity resulted from the averaging process [5], which is assumed a shape dependent constant in this study. We remark that the averaged rotary diffusivity is also possibly orientation dependent; then the "tube-dilation" effect can be modeled by replacing the constant rotary diffusivity D_r^0 by [5]

$$\frac{D_r^0}{(1-\frac{3}{2}\mathbf{Q}:\mathbf{Q})^2}. \tag{31}$$

We note that in the equation of ν up to sixth-order tensors are included. Up to eighth order tensors are present in the orientation tensor equation for $\mathbf{M}$. Following the same procedure, we can derive time evolutionary equation for any moments of even order. The equation for the $2k$, $k=0,1,\ldots$, moment will contain moments of order $2k+6$. With the kinetic equation, we next derive the consistent stress tensor.

2.3 Derivation of the Stress Tensor. We treat the LCP system as incompressible. Then, the stress tensor consists of three parts: the pressure $-p\mathbf{I}$, the viscous stress τ^v and the elastic stress τ^e. We derive the elastic stress first by applying the virtual work principle [3,5] on a finite volume of the LCP material denoted by G called control volume. In order to take into account the nonlocal effect of the intermolecular potential (20), the virtual deformation field $\delta\epsilon=\delta\nabla\mathbf{x}$, the variation of all tensor fields and their first order derivatives are assumed zero at the boundaries of the control volume [20].

Consider a virtual deformation $\delta\epsilon$ of the material in G. We note that the free energy of the LCP system in the material volume is given by (19). According to the virtual work principle [5], the virtual work that the exterior must do to the material to realize $\delta\epsilon$ is

$$\delta W=\int_G \tau^e:\delta\epsilon d\mathbf{x}, \tag{32}$$

where τ^e is the elastic part of extra stress. In response to the virtual deformation $\delta\epsilon$, the variation of f is calculated from the kinetic equation by neglecting all terms except for the convection ones [5]:

$$\delta f=\frac{df}{dt}\delta t=-\mathcal{R}\cdot(\mathbf{m}\times\dot{\mathbf{m}}f)\delta t. \tag{33}$$

The change in the free energy must then equal the work done to the material, i.e.,

$$\delta A=\delta W. \tag{34}$$

This equation yields the elastic stress,

$$\tau^e_{\alpha\beta}=3akT\left[\mathbf{M}-\frac{\nu}{3}\mathbf{I}-\frac{1}{6kT}(\langle\mathbf{m}\times\mathcal{R}(V)\mathbf{m}\rangle+\langle\mathbf{mm}\times\mathcal{R}(V)\rangle)\right]_{\alpha\beta}-\frac{1}{2}[\langle\mathbf{m}\times\mathcal{R}(V)\mathbf{m}\rangle-\langle\mathbf{mm}\times\mathcal{R}(V)\rangle]_{\alpha\beta}$$
$$+\frac{AkT}{2}\left[\frac{\mathcal{L}^2}{24}(\nabla_\alpha\nu\nabla_\beta\nu-\nu\nabla_\alpha\nabla_\beta\nu)+\frac{L^2}{48}(\nabla_\alpha\mathbf{M}_{\mu\beta}\nabla_\mu\nu-\nu\nabla_\alpha\nabla_\mu\mathbf{M}_{\mu\beta}+\nabla_\alpha\nu\nabla_\mu\mathbf{M}_{\mu\beta}-\nabla_\alpha\nabla_\mu\nu\mathbf{M}_{\nu\beta})\right]$$
$$-\frac{3NkT}{4}\left[\frac{\mathcal{L}^2}{24}(\nabla_\alpha\mathbf{M}_{\mu\gamma}\nabla_\beta\mathbf{M}_{\mu\gamma}-\nabla_\alpha\nabla_\beta\mathbf{M}_{\mu\gamma}\mathbf{M}_{\mu\gamma})+\frac{L^2}{48}(\nabla_\alpha\mathbf{M}_{4i\beta\mu\gamma}\nabla_i\mathbf{M}_{\mu\gamma}-\nabla_\alpha\nabla_i\mathbf{M}_{4\beta i\mu\gamma}\mathbf{M}_{\mu\gamma}\right.$$
$$\left.+\nabla_\alpha\mathbf{M}_{\mu\gamma}\nabla_i\mathbf{M}_{4i\beta\mu\gamma}-\nabla_\alpha\nabla_i\mathbf{M}_{\mu\gamma}\mathbf{M}_{4\beta i\mu\gamma})\right]. \tag{35}$$

The details of the derivation is given in Appendix. The antisymmetric part of the elastic stress is

$$\tau^e_{a,\alpha\beta}=\frac{1}{2}[\langle\mathbf{m}\times\mathcal{R}V\mathbf{m}\rangle-\langle\mathbf{mm}\times\mathcal{R}V\rangle]_{\alpha\beta}+\frac{AkT}{2}\left[\frac{L^2}{48}(\nabla_\alpha\mathbf{M}_{\mu\beta}\nabla_\mu\nu\right.$$
$$\left.-\nu\nabla_\alpha\nabla_\mu\mathbf{M}_{\mu\beta}+\nabla_\alpha\nu\nabla_\mu\mathbf{M}_{\mu\beta}-\nabla_\alpha\nabla_\mu\nu\mathbf{M}_{\mu\beta})\right]_{\alpha\beta}$$
$$-\frac{3NkT}{4}\left[\frac{L^2}{48}(\nabla_\alpha\mathbf{M}_{4i\beta\mu\gamma}\nabla_i\mathbf{M}_{\mu\gamma}-\nabla_\alpha\nabla_i\mathbf{M}_{4\beta i\mu\gamma}\mathbf{M}_{\mu\gamma}\right.$$
$$\left.+\nabla_\alpha\mathbf{M}_{\mu\gamma}\nabla_i\mathbf{M}_{4i\beta\mu\gamma}-\nabla_\alpha\nabla_i\mathbf{M}_{\mu\gamma}\mathbf{M}_{4\beta i\mu\gamma})\right]. \tag{36}$$

For the viscous stress, we use the results of Jeffrey's [19], Batchelor's [21] and Hinch and Leal's [22–24] on spheroidal suspensions in viscous solvent to arrive at:

$$\tau^v=2\eta_s\mathbf{D}+3kT[\zeta_1(a)(\mathbf{D}\cdot\mathbf{M}+\mathbf{M}\cdot\mathbf{D})+\zeta_2(a)\mathbf{D}:\langle\mathbf{mmmm}\rangle)], \tag{37}$$

where

$$\eta_s=\eta+\frac{3}{2}\nu kT\zeta_3(a),$$

$$\zeta_3(a)=\frac{\zeta^{(0)}}{I_1},\quad \zeta(a)=\zeta^{(0)}\left(\frac{1}{I_3}-\frac{1}{I_1}\right),$$

$$
\begin{aligned}
\zeta_2(a) &= \zeta^{(0)}\left[\frac{J_1}{I_1 J_3} + \frac{1}{I_1} - \frac{2}{I_3}\right],\\
I_1 &= 2r\int_0^\infty \frac{dx}{\sqrt{(r^2+x)}(1+x)^3},\\
I_3 &= r(r^2+1)\int_0^\infty \frac{dx}{\sqrt{(r^2+x)}(1+x)^2(r^2+x)},\\
J_1 &= r\int_0^\infty \frac{x\,dx}{\sqrt{(r^2+x)}(1+x)^3},\\
J_3 &= r\int_0^\infty \frac{x\,dx}{\sqrt{(r^2+x)}(1+x)^2(r^2+x)},\\
r &= \frac{1+a}{1-a},
\end{aligned}
\tag{38}
$$

η is the solvent viscosity, $\zeta_{1,2,3}(a)$ are three friction coefficients. $3\nu kT\zeta_i(a)$, $i=1,2,3$ are identified as three shape-dependent viscosity parameters due to the polymer-solvent interaction. The total extra stress is given in the *constitutive equation for the extra stress*

$$\tau = \tau^e + \tau^v. \tag{39}$$

From [22,23], it follows that

$$
\begin{aligned}
&\lim_{a\to 1}\zeta_1(a)=0, \quad \lim_{a\to 1}\zeta_2(a)=\infty,\\
&\lim_{a\to -1}\zeta_1(a)=-\infty, \quad \lim_{a\to -1}\zeta_2(a)=\infty.
\end{aligned}
\tag{40}
$$

So, the formulas are not meant to be applied to the two extremes $a=-1$ and $a=1$ at all. To obtain the viscous stress in practice, one should calibrate the coefficients at a fixed aspect ratio $0<r=r_0<\infty$ and then extrapolate the formulas to all the other finite values of r since after all the friction coefficients need to be experimentally determined. In the range of $a\approx 1$ though, the stress contribution from the term $\mathbf{D}\cdot\mathbf{M}+\mathbf{M}\cdot\mathbf{D}$ is negligible, consistent with the Doi theory for rodlike molecules [5].

We recall some results on the "friction coefficients" shown in [1], when $a>0$, $0<\zeta_1(a)<\min(\zeta_2(a),\zeta_3(a))$; when $a<0$, $\zeta_1(a)<0$ and is comparable in magnitudes to $\zeta_2(a)$, giving rise to a non-negligible "shape-induced-antidrag" to the total stress from the term $\mathbf{D}\cdot\mathbf{M}+\mathbf{M}\cdot\mathbf{D}$. This indicates that the oblate spheroidal molecule has the tendency to weaken the viscous stress due to the shape-induced polymer-solvent interaction. However, this will by no means change the dissipative nature of the stress. As shown in [1], the viscous stress part due to the polymer-solvent interaction is indeed dissipative for all values of $a\in(-1,1)$ and all possible orientation despite $\zeta_1(a)<0$ at $a<0$.

The kinetic equation (24), orientation tensor equation (27) and (30), constitutive equation for the extra stress (39), balance of linear momentum (41) and the continuity equation (42), both given next, constitute the hydrodynamical model for flows of spheroidal LCPs.

Balance of linear momentum

$$\rho\frac{d\mathbf{v}}{dt} = \nabla\cdot(-p\mathbf{I}+\tau)+\mathbf{f}, \tag{41}$$

where ρ is the fluid density, p is the scalar pressure and $\mathbf{f}$ the external force. Corresponding to the incompressibility, $\mathbf{v}$ satisfies the *continuity equation*

$$\nabla\cdot\mathbf{v}=0. \tag{42}$$

Balance of angular momentum and the anisotropic elasticity Finally, we want to make sure that the derived theory obeys the balance of angular momentum. From [5], we know that the torque on a test molecule oriented along $\mathbf{m}$ is given by

$$\mathbf{T} = -\mathcal{R}V_{ei}, \tag{43}$$

absence of external effects. In this mesoscopic theory, the material point is implicitly (tacitly) defined as a sphere in which the velocity gradient is assumed constant and all LCP molecules convect spatially in an identical manner within the sphere. Due to the anisotropic elasticity from the intermolecular potential, there exists an additional torque associated to the spatial convection on the "material points." The total torque on a unit volume of the material is given by

$$
\begin{aligned}
\mathbf{t}_k = &\int_{\|\mathbf{m}\|=1}\mathbf{T}_k f(\mathbf{m},\mathbf{x},t)\,d\mathbf{m} + \frac{AkT}{2}\Big[\frac{L^2}{48}(\nabla_\alpha\mathbf{M}_{\mu\beta}\nabla_\mu\nu - \nu\nabla_\alpha\nabla_\mu\mathbf{M}_{\mu\beta}\\
&+\nabla_\alpha\nu\nabla_\mu\mathbf{M}_{\mu\beta} - \nabla_\alpha\nabla_\mu\nu\mathbf{M}_{\mu\beta})\Big] - \frac{3NkT}{4}\Big[\frac{L^2}{48}(\nabla_\alpha\mathbf{M}_{4i\beta\mu\gamma}\nabla_i\mathbf{M}_{\mu\gamma}\\
&-\nabla_\alpha\nabla_i\mathbf{M}_{4\beta i\mu\gamma}\mathbf{M}_{\mu\gamma} + \nabla_\alpha\mathbf{M}_{\mu\gamma}\nabla_i\mathbf{M}_{4i\beta\mu\gamma}\\
&-\nabla_\alpha\nabla_i\mathbf{M}_{\mu\gamma}\mathbf{M}_{4\beta i\mu\gamma})\Big]\boldsymbol{\epsilon}_{\alpha\beta k},
\end{aligned}
\tag{44}
$$

where $\boldsymbol{\epsilon}_{\alpha\beta k}$ is the alternator tensor [25]. Integrating over the control volume G and applying integration by part whenever necessary, our calculations end up with

$$\int_G \tau_{ij}\epsilon_{ijk}\,d\mathbf{x} = \int_G \mathbf{t}_k\,d\mathbf{x}. \tag{45}$$

This equality indicates that the body torque balances the antisymmetric part of the stress tensor on the control volume G, confirming that the balance of angular momentum is maintained [3]. We note that the balance of the angular momentum is achieved on the entire control volume G subject to the assumptions on the zero boundary conditions alluded to earlier rather than in a pointwise sense due to the nonlocality of the intermolecular potential. The presence of the anisotropic elasticity is due to the long-range anisotropic molecular interaction. It is the interaction between the spatial convection and the long-range anisotropic molecular interaction that causes the additional torque on the material point. The role of the anisotropic elasticity needs to be investigated further.

2.4 Entropy Production and Energy Dissipation. In an isothermal process, De Gennes and Prost noted that the entropy production or (energy dissipation) is equal to the decrease in the total energy [3]

$$T\dot{S} = -\frac{d}{dt}\left[\int_G\left(\frac{1}{2}\rho\mathbf{v}\cdot\mathbf{v}\right)dx + A[f]\right], \tag{46}$$

where S denotes the entropy of the control volume G. It is shown that

$$
\begin{aligned}
T\dot{S} = &\int_G\left\langle D_r(\mathbf{m},a)\left\|\mathcal{R}\left(\ln f + \frac{1}{kT}V_{ei}\right)\right\|^2\right\rangle d\mathbf{x} + \int_G\Big\langle\nabla\Big(\ln f\\
&+\frac{1}{kT}V_{ei}\Big)\cdot(D_\parallel(a)\mathbf{mm}+D_\perp(a)(\mathbf{I}-\mathbf{mm}))\cdot\nabla\Big(\ln f\\
&+\frac{1}{kT}V_{ei}\Big)\Big\rangle d\mathbf{x} + \int_G D_{vdisp}\,d\mathbf{x},
\end{aligned}
\tag{47}
$$

where

$$
\begin{aligned}
D_{vdisp} = &2\eta\mathbf{D}:\mathbf{D} + 3\nu kT(\zeta_3\mathbf{D} + \zeta_1(\mathbf{M}\cdot\mathbf{D}+\mathbf{D}\cdot\mathbf{M})\\
&+\zeta_2\mathbf{D}:\langle\mathbf{mmmm}\rangle):\mathbf{D}
\end{aligned}
\tag{48}
$$

is nonnegative definite [1]. It is nonnegative definite provided the translational diffusion coefficient matrix

$$(D_\parallel(a)\mathbf{mm}+D_\perp(a)(\mathbf{I}-\mathbf{mm})) \tag{49}$$

is, which is warranted provided $D_{\parallel}(a)$ and $D_{\perp}(a)$ are nonnegative as implicitly assumed. This concludes that the theory warrants a positive entropy production and thereby obeys the second law of thermodynamics.

2.5 Approximate Theory. The equation for the orientation tensor and the stress expression both contain up to eighth order tensors, indicating a strong coupling to the kinetic equation. Therefore, the kinetic equation is strongly coupled to the stress and the orientation tensor equation (the equation for the second moment of **m**). To decouple the kinetic equation, which often yields a much simpler governing equation system for LCPs, one has to use decoupling or closure approximations [24,26–29]. The simplest among all the choices of the closure approximations are

$$\langle\mathbf{mmmm}\rangle\simeq\frac{1}{\nu}\langle\mathbf{mm}\rangle\langle\mathbf{mm}\rangle,$$

$$\langle\mathbf{mmmmmm}\rangle\approx\frac{1}{\nu^2}\langle\mathbf{mm}\rangle\langle\mathbf{mm}\rangle\langle\mathbf{mm}\rangle,$$

$$\langle\mathbf{mmmmmmmm}\rangle\approx\frac{1}{\nu^3}\langle\mathbf{mm}\rangle\langle\mathbf{mm}\rangle\langle\mathbf{mm}\rangle\langle\mathbf{mm}\rangle. \tag{50}$$

These are exact when the orientation is perfect. Substituting the above closure approximations in the orientation tensor equation and the stress expression given by (30) and (39), respectively, we arrive at the approximate theory for spheroidal LCPs.

An alternative is to use both $\mathbf{M}$ and $\mathbf{M}_4$ as orientational variables and approximate sixth order and eighth order tensors by closures. Of course, more sophisticated closures may be employed to improve the approximation given here [7,8,24,26]. Most of the closures are flow-type dependent so that their performance in different types of flows may vary widely [26–29]. Unless a specific flow problem is identified, we don't see the need for enumerating all the closure approximations here.

3 Reduction to the Ericksen-Leslie Theory

In [1], we showed the kinetic theory developed there yields the torque balance equation of the Ericksen-Leslie theory in the limit of weak flow, weak distortional elasticity, and long time. Here we extend the asymptotic analysis to include a weak translational diffusion and show that the asymptotic limit of the torque balance equation of the theory remains.

We introduce a dimensionless small parameter $0<\epsilon\ll 1$ to quantify the weak effects mentioned above explicitly, i.e., Let

$$D_{\parallel}=\epsilon\tilde{D}_{\parallel},\ D_{\perp}=\epsilon\tilde{D}_{\perp},\ \tilde{t}=t\epsilon,\ \mathbf{D}=\epsilon\tilde{\mathbf{D}},\ \Omega=\epsilon\tilde{\Omega},\ \mathcal{L}^2=\epsilon\tilde{\mathcal{L}}^2,$$
$$L^2=\epsilon\tilde{L}^2. \tag{51}$$

Dropping the tildes, the kinetic equation becomes

$$\begin{aligned}\epsilon\frac{df}{dt}&=\epsilon\frac{\partial}{\partial\mathbf{x}}\cdot\left[(D_{\parallel}(a)\mathbf{mm}+D_{\perp}(a)(\mathbf{I}-\mathbf{mm}))\cdot\left(\frac{\partial f}{\partial\mathbf{x}}+\frac{f}{kT}\frac{\partial V_0}{\partial\mathbf{x}}\right)\right]\\&\quad+\mathcal{R}\cdot\left[D_r(\mathbf{m},a)\left(\mathcal{R}f+\frac{1}{kT}f\mathcal{R}V_0\right)\right]\\&\quad-\epsilon\mathcal{R}\cdot\left[\mathbf{m}\times\dot{\mathbf{m}}f-D_rf\mathcal{R}\frac{V_e}{kT}\right],\end{aligned} \tag{52}$$

where

$$V_0=V_0[f]=AkT\nu-\frac{3N}{2}kT\mathbf{M}:\mathbf{mm},V_e=V_{ei}-V_0. \tag{53}$$

$V_0[f]$ indicates the potential is evaluated at f. We seek an asymptotic expansion of the probability density function

$$f=\sum_{n=0}^{\infty}\epsilon^nf_n(\mathbf{m},\mathbf{x},t). \tag{54}$$

Substituting the ansatz (54) into the Smoluchowski equation, we obtain at leading order $(O(1))$

$$\mathcal{R}\cdot\left[Dr\left(\mathcal{R}f_0+f_0\mathcal{R}\frac{V_0[f_0]}{kT}\right)\right]=0. \tag{55}$$

Clearly, f_0 at leading order is a steady state solution of the Smoluchowski equation with the Maier-Saupe intermolecular potential. A solution of the leading order equation is given by the integral equation

$$f_0=\bar{\rho}e^{-V_0[f_0]/kT}, \tag{56}$$

and $\bar{\rho}=\bar{\rho}(\mathbf{x},t)$. In this paper, we assume $\bar{\rho}=\text{const}$. So, it is the normalizing factor for f_0. Without loss of generality, we also assume

$$\nu=\int_{\{\|\mathbf{m}\|=1\}}f_0d\mathbf{m}=1. \tag{57}$$

This assumption is equivalent to

$$\ln f_0+\frac{V[f_0]}{kT}=\text{const}. \tag{58}$$

Assuming uniaxial symmetry in the base state f_0, i.e.,

$$\mathbf{M}=s\mathbf{nn}-\frac{1-s}{3}\mathbf{I}, \tag{59}$$

where n is the distinguished major director direction of the second moment tensor, we find a steady state solution of f_0 given by

$$f_0=f_0(\cos\theta)$$
$$\frac{df_0}{d\xi}=3sN\cos\theta f_0(\xi), \tag{60}$$

where $\xi=\cos\theta=\mathbf{n}\cdot\mathbf{m}$. The uniaxial director $\mathbf{n}$ is arbitrary since the leading order equation does not tell us how $\mathbf{n}$ varies in time and space. This is the well-known degeneracy of the steady kinetic equation in equilibrium [5]. Let

$$\mathbf{n}=\mathbf{n}(\mathbf{x},t). \tag{61}$$

We then derive its governing equation using higher order equations.

At the next order $(O(\epsilon))$, we have

$$\begin{aligned}\frac{df_0}{dt}&=\mathcal{R}\cdot D_r[\mathcal{R}f_1+f_1\mathcal{R}V_0[f_0]+f_0\mathcal{R}V_0[f_1]]-\mathcal{R}\cdot\left[\left(\mathbf{m}\times\dot{\mathbf{m}}f_0\right.\right.\\&\quad\left.\left.-D_rf_0\left(\mathcal{R}\frac{V_e[f_0]}{kT}\right)\right)\right]+\nabla\cdot\left(D_{\parallel}\mathbf{mm}+D_{\perp}(\mathbf{I}-\mathbf{mm})\right.\\&\quad\left.\cdot\left(\nabla f_0+\frac{f_0}{kT}\nabla V_0[f_0]\right)\right).\end{aligned} \tag{62}$$

The term corresponding to the translational diffusion vanishes because

$$\left(\nabla f_0+\frac{f_0}{kT}\nabla V_0[f_0]\right)=f_0\nabla\left(\ln f_0+\frac{V_0[f_0]}{kT}\right)=f_0\nabla\ \text{const}=0. \tag{63}$$

Thus, (62) reduces to

$$\begin{aligned}\frac{df_0}{dt}&=\mathcal{R}\cdot D_r[\mathcal{R}f_1+f_1\mathcal{R}V_0[f_0]+f_0\mathcal{R}V_0[f_1]]\\&\quad-\mathcal{R}\cdot\left[\left(\mathbf{m}\times\dot{\mathbf{m}}f_0-D_rf_0\left(\mathcal{R}\frac{V_e[f_0]}{kT}\right)\right)\right].\end{aligned} \tag{64}$$

From the solvability condition of (64), detailed in [1], we obtain the torque balance equation for the uniaxial director **n**

$$-\gamma\mathbf{n}+\frac{as}{\lambda}\frac{\nu kT}{D_r^0}\mathbf{N}-as\frac{\nu kT}{D_r^0}\mathbf{D}\cdot\mathbf{n}-\mathbf{h}=0, \tag{65}$$

where γ is a Lagrangian multiplier,

$$\mathbf{N}=\frac{d\mathbf{n}}{dt}-\Omega\cdot\mathbf{n}, \tag{66}$$

h is the elastic field [3]

$$\mathbf{h}=\frac{\nu NkTs}{8}\left[\left(s\mathcal{L}^2+\frac{s-s_4}{7}L^2\right)\Delta\mathbf{n}+\frac{2(s-s_4)}{7}L^2\nabla(\nabla\cdot\mathbf{n})\right.$$
$$+\frac{2s+5s_4}{7}L^2((\nabla\cdot\mathbf{n})\mathbf{n}\cdot\nabla\mathbf{n}+(\mathbf{n}\cdot\nabla\mathbf{n})\cdot\nabla\mathbf{n}$$
$$\left.+\mathbf{nn}:\nabla\nabla\mathbf{n}-\mathbf{n}\cdot\nabla\mathbf{n}\cdot\nabla\mathbf{n}^T)\right], \tag{67}$$

and

$$\lambda=2as\left(\int_{\|\mathbf{m}\|=1}f_{ms}g(\theta)\frac{dV_0}{d\theta}d\mathbf{m}\right)^{-1} \tag{68}$$

is the "tumbling parameter" [16]. This is exactly the torque balance equation in the Ericksen-Leslie theory with the Frank elastic energy given by

$$F=\frac{1}{2}\left[\frac{\nu kTNs}{8}\left(s\mathcal{L}^2+\frac{3L^2}{7}(s-s_4)\right)(\nabla\cdot\mathbf{n})^2\right.$$
$$+\frac{\nu kTNs}{8}\left(s\mathcal{L}^2+\frac{L^2}{7}(s-s_4)\right)(\mathbf{n}\cdot\nabla\times\mathbf{n})^2$$
$$\left.+\frac{\nu kTNs}{8}\left(s\mathcal{L}^2+\frac{L^2}{7}(3s+4s_4)\right)\|\mathbf{n}\times\nabla\times\mathbf{n}\|^2\right]. \tag{69}$$

The stress tensor evaluated at the leading order solution f_0 yields the identical expression as the one in [1]. Therefore, the stress expression does not reduce to that in the Ericksen-Leslie theory; however, it does contain every term in the Ericksen-Leslie stress expression. The Frank elastic constants and the Leslie viscosity coefficients are identical to the ones in [1]. Hence, the inclusion of a weak translational diffusion does not change the asymptotic dynamics in the limit of the weak flows and weak distortional elasticity.

When the translational diffusion competes with the rotary diffusion at the same order, the torque balance equation contains additional gradient terms with up to fourth order spatial derivatives. The asymptotic limit certainly extends the Ericksen-Leslie torque balance equation to account for higher orders effect. The details are cumbersome and therefore omitted here.

4 Conclusion

We have developed a kinetic theory for flows of nonhomogeneous liquid crystalline polymers of spheroidal configurations generalizing the kinetic theory of Kuzuu and Doi for homogeneous liquid crystal polymers as well as that of Wang for nonhomogeneous LCPs to account for translational diffusion and density variation in space. The theory is applicable to flows of rodlike liquid crystal polymers at the large aspect ratios and to those of discotic ones at small aspect ratios. It also accounts for the molecular configurational effect in the viscous stress due to polymer-solvent interaction. The theory is shown to satisfy the second law of thermodynamics and warrant a positive entropy production and, therefore, is well-posed for flows of LCPs. In the asymptotic limit of weak flow, weak distortional elasticity, weak translational diffusion, and long time, the theory yields at leading order the torque balance equation of the Ericksen-Leslie theory. Otherwise, it is a bona fide extension of the Ericksen-Leslie theory that includes higher order effects.

Acknowledgment and Disclaimer

Effort sponsored by the Air Force Office of Scientific Research, Air Force Materials Command, USAF, under grant number F49620-02-1-0086 and F49620-02-6-0086, and the National Science Foundation through grants DMI-0115445, DMS-0204243, DMS-0308019 are gratefully acknowledged. MGF's work is also supported in part by the NASA University Research, Engineering and Technology Institute on Bio Inspired Materials (BIMat) under award No. NCC-1-02037.

Appendix

Derivation of the Elastic Etress Tensor Using Virtual Work Principles. We calculate the variation of the free energy $A[f]$ with respect to the variation of the probability density function defined by

$$\delta f=\frac{df}{dt}\delta t=-\mathcal{R}\cdot(\mathbf{m}\times\dot{\mathbf{m}}f)\delta t. \tag{70}$$

This indicates that not only the rotational configuration of the spheroidal molecule, but also its mass of center are perturbed along the moving trajectory of the material point **x**. Then,

$$\delta A[f]=kT\int_G\int_{\|\mathbf{m}\|=1}\left[\left(\ln f+\frac{V}{kT}\right)\delta f+\frac{1}{2kT}(f\delta V\right.$$
$$\left.-V\delta f)\right]d\mathbf{m}d\mathbf{x}. \tag{71}$$

Assuming the deformation tensor $\mathbf{K}\delta t$ and its derivatives vanish at ∂G and applying integration by part, we have

$$\int_G\int_{\|\mathbf{m}\|=1}\left[\left(\ln f+\frac{V}{kT}\right)\delta f\right]d\mathbf{m}d\mathbf{x}$$
$$=\int_G\mathbf{K}_{\alpha\beta}\delta t:\left\{3a\left(\mathbf{M}-\frac{\mathbf{I}}{3}\right)-\frac{a}{2}[\langle(\mathbf{m}\times\mathcal{R}V)\mathbf{m}\rangle\right.$$
$$+\langle\mathbf{m}(\mathbf{m}\times\mathcal{R}V)\rangle]-\frac{1}{2}[\langle(\mathbf{m}\times\mathcal{R}V)\mathbf{m}\rangle$$
$$\left.-\langle\mathbf{m}(\mathbf{m}\times\mathcal{R}V)\rangle]\right\}_{\alpha\beta}d\mathbf{x}, \tag{72}$$

and

$$\int_G\int_{\|\mathbf{m}\|=1}\left[\frac{1}{2kT}(f\delta V-V\delta f)\right]d\mathbf{m}d\mathbf{x}$$
$$=-\int_G\mathbf{K}_{\alpha\beta}\delta t\left\{\frac{AkT}{2}\left[\frac{\mathcal{L}^2}{24}(\nabla_\alpha\nu\nabla_\beta\nu-\nu\nabla_\alpha\nabla_\beta\nu)\right.\right.$$
$$+\frac{L^2}{48}(\nabla_\alpha\mathbf{M}_{\mu\beta}\nabla_\mu\nu-\nu\nabla_\alpha\nabla_\mu\mathbf{M}_{\mu\beta}+\nabla_\alpha\nu\nabla_\mu\mathbf{M}_{\mu\beta}$$
$$\left.-\nabla_\alpha\nabla_\mu\nu\mathbf{M}_{\mu\beta})\right]$$
$$-\frac{3NkT}{4}\left[\frac{\mathcal{L}^2}{24}(\nabla_\alpha\mathbf{M}_{\mu\gamma}\nabla_\beta\mathbf{M}_{\mu\gamma}-\nabla_\alpha\nabla_\beta\mathbf{M}_{\mu\gamma}\mathbf{M}_{\mu\gamma})\right.$$
$$+\frac{L^2}{48}(\nabla_\alpha\mathbf{M}_{4i\beta\mu\gamma}\nabla_i\mathbf{M}_{\mu\gamma}-\nabla_\alpha\nabla_i\mathbf{M}_{4\beta i\mu\gamma}\mathbf{M}_{\mu\gamma}$$
$$\left.\left.+\nabla_\alpha\mathbf{M}_{\mu\gamma}\nabla_i\mathbf{M}_{4i\beta\mu\gamma}-\nabla_\alpha\nabla_i\mathbf{M}_{\mu\gamma}\mathbf{M}_{4\beta i\mu\gamma})\right]\right\}d\mathbf{x}. \tag{73}$$

In arriving at the above expression, we have used the following identities

$$\nabla \cdot \mathbf{v} = 0,$$

$$\nabla_i \nabla_j (\mathbf{v}_\mu \nabla_\mu) = \mathbf{v}_\mu \nabla_\mu \nabla_j \nabla_i + \nabla_i (\mathbf{K}_{\mu j} \nabla_\mu) + \mathbf{K}_{\mu i} \nabla_\mu \nabla_j . \qquad (74)$$

The extra terms given by (73) are resulted from the interaction of the long range elastic potential and the spatial convection, which contributes additional elastic torque to the macroscopic motion of the material.

References

[1] Wang, Q., 2002, ''A hydrodynamic theory for solutions of nonhomogeneous nematic liquid crystalline polymers of different configuration,'' J. Chem. Phys., **116**, 9120–9136.
[2] Chandrasekhar, S., 1992, ''Liquid Crystals, 2nd ed.,'' Cambridge University Press, Cambridge.
[3] de Gennes, P. G., and Prost, J., 1993, ''The Physics of Liquid Crystals,'' Oxford University Press.
[4] Leslie, F. M., 1979, ''Theory of Flow Phenomena in Liquid Crystals,'' Adv. Liq. Cryst., **4**, 1–81.
[5] Doi, M., and Edwards, S. F., 1986, ''The Theory of Polymer Dynamics,'' Oxford U. Press (Clarendon), London-New York.
[6] Hand, G. L., 1962, ''A theory of anisotropic fluids,'' J. Fluid Mech., **13**, 33–46.
[7] Beris, A. N., and B. J. Edwards, B. J., 1994, ''Thermodynamics of Flowing Systems with Internal Microstructure,'' Oxford Science Publications, New York.
[8] Tsuji, T., and Rey, A. D., 1997, ''Effect of long range order on sheared liquid crystalline polymers, Part 1: compatibility between tumbling behavior and fixed anchoring,'' J. Non-Newtonian Fluid Mech., **73**, 127–152.
[9] Carlsson, T., 1982, ''The possibility of the existence of a positive Leslie viscosity α_2. Proposed flow behavior of disk-like nematic liquid crystals,'' Mol. Cryst. Liq. Cryst., **89**, 57–66.
[10] Wang, L., and Rey, A. D., 1997, ''Pattern formation and non-linear phenomena in stretched discotic liquid crystal fibres,'' Liq. Cryst., **23**(1), 93–112.
[11] Singh, A. P., and Rey, A. D., 1998, ''Microstructure constitutive equation for discotic nematic liquid crystalline materials,'' Rheol. Acta, **37**, 30–45.
[12] Isihara, A., 1951, ''Theory of anisotropic colloidal solutions,'' J. Chem. Phys., **19**(9), 1142–1153.
[13] Colot, J. L., Wu, X. G., Xu, H., and Baus, M., 1988, ''Density-functional, Landau, and Onsager theories of the isotropic-nematic transition of hard ellipsoids,'' Phys. Rev. A, **38**(4), 2022–2036.
[14] Takserman-Krozer, R., and Ziabicki, A., 1963, J. Polym. Sci., Part A: Gen. Pap., **1**, 491–516.
[15] Helfrich, W., 1970, ''Helical bilayer structures due to spontaneous torsion of the edges,'' J. Chem. Phys., **53**(6), 2267–2281.
[16] Kuzuu, N., and Doi, M., 1983, ''Constitutive equation for nematic liquid crystals under weak velocity gradient derived from a molecular kinetic equation,'' J. Phys. Soc. Jpn. **52**(10), 3486–3494.
[17] Baalss, D., and Hess, S., 1988, ''Viscosity coefficients of oriented nematic and nematic discotic liquid crystals; Affine transformation model,'' Z. Naturforsch., **43a**, 662.
[18] Marrucci, G., and Greco, F., 1991, ''The elastic constants of Maier-Saupe rodlike molecular nematics,'' Mol. Cryst., **206**, 17–30.
[19] Jeffrey, G. B., 1922, ''The motion of ellipsoidal particles immersed in a viscous fluid,'' Proc. R. Soc. London, Ser. A, **102**, 161–179.
[20] Feng, J., Sgalari, G., and Leal, L. G., 2000, ''A theory for flowing nematic polymers with orientational distortion,'' J. Rheol., **44**(5), 1085–1101.
[21] Batchelor, G. K., 1970, ''The stress system in a suspension of force-free particles,'' J. Fluid Mech., **41**(3), 545–570.
[22] Hinch, E. J., and Leal, L. G., 1972, ''The effect of Brownian motion on the rhological properties of a suspension of non-spherical particles,'' J. Fluid Mech., **52**(4), 683–712.
[23] Hinch, E. J., and Leal, L. G., 1973, ''Time-dependent shear flows of a suspension of particles with weak Brownian rotations,'' J. Fluid Mech., **57**(4), 753–767.
[24] Hinch, E. J., and Leal, L. G., 1976, ''Constitutive equations in suspension mechanics,'' part 2, ''Approximate forms for a suspension of rigid particles affected by Browian rotations,'' J. Fluid Mech., **76**(1), 187–208.
[25] Bird, B., Armstrong, R. C., and Hassager, O., 1987, *Dynamics of Polymeric Liquids, vol 1 and 2*, John Wiley and Sons, New York.
[26] Feng, J., Chaubal, C. V., and Leal, L. G., 1998, ''Closure approximations for the Doi theory: which to use in simulating complex flows of liquid-crystalline polymers,'' J. Rheol., **42**, 1095–1119.
[27] Chaubal, C. V., Leal, L. G., and Fredrickson, G. H., 1995, ''A comparison of closure approximations for the Doi theory of LCPs,'' J. Rheol., **39 pp**, 73–103.
[28] Wang, Q., 1997, ''Biaxial steady states and their stability in shear flows of liquid crystal polymers,'' J. Rheol., **41**(5), 943–970.
[29] Wang, Q., 1997, ''Comparative studies on closure approximations in flows of liquid crystal polymers: I. elongational flows,'' J. Non-Newtonian Fluid Mech., **72**, 141–162.

Self-Calibrating Sensor for Measuring Density Through Stainless Steel Pipeline Wall

Margaret S. Greenwood

Judith A. Bamberger

Pacific Northwest National Laboratory
P.O. Box 999
Richland, Washington 99352

An ultrasonic instrument to measure the density of a liquid or slurry through a stainless steel pipeline wall is described. By using multiple reflections of the ultrasound within the stainless steel wall, the acoustic impedance (defined as the product of the density of the liquid and the velocity of sound in the liquid) is determined. Thus, the wall is part of the measurement system. The density is obtained by coupling the acoustic impedance measurement with a velocity of sound measurement. By basing the measurement on multiple reflections, instrument sensitivity is increased by the power of the reflection coefficient. The measurement method is self-calibrating because the measurement of the acoustic impedance is independent of changes in the pulser voltage. Data are presented over a range of pulser voltages for two wall thicknesses. These results can be applied to develop an ultrasonic sensor that (1) can be attached permanently to a pipeline wall, possibly as a spool piece inserted into the line or (2) can clamp onto an existing pipeline wall and be movable to another location. The self-calibrating feature is very important because the signal strength is sensitive to the pressure on the clamp-on sensor. A sensor for immersion into a tank could also be developed. [DOI: 10.1115/1.1677462]

Introduction

Recent advances in computers and in particular high-speed A/D signal conversion make on-line real-time ultrasonic measurements an attractive addition to a suite of process measurement capabilities and a tool for chemometrics [1]. An ultrasonic instrument to measure the density of a liquid or slurry [2,3] through a stainless steel (SS) pipeline wall is described. By using multiple reflections of the ultrasound within the SS wall, the acoustic impedance (defined as the product of the density of the liquid and the velocity of sound in the liquid) is determined. Thus, the wall is part of the measurement system. The density is obtained by coupling the acoustic impedance measurement with a velocity of sound measurement. Since methods for measuring the velocity of sound in the fluid [time-of-flight (TOF)] are well known [4], the research presented here will focus on the measurement of the acoustic impedance. The self-calibrating feature is very important because the measurement of the acoustic impedance is *independent* of changes in the pulser voltage. The objective is to develop an ultrasonic sensor that (1) can be attached permanently to a pipeline wall, possibly as a spool piece inserted into the line and (2) can clamp onto an existing pipeline wall and be movable to another location. The self-calibrating feature is very important because the signal strength is sensitive to the pressure on the clamp-on sensor. A sensor for immersion into a tank could also be developed.

Experimental Measurements

A schematic diagram of the experimental apparatus is depicted in Fig. 1. A 5 MHz, longitudinal transducer is mounted upon a thin plate of stainless steel (or other solid material) plate with the base in contact with the liquid. A pulser sends a high-voltage signal to the transducer. The resulting ultrasound makes multiple reflections within the steel plate by reflecting each time the signal strikes the solid-liquid interface or the solid-transducer interface. The multiple echoes are recorded by the same transducer and then amplified by the receiver. They are viewed on a digital oscilloscope, as well as recorded on a file. Figure 2 displays an oscilloscope trace obtained using a stainless steel plate 6.4 mm thick. The plot shows 15 discrete echoes in the plate. Bold numbers along the axis indicate the elapsed time in micro seconds. The data files were analyzed by Matlab, a commercial code.

When the ultrasound strikes the solid-liquid interface, some of the ultrasound is reflected and some is transmitted into the liquid. The amount reflected, defined by the reflection coefficient, is given by:

$$R=\left(\frac{Z_s-Z_{\text{liq}}}{Z_s+Z_{\text{liq}}}\right) \tag{1}$$

where acoustic impedance is the product of the material density and the speed of sound in the material $(Z=\rho\ c)$. Inverting Eq. (1) gives the acoustic impedance of the liquid:

$$Z_{\text{liq}}=Z_s\left(\frac{1-R}{1+R}\right) \tag{2}$$

where Z_{liq} is the acoustic impedance of the liquid and Z_s, that of stainless steel or any other solid.

Using the reflection at a liquid-solid interface is a well-known method for measuring the acoustic impedance of a liquid. However, stainless steel is usually not used for this measurement because of its large acoustic impedance. For water $(Z=1.48\text{E}6\ \text{kg/m}^2\text{s})$ and steel $(Z=4.54\text{E}7\ \text{kg/m}^2\text{s})$, Eq. (1) shows that 93.7% of the ultrasound is reflected back at the stainless steel-water interface, each time the ultrasound strikes the interface. That is, the reflection coefficient is equal to 0.937. As an example, for water the density and speed of sound are 1000 kg/m^3 and 1480 m/s at ambient conditions, while the values for stainless steel are 7900 kg/m^3 and 5790 m/s. From Eq. (1), the reflection coefficient is 0.937. In comparison for 15% sugar water with a density of 1060 kg/m^3, the reflection coefficient is 0.931. These two values differ very little, and determination of the acoustic impedance of a liquid from one echo is very difficult. Little sensitivity occurs to small changes in the density. However, multiple echoes amplify the effect. After 10 echoes, the reflection corresponds to $(0.937)^{10}=0.522$ and similarly, $(0.931)^{10}=0.489$. These values are quite different and can be easily distinguished. Thus, the sensitivity is greatly increased.

Contributed by the Fluids Engineering Division for publication in the JOURNAL OF FLUIDS ENGINEERING. Manuscript received by the Fluids Engineering Division November 1, 2002; revised manuscript received June 4, 2003. Associate Editor: D. Siginer.

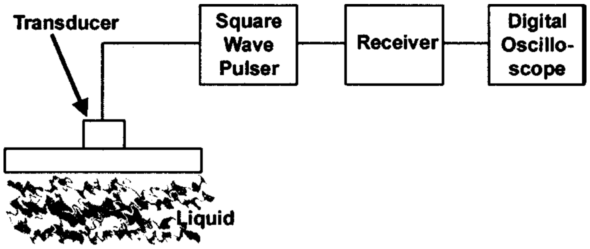

Fig. 1 Schematic diagram of experimental apparatus

Each echo, such as those shown in Fig. 2, is analyzed by taking the fast Fourier transform (FFT) of the signal to determine the amplitude at a frequency of 5 MHz (usually). Figure 3 shows that a straight line results when the logarithm of the FFT amplitude is plotted versus the echo number. A least-squares fit provides the slope of the line. The important point is that, for different liquids, the slopes are different because the reflection coefficients at the solid-liquid interface are different. The goal is to relate the slope of this line to the reflection coefficient for the liquid. Then, using Eq. (2) the acoustic impedance of the liquid is obtained. A separate measurement of the time-of-flight through the liquid yields the density of the liquid.

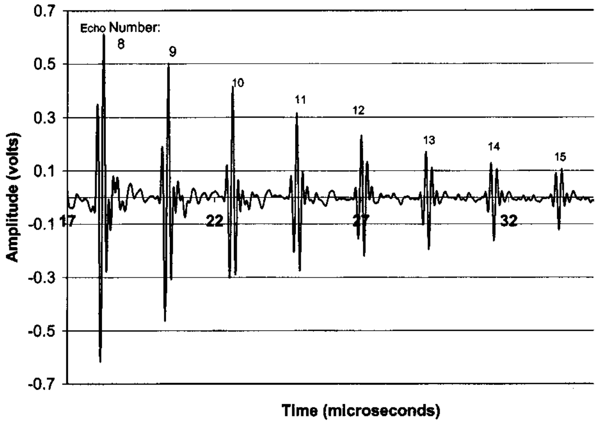

Fig. 2 Oscilloscope trace showing multiple echoes with 6.4-mm-thick steel plate

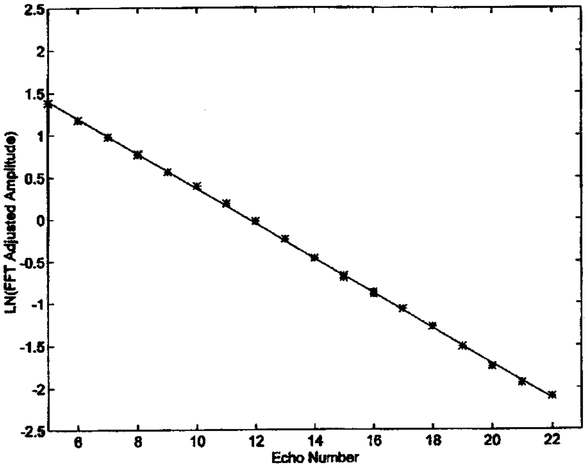

Fig. 3 A graph of the logarithm of the FFT amplitude versus the echo number for 10% sugar water in contact with 6.3-mm-thick SS plate

To obtain the relationship between the slope and the reflection coefficient the relationship for the voltage of the Nth echo is employed.

$$\text{Voltage } \alpha \ (\text{reflection coefficient for liquid})^N \tag{3}$$

Water is the fluid for calibration of the slopes. From Eq. (3) for water and another liquid, the following relationship is obtained for the echo N_1:

$$\frac{V_{\mathrm{liq}N1}}{V_{\mathrm{wtr}N1}}=\frac{R_{\mathrm{liq}}^{N1}}{R_{\mathrm{wtr}}^{N1}} \tag{4}$$

A similar equation can be written for echo N_2. Taking the logarithm of both equations and subtracting yields the desired relationship between slope and reflection coefficient:

$$\frac{R_{\mathrm{liq}}}{R_{\mathrm{wtr}}}=e^{(\text{slope for liquid})-(\text{slope for water})} \tag{5}$$

The term "slope" refers to the slope on a logarithmic plot shown in Fig. 3.

The reflection coefficient for the liquid is determined from Eq. (5), and then Eq. (2) yields the acoustic impedance of the liquid.

Self-Calibrating Feature. Suppose that the pulser voltage changes and is reduced by 5%. The ultrasound produced is likewise reduced, but each echo is reduced by *the same amount*. This means that, while the straight line is located at a slightly different position on the LN(FFT amplitude)-versus-echo graph, its *slope is the same*. Thus, the measurement of slope is independent of the pulser output. This was confirmed experimentally by using a 6.3-mm SS plate in contact with water. A square wave pulse was sent to the 5 MHz transducer, having a voltage of −300 V and a pulse width, which was varied to change the pulser output. Table 1 shows the data obtained for the natural logarithm of the FFT amplitude at 5 MHz for echoes 6, 9, 12, 15, 18, and 21; at the top of the column, the width of the square wave in nanoseconds is given. The data is plotted in Fig. 4. The slopes on a logarithmic plot of the FFT amplitude versus echo number are given in Table 1. For five sets of data, the value of the maximum slope and the minimum slope differ by only 0.2%.

Data for Stainless Steel Plates

Data were obtained for a 5 MHz transducer (diameter =2.5 cm) mounted upon a 6.3-mm-thick stainless steel plate. A square wave pulse with a voltage of −50 V and width of 100 nanoseconds was applied to the transducer. The base of the plate was immersed in water and various concentrations of sugar water. Figure 3 presents a plot of the logarithm of the FFT amplitude at 5 MHz versus the echo number for 10% sugar water. The slope is −0.2070. Table 2 lists the data for two entries of water. One measurement was obtained at the beginning of the experiments and the other, at the end. From the oscilloscope traces for these two sets of data, the amplitudes differed by ~5%. The *very* important point, however, is that the slopes were essentially the same—differing only by 0.1%. These results demonstrate how important the self-calibrating feature really is.

Table 2 presents data obtained for air. At the steel-air interface, all of the ultrasound is reflected and so the reflection coefficient is expected to be equal to 1.0; this is confirmed by the data.

Although the data in Table 1 and Table 2 were obtained using the same stainless steel plate and transducer, different pulser-receivers with different settings were used in each case. Also, the FFT analysis was obtained using the FFT function on the digital oscilloscope for the data in Table 1 and using Matlab for the data in Table 2. These differences are the reason that the slope for water in Table 1 and Table 2 are not the same.

Table 1 Multiple echo data

Echo Number	LN (FFT Amplitude)				
	Pulser Width (ns)				
	102	92	84	78	68
6	3.436	3.408	3.367	3.333	3.247
9	2.821	2.793	2.752	2.717	2.629
12	2.145	2.119	2.082	2.049	1.961
15	1.500	1.476	1.437	1.403	1.320
18	0.813	0.790	0.754	0.722	0.641
21	0.126	0.098	0.057	0.020	−0.067
Slope	−0.2212	−0.2210	−0.2209	−0.2209	−0.2207
R^2	0.9997	0.9997	0.9996	0.9996	0.9996

The independent measurement of the acoustic impedance was carried out by measuring the density of the liquid and determining the velocity of sound in the liquid. The velocity of sound was measured for water, 10% sugar water, and 30% sugar water. For other weight percentages, the velocity was found by interpolation. Therefore, there is some undetermined percentage error in this independent measurement. The independent measurement of density was obtained by weighing a known volume of the sample.

Table 3 lists the data obtained for a 5-MHz transducer mounted upon a stainless steel plate 3.8-mm thick. The dimensions of the transducer are 25 mm by 13 mm. The amplitude data were obtained by using a frequency of 5.5 MHz for the FFT analysis.

While signal averaging took place to obtain the echoes plotted in Fig. 2, only one value of the slope was obtained for each sample shown in Tables 1 and 2. In an automated system, many averages of the slope would be taken—10 at a minimum. The oscilloscope has an 8-bit digitizer, which means that the vertical axis of the oscilloscope (voltage) is divided into 2^8 or 256 bins. More accuracy would be obtained by using a 12-bit digitizer, or 4096 bins along the axis. Thus, the errors in the acoustic impedance can be reduced—possibly to 1% or less.

Summary and Conclusions

Some conclusions are as follows:

- The analysis method provides a way to measure very small changes in reflection coefficient, and hence, very small changes in the density when using stainless steel (or other solids).

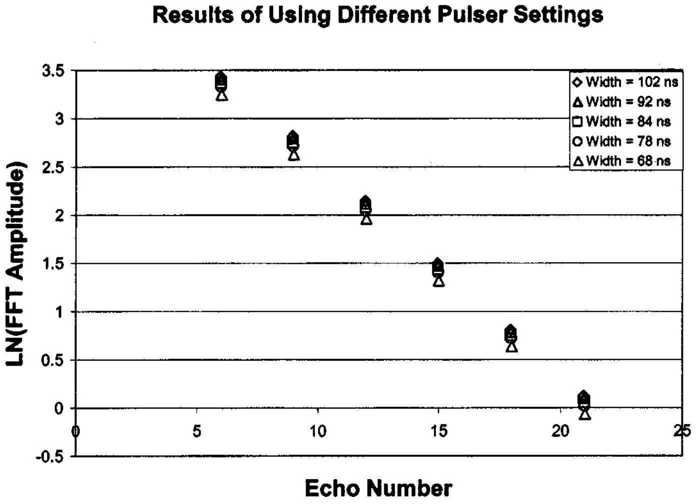

Fig. 4 A graph of the LN (FFT Amplitude) versus echo number for a range of pulse widths

Table 2 Data for 6.3-mm-thick stainless steel plate

Liquid	Independent Measurement of Density, kg/m^3	Slope Log Plot	Sensor Reflection Coefficient	Sensor Measurement of Acoustic Impedance, kg/m^2 sec×10^6	Independent Measurement of Acoustic Impedance, kg/m^2 sec×10^6	Percent Error, %
water-beg	998	−0.2042	0.9382	1.479	1.479	0.0
water-end	998	−0.2040	0.9385	1.472	1.479	−0.5
2.5% SW	1006	−0.2035	0.9389	1.462	1.499	−2.5
5.0% SW	1016	−0.2073	0.9354	1.549	1.521	1.8
7.5% SW	1026	−0.2058	0.9368	1.515	1.545	−1.9
10% SW	1038	−0.2070	0.9357	1.543	1.570	−1.7
15% SW	1065	−0.2094	0.9334	1.598	1.624	−1.6
20% SW	1097	−0.2126	0.9304	1.673	1.684	−0.7
air		−0.1344	1.0061			

Table 3 Data for 3.8-mm-thick stainless steel plate

Liquid	Independent Measurement of Density, kg/m^3	Slope Log Plot	Sensor Reflection Coefficient	Sensor Measurement of Acoustic Impedance, kg/m^2 sec$\times 10^6$	Independent Measurement of Acoustic Impedance, kg/m^2 sec$\times 10^6$	Percent Error, %
water		−0.2943			1.481	
5.0% SW	1010	−0.2968	0.9359	1.538	1.525	0.8
10% SW	1027	−0.2981	0.9347	1.567	1.578	−0.7
15% SW	1057	−0.3020	0.9310	1.658	1.627	1.9
20% SW	1074	−0.3026	0.9305	1.671	1.686	−0.9
30% SW	1115	−0.3153	0.9188	1.965	1.809	8.7
40% SW	1170	−0.3206	0.9139	2.089	1.964	6.4
air		−0.2197	1.0109			

- The self-calibrating feature enables the design of a clamp-on sensor.
- Changes in the pulser voltage do not affect the measurement due to the self-calibrating feature.
- The calibrating time is reduced due to the self-calibrating feature.
- Wireless technology could be utilized to design a sensor to measure density and velocity of sound and thus eliminate the long cables from the sensor to the computer acquisition system.

A computer-controlled system is currently being developed with a 12-bit 100-MHz digitizer for measuring the acoustic impedance and the TOF to determine the density.

A U.S. Patent application has been filed for this measurement technique.

Acknowledgments

Pacific Northwest National Laboratory is operated for the U.S. Department of Energy by Battelle Memorial Institute under Contract No. DE-AC06-76RLO1830.

References

[1] Workman, Jr., J., Veltkamp, D. J., Doherty, S., Anderson, B. B., Creasy, K. E., Koch, M., Tatera, J. F., Robinson, A. L., Bond, L., Burgess, L. W., Bokerman, G. N., Ulhman, A. H., Darsey, G. P., Mozayeni, F., Bamberger, J. A., and Greenwood, M. S., 1999, ''Process Analytical Chemistry,'' Anal. Chem., **71**(12), pp. 121R–180R.

[2] Greenwood, M. S., Skorpik, J. R., Bamberger, J. A., and Harris, R. V., 1999, ''On-line density sensor for process control of liquids and slurries,'' Ultrasonics, **37**, 159–171.

[3] Greenwood, M. S., and Bamberger, J. A., 2002, ''Ultrasonic sensor to measure the density of a liquid or slurry during pipeline transport,'' Ultrasonics .

[4] Povey, M. J. W., 1997, Ultrasonic techniques for fluids characterization, Academic Press (New York).

Sayavur I. Bakhtiyarov*
e-mail: sayavurb@eng.auburn.edu

Ruel A. Overfelt

Sorin G. Teodorescu

Materials Processing Center,
202 Ross Hall, Mechanical Engineering Department,
Auburn University, Auburn, AL 36849-5341, USA
Phone: (334) 844-6198
Fax: (334) 844-3400

Fraction Solid Measurements on Solidifying Melt

A new indirect method to measure fraction solid in molten metals is presented. The method is based on the phenomena that when a metal sample (solid or liquid) rotates in a magnetic field (or the magnetic field rotates around a stationary sample), circulating eddy currents are induced in the sample, which generate an opposing torque related to amount of solid phase in a solidifying melt between the liquidus and solidus temperatures. This new technique is applied for measuring fraction solid on commercial A319 aluminum alloy. The solidification curves obtained by the proposed method at different cooling rates are in good agreement with predictions made by the Scheil model.
[DOI: 10.1115/1.1677450]

Introduction

An understanding of the solidification phenomenon requires knowledge of many thermophysical properties of the metal in both solid and liquid states, and in the mushy zone. Fraction solid is one of the important properties of the metals necessary to optimize the metallurgical processes and to develop mathematical models to predict feedability of casting. Fraction solid is defined as the percentage of solid phase that precipitates in a solidifying melt between the liquidus and solidus temperatures. Thermodynamic and metallographic databases were developed previously, which allow the phase constitution of multicomponent aluminum-based alloys to be predicted [1,2]. Saunders [2] applied computer-aided thermodynamic phase diagram calculations (CALPHAD) method to predict the phase formations in commercial aluminum alloys. Using the assumption of Scheil type conditions, author predicts non-equilibrium solidification behavior such as fraction solid, phase formation and latent heat evolution.

The methods of fraction solid measurements can be categorized in two groups:

- Direct measurements techniques
- Indirect measurements techniques

The direct technique of choice for most materials is the quantitative metallography. This method is based on an image analysis to determine the volume fraction of phases created between the liquidus and solidus temperatures. Under rapid cooling rates small test samples sustain the structure at a given temperature. Structural transformation during quenching is minimized due to high cooling rates.

The thermal analysis technique is another direct method for measuring fraction solid in solidifying metals. The fraction solid is proportional to the amount of heat evolved from the solidifying specimen, which is calculated from the cooling curve as the integrated area between the zero line and the first derivative curve. Differential thermal analysis (DTA) also has been utilized for measuring fraction solid with high accuracy. In laboratory conditions, a differential scanning calorimetry can be used for determining fraction solid. In heat balance model fraction solid (f_s) is determined as a cumulative area between the ''zero'' cooling curve (zc) and the first derivative of the cooling curve (cc) as [3,4]

$$f_s=\frac{C_p}{L}\cdot\int_0^t\left[\left(\frac{dT}{dt}\right)_{cc}-\left(\frac{dT}{dt}\right)_{zc}\right]dt, \tag{1}$$

where C_p is specific heat, L is latent heat of solidification. ''Zero'' cooling curve is a hypothetical cooling curve without phase transformations.

Indirect measurement techniques are based on relationship between fraction solid and physical properties of the test sample. Kiuchi et al. [5] developed a method to estimate the fraction solid from the measured uniaxial flow stress. This method requires calibration tests, which relates fraction solid and decrease ratio of flow stress. Kiuchi and Sugiyama [6] proposed another indirect method to estimate the fraction solid of metals and alloys from the measured change of their electrical resistance or electrical potential difference. The method is based on the knowledge that the electric resistance of an alloy due to impurity and lattice defect is independent of the temperature. However, the resistance due to the lattice vibration is affected by the temperature. The electric resistance of an alloy approximately doubles when it melts and loses its ordered lattice structure. This method utilizes the fact that the electrical resistance of the metal or alloy significantly (1.5–2.0 times) increases when it starts to melt and its increase ratio is related to the amount of liquid fraction in the sample. This method also requires calibration tests to relate fraction solid and electrical potential difference. The estimated values of fraction solid for commercial aluminum and copper alloys were in good agreement with those measured straight by the rapid solidification method. Jeng and Chen [7] determined solidification characteristics of the A356.2 aluminum alloy using differential thermal analysis. The measured fraction solid of the alloy was related to the viscosity changes in the sample during solidification process.

In the methods mentioned above, precipitated impurities will affect the measured values of friction solid. In the method based on the electrical resistance measurements, the effect of impurities and lattice defects is independent of the temperature. However, the electrodes in direct contact with the molten sample contribute some uncertainties to the measured values of the electrical potential difference.

There are various mathematical models with certain assumptions for simulation of fraction solid from experimentally obtained fundamental parameters.

A linear model has been adopted without any theoretical foundation [8]. According to this model the latent heat varies linearly between liquidus and solidus temperatures. Hence fraction solid (f_s) is determined as

$$f_s=\frac{T_l-T}{T_l-T_s}, \tag{2}$$

where T_l, T_s and T are liquidus, solidus and instantaneous temperatures, respectively. Due its straightforwardness this model is used often.

---

*Corresponding author.

Contributed by the Fluids Engineering Division for publication in the JOURNAL OF FLUIDS ENGINEERING. Manuscript received by the Fluids Engineering Division January 26, 2003; revised manuscript received June 30, 2003. Associate Editor: D. Siginer.

Lever rule model assumes a very small solidification rate in binary alloys, so the liquid and solid phases are in equilibrium in the mushy zone [8]. Fraction solid is derived as

$$f_s=\frac{(T_m-T_s)(T_l-T)}{(T_l-T_s)(T_m-T)}, \tag{3}$$

where T_m is a melting temperature of the primary component.

Scheil model presumes a homogeneous liquid phase and no solute back diffusion in solid phase [8]. At aluminum-silicon eutectic growth temperature ($T=T^{\mathrm{AlSi}}{}_{\mathrm{e.g.}}$) fraction solid is maximum ($f_s=1$). At temperatures between eutectic growth and liquids temperature ($T^{\mathrm{AlSi}}{}_{\mathrm{e.g.}}<T<T_l$) fraction solid is determined as

$$f_s=1-\left(\frac{T_m-T}{T_m-T_l}\right)^{(T_m-T_s)/(T_s-T_l)}. \tag{4}$$

Stefanescu et al. [4] proposed to estimate fraction solid according to grain nucleation law, assuming that the grains have spherical shape. The knowledge of average equiaxed grain radius (R_g) and number of particles nucleated per unit volume (N_g) allows calculating fraction solid as

$$f_s=1-\exp\left(-\frac{4}{3}\pi R_g^3 N_g\right). \tag{5}$$

Djurdjevic et al. [9] proposed a model based on a thermal and chemical composition analysis (TCCA). In this model, the temperature range between liquidus and solidus is separated into three distinct segments. Each segment is related to certain metallurgical reactions that occur during solidification. The prediction of fraction solid is based on metallurgical reaction temperatures, which are functions of chemical composition of the alloy. The calculations of the fraction solid for A319 aluminum alloy are in good agreement with the experimental data.

In this paper, we propose a new indirect method to measure fraction solid in molten metals, based on the torque measurements in a moving magnetic field.

Experimental Apparatus and Procedures

We developed a rotational inductive measurement technique to measure the fraction solid of metals and alloys over wide ranges of temperatures. This technique is contactless and thus prevents chemical reactions between molten samples and contacting probes as in previously utilized direct and indirect (electrical potential difference) methods. The method is based on the phenomena that when a metal sample (solid or liquid) rotates in a magnetic field (or the magnetic field rotates around a stationary sample), circulating eddy currents are induced in the sample, which generate an opposing torque proportional to the electrical properties of the sample [10]. On the other hand, the electrical properties of conductors are strongly dependent on temperature and solid/liquid ratio in the melting/solidifying specimen. Hence the measured torque is related to the amount of solid phase that precipitates in a solidifying melt in the mushy zone. In liquid metals and alloys, the applied magnetic field also causes significant rotation of the liquid in the crucible, which decreases the angular velocity between the field and the sample [11]. The experimental apparatus to measure fraction solid of metals and alloys over wide range of temperatures is shown in Fig. 1. A computer controlled Brookfield rheometer Model DV-III was used to provide a constant rotational speed to the metal sample and to measure the torque. This rheometer enables torque measurements from 0 to 673.7×10^{-7} N-m at constant speeds from 0 to 250 rpm in 0.1 rpm increments. The rheometer has an RS232 serial port for communication with a local computer.

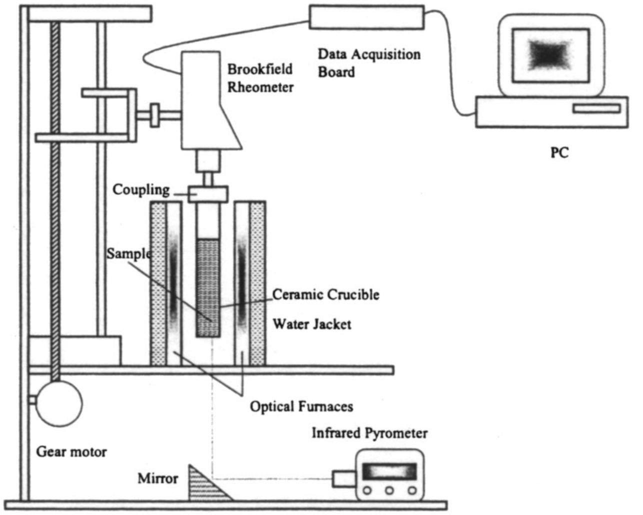

Fig. 1 Schematics of experimental apparatus used for electrical resistivity measurements of solid and molten metals

The temperature of the sample was measured remotely by a portable two-color infrared thermometer M90 focused into a hole in the bottom of the crucible assembly, since thermocouple leads could not be inserted into the rotating samples. Focusing into the hole in the crucible bottom eliminated spurious temperature data from extraneous reflections into the infrared thermometer from the optical heaters. The infrared thermometer output was calibrated to actual temperature by comparing against thermocouple data using a dummy load, with 0.25% accuracy. The pyrometer output was connected to computer and the temperature data obtained were synchronized with data for measured torque and angular velocity of the crucible. As a test material in our experiments we used a commercial A319 aluminum alloy. A composition and thermophysical properties of this alloy are given in Table 1.

Metal samples of aluminum alloy A319 (19.05 mm diameter and 38.1 mm length) were inserted into high purity alumina cylindrical crucibles with flat bottoms. The extruded alumina crucibles (19.05 mm inner diameter and 152.4 mm length) were attached to the spindle of the rheometer through a specially designed coupler to provide concentricity to the rotating shaft, crucible and sample. Molten aluminum alloy tends to oxidize and burn. To avoid oxidation of the test sample, a thin (~1 mm) Boron Nitride film was applied on its top surface. The same sample diameter was maintained for each set of tests. The rotational technique of this geometry is exposed to the end effects in the crucible. The effect was eliminated from the results of two experiments accomplished with the different heights (25.4 mm and 38.1 mm) of the pure metal samples in the crucible at the same angular speed and magnetic induction.

Four quartz infrared line heating elements (2 kW each) housed in elliptical cast aluminum frames were used to heat the samples in the experiments. The heated length of the chamber was 167 mm. The elliptical reflectors concentrated the infrared energy to the crucible surface (Fig. 2). Copper tube connections are pro-

Table 1 Thermophysical properties and composition of A319 aluminum alloys (http://metalcasting.auburn.edu/)

A319 aluminum alloy	
Solidus Temperature	723 K
Liquidus Temperature	869 K
Latent Heat	400 J/g
Density at Melting Point	2.5328 g/cm^3
Composition	Si = 6.1% Fe = 0.68% Mg = 0.3% Cu = 3.01% Mn = 0.32% Zn = 0.71%

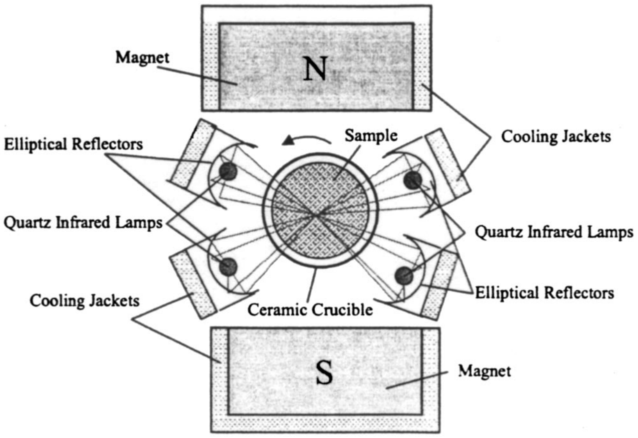

Fig. 2 Diagram of sample-magnetic field-optical furnace arrangement and heating energy focus action

vided for inlet and outlet flow of water to cool the lamp reflector bodies. Tap water at 15°C and 600 kPa was supplied to cool the unit.

The magnetic field was produced by two neodymium-iron permanent magnets. A Hall-effect gaussmeter was used to measure the magnetic field strength. The gaussmeter provides DC and AC field readings from $\pm 10^{-5}$ to ± 2 Tesla with 0.1% resolution. Changing the separation between the magnets allowed us to obtain magnetic fields of different magnitudes. Contour mapping of the magnetic field strength revealed that the magnetic induction varies in both vertical and horizontal directions. Contour lines for the magnetic induction at different distances between the magnets are shown in Fig. 3. It is estimated that the magnetic induction over the test sample varies $\pm 10\%$ in vertical direction and $\pm 7\%$ in horizontal direction compared to its average value. Neither the coupling system nor the alumina crucible had measurable effects upon the applied magnetic field.

Results and Discussions

Figure 4 shows a cooling curve for A319 aluminum alloy in the temperature range between the liquidus and solidus temperature. As seen from the cooling curve, the temperature range between liquidus and solidus has three distinct segments. According to Djurdjevic et al. [9] these segments are related to metallurgical reactions occurring during alloy solidification. The temperature limits for each segment are found as:

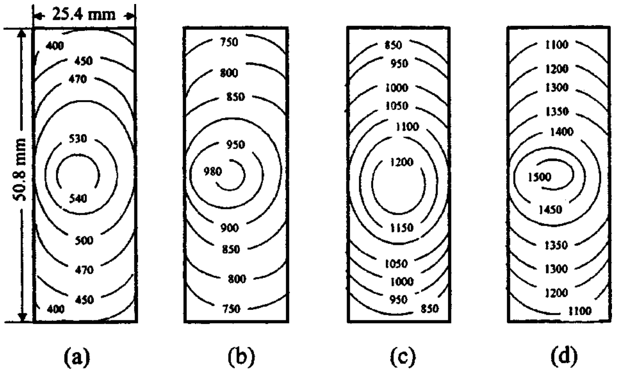

Fig. 3 Contour lines for magnetic induction (in 10^{-4} T) at different distances between magnets: (*a*) 12 cm; (*b*) 9 cm; (*c*) 8 cm; (*d*) 7 cm

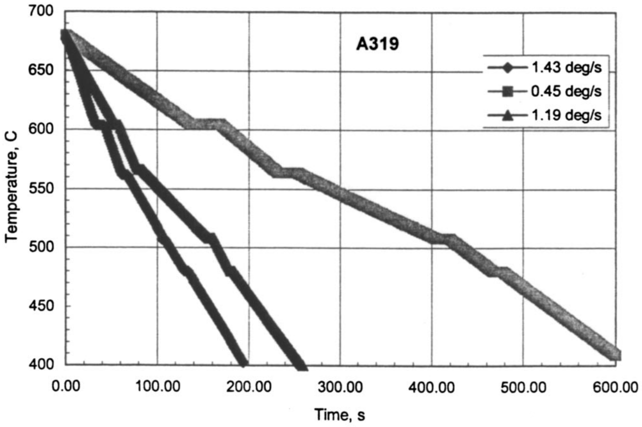

Fig. 4 Cooling curve for A319 aluminum alloy at different cooling rates

i. $T^{\mathrm{AlSi}}_{\mathrm{e.g}} < T < T_l$—nucleation and growth of α-Al dendrite network
ii. $T^{\mathrm{AlCu}}_{\mathrm{e.g.}} < T < T^{\mathrm{AlSi}}_{\mathrm{e.g.}}$—nucleation and growth of Al-Si eutectic
iii. $T_s < T < T^{\mathrm{AlCu}}_{\mathrm{e.g.}}$-nucleation and completion of Al-Cu reaction

Using a thermal analysis technique [12] we determined the characteristic temperatures as shown in Table 2. These values of characteristic temperatures for A319 aluminum alloy are in good agreement with those known from literature. The first derivatives of the cooling curves versus temperature are presented in Fig. 5.

Figure 6 shows a variation of the measured torque for A319 aluminum alloy at different cooling rates. As seen from this figure, inflection points on the torque-time curves correspond to characteristic temperatures determined above (Table 2).

Table 2 Characteristic temperatures determined for A319 aluminum alloy at different cooling rates

Characteristic Temperatures	Cooling Rate 0.45 deg/s	Cooling Rate 1.19 deg/s	Cooling Rate 1.43 deg/s
T_1, °C	605	604	604
$T^{\mathrm{AlSi}}_{\mathrm{e.g.}}$, °C	564	566	562
$T^{\mathrm{AlCu}}_{\mathrm{e.g.}}$, °C	508	508	507
T_s, °C	480	480	480

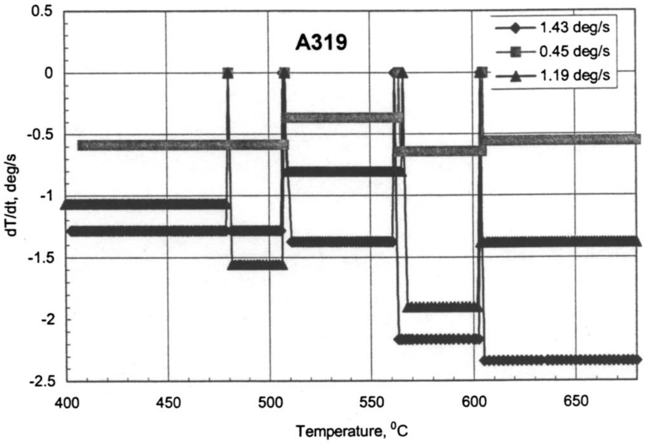

Fig. 5 First derivative curve versus temperature for A319 aluminum alloy at different cooling rates

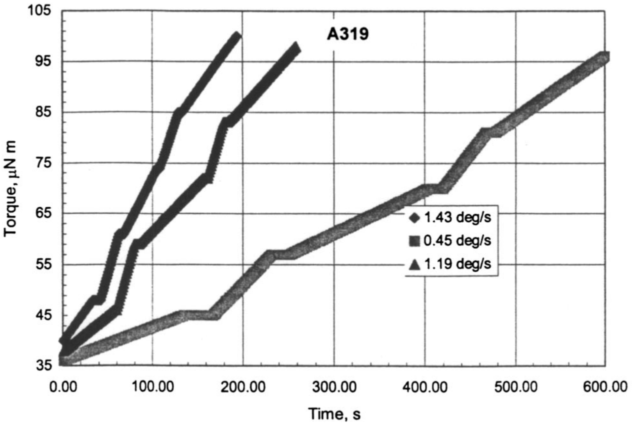

Fig. 6 Measured torque for A319 aluminum alloy at different cooling rates

From data shown in Figs. 4 and 6 we plotted a variation of measured torque versus temperature (Fig. 7). From the measured torque values we calculated a normalized torque ($\bar{M}$) as follows:

$$\bar{M} = \frac{M_s - M}{M_s - M_l}, \tag{6}$$

where M_s and M_l are measured torque at solidus and liquidus temperatures, respectively.

Figure 8 shows a variation of the dimensionless parameter φ with temperature, where φ is defined as

$$\varphi = \left(\frac{T_s - T_l}{T_m - T_s}\right) \cdot \frac{\ln\left(\dfrac{M_m - M}{M_m - M_l}\right)}{\ln\left(\dfrac{T_m - T}{T_m - T_l}\right)}. \tag{7}$$

Here, a technique proposed by Kiuchi and Sugiyama [6] has been used to establish a relationship between normalized torque and fraction solid. The solidification curves (relationship between the normalized torque and the fraction solid) obtained by the technique proposed in this work, and predictions made by the linear and Scheil models are shown in Figs. 9 and 10. As seen from these figures, the measured solidification curves are in a good agreement with the predictions by the Scheil model than those predicted by the linear model.

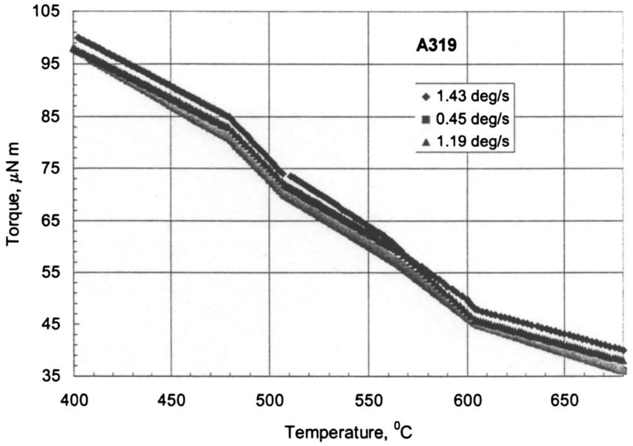

Fig. 7 Variation of measured torque with temperature for A319 aluminum alloy at different cooling rates

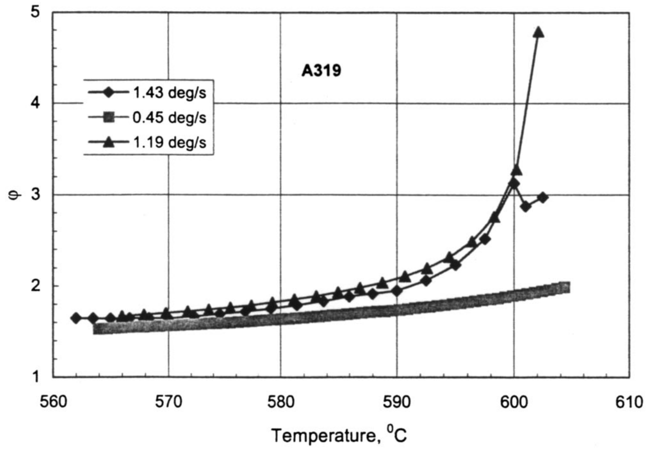

Fig. 8 Variation of parameter φ with temperature for A319 aluminum alloy at different cooling rates

Conclusions

A new indirect method is developed to measure the fraction solid in solidifying metals and alloys. The proposed technique establishes relationship between the fraction solid and the opposing torque in the permanent magnetic field due to the induced

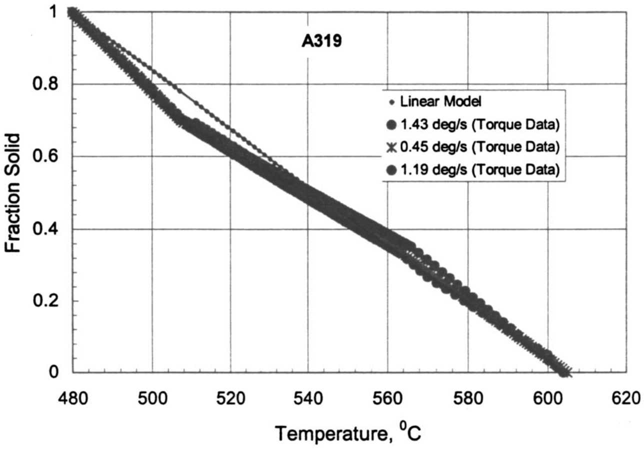

Fig. 9 Solidification curves for A319 aluminum alloy at different cooling rates compared to linear model

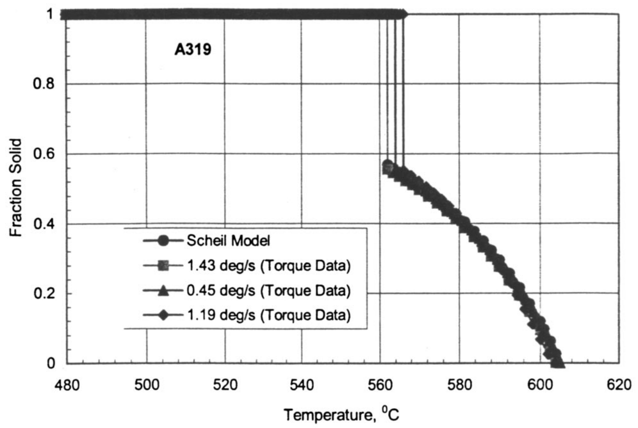

Fig. 10 Solidification curves for A319 aluminum alloy at different cooling rates compared to Scheil's model

eddy currents. The technique was applied to determine the fraction solid for commercial A319 aluminum alloy. The solidification curves obtained by the proposed method at different cooling rates are in good agreement with the predictions made by the Scheil model.

Acknowledgments

The authors gratefully acknowledge the financial support received from NASA's Space Product Development at Marshall Space Flight Center under Cooperative Agreement No. NCC8-240.

References

[1] L. Bäckerud, Chai, G., and Tamminen, J., 1997, ''Solidification Characteristics of Aluminum Alloys,'' **2**, Foundry Alloys, AFS/Skanaluminium.
[2] Saunders, N., 1996, ''Phase Diagram Calculations for Commercial Al-Alloys,'' Mater. Sci. Forum, **217–222**, pp. 667–672.
[3] Huang, H., Suri, V. K., Hill, J. L., and Berry, J. T., 1991, ''Heat Source/Sink Algorithm for Modeling Phase Changes During Solidification in Castings and Water Evaporation in Green Sand Molds,'' AFS Transactions, **54**, pp. 685–689.
[4] Stefanescu, D. M., Upadhya, G., and Bandyopaadhyay, D., 1990, ''Heat Transfer-Solidification Kinetics Modeling of Solidification of Castings,'' Metall. Trans., **2A**, pp. 997–1005.
[5] Kiuchi, M., Sugiyama, S., and Arai, K., 1979, ''Experimental Study on Mushy Metal Forming,'' J. Jpn. Soc. Technol. Plast., **20**(223), pp. 762–765.
[6] Kiuchi, M., and Sugiyama, S., 1994, ''A New Method of Detect Solid Fractions of Mushy/Semi-Solid Metals and Alloys,'' Annals of The CIRP, **43**(1), pp. 1–4.
[7] Jeng, S. C., and Chen, S. W., 1996, ''Determination of The Solidification Characteristics of The A356.2 Aluminum Alloy,'' Mater. Sci. Forum, **217–222**, pp. 283–288.
[8] Flemings, M. C., *Solidification Processing*, McGraw-Hill, 1972.
[9] Djurdjevic, M. B., Kierkus, W. T., Byczynski, G. E., Stockwell, T. J., and Sokolowski, J. H., 1999, ''Modeling of Fraction Solid for the 319 Aluminum Alloy,'' AFS Transactions, **14**, pp. 173–179.
[10] Iida, T., and Guthrie, R. I. L., *The Physical Properties of Liquid Metals*, Clarendon Press, Oxford, 1988, pp. 227–229.
[11] Moffatt, H. K., 1965, J. Fluid Mech., **22**(3), pp. 521–528.
[12] Rappaz, M., 1989, ''Modeling of Microstructure Formation in Solidification Processes,'' Int. Mater. Rev., **34**(3), pp. 93–123.

Adam D. Rosenthal
Massachusetts Institute of Technology,
Department of Electrical Engineering and
Computer Science,
Laboratory for Electromagnetic and Electronic
Systems
Cambridge, MA 02139

Carlos Rinaldi
Massachusetts Institute of Technology,
Department of Chemical Engineering
Cambridge, MA 02139

Thomas Franklin

Markus Zahn

Massachusetts Institute of Technology,
Department of Electrical Engineering and
Computer Science,
Laboratory for Electromagnetic and Electronic
Systems
Cambridge, MA 02139

Torque Measurements in Spin-Up Flow of Ferrofluids

Measurements of magnetic-field-induced torque in applied uniform rotating magnetic fields are presented and compared to theoretical analyses for water- and oil-based ferrofluids. These experiments measure the viscous torque on the inner wall of a stationary hollow polycarbonate spindle that is completely filled with ferrofluid and attached to a viscometer functioning as a torque meter. The spindle remains stationary and is centered inside a three-phase AC 2-pole motor stator winding, creating uniform time-varying rotating magnetic fields. The viscous torque is measured as a function of magnetic field amplitude, frequency, and direction of rotation. These measurements demonstrate that ferrofluid flow and torque are present even in the absence of free surfaces and agree with a recently derived analysis of the torque during spin-up flow of ferrofluids.

[DOI: 10.1115/1.1669030]

1 Introduction

Ferrofluids [1] are suspensions of permanently magnetized colloidal particles coated by a stabilizing dispersant and immersed in a suitably chosen carrier fluid. In the presence of time-varying magnetic fields, ferrofluid particles will rotate in order to align their magnetic dipole moment with the applied field. However, because of the fluid viscosity, the magnetization $\mathbf{M}$ will lag behind the time-varying magnetic field $\mathbf{H}$, thereby resulting in a body-torque density on the ferrofluid, given by $\mu_0 \mathbf{M} \times \mathbf{H}$ (with $\mu_0 = 4\pi \times 10^{-7}$ Henries/m the magnetic permeability of free space), which causes fluid flow. In our experiments, the viscous torque from this magnetic-field-induced flow is measured using a Couette viscometer, as a function of magnetic field amplitude and frequency.

Ferrofluids are a scientifically and commercially important realization of polarizable systems. As such, they are characterized by the presence and effect of long-range body-couples and nonsymmetric viscous stresses, as well as more exotic phenomena, such as couple stresses representing the direct-contact transport of microstructure angular momentum. Due to their physical, chemical, and magnetic properties, ferrofluids are of increasing interest in the design of magneto-responsive colloidal extractants [2], microfluidic pumps and actuators driven by alternating or rotating magnetic fields [3–7], and in biological/biomedical applications such as drug delivery vectors, magnetic cell sorting schemes, and magnetocytolysis treatment of localized tumors [8,9].

The phenomenon of spin-up flow of ferrofluids has received considerable attention [10–15] during the development of the field of ferrohydrodynamics. Experiments are carried out by placing a sample of ferrofluid in an open-top cylindrical container subjected to a rotating magnetic field. In such a stationary cylindrical container, the top surface of the ferrofluid is observed to rotate rigid-body-like in a direction which depends on the applied magnetic field amplitude and frequency. Such essentially rigid-body motion is observed at the top free surface of the fluid right out to the stationary cylindrical vessel wall, except for a thin boundary layer.

The general perception in the literature is that the ferrofluid and magnetic field rotate in opposite directions. However, some authors [11–13] report observations where the ferrofluid switches between co-rotation and counter-rotation with respect to the applied magnetic field depending on magnetic field amplitude and frequency. Explicitly, [12] reports co-rotation of field and fluid for low applied fields and counter-rotation for high applied magnetic fields, whereas [11] and [13] observe counter-rotation for low applied magnetic fields and co-rotation for higher applied fields. We have made similar observations in our laboratory, where a water-based ferrofluid placed in a cylindrical container and subjected to the uniform rotating magnetic field generated by a three-phase two-pole magnetic machine stator winding is observed to co-rotate with the applied magnetic field for small magnetic fields and counter-rotate with respect to the magnetic field for large magnetic fields. In addition to this, we have observed the direction of free-surface rotation change depending on the axial location of the free surface in the gap of the magnetic machine stator.

The confusion regarding field and fluid rotation sense, and the applicability of various theoretical analyses [16–20], is compounded when one considers that all available observations are made at the free-surface of the opaque ferrofluid using various types of tracer beads, with no way to determine the flow profiles prevailing throughout the volume of fluid. It is clear that surface flow observations will be problematic and probably not representative of the bulk-flow situation when one considers that curvature-driven flows have been observed at ferrofluid free surfaces [15]. Thus, there remains a need for accurate, direct measurements of bulk-flow related quantities. One such quantity is the total torque required to restrain the hollow cylinder containing the ferrofluid.

Observations of counter-rotation of field and fluid led [11] to investigate the direction in which the cylindrical container would rotate if it could freely do so. This represents an indirect measurement of the magnetic torque applied on the ferrofluid. One would expect the counter-rotating fluid to drag the cylindrical container with it, but experiments show the container co-rotating with the field whereas the fluid counter-rotates. Such observations have

---

Contributed by the Fluids Engineering Division for publication in the JOURNAL OF FLUIDS ENGINEERING. Manuscript received by the Fluids Engineering Division January 17, 2003; revised manuscript received June 14, 2003. Associate Editor: D. Siginer

Table 1 Physical and magnetic properties at room temperature for water-based and Isopar-M ferrofluids used

Ferrofluid	ρ, [kg/m^3]	η, [Nsm^{-2}]	$\mu_0 M_s$,[†] [Gauss]	ϕ[‡]	χ*
Water-based	1,220	0.007	203	0.036	0.65
Isopar-M	1,180	0.011	444	0.079	2.18

[†]Determined using equation (5).
[‡]Determined using equation (4).
*Determined using Fig. 2.

since been corroborated by [12] and [15]. However, all these observations are of a qualitative nature, not having directly measured the actual torque required to restrain the container. Hence, the motivation of our contribution—to obtain direct quantitative measurements of the torque required to restrain the cylindrical container during spin-up flow of a ferrofluid.

2 Ferrofluid Material and Magnetic Properties

Two types of ferrofluid were obtained from Ferrofluidics Corporation (Nashua, NH): a water-based ferrofluid (MSGW11) and an oil-based ferrofluid with Isopar-M as the carrier fluid (NF1634), each with ~10 nm diameter magnetite particles. Ferrofluid density ρ, viscosity η, and magnetization curves were measured. From the magnetization curves the saturation magnetization $\mu_0 M_s$, volume fraction of magnetic particles ϕ, magnetic susceptibility χ, magnetic particle diameter d, and magnetic time constants (τ_B, τ_N, τ) were determined for both ferrofluids. These results are summarized in Tables 1 and 2.

Physical Properties. The ferrofluid densities were determined gravimetrically using an analytical mass balance and a calibrated burette. The shear viscosity η for each ferrofluid at zero applied magnetic field was measured at room temperature using a Brookfield viscometer Model LVDV-I+. The recommended Brookfield procedure was used, using 500 mL of ferrofluid in a 600 mL beaker and the Brookfield calibrated stainless steel spindle LV1. The resulting values of density and viscosity are shown in Table 1.

Magnetization Characteristics

Demagnetizing Factor. In determining the magnetic properties of the ferrofluid, it is important to differentiate between the externally applied magnetic field and the magnetic field inside the ferrofluid. The difference between the external magnetic field $\mathbf{H}_e$ and the internal magnetic field $\mathbf{H}_i$ is described by the demagnetization factor, D, given by

$$\mathbf{H}_i = \mathbf{H}_e - \mathbf{M}D. \tag{1}$$

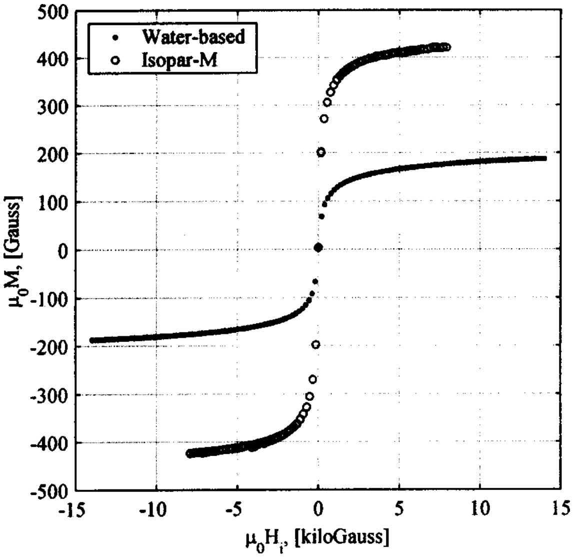

Fig. 1 Magnetization curves for water-based and Isopar-M ferrofluids obtained using a DMS Vibrating Sample Magnetometer at room temperature, $T=299$ K

The demagnetization field arises due to effective magnetic charge induced on the surface of a magnetic material with magnetization **M**, which partially cancels the externally applied magnetic field. Magnetization curves of the ferrofluids were measured using a Digital Measurement Systems (DMS) Vibrating Sample Magnetometer Model 880. Ferrofluid samples were placed in the DMS plastic sample containers, whose dimensions approximate those of an oblate ellipsoid with major to minor axis ratio of $n=2.4$. The demagnetizing factor D corresponding to an oblate ellipsoid is [21]

$$D = \frac{1}{2}\left[\frac{n^2}{(n^2-1)^{3/2}} \arcsin \frac{\sqrt{n^2-1}}{n} - \frac{1}{n^2-1}\right]. \tag{2}$$

Using (2) and $n=2.4$ we obtain a demagnetization factor of $D=0.211$. This value and (1) were used to calculate the internal magnetic field used in the abscissa of the magnetization curves shown in Figs. 1 and 2. This correction is especially important at low magnetic fields, shown in Fig. 2, where the low field magnetic susceptibility is determined.

Saturation Magnetization. For a monodisperse ferrofluid the Langevin equation describes the equilibrium magnetization for a given applied magnetic field [1]:

$$\frac{M}{M_s} = L(\alpha) = \coth \alpha - \frac{1}{\alpha}, \tag{3}$$

where $\alpha = M_d V_p \mu_0 H_i / kT$, with $V_p = \pi d^3/6$ the magnetic core volume per particle. The magnetic volume fraction is defined as

$$\phi = \frac{M_s}{M_d}, \tag{4}$$

Table 2 Estimated magnetic particle diameters and relaxation times at room temperature for water-based and Isopar-M ferrofluids used

Ferrofluid	$d_{\min}$, [nm][†]	$d_{\max}$, [nm][‡]	$d_{\max}$, [nm]*	τ_B, [s]**	τ_N, [s][§]	τ, [s][+]
Water-based	5.5	11.9	11.4	$2\times10^{-6}-10^{-5}$	$5\times10^{-9}-2\times10^{-2}$	$5\times10^{-9}-1\times10^{-5}$
Isopar-M	7.7	13.8	12.6	$7\times10^{-6}-2\times10^{-5}$	$10^{-7}-200$	$10^{-7}-2\times10^{-5}$

[†]Determined using Eq. (5).
[‡]Determined using Eq. (6).
*Determined using Eq. (7).
**Determined using Eq. (9) and assuming 2 nm surfactant bi-layer thickness [2].
[§]Determined using Eq. (10).
[+]Determined using Eq. (11).

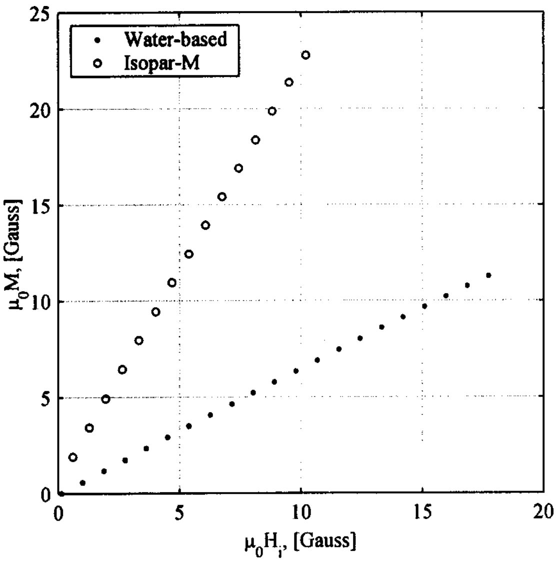

Fig. 2 Linear region (low-field) of the magnetization curves obtained for water-based and Isopar-M ferrofluids at room temperature, T=299 K

where M_d is the domain magnetization ($=446$ kAm^{-1} for magnetite). Obtaining a value of M_s is difficult experimentally since it requires application of a magnetic field of infinite magnitude. Yet ϕ can be calculated from (4) and the high-applied-field asymptote of the Langevin curve [1]:

$$\lim_{\alpha\gg 1} L(\alpha)\approx\left(1-\frac{1}{\alpha}\right)=\left(1-\frac{6}{\pi}\,\frac{kT}{\mu_0 M_d H_i d^3}\right), \tag{5}$$

where T is the absolute temperature, and $k=1.38\times 10^{-23}$ J/K is Boltzmann's constant. Equation (5) is a linear relationship between M and $1/H_i$ and can be rewritten as $\mu_0 M=c+b/(\mu_0 H_i)$ where $c=\mu_0 M_s$ and $b=-6kT\mu_0 M_s/(\pi M_d d^3)$. The parameters b and c are determined by a least-squares fit to the measurements of Fig. 1 in the high field region where $\alpha\gg 1$ to yield estimated values for the saturation magnetization and particle diameter for the smallest magnetic particles. In our study, we fit the uppermost and lowermost 30 data points (60 in total).

Magnetic Susceptibility. In order to determine the initial magnetic susceptibility, the slope of the low-field linear region was determined. The magnetization curves in Fig. 1 do not have enough precision in the low-field region to accurately determine the slope. For this reason, the low-field linear region was separately measured for the water-based ferrofluid and the Isopar-M ferrofluid and is shown in Fig. 2. The slope, corresponding to the initial magnetic susceptibility $\chi=M/H$, was determined through a simple linear least-squares fit of the data and is listed in Table 1.

Magnetic Particle Size. Ferrofluids are expected to have a range of particle sizes that can be determined by examination of the magnetization behavior. The minimum particle diameter was estimated from the high-field asymptote of the Langevin curve, by rearranging the coefficient b of the linear fit for d. Since the coefficient b is most affected by the smallest particles, this calculation provides an estimate for the minimum particle diameter $d=d_{\min}$.

The maximum particle diameter for the water-based ferrofluid was estimated by using the low-field limit of the Langevin curve [1]:

$$\lim_{\alpha\ll 1} L(\alpha)\approx\frac{\alpha}{3}=\frac{\pi}{18}\,\frac{\mu_0 M_d H_i d^3}{kT}, \tag{6}$$

and the value of the initial susceptibility, $\chi=\alpha M_S/(3H_i)$, obtained from the slope of Fig. 2. Here, α is most affected by the larger particles, thus providing an estimate for the maximum magnetic particle diameter.

For suspensions that are non-dilute with respect to the magnetic cores Shliomis [22] gives a correction to (6) using the Debye-Onsager theory of polar fluids [23] to account for the effect of dipole-dipole interactions

$$\frac{\chi(2\chi+3)}{\chi+1}=\frac{\pi}{6}\phi\,\frac{\mu_0 M_d^2 d^3}{kT}. \tag{7}$$

The resulting particle diameter ranges thus obtained are summarized in Table 2, with values given for minimum diameter using (5) and maximum diameter using (6) and (7). Note that these diameters are only estimates. Direct experimental observation shows that the actual diameter of the magnetic particle cores may be as much as 2 nm larger than the estimates obtained from the Langevin relation [2].

Relaxation Times. In studying the dynamics of ferrofluids in time-varying magnetic fields, one must consider how the local magnetization changes, or "relaxes," due to fluid convection, particle rotation, and applied fields. The commonly accepted magnetic relaxation equation for an incompressible, magnetically linear ferrofluid undergoing simultaneous magnetization and reorientation due to fluid convection at flow velocity $\mathbf{v}$ and spin angular velocity $\boldsymbol{\omega}$ is [1,24]:

$$\frac{\partial\mathbf{M}}{\partial t}+\mathbf{v}\cdot\nabla\mathbf{M}-\boldsymbol{\omega}\times\mathbf{M}-\frac{1}{\tau}[\mathbf{M}-\chi\mathbf{H}]=0, \tag{8}$$

where τ is the effective relaxation time constant. Equation (8) is applicable under conditions not far removed from magnetization equilibrium [25–27].

The two commonly accepted mechanisms by which ferrofluid magnetic particles relax are Brownian motion, resulting from collision between the magnetic particle and the constituent molecules of the suspending medium, and Néel relaxation, resulting from rearrangement of the magnetic domains without rotation of the particle. The characteristic time describing Brownian motion is [1]

$$\tau_B=\frac{4\pi\eta_0 R^3}{kT}, \tag{9}$$

where η_0 is the shear viscosity of the suspending fluid, and $R=R_p+\delta$ is the hydrodynamic radius, i.e. the sum of the magnetic particle radius, $R_p=d/2$, and the surfactant layer thickness, δ. In estimating the Brownian relaxation time we have assumed the surfactant layer thickness δ is approximately 2 nm [2].

The Néel relaxation time is given as [1]

$$\tau_N=\frac{1}{f_0}e^{(KV_p/kT)}, \tag{10}$$

where f_0 is a characteristic frequency of the magnetic material ($=10^9$ Hz for magnetite), and K is the anisotropy constant of the magnetic domains. The literature gives different values for the anisotropy constant of magnetite, over the range of 23,000 to 100,000 Joules/m^3. Recent work [28] has used Mossbauer spectroscopy to show that the value of K is size dependent, increasing as particle size decreases and gives a value of $K=78{,}000$ Joules/m^3 for 12.6 nm diameter magnetite nanoparticles, which is the value we use in estimating values of τ_N in this work.

The two relaxation processes described above occur in parallel and therefore the effective time constant describing magnetic particle relaxation is given by

$$\frac{1}{\tau}=\frac{1}{\tau_B}+\frac{1}{\tau_N}\Rightarrow\tau=\frac{\tau_B\tau_N}{\tau_B+\tau_N}. \tag{11}$$

The estimated ranges of the resulting Brownian, Néel, and effective relaxation times thus obtained are summarized in Table 2 based on the estimated range of particle size using (5)–(7). Note that the calculated Néel relaxation times vary by seven orders of magnitude for the estimated particle sizes of water-based ferrofluid and by nine orders of magnitude for the Isopar-M ferrofluid, thus, direct experimental determination would be preferable and will be the subject of future work.

3 Apparatus and Experimental Method

We have used a Brookfield Model LVDV-I+ viscometer as a torque meter. When a fixed rotation speed is selected the spindle rotates counterclockwise as the viscometer applies the necessary torque to keep it rotating at the specified speed. When the magnetic-field-induced shear stress on the spindle is in the clockwise direction, i.e. in the direction opposite to spindle rotation, it is harder to turn the spindle at the specified speed; therefore the viscometer applies a higher torque, larger than the torque required to shear the fluid in the absence of a magnetic field. On the other hand, when the magnetic-field-induced shear stress on the spindle is in the counterclockwise direction, i.e. in the same direction as spindle rotation, it is easier to rotate the spindle at the specified speed; therefore the viscometer applies a lower torque, as compared to the torque required to shear the fluid in the absence of a magnetic field.

For our experiments the spindle was set to remain stationary, hence, with zero applied magnetic field no torque is required from the viscometer to restrain the spindle. Under conditions for which a clockwise magnetic-field-induced shear stress arises, a positive torque will be registered, whereas for a counterclockwise shear stress a negative torque will be measured. The range of measurable torque for our Brookfield viscometer is -6.73 μN-m to $+67.3$ μN-m.

The hollow Lexan® (polycarbonate) spindle used in these experiments was completely filled with ferrofluid. The spindle has an inner diameter of 19.6 mm and a hollow chamber length of 62.4 mm, yielding a total volume of 18.8 mm^3. It is important that the spindle be non-conducting and non-magnetic so that the measured torque on the spindle is entirely due to ferrofluid shear stress. The standard stainless steel spindle would act like an induction motor in a time varying magnetic field due to induced eddy currents, which would cause additional magnetic torque on the spindle and thus confuse separation of ferrofluid viscous torque from induction motor torque.

The plastic spindle was placed so that the fluid is centered along the axis of the three phase, 2-pole motor stator winding (uniform magnetic field source in the absence of ferrofluid) with inner bore of 78 mm diameter and magnetic core height 63 mm. The magnetic fields in the motor stator winding were generated using sinusoidally time varying currents with the appropriate phase differences to create magnetic fields that rotate clockwise or counterclockwise.

Measurements were taken at frequencies of 5, 10, 50, 100, 500, 1,000, 2,000, and 5,000 Hz with an input current of 0, 1, 2, 3, 4, and 5 Amps peak. In the 2-pole stator, each ampere of peak input current corresponds to a uniform external magnetic field of 26 Gauss rms. These magnetic field measurements were made in the absence of ferrofluid, and therefore reflect the external magnetic field and do not incorporate the demagnetizing effect of the ferrofluid. Over the space occupied by the ferrofluid filled spindle, the external magnetic field increased from the radial center of the winding by less than 2% at 10 mm radius with negligible variation over angle from zero to 360 degrees. In the axial direction the magnetic field decreased from the axial center of the winding by less than 18% at the top and bottom of the iron core of the winding, 31.2 mm above and below the axial center of the winding.

For higher frequencies, some trials contain fewer data points. This is either because the torque was outside the maximum operating torque range for the Brookfield viscometer or because the voltage across the motor winding terminals was too high for safe operation. With an applied current at frequency f, the inductive reactance $L\Omega_f$ increases with radian frequency $\Omega_f = 2\pi f$ and limits the current that can be supplied to the stator winding. By adding the appropriate capacitor, C, in series with the motor, a resonant circuit was used so the capacitive reactance $1/[C\Omega_f]$ cancels the inductive reactance, i.e. $L\Omega_f = 1/[C\Omega_f]$, thereby decreasing the high frequency winding impedance so that 1 to 5 ampere currents could be applied. This modification to the experimental setup was needed at frequencies of 500 Hz and above.

4 Measurements of Torque During Spin-Up Flow

Figures 3 and 4 present the measured torque vs. magnetic field amplitude for various frequencies with clockwise magnetic field rotation in the range of 5 Hz–5 kHz. The spindle remained stationary for all measurements. Measurements were performed for both clockwise and counter-clockwise magnetic field rotation, for which the torque just reverses sign. Thus, we mainly present data here for clockwise magnetic field rotation as this results in a clockwise viscometer torque for which our viscometer had the largest operating range.

The torque required to restrain the spindle was measured as a function of magnetic field amplitude for the water-based ferrofluid and Isopar-M ferrofluid as shown in Fig. 3. Both measurement sets show that the measured torque, and therefore the magnetic-field-induced shear stress, increases with magnetic field amplitude. The measured torque also increases with the applied field frequency, particularly for the Isopar-M ferrofluid. For the water-based ferrofluid the torque is seen to scale with applied frequency for the lower frequencies but apparently this dependence saturates at the higher field frequencies.

The data of Fig. 3 is re-plotted in Fig. 4, now with torque as a function of applied-field frequency. Both figures show that the measured torque increases with magnetic field frequency, except for the water-based ferrofluid at frequencies of 500 Hz and above, which show torque saturation with respect to field frequency f.

5 Analysis of Torque on the Hollow Spindle

The torque on the internal wall of the hollow spindle potentially has two components: (i) the torque due to surface-excess magnetic forces stemming from the rapid change in magnetic properties at the wall-fluid interface, and (ii) the torque due to viscous traction and the action of the magnetic fluid's couple-stress pseudodyadic. In general, both must be accounted for when deriving expressions for the experimental torque applied to restrain the stationary hollow spindle.

5.1 Surface-Excess Magnetic Torque.

The surface-excess magnetic torque at the wall-fluid interface may be conveniently obtained by evaluating the jump in the "magnetic stress" tensor (or the so-called Maxwell stress) across the wall-fluid interface. Use of this mathematical technique circumvents the need to know the exact distribution of magnetic fields in this region with rapidly varying magnetic properties. The Maxwell stress applicable to an incompressible ferrofluid is given by [1,29]

$$\mathbf{T}^M = \mathbf{B}\mathbf{H} - \frac{1}{2}\mu_0 H^2 \mathbf{I}; \quad \mathbf{B} = \mu_0(\mathbf{H}+\mathbf{M}) \tag{12}$$

where $\mathbf{I}$ is the identity tensor.

We are interested in determining the θ-directed shear stress component due to the jump in the Maxwell stress tensor across the ferrofluid-spindle wall interface (the r-directed component is of no consequence as it does not contribute to the z-directed torque, which is the experimentally measurable quantity). The θ-directed surface-excess magnetic force per unit area on the cylindrical wall at radius R, f_θ^M, is given by the jump in the $r\theta$-component of the Maxwell stress

$$\begin{aligned} f_\theta^M &= T_{r\theta}^M(r=R^+) - T_{r\theta}^M(r=R^-), \\ &= (B_r H_\theta)|_{r=R^+} - (B_r H_\theta)|_{r=R^-}. \end{aligned} \tag{13}$$

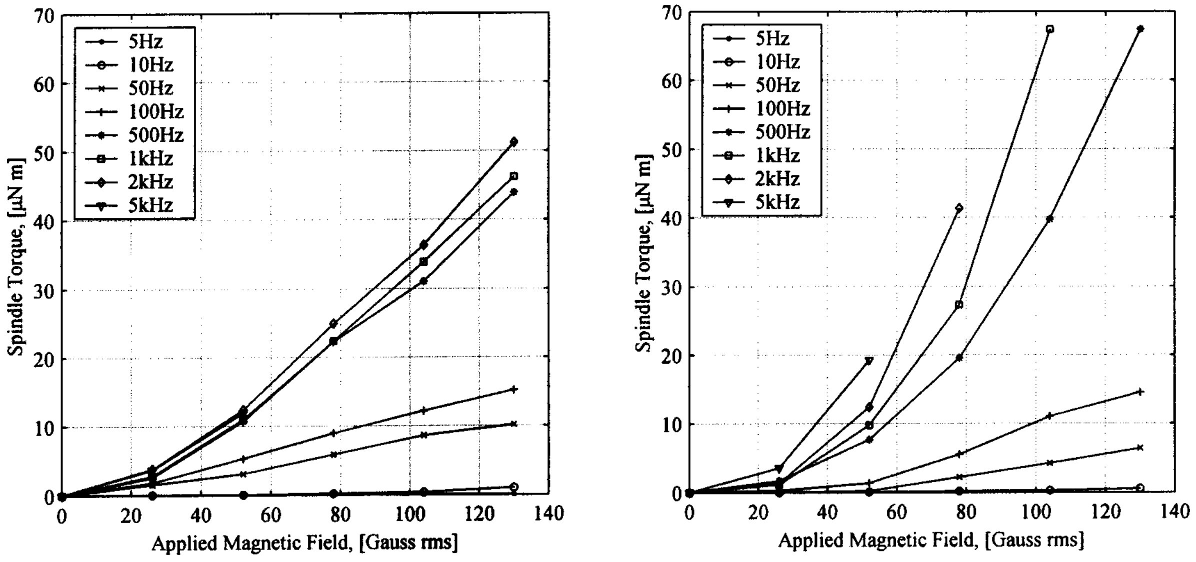

(a)

(b)

Fig. 3 Torque required to restrain the ferrofluid-filled plastic spindle as a function of magnetic field amplitude at various frequencies for the (*a*) water-based and (*b*) Isopar-M ferrofluids in a clockwise rotating uniform magnetic field generated by a two-pole induction motor stator winding. Interpolating lines have been added to aid the reader in distinguishing trends in the data

However, the jump conditions on the magnetoquasistatic field require that the normal component of $\mathbf{B}(\mathbf{x})$, B_r, and the tangential component of $\mathbf{H}(\mathbf{x})$, H_θ, be continuous across the wall-fluid interface, therefore, no surface-excess magnetic force results in the azimuthal direction

$$f_\theta^M = 0. \tag{14}$$

Because there is no surface-excess magnetic force in the azimuthal direction, there is no surface-excess magnetic torque on the cylindrical container wall.

5.2 Viscous Torque and Couple Stress. The torque on the spindle wall due to ferrofluid flow immediately proximate to it arises through two contributions: (i) the torque arising due to the viscous traction on the wall, and (ii) the torque due to gradients in particle spin, embodied in the couple-stress pseudodyadic **C**. The first contribution is that familiar to fluid mechanics and arises due to the Cauchy stress **T** in the suspension, albeit modified to account for antisymmetric stresses. The second is an additional contribution due to the structured continuum nature of the ferrofluid

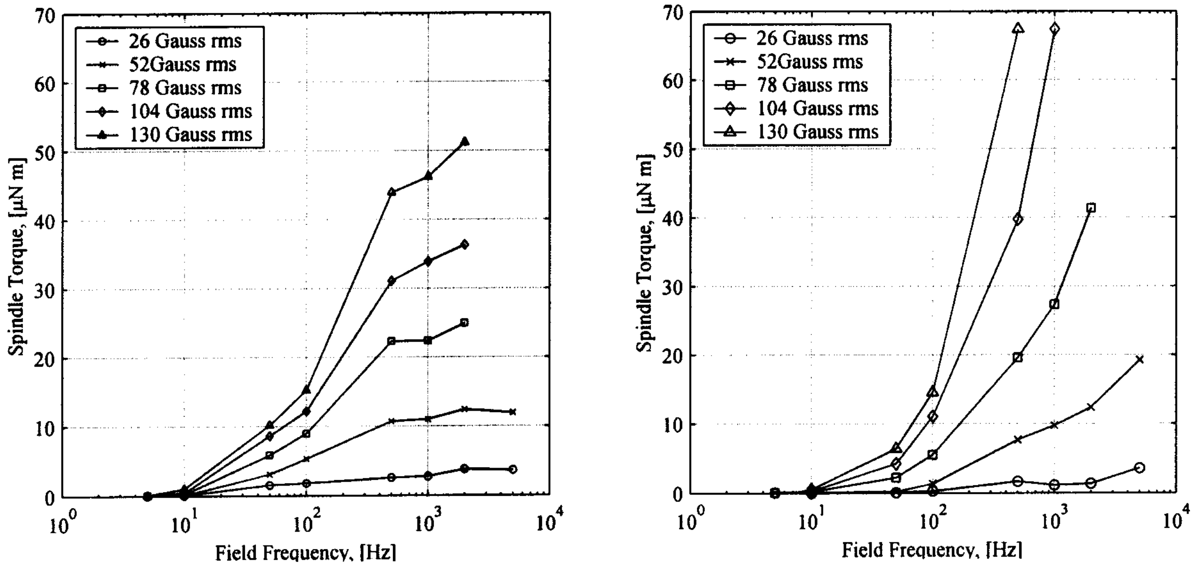

(a)

(b)

Fig. 4 Re-plot of Fig. 3 torque data as a function of magnetic field frequency at various magnetic field amplitudes for (*a*) water-based and (*b*) Isopar-M ferrofluids

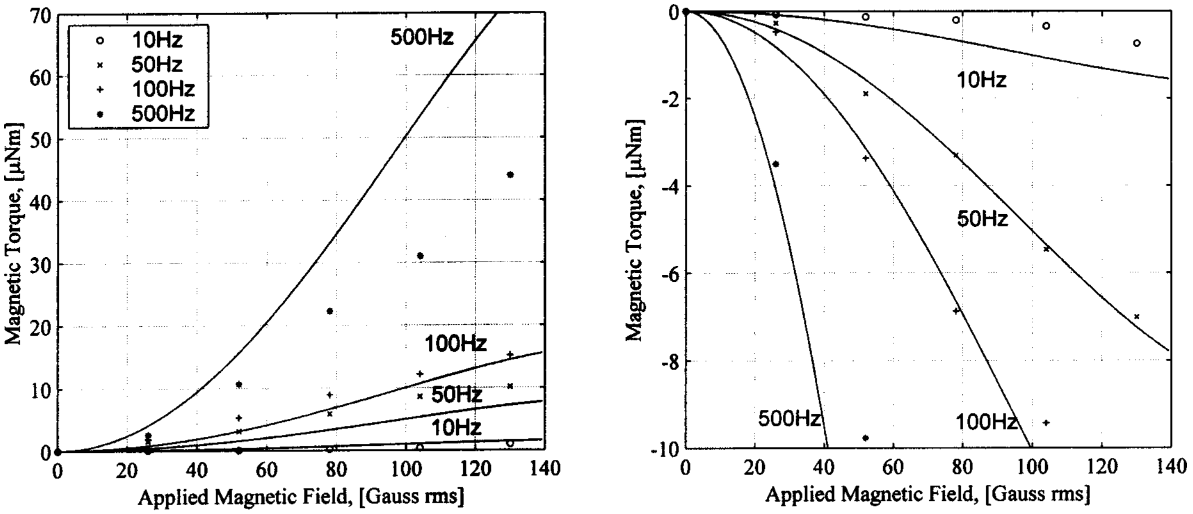

(a) (b)

Fig. 5 Comparison between torque experimental measurements and predictions (solid lines) of (18) for the water-based ferrofluid (obtained using $\chi=0.65$, $\eta=7\times10^{-3}$ Nsm^{-2}, $\zeta=1.4\times10^{-3}$ Nsm^{-2}, $\tau=10^{-5}$ s, and $\kappa=100$). (*a*) Corresponds to clockwise rotation of the magnetic field and (*b*) corresponds to counterclockwise rotation of the magnetic field

suspension [30,31]. In vector form, the torque on a surface *S* relative to an arbitrary origin *O*, from which the position vector **x** is drawn, is given by

$$\mathbf{L}_O=\int_S \mathbf{x}\times(d\mathbf{S}\cdot\mathbf{T})+\int_S d\mathbf{S}\cdot\mathbf{C}. \tag{15}$$

The dynamical quantities **T** and **C** are functionally dependent on the gradient of the velocity field, the spin, the gradient of the spin, and a series of phenomenological material parameters, the so-called viscosities, η (shear dynamic viscosity), λ (bulk dynamic viscosity), ζ (vortex viscosity), η' (shear spin viscosity), and λ' (bulk spin viscosity)

$$\mathbf{T}=-p\mathbf{I}+\eta[\nabla\mathbf{v}+\nabla\mathbf{v}^T]+\lambda[\nabla\cdot\mathbf{v}]\mathbf{I}+\zeta\boldsymbol{\varepsilon}\cdot[\nabla\times\mathbf{v}-2\boldsymbol{\omega}], \tag{16}$$

$$\mathbf{C}=\eta'[\nabla\boldsymbol{\omega}+\nabla\boldsymbol{\omega}^T]+\lambda'[\nabla\cdot\boldsymbol{\omega}]\mathbf{I}. \tag{17}$$

Applying (15) therefore requires knowledge of the velocity, **v**, and spin, $\boldsymbol{\omega}$, fields present in the flow.

A rigorous, regular perturbation analysis of the coupled ferrohydrodynamic problem corresponding to our experimental setup has been made [31], yielding $\mathbf{v}=v_\theta(r)\mathbf{i}_\theta$ and $\boldsymbol{\omega}=\omega_z(r)\mathbf{i}_z$. With these results and using (16) and (17), the axially-directed (*z*-directed) torque for our experimental situation is

$$L_{O,z}=-2\Omega_f\tau\chi\mu_0H^2V_f\left\{1-\frac{\tau\mu_0\chi H^2}{2\zeta}\,\frac{(\eta+\zeta)}{\eta^*}\,\frac{I_2(\kappa)}{I_0(\kappa)}\right\}, \tag{18}$$

where V_f is the volume of ferrofluid, Ω_f is the radian frequency of the magnetic field with rms amplitude *H*, χ is the magnetic susceptibility, ζ is the vortex viscosity, which may be estimated from [32]

$$\zeta=\frac{3}{2}\eta_0\phi_h, \tag{19}$$

where ϕ_h is the hydrodynamic volume fraction of suspended particles, η_0 is the viscosity of the suspending fluid, and η^* and κ are defined parameters, given by

$$\eta^*=\eta+\zeta\frac{I_2(\kappa)}{I_0(\kappa)}, \tag{20}$$

and

$$\kappa=\left(\frac{4\eta}{(\eta+\zeta)}\,\frac{R^2\zeta}{\eta'}\right)^{1/2}, \tag{21}$$

respectively. In (18) and (20), I_0 and I_2 are modified Bessel functions of the first kind and order 0 and 2, respectively. In (21), $R=9.5$ mm is the internal radius of the hollow spindle and η' is the spin viscosity of the ferrofluid. No rigorous theoretical or experimental estimates of the value of η' are currently available. Instead, η' is commonly assumed to be negligibly small, which appears plausible based on scaling arguments which assume that η' is proportional to the particle-scale dimension squared. However, we note that this is not strictly the case, as explained further in [33].

As mentioned before, a regular perturbation expansion scheme in the parameter $\Omega_f\tau$ was used to obtain these results. As such, (18) corresponds to rigorous solution of the governing fluid and magnetic field equations to second order in $\Omega_f\tau$. This regular perturbation expansion ensures that the equations of ferrohydrodynamics and Maxwell's equations [1,33] are rigorously satisfied, without neglecting the effects of spin/magnetization coupling in the magnetization relaxation equation or the demagnetizing fields. However, because of the parameter expansion in $\Omega_f\tau$, this analysis is only applicable when

$$\varepsilon\simeq\frac{\tau\mu_0\chi H^2}{2\zeta}<1. \tag{22}$$

5.3 Comparison With Experimental Observations. Figures 5 and 6 compare our experimental observations of Figs. 3 and 4 to the predictions of (18). The parameters used in obtaining Fig. 5 for the water-based ferrofluid are $\chi=0.65$, $\eta=0.007$ Nsm^{-2}, $\zeta=1.4\times10^{-3}$ Nsm^{-2} (obtained by correcting the previously obtained magnetic core volume fraction ϕ for the effect of adsorbed dispersant layers by adding 2 nm to the particle radius to account for the surfactant layer), $V_f=18.8$ cm^3, $\kappa=100$ (an *ad hoc* value, resulting in $\eta'=4.2\times10^{-11}$ Ns), and $\tau=10^{-5}$ s (adjusted to improve agreement with experimental observations). The parameters used in obtaining Fig. 6 for the Isopar-M ferrofluid are $\chi=2.2$, $\eta=0.011$ Nsm^{-2}, $\zeta=2.0\times10^{-3}$ Nsm^{-2} (again corrected for surfactant), $V_f=18.8$ cm^3, $\kappa=100$ (an *ad hoc* value, resulting in $\eta'=6.1\times10^{-11}$ Ns), and $\tau=2\times10^{-6}$ s (again adjusted to im-

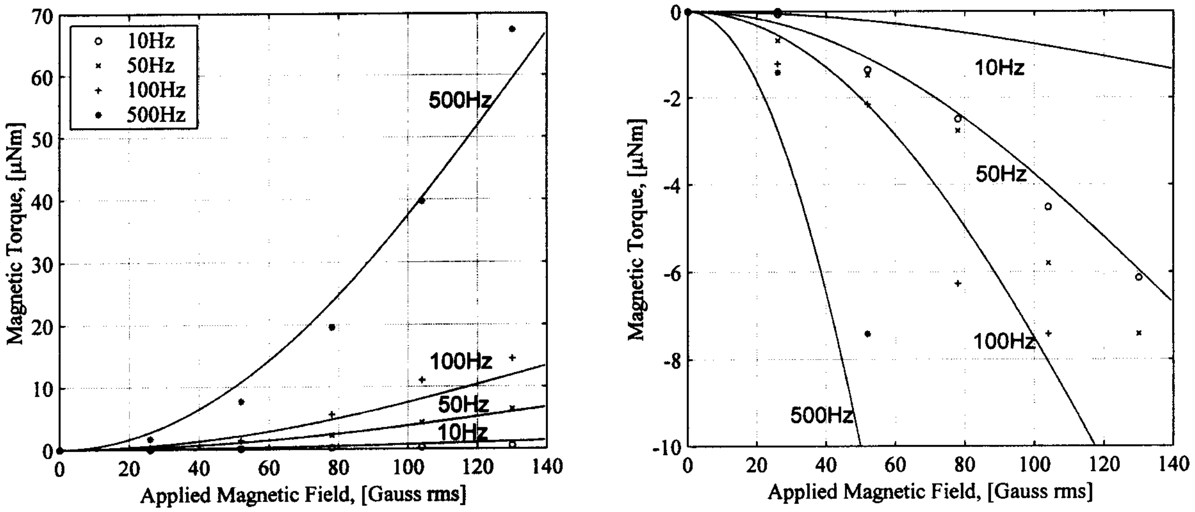

(a) (b)

Fig. 6 Comparison between torque experimental measurements and predictions (solid lines) of (18) for the Isopar-M ferrofluid (obtained using $\chi=2.2$, $\eta=11\times10^{-3}$ Nsm^{-2}, $\zeta=2.0\times10^{-3}$ Nsm^{-2}, $\tau=2\times10^{-6}$ s, and $\kappa=100$). (*a*) Corresponds to clockwise rotation of the magnetic field and (*b*) corresponds to counterclockwise rotation of the magnetic field.

prove agreement with experimental observations). Note that for the values of $\kappa \gg 1$, such as we have assumed here, we are effectively in the zero spin viscosity limit, for which (18) reduces to

$$L_{O,z} = -2\Omega_f \tau\chi\mu_0 H^2 V_f \left\{1-\frac{\tau\mu_0\chi H^2}{2\zeta}\right\}. \qquad (23)$$

The fitted values of τ for the water-based and Isopar-M ferrofluids are in agreement with the Brownian relaxation times obtained in Section 2 (shown in Table 2), and within the calculated effective relaxation time range. This indicates that for our measurements, $\tau_N \gg \tau_B$.

Examining Figs. 5 and 6, we find reasonably good agreement between measured torques and those obtained from our theory, especially for the lower applied field frequencies. For applied field frequencies higher than 500 Hz we find poor agreement indicating perhaps other physical phenomena unaccounted for in our analysis.

Figures 5 and 6 also show low torque data (<10 μN-m) and fitted theory for counter-clockwise magnetic field rotation.

Based on the estimates provided above for the associated physical parameters in (22), we have $\varepsilon=0.35$ for the water-based ferrofluid and $\varepsilon=0.16$ for the Isopar-M ferrofluid, when the applied field strength is 140 Gauss. Higher order terms might be relevant in the analysis of the water-based ferrofluid data because of its high value of ε. The effect of higher-order terms and the analysis beyond the range specified in (22) is left to future communications.

6 Conclusions

The experiments presented herein demonstrate that even without a free surface, there is a significant torque from the viscous shear in a ferrofluid undergoing spin-up flow. Ostensibly this would result from magnetic-field-induced flow throughout the bulk of the fluid, in agreement with a recently derived analysis of the situation [31]. Our measurements show that the effect of magnetic field on torque increases with magnetic field amplitude. For most measurements, the effect on torque increases with magnetic field frequency, except for the water-based ferrofluid at frequencies greater than 500 Hz, where the torque appears to saturate.

We note that the value of ε obtained for the water-based fluid was high, indicating perhaps that higher-order terms may be necessary in analyzing experiments using the water-based ferrofluid. The large difference in τ for the two ferrofluids may also be the reason for the discrepancy. More detailed experimental and theoretical investigations, which should shed light on the observed discrepancy, are currently underway.

Although we cannot directly observe ferrofluid flow inside the opaque spindle, one could argue that the measured torque arises due to shear stresses at the fluid/spindle boundary, and hence is a result of bulk flow in the fluid. Reference [15] argues that surface stresses occurring at a ferrofluid/air interface, rather than stresses occurring throughout the volume, are responsible for magnetic-field-induced flow. Therefore, according to this presumption, in the absence of a free surface there should be no ferrofluid flow and consequently, using a stationary spindle in the viscometer setup described above, there should be no torque. The measurements presented herein show that there is indeed significant torque without a free surface and ostensibly some manner of flow arises inside the fluid.

Acknowledgments

The authors are grateful to Prof. Howard Brenner and Dr. Ronald E. Rosensweig for insightful and stimulating discussions. CR was supported in part by a Graduate Research Fellowship from the U.S. National Science Foundation. This research is supported by the U.S. National Science Foundation Grant #CTS-0084070.

References

[1] R. E. Rosensweig, 1997, *Ferrohydrodynamics*. Mineola, NY: Dover Publications.
[2] Shen, L. F., Stachowiak, A., Fateen, S. E. K., Laibinis, P. E., and Hatton, T. A., 2001, "Structure of alkanoic acid stabilized magnetic fluids. A small-angle neutron and light scattering analysis," Langmuir, **17**, pp. 288–299.
[3] Peréz-Castillejos, R., Plaza, J. A., Esteve, J., Losantos, P., Acero, M. C., Cane, C., and Serra-Mestres, F., 2000, "The use of ferrofluids in micromechanics," Sensors and Actuators A-Physical, **84**, pp. 176–180.
[4] Menz, A., Benecke, W., Pérez-Castillejos, R., Plaza, J. A., Esteve, J., Garcia, N., Higuero, J., and Diez-Caballero, T., 2000, "Fluidic components based on ferrofluids," presented at 1st Annual International IEEE-EMBS, Special Topic Conference on Microtechnologies in Medicine and Biology, Lyon, France.
[5] Hatch, A., Kamholz, A. E., Holman, G., Yager, P., and Bohringer, K. F., 2001, "A ferrofluidic magnetic micropump," J. Microelectromech. Syst., **10**, pp. 215–221.

[6] Berger, M., Castelino, J., Huang, R., Shah, M., and Austin, R. H., 2001, ''Design of a microfabricated magnetic cell separator,'' Electrophoresis, **22**, pp. 3883–3892.
[7] Zahn, M., 2001, ''Magnetic fluid and nanoparticle applications to nanotechnology,'' J. Nanoparticle Res., **3**, pp. 73–78.
[8] Roger, J., Pons, J. N., Massart, R., Halbreich, A., and Bacri, J. C., 1999, ''Some biomedical applications of ferrofluids,'' Eur. Phys. J.: Appl. Phys., **5**, pp. 321–325.
[9] Ramchand, C. N., Pande, P., Kopcansky, P., and Mehta, R. V., 2001, ''Application of magnetic fluids in medicine and biotechnology,'' Indian J. Pure Appl. Phys., **39**, pp. 683–686.
[10] Moskowitz, R., and Rosensweig, R. E., 1967, ''Nonmechanical Torque Driven Flow in Magnetic Suspensions,'' Appl. Phys. Lett., **11**, pp. 1967.
[11] Brown, R., and Horsnell, T. S., 1969, ''The wrong way round,'' Electrical Review, **183**, pp. 235.
[12] Kagan, I. Y., Rykov, V. G., and Yantovskii, E. I., 1973, ''Flow of a dielectric ferromagnetic suspension in a rotating magnetic field,'' Magnitnaya Gidrodynamika, **9**, pp. 135–137.
[13] Calugaru, G. H., Cotae, C., Badescu, R., Badescu, V., and Luca, E., 1976, ''A new aspect of the movement of ferrofluids in a rotating magnetic field,'' Reviews in Roumanian Physics, **21**, pp. 439–440.
[14] Rosensweig, R. E., and Johnston, R. J., 1989, ''Aspects of magnetic fluid flow with nonequilibrium magnetization,'' in *Continuum Mechanics and its Applications*, C. A. C. Graham and S. K. Malik, Eds.: Hemisphere Publishing Company, 1989, pp. 707–729.
[15] Rosensweig, R. E., Popplewell, J., and Johnston, R. J., 1990, ''Magnetic fluid motion in rotating field,'' Journal of Magnetism and Magnetic Materials, **85**, pp. 171–180.
[16] Zaitsev, V. M., and Shliomis, M. I., 1969, ''Entrainment of ferromagnetic suspension by a rotating field,'' J. Appl. Mech. Tech. Phys., **10**, pp. 696–700.
[17] Glazov, O. A., 1975, ''Motion of a ferrosuspension in rotating magnetic fields,'' Magnitnaya Gidrodynamika, **11**, pp. 16–22.
[18] Glazov, O. A., 1975, ''Role of higher harmonics in ferrosuspension motion in a rotating magnetic field,'' Magnitnaya Gidrodynamika, **11**, pp. 31.
[19] Glazov, O. A., 1982, ''Velocity profiles for magnetic fluids in rotating magnetic fields,'' Magnitnaya Gidrodynamika, **18**, pp. 27.
[20] Glazov, O. A., 1990, ''Dynamics of magnetic fluids in rotating magnetic fields,'' Magnitnaya Gidrodynamika, **26**, pp. 83–88.
[21] Bozorth, R. M., 1951, *Ferromagnetism*. New York, NY: IEEE Press.
[22] Shliomis, M. I., 1974, ''Magnetic fluids,'' Sov. Phys. Usp., **17**, pp. 156.
[23] Onsager, L., 1936, ''Electric Moments of Molecules in Liquids,'' J. Am. Chem. Soc., **58**, pp. 1486–1493.
[24] Shliomis, M. I., 1972, ''Effective viscosity of magnetic suspensions,'' Sov. Phys. JETP, **34**, pp. 1291–1294.
[25] Felderhof, B. U., 2000, ''Magnetoviscosity and relaxation in ferrofluids,'' Phys. Rev. E, **62**, pp. 3848–3854.
[26] Shliomis, M. I., 2001, ''Comment on Magnetoviscosity and relaxation in ferrofluids,'' Phys. Rev. E, **6406**.
[27] Felderhof, B. U., 2001, ''Reply to Comment on 'Magnetoviscosity and relaxation in ferrofluids,' '' Phys. Rev. E, **6406**.
[28] Lehlooh, A. F., Mahmood, S. H., and Williams, J. M., 2002, ''On the particle size dependence of the magnetic anisotropy energy constant,'' Physica B, **321**, pp. 159–162.
[29] Melcher, J. R., 1981, *Continuum Electromechanics*. Cambridge, MA: MIT Press.
[30] Dahler, J. S., and Scriven, L. E., 1963, ''Theory of structured continua I. General consideration of angular momentum and polarization,'' Proc. R. Soc. London, **276**, pp. 504–527.
[31] Rinaldi, C., 2002 ''Continuum Modeling of Polarizable Systems,'' Ph.D. Thesis, Massachusetts Institute of Technology, Cambridge, MA.
[32] Brenner, H., 1970, ''Rheology of two-phase systems,'' Annu. Rev. Fluid Mech., **2**, pp. 137–176.
[33] Rinaldi, C., and Zahn, M., 2002, ''Effects of spin viscosity on ferrofluid flow profiles in alternating and rotating magnetic fields,'' Phys. Fluids, **14**, pp. 2847–2870.

O. Petrenko
New Jersey Institute of Technology

E. S. Geskin
New Jersey Institute of Technology,
Newark, NJ 07102-1982
Phone: (973) 596-3338
Fax: (973) 642-4282
e-mail: geskin@njit.edu

G. A. Atanov
Donetsk Open University, Donetsk, Ukraine

A. Semko
University of Donetsk, Donetsk

B. Goldenberg
New Jersey Institute of Technology

Numerical Modeling of Formation of High-Speed Water Slugs

The objective of this work is to investigate acceleration of a water slug by the powder explosion. The process occurs in a device termed the water cannon, which entails a barrel with an attached nozzle. The explosion products expel the slug from the barrel at an extremely high speed. Due to the acceleration in the nozzle the speed of the slug significantly exceeds that of a bullet driven by the similar explosion. The computational procedure was used to evaluate the pressure, velocity and density fields in the course of slug acceleration in the x-t space. The procedure is based on the finite difference method and the method of characteristics. The initial water velocity and pressure are assumed to be zero. The pressure at water-explosion product interface is determined by the conditions of the powder combustion while the pressure at the water-atmosphere interface is equal to zero. The results of the computations enable us to explain the peculiarities of the operation of the water cannon and to optimize device design. [DOI: 10.1115/1.1669421]

1 Introduction

Super-high speed water slugs termed the impulsive water jet (IWJ), constitutes an efficient material removal tools. A water slug impacting the material surface at the speed above 1.5 km/sec affects the substrate similarly to a charge of an explosive deposited on the substrate surface. In fact, IWJ can replace explosion in mining, rocks breakages, structure demolition, etc. [1–3,5]. Various modes of energy injection into water can be used for IWJ formation. During the explosion an expanding gas cavity is generated. The fast moving boundary of the cavity impacts water similarly to the piston and expels the water slug from the barrel via a tapering nozzle. The water slug is accelerated similarly to a conventional projectile expelled from the barrel in the course of explosion. Additional acceleration is due to the fluid converging in the nozzle and to the compression waves developed in the fluid. It was demonstrated that the maximal fluid velocity is attained if the slug maintains a free surface in the course of explosion [1]. A device where this condition is met is termed the water cannon (Fig. 1).

The following phenomenological model describing the water cannon operation was suggested. In the course of the fluid acceleration the compression waves develop in the fluid during the impact as well as during the flow through the converging nozzle. The compression waves are reflected from the free surface (liquid-atmosphere interface) as the rarefaction waves. The formation of the rarefaction waves at the free surface as well as the superposition of the compression and rarefaction waves within the slug body accelerate the front portion of the slug and decelerate the rear portion [1]. Such redistribution of the impact energy in the fluid enables us to generate high-speed liquid projectiles. A numerical technique suitable for evaluation of the conditions of the slug formation in water cannon is discussed in this paper.

2 Mathematical Model

A numerical technique describing the velocity and pressure fields in the water cannon in x-t space was suggested by Atanov [1,4]. The process in question is described by the system

$$\frac{\partial u}{\partial t}+u\frac{\partial u}{\partial x}=-\frac{1}{\rho}\frac{\partial P}{\partial x} \tag{1a}$$

$$\frac{\partial \rho}{\partial t}+\rho\frac{\partial u}{\partial x}+u\left(\frac{\partial \rho}{\partial x}+\rho\frac{1}{F}\frac{\partial F}{\partial x}\right)=0 \tag{1b}$$

$$\frac{P+B}{\rho^{n}}=\text{const} \tag{1c}$$

The system (1) includes the dynamic equations of the momentum and mass balances and the constitutive equation of the one-dimensional isentropic water flow. Validity of the equation (1*c*) was demonstrated by Atanov [1] on the whole range of the pressures generated in water cannon. These equations take into account the change of different parameters due to temperature change in the adiabatic process. Initial velocities and pressure in the barrel are assumed to be zero. The pressure at the gas-liquid interface in the course of the process is equal to the pressure of the combustion product, while the pressure at free surface separating the liquid and the atmosphere is equal to zero. In the performed computations the origin of the space coordinate (the axis x) is the entrance of the nozzle, while the origin of the axis y (time) is the moment of combustion start. Thus the initial and the boundary conditions of the system (1) are defined as:

$$-L_{brl}\leqslant x\leqslant -L_{brl}+L,\quad u(x,0)=0,\quad \rho(x,0)=\rho_0,$$
$$P(x,0)=0,\quad P(-L_{brl},0)=Pg \tag{2}$$

Using the isentropic equation (1*c*) number of variables in the first two equations can be reduced to two and the system (1) can be reduced to the form of:

$$\frac{\partial u}{\partial t}+\frac{\partial}{\partial x}\left(\frac{u^{2}}{2}+\frac{\rho^{n-1}}{n-1}\right)=0 \tag{3a}$$

$$\frac{\partial u}{\partial t}\rho F+\frac{\partial}{\partial x}uF=0 \tag{3b}$$

Equations (3) are written in non-dimensional form. Sound speed and density for water at normal conditions and barrel length were used for scaling. Integration of system (3) over an arbitrary domain in the x-t space yields:

$$\int\int\left[\frac{\partial u}{\partial t}+\frac{\partial}{\partial x}\left(\frac{u^{2}}{2}+\frac{\rho^{n-1}}{n-1}\right)\right]dx\,dt=0 \tag{4a}$$

$$\int\int\left[\frac{\partial u}{\partial t}\rho F+\frac{\partial}{\partial x}uF\right]dx\,dt=0 \tag{4b}$$

Here A is the area of integration. Using the Green formula we can rewrite system (4) in the form of:

Contributed by the Fluids Engineering Division for publication in the JOURNAL OF FLUIDS ENGINEERING. Manuscript received by the Fluids Engineering Division January 15, 2003; revised manuscript received October 30, 2003. Associate Editor: D. Siginer.

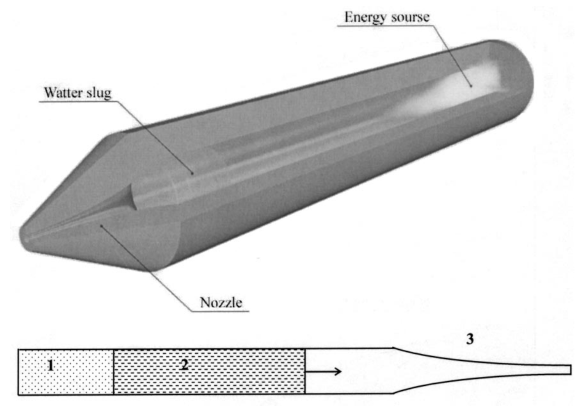

Fig. 1 General schematic of the water cannon 1—powder charge, 2—water load, 3—converging nozzle

$$\oint\left[u\,dx-\left(\frac{u^2}{2}+\frac{\rho^{n-1}}{n-1}\right)dt\right]=0 \tag{5a}$$

$$\oint[\rho F\,dx-u\rho F\,dt]=0 \tag{5b}$$

The computational procedure involved numerical solution of the system (5). The technique is based on the finite difference method while the method of characteristics is used to relate fluid properties at the t and $t+\Delta t$ intervals. Such approach was suggested earlier by Godunov [5]. The process domain was approximated by a trapezoidal grid with a constant number of x-steps equal on each time level (Fig. 2). The example of a grid cell is shown in Fig. 3. Here the horizontal lines represent the state of water at time instances t and $t+dt$. As the slug moves within the converging nozzle its length changes and so does the length of the horizontal sides of a cell.

The distribution of the velocity and density in the slug are approximated by step functions of x that change over time. Then boundary between two cells that are nodes at Figs. 3 and 4 constitutes a discontinuity of u and p functions. The collapse of these discontinuities results in the emanation of two characteristics described by the equations:

$$\frac{dx}{dt}=u\pm\rho^{n-1/2} \tag{6a}$$

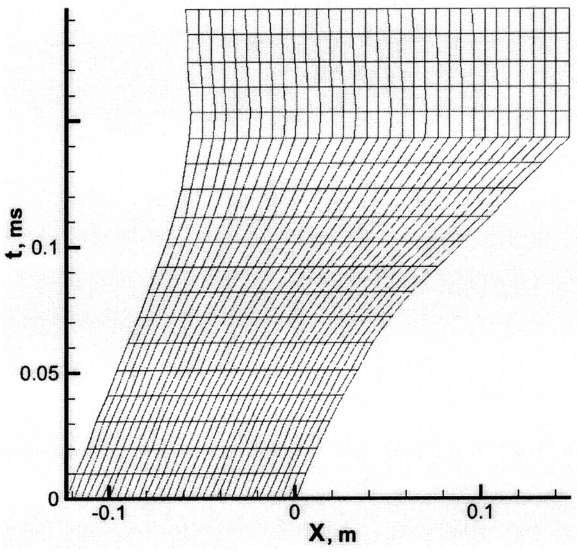

Fig. 2 Schematic of the mesh

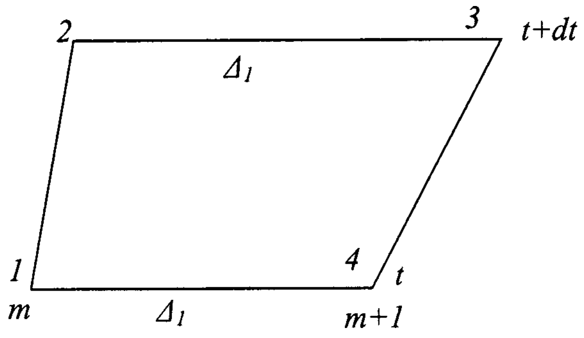

Fig. 3 A grid cell schematic

$$u\pm\frac{2}{n-1}\rho^{n-1/2}=\text{const} \tag{6b}$$

These equations were suggested by Godunov [5].

The finite difference method implies that u and ρ are constant on the lateral sides 1–2 and 4–3. These values of u and ρ on the lateral sides of each cell are calculated from discontinuity decomposition using equations of characteristics: The values on the next time layer are to be found.

A point of discontinuity (the node of the grid) is a common point of the characteristic of the first family, of the characteristic of the second family and the lateral side of the grid. Thus, the following equations hold:

$$u_1-\frac{2}{n-1}\rho_1^{n-1/2}=U-\frac{2}{n-1}Ro^{n-1/2} \tag{7a}$$

$$u_2-\frac{2}{n-1}\rho_2^{n-1/2}=U-\frac{2}{n-1}Ro^{n-1/2} \tag{7b}$$

Using system (7) the value of velocity (U) and density (Ro) at the lateral sides can be determined as follows: For this dt should be sufficiently small so that characteristics do not intersect the lateral sides.

$$U=\frac{1}{2}\left[u_1+u_2-\frac{2}{n-1}(\rho_1^{n-1/2}-\rho_2^{n-1/2})\right] \tag{8a}$$

$$Ro=\left[-\frac{n-1}{4}(u_1-u_2)+\frac{1}{2}(\rho_1^{n-1/2}+\rho_2^{n-1/2})\right]^{2/n-1} \tag{8b}$$

Using values of U and Ro obtained in (8) we can relate u and ρ at the time instances t and $t+dt$ [1,2]:

$$u^{m+1/2}=\frac{1}{\Delta_1}[u_{m+1/2}\Delta_2-dt(c_{m+1}-c_m-U_{m+1}W_{m+1}+U_mW_m)] \tag{9a}$$

$$\rho^{m+1/2}=\frac{1}{F_u\Delta_1}[F_l\rho_{n+1/2}\Delta_2-dt((RUF)_{m+1}-(RUF)_m-(RFW)_m+(RFW)_m)] \tag{9b}$$

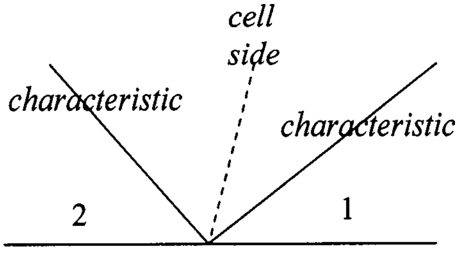

Fig. 4 Schematic for Eq. (7)

$$c_i = \frac{U_i^2}{2} + \frac{Ro_i^{n-1}}{n-1} \tag{9c}$$

$$W_m = (x^m - x_m)/dt \tag{9d}$$

Where:

F_l, F_u, F_m, and F_{m+1} are the average values of nozzle cross-section area corresponding to the sides of a cell *1–4*, *2–3*, *1–2* and *3–4* respectively.

A computer code has been developed for simulation of water cannon operation using this scheme (Eqs. (8) and (9)). A block of code modeling gunpowder combustion was also included in the program. It was assumed that the process of powder combustion is stationary and uniform and the rate of combustion was proportional to the pressure in the combustion chamber and average area of the powder grain surface. The process duration enable us to disregard energy losses on heat exchange in the combustion chamber and the barrel.

3 Experimental Validation of the Computational Results

The following experiment has been carried out in order to validate the developed computational procedure. The schematic of the experimental setup is shown on Fig. 5. Water slugs generated by the water cannon impacted a pendulum located at the distance of 1.2 m from the nozzle. The velocity of the slug prior to the impact was measured by the lasers transit anemometers located at the distance of 8 cm and 110 cm from nozzle exit. In the course of experiments the process conditions were selected as following: the barrel diameter −32 mm, the nozzle exit diameter −1.5 mm, the nozzle length −70 mm, the powder charge −30 g, the water load −230 g. The mass of the ballistic pendulum was 110 kg while the pendant length was 1405 mm.

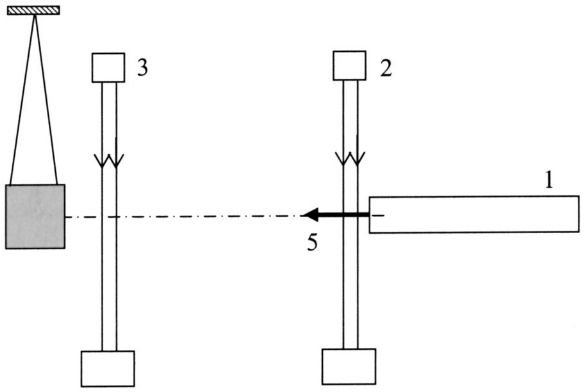

Fig. 5 Experiment Schematic 1—water cannon, 2—first velocimeter, 3—second velocimeter, 4—ballistic pendulum, 5—impulsive water jet

Table 1

No.	V_1, m/s, jet velocity at 8 cm from the nozzle exit	V_2, m/s, jet velocity at 110 cm from the nozzle exit	Θ, deg pendulum deviation angle, deg
1	1020	912	14
2	1219	1107	15
3	1063	1068	15
4	1111	1068	14
5	980	939	14.5

The experimental results are given in the Table 1. The pendulum deviation is determined by the jet momentum, which is a rather stable integral process characteristic, while the laser anemometers show the pulsating instantaneous values of the jet velocity. As it follows from the table the average measured the velocity of the water at the distance of 8 cm from the nozzle exit was 1080 m/s with deviation of ±70 m/s. The average deviation of the pendulum was 14.5 deg with the error of 0.5 deg or 3.5%. The suggested computational technique was used to determine the water velocity variation at the exit of the nozzle. The computed value of this velocity was 1,070 m/s.

The calculated slug impulse is equal to 122 N·s which brings about pendulum deviation equal to 17 deg. Taking into account velocity loss in air, calculated from the table $(\nu_1 - \nu_2)/\nu_1 \cdot 100\% = 5.5\%$ impulse loss becomes 11%. This results in 2 deg smaller angle of pendulum deviation, i.e. $\Theta \simeq 15$ deg. The comparison of the experimental and predicted values of the water velocity and momentum show that the suggested computational technique is sufficiently accurate and can be used at least for estimation of process conditions.

4 Case Studies

The developed computational procedure was used for examination of the cannon operation. The distribution of the velocity and pressure along the barrel and nozzle at different stage of the water expulsion was determined and used was evaluation of the operational process conditions [6]. An example of such computation is shown on Fig. 6. The further application of the developed technique involved process optimization. The developed system of equations is being used as a block of a procedure for optimization of the cannon design. The example of such analysis is given in Fig. 7. The objective of this analysis was the optimization of the nozzle configuration. It was shown that the replacement of a conical nozzle geometry by two converging cones enables us to increase the maximal value of the jet momentum. Figure 6 show optimal relationship characteristic of nozzle geometry. Here axis x shows the length of the first cone, while the total nozzle length of the nozzle is constant, and axis y shows cones intersection radius, axis z shows effective momentum integral (Fig. 8).

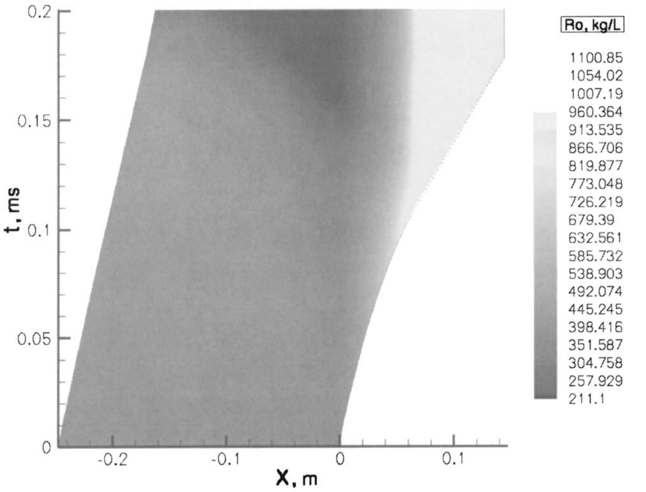

Fig. 6 Distribution of water velocity during the process of 200 g slug flow in the nozzle. Point of origin is shifted up to the moment of inflow.

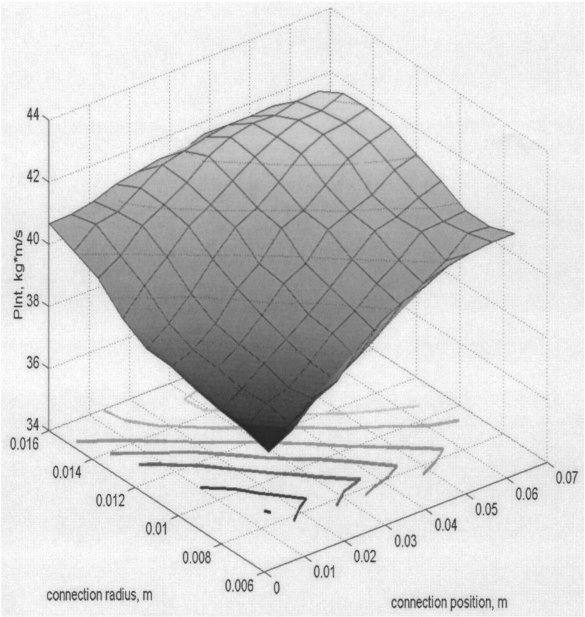

Fig. 7 Effective slug impulse versus connection nozzle radius and position of the connection

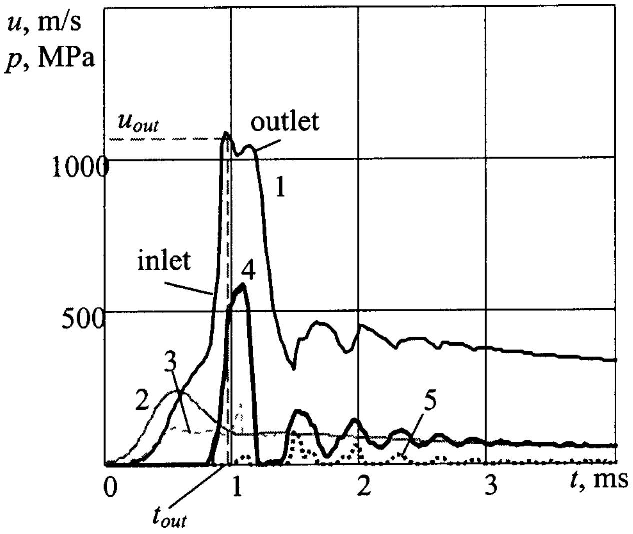

Fig. 8 Velocity of inflow (into the nozzle), outflow (on the exit of collimator), pressure at different points of water cannon versus time. 1—velocity of inflow (inlet) and outflow (outlet) 2—pressure of powder gases in the combustion camera ($x = -450$ mm) 3—pressure in the middle of the water cannon ($x = -200$ mm) 4—pressure in the nozzle inlet ($x = 20$ mm, nozzle length—70 MM) 5—pressure in the collimator inlet ($x = 75$ mm, collimator length 60 mm).

5 Concluding Remarks

The numerical technique for predicting the properties of the slug generated in the course of the powder explosion in a water cannon was developed. The process characteristics obtained as the result of the use of this model correctly represents the known process features. The obtained values of the pressure and velocity correspond to the available experimental data. At the present the model is being used to optimize the cannon design and conditions of its operation. The further improvement will include analysis of the formation and development of shock waves. The effects of the fluid viscosity and the boundary layer on the slug formation will also be accounted for.

6 Acknowledgment

The work was supported by the NSF grant DMI9900247.

Nomenclature

B = constant equal $B = 304.5$ MPa
F = nozzle cross-section area, m^2
L = water load length, m
$\mathrm{L}_{\mathrm{brl}}$ = barrel length, m
n = water adiabatic constant, $n = 7.15$
P = pressure, MPa
ρ = density, $\mathrm{kg/m}^3$
ρ_0 = water density at normal conditions, $\mathrm{kg/m}^3$
Ro = water density on the lateral sides of the grid cell
Θ = pendulum deviation angle, degrees (Table 1)
t = time, ms
u = velocity, m/s
U = water velocity on the lateral sides of the grid cell
V = water velocity at a given distance from the nozzle exit, m/s (Table 1)
V_1 = water velocity at the distance of 8 cm from the nozzle exit, m/s (Table 1)
V_2 = water velocity at the distance of 100 cm from the nozzle exit, m/s
W = water velocity at a grid node
x = space coordinate

Superscript index indicates values at the next time level (Eqs. (7)–(9)

Subscript index indicates values at the previous time level (Eqs. (7)–(9))

References

[1] Atanov, G. A., (1987), *Hydro-Impulsive Installations for Rocks Breaking*, Vishaia Shkola (Russian), Kiev, USSR.

[2] Yie, G. G., Burns, D. J., and Mohaupt, U. H., *Performance of high pressure pulsed waterjet device for fracturing concrete pavement*, 4th Intl. Symposium on Jet Cutting Technology, April 12th–14th, 1978, BHRA, Cranfielid, England.

[3] Chermensky, G. P., *Breaking Coal and Rock With Pulsed Water Jets*, 3rd Intl. Symposium on Jet Cutting Technology, 11th–13th May, 1976, Chicago, U.S.A.

[4] Atanov, G. A., (1977), *Internal Ballistics of Hydro Cannon and Impulsive Water Extruder*, Donetsk State University (Russian), Donetsk, USSR.

[5] Godunov, S. K. et al., *Numerical Solving Multidimensional Problems of Gas Dynamics*, Nauka, Moscow, USSR.

[6] Petrenko, O. P. et al., Investigation of the material fracturing by high speed water slugs. 16th Intl. *Symposium on Jet Cutting Technology, 2002, BHRA, Cranfielid, England.*

N. C. Correia

F. Robitaille

A. C. Long

C. D. Rudd

School of Mechanical, Materials,
Manufacturing Engineering and Management,
University of Nottingham, U.K.

P. Šimáček

S. G. Advani*

Department of Mechanical Engineering,
Center for Composite Materials,
University of Delaware, USA

Use of Resin Transfer Molding Simulation to Predict Flow, Saturation, and Compaction in the VARTM Process

The present paper examines the analysis and simulation of the vacuum assisted resin transfer molding process (VARTM). VARTM differs from the conventional resin transfer molding (RTM) in that the thickness of the preform varies during injection affecting permeability and fill time. First, a governing equation for VARTM is analytically developed from the fundamental continuity condition, and used to show the relation between parameters in VARTM. This analytical work is followed by the development of a numerical 1-D/2-D solution, based on the flow simulation software LIMS, which can be used to predict flow and time dependent thickness of the preform by introducing models for compaction and permeability. Finally, the results of a VARTM experimental plan, focusing on the study of the influence of outlet pressure on compaction and fill time, are correlated with both the analytical and the numerical work. The present work also proposes an explanation for the similarities between VARTM and RTM and shows when modeling VARTM and RTM can result in an oversimplification. [DOI: 10.1115/1.1669032]

1 Introduction

Vacuum Assisted Resin Transfer Molding or VARTM (also known as VI, SCRIMP™, VM, RIFT, etc.) is used widely as an alternative to open mold techniques to produce large components. VARTM employs a single mold tool, with the reinforcement enclosed by a membrane sealed onto the mold to close the cavity. A distribution medium with a high in-plane permeability is usually placed on top of the reinforcement to accelerate the in-plane flow. Air is extracted from the cavity and the atmospheric pressure outside the bag compresses the reinforcement onto the mold, and resin is then drawn into the mold. The process is shown schematically in Fig. 1.

The flexibility of the vacuum bag introduces a novel aspect not present in RTM: the fluid pressure field that induces flow also modifies the local compaction state of the reinforcement and ultimately alters permeability. As fluid pressure changes due to the movement of the flow front, so does the compaction pressure on the reinforcement, which leads to variations in porosity and permeability. This is illustrated in Fig. 2.

In addition flow is inherently 3-D, as fluid advances most rapidly within the distribution medium and then flows through-thickness to impregnate the reinforcement. These aspects should be considered when developing a flow simulation for VARTM.

Throughout this paper, RTM is referred to for comparison purposes. RTM process is significantly better understood than the VARTM and it has been in use for some time. Modeling tools for RTM process are readily available. Moreover, RTM is equivalent to VARTM for an incompressible (or, practically, very stiff) preform and without the use of a distribution media.

Hence, we discuss the analysis of VARTM, beginning with analytical studies of 1-D cases which serve as a building block for the development of a 2-D software simulation, based on the adaptation of a mold filling software, Liquid Injection Molding Simulation (LIMS) developed at University of Delaware. Additionally, an experimental study is presented which validates the concepts of the developed tools. This study also illustrates the fundamental differences between VARTM and RTM and identifies the situations under which one may have to address the pressure dependent properties to obtain a viable solution for VARTM process.

2 VARTM Literature

The VARTM process has been continuously developed for more than half century, from the 1940s with Marco [1] through the later patents by Smith [2] and Green [3] in the 1950s and 1960s up to Seemann's SCRIMP™ [4]. Despite of this, as Williams et al. [5] pointed out, in the mid 1990s, this process' development is slow when compared to other liquid molding techniques such as resin transfer molding (RTM).

Several experimental and analytical studies have since been published on VARTM. Hammami et al. [6] discussed a 1-D model using Darcy's law, assuming elastic equilibrium in the cavity during filling. Calado et al. [7], Luce et al. [8] and Andersson et al. [9] showed the role of flow enhancement layers to reduce filling time. Andersson et al. also demonstrated that the lubrication of the fibers and the time dependence of their compressibility have to be considered when modeling vacuum infusion. Different models proposed in the literature, such as Han et al. [10] and Hammami et al. [6] have been developed for this process. In-depth detailed review of vacuum infusion can be found in [9–13]. The modeling of vacuum infusion with distribution media involves further complications and has been approached by Kang et al. [14] and Anderson et al. [15].

3 Modeling

In this section we will examine the flow through deformable, porous media. First, we will derive a simple analytical model for 1-D flow. Then, we will examine how to adopt the existing RTM simulation tool to model this flow numerically.

3.1 Analytical Modeling. In-plane flow through a porous medium can be modeled using Darcy's law, which for 1-D flow in the x-direction gives fluid velocity (u_x) as:

$$u_x = \frac{K}{\mu}\frac{dP}{dx} \tag{1}$$

---

*Corresponding author; e-mail: advani@me.udel.edu

Contributed by the Fluids Engineering Division for publication in the JOURNAL OF FLUIDS ENGINEERING. Manuscript received by the Fluids Engineering Division March 20, 2003; revised manuscript received October 30, 2003. Associate Editor: D. Siginer

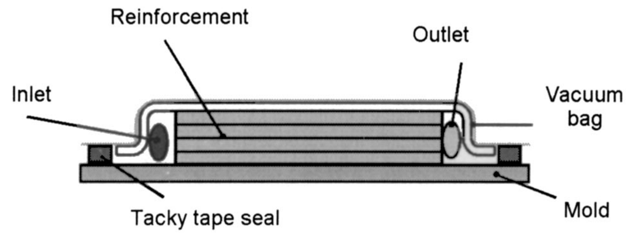

Fig. 1 VARTM mold assembly

where K is the reinforcement permeability, μ is the fluid viscosity, and P is the fluid pressure. Following the analysis of Gutowski et al. [16] the continuity equation for 1-D in-plane flow in a compacting porous medium is:

$$\frac{\partial h}{\partial t} = -\frac{\partial (u.h)}{\partial x} \tag{2}$$

where h is the local material thickness and t is time. This expression differs from that used for flow in an incompressible medium (for example in RTM). Combining Eqs. (1) and (2) for a constant viscosity fluid:

$$\frac{\partial h}{\partial t} = \frac{1}{\mu} \cdot \left[\left(K \cdot \frac{\partial h}{\partial x} + h \cdot \frac{\partial K}{\partial x} \right) \frac{\partial P}{\partial x} + h \cdot K \cdot \left(\frac{\partial^2 P}{\partial x^2} \right) \right] \tag{3}$$

Since both thickness and permeability are functions of pressure, which is a function of position in the mold $x(h[P(x)]$ and $K[P(x)])$, equation (3) can be recast as:

$$\frac{\partial h}{\partial t} = \frac{1}{\mu} \cdot \left[\left(K \cdot \frac{\partial h}{\partial P} + h \cdot \frac{\partial K}{\partial P} \right) \cdot \left(\frac{\partial P}{\partial x} \right)^2 + h \cdot K \cdot \left(\frac{\partial^2 P}{\partial x^2} \right) \right] \tag{4}$$

The Eq. (4) does not feature partial derivatives of h and K on x. Pressure remains constant if it is calculated not at the position x of a point inside the flow but at its relative location between the inlet and the flow front. For example, pressure is constant midway between the inlet and the outlet, even though the physical location of the mid-point changes at each moment. This stems from the fact that permeability K is a function of thickness h. One-dimensional fluid pressure field can therefore be solved once and scaled with flow front movement.

Mathematically this is achieved by performing a variable substitution $\alpha = x/L$ where L is the instantaneous flow front position. In this α-referential scaling, the flow front is located at $\alpha = 1$ while the inlet is at $\alpha = 0$ regardless of time. Assuming that one can ignore rate effects, equation (4) can be written as:

$$-\left[\left(\frac{1}{h} - \frac{\alpha}{[h]_{\alpha=1}} \right) \cdot \frac{dh}{dP} + \frac{1}{K} \frac{dK}{dP} \right] \left(\frac{dP}{d\alpha} \right)^2 = \left(\frac{d^2 P}{d\alpha^2} \right) \tag{5}$$

Equation (5) can be solved using an iterative finite difference method to compute the pressure field, from which flow front progression can be determined using Darcy's law.

3.2 General Solution of VARTM Using LIMS. All numerical research presented here was conducted using LIMS: liquid injection molding simulation, developed at the University of Delaware. LIMS can be described as a dedicated finite element/control volume based simulation of flow through porous media, capable of analyzing both 2-D and 3-D flows [17,18]. LIMS 5.0 has a built in scripting language, LBASIC, which was added so that boundary conditions could be modified during the simulation [19,20]. As is the case with other FE based simulation packages, it is necessary to supply a meshed geometry, preform permeability and porosity values and boundary conditions to carry out the simulations [21].

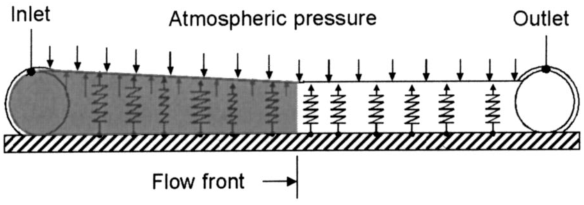

Fig. 2 Effect of fluid pressure on compaction in VARTM

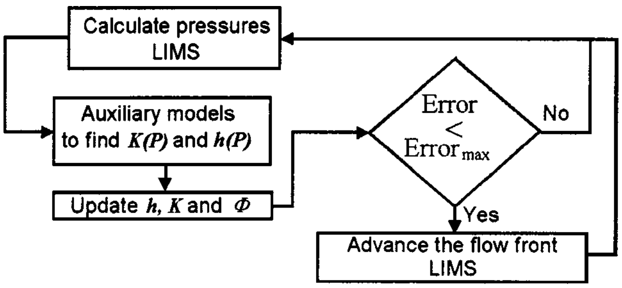

Fig. 3 VARTM algorithm used in Liquid Injection Molding Simulation (LIMS) LBASIC script

The use of an established RTM software was preferred over the development of a stand alone VARTM numerical simulation due to, in essence, the long development time that would be necessary to produce a proven numerical design software package. In fact, due to the extensive research that has gone in to the development of many of today's RTM simulation packages it would hardly be possible to reach the same level of sophistication in a short time.

One of the main advantages LIMS presents over other packages in this case is its extensive scripting capability that allowed the incorporation of VARTM's compaction peculiarities in the approach.

In order to simulate VARTM's flow through a compressible porous medium, the software is required to updates thickness, porosity and permeability locally as a function of compaction pressure. This is accomplished through an LBASIC script, which is able to apply the required changes and check iteratively for convergence by re-solving the pressure field under the new conditions. The flow front is then advanced and the procedure is repeated. A schematic representation of LIMS' LBASIC algorithm is shown in Fig. 3.

Through the use of auxiliary compaction and permeability models the calculation of flow in the compressible medium for cases involving 1-D or 2-D shell components in LIMS becomes possible. Furthermore, the two proposed methodologies are fundamentally different form each other. The analytical approach solves a stand-alone equation, while the numerical approach involves an independent computation mechanism, which is iterated by a controlling script. By comparing the simulation results with the analytic solution one can draw conclusions about the use of RTM simulations for modeling flow in VARTM. The solution to flow and compaction in VARTM, whether analytical or numerical depends on the existence of external auxiliary constitutive models for thickness and permeability as function of compaction pressure: $h(P)$ and $K(P)$. The next subsection discusses these auxiliary models, specifically the ones used to obtain the results.

3.3 Compaction and Permeability Models. Important physics in any model of VARTM is the permeability/compressibility and pressure relationship. This is expressed by the use of a compaction model and a permeability model. These can be seen as separate (or modular) fitting functions, which can be replaced or adapted at any stage and do not form an intrinsic part of the flow model.

Table 1 Compaction model data from reference [22]

Material	Type	layers	vf_0	B
NCS 81053	Stitched bi-directional	6 L	0.11000	0.126
		3 L	0.06780	0.170
Vetrotex U101	Random	6 L	0.02090	0.216
		3 L	0.01850	0.251
Vetrotex U812	Random	6 L	0.00539	0.301
		3 L	0.00504	0.316

Compaction Model. As reported by Robitaille et al. [22] the compaction of fibers can be described by an empirical power law (6), which relates compaction pressure and volume fraction of fibers (ν_f). Note that compaction pressure (P_{Comp}) is seen as the difference between the fluid and atmospheric pressures.

$$\nu f = \nu f_0 \cdot P_{\text{Comp}}^{B} \tag{6}$$

Note also that essentially due to lubrication, dry and wet compaction behaviors are different, and therefore ν_{f0}—the fiber volume fraction at a compaction pressure of 1 Pa—and stiffening index (B) will reflect this difference. Since the model applies to the saturated part of the mold, wet compaction data should be used.

Permeability Model. The most common and easy to use Kozeny-Carman equation, which is used to relate permeability K to fiber volume fraction for oriented fibers, (7) was employed.

$$K = k \cdot \frac{(1-\nu f)^3}{\nu f^2} \tag{7}$$

Here, the Kozeny constant k is determined experimentally and reflects the geometry of the reinforcement. For our fabrics k was chosen as 5×10^{-11} m^2. This equation does not represent the behavior with complete accuracy but was chosen for its simplicity [22]. Combining Eqs. (6) and (7) it is possible to obtain permeability as a function of compaction pressure.

Thickness function of pressure is derived from Eq. (6) and from an expression for fiber volume fraction that can be obtained using the values of area density of the reinforcement S_d and bulk density of glass ρ:

$$h = \frac{S_{\text{d}}}{\rho \cdot \nu f_0 \cdot P_{\text{comp}}^{B}} \tag{8}$$

The results presented here focus mainly on three reinforcement materials in two lay-up categories: 3 and 6 layers. The data used is presented in Table 1. These auxiliary models and corresponding data make it now possible to compare the different approaches and study the effect that material properties have on the modeling results.

4 Results

In this section we will examine the results obtained by the analytic and numerical models and consequently compare them to experimental data. The selection of materials for this work was done in order to show a relevant range of architectures and compaction indexes which comprise of the least and most compressible as well as an intermediate value.

4.1 Analytical Versus LIMS' Numerical Pressure Field Solutions. Figure 4 shows the resulting pressure fields obtained using the models presented above for 1-D flow. It also includes results for flow in an incompressible medium (i.e., RTM) for comparison. For the numerical analysis, 100 1-D (2-noded) elements were sufficient to obtain convergence in the predicted pressure field. Absolute inlet pressure was 0.9 atm (94.5 kPa). Outlet was absolute vacuum and the Kozeny constant k was equal to 5×10^{-11} m^2. However, it should be noted that, according to the analytical model, the Kozeny constant should not affect pressure distribution. It does affect the flow velocity and hence the fill time. Compaction data was obtained from [22,23].

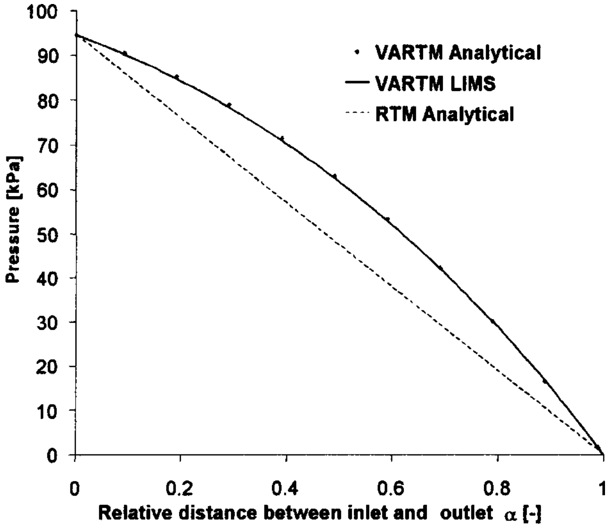

Fig. 4 Pressure field according to LIMS modification to address VARTM, analytical and RTM models for 6 layers of NCS 81053 noncrimp glass reinforcement

Furthermore, Fig. 4 illustrates the differences between VARTM and RTM pressure fields. Secondly, the analytical solution using Eq. (5) is almost identical to the numerical implementation using the LBASIC script in LIMS with the approach illustrated in Fig. 3. Finally, it should be emphasized that, as a consequence of neglecting the compaction rate effects the pressure field behind the flow front is constant in time (when distance is normalized with respect to the filled length).

Table 2 shows the average relative error between LIMS and the analytical solutions in 1-D simulation with 100 nodes. The low error values show that both approaches are interchangeable which, because of the simpler nature of the numerical simulation, expands the analysis possibilities to 2-D cases.

4.2 Experimental Validation: Time-pressure Relationships. As it is difficult to measure the pressure field during VARTM during the mold filling stage, it was decided to compare the experimental mold filling times with the model as a first step towards validation. Future work must however study experimental pressure data since this is directly linked to the solution of the governing equations. An example of pressure data acquisition in VARTM can be found in the work by Grimsley et al. [24]. Nevertheless, one can still measure inlet and outlet pressures of the resin and use this information for comparison with RTM.

4.2.1 The RTM Case. One can easily formulate the well known 1-D integral form of Darcy's law (9) which relates distances covered by infusing fluids to time when the injection is performed under constant pressure:

Table 2 Error between analytical and numerical (VARTM-LIMS) results

Material	Number of layers	
	6 layers	3 layers
NCS 81053	0.60%	0.76%
U 101	1.08%	1.13%
U 812	1.47%	2.04%

$$t_{RTM} = -\frac{\phi\mu}{2K}\cdot\frac{L^2}{\Delta P} \tag{9}$$

where μ, K and ΔP again represent viscosity, permeability and the driving pressure (or difference between inlet and outlet pressures) respectively, and ϕ is the preform porosity. Equation (9) shows that there is a hyperbolic relation between time and the driving pressure. In fact, since viscosity and permeability can be considered constant for the RTM process, one postulates that during filling:

$$t = C\cdot\Delta P^{-1} \tag{10}$$

Here, C is a constant which depends on preform permeability and porosity, resin viscosity and geometry (size). This result points to the essential difference between RTM and VARTM. In VARTM permeability and porosity depend on pressure. In VARTM the power to which the driving pressure is raised will dependent on the compaction behavior of the reinforcement.

4.2.2 The VARTM Case. As previously mentioned, earlier work by Gutowski et al. [14], Hammami et al. [6] and others showed that for VARTM, the governing equation can be written as equation (2). As was shown, the pressure field can be determined by iteration of (5) and takes on the typical nonlinear form that can be observed in Fig. 4. Note that a typical pressure field would be a line (constant gradient) from inlet to the location of the flow front if there were no compressive effects.

One can express the pressure as $P(\alpha)$ where $\alpha = x/L$ and, as the pressure gradient at the flow front governs flow advancement and as the pressure field in Eq. (5) is of a nondimensional nature with regards to the distance from the inlet, it is possible to rewrite the volume averaged velocity of the flow front in VARTM as:

$$\dot{L}(t) = -\frac{1}{\mu\cdot\phi\cdot L(t)}\left[K\cdot\frac{dP}{d\alpha}\right]_{\alpha=1} \tag{11}$$

where K and $dP/d\alpha$ at $\alpha=1$ represent the nondimensional pressure gradient and permeability at the flow front, which remain the same throughout the filling process. Note that in Eq. (11) time is scaled by the term $1/L(t)$. Integrating,

$$t_{VARTM} = -\frac{\phi\mu L^2}{2\left[K\cdot\frac{dP}{d\alpha}\right]_{\alpha=1}} \tag{12}$$

where t is the time for the flow front to reach the distance L. As can be seen, time remains a function of the square of the flow front position, which in turn can be accounted for the similarity between RTM and VARTM. Fill times in 1-D vacuum infusion are therefore directly proportional to those obtained with RTM; this proportionality constant, which will be referred to as C_α, is given by:

$$C_\alpha = \frac{t_{VARTM}}{t_{RTM}} = \frac{\left[\frac{dP}{d\alpha}\right]_{\alpha=1}}{\Delta P} \tag{13}$$

In Eq. (13), C_α may be used in simpler cases to convert standard RTM simulation packages to the modeling of VARTM without the downside of longer computational times (needed to solve the nonlinear coupled flow-compaction problem). This is possible if the software is capable of calculating C_α, which requires the solution of nonlinear equations in 1-D.

4.3 VARTM's Fill Time Versus Outlet Pressure. As discussed earlier, in VARTM unlike RTM, the driving pressure effect on fill time is due to the pressure gradient and also because of change in permeability invoked by the changes in the driving pressure. Therefore, it becomes important to understand VARTM in terms of compaction effects on fill time. This can be done by combining Eqs. (12) and (13) in

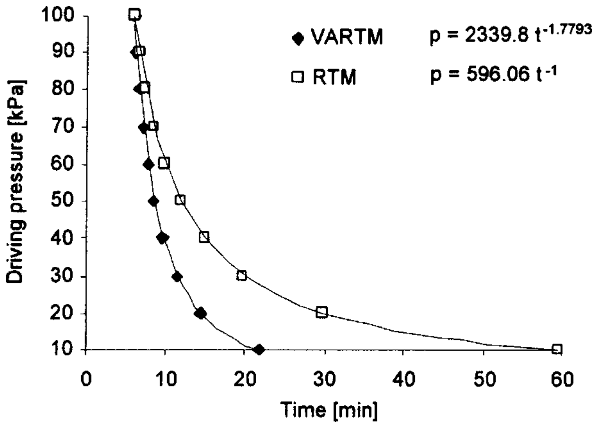

Fig. 5 Difference in fill time vs. ΔP between VARTM and RTM

$$t_{VARTM} = -\frac{L^2\cdot\mu}{2\cdot\Delta P}\cdot\frac{1}{C_\alpha\cdot[K]_{\alpha=1}} \tag{14}$$

Now, by comparing equation (14) with RTM's equivalent equation (9), one can obtain "RTM-equivalent" permeability for VARTM amalgamating the flow-front-compaction-pressure dependent permeability $[K]_{\alpha=1}$ with the constant C_α.

The pressure dependent fill time relation for RTM's (Eq. (9)) and VARTM's (Eq. (14)) can be highlighted by their respective graphical forms. Assuming $\nu_{f0}=0.11$ and $B=0.126$ to represent the compaction behavior of 6 layers of NCS 81053 stitched bidirectional reinforcement and assuming for simplicity that the constant $C_\alpha=1$, fill times for a 1 m long infusion are a function of the driving pressure as illustrated in Fig. 5.

The power exponent fit for VARTM fill time is given by $t_{VARTM}=3.10^{10}.\Delta P^{-1.78}$ while for RTM it is $t_{RTM}=3.10^{10}.\Delta P^{-1}$.

Note that for the case of $C_\alpha=1$, the two lines intersect where compaction pressure in the RTM mold equals the compaction pressure in the VARTM infusion (1E5 Pa inlet pressure). Furthermore, VARTM is faster than RTM since permeability increases in VARTM as compaction pressure is reduced. This in turn is explained by the analysis of the power exponent fit coefficients. If, on one hand, the multiplying term can be seen as the necessary driving pressure to fill the mold in 1 min ($\Delta P_{VARTM}=2339.(1)^{-1.7793}$ kPa), the exponent, on the other, is related to compaction behavior of the power law in Eq. (6). Thus, for RTM the exponent must be 1 in order to satisfy Darcy's Law for incompressible media. VARTM's larger exponent provides a valuable qualitative (if not quantitative) tool for differentiating the two processes.

4.4 Experimental Observations in VARTM. In order to observe the sensitivity of the exponent discussed in the previous section, an experimental plan was formulated in which 4 layers of Vetrotex's 5×4 820 g/m^2 were infused with corn syrup of constant viscosity in each experiment but was different in each experiment. The experimental setup is shown in Fig. 6. The mold was $0.6\times0.25\,[\mathrm{m}^2]$ with infusion introduced as a line injection on the left side (Fig. 7).

Before each experiment, viscosity was measured with a Brookfield viscometer model DV-I and subsequently, these results where used to normalize fill time and plot Fig. 8. This approach eliminates the errors in fill time, which could exist due to evaporation of water from the corn syrup mix (which will change its viscosity over the period of 24 hours).

Since permeability and C_α are both driving-pressure dependent, the fill time in VARTM is of the form

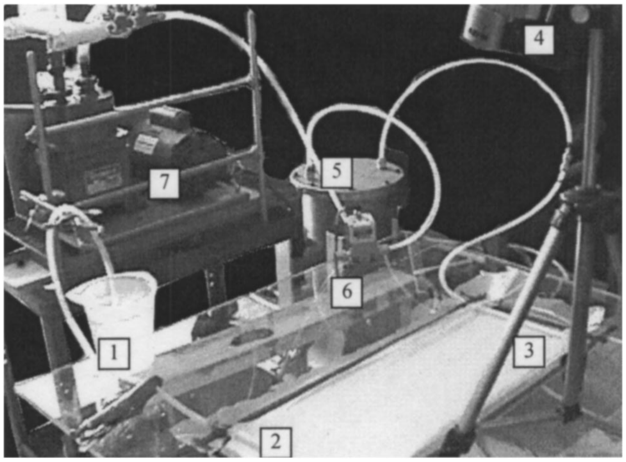

Fig. 6 Experimental setup. 1 resin container, 2 inlet, 3 outlet, 4 digital video camera, 5 resin trap, 6 pressure controller and 7 vacuum pump.

$$t_{VARTM} = C \cdot \Delta P^{D} \tag{15}$$

where C and D are constants but, unlike RTM, D is not -1. It is therefore possible to conclude from Eq. (15) that the deviation of the exponent in Fig. 8 is due to compaction effects on porosity and permeability.

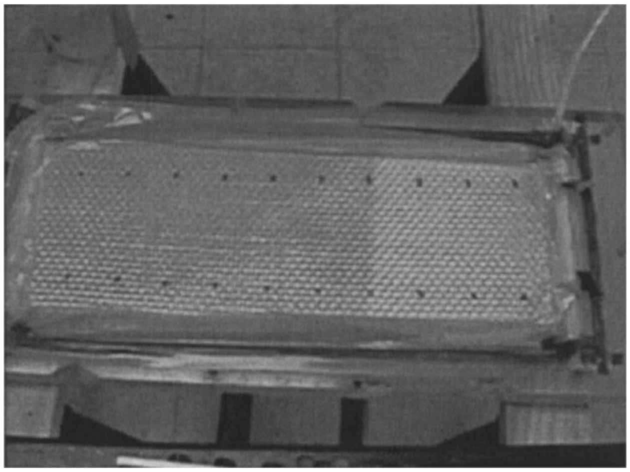

Fig. 7 Example of image captured during an experimental injection

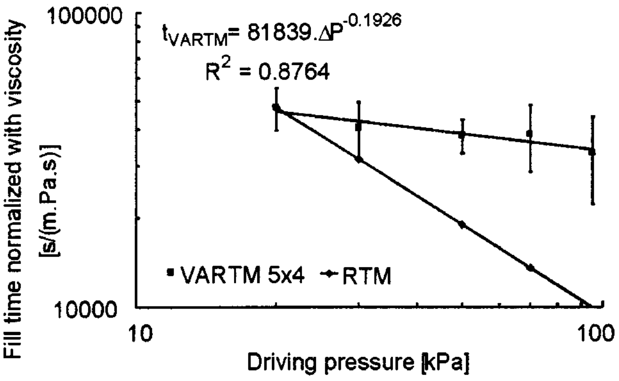

Fig. 8 Experimental results of normalized fill time vs. driving pressure for VARTM of the 5×4 and an ideal RTM curve

The experimental variability which was observed in the 22 experiments with the 5×4 woven is attributable to natural material variations since all other experiments done in the same setup did not show this degree of scatter. The distribution medium showed a high degree of repeatability (typical standard deviations of 10%) while the standalone material presented an average standard deviation of 22% of normalized fill time. This effect dominated the injection of the combined materials, reducing scatter in fill time at both the top and bottom of the lay-up.

5 Conclusions

A new numerical approach was developed for VARTM employing the liquid injection molding simulation (LIMS) software and its scripting capability in LBASIC which has already demonstrated in addressing many important issues in RTM such as dual scale fibrous media, optimization and control of the process [25–30]. Comparing the solution with 1-D analytical prediction of fill time, pressure and pressure dependent properties such as permeability and thickness provided validation of this approach.

The results of an experimental study were shown and they substantiated both the necessity of understanding VARTM's differences and the results of the modeling (Fig. 9). The non-dimensionality of the pressure field was proposed and presented as possible explanation for the similarity in flow patterns between VARTM and RTM. One can therefore use the RTM simulations such as LIMS by coupling them with constitutive auxiliary models for fiber compaction and permeability to estimate mold filling time and distribution of fiber volume fraction in the VARTM process.

Due to the low driving pressure in this process, most industrial applications of VARTM use a high permeability medium to enhance flow, increasing the complexity of the problem. A significant amount of work was done in the past showing that flow is in fact dominated by the higher permeability media and that, within certain limits, the in-plane flow in the reinforcement could be

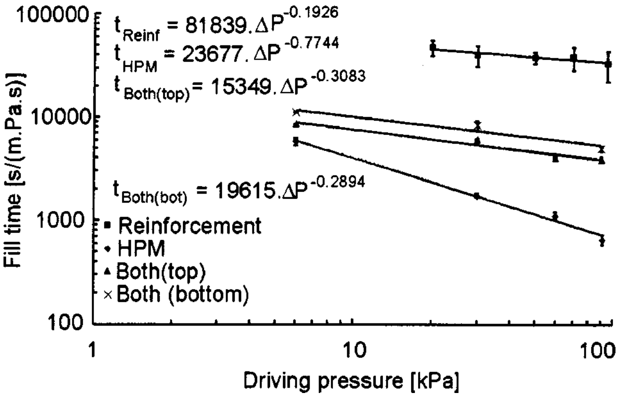

Fig. 9 Experimental VARTM results for (i) 5×4 reinforcement, (ii) High Permeability Media (HPM) (iii) 5×4 reinforcement with High Permeability Media (HPM) on top and (iv) reinforcement 5×4 with HPM on both sides

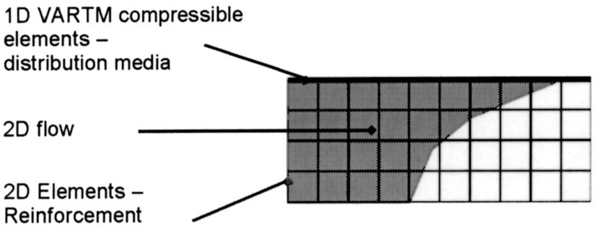

Fig. 10 Finite-element approach for simulation of VARTM in the presence of distribution media

neglected [24]. Nevertheless, it is possible to postulate that because of the flexibility of the membrane, nesting effects, etc., flow in the distribution media is also affected by compaction issues. In light of this, the work presented here should form the basis of future research since it is possible to incorporate different compressing media in the proposed LIMS FE/CV model (Fig. 10) [31].

Acknowledgments

The authors wish to thank the following institutions for their support in this work: The Engineering and Physical Sciences Research Council, DETR, Europrojects (LTTC) Ltd, Halmatic Ltd, LTC Ltd, Southfields Coachworks Ltd, Vosper Thornycroft Ltd in the United Kingdom and ONR's Advanced Materials Intelligent Processing Center Grant ONR contract no M00014-00-C-0333 in the USA.

Nomenclature

u = Fluid filter-velocity [m/s]
K = Permeability [m^2]
μ = Fluid Viscosity [Pa.s]
P = Fluid Pressure [Pa]
t = Time [s]
ρ = Density [Kg/m^3]
B = Compaction stiffening index
vf = Fiber volume fraction
vf_0 = Fiber volume fraction at 1 Pa
L = Length of filled domain [m]
x, y = Rectangular coordinates
h = Laminate thickness [m]
C_α = RTM/VARTM pressure gradient ratio

References

[1] Marco Method, 1950, U.S. Patent Office, Pat No. 2495640.
[2] Smith, G. H., 1959, U.S. Patent Office, Pat No. 2913036.
[3] Green, P. R., 1963, U.K. Patent Office, Pat No. 944955.
[4] Seemann, W. H., 1990, U.S. Patent Office, Pat No. 4902215.
[5] Williams, C., Summerscales, J., and Grove, S., 1996, ''Resin infusion under flexible tooling (RIFT): A review,'' *Composites Part A*, **27A**, pp. 617–524.
[6] Hammami, A., and Gebart, B. R., 2000, ''Analysis of the vacuum infusion molding process,'' Polym. Compos., **21**.
[7] Calado, V. M. A., and Advani, S. G., 1996, ''Effective average permeability of multi-layer preforms in resin transfer molding,'' Compos. Sci. Technol., **56**, pp. 519–531.
[8] Luce, T. L., Advani, S. G., Howard, J. G., and Parnas, R. S., 1995, ''Permeability characterization. Part 2: Flow behavior in multiple layer performs,'' Polym. Compos., **16**.
[9] Andersson, M., Lundstrom, S., Gebart, B. R., and Langstrom, R., 2000, ''Development of guidelines for the vacuum infusion process,'' *Proceedings of FRC 2000*, pp. 113.
[10] Han, K., Jiang, S., Zhang, C., and Wang, B., 2000, ''Flow modelling and simulation of SCRIMP for composites manufacturing,'' Composites, Part A, **31**, pp. 79–86.
[11] Correia, N. C., Ragondet, A., Robitaille, F., Long, A. C., and Rudd, C. D., 2002, ''Modelling the vacuum infusion of composite materials,'' *9th Intl Conf Fibre Reinforced Composites*, Newcastle upon Tyne, UK.
[12] Ragondet, A., Correia, N. C., Robitaille, F., Long A. C., and Rudd, C. D., 2002, ''Experimental investigation and modelling of the vacuum infusion process,'' *10th European Conference on Composite Materials*, Brugges, Belgium.
[13] Acheson, J. A., Simacek, P., and Advani, S. G., ''The implications of fiber compaction and saturation on Fully coupled VARTM simulation,'' Submitted to Composites, Part A.
[14] Kang, M. K., Lee, W. I., and Hahn, H. T., 2001, ''Analysis of the vacuum bag resin transfer molding process,'' Composites, Part A, **32**, pp. 1535–1560.
[15] Anderson, H. M., Lundstrom, T. S., and Gebart, B. R., 2003, ''Numerical model for the vacuum infusion manufacturing of polymer composites,'' Int. J. Numer. Methods Heat Fluid Flow, **13**(3), pp. 283–394.
[16] Gutowski, T. G., and Dillon, G., 1997, ''The Elastic Deformation of Fiber Bundles,'' *Advanced Composites Manufacturing*, T. G. Gutowski, ed., pp. 138–139.
[17] Simacek, P., Ledermann, C., and Advani, S. G., 2001, ''Fast Three Dimensional Numerical Simulation of Isothermal Mold Filling for Liquid Composite Molding Processes,'' *Proceedings of the American Society for Composites Sixteenth Technical Conference*, September 9–12.
[18] Advani, S. G., and Simacek, P., 1999, ''Modeling and Simulation of Flow, Heat Transfer and Cure,'' in *Resin Transfer Molding For Aerospace Structures*, Edited by T. Teresa Krukenberg and R. Paton, Kluwer Academic Publishers, Netherlands, pp. 225–281.
[19] Mathur, R., Advani, S. G., Fink, B. K., 2000, ''A Sensitivity-based Gate Location Algorithm for Optimal Mold Filling During the Resin Transfer Molding Process,'' Advances in Computational Engineering and Sciences, **1**, pp. 138–144.
[20] Kueh, S. R. M., Parnas, R. S., and Advani, S. G., 2002, ''Methodology for using long-period gratings and mold-filling simulations to minimize the intrusiveness of flow sensors in liquid composite molding,'' Compos. Sci. Technol., **62**(2), pp. 311–327.
[21] Bruschke, M. V., and Advani, S. G., 1990, ''A finite element/control volume approach to mold filling in anisotropic media,'' Polym. Compos., **11**, pp. 398–405.
[22] Robitaille, F., and Gauvin, R., 1998, ''Compaction of textile reinforcements for composites manufacturing. II: Compaction and relaxation of dry and H_2O saturated woven reinforcements,'' Polym. Compos., **19**, No. 5, pp. 543–557.
[23] Bruschke, M. V., and Advani, S. G., 1993, ''Flow of Generalized Newtonian Fluids Across a Periodic Array of Cylinders,'' J. Rheol., **37**, pp. 479–498.
[24] B. W. Grimsley, P. Hubert, X. Song, R. J. Cano, A. C. Loos and R. B. Pipes, 2001, ''Flow and compaction during the vacuum assisted resin transfer molding process,'' *International SAMPE Technical Conference*, 4–8 November 2001, Seattle, WA, USA.
[25] Hsiao, K. T., Mathur, R., Advani, S. G., Gillespie, J. W., Jr., and Fink, B. K., 2000, ''A closed form solution for flow during the vacuum assisted resin transfer molding process,'' J. Manuf. Sci. Eng., **122**, pp. 463–475.
[26] Pavel, Simacek, and Advani, S. G., 2003, ''A numerical model to predict fiber tow saturation during liquid composite molding,'' Compos. Sci. Technol., **63**, pp. 1725–1736.
[27] Gokce, Ali, and Advani, Suresh G., 2003, ''Gate effectiveness in controlling resin advance in liquid composite molding processes,'' ASME J. Manuf. Sci. Eng., **125**, Issue 3, pp. 548–555.
[28] Lawrence, Jeffrey M., and Advani, Suresh G., 2003, ''Use of Sensors and Actuators to Address Flow Disturbances During Resin Transfer Molding Process,'' Polym. Compos., **24**, pp. 237–248.
[29] Bickerton, Simon, Simacek, Pavel, Guglielmi, Sarah, and Advani, Suresh G., 1997, ''Investigation of Draping and its Effects on the Mold Filling Process During Manufacturing of a Compound Curved Composite Part,'' Composites, Part A, **28A**, pp. 801–816.
[30] Gokce, Ali, Hsiao, Kuang-Ting, and Advani, Suresh G., 2002, ''Branch and bound search to optimize injection gate locations in liquid composite molding processes,'' Composites, Part A, **33**(9), pp. 1263–1272.
[31] Acheson, Jeffrey A., Simacek, Pavel, and Advani, Suresh G., 2004, ''The implications of fiber compaction and saturation on fully coupled VARTM simulation,'' Composites Part A: Applied Science and Manufacturing, **35**(2), p. 159–169.

Macroscopic Effects of Surface Roughness in Confined Air Flow

M'hamed Boutaous

Patrick Bourgin

Ecole Supérieure de Plasturgie,
85 rue Henri Becquerel,
B.P. 801—01108 Oyonnax, France
e-mail: bourgin@esp-oyonnax.fr

The general framework deals with the winding of thin plastic films, in order to obtain good-quality rolls. This issue is tightly connected to the thickness of the residual air layer entrapped between the film layers. It is then of importance to optimize the surface topography of the films so that to improve the quality of the wound rolls. In a previous work, we proposed a simple model for the flow of an air layer squeezed between a solid smooth substrate and a plastic film sample: it was shown experimentally that the macroscopic characteristics of the flow are connected to the film roughness, but how? In order to answer this question, we assimilated the confined air flow to a flow through a periodic array of cylinders and a mathematical model based on homogenization techniques was developed. In the present paper, we search for pertinent parameters which describe the real surface roughness of plastic films. The experiments were carried out by using a 3-D roughness measurement device and the first observation is that the roughness distribution is not uniform. We made a sampling expressed by the percentage of peaks exceeding some given height threshold. The corresponding experimental parameters are used to define the network of cylinders. For each type of film, the threshold value is the only adjustable parameter and the following results are obtained: It is possible to adjust this parameter so that to obtain a very good agreement between the experimental data and the theoretical predictions. In addition, the smoother the film, the more important the highest peaks are in terms of air leakage. [DOI: 10.1115/1.1669034]

1 Introduction

Web materials such as film or sheet are commonly processed in the form of wound rolls. The overall quality of the product (i.e., plastic, paper, steel . . .) is strongly connected to the roll quality which in turn depends on the residual stresses within the roll [1–5]. In other words, the conditions for a defect to occur can be related to the fact that on component of the stress (at least) is greater than some critical value. For instance if a roll is wound to loosely, two types of defects may occur: (1) one, commonly called ''telescoping'' corresponds to lateral slippage of layers and (2) one, called ''starring'' results from circumferential buckling of layers. In the contrary, winding a roll too tightly can lead to the following defects: (1) a phenomenon called ''blocking'': adjacent layers ''stick'' to each other; more generally, any minor defect occurring locally (for example some dust particle entrapped between two layers) can be enhanced under excessive radial compression. (2) The generation of ''screw'' shaped defects, i.e. buckling in the axial direction due to lateral negative (i.e. compressive) stress resulting from stretching in the longitudinal direction (Poisson effect). In order to achieve a satisfactory stress field within a roll, it is necessary to adapt the processing conditions (tension, velocity, location and mechanical properties of the nip roll, nip force, characteristics of the core, . . .) to the bulk and surface properties of the web being wound (typically paper or plastic film). Of that purpose, various theoretical models have been developed as guide-lines for the choice of optimum processing conditions. All the models aiming to evaluate the internal stresses are based on the theory of accreted bodies [6]. They can be ranked into two categories: (1): Models where the radial Young's modulus is prescribed a priori. The first application of the theory of accreted bodies is probably due to Altmann [7] and Tramposch [8]. Altmann assumed the roll to be an elastic, anisotropic body, with elastic properties (Young's moduli and Poisson' ratio) constant throughout the roll. Yagoda [9] then Connolly and Winarski [10] took the core elastic deformation into account. Pfeiffer [11], Hakiel [12] introduced nonlinearly varying Young's modulus. (2) Models where the roll radial properties are not known a priori, but vary during winding because they result from the stress generated during winding, the stress field itself being dependent on the roll radial properties (among others). These ''second generation'' models are consistent with the experiments devoted to the compressing behavior of stacks of films where the effect of both surface roughness and air interlayers can be evaluated. It is well known that there is a strong link between the roughness of a surface (resulting from micro particles added to the resin) and its behavior in terms of air entrainment and evacuation [6]. Forrest [13] carried out experiments in vacuum in order to climinate any air effect and correlated the stack compression response to surface topography parameters. From a theoretical point of view, most models resort of the theory of hydrodynamic lubrication of rough surfaces: Good and Xu [14] developed a model, based on the classical theory of rough surfaces in contact (see for instance Greenwood and Williamson [15] or Bayada et al. [16]).

The concept of ''roughness'' is somehow difficult to define, because it basically contains much information. For the sake of simplicity, it is useful to characterize ''roughness'' by one single parameter. For example the total roughness (R_t) or the average roughness (Ra) are classically used for describing metallic surfaces. However, they are not adequate for PET film surfaces, see for instance Ref. [2]. We therefore found it necessary to propose a specific approach involving a more sophisticated description of the surface topography and by studying the influence of the static roughness on the aerodynamics phenomena generated by the winding process itself. The influence of the surface roughness on the air flow kinetics was studied by squeezing a rough plastic film on a smooth rigid plate. In order to quantify this influence, a mathematical model, based on homogenization techniques, was developed. In the present model, we represent the surface roughness like a periodic array of cylinders. The macroscopic experimental data can be nicely fitted by adjusting some microscopic parameters such as the cylinder diameters, or their heights.

The question which arises now is: how to connect these parameters to the real surface roughness of a film?

Contributed by the Fluids Engineering Division for publication in the JOURNAL OF FLUIDS ENGINEERING. Manuscript received by the Fluids Engineering Division January 23, 2003; revised manuscript received October 30, 2003. Associate Editor: D. Siginer.

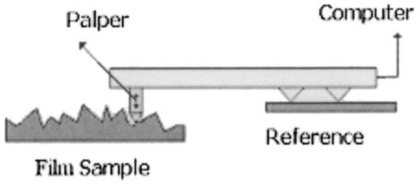

Fig. 1 Sketch of Profilometer

To provide a first answer, we have tested two types of PET films, and found an interesting correlation between the micro and macro experiments.

2 Principle of Roughness Measurement

The profilometer (Fig. 1) used is equipped with a stylus moving on the surface to be tested. The vertical displacement of the apex of the stylus (whose radius of curvature is of the order of a tenth of a micrometer) is analyzed numerically to determine the heights of the bumps. Square PET film samples with 3 mm edge are tested. Continuous measurements are taken over a width, and are repeated every 10 μm in order to scan the whole surface.

The 2-D profile obtained at each traveling is numerically treated so that to remove the defects due to the wavy surface of the film. Mineral fillers are generally incorporated into the polymer during processing so that to generate the film surface roughness. These fillers form agglomerates (Fig. 2). The statistical data processing basically consists in selecting the peaks higher than some prescribed threshold. This assumption is consistent with some observations reported by Bhushan et al. [17]: the highest peaks seem to play an important role in the squeeze flow between two rough surfaces. However, there is no obvious method to determine this threshold. The number of peaks which are taken into account obviously decrease as the threshold level increases. It is then possible to determine the percentage of peaks higher than the threshold value (from which it is deduced the mean distance between the peaks) as well as the mean values of their heights and widths.

These parameters are introduced into the mathematical model based on the representation of the surface roughness by means of a regular array of cylinders. They represent respectively the cylinders heights, the spacing between the cylinders and their diameters.

3 Squeezing Setup

Only the basic features of the experimental setup are summarized here, a more detailed description being found in previously published work [4].

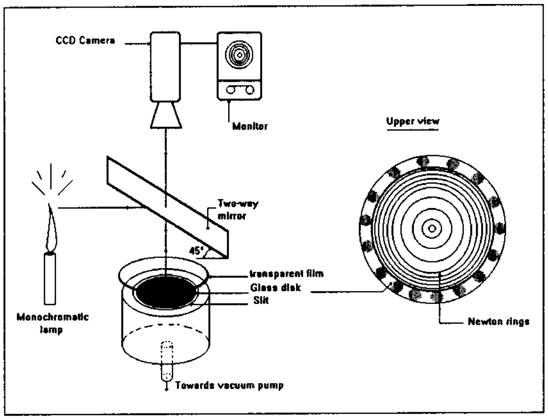

Fig. 3 Squeeze flow experimental set-up

A polished glass disk is put on a flat support having a circular slit connected to a vacuum pump: see Fig. 3.

A sample of plastic film is displayed on the glass plate and sub-ambient pressure is applied by operating the vacuum pump. The air layer which initially separates the film from the glass plate is partially evacuated: a quasi circular front starts from the slit and propagates towards the center.

Monochromatic light ($\lambda = 0.589$ micrometers) is used to insulate the film from above. Newton rings moving towards the center are formed and show the shape of the air gap between the film and the glass plate in the vicinity of the propagating front (Fig. 4). A CCD camera coupled with image processing is used to count the number of rings at the center. The reduction of the air interlayer is easily computed by using elementary optics laws. The corresponding time is measured for each sample. It reveals to be very reproducible for a given type of film (i.e., characterized by its thickness and its roughness). Some typical results are shown in Fig. 5 for two films having the same nominal thicknesses: the air thickness reduction is proportional to time, the slope of the curve being characteristic of the film surface topography (Fig. 5a: "smooth film"; Fig. 5b: "rough film").

The instantaneous thickness of the air layer e(t) at the center of the front is therefore of the form: $e(t) = e_i - k \cdot t$, where e_i is the initial thickness, t, the time and k some parameter characteristic of each sample (slope of the curves in Fig. 5), that we called "dynamic roughness coefficient". Note that it is not necessary to know the initial value of the air layer thickness which is actually difficult to measure.

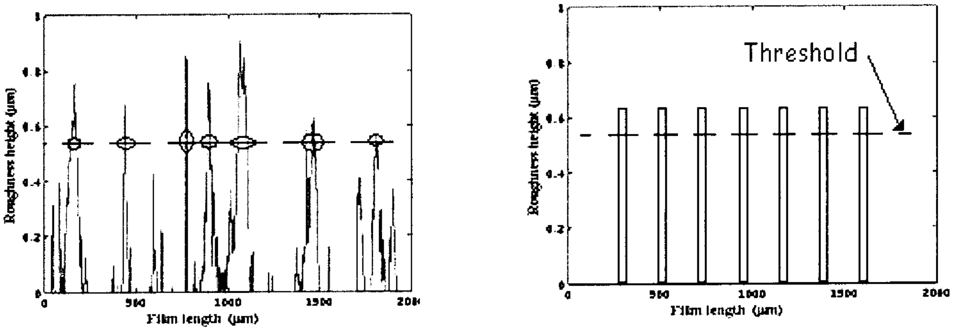

(a) (b)

Fig. 2 Typical roughness profile: (a) Typical roughness profile; (b) Typical roughness profile after homogenization

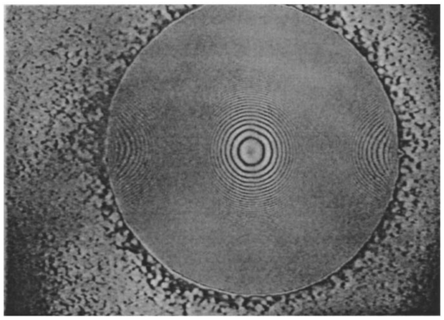

Fig. 4 Evolution of the front radius and Newton rings

4 Mathematical Model

The objective of the model is to establish a relationship between the reduction of the air layer thickness on the one hand and the displacement of the front on the other hand (see Fig. 6) and then to see how this relationship would depend on the surface topography of the plastic film.

The basic idea consists in computing the front radius versus time by equalizing the flow rate between the upstream and the downstream zones defined by the front radius $R(t)$.

The flow is considered to be quasi-static, inertia less and the fluid (air) to be incompressible, which is realistic because of the rather low velocities involved.

As shown in Fig. 6, the flow domain is divided into two zones by the propagating front (as defined by $r = R(t)$), from which it results that there are three unknown time functions to be determined: the thickness reduction of the cavity $e(t)$ (zone 1), the front location $R(t)$ and the thickness reduction of the zone downstream of the front: $e_f(t)$, (zone2).

4.1 Flow in Zone 1: Use of Experimental Data. Upstream the front: ($0 < r < R(t)$), the air gap is much higher than the roughness average value, which means that the surfaces can be considered as smooth, (Fig. 6). The pressure in the cavity is equal to the absolute value of the sub-ambient pressure, as denoted by P_a and the air layer thickness decreases linearly according to the experimental law: $e(t) = e_i - k \cdot t$.

As the front moves towards the center, the volume reduction of this zone is equal to:

$$Qv(t) = \frac{\partial V}{\partial t} = 2\pi(e_f - e(t))R(t)\frac{dR(t)}{dt} - \pi R(t)^2 \frac{de(t)}{dt}$$

Given that $e(t) = e_i - k \cdot t$ where k is a parameter determined experimentally, one gets:

$$Qv(t) = -2\pi(e_i - kt - e_f(t))R(t)\frac{dR(t)}{dt} + \pi R(t)^2 k \qquad (1)$$

4.2 Flow in Zone 2: Flow Rate Conservation and Homogenization Technique. Downstream the front ($R(t) < r < R_0$), the air gap $e_f(t)$ becomes of the same order of magnitude as the film roughness. However, for the sake of simplicity, the instantaneous flow rate is evaluated by means of Reynolds' thin film flow theory [18], which leads to the following expression:

$$Q_v = -\frac{\pi}{6\mu}\frac{P_a}{Ln\frac{R(t)}{R_0}} e_f(t)^3 \qquad (2)$$

where μ denotes the dynamic viscosity coefficient of air.

This flow rate is equal to the volume reduction of the upstream zone, as given by equation (1), which leads to the following ordinary differential equation:

$$kR(t)^2 \ln\left(\frac{R(t)}{R_0}\right) + 2R(t)(-e_i + kt + e_f(t))\ln\left(\frac{R(t)}{R_0}\right)\frac{dR(t)}{dt} + \frac{1}{6}\frac{Pa}{\mu}e_f^3(t) = 0 \qquad (3)$$

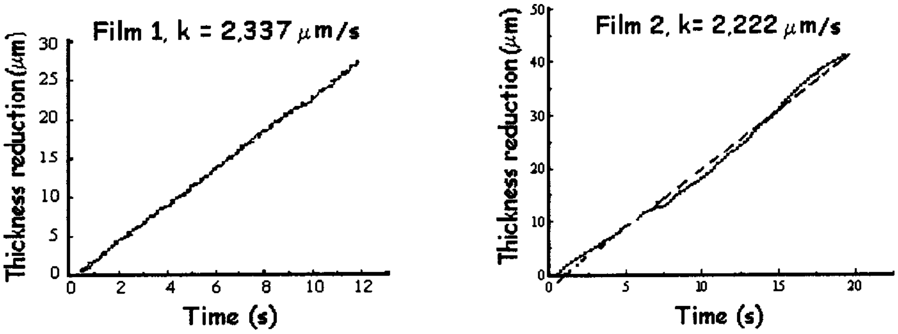

(a) (b)

Fig. 5 Air layer thickness reduction versus time in the central zone: (*a*) rough film; (*b*) smooth film

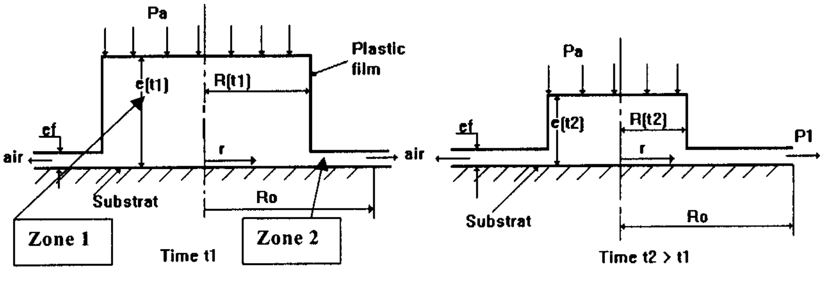

Fig. 6 Model features

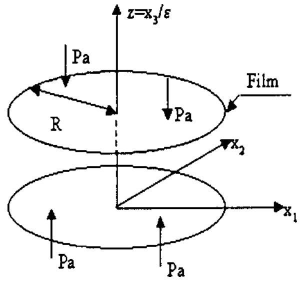

Fig. 7 Flow geometry

This equation shows a coupling between two unknown time functions: *R(t)* and $e_f(t)$. It is therefore necessary to introduce an additional equation. For that purpose, the equation which governs the confined flow in the zone downstream of the front will be searched for.

The general idea here consists in considering a flow through a regular array of identical cylinders confined between two parallel planes and squeezed against each other under a given pressure: see Figs. 7 and 8. The radii of these cylinders and the distance between their axes are respectively denoted by "*a*" and "*ε*". The squeeze flow will be studied by using homogenization techniques in the spirit of [16–21].

4.2.1 Equations of the Problem. The basic equations generally proposed are:

Stokes and continuity equations:

$$\begin{cases}\mu\Delta\vec{\mathrm{u}}=\vec{\nabla}p\\ \vec{\nabla}\cdot\vec{\mathrm{u}}=0\end{cases}$$

The boundary conditions are derived from the following assumptions:

- No-slip boundary conditions,

$$\vec{u}=\vec{0},\quad z=\pm h$$

where h denotes the half distance between the plates.

Prescribed pressure on the boundary of the field

$$p(R)=0$$

Local periodicity of the velocity (for homogenization)

When the problem is solved, the exiting weight flux gives the air thickness reduction:

$$S\frac{dh}{dt}=-Q_v$$

S: the air evacuation surface, *Qv:* volume flow rate.

The distance between the squeezing planes are smaller then the others dimensions. So, we introduce a non-dimensional variable $z=x_3/\omega$ which is of order 1. The distance between the plates is also of order 1:

$$H=\frac{h}{\omega}\approx 1$$

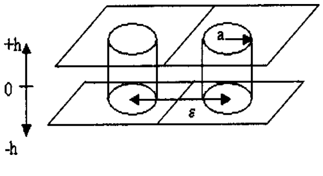

Fig. 8 Roughness modeling

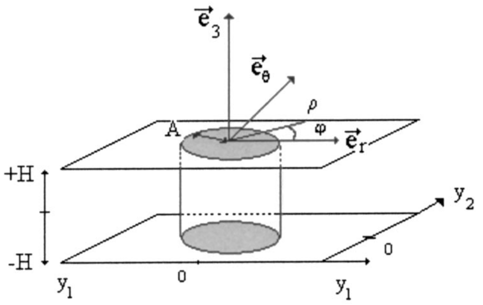

Fig. 9 Elementary cell

By defining "a small" parameter ε, which can be for example the diameter of the cylinders or their spatial period, we can introduce some parameter λ such as:

$$\lambda=\frac{\omega}{\varepsilon}\approx 1.$$

To take into account the local variations, we define the microscopic variable $\vec{y}=\vec{x}/\varepsilon$.

The velocity and pressure fields become dependent of $\vec{x}$ *and* $\vec{y}$, so that the derivative versus the macroscopic variable becomes:

$$\frac{\partial}{\partial x_i}\to\frac{\partial}{\partial x_i}+\frac{1}{\varepsilon}\frac{\partial}{\partial y_i}$$

The following asymptotic developments are classically proposed for the velocity and pressure:

$$\begin{cases}\vec{u}=\sum\limits_{n\geqslant 2}\varepsilon^n\vec{u}^n(\vec{x},\vec{y},z)\\ p=\sum\limits_{n\geqslant 0}\varepsilon^n p^n(\vec{x},\vec{y},z)\end{cases}\qquad(\vec{y}=\vec{x}/\varepsilon\ \ \mathit{local\ \ variable})$$

The boundary conditions become:

$$\vec{u}^n(\vec{x},\vec{y},z=\pm H)=\vec{0},\quad \rho=A,\quad n\geqslant 2,$$

$$p^0(R)=0$$

By introducing this development into the Stokes equations, and by equalizing the terms of the same order, the 1rst order problem becomes:

$$\begin{cases}p^0(\vec{x})\\ \vec{\nabla}_\lambda\cdot\vec{u}^2=0\\ \vec{\nabla}_\lambda\cdot\vec{u}^3=-\dfrac{\partial u_i^2}{\partial x_i}\\ \Delta_\lambda\vec{u}^2=\dfrac{1}{\mu}\vec{\nabla}p^1+\dfrac{1}{\mu}\left(\dfrac{\partial p^0}{\partial x_1},\dfrac{\partial p^0}{\partial x_2},0\right)\end{cases}$$

$$\Delta_\lambda=\frac{\partial^2}{\partial y_1^2}+\frac{\partial^2}{\partial y_2^2}+\frac{1}{\lambda^2}\frac{\partial^2}{\partial z^2}$$

to solve this problem at order 1, we introduce the following local problems defined for one elementary cell:

$$\begin{cases}\mu\Delta\vec{\alpha}^0=\vec{\nabla}q^0\\ \mu\Delta\vec{\alpha}^1=\vec{\nabla}q^1+(1,0,0)\end{cases}$$

and then, in a cylindrical coordinates (Fig. 9), the macroscopic velocity and pressure are of the form:

$$\begin{cases} \vec{u}^2 = \dfrac{dp^0}{dr}\,\vec{\alpha}^1 + \vec{\alpha}^0 \\ p^1 = \dfrac{dp^0}{dr}\,q^1 + q^0 \end{cases}$$

where $\vec{\alpha}^i$, q^i ($i=0$ or 1) are the solutions of the following three local problems:

$$\begin{cases} \mu\Delta\vec{\alpha}^i = \nabla q^i + \vec{f}^i \\ \vec{\nabla}\cdot\vec{\alpha}^i = 0 \end{cases}, \quad \vec{f}^0 = \begin{pmatrix} 0 \\ 0 \\ 0 \end{pmatrix}, \quad \vec{f}^1 = \begin{pmatrix} 1 \\ 0 \\ 0 \end{pmatrix}$$

To solve these local problems, we have chosen the Lee and Fung [21] solution proposed for the Hele-Shaw cell. The periodic boundary condition is replaced here by a Poiseuille flow condition at infinity:

$$V_\infty = U\left(1 - \frac{z^2}{H^2}\right)$$

The characteristic velocity U is determined after solving the problem and equalizing the smooth terms with those corresponding to the solution of the squeeze flow between smooth plates.

4.2.2 *The Two Term Solution for the Velocity by Lee and Fung*

From the local coordinates system (ρ,φ,z) equivalent to (y_1,y_2,z) in our system, Fig. (9), we get the Cartesian components of the velocity from the cylindrical ones by:

$$\alpha_1 = V_\rho\cos(\varphi) - V_\varphi\sin(\varphi)$$

$$\alpha_2 = V_\rho\sin(\varphi) + V_\varphi\sin(\varphi)$$

where V_ρ, V_φ, are the radial and orthoradial "local" velocity components see Fig. (9). They represent the two terms solution of Lee and Fung for the local equations:

$$V_\rho = U\cos\theta\left(\left(1 - \frac{K_2(kA)A^2}{K_0(kA)\rho^2}\right)\right.$$
$$\left.\times\left(1 - \frac{z^2}{H^2}\right) + \frac{2}{k\rho}\frac{K_1(k\rho)}{K_0(kA)}\frac{32\cos(kz)}{\pi^3}\right)$$

$$V_\varphi = -U\sin\theta\left(\left(1 + \frac{K_2(kA)A^2}{K_0(kA)\rho^2}\right)\right.$$
$$\left.\times\left(1 - \frac{z^2}{H^2}\right) + \frac{2}{k\rho}\frac{K_1'(k\rho)}{K_0(kA)}\frac{32\cos(kz)}{\pi^3}\right)$$

where $k=\pi/2H$ and A the cell radius: $a=\varepsilon A$.

The radial component of the velocity, for the problem at order i=0, 1 is then:

$$\alpha_1^i = U_i\left(1 - \frac{z^2}{h^2}\right)\left[\left(1 - \cos(2\varphi)\frac{K_2(kA)A^2}{K_0(kA)\rho^2}\right)\right]$$
$$+ \frac{64\cos(kz)}{\pi^3}U_i\left[\frac{\cos^2\varphi}{k\rho}\frac{K_1(k\rho)}{K_0(kA)} + \sin^2\varphi\frac{K_1'(k\rho)}{K_0(kA)}\right]$$

4.2.3 *Flow Rate and H(t) Differential Equation.*

We can solve the problem numerically, but we have chosen here the two terms analytical solution suggested by Lee et al. [21] for a Hele-Shaw cell, which reported in the velocity expression $\vec{u}^2$ and after a weight balance (similar to that carried out to obtain classical film squeezing equation [18]):

$$-\pi R^2\frac{d}{dt}\left(\frac{h}{2}\right) = \int\int_\Sigma \varepsilon^2\vec{u}^2\cdot\vec{dS}$$

$$then:\ -\pi\frac{R^2}{2}\omega\frac{dH}{dt} = \varepsilon^2\int_{-h}^{h}dx_3\int Rd\theta u_1^2(r=R)$$

for the evaluation of the integrations we do:

$$\int_{-h}^{h}dx_3 \to \omega\int_{-H}^{H}dz$$

$$\int_0^{2\pi}Rd\theta \to N\varepsilon\int_{-\Lambda/2}^{\Lambda/2}dy_2, \quad \text{at } y_1 = \frac{\Lambda}{2}$$

$$where \quad N = \frac{2\pi R}{l} = \frac{2\pi R}{\varepsilon\Lambda}$$

so, we get at end:

$$-\frac{\pi R^2}{2}\omega\frac{dH}{dt} = \varepsilon^2\omega\int_{-H}^{H}dz\int_{-\Lambda/2}^{\Lambda/2}dy_2u_1^2\left(y_1 = \frac{\Lambda}{2}, y_2, z\right)\cdot\frac{2\pi R}{\Lambda}$$

by introducing α_1^i, we have:

$$\int_{-\Lambda/2}^{\Lambda/2}dy_2u_1^2\left(y_1 = \frac{\Lambda}{2}, y_2, z\right) = U_i\left(1 - 2A^2\frac{K_2(kA)}{K_0(kA)}\int_0^{\Lambda/2}dy_2\frac{y_1^2 - y_2^2}{y_1^2 + y_2^2}\right) + \frac{64U_i}{\pi^3}\frac{\cos(kz)}{K_0(kA)}$$
$$\times\left[\underbrace{\int_0^{\Lambda/2}\frac{2K_1(k\sqrt{y_1^2+y_2^2})}{k\sqrt{y_1^2+y_2^2}}\frac{y_1^2}{y_1^2+y_2^2}}_{I} + \underbrace{\int_0^{\Lambda/2}dy_2\frac{2y_2^2}{y_1^2+y_2^2}K_1'(k\sqrt{y_1^2+y_2^2})}_{J}\right]$$

after integration of I by parts, we find:

$$I=\frac{K_1\left(\frac{k\Lambda}{\sqrt{2}}\right)}{\frac{k}{\sqrt{2}}}-J$$

and finally:

$$\int_{-H}^{H}dz\int_{-\Lambda/2}^{\Lambda/2}dy_2\alpha_1^i(y_1,y_2,z)$$

$$=\int_{-H}^{H}dz\left\{U_i\left(1-\frac{z^2}{H^2}\right)\left[1-A^2\left(\frac{\pi}{2}-1\right)\frac{K_2(kA)}{K_0(kA)}\right]\right.$$

$$\left.+\frac{64U_i}{\pi^3}\frac{\cos(kz)}{K_0(kA)}\frac{K_1\left(\frac{k\Lambda}{\sqrt{2}}\right)}{\frac{k}{\sqrt{2}}}\right\}$$

$$=U_i\frac{4H}{3}\left[1-A^2\left(\frac{\pi}{2}-1\right)\frac{K_2(kA)}{K_0(kA)}\right]\frac{4*64}{\pi^3}\frac{Ui}{K_0(kA)}\frac{K_1\left(\frac{k\Lambda}{\sqrt{2}}\right)}{\frac{k}{\sqrt{2}}}$$

by applying this expression in the expression of the flow rate, we obtain:

$$-\frac{R\Lambda}{4\varepsilon^2}\frac{dH}{dt}=\left\{\frac{4H}{3}\left[1-A^2\Lambda\left(\frac{\pi}{2}-1\right)\frac{K_2(kA)}{K_0(kA)}\right]\right.$$

$$\left.\times\frac{4*64}{\pi^3}\frac{1}{K_0(kA)}\frac{K_1\left(\frac{k\Lambda}{\sqrt{2}}\right)}{\frac{k}{\sqrt{2}}}\right\}\left(U_1\frac{dp^0}{dr}+U_0\right)$$

to find the expression of the characteristic velocities U_1 and U_2, we test this equation in the case of smooth surfaces, where $A=0$ and $l=\varepsilon$, then we have:

$$-\frac{R\Lambda}{4\varepsilon^2}\frac{dH}{dt}=\frac{4H}{3}\left(U_1\frac{dp^0}{dr}+U_0\right)$$

so, the term $\varepsilon^2(U_1dp^0/dr+U_0)$ must be the velocity at radius R in the squeeze flow between smooth circular plates.

And from Reynolds equation, we can write:

$$\varepsilon^2\left(U_1\frac{dp^0}{dr}+U_0\right)=\frac{P_aH^2}{8\mu R}\omega^2$$

Finally, the time equation for the squeeze flow like in our problem is:

$$-\frac{1}{H^3}\frac{dH}{dt}=\frac{2Pa}{3\mu R^2}\omega^2\left[1-A^2\frac{K_2(kA)}{K_0(kA)}\right]+\frac{256\sqrt{2}Pa}{\pi^4\mu R^2}\omega^2\frac{K_1(k\sqrt{2})}{K_0(kA)}$$

knowing that $H=h/\omega\approx 1$, $\lambda=\omega/\varepsilon\cdot$, $l=\varepsilon\Lambda$, $k=\pi/2H$ and $a=\varepsilon A$, then, the required time equation is:

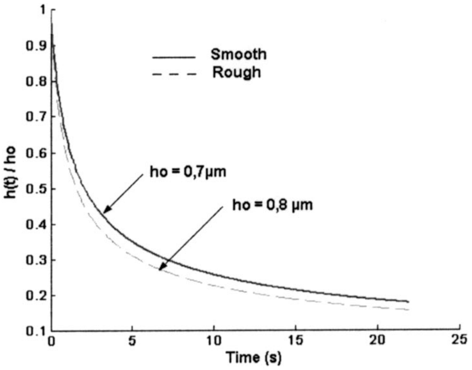

Fig. 10 Air layer thickness reduction in the squeezed zone

$$-\frac{h_0^2}{h^3}\frac{dh}{dt}=\frac{8Pa}{3\mu R^2}h_0^2\left(1-2\frac{a^2}{\varepsilon^2}\frac{K_2\left(\frac{\pi a}{2h}\right)}{K_0\left(\frac{\pi a}{2h}\right)}\right.$$

$$\left.+\frac{768}{\sqrt{2}\pi^5}\frac{hh_0}{h_0\varepsilon}\frac{K_1\left(\frac{\pi\varepsilon}{2\sqrt{2}h}\right)}{K_0\left(\frac{\pi a}{2h}\right)}\right)\tag{4}$$

where K_0, K_1 and K_2 represent the modified Bessel's functions of order 0, 1 and 2, respectively, and $2h_0$ stands for the initial distance between the two planes. These equation is an extension of the classical squeeze film equation for ''rough'' surfaces and reduces to the classical one (Stefan's) for the case of smooth surfaces $(a=0)$.

The coupled problem as defined by equation (3) and the latter equation (4) (where $2h$ is now written e_f like in equation (3)) associated with adequate initial condition for the front: $R(t=0)=R_0$ (slit radius) is solved by using a Runge-Kutta method of the fourth order. The initial value of the air layer thickness close to the slit (i.e. where sucking starts) will be taken equal to the threshold value as defined in the surface topography description. It can be seen in Fig. 10 the nondimensional thickness of the air layer versus time for two samples of films. The tendency is consistent with qualitative observations: the rougher, the faster.

5 Discussion

By introducing the measured roughness parameters into the mathematical model, we search for the threshold value which leads to the best agreement between the experiments and the theoretical predictions, knowing that the spatial period and the cylinders diameter are determined once the threshold value is prescribed. In so doing, we assimilate the measured spacing between the peaks formed by the agglomerates to the distance between the cylinders which simulate roughness (ε), and the peaks width to the diameter of these cylinders ($2a$).

Figures 11 and 12 show the time evolution of the front radius, for two PET films of the same thickness (i.e., stiffness) but of different topographies (rough and smooth, respectively). The ''stars'' correspond to the experimental values.

The experimental data are compared with the theoretical predictions for several values of the threshold, and for two film samples. The results can be summarized as follows:

1. By adjusting one single parameter, ''the threshold value,'' a very good agreement between the experimental data and the theoretical predictions can be obtained. This is not true anymore

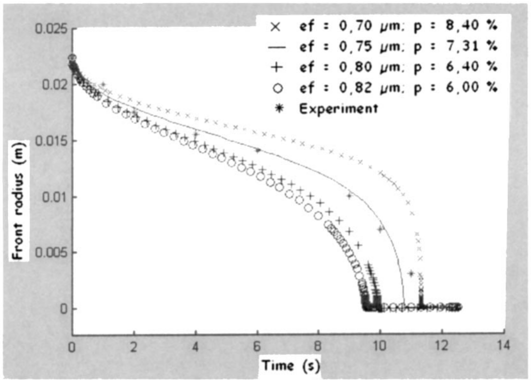

Fig. 11 Rough film: front evolution versus time for several threshold values

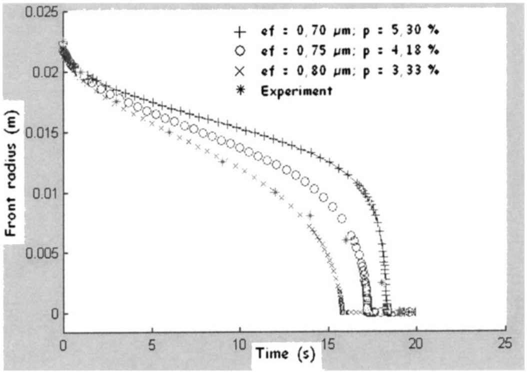

Fig. 12 Smooth film: front evolution versus time for several threshold values

when approaching the end of the squeeze flow process. This discrepancy may be due to some percolation phenomenon of the air flow between the obstacles.

2. Only the very highest peaks (a few percentages whose sizes are over the threshold value) seem to be important for the macroscopic flow. This tendency holds true for each sample and confirms the experimental observations at least qualitatively.

3. The smoother the film, the more important the highest peaks are in terms of air leakage: 7.3% of the peaks higher than 0.75 μm for the ''rough'' film and 3.3% of the peaks higher than 0.80 μm for the ''smooth'' film in terms of roughness mean value.

6 Conclusion

The stress generated within a roll of a flexible medium such as PET film is strongly dependent on the air interlayers. The film roughness plays an important role on the air flows phenomena induced by the winding process. In order to quantify this role, an original experiment was first carried out: it consists in studying the flow of an air layer squeezed between a smooth rigid circular plate and a rough flexible PET film sample. Two parameters were introduced: (1) the thickness reduction of the air layer at the center of the disc which is representative of the film roughness for two samples of the same thickness and allows some ''dynamic roughness coefficient'' to be defined; (2) the propagation of the front (i.e. the time evolution of the front radius). In this paper, a simple model, based on periodic homogeneization techniques, allows the front propagation to be predicted, assuming that the ''dynamic roughness coefficient'' is known and that a pertinent description of the static roughness is given. The main results is that the key role in a squeeze flow is played by the highest peaks, as shown by [17]. This trend is all the more marked as the film is smoother.

The future developments would consist in giving a way to generate only a few ''high enough'' peaks so that to guarantee good mastering of the air interlayers without creating possible defects due to the film roughness.

Acknowledgments

The authors wish to thank Dr. R. Schirrer and Dr. C. Gauthier (Institut Charles Sadron, CNRS, Strasbourg) for giving access to the 3-D profilometer. We acknowledge the reviewers for valuable remarks.

References

[1] Bourgin, P., and Bouquerel, F., 1993, ''Winding Flexible Media: a Global Approach,'' Adv. Info. Storage Sys., ASME, **5**, pp. 493–512.
[2] Bhushan, B., 1996, ''Tribology and Mechanics of Magnetic Storage Devices,'' Chap. 2, Springer, 2nd edition.
[3] Boutaous, M., Bourgin, P., and Woehl, P., 2001, ''Periodic Homogeneization Techniques as a Way to Account for Surface Roughness in a Confined air Flow,'' *Proc. ASME*, I MECE, New York (USA), November 2001.
[4] Boutaous, M., and Bourgin, P., 1997, ''Experimental Study of Squeeze Film Between One Smooth Surface and One Rough Surface,'' *Proceedings of the 4th Int. Conference on Web Handling*, pp. 224–234, Oklahoma, USA.
[5] Boutaous, M., 1998, ''Influence de l'état de Surface des Matériaux Flexibles sur Leur Comportement Mécanique,'' *PhD Thesis*, Louis Pasteur University, Strasbourg, France.
[6] Brown, B. C., and Godmann, L. E., 1963, ''Gravitational Stress in Accreted Bodies,'' Proc. R. Soc. London, **A276**, pp. 571–576.
[7] Altmann, H. C., 1968, ''Formulas for Computing the Stresses in Center Wound Rolls,'' Tappi J., **51**, No. 4, pp. 176–179.
[8] Tramposch, H., 1967, ''Anisotropic Relaxation of Internal Forces in a Wound Reel of Magnetic Tape,'' J. Appl. Mech., **32**, pp. 888–894.
[9] Yagoda, H. P., 1980, ''Resolution of a Core Problem in Wound Rolls,'' ASME J. Appl. Mech., **47**, pp. 847–854.
[10] Connolly, D., and Winarski, D., 1984, ''Stress Analysis of Wound Magnetic Tape,'' Proc. A.S.L.E. Intern. Conf. San Diego.
[11] Pfeiffer, J. D., 1966, ''Internal Stress in a Wound Roll of Paper,'' Tappi J., **49**, No. 8, pp. 342–347.
[12] Hakiel, Z., 1987, ''Non-Linear Model for Wound Roll Stress,'' Tappi J., **70**, pp. 113–117.
[13] Forrest, A. W., 1993, ''A Mathematical and Experimental Investigation of the Stack Compression of Films,'' Proc. Second Intern. Conf. On Web Handling, Stillwater Oklahoma, USA, pp. 196–212.
[14] Good, J. K., and Xu, Y., 1993, ''Computing Wound Roll Stresses Based Upon Web Surface Characteristics,'' Proc. Second Intern. Conf. On Web Handling, Stillwater Oklahoma, USA, pp. 213–227.
[15] Greenwood, J. A., and Williamson, J. B. P., 1966, ''Contact of Nominally Flat Surfaces,'' Proc. R. Soc. London, **A**, No. 295, pp. 300–319.
[16] Bayada, G., and Chambat, M., 1988, ''New Models in the Theory of the Hydrodynamic Lubrication of Rough Surfaces,'' ASME J. Lubr. Technol., **110**, pp. 402–407.
[17] Bhushan, B., and Tonder, K., 1989, ''Roughness-Induced Shear—and Squeeze—Film Effects in Magnetic Recording—Part II: Applications,'' J. Tribol., **111**, pp. 228–236.
[18] Moore, D. F., 1965, ''A Review of Squeeze Films,'' Wear, **8**, pp. 245–263.
[19] Sanchez-Palencia, E., 1980, ''Nonhomogeneous Media and Vibration Theory,'' lecture Notes in Physics, No 127, Springer-Verlag.
[20] Sarkar, K., and Prosperetti, A., 1996, ''Effective Boundary Conditioned for Stokes Flow Over a Rough Surface,'' J. Fluid Mech., **316**, pp. 223–240.
[21] Lee, J. S., and Fung, Y. C., 1969, ''Stokes Flow Around a Cylindrical Post Confined Between Two Parallel Plates,'' J. Fluid Mech., **37**, pp. 657–670.

M. Z. Saghir
T. J. Makriyannis

Ryerson University, Department of Mechanical,
Aerospace and Industrial Engineering,
350 Victoria St,
Toronto, ON, M5B 2K3

D. Labrie
Dalhousie University,
Department of Physics and Atmospheric
Science, Halifax, NS B3H 3J5

Buoyancy Convection During the Growth of Si_xGe_{1-x} by the Traveling Solvent Method (TSM)

The traveling solvent method known as TSM is a process used to produce pure and homogeneous crystals structures. TSM has been tested on many alloys producing uniform and uncontaminated single crystals. In the present study the effect of buoyancy convection on the growth of the $Si_{0.02}Ge_{0.98}$ *crystal grown by the traveling solvent method is investigated under different heating conditions. The full Navier-Stokes equations together with the energy and solutal equations are solved numerically using the finite element technique. The model takes into consideration the losses of heat by radiation and the use of the phase diagram to determine the silicon concentration at the growth interface. Results reveal a strong convection in the solvent, which in turn is detrimental to the growth uniformity in the crystal rod. Additional numerical results show that the convective heat transfer significantly influences the solute distribution in the liquid zone and affects the growth rate substantially. Qualitative comparison of the numerical results with the experiment conducted at Dalhousie University showed a good agreement for the silicon concentration at the growth interface.* [DOI: 10.1115/1.1669414]

Introduction

The traveling solvent method (TSM) or commonly referred to as the traveling heater method (THM) is a process used to produce pure and homogeneous single crystals which can be used for the production of high-quality semiconductors. The way in which the TSM works is, a heated solution zone passes through a polycrystalline feed rod in order to grow a single crystal. The solution zone is heated by radiation for example by a halogen lamp that is encompassed in a furnace. The TSM ampoule which contains the solution zone, the feed rod and the crystal is then translated through the common focus of the furnace's mirrors. This process offers a lowering of the crystal growth temperature and a reduction in its defect density. Matasumoto et al. [1] carried out a numerical simulation of InP crystal growth by the traveling solvent method. It was found that in the case of strong buoyancy convection constitutional supercooling tended to occur near the interface, whereas it does not appear in the case of weak buoyancy convection. Okano et al. [2] applied TSM to the numerical modeling of a simulation for the growth of GaSb from a Ga-solution. Crucible temperature, rotation and material on the crystal interface shape were studied. It was found that with increasing crucible temperature the interface curvature became larger. The application of rotation was successful in suppressing the natural convection in the solution, and in obtaining an interface with less curvature. With lower crucible temperatures the interface shape was slightly convex toward the crystal and the effect of crucible rotation was not significant.

The TSM method was also used for the growth of GaInSb [3]. It was found that the growing crystal's characteristics and stability where influenced greatly on the positioning of the thermal profile. Martinez-Tomas et al. [4] studied the effects of thermal conditions in the TSM growth of HgTe. The study showed the heat transfer between the furnace and the ampoule for central positions increased the length of the liquid zone and the calculated concentration field showed a uniform concentration core in the liquid zone and step concentration along the growth interfaces indicating the importance of convection.

Lent et al. [5] performed a mathematical simulation of TSM growth of ternary semiconductor materials under suppressed gravity conditions. It was found that the position of the thermal profile severely disturbed the characteristics and stability of the growing crystal. Various levels of applied magnetic field where applied aligned and misaligned. An upper limit of misalignment was found at which increased alignment would cause the growth interface to lose stability. The convective flow due to small misalignment was found to increase mixing in the horizontal plane being beneficial for the growth process.

In addition the TSM has been used in conjunction with the rotating magnetic field (RMF) in the attempt to slow buoyancy-induced convection while processing CdTe crystal [6]. The influence of the magnetic field was tested under terrestrial and microgravity conditions. The study showed that under microgravity conditions the application of the RMF can be used to overcome residual buoyancy-induced convection and used to control the uniformity of the solution-zone composition at the growth front without appreciable modification of the growth interface shape [6]. Liu et al. [7] applied a vertical magnetic field to a 3-D simulation model of flow structures in liquid phase electroepitaxy. The results showed that for successful growth the magnetic field must be optimized.

Ye et al. [8] studied the effects of natural convection on temperature and solute distributions, growth rate and growth uniformity along the interface for CdTe single crystal growth by the traveling heater method. A thermosolutal convection model was used to simulate the coupled heat, solute and fluid flow fields in the growth ampoule. Simulation results show that the solute distribution in the liquid zone is significantly influenced by the convective heat transfer and the growth rate increases substantially [8]. The simulations demonstrated the importance of having controlled convection for uniform growth since weaker convection is desired in the interface region. Reig et al. [9] reported on the growth of $Hg_{1-x}Mn_xTe$ by the cold traveling heater method (CTHM). Bulk crystals were produced by the CTHM method in order to obtain crystals with a homogeneous composition and to reduce the Hg high pressure connected to the temperature synthesis reaction between the components in the elemental form.

Nakajima et al. [10] grew Si-rich SiGe crystals by the multicomponent zone melting method. It was found that with a proper pulling rate to keep position and temperature at the growing in-

---

Contributed by the Fluids Engineering Division for publication in the JOURNAL OF FLUIDS ENGINEERING. Manuscript received by the Fluids Engineering Division January 26, 2003; revised manuscript received October 6, 2003. Associate Editor: D. Siginer.

terface constant a crystal of uniform composition can be grown. Also shown was that the supply of Si was very effective in modifying the compositional variation SiGe crystals. Azuma et al. [11] developed an automatic feedback control system of the crystal-melt interface position in order to keep a constant temperature at the growth interface and demonstrated its successful application to uniform composition Si-rich SiGe crystals. Dold et al. [12] experimentally grew GeSi crystals in the range of Si $\leqslant 10\%$ by the vertical Bridgman technique in a radiation heated mirror furnace.

In this paper, we solve the full steady-state momentum, energy and mass transfer equation to study the buoyancy convection and Silicon segregation during the growth of $Si_{0.02}Ge_{0.98}$ Alloy by the traveling solvent method. The growth rate is estimated at the growth interface and its relation with different heating gradients is found. The growth rate obtained numerically was then compared to the experimental data as well as the silicon distribution along the growth interface. Both comparisons showed a reasonable agreement.

Governing Equations and Boundary Conditions

The 2-D axi-symmetric Navier Stokes equations combined with the energy and mass transfer equation were solved numerically using the finite element code FIDAP [13]. Equations (1)–(5) can be nondimensionalized using the following non-dimensional variables:

$$\mathrm{R}=\frac{\mathrm{r}}{\mathrm{L}},\quad \mathrm{Z}=\frac{\mathrm{z}}{\mathrm{L}},\quad \mathrm{U_r}=\frac{\mathrm{u}}{\mathrm{u_o}},\quad \mathrm{U_z}=\frac{\mathrm{v}}{\mathrm{u_o}},$$

$$P=\frac{\mathrm{pL}}{\mu \mathrm{u_o}},\quad \theta=\frac{\mathrm{T}-\mathrm{T_o}}{\Delta \mathrm{T}},\quad \mathrm{C}=\frac{\mathrm{c}-\mathrm{c_o}}{\Delta \mathrm{c}},\quad \mathrm{u_o}=\sqrt{\mathrm{g}\beta_{\mathrm{T}}\Delta \mathrm{TL}}$$

Navier-Stokes Equations
r-direction

$$\rho\left[u_r\frac{\partial u_r}{\partial r}+u_z\frac{\partial u_z}{\partial z}\right]=-\frac{\partial p}{\partial r}+\mu\left[\frac{1}{r}\frac{\partial}{\partial r}\left(r\frac{\partial u_r}{\partial r}\right)+\frac{\partial^2 u_r}{\partial z^2}-\frac{u_r}{r^2}\right] \tag{1}$$

z-direction

$$\rho\left[u_r\frac{\partial u_z}{\partial r}+u_z\frac{\partial (u_z)}{\partial z}\right]=-\frac{\partial p}{\partial z}+\mu\left[\frac{1}{r}\frac{\partial}{\partial r}\left(r\frac{\partial u_z}{\partial r}\right)+\frac{\partial^2 u_z}{\partial z^2}\right]-\rho g[\beta_T(T-T_m)-\beta_C(c-c_0)] \tag{2}$$

Energy-Balance Equation

$$\rho c_{\mathrm{p}}\left[u_r\frac{\partial T}{\partial r}+u_z\frac{\partial T}{\partial z}\right]=k\left[\frac{1}{r}\frac{\partial}{\partial r}\left(R\frac{\partial T}{\partial r}\right)+\frac{\partial^2 T}{\partial z^2}\right] \tag{3}$$

Mass-Balance Equation

$$\left[u_r\frac{\partial c}{\partial r}+u_z\frac{\partial c}{\partial z}\right]=-\alpha_c\left[\frac{1}{r}\frac{\partial}{\partial r}\left(r\frac{\partial c}{\partial r}\right)+\frac{\partial^2 c}{\partial z^2}\right] \tag{4}$$

Continuity Equation

$$\frac{1}{r}\frac{\partial}{\partial r}(ru_r)+\frac{\partial u_z}{\partial z}=0 \tag{5}$$

The finite-element mesh consists of 61 nine-node quadrilateral elements in the radial direction and 101 quadrilateral elements in the axial direction. At each node the unknowns are the temperature, the velocities and the concentration. A linear approximation for the pressure using the penalty method was adopted. The equations were solved simultaneously and the criteria for convergence

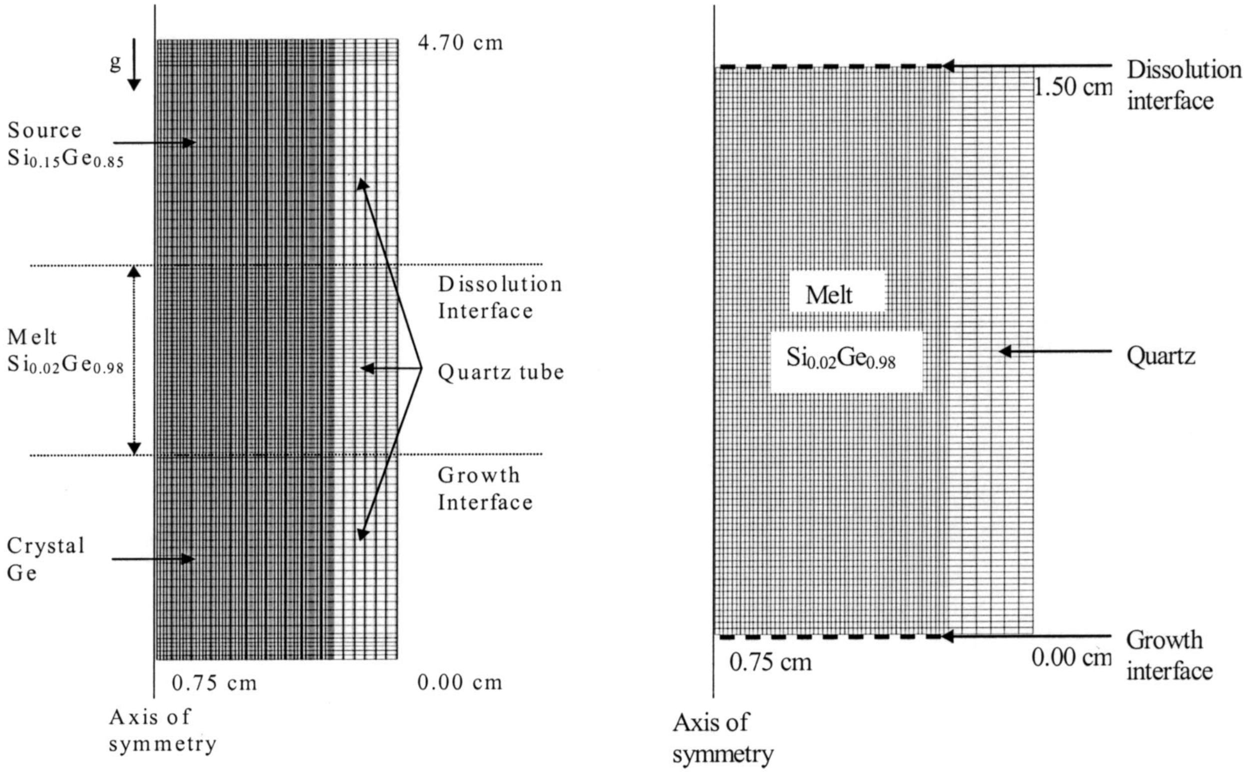

(a) Heat conduction model **(b) Convection model**

Fig. 1 Finite element model for the heat conduction and the fluid flow model

set for the four unknowns, namely the temperature, the two components of velocity and the concentration. Convergence is reached when the primitive variables attain a difference (between two consecutive iterations) less than 10^{-4}. Extensive numerical accuracy was conducted to demonstrate that the chosen grid was adequate for the model.

Boundary Conditions. A temperature profile was applied to the outside quartz wall and a boundary condition of zero velocity flow in the radial and axial directions was applied at the top and bottom of the rod as well as at the quartz tube. Zero velocity in the radial direction was also applied along central axis. This last boundary condition is assuming that the flow will be perfectly symmetric about the central axis. The problem consisted of first solving the heat conduction problem using the mesh displayed in Fig. 1(*a*). Once the temperature at the growth interface and dissolution interface was calculated; the second mesh displayed in Fig. 1(*b*) was used. From the phase diagram, knowing the temperature distribution at the growth interface, the concentration of Silicon is calculated and used as a boundary condition at the growth interface for the second mesh. This mesh consists of 61 elements in the radial direction and 95 elements in the axial direction. Again the nine-node quadrilateral element was used in the analysis. The same temperature profile as in the previous case was applied outside the wall of the quartz tube and the boundary condition for the temperature at the growth and dissolution interface was the one obtained from the conduction model. The full Navier-Stokes equations together with the energy and mass transfer equation were solved. The same convergence criterion as in the previous case was adopted. The flow boundary condition remained the same as in the previous case.

Results and Discussion

The problem consists of a $Si_{0.15}Ge_{0.85}$ feed rod also known as the source rod having a diameter of 1.1 cm and a length of 1.7 cm. This rod is located on top of a $Si_{0.02}Ge_{0.98}$ rod having the same diameter and a length of 1.5 cm identified as the melt rod. Finally a germanium rod known as the crystal rod is located below the two other rods having a length of 1.5 cm and a diameter of 1.1 cm as shown in Fig. 1(*a*). The total sample is enclosed into a quartz tube having an outer diameter of 1.5 cm and a thickness of 0.2 cm. Different heating profiles were applied at the external wall of the quartz tube. The melting temperature of the $Si_{0.02}Ge_{0.98}$ rod is less than the $Si_{0.15}Ge_{0.85}$ rod. Therefore Si will be segregating from the rich SiGe rod toward the bottom rod. Our main objective is to examine the Si segregation in detail in order to gain information as to what is the ideal condition for a heater profile to be used in the crystal growth. Figure 1 depicts the system under consideration.

In this investigation, a normal distribution curve was used to simulate the heater profile along the outside surface of the quartz tube. Two different variations of this curve were used. The first one had a maximum temperature of 1001°C and was perfectly symmetric. The second curve had the same maximum temperature but had a maximum peak shift towards the source rod by 0.15 cm. Figures 2(*a*) and 2(*b*) show the temperature profile adopted outside the Quartz tube. The heating profile displayed in Fig. 2(*b*) was measured experimentally using the Dalhousie furnace. A normal distribution technique was used to provide a smooth temperature variation which was then used in our numerical code.

Figures 3(*a*) and 3(*b*) shows the temperature variation at the growth interface and at the dissolution interface. It is evident that with a symmetrical heating profile; both temperatures at the growth interface and at the dissolution interface are close to each other. However, when the heater is asymmetrical, the large difference between the two interface temperatures is obvious as shown in Fig. 3(*b*).

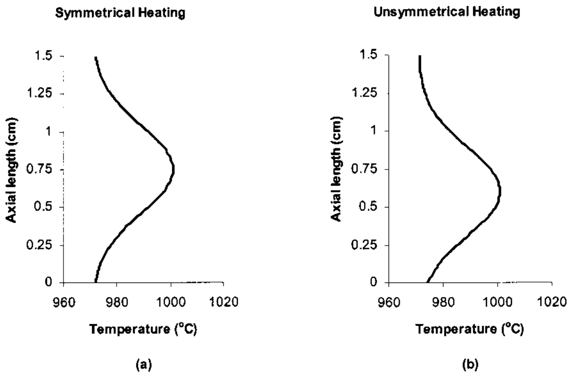

Fig. 2 Temperature boundary condition at the outside wall of the quartz along the solvent

From the phase diagram, using the temperature profiles at the growth interface shown in Fig. 3, the radial variation of Si along the interface is obtained, as shown in Fig. 4, and is used in the fluid, heat and mass transfer model as a boundary condition. Figure 5 presents the temperature and the streamlines obtained from the second model. From the two cases shown the asymmetric case is preferred, as the temperature contour lines are lower along the growth interface, which in turn promotes low flow rate and therefore a more uniform solute distribution resulting in desirable conditions for crystal growth. The temperatures at the growth interface of the two profiles vary from 973.39°C to 974.09°C for the symmetric case and from 971.74°C to 972.52°C for the asymmetric case. The difference in maximum temperature along the two growth interfaces is 1.57°C.

Figures 5(*c*) and 5(*d*) show the simulated streamline contours for the two heater profiles. A single convective cell is formed in

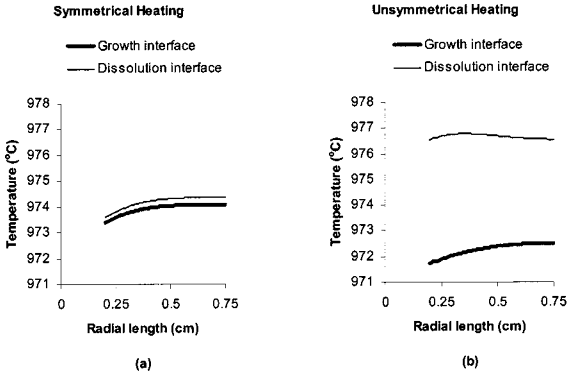

Fig. 3 Temperature boundary condition along the growth and dissolution interface

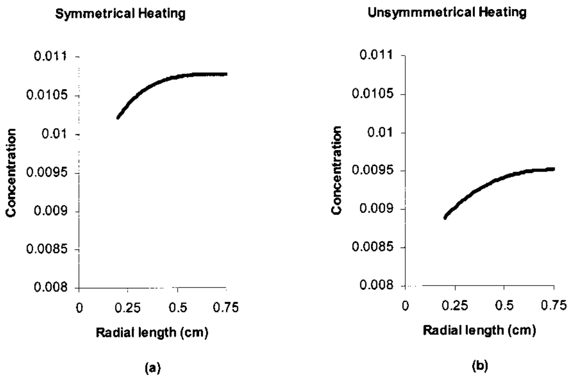

Fig. 4 Solute boundary conditions along the radial direction 0.15 cm above growth interface

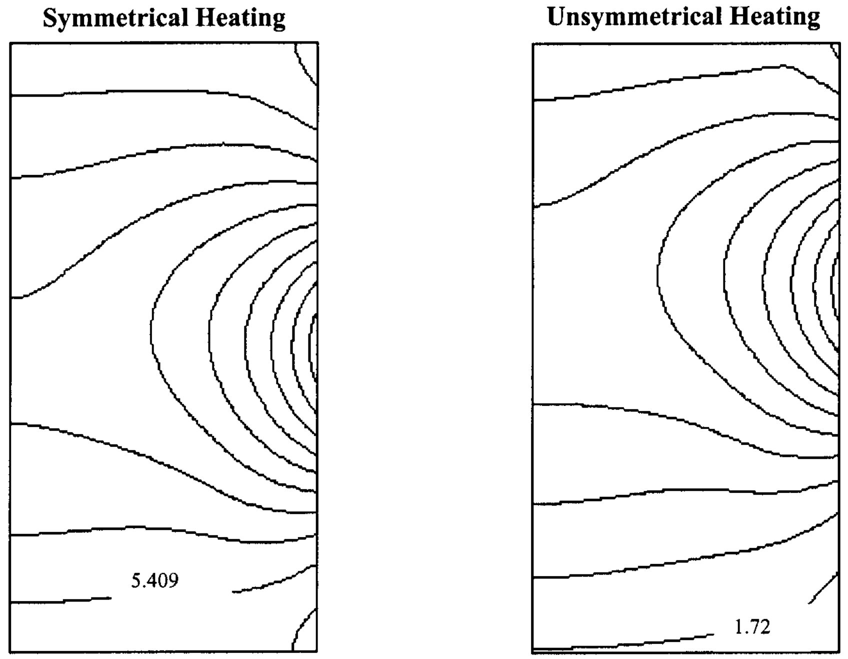

Symmetrical Heating

Unsymmetrical Heating

Left side is the axis of symmetry for a, b

(a) Δθ=2.888

(b) Δθ=2.967

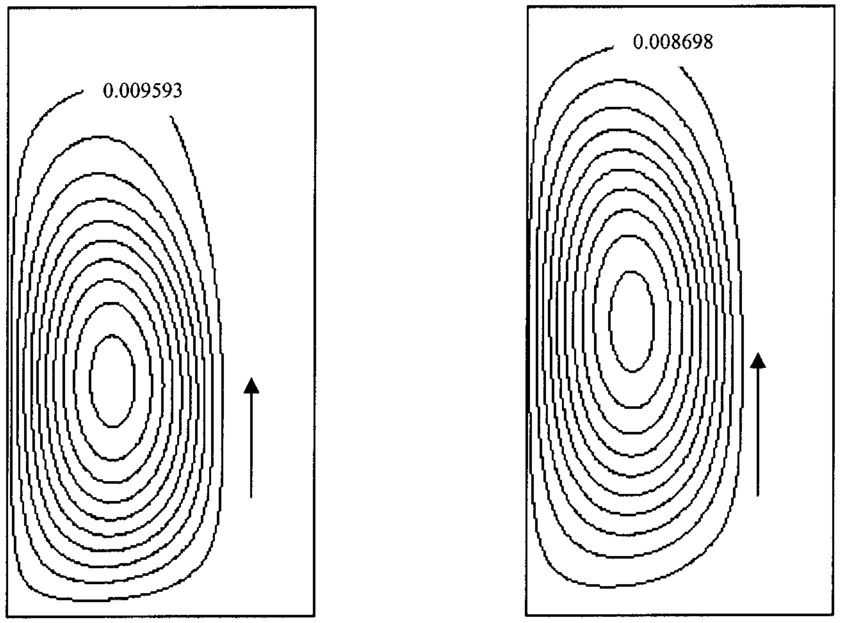

Left side is axis of symmetry for c, d

(c) Δψ=0.0203

(d) Δψ=0.0191

Fig. 5 Temperature and streamlines distribution in the melt

each of the test regions. Due to the effect of buoyancy, the fluid flow along the sides is forced up along the quartz wall where the temperature is higher and moves down along the central axis where the temperature is lower. The maximum flow velocities for the symmetric and asymmetric profiles were 0.788 cm/s and 0.723 cm/s respectively. The center of the flow cell for the symmetric heater profile is located slightly closer to the growth interface than the asymmetric case. This is owed to the fact that the peak temperature for the asymmetric profile is shifted close to the dissolving interface.

Figures 6(*a*) and 6(*b*) show the silicon concentration contours for each of the two heater profiles. A uniform concentration core appears in both figures, the symmetric case reveals a larger area of this constant concentration. Diffusion mass transfer is dominant in

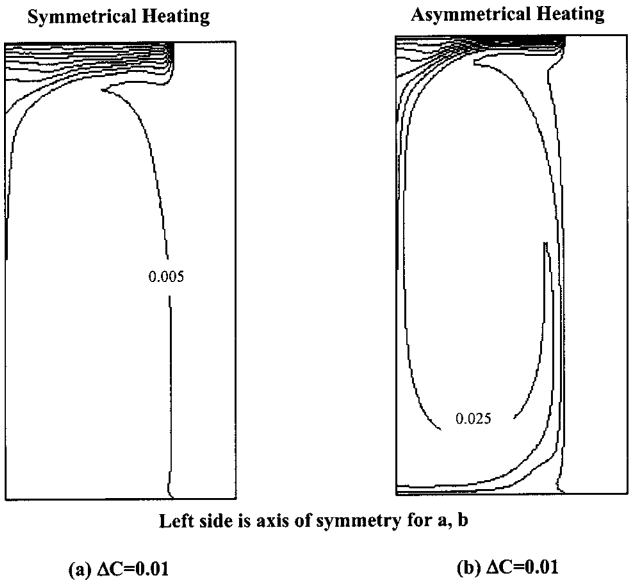

Fig. 6 Silicon concentration distribution in the melt

Table 1 Melt Properties of the solution and the crystal

Parameter	Symbol	Values
Physical Properties of $Si_{0.02}Ge_{0.98}$		
Density	ρ	5.246 g/cm^3
Thermal conductivity	κ	0.511 W/cm·k
Specific heat	c_p	0.0486 J/g·k
Viscosity	μ	7.35×10^{-3} g/cm·s
Kinematic viscosity	ν	1.4011×10^{-3} cm^2/s
Solutal expansion coefficient	β_C	0.005
Thermal expansion coefficient	β_T	1.2×10^{-4}
Solutal diffusivity	α_c	1.0×10^{-4} cm^2/s
Melt temperature	T_m	971°C
Solidification rate	V_g	1.16×10^{-5} mm/s
Physical Properties of $Si_{0.15}Ge_{0.85}$		
Density	ρ	54.924 g/cm^3
Kinematic viscosity	ν	2.7×10^{-3} cm^2/s
Solutal expansion coefficient	β_C	0.005
Thermal expansion coefficient	β_T	1.2×10^{-4}
Solutal diffusivity	α_c	2.6×10^{-4} cm^2/s
Thermal diffusivity	α_T	1.2×10^{-1} cm^2/s
Melt temperature	T_m	1100°C

the high concentration boundary layer near the dissolving interface as a result of a weak flow shown in the previous Figs. 5(*c*) and 5(*d*). Also it is seen that in the asymmetric case there is a thick concentration boundary layer as opposed to none in the symmetric case. This indicates a reduced interaction of fluid flow, leads to a more uniform growth.

In order to calculate the growth rate normal to the growth interface the condition of conservation of mass at the growth interface was used as in Ye et al. [8]:

$$R(c_s - c_l) = \alpha_c \frac{\partial c}{\partial n} \tag{6}$$

Where c_s and c_l are the silicon concentration in the solid and the liquid state across the growth interface. The growth rates calculated for the heater profiles were 0.06 mm/day for the symmetric case and 2.16 mm/day for the asymmetric case. This great difference in growth rate is primarily due to the large temperature difference of 1.57°C at the growth interface between the two cases. It was found that the ideal crystal growth conditions are: (i) having a minimum temperature close to that of the melting point of the solvent along the growth interface, while having a temperature above this melting point along the dissolving interface. This difference in temperature across the two interfaces promotes diffusion of silicon throughout the melt; (ii) having a linear horizontal temperature distribution along the growth interface, giving rise to a uniform concentration distribution and (iii) having almost no flow velocity over the growth interface as shown in Fig. 5(*d*).

The numerical results were compared qualitatively with the experimental results obtained by the co-author Prof. Labrie from Dalhousie University. The heating profile adopted in our numerical modeling, see Fig. 2(*b*), was measured experimentally using a traveling solvent furnace developed at Dalhousie. Using the same sample physical dimension as the one used in the experiment, we obtained some agreement in two important aspects. On the growth rate, we found that in our case and for non-uniform heating (i.e. Fig. 2(*b*) the growth rate was 2.16 mm/day whereas the experimental data showed approximately 4 mm/day. The difference is due to the fact that we are assuming steady state condition whereas on the experimental part, the data was analyzed after processing a full sample which took few days of processing time. The non-uniform heating condition is due to the deformation of the coil with time. Another important point is that the silicon variation on the growth interface was found experimentally to be approximately 2% whereas in our case we had a non uniform distribution of the silicon with a maximum value near 1% for the non-uniform heating condition. From those two observations, because we have shown that the heating condition can have a detrimental effect on the growth rate and silicon distribution, we are in the process of accurately repeating the measurement of the heating profile and repeating the calculation by taking into consideration any misalignment of the sample. Those results will be presented in a later publication.

Conclusion

A study of buoyancy convection in the $Si_{0.02}Ge_{0.98}$ solution has been conducted in order to study this effect on the growth rate of the SiGe crystal. This has been carried out by developing a thermo-solutal model, which accounts for the influence of both thermal and solute convections in the heat and mass transfer. This model also allows for the quasi-state condition of temperature, concentration and convective flow fields in the ampoule. Even though the fluid flow has a small effect on the heat transfer it plays an important role in the concentration distribution within the melt. These results indicate that with the asymmetric heater profile weak flow around the growth interface enables a uniform concentration boundary layer to form.

Acknowledgments

The authors acknowledge the financial support of the Canadian Space Agency (CSA), CRESTech and the Natural Science and Engineering Council (NSERC).

Nomenclature

C = non-dimensional concentration
c = solute concentration
c_o = reference solute concentration
c_p = specific heat at constant pressure (J/g·K)
Δc = change in concentration
g = gravity (cm/s^2)
L = reference length (cm)
P = non-dimensional Pressure
p = pressure (g/cm^3)
R = crystal growth rate (cm/s)
R = non-dimensional radial direction
r = radial direction (cm)
T = temperature (K)

ΔT = change in temperature (K)
U_z = non-dimensional axial velocity
u_z = axial velocity
U_r = non-dimensional radial velocity
u_r = radial velocity (cm/s)
u_o = reference velocity (cm/s)
Z = non-dimensional axial direction
z = axial direction (cm)

Greek Symbols

α_c = Solutal diffusivity of the species (cm^2/s)
β_c = solutal expansion coefficient
β_T = thermal expansion coefficient
θ = non-dimensionalized temperature
κ = thermal conductivity (W/cm·K)
μ = viscosity (g/cm·s)
ρ = density (g/cm^3)

Subscripts

m = melt
Ge = Germanium

References

[1] Matsumoto, Satoshi, Maekawa, Toru, and Takahashi, Katsumi, 1997, ''Numerical Analysis of InP Solution Growth by the Traveling Heater Method: Transient Response in the Case of no Heater Movement,'' Int. J. Heat Mass Transfer, **40**, pp. 3237–3245.

[2] Okano, Yasunori, Nishino, Shin-saku, Ohkubo, Shun-suke, and Dost, Sadik, 2002, ''Numerical Study of Transport Phenomena in the THM Growth of Compound Semiconductor Crystals,'' J. Cryst. Growth, **237–239**, pp. 1779–1784.

[3] Meric, R. A., Dost, S., Lent, B., and Redden, R. F., 1999, ''A Numerical Simulation Model for the Growth of $Ga_xIn_{1-x}Sb$ by the Traveling Heater Method,'' Applied Electromagnetics and Mechanics, **10**, pp. 505–525.

[4] Martinez-Tomas, M. C., Munoz-Sanjose, V., and Reig, C., 2002, ''A Numerical Study of Thermal Conditions in the THM Growth of HgTe,'' J. Cryst. Growth, **243**, pp. 463–475.

[5] Lent, B., Dost, S., Redden, R. F., and Liu, Y., 2002, ''Mathematical Simulation of the Traveling Heater Method Growth of Ternary Semiconductor Materials Under Suppressed Gravity Conditions,'' J. Cryst. Growth, **237–239**, pp. 1876–1880.

[6] Ghaddar, C. K., Lee, C. K., Motakef, S., and Gillies, D. C., 1999, ''Numerical Simulation of THM Growth of CdTe in Presence of Rotating Magnetic Fields (RMF),'' J. Cryst. Growth, **205**, pp. 97–111.

[7] Liu, Y. C., Okano, Y., and Dost, S., 2002, ''The Effect of Applied Magnetic Field on Flow Structuresin Liquid Phase Electroepitaxy—A Three-Dimensional Simulation Model,'' J. Cryst. Growth, **244**, pp. 12–26.

[8] Ye, X., Tabarrok, B., and Walsh, D., 1996, ''The Influence of Thermosolutal Convection on CdTe Growth by the Traveling Heater Method,'' J. Cryst. Growth, **169**, pp. 704–714.

[9] Reig, C., Gomez-Garcia, C. J., and Munoz, V., 2001, ''A New Approach to the Crystal Growth of $Hg_{1-x}Mn_xTe$ by the Cold Traveling Heater Method (CTHM),'' J. Cryst. Growth, **223**, pp. 357–362.

[10] Nakajima, Kazuo, Kusunoki, Toshihiro, Azuma, Yukinaga, Usami, Noritaka, Fujiwara, Kozo, Ujihara, Toru, Sazaki, Gen, and Shishido, Toetsu, 2002, ''Compositional Variation in Si-rich SiGe Single Crystals Grown by Multi-Component Zone Melting Using Si Seed and Source Crystals,'' J. Cryst. Growth, **240**, pp. 373–381.

[11] Azuma, Y., Usami, N., Ujihara, T., Fujiwara, K., Sazaki, G., Murakami, Y., and Nakajima, K., 2003, ''Growth of SiGe Bulk Crystals With Uniform Compostiosn by Utilizing Feedback Control System of the Crystal-Melt Interface Position for Precise Control of the Growth Temperature,'' J. Cryst. Growth, **250**, pp. 298–304.

[12] Dold, P., Barz, A., Recha, S., Pressl, K., Franz, M., and Benz, K. W., 1998, ''Growth and Characterization of $Ge_{1-x}Si_x$ ($x \leqslant 10$ at %) Single Crystals,'' J. Cryst. Growth, **192**, pp. 125–135.

[13] *FIDAP User Manual*, **8.01**, 2002.

Effects of Periodic Inflow Unsteadiness on the Time-Averaged Velocity Field and Pressure Recovery of a Diffusing Bend With Strong Curvature

M. I. Yaras

P. Orsi

Department of Mechanical and Aerospace
Engineering,
Carleton University,
Ottawa, Canada K1S 5B6

This study examines the effects of periodic inflow unsteadiness on the flow development through fishtail-shaped diffusers utilized on small gas-turbine engines. In this application, periodic unsteadiness is caused by a jet-wake type of flow discharging from each passage of the centrifugal compressor impeller. The study consists of detailed measurements in a large-scale fishtail diffuser rig with a geometry that is typical of those used in small gas-turbine engines. Measurements of the transient velocity field have been performed at five cross-sectional planes throughout the diffuser using a miniature hot-wire probe with four wires. These measurements involve frequencies of inflow unsteadiness corresponding to design as well as off-design operating conditions. Results indicate significant effects of inflow unsteadiness at the low end of the tested frequencies on the time-averaged streamwise and cross-flow velocity fields in the diffuser. This is shown to translate into a notable impact on the pressure recovery. In addition to providing insight into the physics of this flow, the experimental results presented here constitute a detailed and accurate data set that can be used to validate computational-fluid-dynamics algorithms for this type of flow. [DOI: 10.1115/1.1667887]

Introduction

Diffusing bends of strong curvature are used in a diverse range of industrial applications. For example, such flow paths are common on small gas-turbine engines utilizing a centrifugal impeller as the last compressor stage. In this application, diffusing bends transfer the high-kinetic-energy flow at the impeller exit through a radial-to-axial turn into the combustion chamber [1–3]. Another example of a diffusing flow path with streamwise curvature is a draft tube, which is utilized for pressure recovery between the impeller discharge and the tailrace in hydraulic turbine installations. It is generally desirable for the diffusion and turning of the flow to take place over the shortest possible length to avoid penalties in size and weight. At the same time, it is important to minimize frictional losses and maintain minimal flow distortion at the diffuser exit, so that the static pressure recovery is maximized. Flow distortion at discharge from the diffusing bend may also be critical with respect to the performance of components installed downstream of the bend.

Despite the difficulty in establishing an optimum trade-off between the conflicting requirements of efficiency, compactness, and discharge conditions with minimal flow distortion, few studies have been conducted on the fundamental physics of the flow evolving in such geometries. The flow through straight diffusers is well understood and detailed performance charts for such configurations have been established [4]. Likewise, the development of streamwise vorticity, cross-stream redistribution of the flow and generation of losses have been investigated fairly extensively for developed as well as developing flows in constant-area bends [5–8]. In contrast, relatively few studies have considered the case of simultaneous diffusion and turning of flows [9–13]. Specifically, none of these studies considered strong curvature or substantial streamwise variation in the cross-sectional geometric aspect ratio, both of which are characteristics of the diffusing bend examined in the present work. The work of Blair and Russo [3] is one study that investigated a similar geometry. In that study, however, the extent of the measurements did not allow for a detailed account of the flow development. In response, an experimental research project was initiated, the first phase of which consisted of detailed measurements providing a clear account of the flow evolution through a fishtail-shaped diffusing bend, the overall total pressure loss, static-pressure recovery and flow distortion levels for a range of spatial distortions of the inlet velocity field [14,15].

Fishtail diffusers on gas-turbine engines experience compressible and periodic-unsteady inflow conditions with highly nonuniform spatial distributions of velocity. The first phase of the research program [14,15] focused on the effects of inlet mean-flow spatial nonuniformities, avoiding the complexities associated with compressibility and periodic unsteadiness. Studies exist in the published literature that have examined the effects of periodic inflow unsteadiness on the performance of vaned and vaneless diffusers [16–19]. However, such studies are not yet available for diffusing bends with diffusion rates, turning rates and cross-sectional shapes that are typical of those of fishtail diffusers. The results presented herein therefore focus on the effects of periodic inflow unsteadiness on the flow development in fishtail diffusers.

While the study provides insight into the performance of fishtail diffusers under unsteady inflow conditions for gas turbine applications, in a broader sense the presented results shed considerable light on the fundamental behavior of the flow through a diffusing bend of strong curvature with a periodic-unsteady inlet flow. In gas turbine installations, and in many other applications utilizing diffusing bends, there is a general thrust towards increased use of computational-fluid-dynamics algorithms in the optimization of the flow path. Flows with substantial streamline curvature and secondary flows developing under the influence of cross-stream pressure gradients continue to defy precise numerical simulation, primarily due to the limitations of current turbulence models. In

---

Contributed by the Fluids Engineering Division for publication in the JOURNAL OF FLUIDS ENGINEERING. Manuscript received by the Fluids Engineering Division October 30, 2002; revised manuscript received October 2, 2003. Associate Editor: A. K. Prasad.

addition to providing a basis for understanding the physics of the flow in fishtail diffusers under periodic unsteady inflow conditions, by virtue of its detail and accuracy, the present set of measurements forms a good test case to guide further development of mathematical models.

Due to space constraints, the paper focuses on the results pertaining to the time-averaged response of the diffuser flow to periodic inflow unsteadiness. The temporal evolution of the velocity field will be the subject of a follow-up paper.

Experimental Apparatus

Test Section. The test section is shown schematically in Fig. 1. Longitudinally, the diffuser consists of four sections, with each section further partitioned into symmetric upper and lower halves. The first section provides a conical flow path with an inlet diameter of 193.7 mm and an included angle of 6.15 deg. In the subsequent three sections, the flow path turns by 90 deg along a centerline with a radius that is 4.36 times the inlet diameter of the diffuser. In these sections, the cross-section of the flow path becomes increasingly more oblong with downstream distance, while the cross-sectional area continues to increase linearly until it reaches a size that is 3.42 times the inlet area of the diffuser. MB1000, a resin based material, was used in the construction of the diffuser. Beyond the 90 deg diffusing turn, the cross section of the flow path remains unchanged through the tail duct, which consists of two symmetric halves constructed of galvanized sheet metal contained in an aluminum frame. Pertinent geometric information on the diffuser flow path is summarized in Fig. 2. This geometry is a large-scale version of typical fishtail diffuser flow paths utilized between the last centrifugal-compressor stage and the combustion chamber on small gas turbine engines, with the inlet of the test section corresponding to the throat of these diffusers. The large scale of the test section has allowed fine-resolution measurements of the flow.

Wind Tunnel. An open-circuit wind tunnel is used as the wind source for the diffuser. A variable-speed centrifugal fan draws in ambient air and delivers it through a honeycomb into a circular settling chamber containing three screens. At the exit of the settling chamber the air passes through two contractions of 9:1 and 4.4:1 area ratios. At the exit of the second contraction, the flow enters a PVC pipe that leads to the inlet of the fishtail-diffuser test section through an unsteady-flow generator.

Unsteady Flow Generator. The unsteady-flow generator (UFG), used to generate wake-type disturbances that sweep periodically across the inlet of the diffuser, is shown schematically in Fig. 3. The device is built around a wheel consisting of a single-groove sheave of 46.4 cm diameter. The wheel is mounted on a support frame that also carries the electric motor used to drive the UFG. Twenty steel bars of 22.9 cm length and 0.635 cm diameter are mounted on the wheel evenly-spaced and pointing radially. 0.875 mm-thick perforated plates are mounted on these support bars in an alternating pattern as shown in Fig. 3. Each perforated plate is shaped to completely fill the space defined by a pair of support bars. The wheel with its perforated plates is placed 2.5 cm downstream of the exit of the second wind-tunnel contraction noted in the preceding section. The length of the steel bars, hence the radial extent of the perforated plates, is chosen to be about 20% greater than the diameter of the air stream exiting the con-

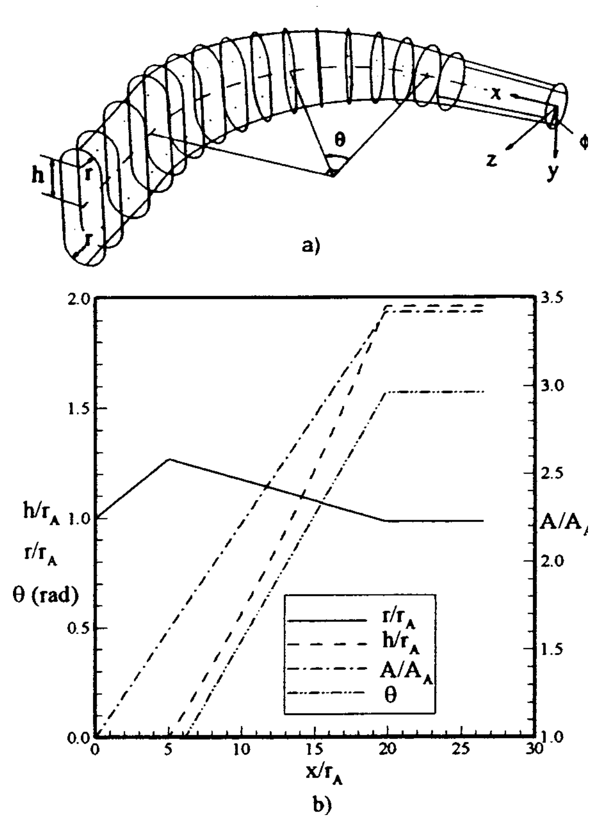

Fig. 2 Geometry of the diffuser flow path

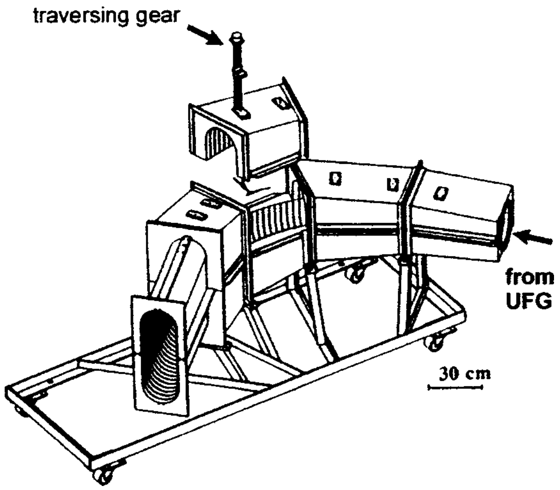

Fig. 1 Fishtail-shaped diffuser test section

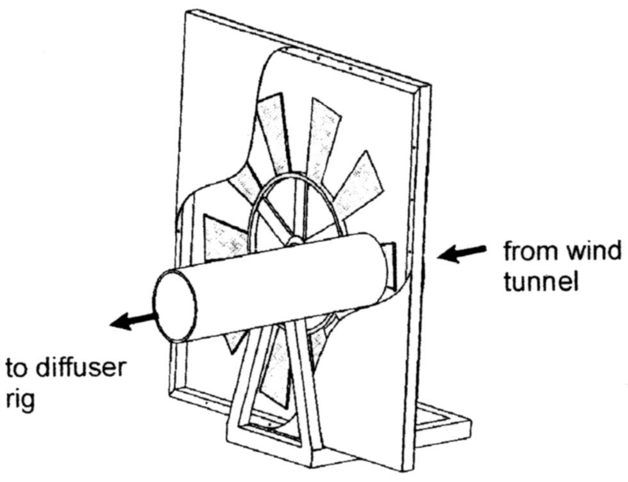

Fig. 3 Unsteady-flow generator

traction to ensure that the complete cross-section of flow is subjected to periodic interruption. The circumferential extent of each perforated plate is set by the spacing of the support bars, which in turn was chosen in relation to the inlet diameter of the diffuser such that approximately half of the inlet plane is blocked by the perforated plates at all times. This is of similar proportion as the width of the wake region at the discharge of each centrifugal impeller passage relative to the inlet diameter of the fishtail diffuser on a typical gas turbine installation.

As the flow discharging from the contraction passes through the spinning patches of perforated plates, the fluid particles are expected to gain some momentum in the direction of rotation of the wheel due to the aerodynamic drag of these patches and their support bars. Upon passing through the unsteady flow generator, to ensure that the complete jet flow is recaptured by the PVC pipe that leads to the diffuser inlet, a bellmouth-shaped entrance of 5.1 cm lip-radius is used on the pipe, which is placed 2.5 cm downstream of the UFG wheel. The length of the pipe between this bellmouth and the diffuser inlet plane is 101.6 cm, which was determined together with the porosity of the perforated plates (51% open area, consisting of staggered holes of 4.76 mm diameter) by trial-and-error, such that the axial-velocity fluctuations at the diffuser inlet plane were about ±25% with relatively small fluctuations in the flow direction. The rationale for this choice will be provided in the section describing the diffuser inflow conditions.

Since the diffuser test section discharges into the laboratory environment, the static pressure at the diffuser entrance is below ambient pressure. Thus, it is necessary to seal the wheel of the UFG from the laboratory environment to prevent ambient air from leaking into the flow path. For this purpose, the complete wheel assembly is placed in a $104\ \mathrm{cm}\times 112\ \mathrm{cm}$ frame made of stock U-shaped steel channels, and both sides of this frame are covered with Garlock™ sheets. In Fig. 3, this sheet is shown open on one side to expose the wheel and the perforated plates for viewing purposes. At the points where the shaft of the wheel passes through these sheets, small bearings are used to prevent leakage.

The wheel assembly is driven by a 3 hp ac motor through a timing belt. The speed of the motor is controlled with a Siemens MicroMaster-Vector variable-frequency drive. Four UFG rotational speeds of 2, 4, 6 and 8 revolutions per second were considered in the experiments. These speeds, together with the aforementioned settings of the perforated-plate patches on the wheel, result in periodic interruption of the diffuser inflow at frequencies of 20, 40, 60, and 80 Hz. The rationale for these frequencies will be provided in the section describing the diffuser inflow conditions. The direction of rotation of the UFG was chosen such that the perforated patches move in the positive y-axis direction (Fig. 2*a*) as they pass through the air stream. The choice of this rotational direction is not critical on the present test section since the geometry is symmetric with respect to the z axis.

Instrumentation. The primary sensor used to measure the three-dimensional velocity and turbulence field throughout the diffuser is a miniature 4-wire probe, controlled by a 4-channel constant-temperature anemometer, both of which were developed in-house. The four tungsten hot-wire sensors on the probe (each of 1.0 mm length and 5-micron diameter) are oriented at about 45 deg relative to the probe axis and are circumferentially positioned at 90 deg from each other to form the shape of a pyramid. The four sensors collectively form a measuring volume of about 2 mm diameter. This volume is quite small compared to most commercial 3- or 4-wire probes, and thus allows measurement of the flow in the diffuser with high resolution. The choice of four sensors instead of three was made to increase the range of flow misalignments for which the flow direction can be determined uniquely. The calibration of the probe is based on the method of directional sensitivity functions, as described by Dobbeling et al. [16]. The directional sensitivity functions are determined through calibration of the probe on a probe-calibration apparatus with motorized motion in pitch and yaw. The flow direction is varied in 5 deg increments up to 45 deg of misalignment relative to the probe axis. Several sets of values are obtained for these functions over a flow velocity range varying from 5 m/s to 25 m/s, to cover the approximate velocity range anticipated in the diffuser. The Reynolds number sensitivity of the directional sensitivity functions was found to be small within this range. The angular calibration was repeated regularly throughout the diffuser experiments to monitor for any possible changes in the sensor geometry that may occur accidentally during handling of the probe. Although the angular calibration of the probe should not change unless the sensor geometry is modified, the velocity calibration of each of the four sensors is prone to relatively rapid changes, primarily due to drift in the conditioning (analog signal amplification and offset) circuitry of the constant-temperature anemometer. For this reason, the velocity calibration, performed with the probe axis aligned to the flow direction in the probe calibration apparatus, was repeated frequently throughout the experiments. Based on the combined uncertainties of the angular and velocity calibrations of the probe (slight changes in the calibration curves between probe recalibrations; interpolation errors associated with the velocity calibration curves and directional-sensitivity calibration surfaces) the velocity magnitude and direction measured with this probe are conservatively estimated to be within 2% and ±1.5 deg of the actual values. For flow misalignments greater than about 30 deg relative to the probe axis, the uncertainty in the flow direction is closer to ±2.5 deg.

During the experiments, the effective cooling velocities of the four wire sensors were non-dimensionalized by the flow centerline velocity in Plane A, one-diameter upstream of the diffuser inlet. Prior to the measurements in the diffuser, this reference velocity, measured with the hot-wire probe, was correlated against the difference between two pressures, one measured on the first contraction of the tunnel, which is close in magnitude to the local stagnation pressure, and the other measured through a static tap on the wall of the PVC pipe in Plane A. This correlation was repeated for each of the rotational speeds of the unsteady-flow generator, and is based on the mean value of the reference velocity determined by time averaging over a duration that is long compared to the period of flow fluctuations caused by the UFG. The aforementioned pressure difference is measured with an MKS differential pressure transducer of ±10 torr range. In order to correct the hot-wire signals for temperature variations as per the procedure described by Bearman [17] (typically a few degrees Celsius over the course of each test run), the temperature of the flow in the diffuser is measured with a thermocouple.

Data Acquisition. The signals from the four wires of the probe, the reference pressure difference and the flow temperature are simultaneously sampled with an Analog Devices RTI-834H data acquisition card interfaced with a sample-and-hold amplifier. The system utilizes a 12-bit A/D converter. Although transient measurements were not intended for the reference temperature and reference pressure, these quantities are sampled together with the hot-wire signals at the same rate to simplify the structure of the data records. The hot-wire signals are low-pass analog filtered with a cut-off frequency that is set to half of the sampling rate.

The data acquisition system is synchronized with the UFG through a slotted optical switch activated once per revolution of the wheel assembly of the UFG, which triggers the sampling cycle on the data acquisition system. Each sampling cycle consists of 19 samples collected at such a rate to cover one full period of flow fluctuation. The data sampling rate was adjusted for each UFG rotational speed to realize this. At each measurement position of the 4-wire probe, 300 cycles of measurements are collected, which has been verified to be adequate for statistical convergence of the mean velocity data.

Measurement Locations and Traverse System. The first measurement plane (Plane A) is located one diameter upstream of

Table 1 Locations of measurement planes

	x/r_A	x/L	θ (deg)
Plane A	-2.0	-0.076	0.0
Plane B	5.0	0.190	0.0
Plane C	10.95	0.416	31.7
Plane D	15.76	0.599	63.5
Plane E	19.79	0.752	90.0

the diffuser inlet, and is far enough upstream to avoid any elliptic influence of the diffusing flow field. Four other cross-sectional measurement planes are distributed throughout the fishtail diffuser. The locations of these measurement planes are listed in Table 1. All measurement planes are traversed with a motorized probe traverse system. Plane A is traversed in the radial direction with the circumferential position of the traverse manually adjusted to 12 evenly spaced locations. The remaining four planes are traversed in the *y* direction as shown in Fig. 1. After each traverse in the *y* direction, the repositioning of the probe in the *z* direction is done manually with the aid of an alignment/positioning device, designed for use on this test rig [18]. This device also provides for referencing the probe position in the *y* direction and establishing its orientation relative to the curvilinear reference axes shown in Fig. 2*a*. The probe position and its orientation relative to the reference axes are estimated to be accurate to within ± 0.20 mm and ±0.1 deg, respectively.

In Plane A, the flow was measured at about 20 locations from the centreline to the pipe wall over each of the 12 radial traverses. The number of data points in the remaining planes varied from about 700 points in Plane B to about 1100 points in Plane E, providing very detailed resolution of the flow.

Experimental Results and Discussion

Diffuser Inlet Flow. All measurements were performed at a Reynolds number of $3.0 \pm 0.1 \times 10^5$ based on the diameter and the centerline velocity in Plane A. This high value of the flow Reynolds number, combined with the presence of the unsteady-flow generator in the inflow path, results in a fully turbulent flow throughout the diffuser. Consequently, the measurement results presented herein are not expected to be sensitive to moderate deviations from the tested Reynolds number. The inflow Mach number was less than 0.1. Even for high-subsonic inflow Mach numbers, the flow would decelerate to Mach numbers below 0.4 before entering the turn. Hence, the three-dimensional flow development in the diffusing bend is not expected to be very sensitive to inflow Mach number variations in the subsonic range.

The rotational speed of the UFG, hence the period of flow fluctuations at the diffuser inlet, was determined such that the ratio of this period to the time a fluid particle would require to travel through the diffuser (accounting for only the streamwise variation of flow velocity) is similar to that observed in a gas turbine installation at design-point operating conditions. This approach yielded a rotational speed of 10 revs/s for the UFG. A slightly lower UFG speed of 8 revs/s was chosen to avoid vibrations on the UFG rig. Additionally, speeds of 6, 4 and 2 revs/s were included in the test matrix to investigate off-design operating conditions.

The temporal and spatial variations of the axial and secondary velocity fields in Plane A are presented in Fig. 4 for all four UFG speeds. The percentage number given at the bottom of each plot in the series indicates the fraction of a full period that has elapsed up to the instant corresponding to the displayed velocity field. Only every other measured time plane is shown for brevity. The axial velocity, given as a flood plot, is normalized by its spatial and temporal average over this measurement plane. This normalization velocity is also shown as a reference vector at the beginning of each series to provide an indication of the strength of the secondary motion in the crossflow (*y-z*) plane.

For all four UFG speeds, the dominant feature in the temporal variation of the axial velocity field is an alternating pattern of about ±25% magnitude between the upper and lower halves of the cross-section. This pattern is more evident for the two lower UFG speeds. These levels of axial-velocity variations are somewhat larger than the ±14% measured on a centrifugal-compressor test rig [19], although those measurements were performed at the throat of vaned diffusers. Generally one would expect a fair range of variations in the amplitude of these fluctuations based on the detailed designs of the centrifugal impeller, the flow path ahead of the diffuser throat sections, and the extent of vaneless space between the impeller and the diffusers. Thus, the present levels of velocity fluctuations are deemed compatible with those that prevail in a turbomachinery setting. The crossflow velocity components in Fig. 4 are noted to be fairly significant at certain instances of the fluctuation period, although a consistent secondary motion, such as a swirl pattern that prevails over a large fraction of the period, is not evident. The range of magnitudes of the secondary velocities is similar for all UFG speeds. The resultant peak temporal variation in the flow direction is about 15 deg, which is very similar to those measured in a centrifugal-compressor rig [19].

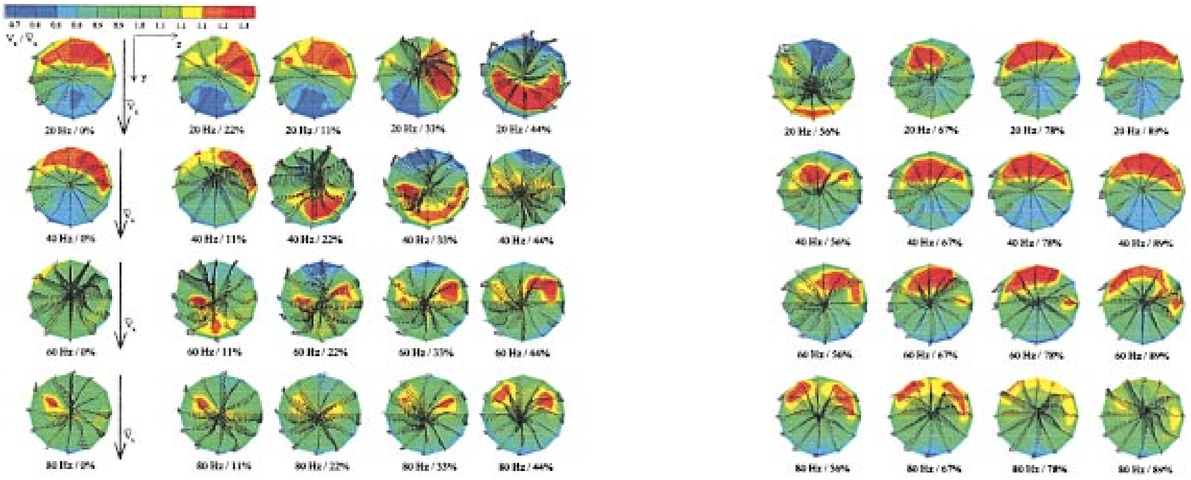

Fig. 4 Ensemble-averaged velocity distribution in Plane A (0 to 89% of period) (uncertainties: ±2% for the velocity magnitude and ±1.5 deg for the flow direction)

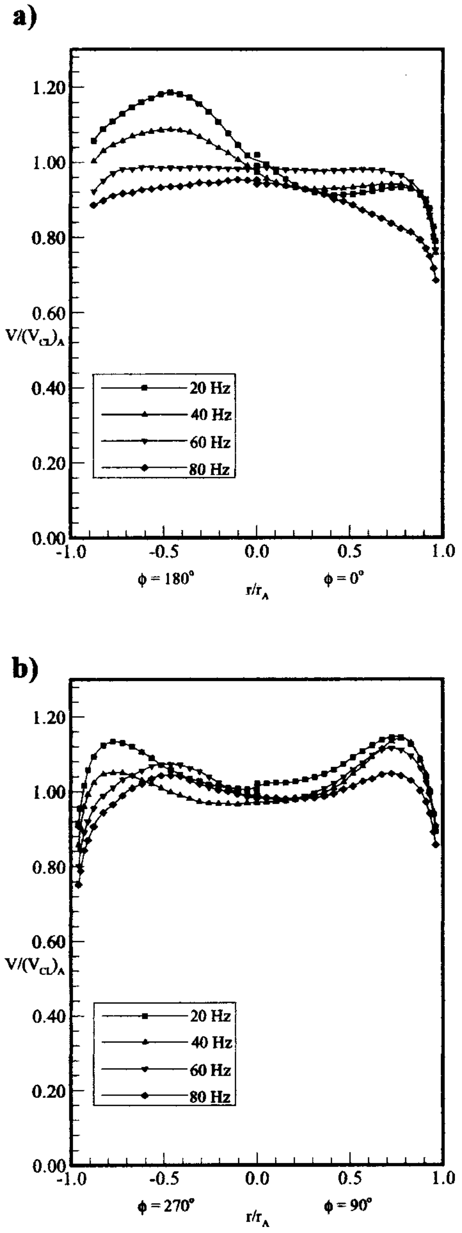

Fig. 5 Time-averaged velocity distributions along the *a*) y axis ($z=0$), *b*) z axis ($y=0$) in Plane A. (Uncertainty in $V/V_{CL_A}=\pm 2\%$.)

Figure 5*a* shows the time-averaged axial velocity distribution in Plane A along the y axis (direction of motion of the UFG) for all four speeds of the UFG. These distributions provide an indication of the extent of symmetry in the alternating pattern of axial velocity observed in the ensemble-averaged results of Fig. 4. It is noted that for the two lower speeds of the UFG, the axial velocity in the upper portion of the measurement plane is biased towards higher values relative to the centerline velocity while the lower side time averages close to the centerline value. For 80 Hz this trend reverses, with the lower portion of the measurement plane being biased towards relatively low time-averaged axial velocities in relation to the centerline value. The most uniform case appears to be associated with 60 Hz. The distribution of the time-averaged axial velocity along the z axis, shown in Fig. 5*b*, is fairly symmetric for all UFG speeds, with a somewhat lower momentum in the core region.

It must be noted that the periodic-unsteady inflow conditions generated on the present fishtail-diffuser test rig are only approximations to what one would expect at the inflow plane of the fishtail diffusers installed downstream of the centrifugal-compressor impeller on gas-turbine engines. In addition to the specifics of the jet-wake flow structure emerging from each passage of the impeller, the details of the flow path between the impeller exit plane and the throats of the diffusers are expected to have substantial influence on the velocity field prevailing at the throat. On the present diffuser test rig, the inlet plane is intended to correspond to the diffuser throat in gas turbine installations. In a gas-turbine installation, between the impeller exit and the throat of the fishtail diffusers, the flow is divided amongst the diffusers by semi-diffuser sections formed through the intersection of the diffuser paths, oriented at quite large angles relative to radial direction, with a circumferential plane representing the outlet of the vaneless space between the impeller and the diffusers. Hub-to-shroud redistribution of the flow and flow separation at the lip of these semi-diffuser sections, with the latter being particularly significant at off-design operation, are flow features that are expected to greatly affect the resultant flow field at the diffuser throat. It is not possible to precisely reproduce these effects on a test rig such as the one used in the present effort, nor would this necessarily be a desirable approach to take. An ideal fishtail diffuser design ought to be one that is not overly sensitive to the fine details of the temporal and spatial flow variations at the inflow plane.

The present work is thus undertaken primarily to document the extent of sensitivity of a typical fishtail diffuser to temporal inflow variations, as a followup of the earlier phase that focussed on the effects of spatial velocity distortions of the inlet flow. Furthermore, as was noted in the Introduction section, the detail and accuracy of the present data set makes it suitable for guiding the development of CFD algorithms tailored for such flows. Such algorithms can then be readily used to predict the details of fishtail diffuser flows with inflow conditions that account for the aforementioned upstream flow history in gas-turbine installations more precisely.

Diffuser Flow Field. The time-averaged 3-D velocity field, obtained from the four-sensor hot-wire probe measurements, and the corresponding streamwise vorticity distributions, are shown in Figs. 6 and 7, respectively. Although study of the results in an ensemble-averaged form should provide considerably more detail on the evolution of the flow, it was decided that prior to analyzing the data in this format, it would be useful to examine the results in a time-averaged form to establish a general sense for the extent of change in the flow pattern due to periodic inflow unsteadiness, and the sensitivity of any such changes to the frequency and amplitude of this unsteadiness. The format of the velocity-field plots given in Fig. 6 is the same as for the inflow velocity plots of Fig. 4. The streamwise vorticity calculated on the basis of the velocity field is nondimensionalized by the spatially and temporally averaged axial velocity in each of the measurement planes and by the radius of the diffuser inlet. The choice of this velocity scale over the inflow centerline velocity for normalizing the vorticity differs from the approach in [15], and makes the comparison of the vorticity magnitudes in different measurement planes somewhat more difficult. However, this choice enables effective comparison of the streamwise vortices in the upper and lower halves of the flow path within each measurement plane, and allows observation of the effects of UFG speed variations. For the velocity field, the same scale is used for the axial velocity contours of all five measurement planes. Although this choice prevents the flow distortions within Plane A (as was evident in Fig. 5) from being visible, it provides a visual guide for the development of axial distortion as the flow makes its way through the diffuser.

For all four speeds of the UFG, the dominant flow feature in the diffuser is noted to be a well-known pair of counter-rotating vortices. The initial development of streamwise vorticity in a bend is

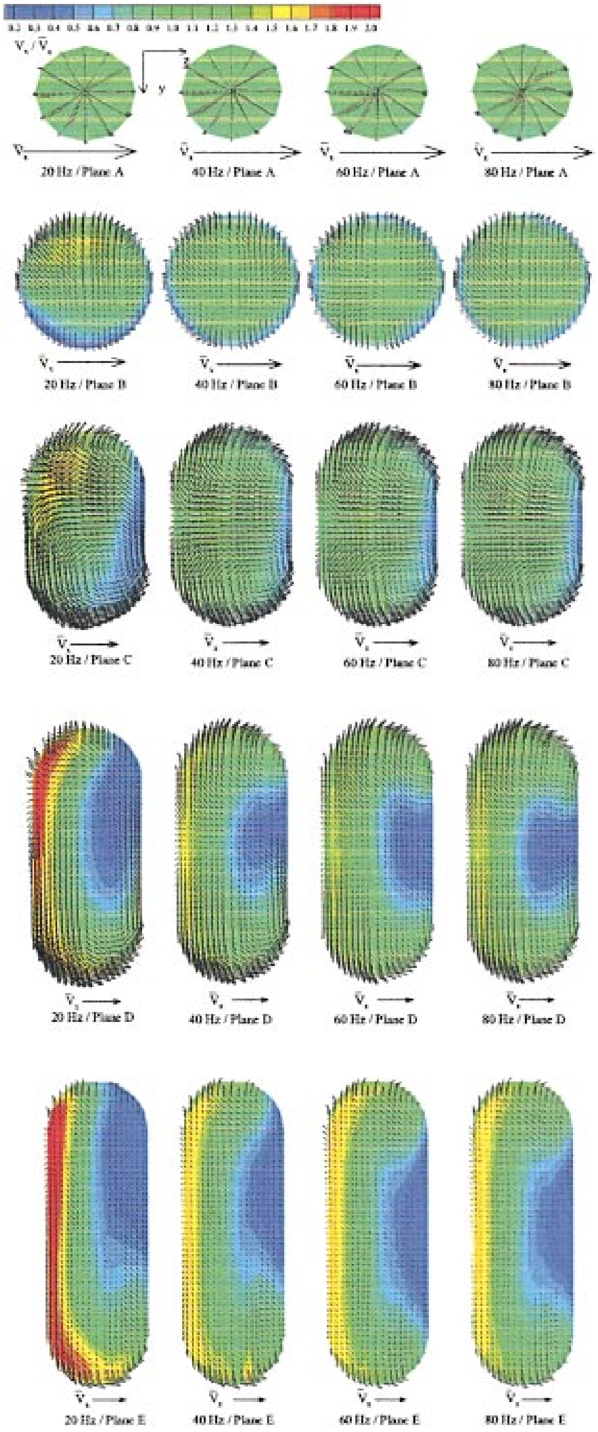

Fig. 6 Time-averaged velocity distribution. (**Uncertainties: ±2% for the velocity magnitude and ±1.5 deg for the flow direction.**)

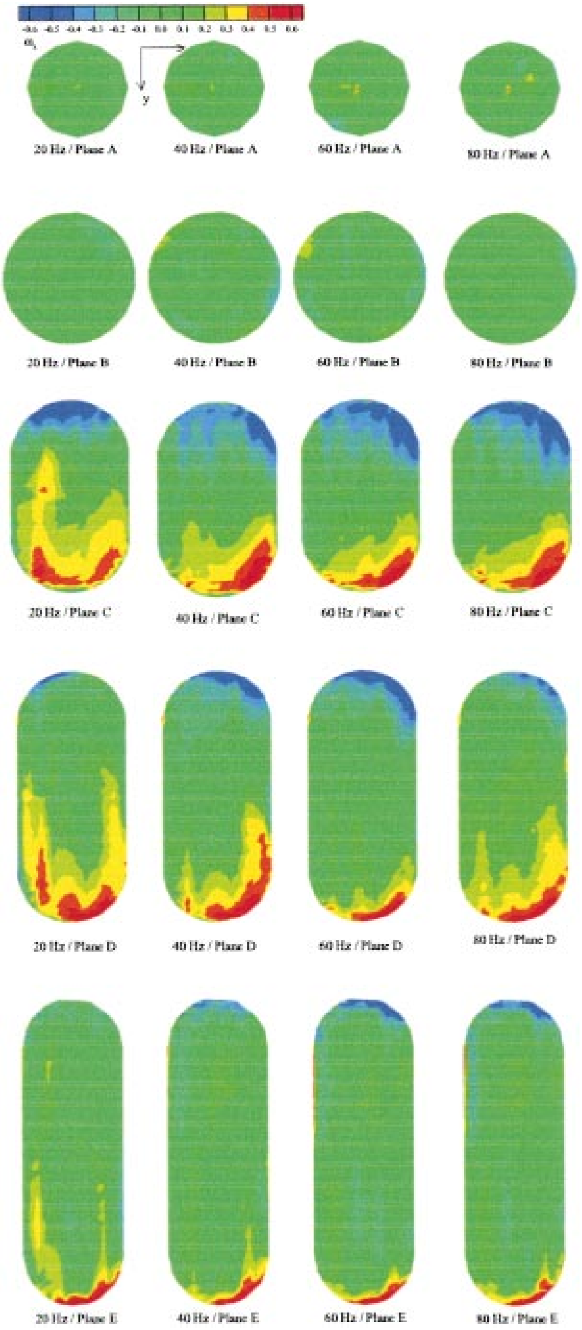

Fig. 7 Time-averaged streamwise vorticity distribution. (**Uncertainty in streamwise vorticity=±0.05.**)

due to the vorticity within the inlet boundary layer developing a streamwise component [15]. In the present diffusing bend, the segments of the circumferential vorticity lines lying in the plane of the bend are expected to rotate during the initial portion of the bend, resulting in the development of streamwise vorticity in the form of a vortex pair. Through inviscid flow theory, the magnitude of this streamwise vorticity can be related to the flow turning and the amount of vorticity contained within the inlet boundary layer in the plane of the bend [20,21]. Considerable redistribution of the streamwise flow between the outer and inner walls of the bend is evident under the influence of the cross-flows induced by this vortex pair. The net radial mass flux associated with the movement of high-momentum fluid towards the outer wall is noted to produce a region of fluid with very small streamwise momentum along the inner wall.

As the speed of the UFG is reduced to the 40 and 20 Hz levels, the streamwise vortex in the upper half is weakened considerably while the one in the lower half becomes stronger. This is clearly visible through inspection of both the cross-stream velocity vectors in Fig. 6 and the vorticity contours in Fig. 7. Distribution of the time-averaged axial velocity along the y axis in Plane B, shown in Fig. 8, provides an explanation for this trend. In this figure, the velocity distributions for 60 and 80 Hz are noted to be

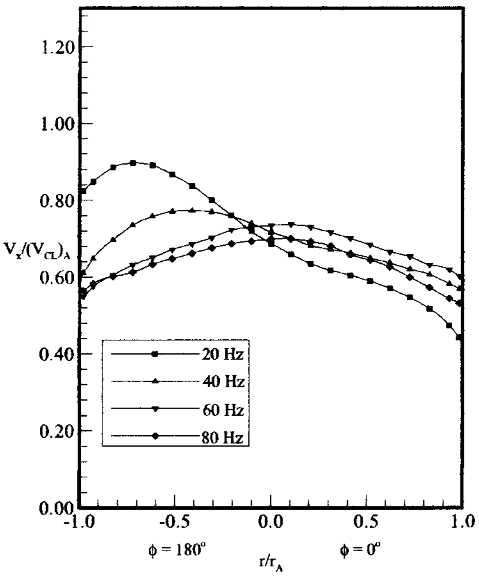

Fig. 8 Time-averaged axial velocity distribution along the y axis ($z=0$) in Plane B. (Uncertainty in $V/V_{CL_A}=\pm 2\%$.)

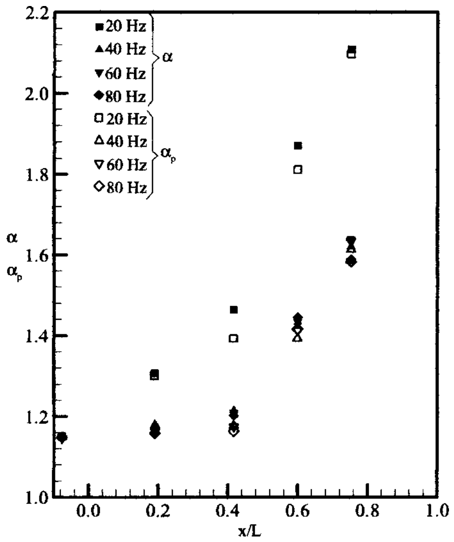

Fig. 9 Streamwise variations of flow distortion. (Uncertainty in α and $\alpha_p=\pm 0.05$.)

symmetric with respect to the z axis. This means that the z component of vorticity contained in the upper and lower halves of the flow path, which are of opposite sense of rotation, are of comparable magnitude. As per the discussion in the preceding paragraph, this is expected to yield a pair of streamwise vortices of similar strength developing inside the bend. For the 40 Hz and 20 Hz cases, the asymmetric velocity distribution in Fig. 8 implies that the z-vorticity in the lower half of the flow path dominates the one in the upper half, with the imbalance being particularly large for the 20 Hz case. Consequently, the streamwise vortex developing inside the bend in the lower half is expected to be stronger as per the measured results. Case V of the preceding phase of this research project [14] involved an inflow axial velocity distortion where the boundary layer was notably thicker near the $\phi=180$ deg position in Plane A. However, the resultant asymmetry in the velocity field with respect to the z axis measured in Plane E was negligible compared to the present results in the 20 Hz and 40 Hz cases. The reason behind this appears to be the relatively large cross-stream motion (in a time-averaged sense) between planes A and B of the unsteady cases, which is visible in Fig. 6. This cross-stream redistribution of mass tends to amplify the difference in the axial velocity distributions between the lower and upper halves of the flow path before the flow enters the bend.

As secondary flows, associated with the aforementioned vortex pair, develop inside the bend, the low momentum fluid along the perimeter is quickly swept towards the inner wall. For the 20 Hz and 40 Hz cases, the imbalance between the induced velocity fields of the upper and lower vortices is noted to result in a shift of the low-momentum fluid by the inner wall towards the upper part of the flow path, with the extent of shift being consistent with the magnitude of the difference in the strength of the vortices. The same imbalance is also responsible for accumulating relatively high momentum fluid in the outer part of the upper half of the cross-sectional plane. By the time Plane D is reached, the low momentum fluid has been collected in the upper portion of the inner wall, which in turn results in relative acceleration of the fluid passing through the outer part of the upper half. Between Planes D and E, the high momentum fluid is distributed along the outer wall while it is amplified in response to the increase in the extent of the low momentum region by the inner wall.

The possibility of such asymmetries developing in this diffusing bend, and the resultant variations in the axial flow distortion, may have significant impact on both the performance of the diffuser in providing pressure recovery and in matching the diffuser outflow conditions with devices installed further downstream. Flow distortion and frictional losses are the two mechanisms that may cause deviation from ideal pressure recovery in a diffuser [15]:

$$\tilde{C}_P=1-\frac{\alpha_E}{\alpha_A}\left(\frac{\overline{V}_{x_E}}{\overline{V}_{x_A}}\right)^2+(\tilde{C}_{P0_A}-\tilde{C}_{P0_E}) \tag{1}$$

In this expression, the kinetic energy factor defined as:

$$\alpha=\frac{1}{A\overline{V}_x^3}\int V^2V_x dA \tag{2}$$

is an indicator of the excess kinetic energy of a flow compared to a unidirectional plug profile of the same flow rate. Comparing α to the primary-flow kinetic energy factor, α_p, defined as:

$$\alpha_p=\frac{1}{A\overline{V}_x^3}\int V_x^3 dA \tag{3}$$

is useful for flows with 3-D flow patterns, as this provides an indication of the relative contributions of axial flow nonuniformity and crossflow motion to the resultant value of α. It is important to point out that, in a general sense, Eq. (1) is not applicable to the case of unsteady flow in a diffuser. However, as was noted earlier, in the present tests half of the inlet flow path is blocked by the perforated plates of the unsteady flow generator at all times. This choice, driven by the objective of creating wake-type disturbances of spatial extent similar to those encountered in gas-turbine installations, resulted in the total mass-flow rate at each of the measurement planes to vary by less than two percent over each period of temporal oscillation in the velocity field. Under these specific conditions of transient flow in the diffuser, it can be easily shown that Eq. (1) remains applicable, with the kinetic energy factors and mass-averaged pressures appearing in this equation being the time-averaged values.

Streamwise variations of the kinetic energy factor, α, and the primary-flow kinetic energy factor, α_p, for different speeds of the UFG are given in Fig. 9. Although some asymmetry of the flow was also noticed in the 40 Hz and 60 Hz cases (Figs. 6 and 7), this is noted to have a very small effect on the extent of flow distortion since the α and α_p values of these cases compare well with the 80 Hz case throughout the diffuser. On the other hand, the kinetic energy factors for 20 Hz are noted to be substantially larger than the remaining cases, with the difference increasing as the exit of the diffuser is approached. One can readily estimate the impact of the larger distortion on the diffuser pressure recovery through Eq. (1). As was demonstrated previously [15], the overall frictional loss in the diffuser is not sensitive to changes in crossflow motion to the extent observed amongst the cases with different UFG speeds. Thus, $\widetilde{C}_{P0}$ can be assumed to be approximately the same for all of these cases. This is also true for α_A, which is noted to be close to unity ($\alpha_A = 1.15$) for all of the unsteady cases as per Fig. 9. Furthermore, noting that for the overall area ratio of the diffuser,

$$(C_P)_{\text{ideal}} = 1 - (\overline{V}_{x_E}/\overline{V}_{x_A})^2 \tag{4}$$

takes a value of 0.91, Eq. (1) reduces to:

$$\widetilde{C}_P = 1 - 0.074\alpha_E + (\widetilde{C}_{P0_A} - \widetilde{C}_{P0_E}) \tag{5}$$

i.e., $\widetilde{C}_P$ is linearly dependent on the value of α_E. As shown in Fig. 9, α_E takes the values of 1.59 and 2.11 for the 80 Hz and 20 Hz cases, respectively. This translates into a reduction of 0.04 in $\widetilde{C}_P$ as the frequency of the inflow unsteadiness is decreased from 80 to 20 Hz. This performance penalty, of about 4.3% with reference to the ideal pressure recovery, is about a quarter of that caused by adjustment of the inflow boundary layer thickness under steady conditions [15].

Finally, comparison of the α and α_p values for each of the UFG speeds shows that the contribution of secondary flows to the overall flow distortion is small (as was the case in the instances of steady inflow, [15]), with this contribution being slightly stronger in Planes C and D, particularly for the 20 Hz case. In Planes B and E the secondary-flow-related distortion is negligible for all speeds of the UFG.

Conclusions

Measurements have been presented on the effects of period-inflow unsteadiness in a fishtail-shaped diffusing bend of strong curvature. The periodic inflow unsteadiness was set up to approximate the conditions encountered in gas-turbine installations due to circumferential nonuniformity of the flow at the centrifugal-impeller discharge. At inflow oscillation conditions approximately corresponding to the design-point operating condition on a gas-turbine engine, the time-averaged velocity field in the diffuser is found to be symmetric with respect to the geometric symmetry plane of the diffuser, dominated by a pair of counter-rotating streamwise vortices. At lower frequencies of inflow velocity fluctuations, however, an asymmetry is observed in the time-averaged cross-flow pattern throughout the diffuser, driven by a substantial mismatch between the strengths of the two streamwise vortices. This is noted to be due to the effect of inflow unsteadiness frequency and amplitude on the time-averaged axial-flow distortion levels, hence vorticity distribution perpendicular to the plane of the bend, just before the 90 deg turn of the flow path. This asymmetry of the flow field in the bend is shown to have a notable effect on the diffuser pressure recovery through its influence on the level of axial flow distortion at the diffuser exit.

Acknowledgments

The author gratefully acknowledges the research grant provided by the Natural Sciences and Engineering Research Council of Canada in support of this project.

Nomenclature

A = local cross-sectional area
$\widetilde{C}_P$ = mass-averaged static pressure coefficient $= (\widetilde{P} - \widetilde{P}_A)/1/2\rho\overline{V}^2_{x_A}\alpha_A$
$\widetilde{C}_{P0}$ = mass-averaged stagnation pressure coefficient $= [\widetilde{P}_{0_A} - \widetilde{P}_0]/1/2\rho\overline{V}^2_{x_A}\alpha_A$
h = half-height of the diffuser side walls; refer to Fig. 2(*a*)
L = diffuser centerline length
P = static pressure
$\widetilde{P}$ = mass-averaged static pressure
P_0 = stagnation pressure
$\widetilde{P}_0$ = mass-averaged stagnation pressure
r = radius of the upper and lower walls; refer to Fig. 2(*a*)
UFG = unsteady-flow generator
V = velocity
$\overline{V}$ = area-averaged velocity
x, y, z = orthogonal curvilinear coordinates; x axis is tangent to the centerline of the flow path with $x = 0$ at the inlet of the diffuser; refer to Fig. 2(*a*)
α = kinetic energy factor (Eq. (2))
α_P = primary-flow kinetic energy factor (Eq. (3))
θ = turning angle of the diffuser centerline; refer to Fig. 2(*a*)
ϕ = circumferential coordinate; refer to Fig. 2(*a*)
ω = vorticity, normalized by the area- and time-averaged axial velocity in the corresponding measurement plane, and by the flow-path radius of Plane A

Subscripts

CL = centerline
x, y, z = components in the x, y and z directions
A, B, C, D, E = cross-sectional measurement planes; refer to Table 1 for their locations

References

[1] Kenny, D. P., 1968, ''A Novel Low Cost Diffuser for High Performance Centrifugal Compressors,'' ASME Paper 68-GT-38.
[2] Reeves, G. B., 1977, ''Design and Performance of Selected Pipe-Type Diffusers,'' ASME Paper No. 77-GT-104.
[3] Blair, L. W. and Russo, C. J., 1980, ''Compact Diffusers for Centrifugal Compressors,'' AIAA Paper No. 80-1077, presented at the AIAA/SAE/ASME 16th Joint Propulsion Conference.
[4] Dolan, F. X. and Runstadler, P. W., 1973, ''Pressure Recovery Performance of Conical Diffusers at High Subsonic Mach Numbers,'' NASA Contractor Report 2299.
[5] Rowe, M., 1970, ''Measurements and Computations of Flow in Pipe Bends,'' J. Fluid Mech., **43**, pp. 771–783.
[6] Agrawal, Y., Talbot, L., and Gong, K., 1978, ''Laser Anemometry Study of Flow Development in Curved Circular Pipes,'' J. Fluid Mech., **85**, pp. 497–518.
[7] Humphrey, J. A. C., Whitelaw, J. H., and Yee, G., 1981, ''Turbulent Flow in a Square Duct with Strong Curvature,'' J. Fluid Mech., **103**, pp. 443–463.
[8] Taylor, A. M., Whitelaw, J. H., and Yianneskis, M., 1982, ''Curved Ducts With Strong Secondary Motion: Velocity Measurements of Developing Laminar and Turbulent Flow,'' ASME J. Fluids Eng., **104**, pp. 350–359.
[9] Fox, R. W., and Kline, S. J., 1962, ''Flow Regimes in Curved Subsonic Diffusers,'' J. Basic Eng., **84**, pp. 303–316.
[10] Sagi, C. J., and Johnston, J. P., 1967, ''The Design and Performance of Two-Dimensional, Curved Diffusers,'' ASME J. Basic Eng., **89**, pp. 715–731.
[11] Parsons, D. J., and Hill, P. G., 1973, ''Effects of Curvature on Two-Dimensional Diffuser Flow,'' ASME J. Fluids Eng., **95**, pp. 349–360.
[12] McMillan, O. J., 1982, ''Mean-Flow Measurements of the Flow Field Diffusing Bend,'' NASA Contractor Report 3634.
[13] Wellborn, S. R., Reichert, B. A. and Okiishi, T. H., 1992, ''An Experimental Investigation of the Flow in a Diffusing S-Duct,'' AIAA-92-3622 presented at the AIAA/SAE/ASME/ASEE 28th Joint Propulsion Conference.
[14] Yaras, M. I., 1996, ''Effects of Inlet Conditions on the Flow in a Fishtail Curved Diffuser With Strong Curvature,'' J. Fluids Eng., **118**, pp. 772–778.
[15] Yaras, M. I., 1999, ''Flow Measurements in a Fishtail Diffuser with Strong Curvature,'' J. Fluids Eng., **121**, pp. 410–417.

[16] Dobbeling, K., Lenze, B., and Leuckel, W., 1990, ''Computer-aided Calibration and Measurements with a Quadruple Hotwire Probe,'' Exp. Fluids, **8**, pp. 257–262.

[17] Bearman, P. W., 1971, ''Corrections for the Effect of Ambient Temperature Drift on Hot-wire Measurements in Incompressible Flow,'' DISA Information Report No. 11, pp. 25–30.

[18] Saroch, M. F., 1996, ''Contributions to the Study of Turbomachinery Aerodynamics, Part I: Design of a Fish-Tail Diffuser Test Section, Part II: Computations of the Effects of AVDR on Transonic Turbine Cascades,'' Masters thesis, Department of Mechanical and Aerospace Engineering, Carleton University.

[19] Krain, H., 1981, ''A Study of Centrifugal Impeller and Diffuser Flow,'' J. Electron Spectrosc. Relat. Phenom., **103**, pp. 688–697.

[20] Squire, H. B., and Winter, K. G., 1951, ''The Secondary Flow in a Cascade of Aerofoils in a Nonuniform Stream,'' Journal of Aeronautical Sciences, **18**, pp. 271–277.

[21] Hawthorne, W. R., 1951, ''Secondary Circulation in Fluid Flow,'' J. Aeronaut. Sci., **206**, pp. 374–387.

Kenneth C. Cornelius
Ph.D., Associate Professor
email: kcorn@cs.wright.edu

Kartik Srinivas
Graduate Student

Department of Mechanical and Materials Engineering,
3640 Colonel Glenn Hwy.,
Wright State University,
Dayton, Ohio 45435-0001,
Phone: (937) 775-5091,
Fax: (937) 775-5009

Isentropic Compressible Flow for Non-Ideal Gas Models for a Venturi

The non-ideal gas equations and mathematical formulation developed in this work using the compressibility factor in the equation of state closely resemble the derivations used for the ideal gas mathematical formulation for a direct comparison of the differences between the ideal versus the non-ideal gas law. The local Mach number is defined for the non-ideal gas. The plenum total variables used in compressible flow are expressed in terms of the local Mach number for the polytrope and Rayleigh models. A power law relationship is derived between the thermodynamic variables that allow an analytical result for the mass flow under certain constraints. [DOI: 10.1115/1.1677499]

Introduction

The measurement of mass flow using a venturi meter is a standard engineering apparatus that is utilized in the laboratory and also widely used to monitor mass flow of gases in industry. We give credit for the venturi geometric device after the pioneering work of Giovanni B. Venturi (1746–1822). The conical streamlined convergence section followed by a gradual expansion of the gas in a conical diffuser downstream of the throat of the venturi meter provides for low energy losses across the device for Mach numbers less than one at the throat. Halmi [1] introduced a novel segmented venturi of short length where the pressure losses were correlated with the diameter ratio as well as the diffuser section with a gradual conical angle of divergence. The discharge coefficient was correlated over a wide Reynolds number range. Miller [2] has compiled a comprehensive overview of differing flow meter designs including the venturi with the data analysis procedures and various correction factors for the evaluation of the mass flow including real gas effects for the polytrope model.

The inclusion of real gas includes the compressibility factor in the equation of state as well as the pressure density relationship along an isentrope contour. The polytropic exponent n which relates the pressure and density variable namely, $P/\rho^n = \text{constant}$ is referred to as the polytrope equation. A second order equation that accounts for a linear variation of n with density along the isentrope namely, $P+B=A_R\rho^{n_R}$ is discussed by Thomson et al. [3] and Sullivan [4] and would be more accurate when $B\neq 0$ at higher pressures. Both of these models allows an expression of the mass flow in terms of the pressure and temperature variables that are used in the experimental evaluation of the mass flow.

The conservation of mass, entropy and the energy equation along with the equation of state provides the mathematical framework for the development of the mass flow in terms of the measured local thermodynamic properties. Closure is defined by the measured discharge coefficient Fox et al. [5], Miller [2] or a calculation scheme using CFD or an integral boundary layer analysis White [6] for the venturi geometry. The discharge coefficient is a function of the Reynolds number that represents the correction for the boundary layer viscous profile effects that exists in the converging flow as applied to the integrated conservation laws. The one-dimensional analysis of the flow is important when measurements are taken at the minimum area to predict the mass flow as there should be no radial pressure gradients at the throat location, Morel [7]. This would require a straight section with constant diameter on the order of one diameter at the end of the contraction geometry before the diffuser section. The insight gained from this analysis demonstrates the essential differences of real gas effects as compared to the analysis of ideal gas with constant properties for venturi applications. Calculations of three refrigerants were analyzed to demonstrate the non-ideal gas effects and the n value approaching one is considered a special case for two of the refrigerants. The polytrope model and the more general Rayleigh model are discussed in the sections below. A similar derivation for the ideal gas model with constant properties for compressible flow can be found in Saad [8].

Mathematical Development for the Isentropic Polytrope Model for Non-Ideal Gas Flow for a Venturi With a Plenum Upstream

The theoretical development of the non-ideal isentropic gas flow through the contraction of the venturi meter is derived in this section. The boundary layer displacement thickness is a small fraction of the radius and therefore a majority of the flow is inviscid. The isentropic expansion of a general non-ideal compressible gas from the total variables can be expressed by the following development from the conservation laws. The equation of corresponding states using $z=z(T_{rv},P_{rv})$ for a non-ideal gas where z is the compressibility factor which is represented in terms of reduced variables. The acentric factor should be included in the evaluation of z for more complex molecular structures. The thermodynamic variables are divided by T_{cr} and P_{cr} which identifies the fluid transition at the top of the (T,s) liquid versus vapor dome which are constants for each individual fluid. The reduced variables are not explicitly used in the following analysis. The compressibility factor can be obtained from the equation of corresponding states from Cengel et al. [9] or Howell et al. [10]. The equations are expressed with gradients in the z plane for a more general evaluation of gases beyond those in which experimental data is available. The equation of state using the gas constant $R_g = R_u/M_{wt}$ can be expressed as

$$P = z\rho R_g T \tag{1}$$

Differentiating this expression provides for the relationship between the variables

$$\frac{dP}{P} = \frac{dz}{z} + \frac{d\rho}{\rho} + \frac{dT}{T} \tag{2}$$

From Gibb's equation, relating entropy change to the change in thermodynamic properties

---

Contributed by the Fluids Engineering Division for publication in the JOURNAL OF FLUIDS ENGINEERING. Manuscript received by the Fluids Engineering Division March 20, 2002; revised manuscript received September 15, 2003. Associate Editor: A. K. Prasad.

$$Tds = dh - \frac{dP}{\rho} \tag{3}$$

with $ds=0$ for the isentropic case, $dh = dP/\rho$, where dh can be expressed for a non-ideal gas in terms of the thermodynamic properties as

$$dh = C_p dT - \left(\frac{T}{z}\right)\left(\frac{\partial z}{\partial T}\right)_P \frac{dP}{\rho} \tag{4}$$

The equation for entropy change from Eq. (3) and Eq. (1)

$$\frac{ds}{R_g} = \frac{C_p}{R_g}\frac{dT}{T} - z\left(1 + \left(\frac{T}{z}\right)\left(\frac{\partial z}{\partial T}\right)_P\right)\frac{dP}{P} \tag{5}$$

The equation for entropy can also be expressed as

$$\frac{ds}{R_g} = \frac{C_v}{R_g}\frac{dT}{T} - z\left(1 + \left(\frac{T}{z}\right)\left(\frac{\partial z}{\partial T}\right)_\rho\right)\frac{d\rho}{\rho} \tag{5a}$$

The equation for the mechanical energy with no work input or heat transfer can be written as

$$\frac{dV^2}{2} + \frac{dP}{\rho} + Tds = 0 \tag{6}$$

Where $Tds=0$ for an isentropic flow through a converging geometry. Integrating along a streamline from the inlet to any downstream location

$$\int \frac{dV^2}{2} = -\int \frac{dP}{\rho} \tag{7}$$

The upstream total plenum variables, where the velocity is zero, are constant. The velocity at the downstream location (i) can be expressed in terms of the integral along a streamline outside the boundary layer flow.

$$\frac{V_i^2}{2} = -\frac{P_T}{\rho_T}\int_1^{P_i/P_T}\left(\frac{\rho_i}{\rho_T}\right)^{-1} d\left(\frac{P_i}{P_T}\right) \tag{8}$$

The mathematical treatment for compressible non-ideal gas flow depends on the power law relationship between the thermodynamic variables, using the isentropic power law analytical result, where $n \neq \gamma$ for a non-ideal gas, the relation between the static and plenum total variables for density and pressure can be expressed as, assuming n remains invariant over the range of investigation,

$$\frac{\rho_i}{\rho_T} = \left(\frac{P_i}{P_T}\right)^{1/n} \quad \text{where,} \quad \rho_T = \frac{P_T}{z_T R_g T_T} \tag{9}$$

The integration along a streamline provides for the velocity at the downstream location (i) where the static pressure P_i is evaluated, and P_T and T_T are constant upstream plenum total variables. Note, valid for $n > 1$.

$$V_i = \left[z_T R_g T_T \left(\frac{2n}{n-1}\right)\left(1 - \left(\frac{P_i}{P_T}\right)^{(n-1)/n}\right)\right]^{1/2}$$

where,

$$n = \gamma \frac{\left(z + (T)\left(\frac{\partial z}{\partial T}\right)_\rho\right)}{\left(z + (T)\left(\frac{\partial z}{\partial T}\right)_P\right)} \tag{10}$$

$$V_i = \left[2 z_T R_g T_T \ln\left(\frac{P_T}{P_i}\right)\right]^{1/2} \quad \text{when} \quad n \to 1 \tag{10a}$$

Combining Eqs. (5) and (5*a*) provides for the exponent *n*. Hence, the magnitude of the ratio $n/\gamma = F(T_{rv}, P_{rv})$ for an individual gas is a unique function of the reduced variables from the principle of corresponding states. Note $(n \to \gamma, z \to 1)$ for the ideal gas assumption.

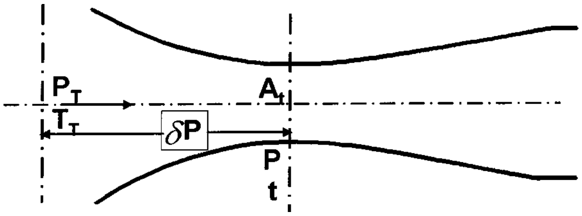

Fig. 1 Venturi meter at the entrance of a plenum

The mass flow rate for a one-dimensional analysis is given by $\dot{m} = C_d \rho_t V_t A_t$. The mass flow can be calculated from the following compressible relation for non-ideal gas. Substituting in terms of the plenum total quantities of the gas upstream of the venturi Eq. (9), the mass flow can be expressed as, note valid for $n > 1$

$$\dot{m} = \frac{C_d A_t P_T}{(z_T R_g T_T)^{1/2}}\left(\frac{2n}{(n-1)}\right)^{1/2}\left(\frac{P_t}{P_T}\right)^{1/n}\left(1 - \left(\frac{P_t}{P_T}\right)^{(n-1)/\mathrm{n}}\right)^{1/2} \quad \text{or} \tag{11}$$

$$\dot{m} = \frac{C_d A_t P_T}{(z_T R_g T_T)^{1/2}}\left(\frac{2n}{(n-1)}\right)^{1/2}\left(1 - \frac{\delta P}{P_T}\right)^{1/n} \times \left(1 - \left(1 - \frac{\delta P}{P_T}\right)^{(n-1)/n}\right)^{1/2} \tag{11a}$$

Where the pressure difference $\delta P = (P_T - P_t)$ is obtained from the difference of the upstream plenum total variable to the minimum static pressure at the throat area A_t. Figure 1 is a sketch of the venturi with the appropriate measured thermodynamic variables. The measurement of δP allows for a more accurate transducer to be used since the magnitude of δP may be much smaller than P_T. In an experimental setup pressure readings from the plenum total variables at the inlet and static pressure at the throat of the venturi meter can be used to calculate the mass flow rate.

The coefficient of discharge C_d is the conventional value tabulated in the manufacture's literature and usually obtained by dividing the measured mass flow by the theoretical (ideal) mass flow using the throat area of the venturi meter. The numerical magnitude of C_d plotted as a function of $R_{nD} = V_t D_t / \nu_t = 4\dot{m}/\pi D_t \mu_t$ provides for the correction to the inviscid flow and the accuracy of the mass flow calculation, Miller [2], Bird et al. [11]. The discharge coefficient provides for a numerical reduction in the actual area for the inviscid flow to pass through the minimum area as the flow moves in a favorable pressure gradient to the throat geometry and has a unique functional relationship for each individual geometry as well as the fluid. The mass flow rate equation can be modified to become non-dimensional by rearranging and squaring to establish a function of $\delta P/P_T$ and n on the right hand side. Note that the speed of sound squared $c_T^2 = (n z_T R_g T_T)$ at the upstream plenum variables, for $n > 1$, the non-dimensional mass expression becomes

$$\Phi_m = \left(\frac{\dot{m}}{C_d A_t P_T}\right)^2 (n z_T R_g T_T) = \left(\frac{2n^2}{n-1}\right)\left(1 - \frac{\delta P}{P_T}\right)^{2/n}\left[1 - \left(1 - \frac{\delta P}{P_T}\right)^{(n-1)/n}\right] \tag{12}$$

$$\Phi_m = \left(\frac{\dot{m}}{C_d A_t P_T}\right)^2 (z_T R_g T_T) = (2)\left(1 - \frac{\delta P}{P_T}\right)^2\left(-\ln\left(1 - \frac{\delta P}{P_T}\right)\right), \quad n \to 1 \tag{12a}$$

The slope of the functional relationship in Eq. (12) asymptotes at the critical or choked value expressed for $n>1$ as

$$\left(\frac{\delta P}{P_T}\right)_c = 1-\left(\frac{2}{n+1}\right)^{n/(n-1)}, \quad \text{and} \quad \left(\frac{\delta P}{P_T}\right)_c = 1-e^{1/2}, \quad n\rightarrow 1 \tag{13}$$

The Mach number for the polytrope model at any location for a non-ideal compressible gas can be expressed by

$$M_i=\frac{V_i}{(z_i n R_g T_i)^{1/2}} \tag{14}$$

The speed of sound, White [6] of the non-ideal gas is defined as $c=(\partial p/\partial\rho)_s^{1/2}=(z_i n_i R_g T_i)^{1/2}$. The isentropic relation between the pressure and temperature variables from Eq. (5) can be written as, assuming r remains invariant over the range of investigation

$$\frac{T_T}{T_i}=\left(\frac{P_T}{P_i}\right)^{(r-1)/r}=\left(\frac{P_T}{P_i}\right)^{(R_g/C_P)(z+(T)(\partial z/\partial T)_P)} \tag{15}$$

The quantity r in the above equation represents the power law for the isentropic expansion of the gas from the plenum to a downstream location (i). The numerical value for r can be expressed in terms of the properties of the gas by the following

$$\frac{r-1}{r}=\frac{R_g}{C_P}\left(z+(T)\left(\frac{\partial z}{\partial T}\right)_P\right) \tag{16}$$

Note, $(r\rightarrow\gamma, z\rightarrow 1, T(\partial z/\partial T)_P\rightarrow 0)$ for the ideal gas assumption. The equation for the Mach number at the minimum area plane can then be derived from Eqs. (10) and (14–16) and can be expressed as $M^2=f(n,z_T,/z,T_T/T,P_T/P)$. For $n>1$

$$M_i^2=\left(\frac{2}{n-1}\right)\frac{z_T}{z_i}\left(\frac{T_T}{T_i}\right)\left(1-\left(\frac{P_T}{P_i}\right)^{-(n-1)/n}\right) \tag{17}$$

$$M_i^2=2\,\frac{z_T}{z_i}\left(\frac{T_T}{T_i}\right)\ln\left(\frac{P_T}{P_i}\right), \quad n\rightarrow 1 \tag{17a}$$

An equation for the ratio of plenum total to static compressibility factor can be obtained utilizing Eq. (1) and combining with Eq. (15). The resultant expression demonstrates that a power law relation must also be satisfied for the ratio z_T/z, namely,

$$\frac{z_T}{z_i}=\left(\frac{P_T}{P_i}\right)^{((n-r)/nr)}, \quad \text{also} \quad \frac{z_T}{z_i}\frac{T_T}{T_i}=\left(\frac{P_T}{P_i}\right)^{(n-1)/n} \tag{18}$$

The Mach number from Eq. (17) and combining with Eq. (18) demonstrates the analytical result as $M^2=f(n,P_T/P)$.

$$M_i^2=\left(\frac{2}{n-1}\right)\left(\left(\frac{P_T}{P_i}\right)^{(n-1)/n}-1\right),$$

$$\text{also} \quad M_i^2=2\ln\left(\frac{P_T}{P_i}\right), \quad n\rightarrow 1 \tag{19}$$

The ratio of plenum total to static temperature downstream in terms of the Mach number is expressed as

$$\frac{T_T}{T_i}=\left(1+\left(\frac{n-1}{2}\right)M_i^2\right)^{n/(n-1)(r-1)/r},$$

$$\text{also} \quad \frac{T_T}{T_i}=e^{(M_i^2\,(r-1)/2r)}, \quad n\rightarrow 1 \tag{20}$$

The critical temperature normalized on the plenum total when the flow is choked at $M_t=1$ can be expressed as

$$\left(\frac{T_t}{T_T}\right)_c=\left(\frac{1+n}{2}\right)^{-n/(n-1)(r-1)/r},$$

$$\text{also} \quad \left(\frac{T_t}{T_T}\right)_c=e^{(-r-1)/2r}, \quad n\rightarrow 1 \tag{21}$$

The mass flow Eq. (11) can also be expressed in terms of the Mach number at the throat see, Saad [8] for the ideal gas model for $n>1$.

$$\dot{m}=\frac{C_{dAt}P_T n}{(n z_T R_g T_T)^{1/2}}M_t\left(1+\frac{n-1}{2}M_t^2\right)^{-1/2(n+1)/(n-1)},$$

$$\text{also} \quad \dot{m}=\frac{C_d A_t P_T}{(z_T R_g T_T)^{1/2}}M_t e^{-M_t^2/2}, \quad n\rightarrow 1 \tag{22}$$

The analysis demonstrates that the replacement of the variables $(n\rightarrow\gamma, z_T R_g\rightarrow R_g)$ in the ideal gas model for the correction for the non-ideal mass flow for engineering applications when n remains invariant over the range of consideration. The static temperature variation with pressure has a different isentropic exponent than the density variation with pressure along the isentrope.

Development for the Isentropic Rayleigh Model for Non-Ideal Gas Flow for a Venturi With a Plenum Upstream

The mathematical treatment for compressible non-ideal gas flow depends on the isentropic relationship between the thermodynamic variables. The Rayleigh model discussed in Sullivan [4] namely, $P+B=A_R\rho^{n_R}$ is a more general expression relevant when n varies over the range under consideration. The numerical value of $n_R\neq n$ for $B\neq 0$ when k or n varies linearly with density from the plenum state to the throat for a non-ideal gas. The relation between the static and plenum total variables for density and pressure can be expressed as; assuming n_R and B remains invariant over the range of investigation,

$$\frac{\rho_i}{\rho_T}=\left(\frac{P_i+B}{P_T+B}\right)^{1/n_R}=\left(1-\frac{n_R}{k_T}\frac{\delta P_i}{P_T}\right)^{1/n_R} \quad \text{also,}$$

$$\left(\frac{c_i}{c_T}\right)^2=\left(1-\frac{n_R}{k_T}\frac{\delta P_i}{P_T}\right)^{(n_R-1)/n_R} \tag{23}$$

where the pressure difference $\delta P_i=(P_T-P_i)$. The salient features of the analysis from [4] are extracted for the sake of completeness in a form conducive to engineering analysis that is exact when k varies linearly with density and the relation between n_R and k is defined as

$$n_R=k_T+\frac{\rho_i}{k_i}\left(\frac{\partial k_i}{\partial\rho_i}\right)_s \quad \text{where} \quad k_T=n_R\left(1+\frac{B}{P_T}\right)=\frac{c_T^2}{z_T R_g T_T} \tag{24}$$

The k and static temperature variation downstream along the Rayleigh isentrope can be derived from Eqs. (1) and (23) as

$$\frac{k_i}{k_T}=\frac{1-\dfrac{\delta P_i}{P_T}}{1-\dfrac{n_R}{k_T}\dfrac{\delta P_i}{P_T}} \quad \text{and}$$

$$\frac{z_i T_i}{z_T T_T}=\left(\left(1-\frac{\delta P_i}{P_T}\right)\left(1-\frac{n_R}{k_T}\frac{\delta P_i}{P_T}\right)^{1/n_R}\right)^{-1} \tag{25}$$

The integration along a streamline from Eq. (8) provides for the velocity at the downstream location (i) where the static pressure P_i is evaluated, and P_T and T_T are constant upstream plenum total variables. Note, valid for $n_R>1$.

$$V_i=\left[k_T z_T R_g T_T\left(\frac{2}{n_R-1}\right)\left(1-\left(1-\frac{n_R}{k_T}\frac{\delta P_i}{P_T}\right)^{(n_R-1)/n_R}\right)\right]^{1/2} \quad \text{and} \tag{26}$$

$$V_i=\left[2(k_T z_T R_g T_T)\left(\ln(k_T)-\ln\left(k_T-\frac{\delta P_i}{P_T}\right)\right)\right]^{1/2} \quad n_R\to 1 \tag{26a}$$

Note that the speed of sound squared $c_T^2=(k_T z_T R_g T_T)$ at the upstream plenum total variables, for $n_R>1$, the non-dimensional mass expression for a venturi application becomes

$$\begin{aligned}\Phi_m&=\left(\frac{\dot m}{C_d A_t P_T}\right)^2(k_T z_T R_g T_T)\\&=\left(\frac{2k_T^2}{n_R-1}\right)\left(1-\frac{n_R}{k_T}\frac{\delta P}{P_T}\right)^{2/n_R}\left[1-\left(1-\frac{n_R}{k_T}\frac{\delta P}{P_T}\right)^{n_R-1/n_R}\right]\end{aligned} \tag{27}$$

$$\begin{aligned}\Phi_m&=\left(\frac{\dot m}{C_d A_t P_T}\right)^2(k_T z_T R_g T_T)\\&=(2k_T^2)\left(1-\frac{1}{k_T}\frac{\delta P}{P_T}\right)^2\left(\ln(k_T)-\ln\left(k_T-\frac{\delta P}{P_T}\right)\right),\quad n_R\to 1\end{aligned} \tag{27a}$$

Note, if a transducer measuring the speed of sound of the gas in the plenum and at the throat location (transverse to the flow direction) was utilized along with upstream plenum and throat temperature measurement with pressure transducers for the evaluation of $\delta P/P_T$, then k_T and n_R can be evaluated from Eqs. (23) and (24*a*) for the evaluation of the non-dimensional mass flow. This would be useful when the property data is not available for a particular gas.

The Mach number at any location along the Rayleigh isentrope for a non-ideal compressible gas can be expressed by

$$M_i=\frac{V_i}{(k_i z_i R_g T_i)^{1/2}} \quad \text{where} \quad k_i=n_R\left(1+\frac{B}{P_i}\right)=\frac{c_i^2}{z_i R_g T_i} \tag{28}$$

The Mach number using Eq. (23) where the choked condition occurs at $M_t=1$ can be expressed in terms of the pressure difference normalized on the plenum total as

$$M_i^2=\left(\frac{2}{n_R-1}\right)\left(\left(1-\frac{n_R}{k_T}\frac{\delta P_i}{P_T}\right)^{-(n_R-1)/n_R}-1\right),$$

$$\text{and}\quad M_i^2=(2)\left(\ln(k_T)-\ln\left(k_T-\frac{\delta P}{P_T}\right)\right)\quad n_R\to 1 \tag{29}$$

When $n_R\to 1$ the Rayleigh model becomes, $P+B=A_R\rho$ and $c_T/c_i=1$. The choked values are

$$\left(\frac{\delta P}{P_T}\right)_c=\frac{k_T}{n_R}\left(1-\left(\frac{2}{n_R+1}\right)^{n_R/(n_R-1)}\right),$$

$$\text{and}\quad \left(\frac{\delta P}{P_T}\right)_c=k_T+(e^{\ln k_T-1/2})\quad n_R\to 1 \tag{29a}$$

The mass flow $\dot m=C_d\rho_t V_t A_t$ can also be expressed in terms of the Mach number at the throat as

$$\dot m=\frac{C_d A_t P_T k_T}{(k_T z_T R_g T_T)^{1/2}}M_t\left(1+\frac{n_R-1}{2}M_t^2\right)^{-1/2(n_R+1)/(n_R-1)},$$

$$\text{and}\quad \dot m=\frac{C_d A_t P_T}{(k_T z_T R_g T_T)^{1/2}}M_t e^{\ln k_T-M_t^2/2}\,n_R\to 1 \tag{30}$$

The analysis demonstrates that the Rayleigh model restricted to Eq. (30) that the replacement of the variables ($n_R\to\gamma$) for the Mach function and ($k_T z_T R_g\to\gamma R_g$) in the denominator as well as ($k_T\to\gamma$) in the numerator of the first term in the model for the non-ideal gas provides for the correction for the ideal mass flow for engineering applications.

The Rayleigh model is a more appropriate mathematical model at higher stagnation density or when $B\neq 0$. When $B=0$ the Rayleigh model reduces to the polytrope model along a fixed isentrope and $k_T=n_R=n$. A least squares curve fit through the property data for a gas will determine the constant model parameters k_T and n_R from Eq. (23) in the analysis for a venturi application. Note, Eq. (19) or (28) is valid for the measurement of the local Mach number from a conventional pitot probe configuration for $M_i\leqslant 1$. Also from Eqs. (10) or (26) the local velocity can be deduced from a modified pitot probe with a thermocouple placed concentric at the entrance of the total pressure hole of the pitot probe for the evaluation of the total temperature. The numerical value of z_T would be calculated from the principle of corresponding states $z_T=z_T\ (T_{rv}, P_{rv})$.

Venturi Meter Application

Figures 2–4 demonstrate the non-ideal gas behavior as well as the power law fit for three common refrigerant gases as compared to air in the isentropic range shown on the graphs that are used in the air conditioning and freezer markets. The symbols are the isentropic relations for the thermodynamic variables for the individual gases and the curves represent a least squares curve using the power law relation. The thermodynamic properties of refrigerant R_{22} and R_{134a} are obtained from fitted non-linear regression analysis of the physical property data using the Martin-Hou equation of state [12]. The measured thermodynamic properties of the individual refrigerants were obtained from the data provided in [13,14], and refrigerant R_{404a} used the Martin-Hou equation of

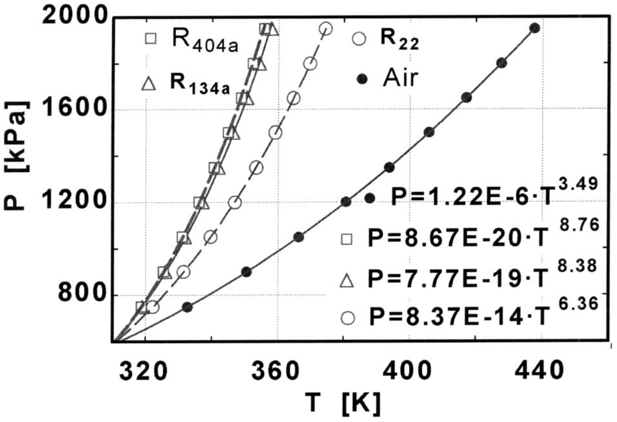

Fig. 2 ***P*** **versus** ***T*** **for refrigerants and air**

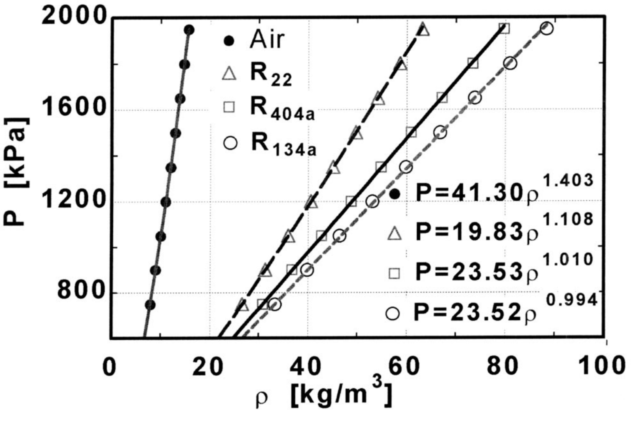

Fig. 3 ***P*** **versus** ***ρ*** **for refrigerants and air**

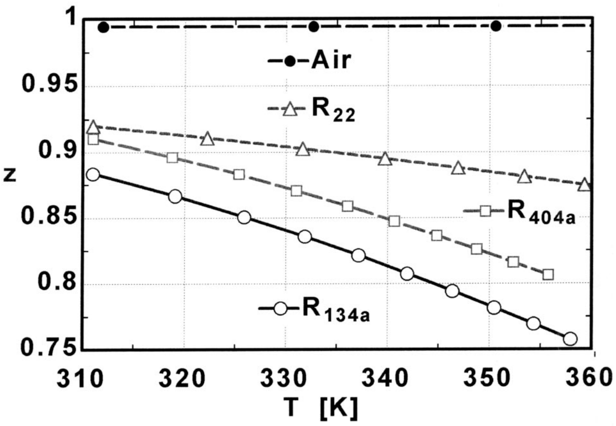

Fig. 4 ***z* versus *T* for refrigerants and air**

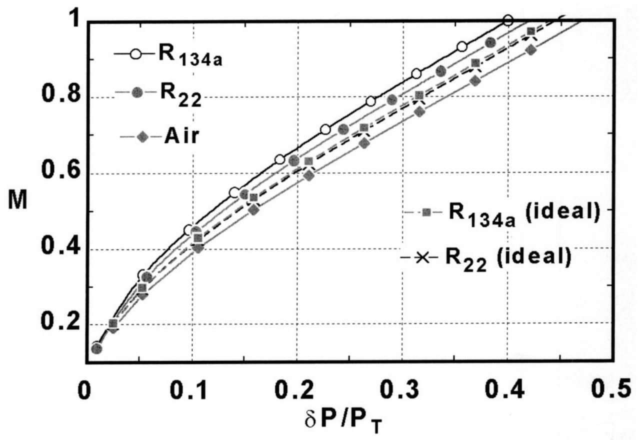

Fig. 7 Mach versus ($\delta P/P_T$) real versus ideal for refrigerants and air

state as modified for mixtures [15]. The numerical value of the compressibility factor z was calculated from Eq. (1). Figures 2–4 demonstrate that air obtained from the physical data provided in [16] which follows closely to the ideal gas behavior with no significant variation in z in the range considered.

The calculations for a venturi application were performed with a total pressure at $P_T = 1.3$ MPa for the region of isentropic expansion for the individual gases. The analysis assumes that the total plenum variables remain constant and the throat pressure is reduced through a range to the choked condition. The calculations were terminated at the critical pressure condition from Eq. (13, 29). For air the static pressure P_t at the throat was 687 kPa, for R_{22}, 748 kPa and R_{134a}, 780 kPa. Figure 5 shows a linear variation of the exponent k for the refrigerants with density and there-

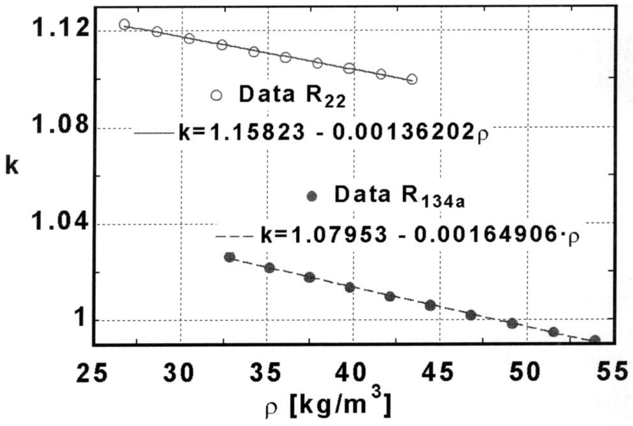

Fig. 5 Exponent *k* versus ρ for refrigerants

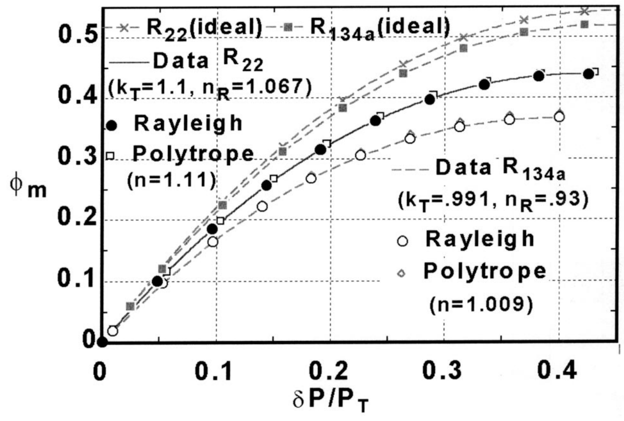

Fig. 6 Φ_m versus ($\delta P/P_T$) real versus ideal comparison for refrigerants

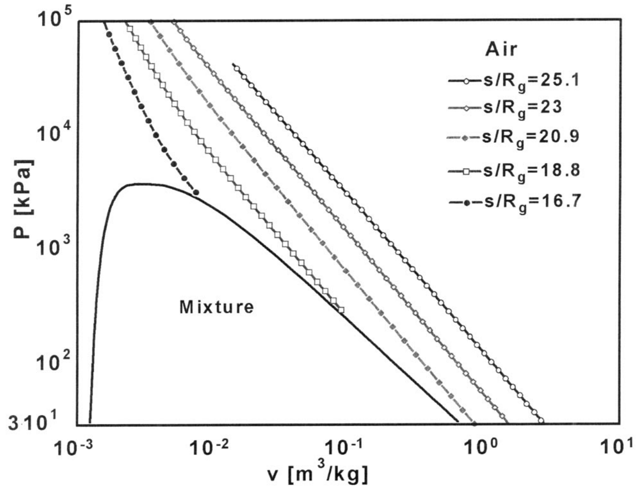

Fig. 8 *P* versus *v* diagram for air with constant isentrope lines

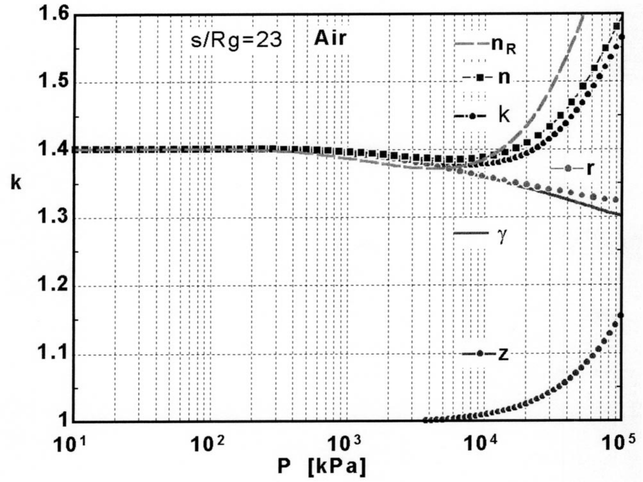

Fig. 9 Exponent values and *z* versus *P* along isentrope for air

fore the Rayleigh model would be more accurate. The refrigerants are non-ideal and have an exponent k that varies by 2% for R_{22} and 4% for R_{134a} between the plenum and choked state under consideration. Figure 6 is a plot of the comparison of the Rayleigh and polytrope model of the non-dimensional mass flow rate Φ_m vs. the non-dimensional pressure difference for R_{22} and R_{134a}. Also plotted on this graph is the ideal gas relation demonstrating the importance of the real gas analysis. A least squares curve fit through the entire range of $(\delta P/P_T)$ to the critical value was used for the calculation for the Polytrope and Rayleigh models. The curves labeled data are considered exact as they were obtained from the experimental property data of the individual gas. The Rayleigh model is superior for the refrigerant gas as the polytrope model over predicts the numerical value of Φ_m by 1% for R_{22} and 1.6% for R_{134a} at the choked condition. Each fluid state has one local curve that applies to a venturi meter over the range of application. If the discharge coefficient is known, the pressure difference normalized on the upstream plenum total pressure can be used to calculate the mass flow for a venturi configuration. The discharge coefficient will be a function of the Reynolds number based on the throat diameter. In the general context of this analysis C_d is a function of (R_{nD_t}, n, M_t) to match the favorable pressure gradient in the contraction geometry and the effects on the boundary layer non-dimensional parameters. The Mach number effects on the discharge coefficient would be insignificant for $M_t \leqslant 0.3$.

Figure 7 is a plot of the throat Mach number vs. the non-dimensional pressure difference from Eq. (17) for air and Eq. (29) for the refrigerants. Since R_{22} has a lower exponent n_R and k_T than air, the Mach number approaches the critical value at a lower normalized pressure differential and R_{134a} has the lowest. Also plotted on this graph is the ideal gas relation demonstrating the importance of the real gas model as the Mach number would be under predicted for compressibility effects. The data would facilitate the industrial usage of the venturi meter for the measurement of mass flow rate of these specific gases in the range investigated.

When $M_t = 1$ at the throat the non-dimensional mass flow rate reaches a local maximum value, and the solution approaches an asymptote similar to the ideal gas model. Once the normalized pressure differential reaches this critical threshold $(\delta P/P_T)_c$ the throat Mach number remains fixed and the critical static variables normalized on their respective plenum total parameters remain invariant. However, if P_T and T_T change there will be variation in the isentropic exponents as well as z_T. Figure 8 shows the P versus v diagram for air with various isentrope contours. A straight line indicates the range of validity of the polytrope model. Figure 9 shows a plot of the exponents and z versus P for one of the isentropes that more clearly demonstrates the range of applicability of the two models. When k and n_R differ significantly from n then the Rayleigh model would give a better prediction of the mass flow to the choked condition.

Uncertainty and Technical Accuracy

The Martin-Hou equation of state has an accuracy of 1% in density [12] for conditions at which the density is less than 1.5 times the critical density defined for each refrigerant or gas [9,10]. All the cases discussed in this work are well below this threshold. Thermodynamic properties at a density greater than this criterion or in the vicinity of the thermodynamic state defined by T_{cr} and P_{cr} should use the equation of state $z = z(T_{rv}, P_{rv})$ including the acentric factor for a non-ideal gas. The power law fit between the thermodynamic variables is an important parameter for accuracy. The range of operation of the venturi meter is important, as the Rayleigh model would provide greater accuracy when the power law exponent n varies linearly with density in the analysis for the mass flow to the choked condition.

Table 1 Property Data of Air and R-22

Property	Air≈(ideal)	R_{22}@inlet	R_{22}@outlet
M_{wt}	28.97	86.47	86.47
R_g (kJ/kg°K)	0.287	0.0961	0.0961
R_g/C_p	0.286	0.124	0.103
γ	1.407	1.27	1.35
n	1.403	1.13	1.105
r	1.402	1.203	1.205
z	0.995	0.894	0.782
c (m/sec)	343.5	168.3	178

Isentropic Compression Work for Open Control Volume

The isentropic work necessary to compress a non-ideal gas from the inlet to the outlet state during a steady state compression process using the one-dimensional assumption is calculated from the energy equation. The isentropic work per unit mass during the compression process can be derived in terms of pressure ratio (P_2/P_1) across the machine and the change in kinetic energy of the flow from outlet to inlet valid for $n > 1$. Note this is the solution for ideal gas model when $(n \rightarrow \gamma, z \rightarrow 1, T(\partial z/\partial T)_P \rightarrow 0)$.

$$
{}_1w_{2s} = \int_1^2 \frac{dP}{\rho} + \int_1^2 d\left(\frac{V^2}{2}\right)
$$

$$
= z_1 R_g T_1 \left(\frac{n}{n-1}\right)\left[\left(\frac{P_2}{P_1}\right)^{(n-1)/n} - 1\right] + \left(\frac{V_2^2}{2} - \frac{V_1^2}{2}\right) \qquad (31)
$$

where n is the coefficient that represents least squares or average value to the true isentropic process i.e. $P = \text{constant}\ \rho^n$. When the exponent $n \rightarrow 1$, which appears to be nearly the case for two of the refrigerants R_{404a} and R_{134a} where the z and T variation from Eq. (2) almost uniquely cancel as this is certainly not an isothermal case, then the isentropic work can be mathematically expressed as

$$
{}_1w_{2s} = \int_1^2 \frac{dP}{\rho} + \int_1^2 d\left(\frac{V^2}{2}\right) = z_1 R_g T_1 \ln\left(\frac{P_2}{P_1}\right) + \left(\frac{V_2^2}{2} - \frac{V_1^2}{2}\right),
$$

$$
\text{when} \quad n \rightarrow 1 \qquad (31a)
$$

The isentropic work per unit mass during the compression process for the Rayleigh Model is

$$
{}_1w_{2s} = \int_1^2 \frac{dP}{\rho} + \int_1^2 d\left(\frac{V^2}{2}\right)
$$

$$
= (k_T z_T R_g T_T)\left(\frac{1}{n_R - 1}\right)\left(\left(1 + \frac{n_R}{k_T}\left(\frac{P_2}{P_1} - 1\right)\right)^{(n_R-1)/n_R} - 1\right)
$$

$$
+ \left(\frac{V_2^2}{2} - \frac{V_1^2}{2}\right) \qquad (32)
$$

When $n_R \rightarrow 1$

$$
{}_1w_{2s} = \int_1^2 \frac{dP}{\rho} + \int_1^2 d\left(\frac{V^2}{2}\right)
$$

$$
= (k_T z_T R_g T_T)\left(\ln\left(k_T + \left(\frac{P_2}{P_1} - 1\right)\right) - \ln(k_T)\right) + \left(\frac{V_2^2}{2} - \frac{V_1^2}{2}\right) \qquad (32a)
$$

The isentropic work per unit mass ${}_1w_{2s}$ is for the compressor work input to the gas during the steady state compression process that is used as the reference work input for calculation and comparison to the actual hardware to define the isentropic efficiency.

Table 1 compares the properties of air and R_{22} at the inlet and exit states based on the conditions established by the American Refrigeration Institute (ARI) for an air conditioning standard reference state. The standard is $P_1 = 620.5$ kPa (90 psi), T_1

$=291.7^\circ$K (525°R) at the inlet; at the outlet $P_2=2.14$ MPa (310 psi), $T_2=347.3^\circ$K (625°R). From Eq. (31) for this condition with a pressure ratio of 3.44, the isentropic work for R_{22} becomes ${}_1w_{2s}=32.7$ kJ/kg. The values of the different properties have been extracted from the data presented in [13]. The z value from Table 1 has the most significant change for the non-ideal R_{22} gas and the difference between γ and n would have a significant impact on the prediction of the isentropic work for the real gas.

Conclusion

A mathematical model using the non-ideal equation of state has been derived in conjunction with the isentropic flow methodology. The development closely follows the ideal gas model in compressible flow and demonstrates an equivalence of the mathematical results $(n\rightarrow\gamma, r\rightarrow\gamma T(\partial z/\partial T)\rightarrow 0, z\rightarrow 1)$ for the ideal gas assumption. The polytrope and Rayleigh model relations appear to be valid over a significant range of the thermodynamic variables allowing a closed parametric model for the mass flow equation for venturi applications. With the conventional measurement of the appropriate thermodynamic variables the Mach number and static parameters can be mathematically correlated for a wide range of gasses. The mass flow for non-ideal gasses can be theoretically evaluated using a venturi meter and the analysis identifies the appropriate measurements for applications in compressible gas flow.

Various non ideal gases can be used with the venturi meter with standard measurement transducers to calculate the mass flow rate with greater precision than the standard assumption of using the isentropic flow formulation with the equation of state as the ideal gas law. Results for three common refrigerants have been analyzed identifying the power law relationship and the Reyleigh parameters from the thermodynamic variables for the isentropic, non-ideal gas. Thus many engineering problems can be addressed including the isentropic single stage compressor design for gases that deviate from the ideal gas law at higher temperature and pressure using the theoretical framework discussed in this analysis. If the exponent n deviates significantly as is the case for higher temperature and pressure then the dimensionless mass as well as Mach number can be correlated in terms of $(\delta P/P_T)$ from the basic fundamentals with the Rayleigh model for venturi applications.

Acknowledgments

The authors would like to acknowledge partial support of this research funded from a grant from Copeland Corporation. I would also like to acknowledge the support and encouragement of my colleagues and the many students I have taught over my tenure in the academic environment, without which the incite of this work would not have come to fruition. I would like to pay tribute to the authors of the well-written textbooks that have laid the foundation upon which this work is based for a general non-ideal gas model in the simplest form possible.

Nomenclature

A = area
B = Rayleigh model constant, see Eq. (23)
c = speed of sound, see Eqs. (14, 23)
C_d = discharge coefficient
C_p = specific heat at constant pressure
C_v = specific heat at constant density
D = diameter
h = specific enthalpy
k = Rayleigh model parameter, see Eqs. (24, 28)
M = Mach number
$\dot{m}$ = mass flow rate
M_{wt} = molecular weight
n = isentropic exponent relating P and ρ, see Eqs. (10, 24)
r = isentropic exponent relating P and T, see Eq. (15)
P = static pressure
P_T = plenum total pressure
R_g = gas constant
R_{nD} = Reynolds number
R_u = universal gas constant
s = specific entropy
T = static temperature
T_T = plenum total temperature
v = specific volume
V = velocity
${}_1w_{2s}$ = isentropic work per unit mass, see Eqs. (31, 32)
z = compressibility factor, see Eq. (1)
δP = pressure difference (P_T-P_t)
γ = C_P/C_v ratio of specific heats
μ = absolute viscosity
ν = kinematic viscosity
Φ_m = non-dimensional mass flow rate, see Eqs. (12, 27)
ρ = density
1 = inlet
2 = outlet
c = critical or choked, see Eqs. (13, 29*a*)
cr = saturated liquid-vapor transition point
i = plane downstream of inlet
R = Rayleigh model
rv = reduced variables
t = throat
T = plenum total

References

[1] Halmi, D., 1974, ''Metering Performance Investigation and Substantiation of the ''Universal Venturi Tube'' (U.V.T.),'' ASME J. Fluids Eng., **96**, pp. 124–131, 132–138.
[2] Miller, R. W., 1996, *Flow Measurement Engineering Handbook*, 3rd Edition, McGraw Hill, NY, pp. 2.15–2.21, 2.110–2.112, 13.3–13.33, I1–I13.
[3] Thompson, P. A., and Sullivan, D. A., 1978, ''Exact and Approximate Equations for Real-Fluid Isentropic Flow,'' ASME J. Fluids Eng., **100**, pp. 413–418.
[4] Sullivan, D. A., 1981, ''Historical Review of Real-Fluid Isentropic Flow Models,'' ASME J. Fluids Eng., **103**, pp. 258–267.
[5] Fox, R. W., and McDonald, A. T., 1998, *Introduction to Fluid Mechanics*, 5th Edition, John Wiley and Sons, Inc., NY, pp. 353–357.
[6] White, F. M., 1991, *Viscous Fluid Flow*. McGraw Hill, NY, pp. 42–48, 406–422.
[7] Morel, T., 1975, ''Comprehensive Design of Axisymmetric Wind Tunnel Contractions,'' ASME J. Fluids Eng., **97**(2), pp. 225–233.
[8] Saad, M., 1992, *Compressible Fluid Flow*, 2nd edition, Prentice-Hall, NJ, pp. 87–116.
[9] Cengel, Y. A., and Boles, M. A., 2002, *Thermodynamics an Engineering Approach*, 4th edition, McGraw Hill, NY, pp. 664–690, 867–869.
[10] Howell, J. R., and Buckius, R. O., 1992, *Fundamentals of Engineering Thermodynamics*, 2nd edition, McGraw Hill, NY, pp. 622–628.
[11] Bird, R. B., Stewart, W. E., and Lightfoot, E. N., 1966, *Transport Phenomena*, 2nd Edition, John Wiley & Sons, Inc., NY, pp. 469–473.
[12] Martin, J. J., and Hou, Y. C., 1955, ''Development of an Equation of State for Gases,'' AIChE J., **1**:142, pp. 142–151.
[13] Downing, A., and Knight, K., 1971, ''The Thermodynamic Properties of Refrigerant R-22,'' DuPont Technical Bulletin RT-52.
[14] McLinden, M. O., Gallagher, J. S., and Weber, L. A., 1989, ''Measurement and Formulation of the Thermodynamic Properties of R-134a and 123,'' ASHRAE Trans., **95**(2), pp. 263–283.
[15] Bivens, D. B., and Yokozeki, A., 1996, ''A Blend of R125/R143a/R134a With Mass Percentages of 44%/52%/4%, R-404a,'' *Intl. Conference on Ozone Protection Technologies*, Washington, DC, also''The Thermodynamic Properties of SUVA HP62 Refrigerant R-404a,'' DuPont Technical Bulletin T-HP62.
[16] Lemmon, E. W., Jacobsen, R. T., Penoncello, S. G., and Friend, D. S., 2000, ''Thermodynamic Properties of Air and Mixtures of Nitrogen, Argon, and Oxygen from 60 to 2000 K at Pressures to 2000 MPa,'' J. Phys. Chem., **29**(3), pp. 12–32.

Closely Spaced Circular Cylinders in Cross-Flow and a Universal Wake Number

David Sumner
Department of Mechanical Engineering,
University of Saskatchewan,
57 Campus Drive,
Saskatoon, Saskatchewan, S7N 5A9
Canada

To investigate the effectiveness of a universal wake number for groups of closely spaced bluff bodes, staggered cylinder configurations with center-to-center pitch ratios of $P/D=1.125$ and 1.25, and incidence angles from $\alpha=0$ deg–90 deg, were tested in the subcritical Reynolds number regime. The aerodynamic forces, base pressure, and vortex shedding frequencies were measured for the upstream and downstream cylinders, and were found to be strongly dependent on the incidence angle and small changes in the flow pattern. The Griffin number was found to be an appropriate universal wake number for the closely spaced staggered cylinders, based on the total drag force acting on the two cylinders, and the average base pressure for the two cylinders. The results suggest that the single vortex wake of a pair of closely spaced staggered cylinders is broadly comparable to the wake of a solitary bluff body, and that the universal wake number concept can be extended to groups of closely spaced bluff bodies. [DOI: 10.1115/1.1667881]

1 Introduction

A circular cylinder immersed in a uniform cross-flow has been a well-studied problem in fluid mechanics. For a wide range of Reynolds number, Re, including the subcritical, supercritical, and postcritical regimes, the flow around the circular cylinder is characterized by the periodic alternate shedding of Kármán vortices. The regular spacing of vortices in the wake of the cylinder, known as the Kármán vortex street, can persist for many cylinder diameters downstream. Using the cylinder diameter, D, as a reference length, and the freestream velocity, U, as a reference velocity, the vortex shedding frequency, f, is expressed in dimensionless form as the Strouhal number, $\mathrm{St}(=fD/U)$.

Periodic alternate vortex shedding and a vortex street also characterize the wakes of other 2-D bluff bodies, including the square cylinder, rectangular cylinder, and flat plate, for example. For these non-circular shapes, the Strouhal number uses the cross-stream or transverse width of the bluff body as the reference length. The study of bluff body wakes from different wake generating bodies has been motivated by many practical applications, many of which involve the tendency of the structure to experience vortex-induced vibrations.

The possibility that similar vortex wakes may develop behind vastly different two-dimensional bluff bodies has led researchers to explore the concept of a universal wake number, which is independent of the cross-sectional geometry of the vortex wake generating body. Several different definitions have been proposed in the literature, including the universal Strouhal numbers of Roshko [1] and Bearman [2] and the universal wake number of Griffin [3]. These numbers have variously involved the vortex shedding frequency, drag force, and base pressure of the bluff body. To achieve their universal nature, they have used length and velocity scales associated with the vortex wake, rather than the body shape or the freestream.

The universal Strouhal number, St^*, uses the wake width, D', and the velocity just outside the shear layer near the point of separation, U_s, as the reference length and velocity scales, respectively, for the vortex shedding frequency [1,2,4]. It is related to the actual Strouhal number as shown below:

$$\mathrm{St}^* = \frac{fD'}{U_s} = \mathrm{St}\,\frac{D'}{D}\,\frac{U}{U_s}. \tag{1}$$

Through Bernoulli's equation, the velocity just outside the shear layer, U_s, can be related to the base pressure coefficient, C_{PB}, and a base pressure parameter, K, can be defined:

$$C_{PB} = 1 - \left(\frac{U_s}{U}\right)^2 \tag{2}$$

$$K = (1 - C_{PB})^{1/2} = \frac{U_s}{U} \tag{3}$$

The universal Strouhal number then becomes

$$\mathrm{St}^* = \frac{fD'}{U_s} = \mathrm{St}\,\frac{D'}{D}\,\frac{U}{U_s} = \frac{\mathrm{St}}{K}\,\frac{D'}{D}. \tag{4}$$

Both analytical [1,2] and experimental [3] methods have been used to define D', however a semiempirical approximation for the wake width is often used [3], where C_D is the mean drag coefficient:

$$\frac{D'}{D} = \frac{C_D}{-C_{PB}}. \tag{5}$$

The universal Strouhal number, St^*, then becomes

$$\mathrm{St}^* = -\frac{\mathrm{St}}{K}\,\frac{C_D}{C_{PB}}. \tag{6}$$

By using similar scaling relationships, a modified drag coefficient, C_D^*, was defined by Griffin [3]:

$$C_D^* = \frac{C_D}{K^2}\,\frac{D}{D'} = \frac{-C_{pb}}{K^2}. \tag{7}$$

The product $\mathrm{St}^* C_D^*$ was found to remain nearly constant for a wide range of bluff-body flows, including: cylinders of various cross-sections; cylinders with splitter plates, base bleed, and rough surfaces; fixed and oscillating cylinders; and cylinders in the subcritical, critical, and postcritical regimes [3]. This product has subsequently become known as the Griffin number, G [5–7]:

$$\mathrm{G} = \mathrm{St}^* C_D^* = \frac{\mathrm{St}C_D}{K^3}. \tag{8}$$

Contributed by the Fluids Engineering Division for publication in the JOURNAL OF FLUIDS ENGINEERING. Manuscript received by the Fluids Engineering Division February 12, 2003; revised manuscript received September 30, 2003. Associate Editor: M. V. Ötügen.

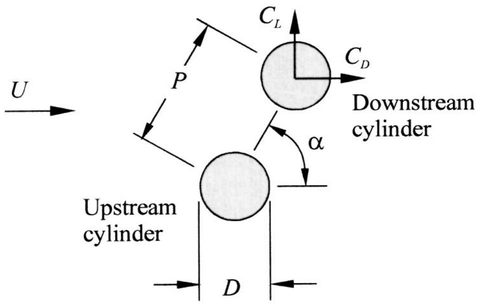

Fig. 1 Staggered configuration of two circular cylinders of equal diameter, immersed in a steady mean cross-flow. Included is the force convention for the downstream cylinder.

Both St* and G have been applied with varying degrees of success to isolated 2-D bluff bodies of various cross-sections over a wide range of Reynolds number [3]. Collapse of the data is seen for bodies with both moveable and fixed separation points; with smooth and rough surfaces; with splitter plates and base bleed; in steady and confined flow; undergoing forced and free vibration; at pitch angle and yaw angle with the freestream; and through the subcritical, supercritical, and postcritical Reynolds number regimes [1–9].

Some groups of closely spaced bluff bodies immersed in cross-flow, such as a pair of circular cylinders, are also found to generate a single vortex street, depending on their proximity to one another [10,11]. Cylinder groups can be found in many practical applications, such as the designs for heat exchangers, cooling systems for nuclear power plants, offshore structures, buildings, chimneys, and power transmission lines, and therefore the relevance of the universal wake number concept to these configurations needs to be explored. If applicable, this would indicate that a single vortex wake generated by a group of bluff bodies is similar to that of a solitary bluff body.

The most general configuration of two circular cylinders, of equal diameter, D, immersed in a steady mean cross-flow of velocity, U, is known as the staggered arrangement (Fig. 1). Here, the cylinders are spaced at a center-to-center distance, P, and at an angle, α, to the oncoming mean flow. The flow pattern, vortex shedding frequency, and aerodynamic forces are highly sensitive to the combination of the nondimensional pitch ratio, P/D, and the incidence angle, α [11–15]. When these cylinders are closely spaced, $P/D<1.5$, their behavior is similar to that of a single bluff body, and a single vortex street is generated [11,14]. This behavior is illustrated schematically in Fig. 2, where a familiar Kármán vortex street forms in the combined wake of the cylinders in spite of the complexity of the flow close to and around the cylinders, which may include the actions of shear layer reattachment and base bleed. In the present study, closely spaced pairs of circular cylinders of equal diameter arranged in the staggered configuration are tested in the subcritical regime, and a suitable definition of the universal wake number is explored.

2 Experimental Approach

Experiments were conducted in a low-speed, closed-return wind tunnel, with a test-section of 0.91 m (height) ×1.13 m (width)×1.96 m (length). A ground plane was installed in the test section. The longitudinal freestream turbulence intensity was no greater than 0.6% and the freestream nonuniformity in the central portion of the test-section, outside the test-section-wall boundary layers, was no greater than 0.5%.

Two circular cylinders of equal diameter, $D=0.032$ m, were arranged in staggered configurations of $P/D=1.125$ and 1.25, similar to that adopted by [14–16]; see Fig. 3. Experiments were conducted in the subcritical Reynolds number range, Re=3

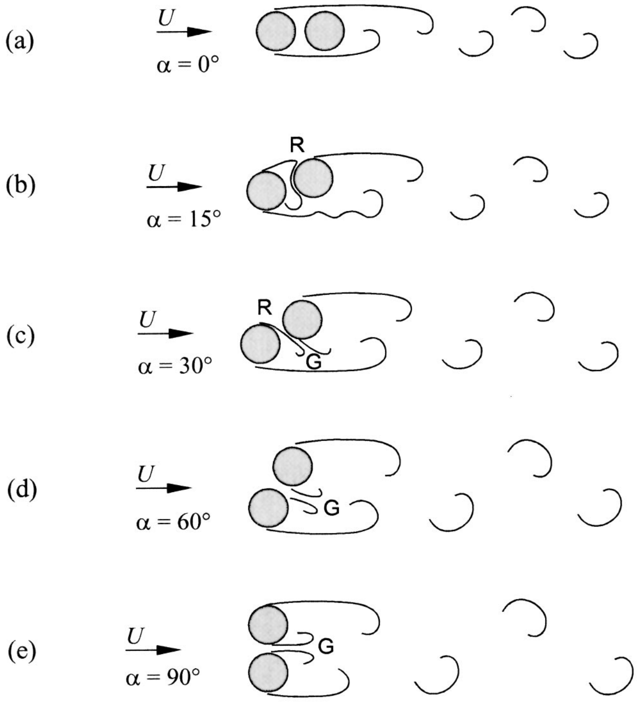

Fig. 2 Single bluff-body behavior of two closely spaced staggered circular cylinders of equal diameter: (*a*) tandem, α=0 deg; (*b*) α=15 deg; (*c*) α=30 deg; (*d*) α=60 deg; (*e*) side-by-side, α=90 deg, R=shear layer reattachment, G=gap flow.

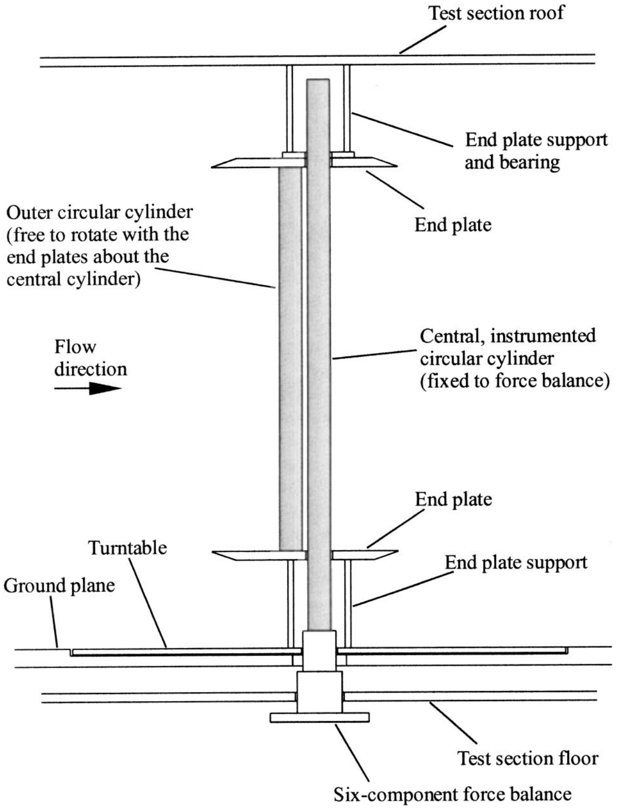

Fig. 3 Schematic of the experimental setup in the wind tunnel

$\times 10^4$–7×10^4. The first cylinder was mounted vertically from a six-component force balance located outside and below the wind tunnel test section (Fig. 3). The uncertainty in the mean aerodynamic force coefficients, C_L and C_D, was estimated at ±2% at $\mathrm{Re}=5\times 10^4$. This cylinder was centrally located in the test section and was instrumented with base static pressure taps along its span. The second cylinder was mounted between a pair of circular end plates, isolated from the force balance, and could be rotated in α about the central cylinder using a computer-controlled turntable embedded in the ground plane (Fig. 3). In this way, the central cylinder could represent either an upstream or downstream cylinder, over the full range of incidence angle, $\alpha=0$ deg–90 deg. The uncertainty in angular position was estimated at ±0.25°. With the end plates in position, the length of cylinder exposed to the flow was $L=0.563$ m, giving an aspect ratio of $\mathrm{AR}=L/D=17.6$ and a solid blockage ratio of 1.75% per cylinder.

Reference flow conditions were measured with a Pitot-static probe (United Sensor, 3.2-mm diameter) and Datametrics Barocell absolute and differential pressure transducers. Base pressure measurements on the central cylinder were obtained with a Validyne differential pressure transducer. The measurement uncertainty in the mean base pressure coefficient, C_{PB}, was estimated at ±1% at $\mathrm{Re}=5\times 10^4$. Data from the pressure transducers and the force balance were acquired with a Pentium II microcomputer, a National Instruments AT-MIO-64F-5 12-bit multifunction board and LabVIEW software. Vortex shedding frequencies were acquired with a TSI 1210-T1.5 single-component hot-wire probe, an IFA-100 anemometer, a National Instruments PCI-6024E data acquisition board, and the Virtual Bench Digital Signal Analyzer. Since the detection of a Strouhal number for the upstream cylinder is highly sensitive to the measurement location [11,13], the hot-wire probe was located at various positions to ensure the reliability and repeatability of the power spectra. The probe was typically positioned at $x/D=3.0$ and $y/D=1.0$ from the downstream cylinder, and at $x/D=3.0$ and $y/D=1.0$ from the upstream cylinder. The measurement uncertainty in St and the universal wake numbers, St* and G, was estimated at ±4% at $\mathrm{Re}=5\times 10^4$.

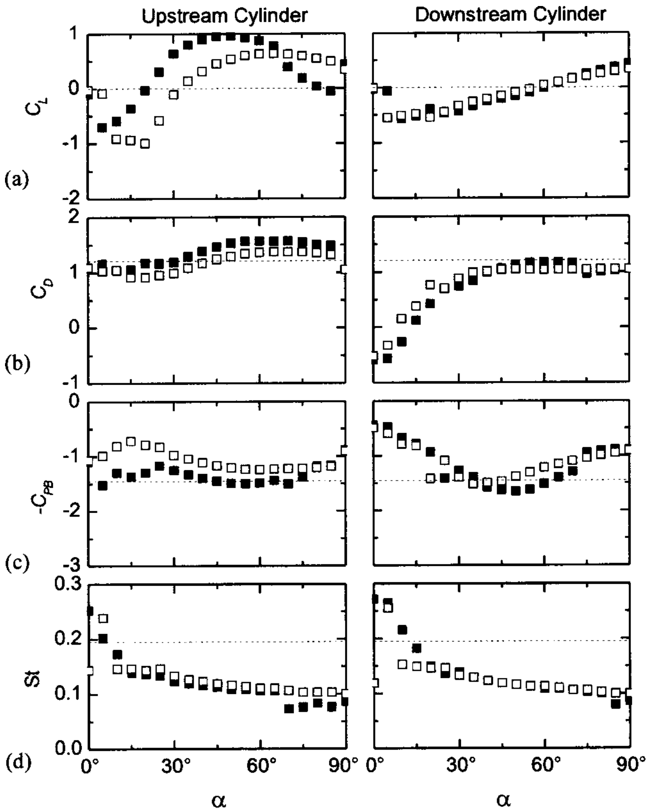

Fig. 4 Experimental data for two closely spaced staggered cylinders, $\mathrm{Re}=5\times 10^4$: (*a*) mean lift coefficient, uncertainty ±2%; (*b*) mean drag coefficient, uncertainty ±2%; (*c*) mean base pressure coefficient, uncertainty ±1%; (*d*) Strouhal number, uncertainty ±4% ■, $P/D=1.125$; □, $P/D=1.25$; -----, single cylinder.

3 Results and Discussion

The flow field for staggered configurations of $P/D=1.125$ and 1.25 is similar to a single bluff body for nearly the entire range of α, since the cylinders are situated very close to one another and the gap between them is small [11,14,16]. Kármán vortex shedding tends to occur from the cylinder group as a whole, rather than from the individual cylinders, and there is single Kármán vortex street in the combined wake. In a tandem configuration, $\alpha=0$ deg [Fig. 2(*a*)], the shear layers from the upstream cylinder wrap around and enclose the downstream cylinder. As the incidence angle is increased, $\alpha=15$ deg and 30 deg [Figs. 2(*b*,*c*)], the inner shear layer (closest to the flow centreline) from the upstream cylinder either wraps around, or reattaches onto, the downstream cylinder. At larger incidence angles, $\alpha=60$ deg [Fig. 2(*d*)], shear layer reattachment onto the downstream cylinder can no longer be maintained. Instead, some of the approach flow is directed through the gap between the cylinders and enters the near-wake region. This weak gap flow is similar to "base bleed," which refers to the injection of low-momentum fluid into the near-wake of a bluff body. In the side-by-side configuration, $\alpha=90$ deg [Fig. 2(*e*)], the two cylinders continue to behave as if a single bluff body with base bleed [10].

3.1 Behavior of the Experimental Data.

The aerodynamic force data, base pressure data, and Strouhal number data for $P/D=1.125$ and 1.25 are shown in Fig. 4. Here, an outward-directed lift force on a cylinder is considered positive, and an inward-directed lift force on a cylinder is considered negative (defined in Fig. 1). The behavior of the aerodynamic forces, base pressure, and Strouhal number with incidence angle are similar for the two pitch ratios. The data were found to be independent of the Reynolds number, similar to [14–16], and the results in Fig. 4 are shown for $\mathrm{Re}=5\times 10^4$ only.

The mean lift coefficient, C_L [Fig. 4(*a*)], for the upstream cylinder experiences large changes in magnitude and direction, which correspond to changes in the flow patterns [11,14,16]. The drag coefficient [Fig. 4(*b*)] of the upstream cylinder may be up to 30% higher (unfavorable) or 25% lower (favorable) than the value for a single circular cylinder, depending on the incidence angle. For the downstream cylinder, the shielding effect of the upstream cylinder causes its drag coefficient to be lower than the value for a single cylinder. At very small incidence angles, the shear layers from the upstream cylinder completely enclose the downstream cylinder [Fig. 2(*a*)], and the drag force on the downstream cylinder becomes negative, indicating that it experiences a thrust force. The behavior of the base pressure coefficient [Fig. 4(*c*)] tends to mirror that of the drag coefficient. The small increase in C_{PB} at high incidence angles is a result of the base-bleed effect of the weak gap flow between the cylinders.

The Strouhal number data [Fig. 4(*d*)] show that the same Strouhal number is measured behind the upstream and downstream cylinders, which indicates that a single vortex shedding process is present [11]. In staggered configurations with higher pitch ratios than in the present study, two distinct Strouhal numbers are measured at most incidence angles, where the cylinders no longer behave as if a single bluff body [11,13,15]. The Strouhal number generally remains lower than that of a single, isolated circular cylinder for nearly the entire range of α. The Strouhal number steadily decreases with α to a value of $\mathrm{St}\sim 0.1$ (one-half the vortex shedding frequency for an isolated circular cylinder). The lowering of the Strouhal number occurs as the near-wake region

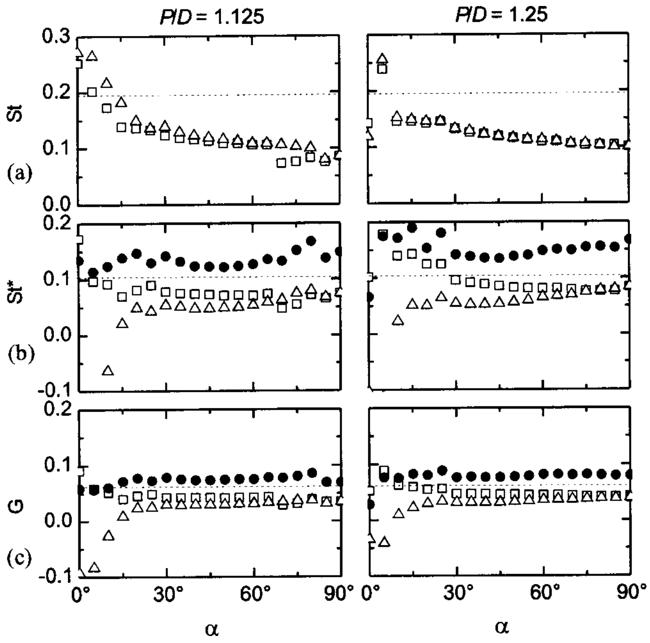

Fig. 5 Universal wake number data for two closely spaced staggered cylinders, Re=5×10⁴: (*a*) Strouhal number, uncertainty ±4%; (*b*) universal Strouhal number, uncertainty ±4%; (*c*) Griffin number, uncertainty ±4%. □, Upstream cylinder data only; △, downstream cylinder data only; ●, data for both cylinders together; - - - - -, single cylinder.

lengthens and widens with increasing α. In the nearly tandem configuration, $\alpha < 15$ deg, the Strouhal number is higher than the single-cylinder value. The high frequencies measured at small incidence angles are also found in the tandem configuration [17], and are caused by a shortening and narrowing of the near-wake region compared to the case of a single cylinder [11]. The small degree of scatter in the St data for $\alpha < 30$ deg, particularly for the upstream cylinder, is related to the dynamics of the shear layer reattachment process [15,16]. Coincidentally, at these smaller incidence angles, the peaks in the power spectra are smaller and more broad-banded [16]. At high incidence angles, there are discontinuous changes in C_L, C_D, C_{PB} and St, which are thought to be caused by changes in the strength and deflection angle of the base-bleed gap flow [14,16]. The power spectra for incidence angles near the discontinuity show two small vortex shedding peaks; this suggests that two base-bleed gap flow patterns may appear alternately, i.e. intermittently switch from one flow pattern to the other, on or about the critical incidence angle [16].

3.2 Universal Wake Numbers. The universal wake number data are presented in Fig. 5, where the Strouhal number data have been included, in Fig. 5(a), for comparison purposes. The results are mostly similar for the two pitch ratios, $P/D = 1.125$ and 1.25.

The cylinders comprising the staggered configuration were initially considered on an individual basis, as either an upstream or downstream cylinder, despite the fact that together they produce a single vortex street and have the same Strouhal number (Fig. 5(*a*)). Separate universal Strouhal numbers, St*, for the upstream and downstream cylinders were therefore calculated from Eq. (6) using each cylinder's individual data for C_D, C_{PB}, and St. A similar approach was followed to calculate the Griffin number, G, for each cylinder, using Eq. (8). The results for St* and G are shown as the open symbols in Figs. 5(*b*,*c*), respectively.

From Fig. 5(*b*), it is seen that the St* data become nearly pitch-angle independent for $\alpha > 30$ deg. In the side-by-side configuration, corresponding to $\alpha = 90$ deg (Fig. 2(*e*)), the wake data for both the upstream and downstream cylinders collapse to universal Strouhal numbers of $\mathrm{St}^* \approx 0.075$ and 0.084 for $P/D = 1.125$ and 1.25, respectively. These values at $\alpha = 90$ deg are 30% lower than the measured single-cylinder value of $\mathrm{St}^* = 0.104$ (shown by the dashed line in Fig. 5(*b*)) and the values are different for the two P/D ratios. For lower values of α, the upstream and downstream cylinder values of St* begin to diverge from one another and St* is not universal with the incidence angle. This is particularly evident for $\alpha < 30$ deg, where the St* data for the downstream cylinder become negative, which happens because this cylinder experiences a thrust force (Fig. 4(*b*)) in the nearly tandem configuration (Figs. 2(*a*,*b*)).

The Griffin number data in Fig. 5(*c*), calculated separately for the individual cylinders, collapse to a common Griffin number at $\alpha = 90$ deg of $\mathrm{G} \approx 0.035$ and 0.040 for $P/D = 1.125$ and 1.25, respectively. These values are more than 45% lower than the measured single-cylinder value of $\mathrm{G} = 0.062$ (shown by the dashed line in Fig. 5(*c*)) and different values are obtained for the two P/D ratios. However, as in the case of the St* data, the Griffin number data are not universal with the incidence angle, and G for the downstream cylinder becomes negative for $\alpha < 30$ deg.

The ineffectiveness of the universal wake numbers, particularly when the cylinders are nearly tandem, may be caused by the gap between the two cylinders. Nakamura [9] reported that the afterbody shape could have a strong influence on the base pressure, the interactions between the separated shear layers, and the flow in the vortex formation region, and therefore the universal Strouhal number. This was particularly evident for the contrasting cases of a H-section cylinder and two tandem normal flat plates (of similar geometry but without the horizontal bar joining the flat plates), which had different universal Strouhal numbers despite the similar geometry [9]. The behavior of the two nearly tandem circular cylinders in the present study, where the downstream cylinder is separated by a gap from the upstream cylinder, is similar.

A second approach was to consider the cylinders together as a single body rather than as separate upstream and downstream cylinders, which is more consistent with the actual fluid behavior. This was done by using the total drag force experienced by the cylinder group, the average base pressure coefficient of the two cylinders, and the Strouhal number data for the downstream cylinder, when calculating St* and G using Eqs. (6) and (8). (The choice of the Strouhal number data from the downstream cylinder was arbitrary, and was made for calculation purposes only, since the St data were essentially identical for the two cylinders, see Fig. 5(*a*).) The St* and G results for the single-body approach are shown as solid symbols in Figs. 5(*b*,*c*), respectively.

The universal Strouhal number data calculated using the single-body approach, Fig. 5(*b*), are improved for $\alpha < 30$, compared to the individual-cylinder approach, since St* remains positive. However, the St* data still vary considerably with α and P/D, and a universal value is not obtained. The Griffin number data, Fig. 5(*c*), calculated following the single-body approach are significantly improved over the individual-cylinder results, however. Average universal wake numbers of $\mathrm{G} = 0.073$ (10% standard deviation) and 0.077 (15% standard deviation) are obtained for $P/D = 1.125$ and 1.25, respectively, over the entire range of α. The close agreement of these values for the two pitch ratios suggests that the Griffin number is independent of P/D. These values of Griffin number are now within 25% of the measured single-cylinder value, indicating the vortex street wake of the closely spaced staggered cylinders is to some extent similar to that of single, isolated bluff bodies.

The overall effectiveness of the universal wake number depends on a finding a suitable definition for the base pressure measurement [5], one which represents the combined wake of the staggered cylinders and is consistent with the semi-empirical definition of the wake width, D', in Eq. (5). In the present study, the greatest improvement in the collapse of the data was obtained by using the average base pressure coefficient of the two cylinders. This approach is most reasonable when the cylinders are nearly side-by-side, at higher incidence angles [Figs. 2(*d*,*e*)], considering that the base regions of the two cylinders are completely open to the near-wake region. This approach is less satisfactory from a physical standpoint when the cylinders are nearly tandem, at low incidence angles (Figs. 2(*a*,*b*)), since the base pressure for the upstream cylinder is more a measure of the pressure in the interstitial region (or gap) between the cylinders rather than the wake. However, using the base pressure from the downstream cylinder only (as opposed to the average of the two cylinders), which is the one most closely associated with the wake at all α, was less effective (results not shown).

Interestingly, it is found that the product of the Griffin number and the inverse of the pitch ratio, $\mathrm{G}(P/D)^{-1}$, improves the agreement with the single-cylinder value, with $\mathrm{G}(P/D)^{-1}=0.065$ (10% standard deviation) and 0.062 (15% standard deviation) for $P/D=1.125$ and 1.25, respectively, over the entire range of α. These values are within 0.5% of the measured single-cylinder value for the Griffin number. The use of the center-to-center pitch ratio, P/D, to improve the collapse of the universal wake number data indicates that the mechanism of vortex formation from a cylinder group, even when the cylinders are closely spaced, has some small but fundamental differences compared to the case of a single, isolated bluff body.

4 Conclusions

The flow around two closely spaced circular cylinders of equal diameter arranged in a staggered configuration behaves in a manner similar to a single bluff body. When the cylinders are closely spaced as such, periodic alternate vortex shedding occurs from the cylinder group rather than from the individual cylinders, and a single vortex street is found in the wake. This behavior suggested that the universal wake number concept might be suitable for such a flow. Wind tunnel experiments were conducted for staggered cylinder groups with dimensionless pitch ratios of $P/D=1.125$ and 1.25 for the complete range of incidence angle, $\alpha=0$ deg–90 deg, in the subcritical Reynolds number regime. Measurements of the mean aerodynamic forces, base pressure, and Strouhal number were obtained for each cylinder. By considering the cylinders as a single body, using the total drag force acting on the cylinders and the average base pressure coefficient of the two cylinders, the Griffin number was found to be an effective universal wake number for two closely spaced staggered circular cylinders, with an average value of $\mathrm{G}=0.073$ (standard deviation of 15%) for the data from the two pitch ratios. This value is within 25% of the measured single-cylinder value of $\mathrm{G}=0.062$. The results imply that the vortex wake developing behind a group of ylinders is, to some extent, similar to that of a single bluff body. In addition, there exists the potential for the universal wake number concept to be extended from single bluff bodies to groups of closely spaced bluff bodies.

Acknowledgments

The support of the Natural Sciences and Engineering Research Council (NSERC) of Canada is gratefully acknowledged. The assistance of O. O. Akosile, D. Deutscher, J. L. Heseltine, M. D. Richards, and the staff of Engineering Shops is greatly appreciated.

References

[1] Roshko, A., 1955, "On the wake and drag of bluff bodies," J. Aero. Sci., **22**, pp. 124–132.
[2] Bearman, P. W., 1967, "On vortex street wakes," J. Fluid Mech., **28**, pp. 625–641.
[3] Griffin, O. M., 1981, "Universal similarity in the wakes of stationary and vibrating bluff structures," ASME J. Fluids Eng., **103**, pp. 52–58.
[4] Griffin, O. M., 1978, "A universal Strouhal number for the 'locking-on' of vortex shedding to the vibrations of bluff cylinders," J. Fluid Mech., **85**, pp. 591–606.
[5] Buresti, G., 1983, "Appraisal of universal wake numbers from data for roughened circular cylinders," ASME J. Fluids Eng., **105**, pp. 464–468.
[6] Adachi, T., Ozaki, T., Yamamoto, T., Eguchi, Y., Matsuuchi, K., and Kawai, T., 1996, "Study of the universal Strouhal number over the wide Reynolds number flow range (effect of surface roughness)," JSME Int. J., **39**(2), pp. 335–342.
[7] Adachi, T., 1997, "Effects of surface roughness on the universal Strouhal number over the wide Reynolds number range," J. Wind. Eng. Ind. Aerodyn., **69–71**, pp. 399–412.
[8] Chen, J. M., and Fang, Y.-C., 1996, "Strouhal numbers of inclined flat plates," J. Wind. Eng. Ind. Aerodyn., **61**, pp. 99–112.
[9] Nakamura, Y., 1996, "Vortex shedding from bluff bodies and a universal Strouhal number," J. Fluids Struct., **10**, pp. 159–171.
[10] Sumner, D., Wong, S. S. T., Price, S. J., and Païdoussis, M. P., 1999, "Fluid behavior of side-by-side circular cylinders in steady cross-flow," J. Fluids Struct., **13**, pp. 309–338.
[11] Sumner, D., Price, S. J., and Païdoussis, M. P., 2000, "Flow-pattern identification for two staggered circular cylinders in cross-flow," J. Fluid Mech., **411**, pp. 263–303.
[12] Zdravkovich,, M. M. and Pridden, D. L., 1977, "Interference between two circular cylinders; series of unexpected discontinuities," J. Ind. Aerodyn., **2**, pp. 255–270.
[13] Kiya, M., Arie, M., Tamura, H., and Mori, H., 1980, "Vortex shedding from two circular cylinders in staggered arrangement," ASME J. Fluids Eng., **102**, pp. 166–173.
[14] Sumner, D., and Richards, M. D., 2002, "A closer investigation of the mean aerodynamic forces for two staggered circular cylinders in cross-flow," Proceedings of the 5th International Symposium on Fluid-Structure Interactions, Aeroelasticity, Flow-Induced Vibration & Noise, New Orleans, USA, Paper No. IMECE2002-32179, New York: ASME.
[15] Sumner, D., and Richards, M. D., 2003, "Some vortex-shedding characteristics of the staggered configuration of circular cylinders," J. Fluids Struct., **17**, pp. 345–350.
[16] Akosile, O. O., and Sumner, D., 2003, "Staggered circular cylinders immersed in a uniform planar shear flow," J. Fluids Struct., **18,** pp. 613–633.
[17] Ljungkrona, L., Norberg, C., and Sundén, B., 1991, "Free-stream turbulence and tube spacing effects on surface pressure fluctuations for two tubes in an in-line arrangement," J. Fluids Struct., **5**, pp. 701–727.

The Effect of Wake Passing on a Flow Separation in a Low-Pressure Turbine Cascade

Michael J. Brear
Department of Mechanical and
Manufacturing Engineering,
University of Melbourne, Australia
e-mail: mjbrear@unimelb.edu.au

Howard P. Hodson
Whittle Laboratory
Engineering Department,
Cambridge University, UK
e-mail: hph@eng.cam.ac.uk

This paper describes an investigation into the effect that passing wakes have on a separation bubble that exists on the pressure surface and near the leading edge of a low-pressure turbine blade. Previous experimental studies have shown that the behavior of this separation is strongly incidence dependent and that it responds to its disturbance environment. The results presented in this paper examine the effect of wake passing in greater detail. Two-dimensional, Reynolds averaged, numerical predictions are first used to examine qualitatively the unsteady interaction between the wakes and the separation bubble. The separation is predicted to consist of spanwise vortices whose development is in phase with the wake passing. However, comparison with experiments shows that the numerical predictions exaggerate the coherence of these vortices and also overpredict the time-averaged length of the separation. Nonetheless, experiments strongly suggest that the predicted phase locking of the vortices in the separation onto the wake passing is physical. [DOI: 10.1115/1.1667884]

Introduction

Brear et al. [1] discussed that the design of modern aircraft engines often involves manipulation of the blade surface boundary layers through the exploitation of the engine's disturbance environment. This is done to sustain or improve the engine performance whilst reducing its weight and/or cost. For example, upstream blade rows shed wakes that cause a periodic forcing of the boundary layers on downstream blades. Several low-pressure turbine designs have exploited this phenomenon to achieve improvements in performance [2,3].

This study examines the effect of wake passing on a separation that exists on the pressure surface and near the leading edge of a current, low-pressure turbine blade. Two dimensional, Reynolds averaged numerical predictions are first used to study the interaction between passing wakes and the separation. These predictions are then compared to experiments, and while both sets of results do not agree in all respects, a complex interaction between the passing wakes and the separation is seen in both cases.

Experimental and Numerical Methods

All experiments were performed in low speed, open return wind tunnels at the Whittle Laboratory, Cambridge University. The blade, cascade and tunnel studied in this paper is the same as that studied in Brear et al. [1]. A ''moving bar cascade'' consisting of seven turbine blades (Fig. 1*a* and Table 1), was used and is discussed in more detail in Brear [4]. Wakes shed from an upstream blade row were simulated by circular bars of 2 mm diameter that translated circumferentially along a plane located 50% C_X upstream of the cascade leading edge. All results presented in this paper were performed at a cascade exit Reynolds number Re_2 of 130,000, which is representative of cruise conditions for this blade.

The 2 mm bar diameter and axial location was shown by Howell et al. [3] to generate wakes that are a reasonable representation of those inside the low-pressure turbine. Specifically, Howell et al. [3] showed that bars of the stated diameter produced wakes with a profile loss and peak velocity deficit that were very similar to the those shed by a real upstream blade row. While this is not an exact replication of the true wakes, the simulated wakes are reasonable for the present study because the wake passing frequency and root mean square (RMS) intensity of the wakes appear to be the characteristics that primarily determine the nature of the interaction between the wakes and the separation.

The blade shown in Fig. 1*a* is based on a 50% reaction design. The ''reduced frequency'' of the wake passing is a nondimensional frequency that is defined as

$$\bar{f} \equiv \frac{fC}{V_2} = \frac{C}{\phi s_{BAR}} \cos \alpha_2 = \frac{C}{s_{BAR}} \cos \alpha_2 (\tan \alpha_2 - \tan \alpha_1). \quad (1)$$

On a given blade with set inlet angle (i.e., blade incidence) and exit angle, the reduced frequency is essentially an indicator of the pitch of the upstream blade row. A low-speed, one-and-a-half stage, low-pressure turbine with the blade shown in Fig. 1*a* as its mid-span section and engine representative blade counts was studied in the Whittle Laboratory previously and had a reduced frequency of 0.62 for the stators and 1.29 for the rotors. Neither of these values could be matched exactly on the moving bar cascade because of geometry constraints, and a datum value of 0.58 was chosen for the experiments. Given that the highest and lowest values of the reduced frequency studied were 1.16 and 0.29, respectively, and that the main conclusions of this paper are largely independent of the reduced frequency, this datum value was considered suitable for more detailed investigation.

The hot-wire measurements were performed with ''Dantec 55P15,'' single sensor, streamwise normal hot wires, and related Dantec equipment. In order to resolve events within the wake passing cycle, ensemble averaging over a number of wake passing periods was also performed. The ensemble averaged mean velocity was defined as

$$\tilde{u}_j = \frac{1}{M} \sum_{i=1}^{M} u_{i,j} \, , \quad (2)$$

where M is the number of ensembles and $u_{i,j}$ is the velocity at instant j of ensemble i. The ensemble averaged, RMS velocity was therefore

$$\tilde{u}_{j,RMS} = \sqrt{\frac{1}{M} \sum_{i=1}^{M} (u_{i,j} - \tilde{u}_j)^2}, \quad (3)$$

as opposed to the more usual, RMS velocity

Contributed by the Fluids Engineering Division for publication in the JOURNAL OF FLUIDS ENGINEERING. Manuscript received by the Fluids Engineering Division March 4, 2003; revised manuscript received October 30, 2003. Associate Editor: W. W. Copenhaver.

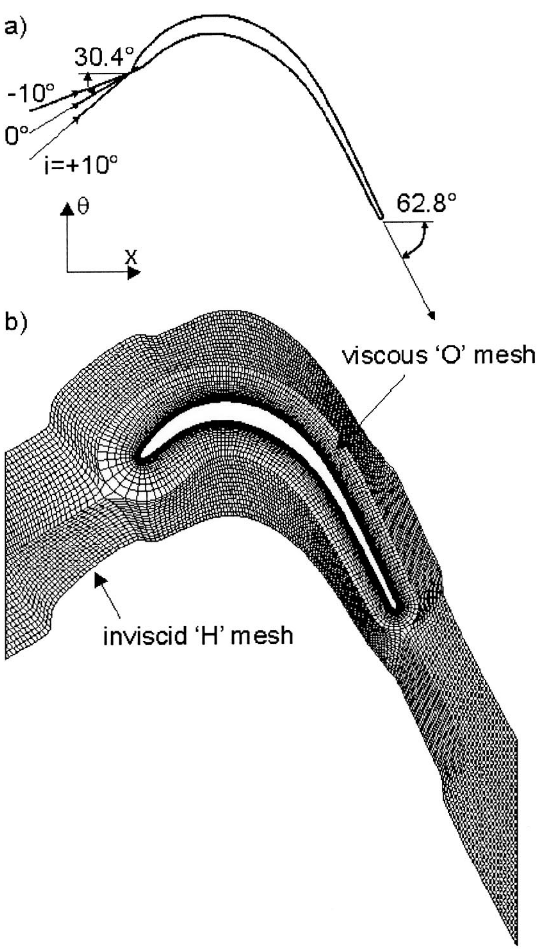

Fig. 1 ***a*) The low-pressure turbine blade and *b*) the 'Unsflo' computational mesh**

$$u_{RMS}=\sqrt{\frac{1}{N}\sum_{j=1}^{N}(u_j-\overline{u})^2}, \tag{4}$$

where N is the number of samples and $\overline{u}$ is the mean velocity.

All results were sampled at a logging frequency of 25 kHz, with a low pass filter set at a 10 kHz cutoff frequency. The ensemble averaged results consisted of 100 ensembles of 4096 samples. The entire pressure surface flow was mapped out with 19 circumferential traverses from 95% to 5% C_X along the pressure surface in 5% C_X increments and a further traverse at 1% C_X. All traverses extended 0.1 mm circumferentially above the pressure surface to one third of the blade pitch. Details of the calibration procedure are given in Brear [4]. Including hot-wire positioning and regular calibration, a complete set of ensemble averaged measurements took approximately 9–10 hours of continual experimentation. Further increases in the number of ensembles was not considered practical, and the results presented are of sufficient quality for the arguments put forward in this paper.

Table 1 Parameters of the cascade blade

chord, C (mm)	148.3
axial chord, C_x (mm)	126.8
pitch, s (mm)	103.8
span, h (mm)	375
inlet flow angle at $i=0$ deg, α_1 (deg)	30.4
exit flow angle, α_2 (deg)	62.8

The limitations in the accuracy of a stationary hot wire in a recirculating flow are acknowledged. However, the complexity of the geometry under investigation as well as the proximity of the separated shear layer to the blade surface in some cases made measurements with flying hot wires or lasers just as, or even more, problematic. Nonetheless, likely systematic errors should be kept in mind when interpreting RMS velocity fluctuations quantitatively. Kiya & Sasaki [5] found that stationary hotwire measurements can significantly overpredict the streamwise velocity fluctuations in separation bubbles by as much as 30% of the local mean velocity at the center of the separated shear layer. It is nonetheless emphasised that these main sources of error are systematic, and the repeatability of the RMS velocities was found to be within $\pm 0.01\ V_2$.

The surface static pressure was measured at 43 points around the blade with a 'Scanivalve' pressure switch and a Druck PDCR-22 differential pressure transducer of ±35 mbar range. The uncertainty of V/V_2 was estimated to be ±0.02.

The smoke wire visualizations were performed with a length of resistance wire placed upstream of the cascade. This wire was coated with a heavy automotive oil and was then subjected to a DC voltage. A light sheet generated by a 1 kW halogen lamp illuminated the midspan section of the cascade, allowing images to be captured by a Kodak Ektapro, high-speed digital video camera, placed outside an endwall viewing port.

The numerical predictions were performed with a 2-D solver named 'Unsflo'. Unsflo is a coupled solver which solves the Euler equations in a H mesh further from the blade surface, and the Reynolds averaged, thin shear layer equations in an 'O' mesh surrounding the blade (Fig. 1*b*). In this investigation, the single blade passage predictions were performed at a cascade exit Mach number of 0.2 in order to accelerate convergence and used a *k*-*l* turbulence model and fourth order smoothing. The surface normal extent of the O mesh was carefully chosen to contain the separation bubble and had 200 points around the blade surface and 30 points normal to the blade surface. The first point in the viscous mesh was always less than 2 wall units away from the blade surface. The inviscid, H mesh had 200 streamwise and 30 pitchwise points. Mesh independence was defined as occurring if the time averaged reattachment point of the separation bubble was unchanged with further mesh refinement. This was achieved with the mesh shown in Fig. 1*b*. Whilst the difficulties in using two dimensional, Reynolds averaged solvers in unsteady separated flows are acknowledged, they can give reasonable results, although their shortcomings are well documented [6]. Further details of Unsflo are contained in Giles & Haimes [7] and Brear [4].

Both steady inflow and wake passing conditions were studied in the numerical predictions. For the wake passing cases, the incoming wakes were Gaussian in shape and defined to have the same peak velocity deficit and width as the measured wake of the blade shown in Fig. 1*a*. It is also noted that the reduced frequency was 0.89 for all the numerical predictions presented in this paper. This value arises when the pitch of the upstream blade row is the same as the pitch of the bladerow under investigation, and was chosen so that only one blade passage needed to be modeled, thus minimizing the required computational effort. Whilst not presented, numerical predictions performed at half (0.44) and twice (1.78) the reduced frequency revealed the same basic interaction between the wakes and the separation. This is in keeping with the trends seen in experiments discussed earlier, which suggests that the choice of a reduced frequency of 0.89 for further investigation was also reasonable.

Discussion

Figure 2 shows a comparison between the measured and predicted isentropic velocity distributions around the blade *under steady inflow conditions*. The experimental and unsteady (time accurate) numerical results agree closely, except in the region from the leading edge to roughly 50%C_X on the pressure surface,

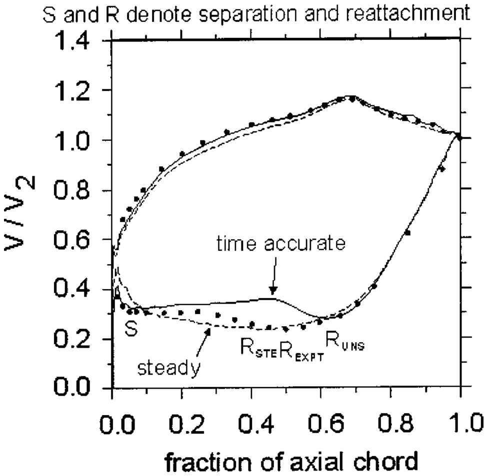

Fig. 2 Isentropic velocity distribution from experiment and timed averaged numerical predictions for steady inflow and $i=0$ deg (S and R denote separation and reattachment points respectively)

which is the region occupied by the flow separation studied in this paper. By comparing the isentropic velocity distributions with surface flow visualization and hot-wire measurements, Brear et al. [1,8] showed that the local minimum in isentropic velocity occurs at the time-averaged reattachment point of the separation R_{EXPT}. Thus, the unsteady numerical predictions can be seen to significantly overpredict the axial length of the separation with steady inflow (Table 2). Figure 2 also shows the isentropic velocity distribution for a steady prediction, where 'steady' is taken to mean that the time-step at each cell varies, and depends on the local velocity. Thus, with the same steady inflow boundary condition, the steady prediction shows reattachment at 40%C_X, compared to the unsteady predictions in Table 2. This illustrates the strong time dependence of the equations of motion within this region.

The difference between the steady and unsteady predictions on the suction surface prior to peak isentropic velocity in Fig. 2 is thought to be due to blockage effects of the separation. Since the steady prediction produces a significantly smaller separation, the velocities outside the separation will be smaller than those for the larger separation produced by the unsteady numerical predictions, for a given mass-flow through the blade passage.

Figure 3 shows contours of entropy coefficient ξ_S at an arbitrary instant during the unsteady prediction with steady inflow. The entropy coefficient is defined as:

$$\zeta_s=\frac{2T_0(s-s_{ref})}{V_2^2}, \tag{5}$$

where the reference entropy s_{ref} for this quantity is defined along the uniform inlet boundary of the computational domain. Since entropy is a passive scalar when no entropy generation is occurring [9], Fig. 3 shows both the generation of significant levels of entropy within the separation in addition to the entropy transport. The instantaneous streamlines in Fig. 3 show two counter-clockwise vortices (center critical points) separated by a saddle critical point [10]. A third vortex with clock-wise sense exists closer to the blade surface. Animations of this instantaneous streamline structure show that the separation periodically produces a pair of vortices of opposing sense. This behavior is shown more clearly when wake passing is included later in this paper; the larger, counter-clockwise vortex merges with that immediately downstream of it, whilst the clockwise vortex lifts off the surface as it dissipates.

Table 2 Time averaged axial location of reattachment from experiments and unsteady numerical predictions for $i=0$ deg

inlet boundary condition	reattachment (x/C_x)	
	expt.	pred.
steady inflow	0.5	0.61
wake passing	0.4	0.61

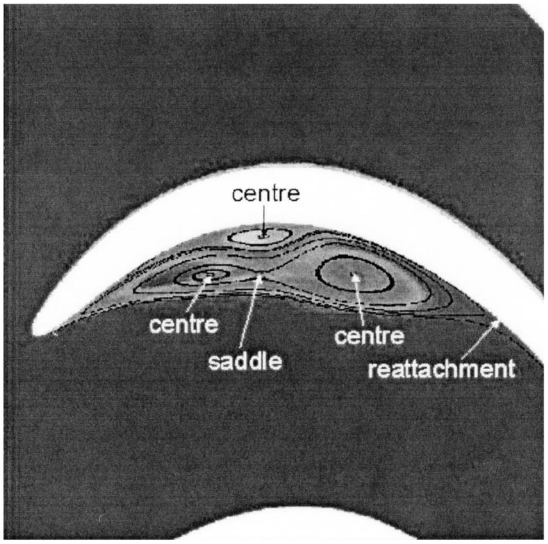

Fig. 3 Instantaneous entropy coefficient and instantaneous streamlines from unsteady predictions with steady inflow and $i=0$ deg (scale as in Fig. 6)

The instantaneous streamline structure would therefore seem to be in partial agreement with the topology of a shedding separation bubble put forward by Theofilis et al. [11], as well as a number of 2-D numerical studies [12–14]. These other investigations all observed a periodic growth of vortices of both senses that are transported downstream as they decay. This is in contrast to the present *numerical* predictions, where the vortices are not observed to shed downstream of the separation. Rather, the counter-clockwise vortices are seen to continuously merge, although the reason for this is only speculated upon. These other, cited studies of two-dimensional separation bubbles featured the flow downstream of the separation relaxing to a zero pressure gradient. In a manner that is possibly analogous to two dimensional cavity flows [15], the turning of the blade in the present study causes the flow to accelerate strongly towards the trailing edge, and perhaps captures vortices shed from the separation rather than letting them convect downstream. Certainly, separated flows cannot exist in regions of favorable pressure gradient such as that seen downstream of reattachment in Fig. 2, and this lack of shedding was also observed when other, or no, turbulence models were used. Thus, the present geometry could modify the behavior of the separation from that observed in other, more simplified geometries. However, Alam & Sandham [12] also warn that 2-D simulations of separation bubbles are likely to exaggerate the coherence of these vortices both within the separation and downstream of reattachment. Since this is consistent with the isentropic velocity distributions in Fig. 2 and the smoke-wire visualizations presented later, the numerical predictions presented should therefore be treated with some caution.

Experiments confirm that the periodic growth of spanwise vortices is physically reasonable behavior although, as expected, the numerical predictions appear to exaggerate it. Figure 4 shows that the smoke wire visualization at 0° incidence reveals a strongly unsteady separated region, in which large coherent vortices such as those seen in the numerical predictions are not observed. How-

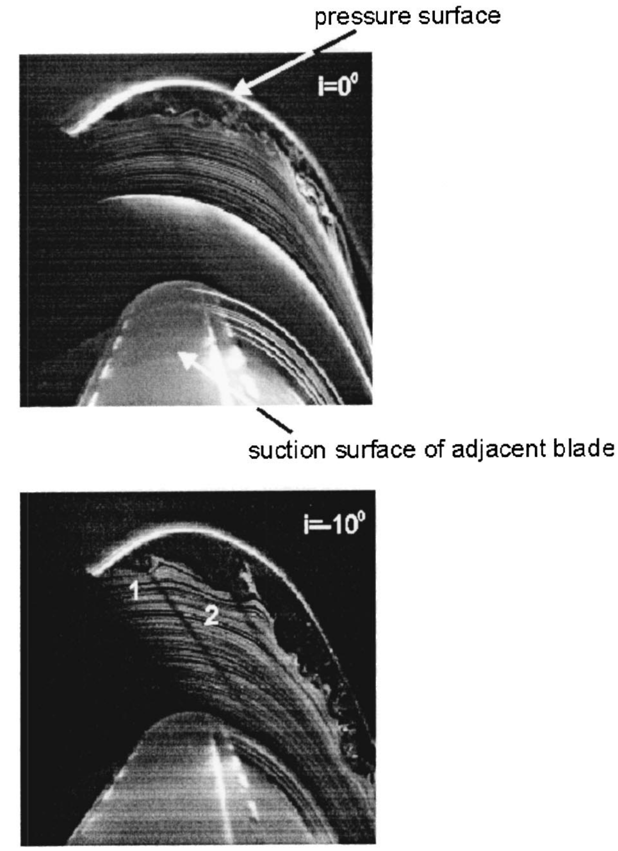

Fig. 4 Smoke-wire flow visualization of the separation at 0 deg and −10 deg incidence under steady inflow

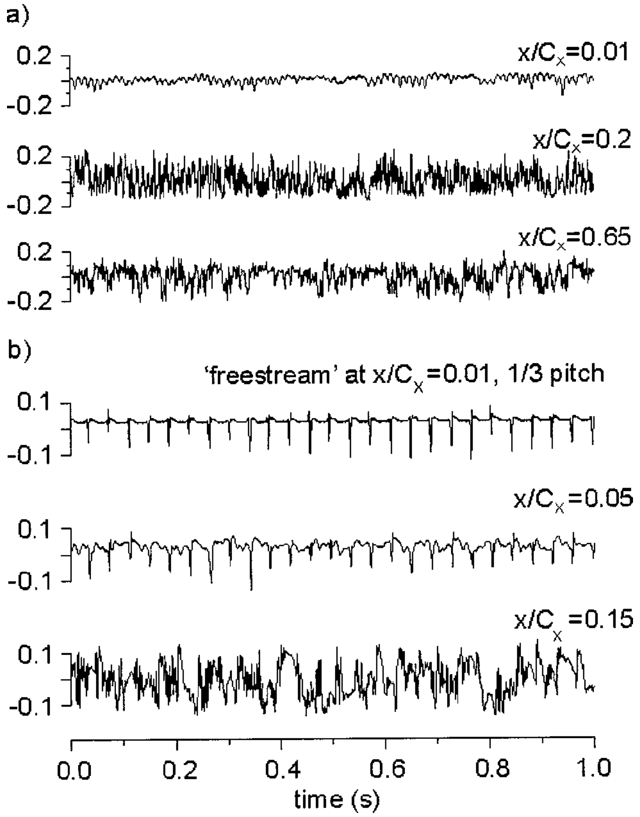

Fig. 5 Measured time traces of $(u_{RAW}-\bar{u})/V_2$ along the center of the separated shear layer for *a*) $i=-10$ deg, steady inflow and *b*) $i=0$ deg, $\bar{f}=0.29$

ever, Fig. 4 also suggests that the separation at −10 deg incidence features periodic formation and convection of large, spanwise vortices (labeled 1 and 2). This behavior is in keeping with the shedding, 2-D separations discussed earlier, and suggests that a significant change in the dynamics of the separation occurs between 0 deg and −10 deg incidence in the experiments.

Contours of entropy can also be considered smoke-like by considering again the passive scalar behavior of entropy in the absence of entropy generation. The smoke-wire visualization at −10 deg incidence in Fig. 4 then perhaps shows some qualitative similarities to the contours of entropy in Fig. 3 at 0 deg incidence, excepting that the smoke is generated outside of the bladerow whereas the entropy is generated within the shear layers. In both cases, the quantity in question appears to wrap around the spanwise counter-clockwise vortices as they travel downstream. It therefore appears that the numerical predictions are correct in so far as they do not show any shedding of large vortices at 0 deg incidence. However, as discussed earlier, they are incorrect in that they exaggerate the size and coherence of these vortices within the separation.

The frequency of formation of these vortices in the smoke wire visualization at −10 deg incidence corresponds to that seen in the hot-wire trace at the same incidence and $1\%C_X$ in Fig. 5*a*. Thus, the separation at −10 deg incidence has a clear, natural frequency that is observed in both the smoke-wire visualizations and the hot-wire traces. As Brear et al. [1] showed, hot-wire measurements at 0 deg incidence and +10 deg incidence also showed that the separation had a natural frequency (Table 3) but, as Fig. 4 showed, they lacked the clear vortices in the smoke wire visualizations. Thus, hot-wire results suggest that the separated flow transition is characterized first by the growth and then breakdown of these spanwise vortices. However, as the incidence becomes more positive, the smoke-wire visualizations suggest that these vortices appear to loose their coherence more quickly. Thus, as Alam & Sandham [12] argued, a 2-D, numerical prediction that cannot model this inherently three dimensional phenomenon will most likely exaggerate the streamwise extent of these spanwise vortices.

Figure 6 shows predicted contours of the entropy coefficient at equally spaced instants during a wake passing cycle. The reference entropy s_{ref} for these contours is defined as occurring midway between two wakes at the inlet boundary of the computational domain. Figure 6 shows the mainly inviscid distortion of the wakes shed from the simulated upstream bladerow as they are transported through this bladerow. This behavior is qualitatively similar to that of several other studies [16,17], and also shows that the wakes extend into the region occupied by the separation bubble under investigation.

Figure 6 also illustrates the predicted interaction between the separation and the wakes during one wake passing period *T*. At time t=0, the separation can be seen to consist of three structures; counter-clockwise vortices 1 and 3 are separated by the clockwise vortex 2. As time progresses past instants t=*T*/4 and t=*T*/2, vortex 2 can be seen to draw away from the pressure surface and become smaller whilst vortex 3 grows in size and moves towards

Table 3 Shear layer and wake passing frequencies at 0 deg incidence from experiments and unsteady numerical predictions

	expt.	pred.
Unforced, shear layer freq. (Hz)	87	75
Wake passing freq. (Hz)	52 ($\bar{f}=0.58$)	80 ($\bar{f}=0.89$)

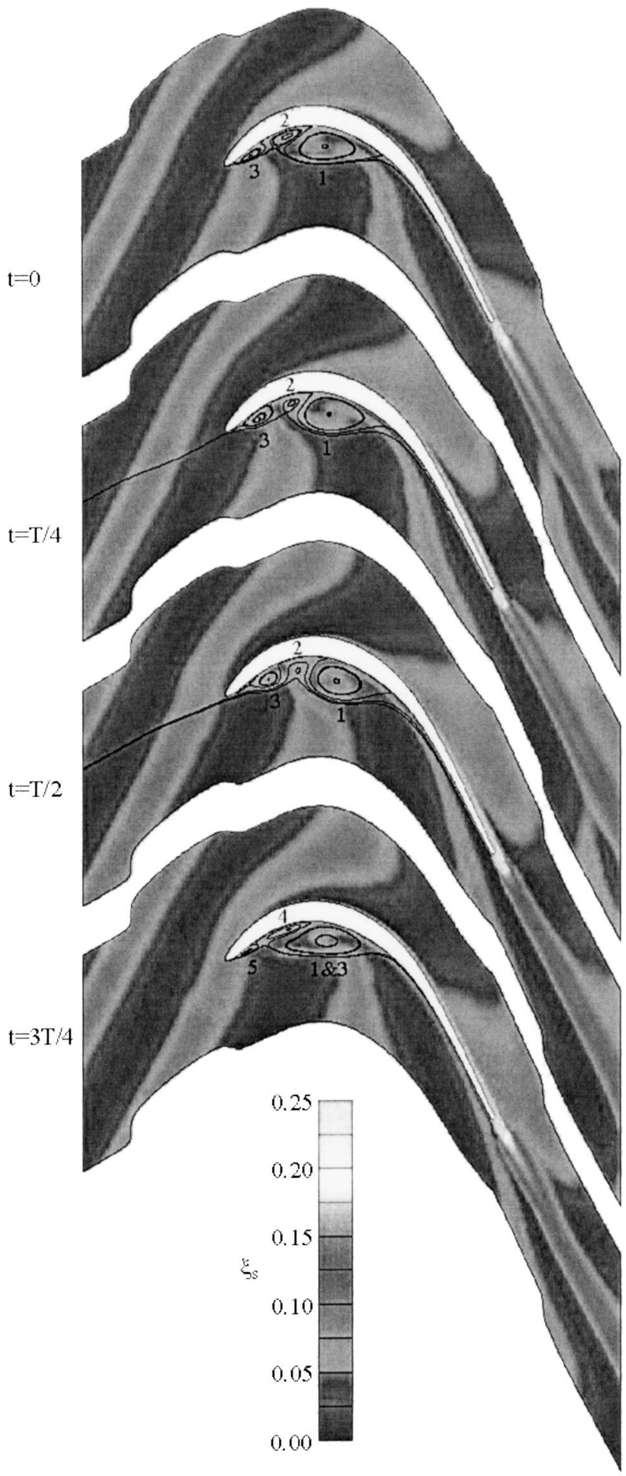

Fig. 6 Predicted instantaneous streamlines superimposed onto contours of entropy coefficient ($\bar{f}=0.89, i=0$ deg)

vortex 1. By t$=3T/4$, vortex 2 has disappeared, vortices 1 and 3 have merged into a single counter-clockwise vortex and two new structures, clockwise vortex 4 and counter-clockwise vortex 5, have also formed. The separation at t$=3T/4$ is therefore similar to that at t$=0$, illustrating that this overall behavior is periodic and in phase with the wake passing.

A comparison of the instantaneous streamlines with the vorticity field reveals the origin of each of these vortices. Figure 7 shows that at t$=0$, counter-clockwise vortices 1 and 3 contain mainly positive vorticity. As expected, this is vorticity of the same sense as the boundary layer downstream of reattachment. However, there must also be vorticity of opposite sense next to the blade surface because of the no-slip condition. The clockwise vortex 2 originates from this region. Importantly, the separated flow structure in Figs. 6 and 7 is the same as that shown in Fig. 3 for steady inflow. Thus, wake passing is predicted to only modulate the separation's structure rather than fundamentally change it.

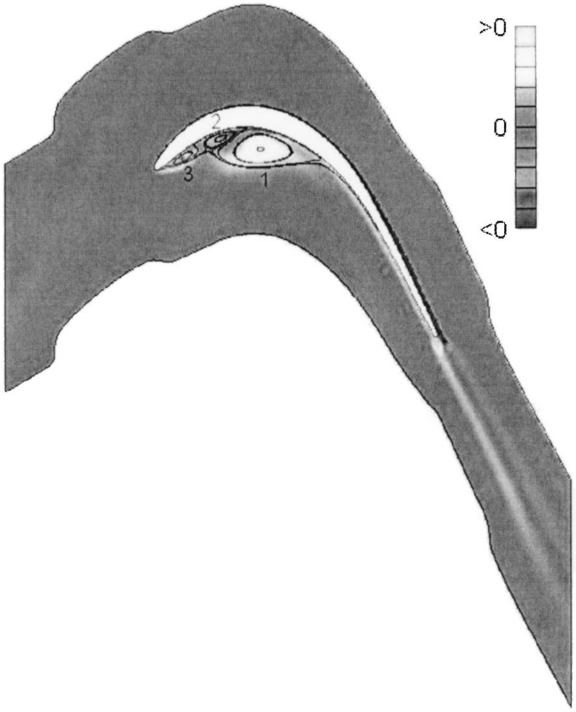

Fig. 7 Predicted contours of vorticity with instantaneous streamlines superimposed at t$=0$ ($\bar{f}=0.89, i=0$ deg)

Figure 8 shows that in experiments, the separation bubble with steady inflow exhibits a peak in u_{RMS} some distance away from the blade surface. As Brear et al. [1] showed, this peak in u_{RMS} always occurred at the inflection point of the mean velocity profile, and which will therefore be defined as the center of the separated shear layer in this paper.

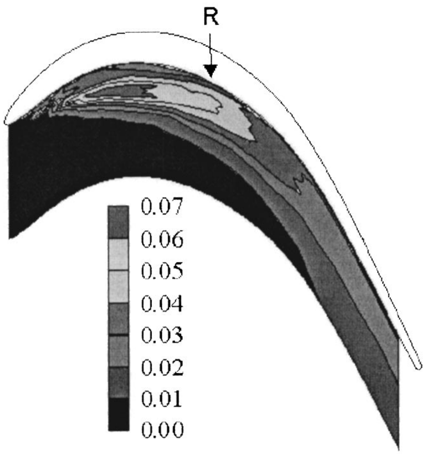

Fig. 8 Measured contours of u_{RMS}/V_2 at $i=0$ deg and steady inflow

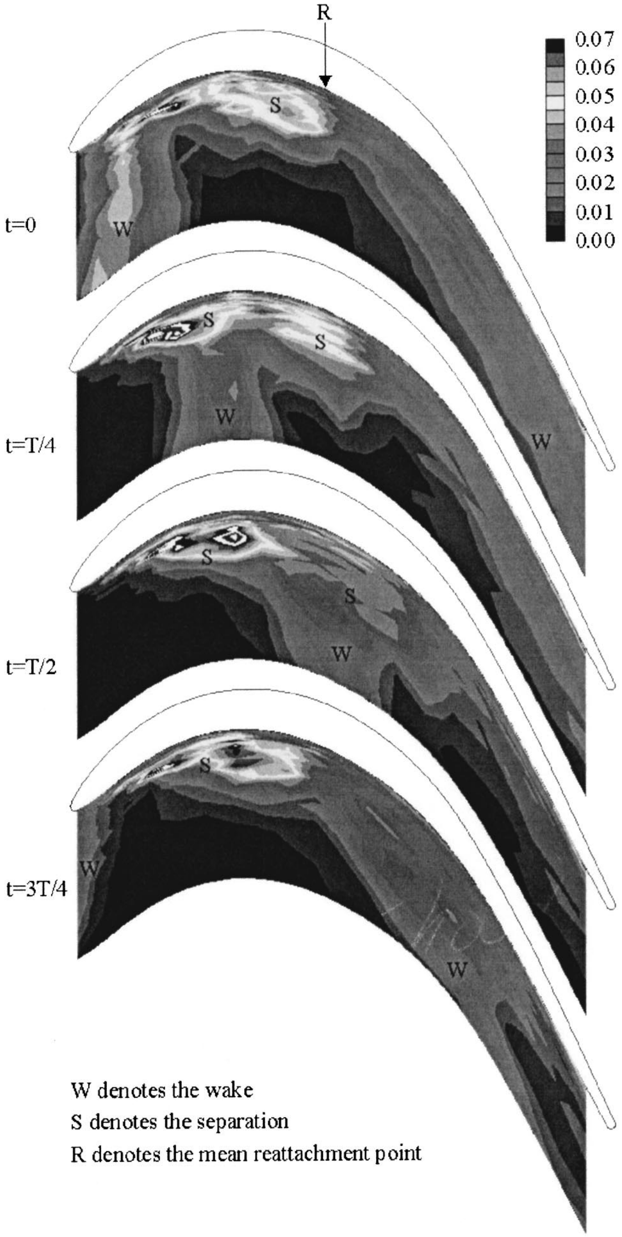

Fig. 9 Measured contours of $\tilde{u}_{RMS}/V_2$ during one wake passing period ($\bar{f}=0.58, i=0$ deg)

In comparison to u_{RMS}, contours of $\tilde{u}_{RMS}$ quantify the unsteadiness that is not in phase with the wake passing. Since the wake is turbulent, it should be observable with this quantity since it should contain a range of scales that will not be in phase with the wake passing. The separation bubble should also be identifiable from contours of $\tilde{u}_{RMS}$. At 0 deg incidence, Fig. 8 suggests a rapid transition under steady inflow, and the smoke-wire visualizations in Fig. 4 suggested unsteadiness of a range of scales once transition has begun. Figure 9 therefore shows two structures identified by these means: the wake (W) and the separation (S). Assuming the validity of identifying the wakes and separation in this way, the separation can be seen to respond to the wake passing. At $t=0$, the separation can be seen to exist between two wakes. By $t=T/4$, the separation seems to have broken into two regions which lie either side of the passing wake. These two portions of the separation are transported downstream. By $t=T/2$, the structure furthest downstream has merged with a wake. By $t=3T/4$, the region which lay behind the wake at $t=T/4$ has grown considerably and begins to resemble the separation at $t=0$. The overall process is therefore in phase with the wake passing.

The numerical predictions discussed earlier showed that the large vortices of counter-clockwise sense behaved in a qualitatively similar manner to the structures labeled *S* in Fig. 9. This may suggest that the structures labeled *S* in Fig. 9 can be identified as counter-clockwise vortices that are shed from the separation, although it is emphasised that in a real, turbulent flow, a single, large vortex such as those observed in the Reynolds averaged numerical predictions is unlikely to occur. Instead, a highly 3-D flow such as that suggested by the smoke-wire visualizations in Fig. 4 is expected. Thus, when identifying the structures labeled *S* as vortices, it should be kept in mind that ensemble averaging only shows the phase averaged behavior. For a strongly turbulent flow such as in the present example, the ensemble averaged picture can be quite different to the instantaneous behavior.

Examination of individual time traces further illustrates the response of the separated shear layer to wake passing. Figure 5*b* shows clearly that the shear layer at the separation point (5% C_X) responds to the wake passing at the lowest wake passing frequency studied. Similar behavior was also observed at reduced frequencies of 0.58 and 1.16. This is perhaps not surprising since the wake passing frequency is of the same order of magnitude as the natural frequency (87 Hz) of the separation bubble under steady inflow at 0 deg incidence (Table 3). The wake passing frequency can be seen in traces further along the separated shear layer in Fig. 5*b*, together with a range of other scales. If transition of the separated shear layer is characterized by the initial growth and breakdown of spanwise vortices, the effect of wake passing in the present study appears to have an analogous effect to that of strong, acoustic forcing of separations in some other studies. Several authors have observed that acoustic waves of appropriate frequency can lock the phase of the formation of spanwise vortices in separated shear layers, and encourage their growth [18,19,15].

Brear et al. [1] showed that wake passing excited stronger unsteadiness in the separated shear layer, and that this had the effect of reducing the time-averaged length of the separation (Table 2). At the inlet to the cascade, the measured RMS intensities of the freestream disturbance caused by the wake passing were $u_{RMS}/V_1=4.0\%$, 5.9% and 7.3% at reduced frequencies of 0.29, 0.58 and 1.16, respectively. These levels of unsteadiness can reasonably be considered strong levels of forcing, and it was therefore argued that the wake passing provided strong forcing of the unstable, separated shear layer, thereby causing earlier transition. In keeping with numerous studies of the response of laminar separation bubbles to freestream disturbances, the separation was therefore observed to become smaller [20].

It is also noted that the numerical predictions found that wake passing had little effect on the time-averaged length of the separation (Table 2). This further exposes the limitations of the numerical predictions. Whilst the causes of this discrepancy are not definitely known, there are several non-physical aspects of the wake modelling that may be involved. Since the wakes convect into the computational domain through an inviscidly modelled region (Fig. 1*b*), the wakes do not contain any turbulent viscosity. This is compared to the wakes observed in experiment in Fig. 9, which contain *non-phase locked* unsteadiness that is of similar intensity to that which is generated by the separated shear layer. Thus, the wakes in the numerical predictions are only a large amplitude, periodic disturbance to the separation, unlike the experiments where smaller, aperiodic disturbances will also exist. Of course, the two-dimensionality of the numerical predictions is also expected to have a significant effect, since any modelling of an inherently 3-D transition of the separated flow is ignored.

It should also be kept in mind that this study used a linear cascade. Whilst this is common practice in turbomachinery research, use of the linear cascade ignores certain effects that are present in the real engine, the most significant of which are ex-

Table 4 Shear layer natural frequency and mean reattachment point from Brear et al. [1] (steady inflow)

i (deg)	shear layer frequency (Hz)	mean reattachment location (x/C_x)
−10	90	0.4
0	87	0.5
+10	83	0.65

pected to be centrifugal forces and the radial pressure gradient. Table 4 shows results from Brear et al. [1] in which the incidence of the blade was varied, causing large changes in the separation size. It is expected that most thin, solid low pressure turbine blades will feature separations on the pressure surface with a size within these limits at design conditions. Interestingly, there is only a relatively small change in the separated shear layer's natural frequency over the range of incidences studied. As stated earlier, the phase locking of the separation onto the wake occurred over the range of reduced frequencies from 0.29 (26 Hz) to 1.16 (103 Hz). Since the separation frequency was found not to vary greatly over a wide range of separation sizes, and phase locking occurred over a broad range of wake passing frequencies, phase locking is therefore expected to occur in the real engine if the use of a linear cascade is reasonable. Of course, further studies of full engine geometries are required to verify this.

Conclusions

This paper showed that the wakes shed from a simulated, upstream bladerow excited periodic behavior in a separation that existed on the pressure surface and near the leading edge of a low pressure turbine blade. This excitation was suggested to occur because the wake passing frequencies studied in both the numerical predictions and experiments were similar to the unforced, natural frequency of the separation observed under steady inflow conditions.

Two-dimensional, Reynolds averaged, numerical predictions were first used to examine the unsteady interaction between the wakes and the separation bubble. The separation was predicted to consist of spanwise vortices whose development was in phase with the wake passing. However, comparison with experiments showed that the numerical predictions exaggerate the streamwise extent of these vortices and significantly overpredict the time-averaged length of the separation. It was also found that the numerical predictions showed that wakes had little effect in changing the time-averaged length of the separation, when previous experiments showed that wakes reduced the separation length. Nonetheless, the numerical predictions agreed with experiments in showing that the separation bubble 'locked on' to the periodic excitation provided by the wake over the wide range of wake passing frequencies that are likely to occur in an engine.

Acknowledgments

The authors would like to thank Rolls-Royce, plc and the Defense Evaluation and Research Agency (MOD and DTI CARAD) for their financial support.

Nomenclature

C = chord (m)
C_X = axial chord (m)
$C_P = (P_{01} - P)/(P_{01} - P_{02})$ = static pressure coefficient
$\bar{f} = fC/V_2$ = reduced frequency of bars
i = incidence (deg)
P = pressure (Pa)
R = reattachment point
$\mathrm{Re}_2 = V_2 C/\nu$ = cascade exit Reynolds number
S = separation point
s = entropy (J/kg.K)
s = pitch (m)
T = temperature (K)
$\bar{T}$ = wake passing period (s)
$\bar{u}$ = mean velocity (m/s)
u_{RAW} = raw velocity (m/s)
u_{RMS} = RMS velocity (m/s)
$\tilde{u}_{RMS}$ = ensemble averaged RMS velocity (m/s)
U = blade speed (m/s)
$V = V_2\sqrt{C_P}$ = isentropic velocity (m/s)
V_X = axial velocity (m/s)
α = blade flow angle (deg)
ζ_s = entropy coefficient
$\phi = V_X/U$ = flow coefficient

Subscripts

0 = stagnation
1 = cascade inlet
2 = cascade exit
BAR = upstream bars (i.e., simulated upstream blade row)
$EXPT$ = experimental result
STE = steady numerical prediction
UNS = unsteady (time accurate) numerical prediction

References

[1] Brear, M. J., Hodson, H. P., and Harvey, N. W., 2002, "Pressure surface separations in low pressure turbines-part 1: midspan behavior," ASME J. Turbomach., **124**, pp. 393–401.
[2] Halstead, D. E., Wisler, D. C., Okiishi, T. H., Walker, G. J., Hodson, H. P., and Shin, H. W., 1997, "Boundary layer development in axial flow compressors and turbines: part 1 of 4-composite picture," ASME J. Turbomach., **119**, pp. 114–127.
[3] Howell, R. J., Ramesh, O. N., Hodson, H. P., Harvey, N. W., and Schulte, V., 1999, "High lift and aft loaded profiles for low pressure turbines," ASME paper no. 2000-GT-261.
[4] Brear, M. J., 2000, "Pressure surface separations in low pressure turbines," Ph.D. dissertation, University of Cambridge.
[5] Kiya, M., and Sasaki, K., 1983, "Structure of a turbulent separation bubble," J. Fluid Mech., **137**, pp. 83–113.
[6] Lubcke, H., Schmidt, St., Rung, T., and Thiele, F., 2001, "Comparison of LES and RANS in bluff-body flows," J. Wind. Eng. Ind. Aerodyn., **89**, pp. 1471–1485.
[7] Giles, M., and Haimes, R., 1995, "Unsflo user's manual, version 6.0," MIT Computational Aerospace Sciences Laboratory.
[8] Brear, M. J., Hodson, H. P., Gonzalez, P., and Harvey, N. W., 2002, "Pressure surface separations in low pressure turbines-part 2: interactions with the secondary flow," ASME J. Turbomach., **124**, pp. 402–409.
[9] Denton, J. D., 1993, "Loss mechanisms in turbomachines," ASME J. Turbomach., **115**, pp. 621–656.
[10] Chong, M. S., Perry, A. E., and Cantwell, B. J., 1990, "A general classification of three-dimensional flow fields," Phys. Fluids, **2**(5), pp. 765–777.
[11] Theofilis, V., Hein, S., and Dallmann, U., 2000, "On the origins of unsteadiness and three-dimensionality in a laminar separation bubble," Philos. Trans. R. Soc. London, Ser. A **358**, pp. 3229–3246.
[12] Alam, M., and Sandham, N. D., 2000, "Direct numerical simulation of 'short' laminar separation bubbles with turbulent reattachment," J. Fluid Mech., **410**, pp. 1–28.
[13] Ghosh Chaudhuri, P., and Knight, D. D., 1994, "Two-dimensional unsteady leading-edge separation on a pitching airfoil," AIAA J., **32**(4), p. 673–681.
[14] Ripley, M. D., and Pauley, L. L., 1993, "The unsteady structure of two-dimensional separation," Phys. Fluids A, **5**, pp. 3099–3106.
[15] Rowley, C. W., Colonius, T., and Basu, A. J., 2002, "On self-sustained oscillations in two-dimensional compressible flow over rectangular cavities," J. Fluid Mech., **455**, pp. 315–346.
[16] Dorney, D. J., Filtan, H. C., Ashpis, D. E., and Solomon, W. J., 2000, "Effects of blade count on boundary layer development in a low-pressure turbine," AIAA paper, no. AIAA 2000-0742.
[17] Hodson, H. P., 1984, "An inviscid blade-to-blade prediction of a wake-generated unsteady flow," ASME paper no. 84-GT-43.
[18] Freymuth, P., 1966, "On transition in a separated laminar boundary layer," J. Fluid Mech., **25**, part 4, pp. 683–784.
[19] Niew, T. R., 1993, "The stability of the flow in a laminar separation bubble," Ph.D. dissertation, University of Cambridge.
[20] Gad-el-Hak, M., 1990, "Control of low speed aerodynamics," AIAA J., **28**(9), pp. 1537–1552.

Qiang Zhang
Convective Heat Transfer Laboratory,
Department of Mechanical Engineering,
University of Utah, Salt Lake City,
Utah 84112-9208 USA

Sang Woo Lee
School of Mechanical Engineering,
Kumoh National Institute of Technology, Gumi,
Gyongbook 730-701 Korea

Phillip M. Ligrani*
Convective Heat Transfer Laboratory,
Department of Mechanical Engineering,
University of Utah, Salt Lake City,
Utah 84112-9208 USA

Effects of Surface Roughness and Turbulence Intensity on the Aerodynamic Losses Produced by the Suction Surface of a Simulated Turbine Airfoil

The effects of surface roughness on the aerodynamic performance of turbine airfoils are investigated with different inlet turbulence intensity levels of 0.9%, 5.5% and 16.2%. Three symmetric airfoils, each with the same shape and exterior dimensions, are employed with different rough surfaces. The nonuniform, irregular, 3-D roughness is characterized using the equivalent sand grain roughness size. Mach numbers along the airfoil range from 0.4 to 0.7. Chord Reynolds numbers based on inlet and exit flow conditions are 0.54×10^6 *and* 1.02×10^6*, respectively. The contributions of varying surface roughness and turbulence intensity level to aerodynamic losses, Mach number profiles, normalized kinetic energy profiles, and Integrated Aerodynamics Losses (IAL) are quantified. Results show that effects of changing the surface roughness condition on IAL values are substantial, whereas the effects of different inlet turbulence intensity levels are generally relatively small.* [DOI: 10.1115/1.1667886]

Introduction

The overall efficiency and operational behavior of aero-engines, as well as gas turbine engines used for utility power generation, are greatly influenced by the surface finish of the rotor and stator blades contained in the turbine. In many cases, these surfaces are roughened because of the manufacturing methods employed. During operation, the roughness of the test surfaces often then increases because of corrosion, erosion, particulate deposition, and spallation. Here, the effects of such surface roughness on the aerodynamic losses produced by a turbine airfoil, operating in a compressible, high-speed environment, are considered at different freestream turbulence levels.

The influences of surface roughness on adjacent flow behavior has been of interest for researchers for almost 100 years. The use of equivalent sandgrain roughness size, k_s, to characterize and quantify rough surfaces was first proposed and utilized by Nikuradse [1] and Schlichting [2]. This quantity represents the size of sand grains which give the same skin friction coefficients in internal passages as the roughness being evaluated. This measure of roughness size continues to be used widely in empirical correlation equations (which are based on experimental data) to represent rough surface behavior, and for closure models employed in a variety of numerical prediction codes. Coleman et al. [3] later re-evaluated Schlichting's [2] surface roughness experiments by using more accurate and physically plausible assumptions in the analysis of the original experimental data. These investigators then utilized the corrected results to determine skin friction coefficients, $C_f/2$, and magnitudes of equivalent sand grain roughness, k_s. Sigal and Danberg [4,5] made additional important advances in accounting for roughness geometry considerations for uniformly shaped roughness elements spread in a uniform pattern over a test surface. For this type of "2-D roughness," the authors provide equations for the dependence of the ratio of equivalent sand grain roughness to mean roughness height, k_s/k, upon a roughness parameter, Λ_s, which is determined from roughness geometry.

Bons et al. [6] present measurements of detailed surface roughness characteristics from a wide variety of in-service turbine blades and vanes. Different surface degradation mechanisms are evaluated and related to three-dimensional maps of the different rough surfaces which are evaluated. Van Rij et al. [7] give a modified version of the Sigal and Danberg correlation for the dependence of k_s/k on Λ_s for randomly-placed, non-uniform, 3-D roughness with irregular geometry and arrangement. Also described are analytic procedures for determination of roughness height k and Λ_s from roughness geometry. With this approach, magnitudes of equivalent sandgrain roughness size k_s are determined entirely from 3-D roughness geometry. The investigators verify the results, and analytic procedures employed, using: (i) experimental results obtained with the same type of 3-D roughness, and (ii) analytic descriptions of the geometry of uniformly shaped roughness elements arranged in a regular pattern on the test surface.

In a paper published in 1975, Bammert and Sandstede [8] describe the influences of different manufacturing tolerances and turbine airfoil surface roughness characteristics on the overall performance of turbines. Particular attention is devoted to the effects of these parameters on efficiency, relative mass flow, enthalpy drop, and outlet flow angle. Later work by the same authors [9] considers the effects of the surface roughness on the boundary layer development along blades arranged in a stationary cascade. Momentum thicknesses are as much as three times values measured on smooth airfoils in regions of decelerating flow. Kind et al. [10] investigate the effects of partial roughness coverage of the blade surfaces by measuring pressure distributions, profile losses, and the flow deviations produced by a planar turbine cascade. Different roughness heights, and different roughness element spacings are considered. According to the authors, the largest profile loss increases are produced by roughness located on the suction surface. Bogard et al. [11] analyze the surface roughness characteristics of turbine vanes that have undergone a significant number of hours of operation. Flat plate surfaces with cone

---

*Corresponding author.

Contributed by the Fluids Engineering Division for publication in the JOURNAL OF FLUIDS ENGINEERING. Manuscript received by the Fluids Engineering Division May 6, 2003; revised manuscript received October 30, 2003. Associate Editor: W. W. Copenhaver.

shaped elements are used to simulate the roughness which is present on vane surfaces. According to the authors, the effects of surface roughness and high free-stream turbulence are additive along flat plates, and can produce heat transfer rate increases that are as much as 100% greater than smooth surface values. Abuaf et al. [12] quantify heat transfer and aerodynamics performance characteristics of turbine airfoils with different surface finish treatments. Experimental results show that tumbling and polishing reduce the average roughness size and improve overall performance. The authors also employ a Reynolds analogy to determine skin friction coefficients, drag forces, and aerodynamic efficiencies from airfoil surface heat transfer data. Leipold et al. [13] employ a compressor cascade to investigate the influences of surface roughness at different inlet flow angles and Reynolds numbers. The investigators indicate that surface roughness has no effect upon the presence or location of laminar separation, and that the roughness causes the turbulent boundary layer to separate at high Reynolds numbers. In addition, the roughness appears to have much larger effect for positive incidence angles than for negative incidence angles. Guo et al. [14] report on the influences of localized pin-shaped surface roughness on heat transfer and aerodynamic performance of a fully film-cooled engine aerofoil. When located on the downstream part of the suction surface, the pins do not produce any reduction of airfoil aerodynamic efficiency, however, substantial loss increases are present when the pins are located on the pressure side of the airfoil.

Of the investigations which also examine the effects of augmented free-stream turbulence levels, Gregory-Smith and Cleak [15] show that the mean flow field is not affected significantly by inlet turbulence intensity levels as high as 5%. Variations of the different Reynolds stress tensor components and spectra are given for different cascade locations, which show important changes near the endwall from augmented mainstream turbulence levels. Hoffs et al. [16] investigate heat transfer on a turbine airfoil with different surface roughness characteristics at different Reynolds numbers, with turbulence intensity levels as high as 10%. The authors indicate that measured leading heat transfer distributions agree with correlations, provided the turbulence length scale is taken into account. Giel et al. [17] employ an active blowing grid of square bars to produce a turbulent intensity and length scale of 10% and 22 mm, respectively, at the entrance of a transonic cascade. Heat transfer results are given along a turbine airfoil, which show the effect of strong secondary flows, laminar-to-turbulent transition, and variations near the stagnation line. Boyle et al. [18] provide turbine vane aerodynamic data at low Reynolds numbers made at midspan locations downstream of a linear cascade with inlet turbulence intensity levels as high as 10%. Nix et al. [19] describe the development of a grid which produces freestream turbulence characteristics of the flow exiting the combustor of advanced gas turbine engines. Intensities as high as 12% are produced using the device, with length scales of about 20 mm.

In a study of aerodynamic losses downstream of subsonic turbine airfoil with no film cooling, Ames and Plesniak [20] demonstrate important connections between wake growth and the level of free-stream turbulence. Wake mixing and eddy diffusivity magnitudes, in particular, are altered by different levels of freestream turbulence. Jouini et al. [21] present detailed measurements of midspan aerodynamics performance characteristics of a transonic turbine cascade at off-design conditions. Measurements of blade loading, exit flow angles, and trailing edge base pressures at different Mach numbers show that profile losses at transonic conditions are closely related to base pressure behavior. Radomsky and Thole [22] present measurements of time-averaged velocity components and Reynolds stresses along a turbine stator vane at elevated free-stream turbulence levels. As the freestream turbulence level increases, transition occurs farther upstream on the suction side, with increased velocity fluctuations near the pressure side. Boyle et al. [23] provide aerodynamic data for a linear turbine vane cascade, including surface pressure distributions and aerodynamic losses for different Reynolds numbers, Mach numbers, and levels of inlet turbulence.

The present study focuses on the effects of surface roughness and increased freestream turbulence levels on aerodynamics losses downstream of airfoils in compressible, high-speed subsonic flow. The present study is different from the other investigations mentioned because the combined effects turbulence and roughness are considered as they affect aerodynamic performance. Three symmetric airfoils are employed, with different rough surfaces which are characterized using equivalent sandgrain roughness size. Magnitudes of equivalent sandgrain roughness size for each surface are determined using 3-D optical profilometry data, and procedures described by van Rij et al. [7]. The magnitudes of longitudinal turbulence intensity used at the inlet of the test section are 0.9%, 5.5%, and 16.2%, where the latter values are produced using a mesh grid and cross bars, respectively. The contributions of roughness and inlet turbulence levels to local total pressure losses, local kinetic energy distributions, local Mach number distributions, and Integrated Aerodynamic Losses are described.

Experimental Apparatus and Procedures

Transonic Wind Tunnel (TWT). The University of Utah Transonic Wind Tunnel (or TWT) produces Mach numbers, pressure variations, Reynolds numbers, passage mass flow rates, and scaled physical dimensions which match values along airfoils in operating aero-engines and in gas turbines used for utility power generation. The TWT blow-down type facility consists of two main parts: (i) compressor and storage tanks, and (ii) wind tunnel. The wind tunnel consists of five major sub-sections: (i) flow rate and pressure level management apparatus, (ii) plenum tank, (iii) inlet ducting and test section, (iv) plenum, exit ducting, and ejector, and (v) control panel. More detailed descriptions are provided by Jackson et al. [24] and Furukawa and Ligrani [25].

A Gardner Denver Co. model RL-1155-CB compressor is used to pressurize the array of eight tanks whose total volume is 11.9 m^3. The operating pressure of these supply tanks is about 2.2 MPa. A VanAir VAS93039 model D16-5 Deliquescent desiccant dryer, a Pall Corp. 5EHG-4882-207 oil filter, and two Permanent Filter Corp. No. 13846 particulate filters are located just downstream of the compressor to remove particulates and moisture from the air. A Fisher pressure regulator with a 6X4 EWT design sliding gate valve, a Fisher type 667 diaphragm actuator, a 3582 series valve positioner, and a Powers 535 1/4 DIN process controller are used to regulate the pressure in the facility as the storage tanks discharge. A plenum tank, a 30.48 cm inner diameter pipe, a circular-to-square transition duct, a nozzle, and the test section then follow the pressure regulator.

Relative humidity at the test section inlet is typically 20%–30%. The test section is connected to a large 92.71 cm by 91.44 cm by 91.44 cm plenum with a square rubber flange at its outlet. The plenum diffuses high speed air from the test section exit into a reservoir of low velocity air. This plenum is then connected to two ducts which are subsequently connected to the atmosphere.

Pressure and Temperature Measurements. As tests are conducted, Validyne Model DP15-46 pressure transducers (with diaphragms rated at either 345 kPa or 1380 kPa), and calibrated copper-constantan thermocouples are used to sense pressures and temperatures at different locations throughout the facility. Signals from the transducers are processed by Celesco Model CD10D carrier demodulators. All pressure transducer measurement circuits are calibrated using a Wallace and Tiernan FA145 bourdon tube pressure gage as a standard. A United Sensor PLC-8-KL pitot-static probe with an attached copper-constantan thermocouple, and a four-hole conical-tipped pressure probe with an attached copper-constantan thermocouple are used to sense total pressure, static pressure, and recovery temperature at the inlet and exit of the test section, respectively, during each blow down. Mach numbers, sonic velocities, total temperatures, and static temperatures are determined from these data. The conical probe is aligned using two yaw ports placed on either side of the probe. As a blow down is underway, the probe is located one chord length downstream of the airfoil. It is traversed using a two-axis traversing sled with two Superior Electric M092-FF-206 synchronous stepper motors, connected to a Superior Electric Model SS2000I programmable motion controller and a Superior Electric Model SS2000D6 driver. Commands for the operation of the motion controller are provided by LABVIEW 6.1 software and pass though a serial port after they originate in a Dell Precision 530 PC work station.

Voltages from the carrier demodulators and thermocouples are read sequentially using Hewlett-Packard HP44222T and HP44222A relay multiplexer card assemblies, installed in a Hewlett-Packard HP3497A low-speed Data Acquisition/Control Unit. This system provides thermocouple compensation electronically such that voltages for type T thermocouples are given relative to 0°C. The voltage outputs from this unit are acquired by the Dell Precision 530 PC workstation through its USB port, using LABVIEW 6.1 software and a GPIB-USB-B adaptor made by National Instruments.

Test Section and Test Airfoil

Test Section. A schematic diagram of the non-turning airfoil cascade test section is shown in Fig. 1. The inlet of the test section is 12.70 cm by 12.70 cm. The test section is made up of two acrylic side walls, and top and bottom walls made of steel and acrylic. The two side walls are flat, whereas the top and bottom walls are contoured to form a converging-diverging shape which produces the desired Mach number distribution along the symmetric test airfoil. Because significant flow turning is not included, the camber curvature, present in many cascades with multiple airfoils, is not present.

The present test section is useful and advantageous over cascade arrangements with multiple airfoils and significant flow turning because: (i) the test section produces Mach numbers, pressure variations, Reynolds numbers, passage mass flow rates, and physical dimensions which match values along airfoils in operating engines, (ii) the airfoil provides the same suction surface boundary layer development (in the same pressure gradient without flow turning) as exists in operating engines, (iii) aerodynamic loss data are obtained on airfoil surfaces without the complicating influences of vortices present near airfoil leading edges, in the blade passages, and along airfoil pressure surfaces, (iv) only one airfoil is needed to obtain representative flow characteristics, and (v) the entire airfoil surface is accessible to optical, surface temperature measurement schemes such as infrared thermography (results from which are reported elsewhere). Thus, the present experiment is designed to isolate the effects of surface roughness and turbulence intensity on wake aerodynamic losses, while matching Reynolds numbers, Mach numbers, pressure gradients, passage flow rates, boundary layer development, and physical dimensions of airfoils in operating engines.

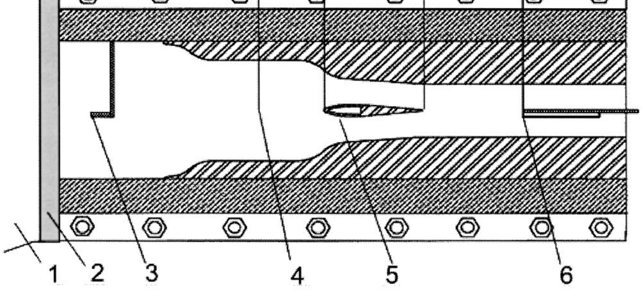

Fig. 1 Schematic diagram of the test section

Augmenting Mainstream Flow Turbulence Levels. Three different arrangements are used at the inlet of the test section to produce three different levels of mainstream turbulence intensity: (i) no grid or bars, (ii) fine mesh grid, and (iii) cross bars. The fine mesh grid consists of an array of 4 square rods arranged horizontally and 4 square rods arranged vertically. Each rod is spaced 25.4 mm from adjacent rods, and is 5 mm on each side. The open area amounts to 48% of the inlet area. The bar device consists of two parallel bars, where each is 25.4 mm in width, with 25.4 mm spacing from the adjacent bar, and 25.4 mm spacing from the top and bottom walls of the inlet duct. The open area amounts to 60% of the inlet area.

Longitudinal Turbulence Intensity Measurements. A single, horizontal-type platinum-plated tungsten hot-wire sensor, with a diameter of 12.7 μm and a length of 2.54 mm, is employed to measure the time varying longitudinal component of velocity at the inlet of the test section. The time-averaged longitudinal velocity, longitudinal turbulence intensity, and turbulence length scale are then determined from these measurements. The mount for the hot-wire probe is attached to an airfoil, which is employed only for this purpose. With this arrangement, the hot-wire sensor is located 6.6 cm (or 87% of one chord length) upstream of the airfoil leading edge. This position is then 16.9 cm downstream the turbulence generator. The vertical position of the probe, relative to the airfoil centerline, is adjustable so that the spatial uniformity of the flow can be checked at this streamwise location.

The hot-wire probe is driven by a Disa 55M10 constant-temperature hot-wire anemometer bridge with an overheat ratio of 1.6. The analog signal from this bridge is then processed using a Dantec 56N20 signal conditioner with a low-pass, anti-aliasing filter set to 100 kHz. The time-varying output voltage signal is then sampled at a 200 kHz rate using a DATEL PCI441D I/O board installed in the Dell Precision 530 PC work station. During each measurement, 1,000,000 voltage values are sampled over a 5-s period. Data are acquired using LABVIEW 6.1 software and then processed further using Matlab 6.1 software, including determination of the turbulence length scale. This is accomplished by integrating the autocorrelation functions which are deduced from the time-varying longitudinal velocity signals. The entire measurement system, including the hot-wire sensor, is calibrated in the free-stream of the TWT over a range of velocities from 71 m/s to 103 m/s. A Kiel type pressure probe, wall static taps, and a copper-constantan thermocouple are used to measure and determine the total pressure, static pressure, recovery temperature, and velocity at the inlet of the test section as the calibration is conducted.

Test Airfoil and Surface Roughness. A schematic diagram of the cross-section of one symmetric airfoil tested is shown in Fig. 2. The airfoil chord length c is 7.62 cm. The effective pitch p is 5.08 cm. The trailing edge of the symmetric airfoil is a 1.14 mm radius round semi-circle, designed to produce the wake flows of turbine airfoils employed in operating engines. The airfoil is scaled to provide similar boundary layer development and trailing edge thickness, as for airfoils which are used in operating aero-engines and in gas turbines used for utility power generation. Geometric dimensions of the contoured test walls and airfoil are given by Jackson [26].

Three different airfoils, all with the same exterior dimensions but with different surface roughness characteristics, are used. One airfoil has a smooth surface, and two other airfoils have rough surfaces. The roughness simulates the actual roughness which develops on operating turbine airfoils, over long operating times, due to particulate deposition and to spallation of thermal barrier

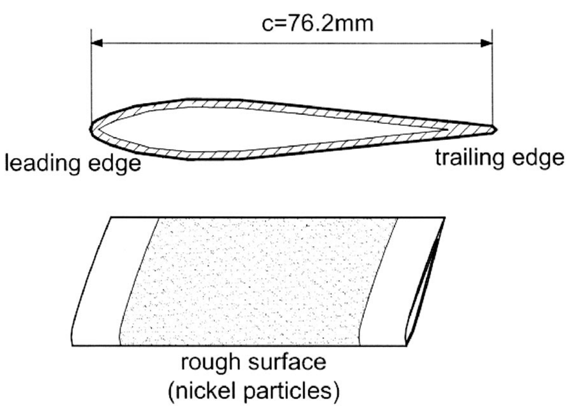

Fig. 2 Schematic diagram of the test airfoil

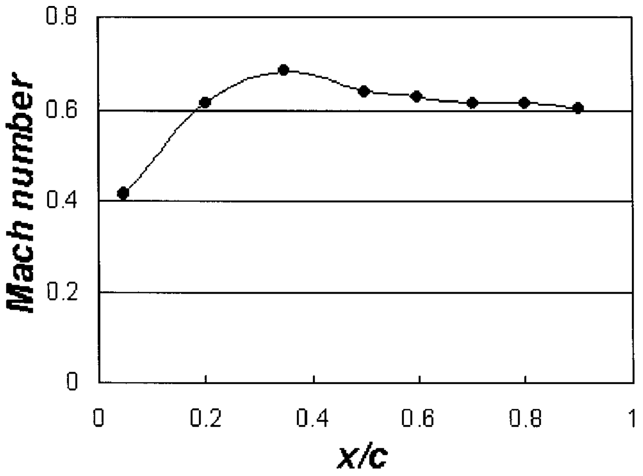

Fig. 3 Airfoil Mach number distribution

coatings (TBCs). The roughness is applied by bonding nickel particles, manufactured by Praxair Surface Technologies Inc., to the airfoil surfaces. The airfoil with the smaller-sized roughness elements has Praxair T1166F particles, which range in size from 20 μm to 53 μm. The airfoil with the larger-sized roughness elements has Praxair NI-914 particles, which range in size from 88 μm to 149 μm. The bonding is implemented using a layer of Contronics Corp. Duralco 132 aluminum-filled, high thermo-conductivity epoxy. This epoxy (and the roughness particles) are applied to an indented region located across the central span of the airfoil, which means that the mean level of the roughness is at about the same level as the surrounding smooth surface. This approach is used to give the same exterior dimensions to the surfaces of all three airfoils, regardless of whether their surfaces are smooth or rough.

Experimental Uncertainties. Uncertainty estimates are based on 95% confidence levels, and determined using procedures described by Kline and McClintock [27] and by Moffat [28]. Mach number uncertainty is ± 0.002. Uncertainty of temperatures is 0.15°C. Pressure uncertainty is 0.25 kPa. Uncertainties of C_p, $M_e/M_{e,\infty}$, and KE are ± 0.0013 (0.07), ± 0.0023 (0.96), and ± 0.03 (0.90), respectively, where typical nominal values of these quantities are given in parenthesis. IAL uncertainty is ± 0.04 N/cm (0.800 N/cm). Magnitudes of IAL, determined from replicate runs, are always within IAL uncertainty ranges.

TWT Qualifying Characteristics and Mainstream Air Flow Conditions

The Mach number distribution along the airfoil is shown in Fig. 3 and is similar to values present on turbine airfoil suction surfaces. Magnitudes range from 0.4 to 0.7 from the leading edge to $x/c = .35$, and from 0.7 to 0.6 along the remaining part of the airfoil. These values are based upon measurements of total pressure at the test section inlet and static pressures measured along the mid-span line of a smooth airfoil, which is employed especially for this task. The eight measured values shown in Fig. 4 are based on measurements made along the top of surface of the airfoil. These values are in excellent agreement with Mach numbers measured at three different locations on the bottom surface of the airfoil.

During each test, the inlet total pressure at the inlet of the test section, P_{oi}, is 114 kPa. With no turbulence grid employed at the test section inlet, the magnitude of the longitudinal turbulence intensity is 0.9%. With the fine mesh turbulence generating grid, the intensity and length scale are 5.5%, and 15.24 mm, respectively. With the cross bar turbulence generating grid, the intensity and length scale are 16.2%, and 19.70 mm, respectively. As mentioned, these values are measured at a location which is 87% of one chord length upstream of the airfoil leading edge. During each blow-down test, these conditions are maintained in the test section for 45-s long time intervals. Such characteristics are not only due to the TWT design, but also to the excellent performance characteristics of the TWT mainstream air pressure regulator and its controller. Chord Reynolds numbers based on inlet and exit flow conditions are 0.54×10^6 and 1.02×10^6, respectively.

With no turbulence grid employed, the total pressure and static pressure show excellent spatial uniformity at the inlet of the test section. Total pressure and static pressure values vary by less than 0.42 kPa (or 0.37% of mean values) as measurements are made at

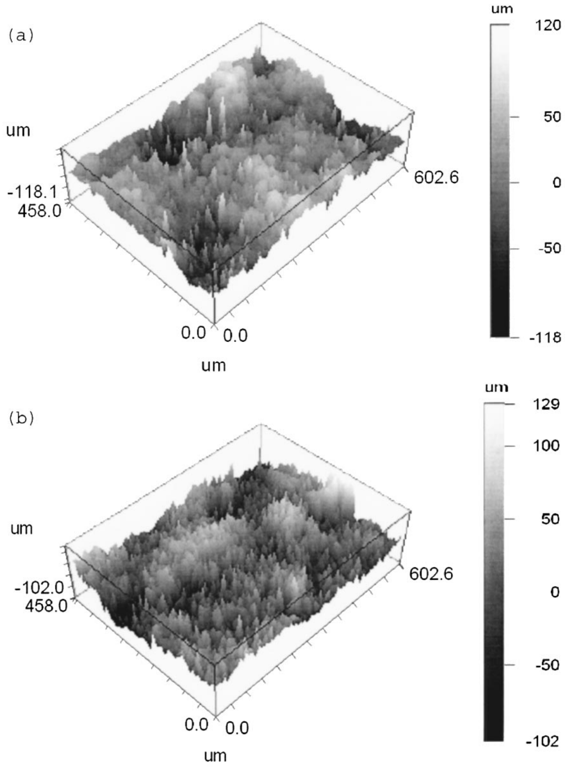

Fig. 4 Three-dimensional Wyko profilometry traces of portions of the rough surfaces. (*a*) Simulated rough surface with small-sized roughness elements. (*b*) Rough surface from the trailing-edge pressure side of a turbine blade with particulate deposition from a utility power engine.

9 different probe locations. For the central portion of the inlet duct, these variations amount to less than 0.35 kPa (or 0.3% of mean values). Much numbers determined from these data then vary by less than .002. Similar variations are also measured at a location which is 87% of one chord length upstream of the airfoil leading edge.

Spatial variations of the flow are about the same when the fine mesh grid is used at the inlet of the test section. Slightly larger variations are present when the cross bars are used to augment turbulence intensity levels. These are also based upon measurements made at multiple vertical locations, which are positioned at a streamwise location which is 87% of one chord length upstream of the airfoil leading edge. The vertical positions of the hot-wire probe employed, relative to the airfoil centerline, are adjustable, and are 0 mm, 12.7 mm and 25.4 mm above the centerline. The variations of turbulent intensity level measured at different probe locations are approximately 1.4% for the cross-bars and 0.3% for the fine mesh grid.

Such spatial non-uniformities, if present, are compensated by the procedures employed to measure profiles of normalized local total pressure losses C_p, normalized local Mach numbers $M_e/M_{e,\infty}$, and normalized local kinetic energy *KE*. With either mesh grid or bars employed, this is accomplished by measuring these profiles both with and without an airfoil located in the test section. Experimental data obtained with on blade in the test section indicate that the flow has excellent spatial uniformity. Experimental data, obtained with no blade in the test section, show excellent flow spatial uniformity. The magnitudes of the no blade losses are less than 0.5 kPa for both the fine mesh grid and cross bars cases. Differences in measured quantities obtained with and without an airfoil in the test section thus provide information on the effects of the airfoil and its surface condition, irrespective of any non-uniformities produced by the turbulence generating device which is used.

Experimental Results and Discussion

Roughness Characterization. The magnitudes of equivalent sandgrain roughness are determined for all three surfaces tested using procedures which are described by van Rij et al. [7].

The first step in this approach is a detailed determination of surface contour coordinates using a Wyko high-resolution optical Surface Profilometer. Figure 4*a* shows an enlarged image of a portion of the test surface with small-sized roughness elements, obtained from optical profilometry data. The image of a rough surface from the pressure side of a turbine blade with particulate deposition from a utility power engine is shown in Fig. 4*b*. The similarity of irregularity, nonuniformity, and three dimensional nature of the roughness elements, including their irregular arrangement, are evident from these plots. Equivalent sand grain roughness size of this turbine blade surface is about 62.3 μm, which is close to the size of test surface of small-sized roughness elements (52.59 μm). Table 1 also show that magnitudes of other surface roughness statistics from the utility power engine turbine blade are also similar to test surfaces employed with small-sized and large sized roughness elements.

The next step in the procedure is numerical determination of a modified version of the Sigal and Danberg roughness parameter Λ_s [4,5,7]. The procedures to accomplish this are described by Van Rij et al. [7], and involve determination of the rough surface flat reference area, the total roughness frontal area, and the total roughness windward wetted surface area. With Λ_s known, the ratio of equivalent sandgrain roughness size to mean roughness height, k_s/k, is determined using a correlation for three-dimensional, irregular roughness with irregular geometry and arrangement, which is given by van Rij et al. [7].

Table 1 Characteristics of rough surfaces investigated

Surface	Λ_S	k_s/k	k (μm)	k_s (μm)	k_s/c
large-sized roughness	15.447	1.959	64.03	125.19	0.00164
small-sized roughness	20.101	1.889	27.92	52.59	0.00069
smooth	3020.7	.0026	3.50	.0094	0
turbine blade from a utility power engine	43.455	1.641	40.815	62.30	0.00082

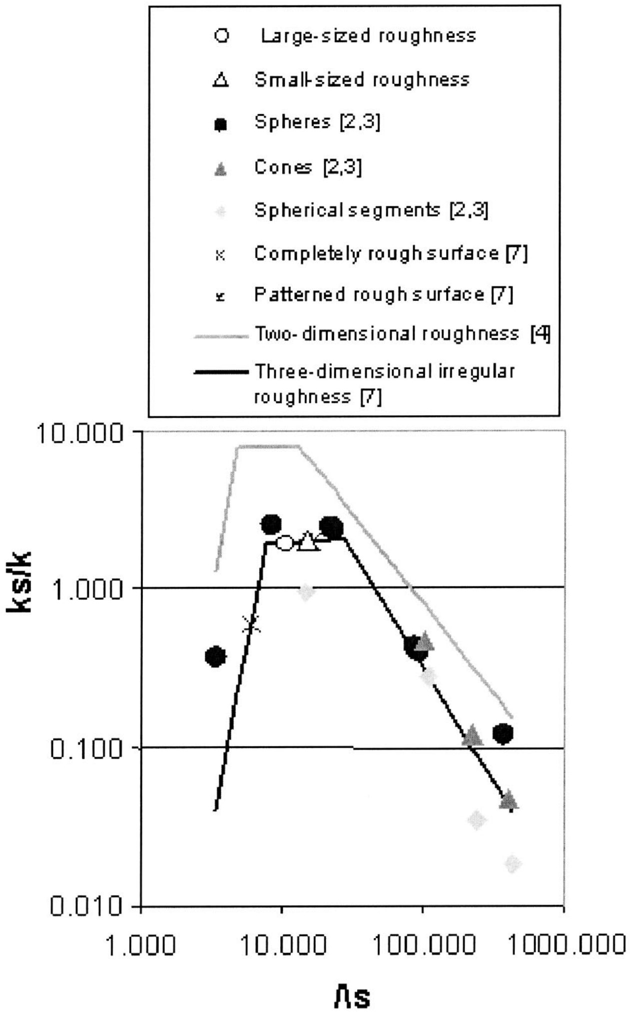

Fig. 5 Dependence of the ratio of equivalent sandgrain roughness size to mean roughness height on the Sigal and Danberg [4] roughness parameter for the present study, and the Schlichting [2], Coleman et al. [3], and the van Rij et al. [7] investigations

$$\frac{k_s}{k}=\begin{cases} 1.584\times 10^{-5}\Lambda_S^{5.683} & \Lambda_S\leq 7.842 \\ 1.802\Lambda_S^{0.0304} & 7.842\leq\Lambda_S\leq 28.12 \\ 255.5\Lambda_S^{-1.454} & 28.12\leq\Lambda_S \end{cases} \tag{1}$$

The mean roughness height is then also estimated by taking the distance between the maximum point of the ensemble-average of all of the roughness peaks in any roughness sample, and a base height. Determination of this base location is based on analytic procedures which are also given by van Rij et al. [7].

With this approach, magnitudes of equivalent sand grain roughness size for the 3-D, irregular roughness of the present study are determined. Values are given in Table 1, which are based on an average of 8 profilometry scans. The variation of k_s/k is 3% among eight traces for the surface with the large-sized roughness,

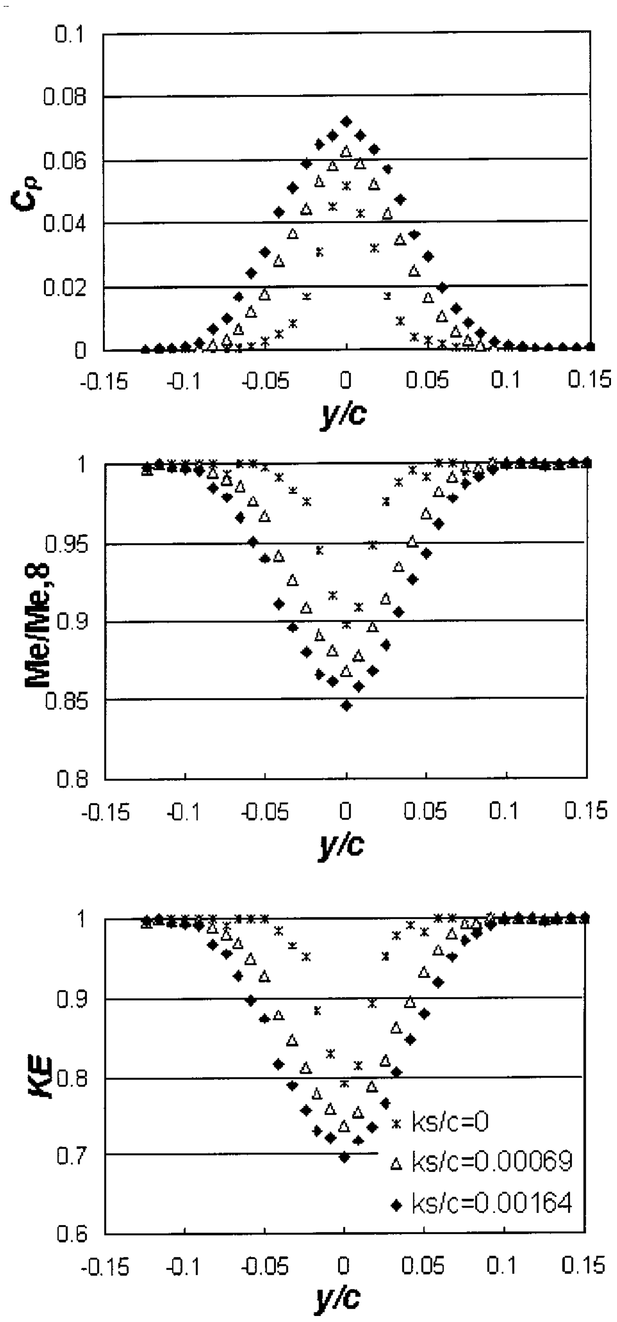

Fig. 6 Profiles measured with inlet turbulence intensity of 0.9%. (*a*) Normalized local total pressure losses. (*b*) Normalized local Mach numbers. (*c*) Normalized local kinetic energy.

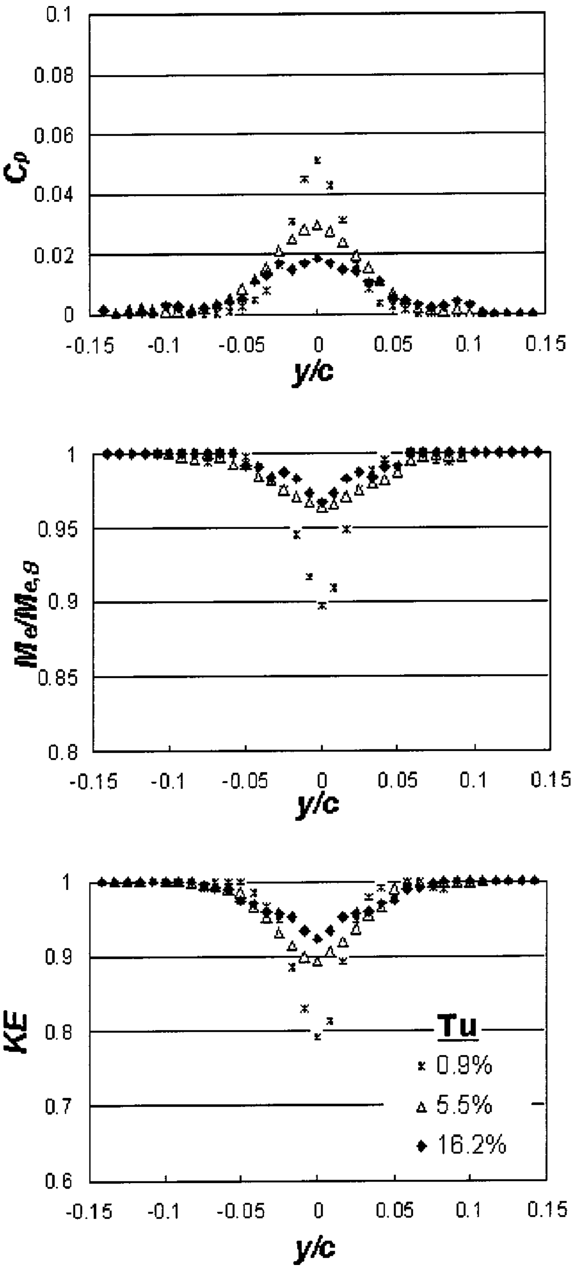

Fig. 7 Profiles measured using the smooth airfoil ($k_s/c=0$) with different turbulence intensity levels. (*a*) Normalized local total pressure losses. (*b*) Normalized local Mach numbers. (*c*) Normalized local kinetic energy.

and 2.6% among six traces for the surface with the small-sized roughness. Magnitudes of Λ_s and k_s/k from the present study are also shown plotted in Fig. 5, along with Eqn. (1), and values from the Schlichting [2], Coleman et al. [3], Sigal and Danberg [4], and van Rij et al. [7] investigations.

Local Aerodynamics Losses, Mach Number, and Kinetic Energy Distributions. Figures 6*a–c* show the effects of surface roughness on normalized local total pressure losses C_p, normalized local Mach numbers $M_e/M_{e,\infty}$, and normalized local kinetic energy *KE* profiles for an inlet turbulence intensity level of 0.9%. Data are given for k_s/c values of 0, .00069, and .00164, which correspond to the smooth, small-sized roughness, and large-sized roughness, respectively. The results in this set of figures are given for a low value of inlet turbulence intensity because variations due to roughness are generally more apparent than for higher inlet turbulence intensity levels.

Figure 6 shows that total pressure losses, Mach number deficits, and deficits of kinetic energy all increase at each y/c location as k_s/c increases. This is especially apparent at peak value locations, and is accompanied by increases in the width of the profiles as roughness size becomes larger. This is largely due to increased thickening of the boundary layers along the airfoil surfaces as k_s/c increases, which is accompanied by higher magnitudes of Reynolds stress tensor components, higher magnitudes of local turbulent transport, and higher surface skin friction coefficients. The likely causes of the broader wakes with increased roughness size in Fig. 6 are: (i) thicker boundary layers at the airfoil trailing edge, and (ii) increased turbulent diffusion in the transverse direc-

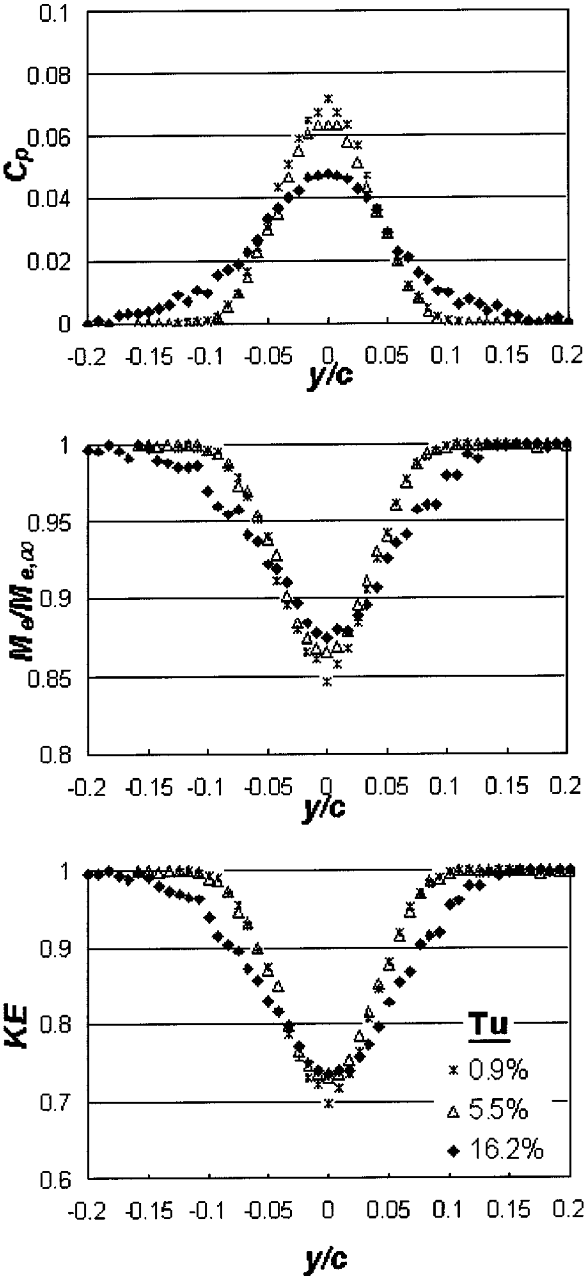

Fig. 8 Profiles measured using the airfoil with large-sized roughness ($k_s/c=.00164$) with different inlet turbulence intensity levels. (*a*) Normalized local total pressure losses. (*b*) Normalized local Mach numbers. (*c*) Normalized local kinetic energy.

tion *within* the wake as it advects downstream. For the present airfoil shape and configuration, numerical predictions show that flow separation regions (as well as associated form drag contributions) are about the same for all three airfoils, regardless of their k_s/c values of 0, .00069, and .00164. Numerical results also show that boundary layers are almost entirely turbulent along the entire length of all three tested airfoils.

Figures 7*a–c* present results which illustrate the effects of different inlet free-stream turbulence levels on normalized local total pressure losses C_p, normalized local Mach numbers $M_e/M_{e,\infty}$, and normalized local kinetic energy *KE* profiles for the smooth airfoil with $k_s/c=0$. Results are presented for *Tu* magnitudes of 0.9%, 5.5%, and 16.2%. As the inlet turbulence intensity increases, distributions of C_p, $M_e/M_{e,\infty}$, and *KE* show that the wake downstream of the airfoil becomes wider. At the center of the wake at $y/c=0$, C_p values drop dramatically, and $M_e/M_{e,\infty}$ and *KE* values increase substantially as inlet turbulence intensity increases.

In their low speed cascade experiments, Ames and Plesniak [20] also observe wake broadening with increasing mainstream turbulence intensity, and associate these with smaller peak velocity deficits. As mentioned, increased diffusion *from* the wake *to* surrounding free-stream flow plays an important role in producing such trends. Note that aerodynamic loss contributions in the freestream are also substantial in the results obtained by Ames and Plesniak. As a result, elevated free-stream turbulence intensity levels substantially increase overall loss magnitudes in their experiments. In the present study, a symmetric airfoil is used with a zero angle of inclination, and the total pressure at inlet of test section is almost the same as the total pressure in the freestream at the outlet. This means that losses in the free-stream are negligible in the present investigation, as shown in Figure 8*a*. In the investigation described by Boyle et al. [23], the variation in turbine vane aerodynamic losses is either positive or negative, depending on the Reynolds and Mach numbers. Cases that correspond closely to present study show similar minimal turbulence intensity effects. However, the local profile of pressure loss coefficient from Boyle et al. [23] at an exit Mach number of 0.9 shows different trends from Ames and Plesniak [20] as well as the present study, since peak total pressure loss magnitudes increase as the level of mainstream turbulence increases.

Figure 8*a–c* are obtained using the airfoil with large-sized roughness ($k_s/c=.00164$) and *Tu* magnitudes of 0.9%, 5.5%, and 16.2%. These results are presented to illustrate the combined effects of inlet turbulence intensity and airfoil surface roughness on aerodynamics losses, $M_e/M_{e,\infty}$ profiles, and *KE* distributions. When *Tu* increases from 0.9% to 5.5%, the normalized profiles only show very small variations. For example, in Fig. 9*a*, C_p magnitudes drop slightly at $y/c=0$, whereas distributions for *Tu* of 0.9% and 5.5% are very similar in other parts of the plot. As the inlet turbulence intensity increases from 5.5% to 16.2%, C_p peak values drop more substantially at $y/c=0$, and the wake region spanned by the C_p distribution is widened. The variations of normalized kinetic energy and normalized exit Mach number with *Tu* are qualitatively similar, as illustrated by Figs. 8*b* and 8*c*.

Comparing the profiles in Figs. 6*a–c*, 7*a–c*, and 8*a-c* shows that C_p, $M_e/M_{e,\infty}$, and *KE* distributions are less sensitive to variations of the freestream turbulence intensity than to the changes of surface roughness on the airfoil. This means the wake downstream of the airfoil is dominated by upstream roughness influences. This is partially a result of the augmentations of mixing and turbulent transport in the boundary layers which develop along the airfoil. It also means that the effects of roughness and inlet turbulence intensity in wakes are not "additive," unlike the behavior observed in boundary layers developing over rough, flat plates by Bogard et al. [11].

Integrated Aerodynamics Losses

Dimensional magnitudes of Integrated Aerodynamics Loss, *IAL*, are determined by integrating profiles of $(P_{oe,\infty}-P_{oe})$ with respect to y in the transverse flow direction across the wake. The integration range is from free-stream to wake, and then to the freestream. *IAL* magnitudes thus represent boundary layer and mixing losses in the wake.

Such *IAL* magnitudes are presented in Fig. 9 as dependent upon the inlet turbulence intensity level for the airfoils with the smooth surfaces ($k_s/c=0$), small-sized roughness ($k_s/c=.00069$), and large-sized roughness ($k_s/c=.00164$). When the smooth airfoil is employed, *IAL* magnitudes decrease only slightly as the magnitude of the inlet turbulence intensity increases. When the surface roughness level increases and k_s/c equals .00069 and .00164, *IAL* variations with *Tu* are again quite small. For airfoil with large-sized roughness, changing inlet turbulence intensity levels have almost no effect on *IAL* magnitudes. Fig. 9 also shows important

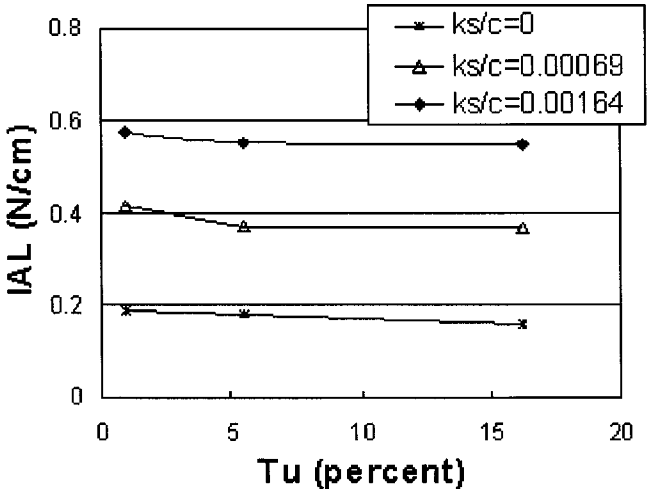

Fig. 9 Comparison of dimensional Integrated Aerodynamic Loss as dependent upon the inlet turbulence intensity level for the smooth airfoil ($k_s/c=0$), the airfoil with small roughness ($k_s/c=.00069$), and the airfoil with large roughness ($k_s/c=.00164$)

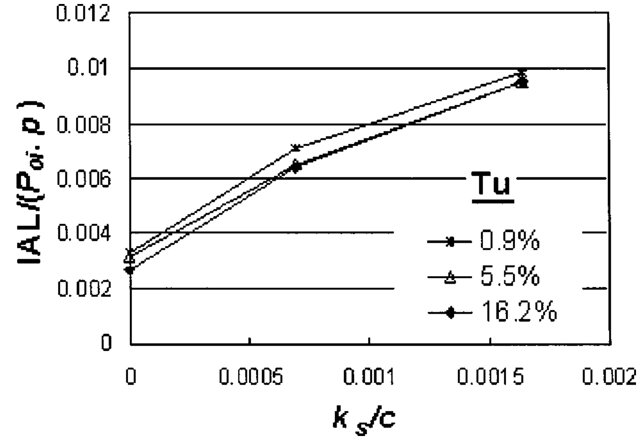

Fig. 10 Comparison of normalized Integrated Aerodynamic Loss as dependent upon the normalized equivalent sand grain roughness size for different inlet turbulence intensity levels

IAL increases with airfoil surface roughness at each value of *Tu*, which again illustrates that roughness contributions to *IAL* magnitudes are quite significant.

IAL data normalized using the airfoil passage effective pitch p and test section inlet stagnation pressure P_{oi}, are presented in Fig. 10, as they depend upon k_s/c for different *Tu* values. The overall trend of the data in this graph illustrate the dominating influences of airfoil surface roughness on aerodynamic losses, and weak dependence of these losses on inlet freestream turbulence intensity level. Similar trends are reported by Kind et al. [10], but for different ranges of equivalent sand grain roughness sizes.

Additional Comparisons With Ames and Plesniak

Figure 11 compares smooth airfoil $(P_{oi}-P_{oe})/(P_{oi}-P_{se})$ total pressure loss coefficient profiles for different turbulence intensity levels to ones from Ames and Plesniak [20]. For both studies, mean coefficients decrease at $y/c=0$, with broader distributions over larger ranges of y/c values, as *Tu* increases. Similar qualitative trends are thus evident, even though quantitative values are different. Quantitative differences are due to a number of factors, including different airfoil configurations (curved, straight), different flow conditions (low-speed, high subsonic compressible), and different measuring locations downstream of the airfoil (0.11 chord lengths, 1.0 chord length). In contrast to the present study, Ames and Plesniak also report substantial losses in the freestream, as mentioned. Such freestream losses increase mass-averaged loss coefficients substantially, which precludes comparisons of such coefficients with ones from the present investigation.

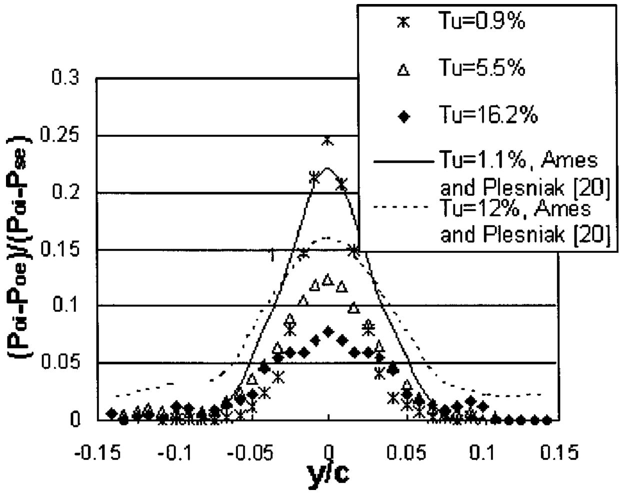

Fig. 11 Comparisons of total pressure loss coefficients with ones from Ames and Plesniak [20] for smooth airfoils ($k_s/c=0$)

Summary and Conclusions

The effects of surface roughness on the aerodynamic performance of turbine airfoils are investigated with different inlet turbulence intensity levels of 0.9%, 5.5%, and 16.2%. Three symmetric airfoils, each with the same shape and exterior dimensions, are employed with ratios of equivalent sandgrain roughness size to airfoil chord length k_s/c of 0, .00069 and .00164. These magnitudes of equivalent sandgrain roughness are determined for all three surfaces tested using 3-D optical profilometry traces of the rough surfaces and procedures which are described by van Rij et al. [7]. For the latter two airfoils, the roughness is randomly placed, nonuniform, irregular, and 3-D, with irregular geometry and arrangement. It is created to match the roughness which exists on operating turbine vanes and blades subject to extended operating times and significant particulate deposition on the surfaces.

Mach numbers along the airfoil range from 0.4 to 0.7. These results are obtained using the University of Utah Transonic Wind Tunnel (TWT), which, with the test section employed, is designed to isolate the effects of surface roughness and turbulence intensity on wake aerodynamic losses, while matching Reynolds numbers, Mach numbers, pressure gradients, passage flow rates, boundary layer development, and physical dimensions of airfoils in operating engines. This facility provides steady flows for 45-s long time intervals with excellent spatial uniformity at the inlet of the test section.

Changing the airfoil surface roughness condition has a substantial effect on the normalized and dimensional magnitudes of Integrated Aerodynamic Losses produced by the airfoils. This is illustrated by data trends which show the dominating influences of airfoil surface roughness on aerodynamic losses, and weak dependence of Integrated Aerodynamic Losses on inlet freestream turbulence intensity level.

With an inlet turbulence intensity level of 0.9%, normalized local total pressure losses C_p, deficits of normalized local Mach numbers $M_e/M_{e,\infty}$, and deficits of normalized local kinetic energy *KE* generally become larger in spatial extent and increase in magnitude at each wake location as k_s/c increases. Relative to smooth airfoils, this is due to: (i) augmentations of mixing and turbulent transport in the boundary layers which develop along the roughened airfoils, (ii) thicker boundary layers at the trailing edges of roughened airfoils, (iii) increased turbulent diffusion in the transverse direction *within* the wakes of roughened airfoils as they advect downstream. When the turbulence intensity increases, diffusion *from* the wake *to* surrounding freestream flow becomes important, and results in broader wakes with more uniform aerodynamics loss distributions.

Relatively small variations of local C_p, $M_e/M_{e,\infty}$, and KE distributions are present when the turbulence intensity is varied around an airfoil with large-sized roughness ($k_s/c=.00164$). These quantities are thus less sensitive to variations of the freestream turbulence intensity than to the changes of surface roughness on the airfoil, which provides evidence that the wake downstream of the airfoil is generally dominated by upstream roughness influences even when the inlet turbulence intensity level is as high as 16.2%.

Acknowledgments

The research reported in this paper was sponsored by the National Science Foundation (NSF Grant Number CTS-0086011). Dr. Stefan Thynell and Dr. Richard Smith were the NSF program monitors. The authors also acknowledge Dr. Mike Blair of Pratt & Whitney Corp., Dr. Hee-Koo Moon of Solar Turbines Inc., Dr. Ed North and Dr. Ihor Diakunchak of Siemens-Westinghouse Corp. and Dr. Ricardo Trindade of Pratt & Whitney-Canada Corp. for guidance and suggestions on this research effort, and for providing roughened turbine blade hardware from engines for analysis and comparison.

Nomenclature

A = test section exit area
c = chord length of airfoil
$C_f/2$ = skin friction coefficient
C_p = pressure coefficient, $(P_{oi}-P_{oe})/P_{oi}$
IAL = integrated aerodynamic losses
M_e = exit local Mach number
$M_{e,\infty}$ = exit free-stream mach number
k = mean roughness height
KE = normalized kinetic energy, $(P_{oe}-P_{se})/(P_{oe}-P_{se})_\infty$
k_s = equivalent sand grain roughness
p = airfoil passage effective pitch
P_o = stagnation pressure
P_{oe} = exit local stagnation pressure
$P_{oe,\infty}$ = exit free-stream stagnation pressure
P_{oi} = inlet stagnation pressure
P_s = static pressure
P_{se} = exit static pressure
Tu = turbulence intensity at test section inlet
u = local streamwise velocity
x = linear distance along airfoil centerline from airfoil leading edge
y = normal coordinate measured from airfoil centerline

Greek symbols

ρ = local air static density
γ = ratio of specific heats
Λ_s = roughness parameter

References

[1] Nikuradse, J., 1933, “Laws of Flow in Rough Pipes,” NACA TM 1292, National Advisory Committee on Aeronautics.
[2] Schlichting, H., 1936, “Experimental Investigation of the Problem of Surface Roughness,” NACA TM-832, National Advisory Committee on Aeronautics.
[3] Coleman, H. W., Hodge, B. K., and Taylor, R. P., 1984, “a Re-Evaluation of Schlichting’s Surface Roughness Experiment,” ASME Trans. J. Fluids Eng., **106**, pp. 60–65.
[4] Sigal, A., and Danberg, J. E., 1990, “New Correlation of Roughness Density Effect on Turbulent Boundary layer,” AIAA J., **28**, No. 3, pp. 554–556.
[5] Sigal, A., and Danberg, J. E., 1988, “Analysis of Turbulent Boundary Layer Over Roughness Surface With Application to Projectile Aerodynamics,” Amy Ballistic Research Lab, Aberdeen Proving Grounds MD, Technical Report BRL-TR-2977.
[6] Bons, J. P., Taylor, R. P., McClain, S. T., and Rivir, R. B., 2001, “The Many Faces of Turbine Surface Roughness,” ASME Trans. J. Turbomach., **123**, pp. 739–748.
[7] van Rij, J. A., Belnap, B. J., and Ligrani, P. M., 2002, “Analysis and Experiments on Three-Dimensional, Irregular Surface Roughness,” ASME Trans. J. Fluid Eng., **124**, pp. 1–7.
[8] Bammert, K., and Sandstede, H., 1975, “Influence of Manufacturing Tolerances and Surface Roughness of Blades on the Performance of Turbines,” ASME Paper No. 75-GT-35.
[9] Bammert, K., and Sandstede, H., 1980, “Measurements of the Boundary layer Development along a Turbine Blade with Rough Surfaces,” ASME J. Eng. Power, **102**, pp. 978–983.
[10] Kind, R. J., Serjak, P. J., and Abbott, M. W. P., 1996, “Measurements and Prediction of The Effects of Surface Roughness on Profile Losses and Deviation In a Turbine Cascade,” ASME Paper No. 95-GT-203.
[11] Bogard, D. G., Schmidt, D. L., and Tabbita, M., 1998, “Characterization and Laboratory Simulation of Turbine Airfoil Surface Roughness and Associated Heat Transfer,” ASME J. Trans. Turbomach., **120**, pp. 337–342.
[12] Abuaf, N., Bunker, R. S., and Lee, C. P., 1998, “Effects of Surface Roughness on Heat Transfer and Aerodynamics Performance of Turbine Airfoils,” ASME Trans. J. Turbomach., **120**, pp. 522–529.
[13] Leipold, R., Boese, M., and Fottner, L., 2000, “The influence of Technical Surface Roughness Caused by Precision Forging on the Flow Around a Highly Loaded Compressor Cascade,” ASME Trans. J. Turbomach., **122**, pp. 416–425.
[14] Guo, S. M., Oldfield, M. L. G., and Rawlinson, A. J., 2002, “Influence of Discrete Pin Shaped Surface Roughness(P-Pins) on Heat Transfer and Aerodynamics of Film Cooled Aerofoil,” ASME Paper No. GT-2002-30179.
[15] Geogory-Smith, D. G., and Cleak, J. G. E., 1992, “Secondary Flow Measurements in a Turbine Cascade With High Inlet Turbulence,” ASME Trans. J. Turbomach., **114**, pp. 173–183.
[16] Hoffs, A., Drost, U., and Bolcs, A., 1996, “Heat Transfer Measurements on a Turbine Airfoil at Various Reynolds numbers and Turbulence Intensities Including Effects of Surface Roughness,” ASME Paper No. 96-GT-169.
[17] Giel, P. W., Bunker, R. S., Van Fossen, G. J., and Boyle, R. J., 2000, “Heat Transfer Measurements and Predictions on a Power Generation Gas Turbine Blade,” ASME Paper No. 2000-GT-209.
[18] Boyle, R. J., Luci, B. L., Verhoff, V. G., Camperchioli, W. P., and La, H., 1998, “Aerodynamics of a Transitioning Turbine Stator Over a Range of Reynolds Numbers,” ASME Paper No. 98-GT-285.
[19] Nix, A. C., Smith, A. C., Diller, T. E., Ng, W. F., and Thole, K. A., 2002, “High Intensity, Large Length-scale Freestream Turbulence Generation in a Transonic Turbine Cascade,” ASME Paper No. GT-2002-30523.
[20] Ames, F. E., and Plesniak, M. W., 1997, “The Influence of Large-Scale, High Intensity Turbulence on Vane Aerodynamics Losses, Wake Growth, and the Exit Turbulence parameters,” ASME Trans. J. Turbomach., **119**, pp. 182–192.
[21] Jouini, D. B. M., Sjolander, S. A., and Moustapha, S. H., 2001, “Aerodynamic Performance of a Transonic Turbine Cascade at Off-Design Conditions,” ASME Trans. J. Turbomach., **123**, pp. 510–518.
[22] Radomsky, R. W., and Thole, K. A., 2002, “Detailed Boundary Layer Measurements on a Turbine Stator Vane at Elevated Freestream Turbulence Levels,” ASME Trans. J. Turbomach., **124**, pp. 107–118.
[23] Boyle, R. J., Lucci, B. L., and Senyitko, R. G., 2002, “Aerodynamics Performance and Turbulence Measurements in a Turbine Vane Cascade,” ASME Paper No. GT-2002-30434.
[24] Jackson, D. J., Lee, K. L., Ligrani, P. M., Johnson, P. D., 2000, “Transonic Aerodynamics Losses Due to Turbine Airfoil, Suction Surface Film Cooling,” ASME Trans. J. Turbomach., **122**, pp. 317–326.
[25] Furukawa, T., and Ligrani, P. M., 2002, “Transonic Film Cooling Effectiveness From Shaped Holes on a Simulated Turbine Airfoil,” AIAA Journal of Thermophysics and Heat Transfer, **16**, pp. 228–237.
[26] Jackson, D. J., 1998, “Aerodynamics Mixing Losses and Discharge Coefficients Due to Film Cooling From a Symmetric Turbine Airfoil in Transonic Flow,” M. S. Thesis, Department of Mechanical Engineering, University of Utah.
[27] Kline, S. J., and McClintock, F. A., 1953, “Describing Uncertainties in Single Sample Experiments,” Mechanical Engineering, **75**, pp. 3–8.
[28] Moffat, R. J., 1988, “Describing the Uncertainties in Experimental Results,” Exp. Therm. Fluid Sci., **1**, pp. 3–17.

Michael J. Brear
Department of Mechanical and Manufacturing Engineering,
University of Melbourne,
Australia
e-mail: mjbrear@unimelb.edu.au

Zachary Warfield
Structures and Configuration Group,
Mechanical Engineering Section,
Jet Propulsion Laboratory

John F. Mangus
Integrated Systems,
Northrop Grumman Corporation

Cpt. Steve Braddom
Department of Civil & Mechanical Engineering,
West Point

James D. Paduano
Gas Turbine Laboratory,
Massachusetts Institute of Technology

Jeffry S. Philhower
Integrated Systems,
Northrop Grumman Corporation

Flow Separation Within the Engine Inlet of an Uninhabited Combat Air Vehicle (UCAV)

This paper discusses the structure of the flow within the engine inlet of an uninhabited combat air vehicle (UCAV). The UCAV features a top-mounted, serpentine inlet leading to an engine buried within the fuselage. The performance of the inlet is found to depend strongly on a flow separation that occurs within the inlet. Both the time-averaged and the unsteady structure of this separation is studied, and an argument relating the inlet performance to the behavior of this separation is suggested. The results presented in this paper also suggest that there are considerable aerodynamic limitations to further shortening or narrowing of the inlet. Since there are substantial, system level benefits from using a smaller inlet, the case for separated flow control therefore appears clear. [DOI: 10.1115/1.1667885]

Introduction

The engine inlets of uninhabited combat air vehicles (UCAV's) are often serpentine. Furthermore, the structural weight of UCAV's is minimized by making the inlet as short and as narrow as possible. If it is necessary to maintain the serpentine inlet design, reduced inlet length implies greater flow turning. A narrow inlet requires flow that is close to choking at peak mass-flow conditions. The combination of aggressive flow tuning and high subsonic Mach numbers makes strong adverse pressure gradients unavoidable. As previous investigations have found, the flow within serpentine inlets therefore often separates, leading to reduced inlet pressure recovery and increased unsteadiness within the inlet [1–3].

Of course, reduced inlet pressure recovery and increased inlet unsteadiness cause a deterioration in the performance of the propulsion system. The mechanisms by which this occurs are numerous and complex. Most obviously, the specific thrust and specific fuel consumption are related to the inlet pressure recovery. However, distortions generated within the inlet also adversely affect the performance of the engine, primarily in terms of reduced compressor efficiency and reduced stall/surge margin [4].

This paper therefore presents a study of the mechanisms that determine reduced pressure recovery and increased unsteadiness within a UCAV inlet during cruise. At this flight condition, the flow entering the inlet has a uniform stagnation pressure and does not experience lip separations and other phenomena characteristic of take-off, landing and maneuvering. As such, any deterioration of the flow that enters the compressor is the result of phenomena that are internal to the inlet. Specifically, the inlet performance is related to the detailed structure of a flow separation. Both the steady and unsteady structure of this separation is studied using experimental and computational methods. From these results, it is then suggested that further shortening of the inlet can only be achieved with the use of separated flow control.

Experimental Methods

All experiments presented in this paper were performed at the Gas Turbine Laboratory, Massachusetts Institute of Technology. A one-sixth scale model of a UCAV inlet formed the entrance to an open loop system driven by a 1 MW De Laval compressor (Fig. 1). A bellmouth contraction was placed upstream of the inlet so that the smooth inlet flow of cruise conditions was simulated on the stationary rig, i.e. the lip separations and other phenomena that are characteristic of take-off, landing and maneuvering were avoided. An instrument can which contained a rake of 40 stagnation pressure probes (either steady or unsteady) was located downstream of the inlet. The layout of these probes complied with ARP 1420 [4] such that an average of the stagnation pressures read by the probes was the area averaged stagnation pressure at the AIP. The location of the probe rake represented the entrance to the engine (the fan face) and is referred to as the aerodynamic interface plane (AIP). The inlet massflow rate was controlled with a translating plug that acted as a throttle, and the uncertainty in the mass-flow measurement was estimated to be ±0.08 lb/s. Flight representative inlet Mach numbers were achieved during the experiments (Table 1). Of course, inlet Reynolds number similarity could not be achieved due to the scaling of the inlet. Further details of all experimental methods employed are contained in [5].

Steady pressure measurements were taken with static pressure taps and pitot tubes that were connected by pneumatic tubing to a 10 psi Scanivalve differential pressure transducer. When measuring the inlet pressure recovery, the stagnation pressure measured at the AIP was nondimensionalized by the ambient pressure in the laboratory. The uncertainty in the inlet pressure recovery measured in this way was estimated to be ±0.0025 [5]. Unsteady stagnation pressure measurements at the AIP were performed with 5 psi Kulite unsteady pressure transducers that were connected to strain gauge conditioning amplifiers from Measurements Group,

---

Contributed by the Fluids Engineering Division for publication in the JOURNAL OF FLUIDS ENGINEERING. Manuscript received by the Fluids Engineering Division March 17, 2003; revised manuscript received October 6, 2003. Associate Editor: W. W. Copenhaver.

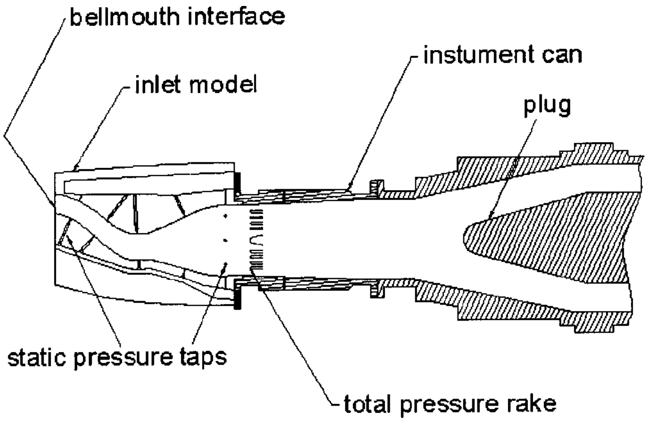

Fig. 1 Cross-section of experimental rig

Inc. Figure 9*c* shows the location of a surface mounted hot film sensor that was placed within the separated region. This was a SENFLEX SF9902 single element shear stress sensor, and was controlled by a DANTEC constant temperature anemometer bridge. Both the unsteady pressure and hot film measurements were logged at a frequency of 20 kHz and statistically stationary data was obtained in all experiments by varying the sampling duration. The sampling duration was at most 12 s.

Oil and dye flow visualisation was used to produce portraits of the limiting streamline structure within the inlet. This technique used a thick, black mixture of silicon oil and powdered charcoal painted uniformly over the inner surface of the laboratory scale inlet. The model was then run at cruise representative Mach-numbers, and the limiting surface patterns shown in this paper arose after roughly 10 minutes of operation. The surface flow visualization results presented in this paper used an inlet massflow rate of 3.6 lb/s, rather than the design massflow rate of 3.13 lb/s (Table 1). This was because the higher mass-flow rate gave clearer results within the separated region. It is emphasized, however, that the *structure* of the separated region appeared to be the same at both of these massflow rates.

Table 1 Parameters at full scale and model scale

case	alt. (kft)	Ma_∞	$Re_{AIP}(.10^6)$	$\dot{m}$ (lb/s)
full scale	35	0.8	7.63	111.5
model scale	0	0.0	1.28	3.13

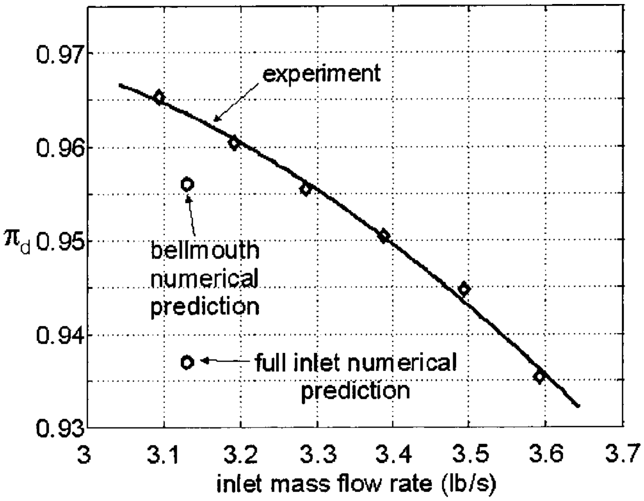

Fig. 2 Measured and predicted π_d as a function of the scaled inlet massflow

Numerical Methods

The numerical predictions presented in this paper used a proprietary version of the NASA CNS program. This solver used a diagonalized Beam Warming solution algorithm with a finite volume spatial discretization. For the current work, a four-block grid system with patched and overset grid boundaries was utilized. The grid was generated for a complete half model of the full scale aircraft and its farfield, and consisted of over one million nodes. The numerical prediction was performed at the full-scale cruise condition given in Table 1, meaning that the Reynolds numbers of the predictions were roughly six times the equivalent Reynolds number of the model because of the scale difference. Possible consequences of this are discussed in this paper. The results presented in this paper used an inlet modeled with 462,429 nodes, although higher resolution grids were also used in other cases to establish grid independence. All of the runs utilized local time stepping and a $K-\Omega$ turbulence model.

Discussion

Inlet Pressure Recovery and Flow at the AIP. Figure 2 shows the area averaged inlet pressure recovery versus the inlet mass-flow rate. The inlet pressure recovery is reasonable at the design mass-flow rate of 3.13 lb/s (Table 1), although it is roughly 2% below the pressure recovery of current, civil aircraft engine inlets cruising at similar flight conditions [1]. The lower inlet pressure recovery is of course due to the complex, serpentine geometry of the UCAV inlet. Excluding any form of separation within the inlet (which will serve only to further reduce the inlet pressure recovery), its considerable length compared to a typical civil inlet design will inevitably cause reduced inlet pressure recovery through the losses generated in the inlet boundary layers.

Figure 2 also shows that the inlet pressure recovery decreases as the mass-flow rate is increased above design conditions. This is not expected to be Reynolds number related since the Reynolds number is increasing with increased mass-flow rate. In most high Reynolds number flows, increased Reynolds number will tend to reduce the thickness of the boundary layers [6], thereby increasing the inlet pressure recovery. Instead, the decrease in inlet pressure recovery is expected to be a Mach number effect. This is thought to be analogous to the increase in the drag of an airfoil at a fixed angle of attack, but with a subsonic, free-stream Mach number increasing towards unity. In such cases, the severity of the adverse pressure gradient downstream of the point of peak velocity typically increases with increased freestream Mach number, causing the boundary layers to thicken and to even separate. Higher levels of aerodynamic loss are therefore created [7]. A similar argument appears reasonable in the present study, since the choking of the inlet must occur at some massflow rate. Indeed, it is argued that a

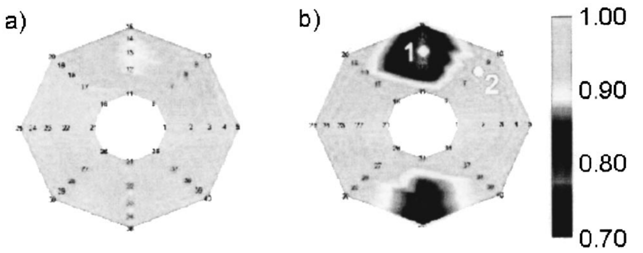

Fig. 3 Contours of P_t/P_∞ at the AIP from experiment for *a*) low massflow rate (2.9 lb/s) and *b*) design massflow rate (3.6 lb/s), showing the location of the unsteady, stagnation pressure probes 1 and 2

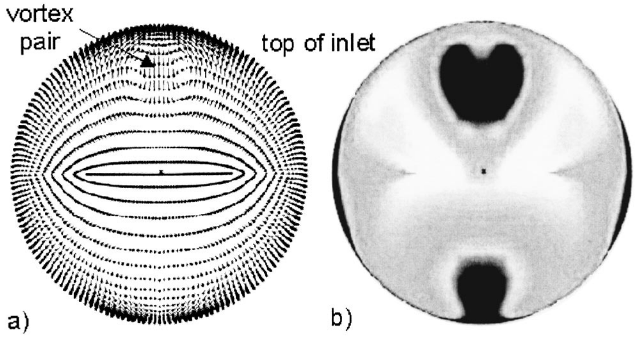

Fig. 4 Predicted *a*) secondary flow vectors and *b*) contours of P_t/P_∞ (see Fig. 3 for scale) at the AIP

separation within the inlet is a significant contributor to this fall in the inlet pressure recovery, and this separation occurs immediately downstream of the inlet throat.

Further understanding of the origins of the inlet loss can be obtained from contour plots of nondimensional stagnation pressure at the AIP. As Fig. 3*a* shows, the stagnation pressure contours at low massflow rate are reasonably uniform, although there are relatively minor deficits at the top and bottom of the AIP. However, Figure 3*b* shows that significant deficits in stagnation pressure occur at the AIP's top and bottom at the higher mass-flow rate. Mass-flow rates between those shown in Figs. 3*a* and 3*b* give intermediate stagnation pressure portraits. These results show that the stagnation pressure deficits at the top and bottom of the AIP are responsible for the variations in inlet pressure recovery shown in Fig. 3.

The numerical prediction of the nondimensional stagnation pressure contours at the AIP appears to compare favorably with experiment, although it is emphasised that the experimental result in Fig. 3*b* is at a higher scaled mass-flow rate than the predicted result in Fig. 4*b*. Like Fig. 3*b*, Fig. 4*b* also shows the regions of stagnation pressure deficit at the top and bottom of the AIP, although the resolution of the predicted flow is of course much better since the number of stagnation pressure probes in experiment was limited to 40. Regions of stagnation pressure loss are also evident on the sides of the AIP. These are not seen in the experiments (Fig. 3*b*) because the stagnation pressure probes were not close enough to the inlet walls.

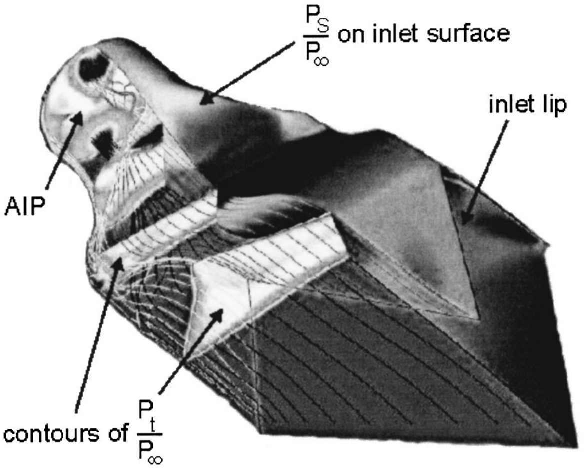

Fig. 5 Computed inlet flow showing contours of P_t/P_∞ at fixed axial locations (see Fig. 8 for scale) and P_s/P_∞ on the inlet surface

The qualitative similarity between the results at different scaled mass-flow rates in Figs. 3*b* and 4*b* can be further explained by reference to Fig. 2. As stated earlier, the numerical predictions were performed for the full aircraft, whereas experiments used a bellmouth contraction to simulate cruise conditions on a stationary rig. Thus, the predicted stagnation pressure distribution at the AIP includes the boundary layer loss created upstream of the inlet. However, Fig. 2 shows that the predicted inlet pressure recovery at the design mass-flow rate of 3.13 lb/s in Fig. 4*b* is very similar to that measured at 3.6 lb/s in Fig. 3*b*. Fig. 2 also shows that equivalent numerical predictions with the bellmouth inlet resulted in an inlet pressure recovery that is roughly 2% greater than the full aircraft predictions, and these are in better agreement with the experimental results at the same massflow rate. Thus, the similarity in the inlet pressure recoveries in Figs. 3*b* and Fig. 4*b* is partially because the increased massflow condition of Fig. 3*b* gives a similar drop in the pressure recovery to that caused by the inclusion of the upstream boundary layers. The bellmouth and full aircraft predictions in Fig. 2 nonetheless revealed the same inlet flow structure. Specifically, the size of a separation on the top surface of the inlet was the same in both sets of numerical predictions.

Figure 4*b* also shows that the deficit in the stagnation pressure at the top of the inlet has a lobed appearance. Examination of the secondary flow vectors (which are defined as perpendicular to the axial direction) in Fig. 4*a* reveals a related feature. A pair of counter-rotating vortices exist within the region occupied by the stagnation pressure deficit in Figure 4*a*. It is also noted, however, that the secondary flow associated with the bottom deficit in stagnation pressure does not appear to be as strongly vortical. Nonetheless, close examination of this region also shows a pair of weak, counter-rotating vortices. Later results suggest that the origins of the top and bottom vortex pairs are different.

Overall Inlet Flow. Figure 5 shows an overall view of the predicted flow within the inlet during cruise. The inlet lip is serrated, which was removed in the experiments and replaced with the bellmouth contraction to avoid gross separation at static freestream conditions. However, at the cruise Mach number of 0.8, Fig. 5 shows that the streamlines are roughly parallel at the inlet lip. These streamlines have become bundled at the top, and bottom of the inlet by the time the flow has reached the AIP. In keeping with Fig. 4*a*, the streamlines at the top of the inlet exhibit a relatively strong swirling motion immediately upstream of the AIP, although this does not appear to be the case further towards the inlet lip. Thus, this vortical flow at the top of the inlet appears confined to the region immediately before the AIP. As is argued in this paper, this motion primarily results from the flow separating within the latter part of the inlet. This separation is caused by a strong adverse pressure gradient that can also be inferred from Fig. 5 and is shown more clearly in Fig. 6.

Figure 5 may also suggest that the pair of weak, counter-rotating vortices that occur at the bottom of the AIP originate further towards the inlet lip. Surface flow visualisation of the lower surface of the inlet in Fig. 9*a* supports this result by showing that separation does not occur immediately upstream of the AIP, as is the case for the top surface of the inlet. Instead, this visualisation shows some secondary flow further towards the inlet lip, in keeping with the behavior of the lower surface streamlines in Fig. 5. It is therefore thought that the weak vortex pair at the bottom of the AIP originates from the bottom inlet surface closer to the inlet lip.

Centerplane Flow. Figure 6 shows the predicted surface static pressure along the centerline of the inlet's top surface. It is clear that there is a strong favorable pressure gradient along most of the centerline from the inlet lip to roughly halfway along the inlet. The minimum in static pressure represents the inlet throat, downstream of which is a strong adverse pressure gradient and then two local minima in static pressure. These local minima

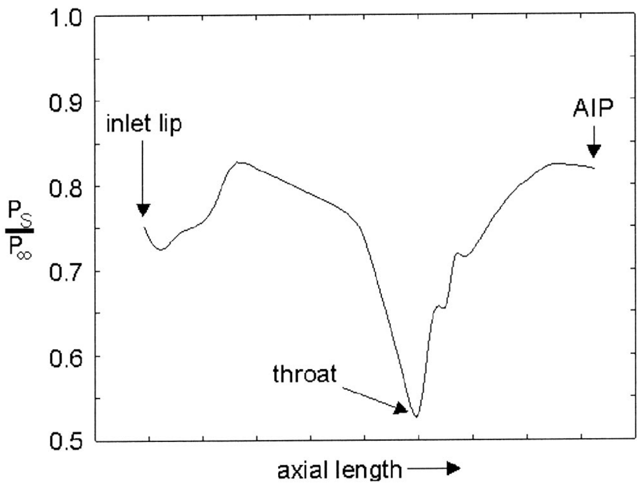

Fig. 6 Predicted static pressure along the top surface of the inlet

could most likely be removed with more careful design, although the requirement of compressor inlet Mach numbers of between 0.5 and 0.6 inevitably means that an adverse pressure gradient must exist downstream of the inlet throat if the flow at the throat is close to choking. Since there are strong system level incentives for maximizing the inlet throat Mach number, strong adverse pressure gradients within the last part of the inlet are always expected to be the case in practice. As is shown in this paper, the separation of interest exists downstream of the second local minimum in surface static pressure.

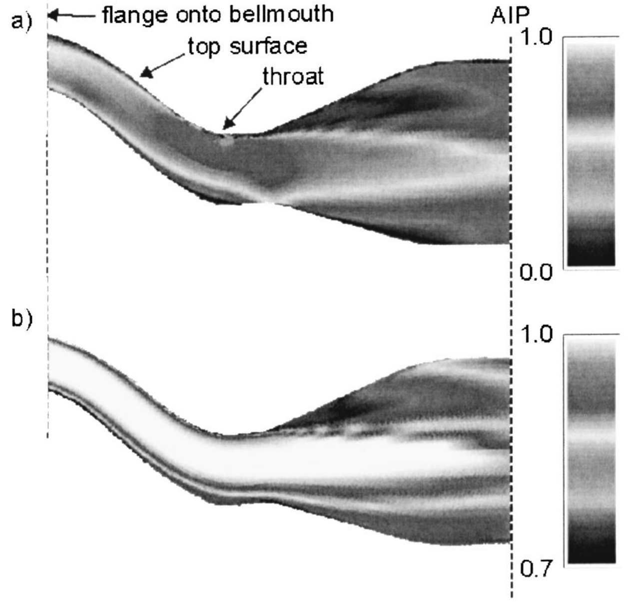

Fig. 7 Experimental surface flow visualisation showing *a*) the bottom and *b*) the top surfaces of the inlet and *c*) the top surface's separated region with inferred flow topology (lines) and the location of the hot-film sensor (white cross)

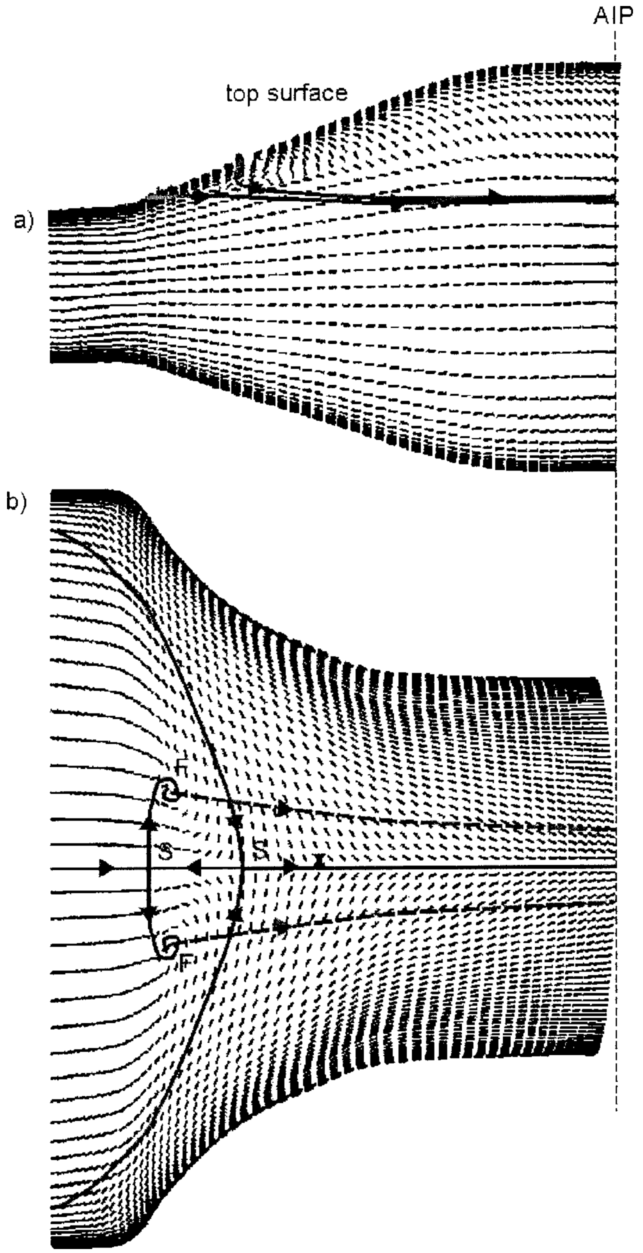

Fig. 8 Predicted contours of *a*) Mach number and *b*) P_t/P_∞ along the center-plane of the inlet

The centerplane Mach number contours that correspond to this surface static pressure distribution are shown in Fig. 7*a*. The inlet throat is apparent, and appears to be close to choking. Importantly, the Mach number is very low nearer the top and bottom inlet surfaces downstream of the inlet throat, which is the region that the inlet broadens to the AIP diameter. This is particularly marked on the top of the inlet, where flow separation is shown to occur.

Contours of stagnation pressure on the centerplane show the aerodynamic loss associated with this region of low Mach number flow (Fig. 7*b*). Up to the inlet throat, the strongly favorable pressure gradient along the top surface causes the surface flow along the centerplane to be characterized by relatively thin, *attached* boundary layers. However, a large region of low stagnation pressure occurs downstream of the inlet throat. This compares to the loss free flow in the middle of the centerplane, which does not extend to the AIP since the two large lobes of low stagnation pressure shown earlier in Figs. 3*b* and 4*b* eventually coalescence. It is therefore reasonable to suggest that a significant proportion of the loss observed at the AIP originates within this last section of the inlet, where the adverse pressure gradient has been shown to be strong, and the flow is later shown to separate.

Figures 6 and 7 also suggest that further modifications to the inlet design will have important consequences. The weight and drag of the aircraft can be minimized in two ways: by either shortening the inlet or making the inlet narrower. However, a given engine with a specified inlet Mach number of between 0.5 and 0.6 provides the downstream boundary condition to the inlet flow. If it is necessary to maintain a serpentine inlet design, reduced inlet length necessarily implies more aggressive flow turning. Once again invoking the analogy with a single airfoil at a now constant free-stream Mach number but with an increasing angle of attack, increased flow turning will increase the peak Mach numbers within the inlet. Similarly, continuity requires that peak inlet Mach numbers will be increased if the inlet is made narrower. Thus, shortening or narrowing the inlet have the same qualitative effect. Both will increase the peak Mach numbers within the inlet, whilst a given choice of engine will require that the flow at the AIP is maintained at roughly the same Mach number. The intensity of the adverse pressure gradient downstream of the inlet throat will therefore inevitably be increased, causing reduced inlet pressure recovery and, as is suggested in the present case, stronger separation and higher levels of its associated inlet unsteadiness.

Separated Flow Structure. The predicted velocity vectors within the last section of the inlet reveal the structure of the separation. Figure 8*a* shows a region of reversed flow near the top wall on the centerplane, with the estimated dividing streamlines also shown. Figure 8*b* shows the limiting surface flow on the top surface of the inlet. Four stagnation points are visible: two foci (F) and two saddles (S). The dashed lines originating from the two foci represent the approximate location of two vortices that extend away from the surface and downstream to the AIP. As discussed earlier, the swirling streamlines associated with these vortices are visible near the top of the inlet in Fig. 5.

Figure 9*b* and *c* shows that the numerical predictions and experiments give the same flow topology along the top of the inlet, even though the size of the separation is significantly larger in experiment. Experiments show that the flow along the entire top surface is attached up to the inlet throat. However, just downstream of the inlet throat the flow becomes strongly three dimensional and, in keeping with the limiting streamline pattern shown in Fig. 8*b*, the inferred surface topology in Fig. 9*b* also shows two foci and two saddles. Perry & Chong [8] call a separation with this limiting streamline topology an ''owl face of the first kind.'' Similar *predicted* flow structures in serpentine engine inlets have been reported in Seddon and Goldsmith [1] and Anderson et al. [2], although this paper is thought to be the first that verifies the existence of this structure experimentally.

A clearer picture of this basic separation structure is shown in Fig. 10, where the vortex pair that extends downstream is seen to originate at the two foci. Thus, the two vortices that are observed at the top of the AIP in Fig. 4*a* appear to originate at the two foci within the separated region. This is consistent with the swirling streamline patterns near the top surface in the last section of the inlet in Fig. 5. It is emphasized that this structure is not a typical separation bubble such as that classified by Horton [9]: it is not characterized by a reattachment point and recirculating flow. Nonetheless, the mean, surface normal velocity profiles throughout the separated region must be inflectional. In keeping with the many other inviscidly unstable shear layers such as mixing layers and more usual separation bubbles, it is therefore expected that the separation will be strongly unsteady and may respond to freestream disturbances [10].

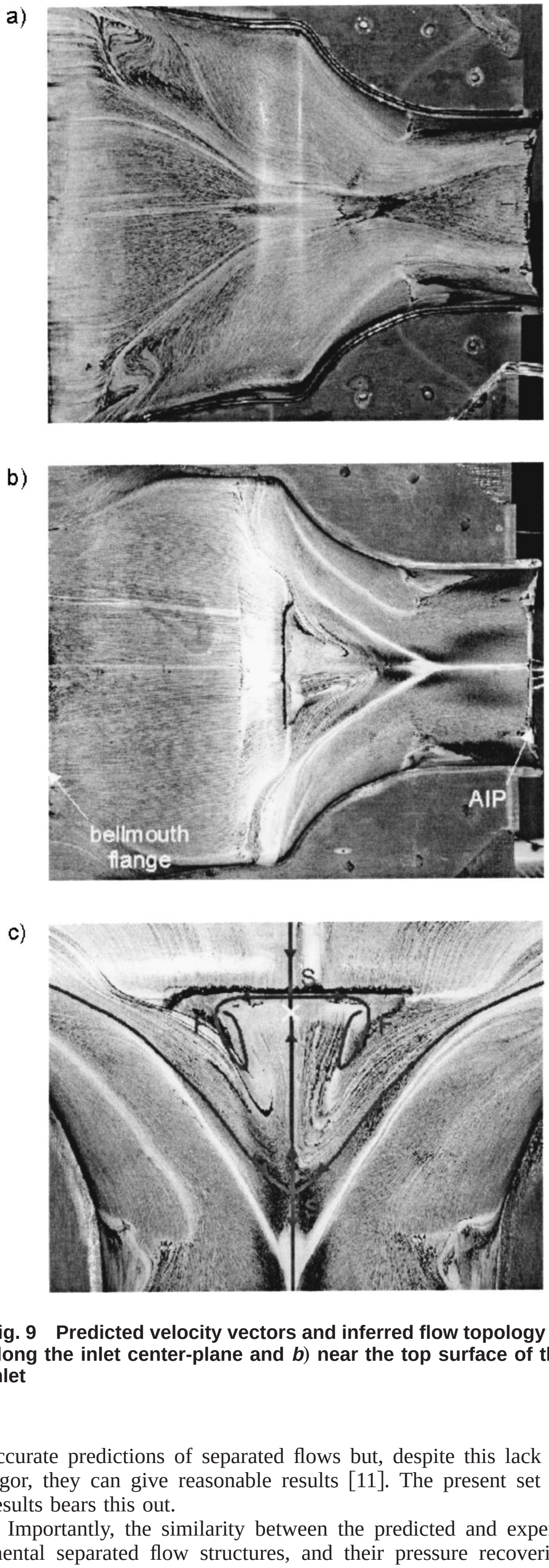

Fig. 9 Predicted velocity vectors and inferred flow topology *a*) along the inlet center-plane and *b*) near the top surface of the inlet

The differing size of the separated regions in experiment and the numerical prediction is not surprising. The numerical prediction was performed at a higher Reynolds number and lower Mach number than the experimental flow visualisations in Fig. 9, and the numerical prediction is a steady, Reynolds averaged solution of what is expected to be a strongly unsteady flow. Reynolds averaged turbulence models should not be expected to produce accurate predictions of separated flows but, despite this lack of rigor, they can give reasonable results [11]. The present set of results bears this out.

Importantly, the similarity between the predicted and experimental separated flow structures, and their pressure recoveries (Fig. 2), suggests that the separation has a significant impact on the inlet pressure recovery. A comparison of Figure 7*b* and 8*a* shows that the separation is also a region of considerable deficit in stagnation pressure. This compares to the attached boundary layers upstream of the separation in Fig. 7*b*, where the stagnation

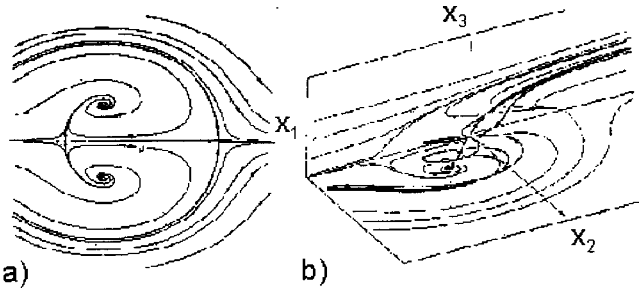

Fig. 10 An "owl-face of the first kind" [8]

pressure is significantly higher. Thus, large stagnation pressure losses appear to be produced within the separated region, and this high loss fluid should then convect to the AIP.

The creation of low stagnation pressure within separated regions is often observed in steady, Reynolds averaged numerical predictions of separated flows [12]. As was found in the present numerical prediction, the turbulence model can predict levels of turbulent viscosity within the separated region that can be several orders of magnitude greater than the laminar viscosity. As Brear et al. [12] show, the entropy generation rate per unit volume is directly proportional to the turbulent viscosity, and the turbulence model is therefore predicting that the primary sources of loss generation within the separation are the Reynolds stresses. Laminar stresses are less significant. Because the numerical prediction is steady, increased entropy is manifested as reduced stagnation pressure. Furthermore, Brear [13] showed that the Reynolds stresses within numerous separated flows can be an order of magnitude higher than those that occur in attached boundary layers. Thus, the numerical prediction of very high turbulent viscosity is physical, even though the absolute values of predicted turbulent viscosity are not expected to be accurate. It is therefore perhaps surprising that the predicted and measured inlet pressure recoveries agree as closely as they do (Fig. 2), and this serves to further the utility of steady, Reynolds averaged numerical predictions despite the lack of rigour of applying them to separated flows.

Large Reynolds stresses within separated flows are not surprising, given that such flows can feature large, coherent structures that often have some periodicity [10,11,14]. These structures can be long-lived and convect downstream for a considerable distance [15]. Whilst the Reynolds stresses within the separated region were not measured in the present investigation, coherent structures that either pass through the separation or are created within it are observed to convect to the AIP. As Fig. 11*a* shows, there is significant cross correlation between the surface mounted, shear stress sensor within the separated region (Fig. 7*c*) and the unsteady stagnation pressure sensor 1 located close to the center of the stagnation pressure deficit at the AIP (Fig. 3*b*). Figure 11*a* shows that there is a lag of approximately 1 ms between events occurring at probe 1 at the AIP and those occurring within the separation. This lag is similar to the calculated convection time from the separation point to the AIP of 0.75 ms [5,16] and, since the shear stress sensor cannot measure acoustic fluctuations, this correlation must involve some form of flow structure. Furthermore, Figure 11*a* also shows that this structure has a dominant frequency of approximately 500 Hz. Figure 11*b* also shows this characteristic frequency, as well as showing that the structures arriving at the AIP have significant spatial extent because there is no lag between probes 1 and 2. Figure 11 is therefore strong evidence for suggesting that the separation has characteristics that are typical of separated flows. It appears that the separation creates large structures with a characteristic frequency, and that these structures convect downstream to the AIP.

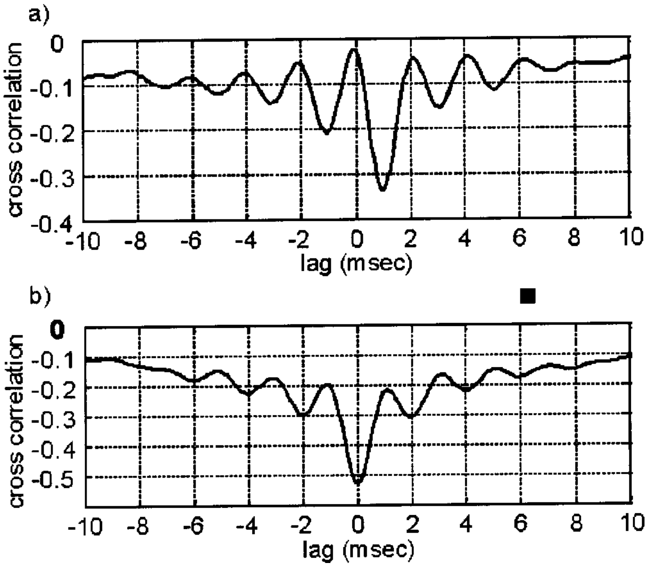

Fig. 11 Cross correlations at design massflow rate between *a*) the unsteady stagnation pressure probe 1 at the AIP in Fig. 3*b* and the hot-film sensor located at X in Fig. 7 and *b*) the two unsteady stagnation pressure probes at the AIP in Fig. 3*b*

Conclusions

This paper presented an experimental and computational study of the engine inlet on an uninhabited combat air vehicle (UCAV) operating at cruise conditions. At this flight condition, the flow entering the inlet had a uniform stagnation pressure and did not experience lip separations and other phenomena that are characteristic of take-off, landing and maneuvering. As such, any deterioration of the flow that enters the compressor is the result of phenomena that are internal to the inlet.

A separation on the top surface of the inlet appeared to be a significant contributor to reduced inlet pressure recovery and increased inlet unsteadiness. The time-averaged structure of this separation was identified by reference to a more fundamental study, and featured two vortices that extended downstream to the fan face. Furthermore, measurements suggested that the separation created large, unsteady structures that were observed at the fan face. The numerical predictions also indirectly suggested that this unsteady phenomenon caused large Reynolds stresses within the separated region that in turn generated significant loss. Thus, the separation seemed to be the cause of both a reduction in inlet pressure recovery and an increase in inlet unsteadiness by the same basic mechanism.

This unsteady behavior of the separation has important consequences for inlet design. An increase in the inlet Mach number or a reduction in the length of the inlet should increase the intensity of the adverse pressure gradients within the inlet. Stronger adverse pressure gradients cause stronger separations, which should therefore lead to reduced pressure recovery and increased inlet unsteadiness. Thus, further reductions in the inlet length or width either requires that the designer accepts the reduced performance, or finds some means of decoupling the inlet performance from changes in the geometry. Since both the unsteadiness and the pressure recovery appear to be the result of phenomena that originate from a contained region, this inlet is therefore a clear candidate for the application of separated flow control.

Acknowledgment

This work was supported by the Defense Advanced Research Projects Agency (DARPA), under the guidance of Dr. Richard Wlezian.

Nomenclature

AIP = aerodynamic interface plane (fan face)
$\dot{m}$ = mass-flow rate (lb/s)
Ma_∞ = flight Mach number
P_s = static pressure (Pa)
P_t = stagnation pressure (Pa)
P_∞ = free-stream stagnation pressure (Pa)
$\mathrm{Re}_{\mathrm{AIP}}$ = Reynolds number based on AIP diameter
x_{1-3} = cartesian axes
π_d = area averaged inlet pressure recovery

References

[1] Seddon, J., and Goldsmith, E. L., 1999, ''Intake aerodynamics,'' 2nd edition, AIAA education series, AIAA.
[2] Anderson, B. H., Miller, D. N., Yagle, P. J., and Truax, P. P., 1999, ''A study of MEMS flow control for the management of engine face distortion in compact inlet systems,'' Proc. 3rd ASME/JSME Conference, San Francisco, ASME paper no. FEDSM99-6920.
[3] Ng, W., and Burdisso, R. A., 2001, ''Active acoustic and flow control for aeropropulsion,'' 39th AIAA Aerospace Sciences Meeting & Exhibit, Reno, AIAA paper no. AIAA 2001-0220.
[4] SAE Committee S-16, 1977, ''ARP 1420-Gas turbine engine inlet flow distortion guidelines.''
[5] Warfield, Z., 2001, ''Active control of separation induced distortion in a scaled tactical aircraft inlet,'' M.S. Thesis, Massachusetts Institute of Technology.
[6] Schlichting, H., 1979, ''Boundary layer theory,'' McGraw-Hill, New York.
[7] Abbott, I. H., and von Doenhoff, A. E., 1959, ''Theory of wing sections,'' Dover, New York.
[8] Perry, A. E., and Chong, M. S., 1986, ''A series expansion study of the Navier-Stokes equations with applications to three-dimensional separation patterns,'' J. Fluid Mech., **173**, pp. 207–223.
[9] Horton, H. P., 1969, ''A semi-empirial theory for the growth and bursting of laminar separation bubbles,'' ARC current papers, no. 1073.
[10] Gad-el-Hak, M., 1990, ''Control of low speed aerodynamics,'' AIAA J., **28**, no. 9, pp. 1537–1552.
[11] Lubcke, H., Schmidt, St., Rung, T., and Thiele, F., 2001, ''Comparison of LES and RANS in bluff-body flows,'' J. Wind. Eng. Ind. Aerodyn., **89**, pp. 1471–1485.
[12] Brear, M. J., Hodson, H. P., and Harvey, N. W., 2002, ''Pressure surface separations in low pressure turbines-part 2: interactions with the secondary flow,'' ASME J. Turbomach., **124**, pp. 402–409.
[13] Brear, M. J., 2000, ''Pressure surface separations in low pressure turbines,'' Ph.D dissertation, Cambridge University.
[14] Brear, M. J., Hodson, H. P., and Harvey, N. W., 2002, ''Pressure surface separations in low pressure turbines-part 1: midspan results,'' ASME J. Turbomach., **124**, pp. 393–401.
[15] Castro, I. P., and Epik, E., 1998, ''Boundary layer development after a separated region,'' J. Fluid Mech., **374**, pp. 91–116.
[16] Braddom, S., 2002, ''Design and Characterization of Robust Hot Film Sensors for Tactical Aircraft Inlets,'' M.S. Thesis, Massachusetts Institute of Technology.

Kenji Kawashima
Precision and Intelligence Laboratory,
Tokyo Institute of Technology,
4259 Nagatsuta-cho,
Midori-ku, Yokohama,
Kanagawa, 226-8503
e-mail: kkawashi@pi.titech.ac.jp

Yukio Ishii[1]
[1]Department of Precision Machinery Systems,
Tokyo Institute of Technology

Tatsuya Funaki

Toshiharu Kagawa

Precision and Intelligence Laboratory,
Tokyo Institute of Technology,
4259 Nagatsuta-cho,
Midori-ku, Yokohama,
Kanagawa, 226-8503

Determination of Flow Rate Characteristics of Pneumatic Solenoid Valves Using an Isothermal Chamber

In this paper, two new methods for obtaining the sonic conductance and the critical pressure ratio of pneumatic valves are proposed. Both methods use a chamber that can approximate isothermal conditions. This was achieved by filling the chamber with metal wire, which creates a larger heat transfer area and heat transfer coefficient. The sonic conductance and the critical pressure ratio are obtained by measuring the pressure in the chamber during charging and discharging. These methods take only seconds to perform and require less energy than the ISO 6358 procedure. The major factor in the error for the pressure response during the charging of the isothermal chamber is the upstream pressure change. Nevertheless, the sonic conductance can be determined within a 3% uncertainty. In addition, the sonic conductance calculated from the pressure response during the discharging of the chamber can be determined within a 1.2% uncertainty.
[DOI: 10.1115/1.1667888]

1 Introduction

Recently pneumatic systems have been used in a precise positioning stage to isolate vibration [1], or an accurate position control [2] because air has advantages such as compressibility, clean energy, high power ratio, nonmagnetic etc. These systems are typically applied in the semiconductor manufacturing process.

In pneumatic systems, power is transmitted and controlled through a gas under pressure with solenoid valves and servo valves. Therefore, the flow rate of such valves is the most important characteristic in construction of pneumatic systems and controller design. Since air is a compressible fluid, the flow rate characteristic is nonlinear [3]. At the sonic (choked) condition the flow rate is constant, and at the subsonic condition the flow rate decreases due to the rise of the downstream pressure.

According to the ISO standard (ISO 6358, 1989) [4] and JIS (JIS B 8390, 2000) [5], the flow rate of pneumatic components is characterized by the sonic conductance and the critical pressure ratio. The sonic conductance to indicates the ability of flow to pass under the sonic condition. In a nozzle, the boundary between the sonic and the subsonic condition is given by the pressure ratio between downstream and upstream of the nozzle, the critical pressure ratio, which is 0.5283 obtained from the Bemoullis' Law and isentropic process [6]. However, as the flow pathway is complicated in actual valves, it is known that the critical pressure ratio differs from the ideal value [3]. Therefore, the sonic conductance and the critical pressure ratio are calculated from the mass flow rate through the test valve, and the differential pressure across the valve with methods detailed by the ISO 6358 standards. These methods, however, have a disadvantage. Because the pressure and the flow rate must be measured under steady-state flow, a long measurement time is needed. As a result, these methods consume much time and energy.

However, the process of charging and discharging air into a chamber requires only seconds and a minimal amount of energy consumption. Therefore, if a pressure response process can be used to measure the sonic conductance and the critical pressure ratio, it will be a useful energy saving method.

A pressure response method that utilizes a charging process has been proposed by Kuroshita [7]. This method determines the flow rate characteristics under the vacuum condition and, hence, has the disadvantage of needing a vacuum pump, which can also induce a temperature change error. In fact, the air temperature in a normal chamber can vary up to 40 K, which affects the accuracy of the flow rate measurements. There are other proposed methods for determining the flow rate characteristics during discharge [8], and these methods have room for consideration of the error due to temperature change in the chamber.

However, if the air charge and discharge is performed under isothermal conditions, the flow rate characteristics can be measured easily and accurately due to exclusion of the temperature change influence. The authors have proposed a chamber filled with steel wool [9] that can approximate an isothermal condition. By using this isothermal chamber, the instantaneous flow rate can be measured within a 1% error [9,10]. Therefore, it is highly probable that the pressure response method can be used for measuring the flow rate characteristics of pneumatic valves if the isothermal chamber is used.

In this study, the pressure response from the charge and discharge of air in an isothermal chamber is used to determine the sonic conductance and the critical pressure ratio of pneumatic valves. Four solenoid valves were tested, and the effectiveness of the proposed method was confirmed.

2 ISO Method for Measuring Flow Rate Characteristics

Two methods for measuring the sonic conductance and the critical pressure ratio are defined in ISO 6358. The first method involves maintaining a steady flow rate and keeping the upstream pressure constant while the downstream pressure is decreased. In this paper, this method is referred to as the $\mathrm{ISO_u}$ method. In the second method, the downstream pressure is set to atmospheric pressure and the upstream pressure is changed, while a steady flow rate is maintained. This method is called the $\mathrm{ISO_d}$ method. The experimental setup for the $\mathrm{ISO_u}$ method is provided in Fig. 1 and the experimental setup for the $\mathrm{ISO_d}$ method is provided in Fig.

Contributed by the Fluids Engineering Division for publication in the JOURNAL OF FLUIDS ENGINEERING. Manuscript received by the Fluids Engineering Division April 2, 2003; revised manuscript received October 6, 2003. Associate Editor: M. J. Andrews.

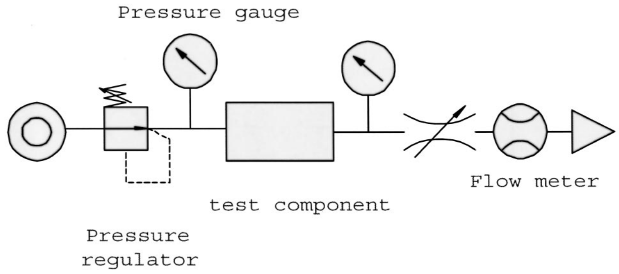

Fig. 1 Experimental apparatus of ISO method fixing upstream pressure

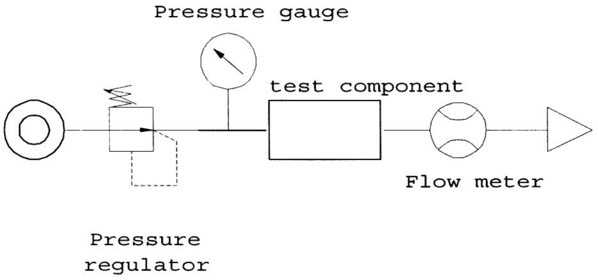

Fig. 2 Experimental setup for the ISO method fixing the downstream pressure

2. A pressure sensor, accurate within 0.2%, and a gas meter, accurate within 1%, are used to measure the average flow rate.

In the $\mathrm{ISO_u}$ method, the sonic conductance is determined from the flow rate at the choked flow, and the critical pressure ratio is calculated using the data from four points in the subsonic flow. The flow rate characteristics calculated from the $\mathrm{ISO_u}$ method, however, are sometimes different from the actual values [11]. Therefore, this study uses experimental values instead of those obtained with the $\mathrm{ISO_u}$ method. After calculating the sonic conductance from the flow rate at the choked flow, more than 10 points from the experimental data in the subsonic flow are used to calculate the critical pressure ratio. This method is called the modified ISO method. In this paper, this ISO method is used instead of the $\mathrm{ISO_u}$ or the $\mathrm{ISO_d}$ method.

3 Pressure Response Method for Measuring the Flow Rate Characteristics Using the Isothermal Chamber

3.1 Charge Method. The proposed method for determining the flow rate characteristics from the charge response in an isothermal chamber is called the "charge method." The experimental setup for the charge method, shown in Fig. 3, consists of an air supply, a pressure regulator, a sub tank, a solenoid valve, an isothermal chamber, and a pressure sensor. The pressure sensor was a semi-conductor type made by Toyoda machine works, LTD. The linearity of the pressure sensor is 1% and the hysteresis is 0.5% against full scale. We calibrated this sensor with an accurate pressure gauge of uncertainty less than 0.2%. A 12-bit A/D board is used to obtain the pressure data. The internal volume of the isothermal chamber was 3.0×10^{-3} m^3 and the volume of the sub tank is 30×10^{-3} m^3. The supply pressure is set to 588 kPa. The supply pressure was measured at the sub tank. The pressure in the isothermal chamber was measured at the both side of cylindrical chamber and confirmed that there was no pressure distribution in the chamber. The resolution of the pressure sensor was 0.5 Pa and the sampling time is 5 ms.

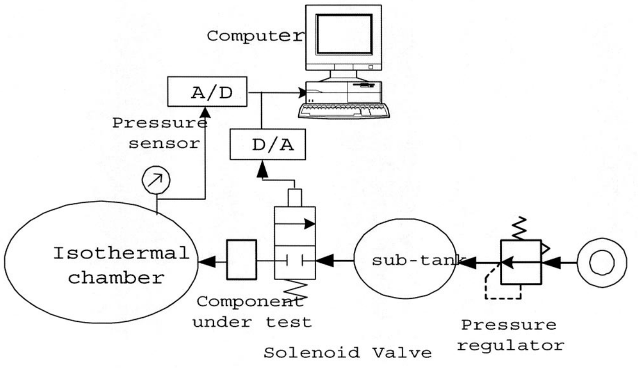

Fig. 3 Experimental setup for the charge method

When an isothermal chamber was used, it is assumed that the air in the chamber remains isothermal [9,10]. Therefore, Eq. (1) can be obtained from the state equation of ideal gases.

$$V\frac{dP}{dt}=GR\theta \tag{1}$$

The flow rate through a pneumatic valve is represented in the following two formulas [4].

1. The case of choked flow

$$G=C\rho_0P_1\sqrt{\frac{\theta_0}{\theta}} \tag{2}$$

2. The case of subsonic flow

$$G=C\rho_0P_1\sqrt{\frac{\theta_0}{\theta}}\sqrt{1-\left(\frac{\frac{P_2}{P_1}-b}{1-b}\right)^2} \tag{3}$$

where C is the sonic conductance which represents the flow passes ability and b is the critical pressure ratio. The pressure response equations in the chamber, which can be derived from Eqs. (1), (2) and (3), are provided below when we assume the supply pressure P_1 is Ps and downstream pressure P_2 is the pressure in the chamber P.

1. The case of choked flow

$$P=P_a+\frac{C\rho_0P_s}{V}R\sqrt{\theta_0\theta_a}t=f_1(t) \tag{4}$$

2. The case of subsonic flow

$$P=P_s(1-b)\cdot\sin\left(\frac{C\rho_0}{(1-b)V}R\sqrt{\theta_0\theta_a}(t-t_c)\right)+bP_s=f_2(t) \tag{5}$$

Equations (4) and (5) represent the theoretical pressure response equations. For the choked flow, when the air in the chamber is isothermal, the pressure increases linearly with time, as shown in Fig. 4. The proposed method determines the sonic conductance and the critical pressure ratio by fitting the experimental pressure response with the theoretical pressure response given by Eqs. (4) and (5). The Gauss-Newton method, a nonlinear least square method, is used to fit the pressure response. The details of this procedure can be found in the appendix. This fitting method allows for the sonic conductance and the critical pressure ratio to be obtained quickly and accurately.

3.2 Discharge Method. The proposed method for determining the flow rate characteristics from the discharge response in an

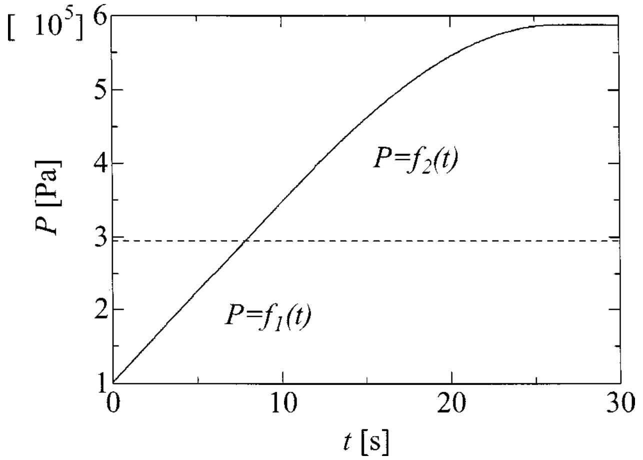

Fig. 4 Pressure response during charging (sampling time 5 ms)

isothermal chamber is called the "discharge method." The experimental setup for the discharge method, shown in Fig. 5, consists of an air supply, a pressure regulator, a solenoid valve, an isothermal chamber, and a pressure sensor. The pressure sensor was a semi-conductor type, and an A/D board was used to obtain the pressure data. The internal volume of the isothermal chamber was 3.0×10^{-3} m^3 and the supply pressure was set to 588 kPa. The resolution of the sensor and the sampling time was same as charge method. The supply air was charged in to the isothermal chamber in advance, and the shut the upstream valve. Then the test valve was opened to start discharge.

When an isothermal chamber is used, it is assumed that the air in the chamber remains isothermal. Therefore, the pressure response equations, Eqs. (1), (2), and (3), are also valid during discharge.

1. The case of choked flow

$$P=P_i e^{-1/T_p} \qquad T_p=\frac{V}{R\theta C\rho_0}\sqrt{\frac{\theta}{\theta_0}} \tag{6}$$

1. The case of subsonic flow

(a) $0.0<b<0.5$

$$P=\frac{-bP_a}{1-2b}+\frac{(1-b)P_a}{1-2b}\cosh\frac{1}{T_p}\frac{\sqrt{1-2b}}{1-b}\times\left\{t-T_p\ln\left(\frac{bP_i}{P_a}\right)+T_p\frac{1-b}{\sqrt{1-2b}}\ln\frac{1-\sqrt{1-2b}}{1+\sqrt{1-2b}}\right\} \tag{7}$$

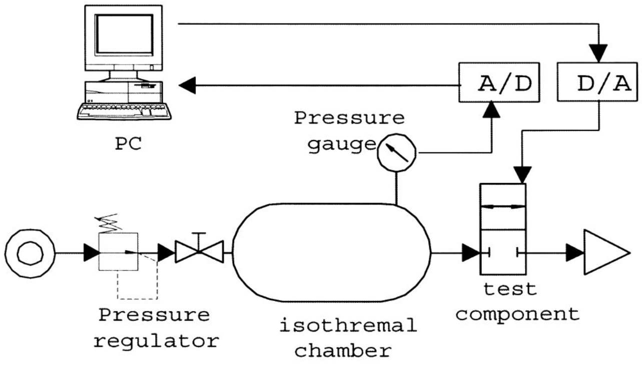

Fig. 5 Experimental setup for the discharge method

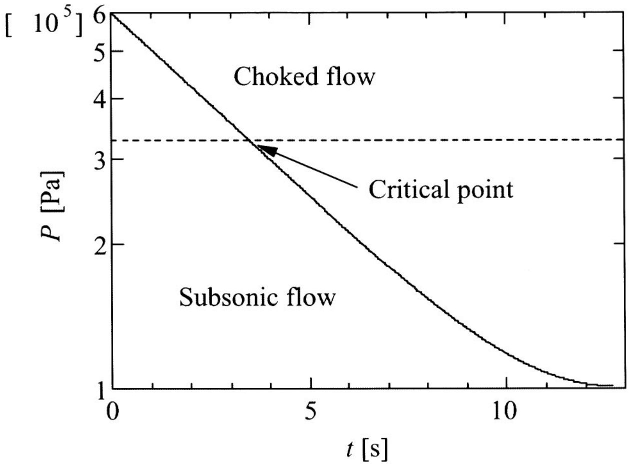

Fig. 6 Pressure response during discharge (sampling time 5 ms)

(b) $b=0.5$

$$P=\frac{P_a}{T_p^2}\left\{t-T_p\ln\left(\frac{bP_i}{P_a}\right)-T_p\right\}^2+P_a \tag{8}$$

(c) $0.5<b<1.0$

$$P=\frac{bP_a}{2b-1}+\frac{(1-b)P_a}{2b-1}\cos\left[\frac{\sqrt{2b-1}}{1-b}\times\left\{\frac{1}{T_p}-\ln\left(\frac{bP_i}{P_a}\right)\right\}+2\arctan\frac{1}{\sqrt{2b-1}}\right] \tag{9}$$

During discharge, the pressure decreases logarithmically with time, as shown in Fig. 6. Therefore, the flow rate characteristics for the discharge method can be calculated with the nonlinear least square method, the same as in the charge method.

4 Experimental Results and Discussions

The purpose of the experiment was to investigate the influence of changes in air temperature on the accuracy of the system. Steel wool with a diameter of approximately 25 μm and copper wire with a diameter of approximately 50 μm were used in the experiments. The density of the steel wool is 7.86×10^3 $\mathrm{kg/m}^3$ and that of copper is 8.96×10^3 $\mathrm{kg/m}^3$.

The sonic conductance and the critical pressure ratio were determined using the proposed methods, with the isothermal chambers filled with metal wires. The results of the experiments are presented in the following subsection.

4.1 Temperature Changes in the Isothermal Chamber. A chamber can approximate isothermal characteristics when it is filled with metal wire. The temperature change is dependent on the diameter of the metal wire because we have already studied that the heat transfer area is a very important factor [12]. In this experiment, steel wool with a diameter of about 25 μm and copper wire with a diameter is about 50 μm were used. The heat capacitance of the both types of wire was almost the same, at about 3,000 times larger than that of air.

To realize isothermal condition, the heat transfer area [13] becomes very important [12]. When the steel wool, with diameter 25 μm was used, the heat transfer area became about 18 m^2 against the chamber size of 3.0×10^{-3} m^3 assuming the wire is cylindrical. When the copper wire with diameter 50 μm was used the area became 8 m^2.

The stop method [9] was used to investigate the degree of temperature change between the different kinds of metal wool. The

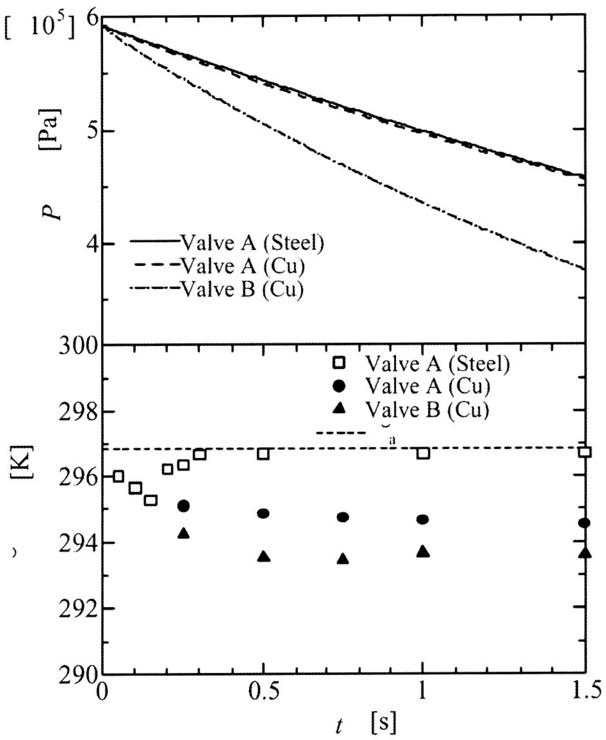

Fig. 7 Temperature changes in the isothermal chambers

stop method is introduced as follows: Stop the solenoid valve at the time we want to know the temperature $\overline{\theta}(t)$. Measure the pressure at that time $P(t)$ and the pressure when it becomes stable P_∞ using a pressure sensor. When the pressure becomes stable, the temperature in the chamber recovers to the room temperature. Hence, we can measure the average temperature at the time t using the Law of Charles.

$$\overline{\theta}(t)=\frac{P(t)}{P_\infty}\theta_a \tag{10}$$

By changing the time to stop discharge or charge, the average temperature at any time could be measured. We confirmed that the uncertainty of this method is within 3% [9].

The experimental results are shown in Fig. 7. The upper graph in Fig. 7 shows the pressure responses, and the lower graph represents the temperature changes. After 1.5 s the temperature becomes almost constant. Therefore, the experimental results before 1.5 s is shown in Fig. 7.

When the steel wool was used, the temperature dropped a maximum of 1.5 K, and then the temperature quickly returned to room temperature as shown in Fig. 7. On the other hand, when the copper wire was used, the temperature changed a maximum of 3 K. Compared with the steel wool, the temperature of the copper wire changed gradually. These results show that the chamber filled with metal wire is able to closely simulate isothermal conditions, when compared with a normal chamber that can have a maximum decrease in temperature of 40 K.

4.2 Experimental Results of the Charge Method. Table 1 shows the flow rate characteristics determined by the charge method when the chamber was filled with steel wool. Table 2 shows the calculated flow rate characteristics determined by the charge method when the chamber was filled with copper wire. It is clear from Table 1 that the sonic conductance error of the charge method remains within 3% from Table 1. The maximum difference in the critical pressure ratio between the value calculated from the modified $\mathrm{ISO_u}$ method and the charge method is 0.08, which is 53.3%.

The critical pressure ratio is especially hard to measure correctly, due to the ellipse approximation for the subsonic flow. Therefore, the critical pressure ratio will always contain a slight error. However, from the viewpoint of calculated flow rate characteristics, these experimental results are adequate enough for practical use, as illustrated in Fig. 8. Even though the critical ratio difference is 53.3%, the black dots and the solid line show good agreement on the whole. So the flow characteristics of the valve can be represented even though the critical ratio differs 0.08.

When the copper wire is used, as depicted in Table 2, the proposed method is proven effective.

4.3 Influence of the Upstream Pressure Change. When the charge method is performed with the isothermal chamber and a solenoid valve with a high sonic conductance, the upstream pressure decreases. This decrease in upstream pressure affects the accuracy of the measured flow rate characteristics.

The upstream pressure change was investigated by placing a pressure sensor on the upstream chamber. The response character-

Table 1 Experimental results using the charge method with the chamber with stuffed steel wool

	Sonic conductance 10^{-9} [$\mathrm{m^3/(sPa)}$]			Critical Pressure Ratio		
Solenoid Valve	Modified $\mathrm{ISO_u}$ method	Charge method	Error Percentage	Modified $\mathrm{ISO_u}$ method	Charge method	Error Percentage
A	4.84	4.81	−0.62	0.15	0.23	53.3
B	8.42	8.24	−2.14	0.33	0.37	12.2
C	2.76	2.76	0	0.35	0.41	17.1
D	5.61	5.58	−0.53	0.39	0.45	13.3

Table 2 Experimental results using the charge method with the chamber stuffed with copper wire

	Sonic conductance 10^{-9} [$\mathrm{m^3/(sPa)}$]			Critical Pressure Ratio		
Solenoid Valve	Modified $\mathrm{ISO_u}$ method	Charge method	Error Percentage	Modified $\mathrm{ISO_u}$ method	Charge method	Error Percentage
A	4.84	4.87	0.62	0.15	0.18	20.0
B	8.42	8.32	−1.18	0.33	0.34	3.0
C	2.76	2.78	0.72	0.35	0.38	8.6
D	5.61	5.54	−1.25	0.39	0.40	2.6

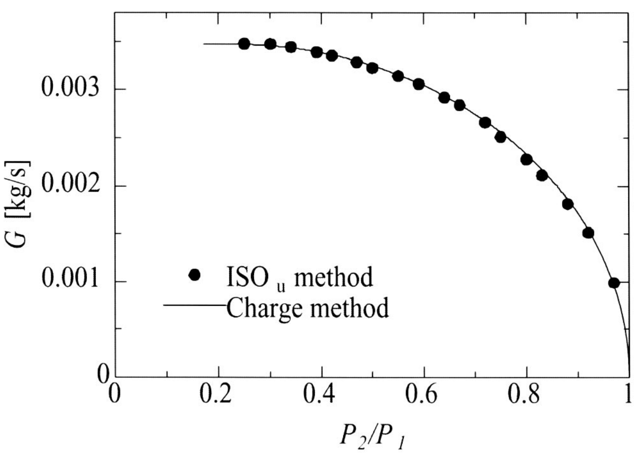

Fig. 8 Flow rate characteristics by charge method (Valve A steel wool)

istics of Valve B, which had the worst upstream pressure change, are shown in Fig. 9. In this figure, the horizontal axis represents the time from the start of the charging process. Immediately after the start of charging, the upstream pressure decreased about 16 kPa. After the initial drop, the upstream pressure linearly recovered to the designated regulator pressure, 588 kPa. In this experiment, the volume of the chamber was 30×10^{-3} m^3. If a bigger chamber is used, the upstream pressure change decreases. Therefore, the sonic conductance measuring error could be reduced by using a larger chamber.

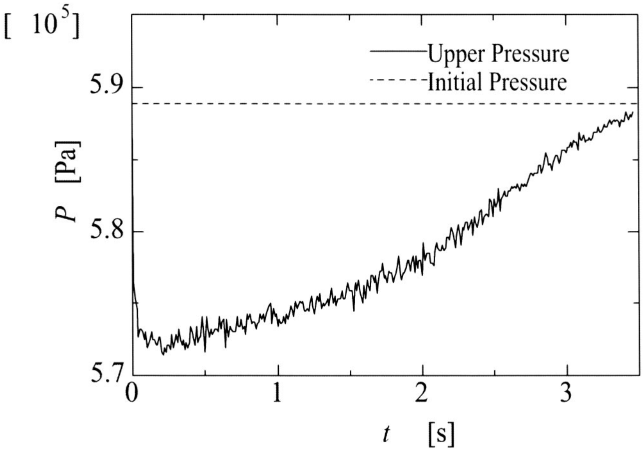

Fig. 9 Upstream pressure change during charge

4.4 Experimental Result with the Discharge Method

Table 3 shows the flow rate characteristics determined by the discharge method when the chamber was filled with steel wool. Table 4 shows the flow rate characteristics determined by the discharge method when the chamber was filled with copper wire.

The results from both the discharge method and the ISO_d method are provided in Table 3, as well as the error of the ISO_d method. The graphs of Valve A's flow rate characteristics are shown in Fig. 10.

The error for Valve A is higher than the other solenoid valves because its critical pressure ratio is lower than its initial pressure ratio. These values don't produce a choked flow state, and the sonic conductance can not be estimated accurately. The initial pressure in this experiment was 591 kPa, and the initial pressure ratio was 0.17. Therefore, to obtain an accurate measurement, the critical pressure ratio for the solenoid valve must be higher than this value. The other solenoid valves produced the choked flow state and their sonic conductance values were measured within 1% accuracy.

These results suggest that an accurate sonic conductance can be obtained by setting the proper initial pressure ratio. Also, it was determined that the minimum pressure time constant should be 3.5 s to obtain accurate experimental results.

The experimental results for the copper wire-filled chamber are shown in Table 4. By comparing these results with those of the steel wool-filled chamber, it was found that the steel wool produced a lower error. This can be attributed to the ability of steel wool to more accurately simulate the isothermal condition. As the temperature change increases, the sonic conductance values are determined to be larger than their actual values. The experimental results reflect this trend.

The sonic conductance of Valve A is difficult to determine. Because the sonic conductance values were measured to be larger than their actual values, so the calculated critical pressure ratio is smaller than its actual value. The ISO_d method calculated the Valve A critical pressure ratio to be 0.10, a particularly small value. For the purposes of this research, critical pressure ratios

Table 3 Experimental result using the discharge method with the chamber stuffed with steel wool

	Sonic conductance 10^{-9} [m^3/(sPa)]			Critical Pressure Ratio		
Solenoid Valve	Modified ISO_d method	discharge method	Error Percentage	Modified ISO_d method	discharge method	Error Percentage
A	4.84	4.98	2.89	0.1	0.08	25.0
B	8.51	8.55	0.47	0.25	0.25	0.0
C	2.77	2.79	0.72	0.28	0.27	3.7
D	5.71	5.72	0.18	0.35	0.35	0.0

Table 4 Experimental result using the discharge method with the chamber stuffed with copper wool

	Sonic conductance 10^{-9} [m^3/(sPa)]			Critical Pressure Ratio		
Solenoid Valve	Modified ISO_d method	discharge method	Error Percentage	Modified ISO_d method	discharge method	Error Percentage
A	4.84	-	-	0.1	-	-
B	8.51	8.66	1.76	0.25	0.17	−32.0
C	2.77	2.79	0.72	0.28	0.21	−25.0
D	5.71	5.72	0.18	0.35	0.29	−17.1

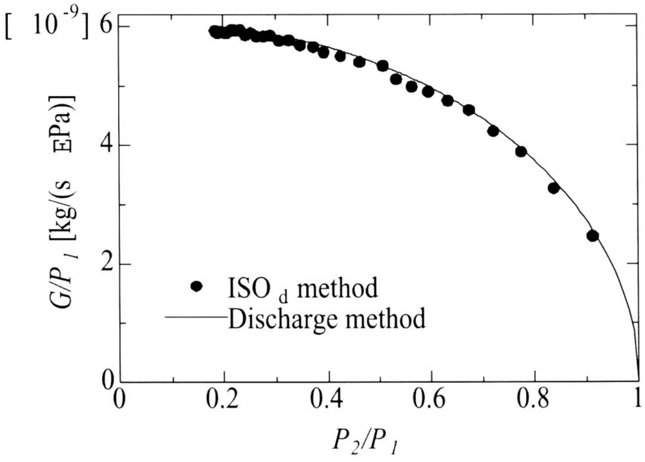

Fig. 10 Flow rate characteristics by discharge method (Valve A steel wool)

less than 0.10 were not considered. Therefore, the flow rate characteristics for Valve A could not be obtained by the proposed method.

4.5 Uncertainty. The quality of the isothermal condition in the chamber depends on the weight per unit volume of the metal wire [9]. For example, when the chamber is stuffed with 300 kg/m^3 of steel wool with a diameter of 25 μm, as shown in Fig. 4, the temperature decreases a maximum of 2 K. Also, when the pressure change velocity increases, the isothermal quality of the chamber deteriorates. It was determined that the pressure change velocity needs to remain below 100 kPa/s for the temperature change error to remain within 0.5%.

The error for the proposed charge response method is given by the following formula.

$$\frac{\delta C}{C} = \sqrt{\left(\frac{\delta P}{P}\right)^2 + \left(\frac{\delta P_s}{P_s}\right)^2 + \left(\frac{\delta V}{V}\right)^2 + \left(\frac{\delta t}{t}\right)^2 + \frac{1}{4}\left(\frac{\delta \theta}{\theta}\right)^2} \tag{11}$$

The error for the pressure sensor δP is 0.5%. The error due to the change in the supply pressure δP_s is a maximum of 3%, as determined from the experimental results shown in Fig. 6. The chamber volume measurement error δV is 0.5%. The time lag for the solenoid valve δt is 0.01 seconds, resulting in a time measurement error of 0.1% when the measurement time is 10 s. The temperature measurement error $\delta \theta$ is 1 K, resulting in an error rate of 0.3%. The sonic conductance error has a maximum of 3%. Using the Table 1 results, the sonic conductance is within this error range. Therefore, this method has sufficient accuracy for practical use.

The error of the proposed discharge response method is given by the following formula.

$$\frac{\partial C}{C} = \sqrt{\left(\frac{\delta P}{P \ln(P/P_1)}\right)^2 + \left(\frac{\delta P_i}{P_i \ln(P/P_i)}\right)^2 + \left(\frac{\delta V}{V}\right)^2 + \left(\frac{\delta t}{t}\right)^2 + \frac{1}{4}\left(\frac{\delta \theta}{\theta}\right)^2} \tag{12}$$

The pressure error includes the logarithmic portion of the error equation, and the critical pressure ratio is applied to the pressure ratio as a natural logarithm. Therefore, the sonic conductance error determined by the discharge method has a maximum of 1.2%.

5 Conclusion

Two new methods for obtaining the sonic conductance and the critical pressure ratio were proposed. The charge method determines the flow rate characteristics from the pressure response during the charging of an isothermal chamber. The discharge method determines the flow rate characteristics from the pressure response during the discharge.

The major factor affecting the accuracy of the charge method is the change in the upstream pressure. With the proposed experimental system, the uncertainty remained within 3% and, therefore, is sufficient for practical use. The discharge method with the isothermal chamber resulted in a maximum sonic conductance uncertainty of 1.2%.

The proposed methods have several advantages over the ISO method, such as short measurement time and air consumption. Therefore, these methods are preferred for everyday use.

Acknowledgments

The authors are grateful to Mr. Oneyama, Dr. Zhang and Mr. Seno of the SMC Corporation for their advice and support.

Nomenclature

b = Critical pressure ratio []
C = Sonic conductance [m^3/(sPa)]
G = Mass flow [kg/s]
P = Pressure [Pa]
R = Gas constant [J/(kg·K)]
t = Time [s]
V = Volume of chamber [m^3]
θ = Temperature [K]
ρ = Air density [kg/m^3]
T_p = Pressure time constant [s]

Subscripts

0 = Normal condition
1 = Upper Pressure
2 = Lower Pressure
a = Atmosphere
s = Supply
c = Choke state

Appendix

The calculation process for determining the sonic conductance and the critical pressure ratio by the Gauss-Newton method is performed as follows:

1. Initial values C_0 and b_0 are given for the pressure response equations, Eq. 4 and 5: $P=f_1(t)$, $P=f_2(t)$.
2. The square residual error S_0 is calculated by: $\Sigma(P_i - f(t_i, C_0, b_0))^2$.
3. The elements $\partial f/\partial C$, $\partial f/\partial b$ and $P_i - f(t_i, C, b)$, are calculated for $i = 1 \sim n$.
4. The linear equation

$$\sum \left(\frac{\partial f_i}{\partial b}\right)^2 \Delta b + \sum \frac{\partial f_i}{\partial C}\frac{\partial f_i}{\partial b}\Delta C = \sum \frac{\partial f_i}{\partial b}(P_i - f(t_i, C, b))$$

is solved using the modified values $\Delta C, \Delta b$.

5. Determine C and b by using the equation $C = C_0 + \Delta C$, $b = b_0 + \Delta b$.

6. Calculate $s = \Sigma(P_i - f(t_i, C_0, b_0))^2$. If this value satisfies the convergence condition $|(s - s_0)/s| < \varepsilon$, the determination process is ended. If it does not satisfy the condition, the aforementioned process is repeated by setting C and b to C_0 and b_0.

References

[1] Wakui, S., 2003, Incline Compensation Control Using an Air-Spring Type Active Isolated Apparatus, Prec. Eng., **27**, pp. 170–174.

[2] Kagawa, T., Tokashiki, L., Fujita, T., and Sakaki, T., 2000, Accurate Positioning of a Pneumatic Servosystem with Air Bearings, Bath Workshop on Power Transmission and Motion Control, pp. 257–268.

[3] Andeersen, B., 1967, The Analysis and Design of Pneumatic Systems, John Wiley and Sons, Inc.

[4] ISO6358: Pneumatic Fluid Power-Components Using Compressible Fluids-Determination of Flow-rate Characteristics, (1989).

[5] JIS B 8390: Pneumatic Fluid Power Components Using Compressible Fluids-Determination of Flow-rate Characteristics, (2000) (In Japanese).

[6] Blaine W. Andersen, 1967, The Analysis and Design of Pneumatic Systems, John Wiley & Sons, Inc.

[7] Kuroshita, K, 2002, Study on Measurement Method of Flow-rate Characteristics of Pneumatic Solenoid Valve, Proceedings of the 5th JFPS International Symposium on Fluid Power, Vol. 1, pp. 73/78.

[8] de las Heras, S., 2001, A New Experimental Algorithm for the Evaluation of the True Sonic Conductance of Pneumatic Components Using the Characteristic Unloading Time, Journal of Fluid Power, **2**, No. 1.

[9] Kawashima, K., Kagawa, T., Fujita, T., 2000, Instantaneous Flow rate Measurement of Ideal Gases,'' ASME J. Dyn. Syst., Meas., Control, **122**, 174/178.

[10] Kawashima, K., Kagawa, T., 2003, Unsteady Flow Generator For Gases Using An Isothermal Chamber, Measurement Journal of the International Measurement Confedeferation, **33**, No. 4, 333/340.

[11] Han, B., Fujita, T., Kagawa, T., and Kawashima, K., 2001, Flow Rate Characteristics Measurement of Pneumatic Valve by Pressure Response, Proceedings of The 5th International Conference on Fluid Power Transmission and Control, 200/204.

[12] Kawashima, K., Fujita, T., and Kagawa, T., 2001, Flow Rate Measurement of Compressible Fluid Using Pressure Change in the Chamber, Trans. of the Society of Instrument and Control Engineering, Vol. E-1, No. 1, 32, 252/258.

[13] Kagawa, T., 1985, Heat Transfer Effects on the Frequency Response of a Pneumatic Nozzle Flapper, ASME J. Dyn. Syst., Meas., Control, **107**, 332/336.

Robert P. Evans
Advisory Engineer, Idaho National Engineering
and Environmental Laboratory,
P.O. Box 1625, Idaho Falls, Idaho 83415
e-mail: rpe@inel.gov

Jonathan D. Blotter
Associate Professor, Mechanical Engineering
Department,
Brigham Young University,
Provo, Utah 84602
e-mail: jblotter@byu.edu

Alan G. Stephens
Professor, College of Engineering,
Idaho State University,
Pocatello, Idaho 83206

Flow Rate Measurements Using Flow-Induced Pipe Vibration

This paper investigates the possibility of developing a nonintrusive, low-cost, flow-rate measurement technique. The technique is based on signal noise from an accelerometer attached to the surface of the pipe. The signal noise is defined as the standard deviation of the frequency-averaged time-series signal. Experimental results are presented that indicate a nearly quadratic relationship over the test region between the signal noise and flow rate in the pipe. It is also shown that the signal noise–flow rate relationship is dependent on the pipe material and diameter. [DOI: 10.1115/1.1667882]

1 Introduction

Flow measurements are used in many applications for various purposes. Some of these include providing data for system control, process analysis, accounting of yield, and consumption. Recent developments in technology have provided improved sensor designs and measurement techniques. Coriolis, magnetic, and ultrasonic flow meters are a few examples of this improved technology. Although many high-quality pipe-flow sensors and measurement techniques exist, there is a need for the development of a low-cost, nonintrusive, flow sensor. The geothermal industry is in particular need of such a sensor for the measurement of brine flows. Geothermal brine typically consists of hot, pressurized liquid, carrying dissolved solids. As the pressure of the liquid drops, some of the dissolved solids precipitate out of solution coating any surface in contact with the fluid. This coating renders an intrusive flow meter inoperable after a short time. Similar nonintrusive measurements are also needed in the nuclear industry.

This paper explores the possibility of developing a low-cost, nonintrusive, flow-rate sensor based on the signal noise from an accelerometer attached to the outside surface of the pipe. Signal noise in this paper refers to the standard deviation of a time-series signal acquired from the transducer. This signal noise is a result of turbulence-induced pressure fluctuations in the fluid flow which are imparted to the pipe wall. This type of signal noise analysis has shown promise in providing nonintrusive flow measurements. The method was first considered at the Idaho National Engineering and Environmental Laboratory (INEEL) as a diagnostic tool for pump performance in nuclear applications [1]. During the Loss-of-Fluid Test nuclear reactor safety testing program, measurements were analyzed to determine their uncertainty and limitations. It was noticed that in turbulent single-phase flow, the standard deviation of the signal increased with flow rate for flow-measuring instrumentation [2]. Based on these results, initial laboratory tests were performed by the authors. These tests demonstrated that it was possible to use signal noise from an accelerometer to sense flow noise in a pipe [3,4]. These preliminary results were used to obtain funding from the Department of Energy (DOE) through an INEEL Laboratory Directed Research and Development (LDRD) award to construct an air-water flow loop and continue to investigate the relationship between signal noise and flow rate. This paper presents the results of this investigation.

Pipe vibration due to internal flow has been investigated by various researchers using analytical, numerical and experimental methods [2,5–10]. This research builds on these efforts and the signal noise concepts and presents experimentally based relationships between signal noise and the flow rate in a pipe. This paper first describes an empirical approach to the basic theory on which the accelerometer-based flow sensor is founded. The paper then describes the experimental test set up and procedure used to acquire the data. The data are then presented and discussed. The data indicate that there is a strong relationship between the accelerometer based signal noise and the flow rate in the pipe. Over the range of flow rates investigated, it is shown that the relationship between signal noise and flow rate is nearly quadratic and a function of pipe material and pipe diameter.

2 Theoretical Overview

When describing turbulent flow, it is convenient to recognize that the local velocity at a point may be regarded as superposition of an average value and instantaneous fluctuating value. The instantaneous velocity, u, can then be written in terms of the time average velocity, $\overline{u}$, also called the mean velocity, and a fluctuation velocity u' as shown by Eq. (1).

$$u=\overline{u}+u' \tag{1}$$

The time average velocity $\overline{u}$ is defined as shown by Eq. (2) where T_1 is a time large enough that $\overline{u}$ is the same for any longer time for steady flow. Therefore, the mean is independent of time and the time-averages of the fluctuations are equal to zero.

$$\overline{u}\equiv\frac{1}{T_1}\int_0^{T_1}u\,dt \tag{2}$$

As the molecules of the fluid approach the wall, they have kinetic energy. This kinetic energy must be converted to another form of energy as the molecules reach the pipe wall. According to the first law of thermodynamics, some of the kinetic energy is converted to heat as the turbulent eddies dissipate, but most is converted into potential energy in the form of pressure [11].

Consider a turbulent flow through a horizontal pipe of circular cross section. The velocities of the fluid can be expressed in terms of a time average and a fluctuation as shown by Eqs. (3) and (4).

$$u=\overline{u}+u' \tag{3}$$

$$v=\overline{v}+v'=v' \tag{4}$$

In Eqs. (3) and (4), u is the velocity in the direction of the primary pipe axis and v is the velocity perpendicular to the pipe axis. Since there is no net flow in the direction perpendicular to

---

Contributed by the Fluids Engineering Division for publication in the JOURNAL OF FLUIDS ENGINEERING. Manuscript received by the Fluids Engineering Division April 28, 2003; revised manuscript received November 7, 2003. Associated Editor: J. Lee.

the pipe axis, the time-averaged flow in that direction is zero and so the instantaneous flow is just equal to the fluctuation.

Although the time averages of the fluctuations in any direction are zero, the time average of the products, such as $u'v'$ are not equal to zero. Prashun [12] states that in general, it can be shown that the time average of the product of the velocity fluctuations is less than zero as shown by Eq. (5).

$$\overline{u'v'} < 0 \tag{5}$$

Prashun [12] also demonstrated that for a circular conduit of radius r, the shear stress, τ, at the wall can be related to the pressure, p, as shown by Eqs. (6) and (7).

$$\tau = -\frac{r}{2}\frac{dp}{dx} \tag{6}$$

$$\frac{dp}{dx} = p' = -\frac{2\tau}{r} \tag{7}$$

From the Navier-Stokes equations, Prashun also demonstrated that for turbulent flow, the turbulent shear stress can be expressed as shown by Eq. (8)

$$\tau = -\rho\overline{u'v'} \tag{8}$$

Combining Eqs. (7) and (8) shows that the pressure fluctuation is proportional to the fluctuation of the fluid velocity as shown by Eq. (9)

$$p' \propto \overline{u'v'} \tag{9}$$

It can also be shown that the pipe vibration is proportional to the pressure fluctuations in the fluid. For this analysis, the fluid-filled piping system can be depicted as a one-dimensional model of a beam. It is well known from structural mechanics that the rate of change of the moment along a beam is equal to the shear and the rate of change of shear, dV/dx, along the length of the beam is equal to the pressure fluctuations, $p'(x)$, per unit length as shown by Eq. (10) [13].

$$\frac{d^2M}{dx^2} = \frac{dV}{dx} = p'(x) \tag{10}$$

When a beam is subjected to bending, one side of the beam is in tension while the other side is in compression. Differentiating the well known Flexure Equation, given by Eq. (11), twice with respect to x, then using the relationship for p' from Eq. (11) gives the results in Eq. (12).

$$M = EI\frac{d^2y}{dx^2} \tag{11}$$

$$\frac{d^2M}{dx^2} = EI\frac{d^4y}{dx^4} = p'(x) \tag{12}$$

In order to relate the pressure fluctuations to the pipe acceleration d^2y/dt^2, consider the differential equation of motion for transverse vibration of a beam as given by Seto [14] in Eq. (13).

$$\frac{\partial^2 y}{\partial t^2} = -\frac{EIg}{A\gamma}\frac{\partial^4 y}{\partial x^4} = -\frac{g}{A\gamma}EI\frac{\partial^4 y}{\partial x^4} \tag{13}$$

where:

A = cross sectional area of the beam
γ = specific weight of the beam
g = acceleration of gravity
EI = flexural rigidity

Since g, A, and γ are constants, Eq. (13) can be rewritten as shown by Eq. (14).

$$\frac{\partial^2 y}{\partial t^2} = -CEI\frac{\partial^4 y}{\partial x^4} = -Cp'(x) \tag{14}$$

where:

$$C = \frac{g}{A\gamma}$$

Equation (14) indicates that the acceleration of the pipe is proportional to the pressure fluctuations in the fluid. This experimental research is based on this premise.

The last relationship to be demonstrated is the relationship between the standard deviation of the pipe vibrations and the mean flow rate of the fluid in the pipe. Blake [15] stated that the generation of vibrations by fluid motion involves the reactions of fluids and solids to stresses imposed by time-varying flow. For dynamically similar flows, the ratio of the flow fluctuations to the average flow is constant. Bird et al. [16] clarified this relationship by noting that the oscillatory term is the time average of the absolute magnitude of the oscillation, given by $\sqrt{m}$ where $m = u'^2$. They defined this relationship as ''intensity of turbulence,'' which is a measure of the magnitude of the turbulent disturbance, and is given by Eq. (15).

$$\frac{\sqrt{\overline{m}}}{\overline{u}} = \text{intensity of turbulence} \tag{15}$$

From the definition of turbulent flow given in Eq. (1) the intensity of turbulence expression can be rearranged as shown by Eq. (16)

$$\frac{\sqrt{\overline{m}}}{\overline{u}} = \frac{\overline{m}}{\overline{u}^2} = \frac{\frac{1}{N}\sum_{i=1}^{N}[u_i(t)-\overline{u}]^2}{\overline{u}^2} = C \tag{16}$$

Multiplying both sides by the number of points N and $\overline{u}^2$ and dividing by $N-1$ results in Eq. (17) where the left hand side is the definition of the sample standard deviation.

$$\frac{1}{N-1}\sum_{i=1}^{N}[u_i(t)-\overline{u}]^2 = \frac{NC}{N-1}\overline{u}^2 = K\overline{u}^2 \tag{17}$$

Since, as was demonstrated above, the flow fluctuations are proportional to the pressure fluctuations and the pressure fluctuations are proportional to the pipe vibrations, it follows that the standard deviation of the pipe vibrations is proportional to the average flow rate.

3 Experimental Test Facility

The air-water flow loop at Idaho State University (ISU) was used as the experimental test facility. A schematic of the flow loop is shown in Fig. 1. This flow loop will be described as two main components. These are the water system and the test section.

3.1 Water System. Although this research is focused on single phase (all water) flow, the ISU flow loop was designed to have two phase (air-water) flow capability. The water system supplies the liquid phase of the test fluid and consists of a primary pump, air- and manually-operated flow control valves, a test loop, a bypass loop with a water clean-up system, two air-water separator tanks with an air discharge system, plus the interconnecting piping, loop pressure, and pump speed instrumentation. These components are shown in Fig. 1.

Water is circulated through the flow loop by a Goulds 10 in. diameter impeller, centrifugal pump driven by a Reliance 75 HP, 2,500 rpm, Model Super RPM DC, direct current motor with a variable-speed controller. Water from the pump can be routed through the test section, the by-pass section, or both so that the amount of water passing through the test section can be controlled. The flow path for the water is controlled by two air-operated Valtek, size 3, Class 150 valves at the outlet of the pump. Each valve opening can be controlled to allow the desired flow through the test section and the bypass.

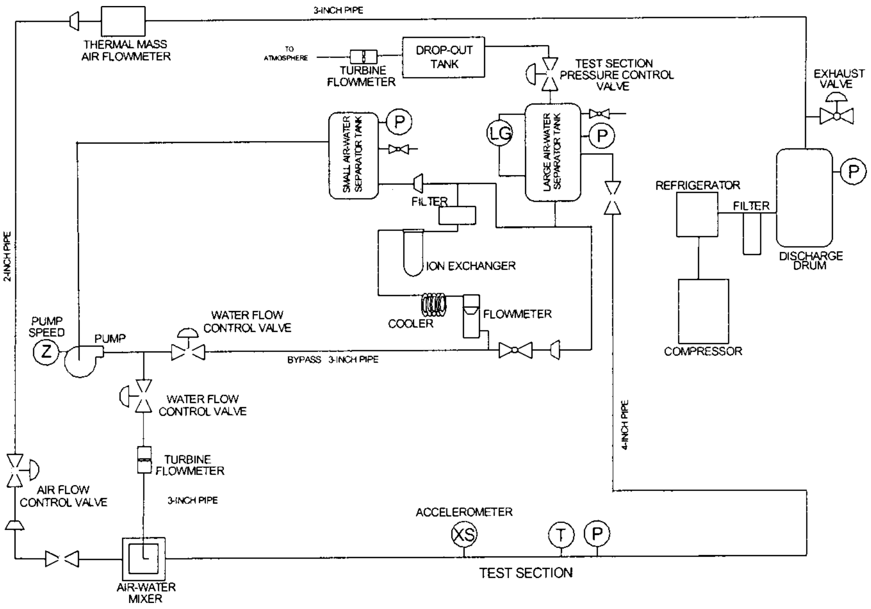

Fig. 1 Flow loop schematic

The water for the test section goes from the pump, through the control valve and then through an air-water mixer before entering the test section. In this research, air was not mixed with the water but the flow still passes through the mixing chamber. After passing through the test section, the water enters the first of two air-water separator tanks which allow any entrained air to separate from the water by gravity. The pressure and water level in the tank are monitored by a pressure gage and level indicator, respectively. The water from the first air-water separator tank passes out of the bottom of the tank into a second, smaller air-water separator tank, where any additional air can be removed from the water. The water then goes to the pump to start the cycle again.

The bypass loop provides two functions: it provides an alternate path for the water so that the amount of water flowing through the test section can be controlled without changing the pump speed, and it also provides a system to cool and clean the loop water. The water can become heated as it passes through the pump. After several passes through the pump, the water can become relatively warm. Some of the water flowing through the bypass loop can be diverted through a system to cool and clean the water. The cooling is accomplished by passing the water through a heat exchanger which transfers some of the heat to secondary cooling water. The water also passes through an ion exchanger and filter to clean the water before re-entering the flow path between the first and second air-water separator tanks. The amount of water passing through the cooling and cleanup system is monitored by a variable-area, rotameter and controlled by a hand-operated valve in the bypass line. The remainder of the water from the bypass loop re-enters the flow path at the outlet of the first air-water separator tank. The loop water piping is primarily 0.0762 m or 0.102 m (3 or 4 in) nominal pipe size and primarily of 304 stainless steel and polyvinyl chloride (PVC).

The structural support for the test section was designed to minimize any external vibration. The test section was connected to the flow loop through rubber isolators and the pump was mounted to isolate as much vibration as possible. Background noise tests indicated a quiet system and the data required minimal filtering for extraneous noise.

For normal operation, the system is started from an uncirculated, cold water condition and brought up to a flow rate that completely fills the pipe. The system is then allowed to run until the piping is free of air and a steady temperature and flow rate have been reached.

3.1.1 Control System. The pump and valves in the flow loop are controlled from a control panel in an adjacent room. The control panel has an on-off switch for the pump motor as well as a variable speed control. A dial gage, which receives input from the pump speed controller, displays the speed in revolutions per minute. The air-operated valves are controlled by electric potentiometers on the control panel. The panel is situated so that the loop can be viewed during operation.

3.1.2 Test Measurement Transducers. The flow loop instrumentation consisted of: a) a PCB Piezotronics Model 352B68 piezoelectric accelerometer to measure pipe vibration in the test section, b) a Flow Technology FT Series full-bore turbine flow meter with a 0.0762-m (3 in) nominal diameter, operating range of 250 to 2,500 liters/min (l/m), repeatability of ±0.5% of reading, and linearity of ±0.5% of reading to measure water flow through the test section, c) a 0 to 1.034 MPa (0 to 150 psi) Heise pressure gage to measure test section pressure, and d) a bimetallic thermometer temperature gage to measure the test section temperature.

3.1.3 Data Acquisition and Recording System. Data from the flow loop transducers were recorded simultaneously on a HP35670 Spectrum Analyzer and a PC based data acquisition system as shown in Fig. 2. As shown, the accelerometer data were recorded using the spectrum analyzer while all other data were recorded using the PC data acquisition system.

3.2 Test Section. The flow loop test section consists of a 6.1 m (240 in) interchangeable section of pipe. In this effort, five different test sections were used. The first three sections, were nominal 0.0762-m (3 in) diameter schedule 40 pipe made of clear PVC, 304/304 L stainless steel, and aluminum. These three sections were used to determine the effects of material properties on the signal noise–flow rate relationship. Two other test sections, one of 0.1016-m (4 in) nominal diameter clear PVC and the other of 0.0381-m (1.5 in) diameter stainless steel were used to investigate the effects of pipe diameter. The various test sections were inserted into the flow loop one at a time by flanged connections. The accelerometer was mounted on the top of the pipe test section 2.34 m (92 in) downstream of the inlet.

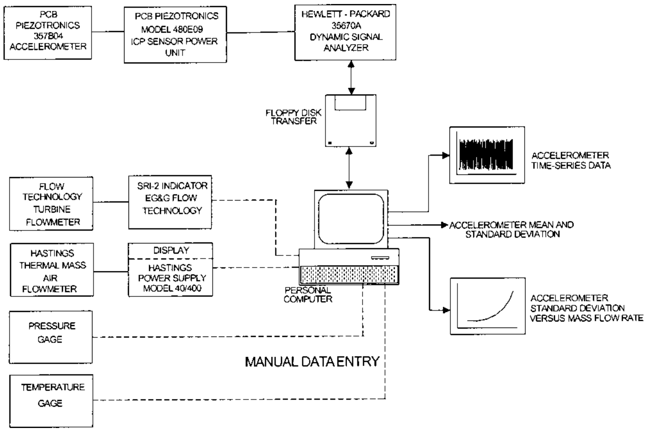

Fig. 2 Data acquisition schematic

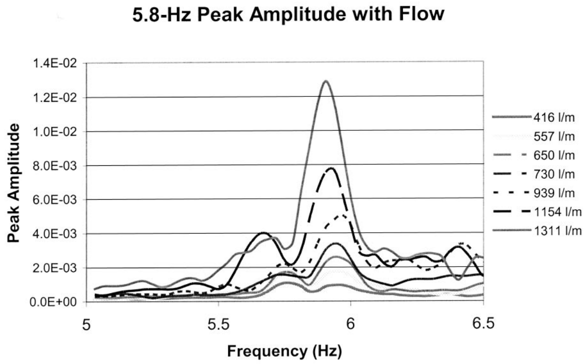

Fig. 3 Frequency domain plots of the accelerometer data with various flow rates

4 Data Acquisition, Results, and Analysis

One focus of this research is to determine the relationship between flow rate and the signal noise as measured by an accelerometer attached to the pipe. The purpose is to determine if a relationship exists such that a nonintrusive flow-rate sensor or measurement technique could be developed. This section first presents the data acquisition process followed by the presentation and discussion of the results.

4.1 Data Acquisition. The data acquisition system previously discussed and shown in Fig. 2 was used. The accelerometer data was initially acquired using various sample rates and time spans. Based on these results, a 2 s time span and a sample rate of 2,048 samples/s were used to acquire the data presented. Anti-aliasing filters were used with a cut off frequency of 800 Hz. The accelerometer time series data were transformed to the frequency domain using a Fast Fourier Transform. Ten data sets were averaged in the frequency domain and the data were transformed back to the time domain. Initially, 50 data sets were used to compute the average. However, the data was such that the difference between the signals based on 50 averages and the signals based on 10 averages were indiscernible at all flow rates. Therefore, only 10 data sets were used in the averaging. The standard deviation of the frequency domain average time series signal was then used to compare with the flow rate. It should also be noted that care was taken to vibrationally isolate the pump from the test section and the prominent pump frequencies were filtered from the accelerometer data before the data were transformed back to the time domain.

Fourteen flow rates between 400 and 1,500 l/m were used for all data sets for the 0.0762-m (3 in) test sections. The minimum flow rate of 400 l/m was required to keep the pipe full of water. The 1,500 l/m limit was the highest flow rate obtainable with the pump and system components. The flow steps were repeatable within a ±2 l/m range. The flow rate was held relatively constant with a maximum fluctuation of ±1 l/m during testing. This results in a less than 1% error in the flow rate input. The same accelerometer position, sample rate, and flow rates were used in the testing of the five test sections.

4.2 Results and Analysis. The results and analysis are presented in two sections. First, experimental data will be compared with a frequency analysis to show that the data follows expected trends. The data that identifies the relationship between signal noise and flow rate will then be presented and discussed.

4.2.1 Frequency Domain Results and Analysis. It is well known that the fundamental natural frequency of a pipe containing a flowing fluid decreases as the flow rate increases. A flow measurement technique based on this natural frequency shift would then be plausible. However, the changes in natural frequency are typically very small (on the order of tenths of a Hz or less) for turbulent flow that is well below the critical flow rate (i.e., $v/v_{\text{critical}} < 0.1$). Therefore, the sensitivity of such a technique for relatively slow-flow rates would be very poor. For flow rates that provide a v/v_{critical} ratio greater than 0.3 the natural frequency shifts become significantly larger. If estimates of the flow rate are acceptable and relatively high-flow rates are expected it may then be plausible to develop a technique based on these concepts [17].

To illustrate the ability to measure the flow rate based on natural frequency shifts, frequency domain plots of the accelerometer data for the various flow rates were generated. Portions of these are shown in Fig. 3. The data shown in Fig. 3 represents an average of 10 data sets where 4,096 data points were acquired over 2 s as previously discussed. By comparing the main peaks for each flow rate as shown in Fig. 3, the downward shift of the natural frequency due to the increase in flow rate is clearly apparent. However, for a flow rate of 1,311 l/m the peak occurs at 5.906 Hz and at a flow rate of 416 l/m the peak occurs at 5.937 Hz. Therefore, a factor of 3.15 decrease in flow rate results in a frequency factor increase of 1.094. This is a small increase in frequency for a large decrease in flow and would make for a system with a very low sensitivity. An increase in the amplitude of the peak response as the flow rate increases is also shown to occur. Although this data is shown to contain multiple peaks, which may be difficult to distinguish under various conditions, it does verify that the measurements are responding according to theory and gives some feel that the accelerometer is indeed sensing changes in the flow. It is also noted that the first mode frequency peaks can be identified because they follow the expected trends where the other small, yet somewhat significant peaks, appear to have random shifts and do not follow the expected trends. To build on these results and investigate techniques with higher sensitivity, this paper now continues with the focus of this research, which is to determine the possibility of using signal noise to measure the flow rate.

4.2.2 Signal Noise Results and Analysis. The signal noise, computed as the standard deviation of the frequency domain averaged time-series signal, versus flow-rate plots for the three pipe materials are shown in Figs. 4–6. The diamond shaped points indicate the experimental data and the solid lines represent a second-order least squared error fit to the data. The equation for the curve fit and the R^2 value for the fit are also shown as part of each figure. In the curve fit equations shown, x, represents the flow rate in liters/minute. The PVC and stainless steel curves have R^2 values of 0.997 and 0.991, respectively, while the aluminum fit drops to an R^2 value of 0.983. There is no apparent reasoning as to why the aluminum pipe appears slightly less quadratic in the measured flow range except for possible background noise detected by the accelerometer. These curves clearly illustrate that there is a strong correlation between accelerometer based signal

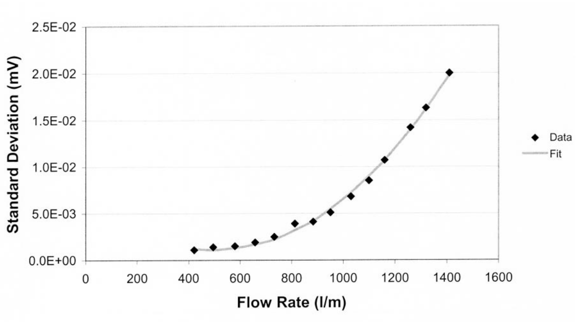

$$STD = 2.43e\text{-}08\, x^2 - 2.61e\text{-}05\, x + 8.29e\text{-}03 \qquad R^2 = 0.997$$

Fig. 4 Signal noise and curve fit for 0.0762-m (3-in) PVC pipe

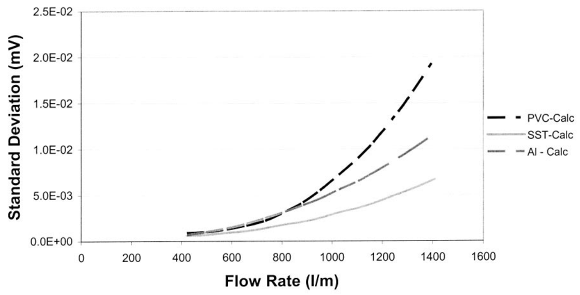

Fig. 7 Comparison of the curve fit of the standard deviation of the vibrations in the test section with mass flow for various test section materials

noise and flow rate. Although these curve fits are good it is noted that if the flow rate went to zero this curve would most likely still be deterministic but not quadratic. These curves also illustrate that a system based on signal noise potentially has a much higher sensitivity than a frequency shift based method.

Figure 7 is a superposition plot of the signal noise versus flow rate for all three materials. This plot clearly indicates that the pipe material properties significantly change the shape of the curve and would need to be accounted for in the development of a measurement technique. These curves indicate that as the density and stiffness of the material are increased, the slope of the signal noise—flow rate curve decreases. A focus for future work would be to determine relationships between density, stiffness, and signal noise.

Pipe diameter was another system parameter that was considered to likely shift or change the shape of the signal noise−flow rate curve. To investigate this, two cases were investigated.

The first case consisted of comparing the results of a 0.0762-m and a 0.1016-m (3 and 4 in) diameter pipe. The raw data for these two diameters are shown in Fig. 8. Figure 8 indicates that the dependence on pipe diameter is not constant over the flow domain investigated. It also shows that the larger diameter pipe has less signal noise than the smaller pipe as might be expected.

The second case consisted of comparing the 0.0762-m (3 in) stainless steel pipe to a 0.0381-m (1.5 in) diameter stainless steel pipe. The signal noise data for this case is shown in Fig. 9. Because of limitations in the flow system, the maximum flow rate for this case was approximately 1,200 l/m. The difference between the curves in this case is more significant as is the change in pipe diameter. Furthermore, as in the previous case, the larger pipe diameter has lower signal noise values for the same flow rate.

To further investigate the significance of the data a nondimensional plot with all the data was developed as shown in Fig. 10. The vertical axis is a nondimensional form of the standard deviation of the accelerometer data and the horizontal axis is the Reynolds number. This plot clearly indicates a strong relationship be-

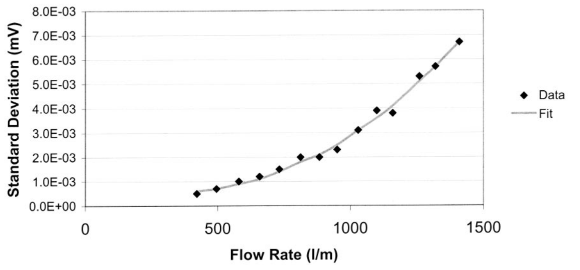

$$STD = 5.48e\text{-}09\, x^2 - 3.92e\text{-}06\, x + 1.32e\text{-}03 \qquad R^2 = 0.991$$

Fig. 5 Signal noise and curve fit for 0.0762-m (3-in) stainless steel pipe

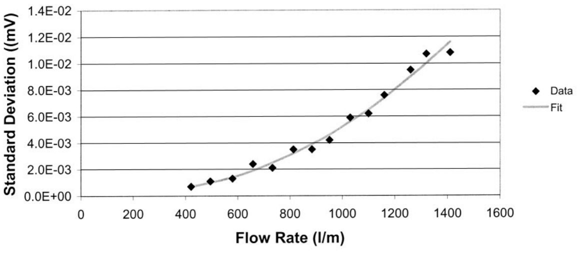

$$STD = 7.99e\text{-}09\, x^2 - 3.63e\text{-}06\, x + 8.62e\text{-}04 \qquad R^2 = 0.983$$

Fig. 6 Signal noise and curve fit for 0.0762-m (3 in) aluminum pipe

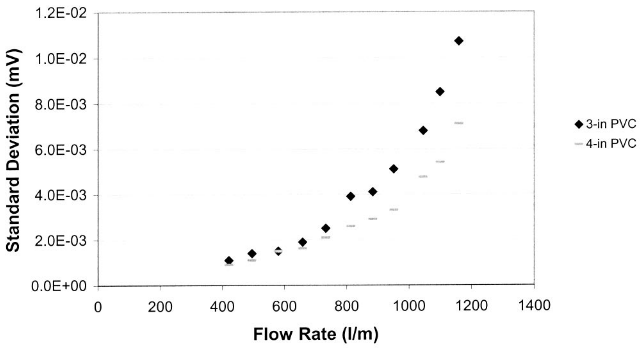

Fig. 8 Signal noise versus flow rate for 0.1016 m and 0.0762 m diameter PVC pipe

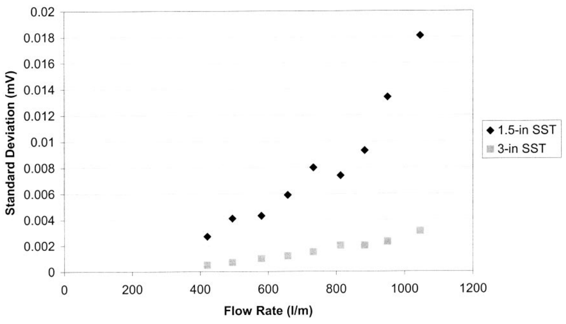

Fig. 9 Signal noise versus flow rate for 0.0762 m and 0.0381 m diameter stainless steel pipe

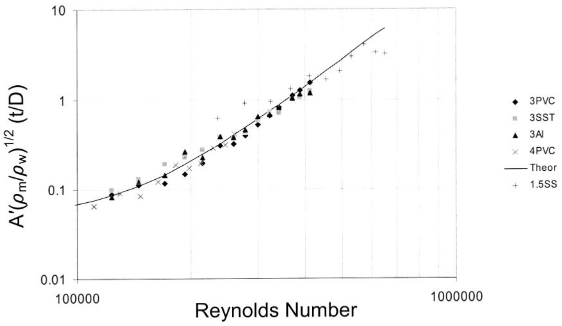

Fig. 10 Nondimensional plot of acceleration data versus Reynolds number for all data sets

tween flow noise and flow rate and provides promise for the development of a flow sensor based on the flow noise approach presented in this paper.

5 Summary

In summary, it can be concluded that noise from an accelerometer mounted to the surface of a pipe has a strong (deterministic) relationship with the flow rate. Based on measurement sensitivity, it can also be concluded that a flow rate measurement technique, based on the signal noise method presented, has significantly more potential, than a frequency shift based technique. It was also shown that pipe material and the diameter have effects on the relationship. Based on this research, it can also be concluded that a signal-noise based, flow-measurement technique has potential for development but that continued research into calibration techniques and methods to account for parameters that affect the relationship such as pipe material and diameter needs to be performed.

Acknowledgment

The authors would like to thank the DOE and the INEEL for the support of this research through the LDRD program. They would also like to thank Dr. Dan Maynes and Matt Pittard for their suggestions to the paper and involvement with the research.

References

[1] Evans, R. P., and Goodrich, L. D., 1992, ''Determination of Void Fraction in a Fluid Through Analysis of the Flow-Induced Noise on a Drag Disk Signal,'' 38th ISA International Instrumentation Symposium, Instrument Society of America, Paper #92,0178.

[2] Lassahn, G. D., 1983, ''LOFT Experimental Measurements Uncertainty Analysis-Methodology and Summary,'' **I**, NUREG/CR-0169, EGG-2037.

[3] Evans, R. P., Blotter, J. D., and Stephens, A. G., 1998, Determination of Flow Parameters in Two-Phase Flow Through Analysis of Flow-Induced Noise on an Accelerometer Signal; Geothermal Mass Flow Measurement Feasibility Report, Idaho National Engineering and Environmental Laboratory internal report.

[4] Evans, R., 1999, ''Two-phase Mass Flow Measurement Using Noise Analysis,'' 45th International Instrumentation Symposium, Albuquerque, NM, ISA-International Society for Measurement and Controls.

[5] Weaver, D., Ziada, S., Au-Yang, M., Chen, S., Paidoussis, M., and Pettigrew, M., 2000, ''Flow-Induced Vibrations in Power and Process Plant Components-Progress and Prospects,'' ASME J. Pressure Vessel Technol., **123**, pp. 339–348.

[6] Saito, N., Miyano, H., and Furukawa, S., 1990, ''Study on Vibration Response of Pipes Induced by Internal Flow,'' *Pressure Vessels and Piping Conference*, ASME Pressure Vessels Piping Div Publ PVP, pp. 233–238.

[7] Durant, C., Robert, G., Filippi, P., and Mattei, P., 2000, ''Vibroacoustic Response of a Thin Cylindrical Shell Excited by a Turbulent Internal Flow: Comparison Between Numerical Prediction,'' J. Sound Vib., **229**, pp. 1115–1155.

[8] Durant, C., and Robert, G., 1998, ''Vibroacoustic Response of a Pipe Excited by a Turbulent Internal Flow,'' Flow, Turbul. Combust., **61**, pp. 55–69.

[9] Brevart, B., and Fuller, C., 1993, ''Effect of an Internal Flow on the Distribution of Vibration Energy in an Infinite Fluid Filled Thin Cylindrical Elastic Shell,'' J. Sound Vib., **167**, pp. 149–163.

[10] Kim, Y. K., and Kim, Y. H., 1996, ''Three Accelerometer Method for the Measurement of Flow Rate in Pipe,'' J. Acoust. Soc. Am., **100**, pp. 717–726.

[11] Pittard, M. T., and Blotter, J. B., 2003, ''Numerical Modeling of LES Based Turbulent-Flow Induced Vibration,'' ASME International Mechanical Engineering Congress & Exposition, Washington, D.C.

[12] Prashun, A. L., 1980, *Fundamentals of Fluid Mechanics*, Prentice Hall, Englewood Cliffs, NJ, pp. 202–222, Chap. 7.

[13] Thomson, W. T., and Dahleh, M. D., 1998, *Theory of Vibration with Applications 5th ed.*, Prentice-Hall, Inc., Upper Saddle River, NJ, pp. 258–286, Chap. 9.

[14] Seto, W. W., 1964, *Theory and Problems of Mechanical Vibrations*, Schaum Publishing Co., NY, pp. 128, Chap. 5.

[15] Blake, W. K., *Mechanics of Flow-Induced Sound and Vibration*, Academic Press Inc., Harcort Brace Jovanokich Publishers, Orlando, FL, pp. 1–43, **1**, Chap. 1.

[16] Bird, R. B., Stewart, W. E., and Lightfoot, E. N., 1960, *Transport Phenomena*, John Wiley and Sons Inc., NY, pp. 153–179, Chap. 5.

[17] Blevins, R. D., 1977, *Flow-induced Vibration*, Van Nostrand Reinhold Co., NY, pp. 287–311, Chap. 10.

Journal of Fluids Engineering
Technical Briefs

An Experimental Study of the Effect of Grid Turbulence on Shear Layer Evolution

Amy Warncke Lang
e-mail: langaw@slu.edu

Begoña Gomez
e-mail: gomezmb@slu.edu

Aerospace and Mechanical Engineering,
Parks College of Engineering and Aviation,
Saint Louis University,
3450 Lindell Blvd.,
St. Louis, MO 63103
Phone: (314) 977-8419

An experiment was performed in a shear layer water tunnel to determine the effect that grid turbulence, introduced within the meeting of the two streams, had on the evolution of a free shear layer. DPIV results show that the presence of grid turbulence inhibited the growth of the large coherent structures formed in the undisturbed shear layer, and thus led to an alteration of the entrainment process of free stream fluid into the shear layer. This caused more symmetry and various growth rates in the shear layer evolution. Also, the peak Reynolds stress magnitudes increased with the presence of grid turbulence.
[DOI: 10.1115/1.1677486]

Introduction

The incompressible shear layer is a widely observed flow phenomenon experimentally. One of the earlier experimental observations of such a shear layer was performed by Dimotakis & Brown [1]. Here they argue that with the presence of the large coherent structures, known to form in the free shear layer, that the ''mixing-layer dynamics at any point are coupled to the large structure further downstream.'' Here they also observed that the entrainment of fluid from the irrotational free streams took place largely due to the presence of the large coherent structures, while the fine-scale mixing within the shear layer corresponds with the amalgamation processes of the large structures. This first phase of entrainment was later termed induction by Dimotakis [2]. The latter phase of smaller scale mixing was then termed diastrophy, which is dominated by the viscous diffusive process at scales on the order of the Kolmogorov length scale of the flow.

Other studies have shown that the shear layer growth rate is highly dependent on the inflow conditions of the free streams, hence this study to determine the effect of grid turbulence. For instance, it was observed by Browand & Latigo [3] that the tripping of the boundary layer, on the splitter plate dividing the two free streams, had the effect of reducing the shear layer growth rate. Hence, a laminar state of the incoming flow must result in larger coherent structures to have the shear layer grow faster spatially while any presence of turbulence may inhibit the larger growth of these structures. In addition, it is well understood and observed that a shear layer entrains fluid from the two streams in an asymmetric way, and that the shear layer grows into the low speed side at a faster rate. One of the first observations of this behavior experimentally was by Konrad [4]. One objective of this study was to observe whether the presence of grid turbulence altered this behavior in any way and to what degree.

Finally, the distribution of Reynolds stress, $\langle u'v'\rangle$, within the shear layer with and without the presence of grid turbulence was observed. Previous observations by Maheo [5] of the bulk incompressible shear layer discussed again the possible increase or decrease of peak Reynolds stress as the flow progressed downstream could be a function of inflow conditions. In his case, the presence of turbulence in the free stream lead to a slight decrease in Reynolds stress peak value with downstream distance. To understand the production of Reynolds stress one must consider the Reynolds stress equation. If the incompressible shear layer is modeled as approximately 2-D with large lateral changes in flow properties as compared to longitudinal changes, one can equate the rate of change of turbulent Reynolds stress in the shear layer as given by White [6]

$$\begin{aligned}\langle u\rangle \frac{\partial\langle u'v'\rangle}{\partial x} + \langle v\rangle \frac{\partial\langle u'v'\rangle}{\partial y} &\approx 2\langle u'v'\rangle \frac{\partial\langle u\rangle}{\partial y} - \frac{\partial}{\partial y}\left(\left\langle u'v'^2 + \frac{p'u'}{\rho}\right\rangle\right) \\ &\quad - 2\nu\left\langle \frac{\partial u'}{\partial y}\frac{\partial v'}{\partial x}\right\rangle + \left\langle \frac{p'}{\rho}\left(\frac{\partial u'}{\partial y}+\frac{\partial v'}{\partial x}\right)\right\rangle + \nu\frac{\partial^2\langle u'v'\rangle}{\partial y^2}\end{aligned} \tag{1}$$

where time averaging is denoted by $\langle\ \rangle$. Here the first term on the right hand side of the equation is the production of Reynolds stress due to the presence of an overall average shear present in the flow field. The additional terms account for pressure-strain effects, dissipation, and diffusion. Thus the higher the average shear in the flow, or the thinner the shear layer if the same difference in free stream values is used, should lead to a higher peak Reynolds stress in the shear layer.

Experimental Setup

A small recirculating shear layer water tunnel was used for the study with a test section of 12 inches wide by 30 inches long by 6

Contributed by the Fluids Engineering Division for publication in the JOURNAL OF FLUIDS ENGINEERING. Manuscript received by the Fluids Engineering Division March 22, 2003; revised manuscript received October 28, 2003. Associate Editor: A. K. Prasad.

inches deep. As a result two streams, each 6 inches wide, met after a splitter plate at the beginning of the test section to form the shear layer. Grid turbulence was introduced into each of the streams by placing metal grids 25.4 mm upstream of the splitter plate edge. Two grid sizes were used, the larger with a mesh size of 25.5 mm and the smaller with a mesh size of 16.3 mm. The size of the struts in the grids had a thickness each of 10.3 mm and 8.75 mm correspondingly. The grid struts touched the surfaces of the splitter plate upstream. In this way no frame edge of the grid interfered with the boundary layer growth on the splitter plate. The grid pattern was square with the struts orientated at 45° angles to the water free surface. This was done so as to not give any preferential direction to the eddies produced by the grid possibly interacting with the 2-D coherent vortex structures known to be produced in the bulk shear layer. A case without grids was also performed where the free stream velocities were 26.4 and 14.4 cm/s resulting in a speed ratio of $r=U_2/U_1=0.546$ between the low and high speed streams. Without the presence of grids the turbulence levels in the free-streams are negligible, as can be observed in the results. It should also be noted that for this study the Kolmogorov scale is on the order of 0.1 mm, much less than the scales produced by the grid turbulence. Thus the introduction of grid turbulence to the mixing layer should affect the induction processes within the shear layer and not that associated with diastrophy.

It should be noted that for the cases with grids the RPM reading of each of the pumps was not changed from that of the case without grids. However, a change in free-stream velocities measured did occur due to both the blockage of the grids and the increased growth rate of the boundary layers on the tunnel walls due to the presence of the free-stream turbulence. This resulted in average free stream velocities for the case with small grids of 18 and 28 cm/s and for the large grids 19 and 34 cm/s. Note that for the small grids the ΔU value was in the range of 10 to 12 cm/s while that for the case with large grids changed to about 15 cm/s. Finally, comparing the three cases with their corresponding speed ratios defined as $r_2=(U_1-U_2)/(U_1+U_2)$ one obtains the experimental parameters as given in Table 1 with the corresponding Reynolds number ($\mathrm{Re}=\Delta U\delta/v$) based on the shear layer thickness at a downstream distance of $x=15$ cm for each case. With this downstream distance being approximately halfway through the measurement region, one can assume that this approximates the average shear layer thickness for each case. Here the edges of the shear layer are defined where the velocity reaches 99% of the free-stream value to calculate the shear layer thickness, δ.

Velocity measurements were performed using a DPIV (digital particle image velocimetry) system with the software PIXELFLOW. This system utilizes a Nd:YAG laser and a CCD camera with an image size of 768×480 pixels. An interrogation window size of 32×32 pixels was used, and the imaged area was approximately 11 cm in width. The time difference between images was 3 ms. The flow was seeded with silver-coated glass spheres that are neutrally buoyant in water and have an average diameter of 15 μm. Data was taken at three consecutive downstream stations starting at an origin ($x=0$) located 9 cm downstream of the splitter plate. This initial position for the acquisition of the data was chosen due to the fact that the boundary layers shed from the splitter plate were no longer observed. A plane of the flow parallel to the water free surface and at a depth of 5 cm was illuminated with the laser sheet to acquire the DPIV images as shown in Fig. 1. To obtain Reynolds stress measurements and averaged flow fields, 3000 image pairs were acquired for each data set. A large number of pairs was used to assure accuracy in the averaged values. PIXEFLOW's image analysis software is capable of sub-pixel accuracy and gave an uncertainty in the velocity measurements of 4% and 8% in vorticity.

Results

To observe the differences in the instantaneous flow fields for the three cases, three arbitrarily chosen instantaneous vorticity plots at the second downstream station for each of the three cases are shown in Fig. 2. Without the presence of grid turbulence in the free stream flow, the formation of large coherent vortex structures within the shear layer is observed. The plots are useful to distinguish that first of all with the smaller grids, smaller scale vortical structures are observed in the free streams, while with the larger grids slightly larger scale structures on average are observed. In addition, it is noticed that for the case with the smaller grids, some evidence of the larger scale coherent structures observed for the case with no grids is still seen. However, with the case of the larger grids the flow in the shear layer is dominated by the turbulent structure size shed from the large grids. This leads to the conclusion that the larger scale turbulence is inhibiting to a higher degree the formation of the normally dominant coherent vortex structures.

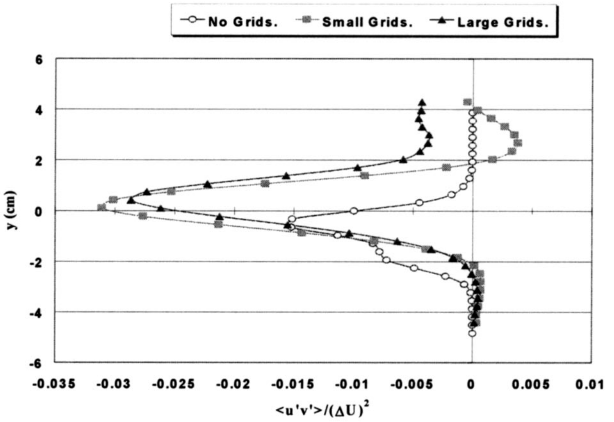

Fig. 4 Normalized Reynolds stress profiles through the shear layers at a distance of 14 cm downstream of the splitter plate

Next is shown the averaged vorticity fields for the three cases in Fig. 3. It should be noted that the shear layer appears to have the smallest growth rate for the case with small grids. First, this is consistent with the fact the mixing layer is known to grow as a function of r_2. Thus this trend is observed regardless of the turbulence levels in the free stream. However, the presence of smaller scale turbulence to the inflow stream leading to a smaller growth rate is also consistent with previous observations by Browand & Latigo [3]. Thus both effects must be taken into account as leading to the smaller growth rate for the case of the smaller grids. However, with the use of larger grids two important observations are made. First, that the growth rate of the shear layer appears to be larger than that for the case with small grids. This is consistent with the idea that larger turbulent structures will entrain fluid at a faster rate into the shear layer. The second observation is that the shear layer is shifted more into the high-speed side even though a higher difference in average free stream velocity was measured for this case. This must be due to a more even entrainment rate from both streams into the shear layer due to the presence of equal size turbulent structures within the free streams, and also an effect of the absence of the large coherent structures formed in the case without grids.

This same effect is also observed in Fig. 4 where a cut through the shear layer at 14 cm downstream of the splitter plate shows the Reynolds stress magnitudes for the three cases. A shift in the peak of the Reynolds stress to the high-speed side is observed for the cases with grids. It should be noted that the Reynolds stress has been normalized with respect to the difference in free stream speeds measured for each case. So while the measured magnitudes of the Reynolds stress are larger for the case with the larger grids, after normalizing the data it is observed that the fluctuations are approximately doubled for the case with grids at this downstream distance.

Table 1 Experimental parameters for all three cases. Re based on shear layer thickness at a downstream distance of x=15 cm.

Case	r_2	δ (cm)	Re
Without grids	0.294	5.483	6580
Small grids	0.207	6.128	6100
Large grids	0.288	6.773	10,160

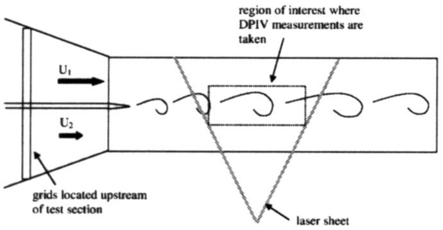

Fig. 1 Schematic of experimental test section as viewed from the top of the water tunnel with flow moving from left to right

Finally, Fig. 5 presents the normalized Reynolds stress peak value as a function of downstream distance for each of the three cases. It is noted that while initially the smaller grid case has a larger normalized value of Reynolds stress, the larger grid case sustains higher magnitudes of Reynolds stress further downstream. This could in part be due to the larger average shear produced across the shear layer, which according to Equation 1 would lead to a larger production of Reynolds stress in the shear layer. Although the peak values of the average vorticity in the shear layer are comparable for the cases with grids, it is evidently less only for the case with no grids as seen in Fig. 3. Thus even though the small grid and no grid cases have approximately the same ΔU across their corresponding shear layers, the overall effect of the grid turbulence is to both increase the Reynolds stress in the layer as well as slightly increasing the growth rate. Another reason for the trend in peak Reynolds stress, observed in Fig. 5, could also be the longer decay time of the eddies produced by the larger grid. This would lead to the higher value of peak Reynolds stress observed for the larger grid case being sustained over the measurement region.

Conclusions

The presence of grid turbulence inhibits the growth and formation of the large coherent structures known to form in the free shear layer. In particular, for the case with smaller grids some evidence of larger structures appears to be present, but the size of the structures is less than that with no grid turbulence. Thus the turbulence in the free stream inhibits the amalgamation process that causes the coherent structures to grow in size. As a result the shear layer grows at a slower rate than the undisturbed shear layer.

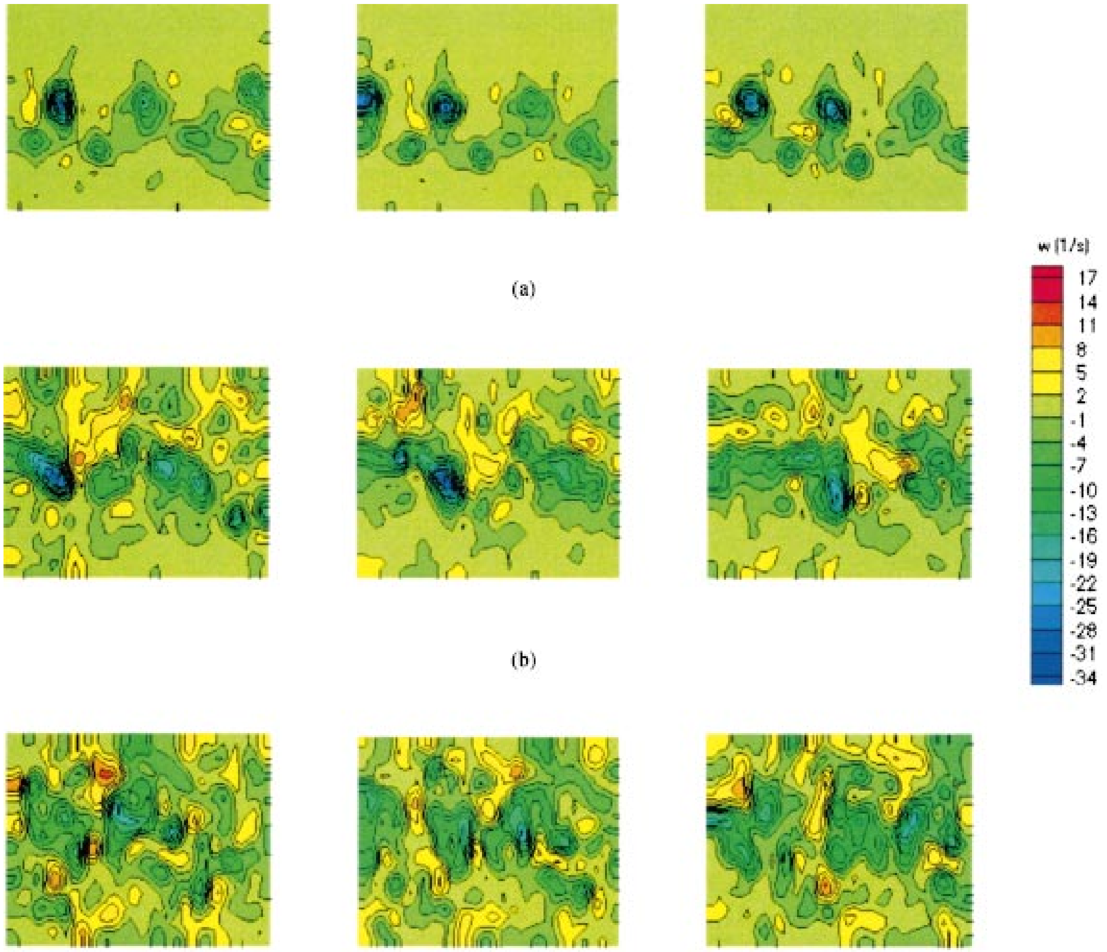

Fig. 2 Three arbitrarily chosen instantaneous vorticity fields located at the second station downstream (from 12 to 24 cm downstream of the splitter plate) for the cases of (a) no grid turbulence (b) smaller grids and (c) larger grids

(c)

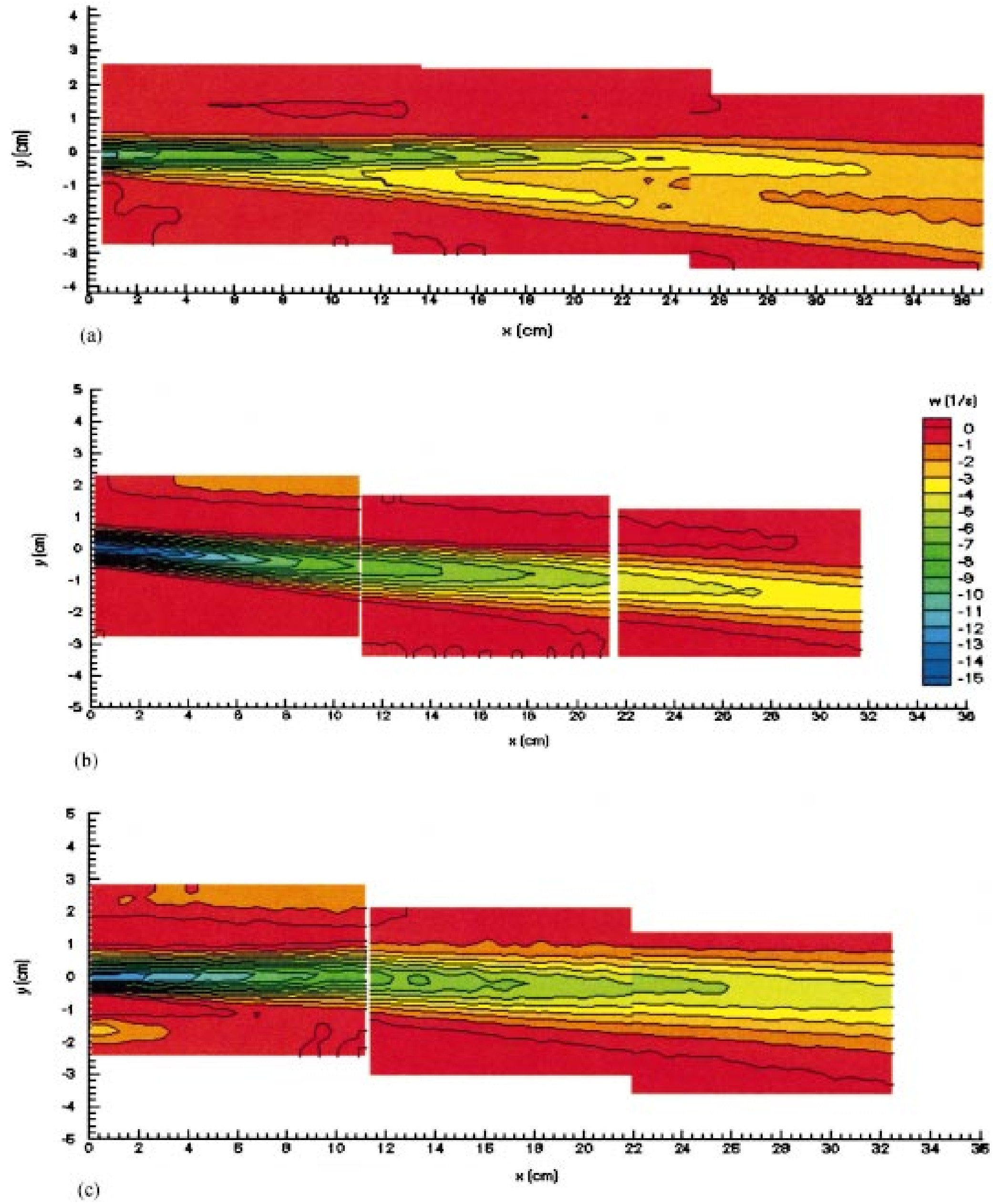

Fig. 3 Averaged vorticity fields for the cases of (a) no grid turbulence (b) smaller grids and (c) larger grids

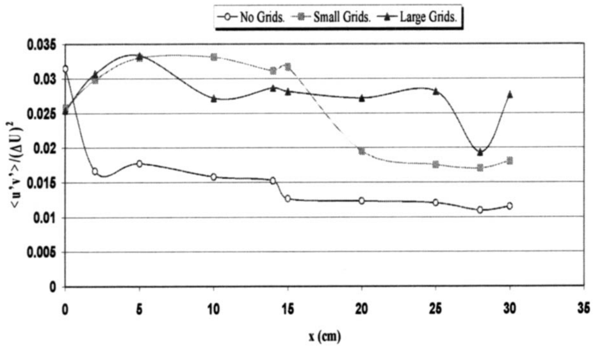

Fig. 5 The progression of normalized Reynolds stress peak values as a function of downstream distance for each of the three cases

However for the case of larger grids and larger-sized vortical structures within the free stream, the shear layer is dominated by vortical structures of similar size as the grid turbulence. As a result, the Reynolds stress magnitudes in the cases with grid turbulence are noticeably larger. This is an expected result as the larger vortex structures in the undisturbed shear layer would result in less velocity fluctuations than a series of smaller structures at a particular point in the flow. The larger average vorticity for the cases with grids is also evidence of this result. Finally, the formation of larger coherent structures is not observed in the case with the larger grids.

An additional result is that for the cases of grid turbulence the entrainment process is controlled by both the grid turbulence and eddies of comparable size formed in the shear layer. However, in the case of the undisturbed shear layer, the large coherent structures are primarily responsible for the entrainment of free stream flow into the shear layer as stated by Dimotakis [2]. Thus for the cases of grid turbulence the shear layer is shifted back towards the high-speed side making the flow more symmetric, but still growing into the low-speed stream. This effect is more pronounced with the larger sized grids, and thus larger-sized vortical length scales in the free stream turbulence.

Acknowledgments

This work was in part made possible through the SLU 2000 Research Assistant program at Saint Louis University, as research assistant Ana De Leon worked with Begoña Gomez in acquiring the data. In addition, some of the equipment used for the study was acquired through the Beaumont Faculty Development Fund at Saint Louis University.

References

[1] Dimotakis, P., and Brown, G., 1976, ''The Mixing Layer at High Reynolds Number: Large-Structure Dynamics and Entrainment,'' J. Fluid Mech., **78**, pp. 535–560.

[2] Dimotakis, P., 1986, ''Two-Dimensional Shear Layer Entrainment,'' AIAA J., **24**(**11**), pp. 1791–1796.

[3] Browand, F., and Latigo, B., 1979, ''Growth of the Two-Dimensional Mixing Layer From a Turbulent and Nonturbulent Boundary Layer,'' Phys. Fluids, **22**(**6**), pp. 1011–1019.

[4] Konrad, J., 1976, ''An Experimental Investigation of Mixing in Two-Dimensional Shear Flows With Application to Diffusion-Limited Chemical Reactions,'' Ph.D. thesis, California Institute of Technology, Pasadena, CA.

[5] Maheo, P., 1998, ''Free-Surface Turbulent Shear Flows,'' Ph.D. thesis, California Institute of Technology, Pasadena, CA.

[6] White, F., 1991, Viscous Fluid Flow, McGraw-Hill, Inc., New York, NY, pp. 407–409.

Lock-Exchange Flows in Non-Rectangular Cross-Section Channels

Luis Thomas and Beatriz Marino
IFAS, UNCPBA, Pinto 399, B7000GHG Tandil,
Argentina Researchers of CONICET

Lock-exchange flows driven by density differences in non-rectangular cross-section channels are investigated in situations that resemble estuaries, navigation canals and hydraulic engineering structures. A simple analytical model considering stratified flows suggests practical relationships corroborated by results of laboratory experiments carried out in a straight channel of triangular cross-section. [DOI: 10.1115/1.1677475]

Introduction

The lock-exchange flows consist of a gravity current of less-dense fluid moving along the surface and a dense current flowing beneath it in the other direction. Main physical mechanisms underlying many natural phenomena associated with this kind of flows can be understood in terms of gravity current theory by means of a simple experimental system constituted by a channel that is temporarily divided into two sections by a thin vertical gate (Fig. 1a). Freshwater fills one section and saltwater the other, and the free surface levels are made equal. As soon as the barrier is raised, the dense fluid starts to collapse and counter-currents begin to flow in opposite directions (Fig. 1(*b*)).

Measurements on the flows present in estuaries and nearby continental shelves, together with theoretical, numerical and laboratory studies have provided understanding regarding the front dynamics and their role in estuarine flows. Most of the analytically simplified models of estuaries assume rectangular cross-sections, or laterally averaged flows, minimizing the influence of the transverse variations over the flow [1–3] and several attempts to model theoretically the flow driven by lateral variation of bathymetry were performed [4–7]. Particularly, Simpson [8] reported the values of the ratio between the initial front velocities of the saltwater and freshwater flows and the thickness of the channel provided by laboratory experiments carried out in trapezoidal, triangular and circular cross-section flumes, but no theoretical model is proposed to explain the findings.

The present work concentrates on lock-exchange flows driven by gravity in open channels with a constant arbitrary cross-section in order to reveal the possible roles of the shape of the cross-section on the flows present in estuaries and engineering structures. A simple analytical model is introduced to explain the relationship between the front velocities and the channel cross-section, and laboratory results from experiments carried out in a straight channel of triangular cross-section are provided.

A Model for the Front Velocities

After removing the gate at time $t=0$ (Fig. 1), the stratification is simplified assuming an unmixed two-layer structure, and the well-known *box model* that has provided good results in many other contexts is invoked. In this conceptual frame, depths and velocities of both liquid layers are considered as uniform along x. From continuity it follows that the mass flux through a cross-section at any x-position along the channel must be the same,

$$\rho_1 \cdot A_1 \cdot u_1 = \rho_2 \cdot A_2 \cdot u_2 , \tag{1}$$

leading to $u_1 = u_2$ and $h_1 = h_2$ when $\rho_2/\rho_1 \approx 1$, the upper and lower boundary conditions are the same and a symmetric cross-section channel is used (i.e., closed pipes). If the channel is open, the different upper and lower boundary conditions give front velocities that differ about 20% [8]. An asymmetric cross-section (Fig. 1c) imposes an additional condition that has to be settled. Neglecting the friction due to the sidewalls, the momentum balance at the leading edge regulates the front velocity by means of a constant densimetric Froude number $F_{1,2} = u_{1,2}/(g' h_{1,2})^{1/2}$. For high Reynolds numbers, well-established theoretical considerations supported by laboratory experiments and field observations in rivers, lakes and oceans suggest that F is of the order of unity for plumes and tidal intrusion fronts [8].

Therefore,

$$\frac{u_1}{\sqrt{g' h_1}} = \Gamma \frac{u_2}{\sqrt{g' h_2}} \tag{2}$$

with $\Gamma = F_1/F_2 \approx 1$. Suppose that the contour of the channel is defined by

$$\frac{z}{H} = \beta \left(\frac{|y|}{D} \right)^{\alpha}, \tag{3}$$

where α and β are constants. As Fig. 2 displays, the value $\alpha=1$ determines a triangular cross-section, $\alpha>1$ provides convex cross-sections (almost rectangular if $\alpha \gg 5$), and $\alpha \leqslant 1$ indicates a cross-section with a central depression.

Using Eq. (3) and introducing the fractional depth $\xi = h_1/H$ of the bottom current, Eqs. (1–2) become

$$\frac{u_1}{u_2} = \frac{\rho_2 A_2}{\rho_1 A_1} = \frac{\rho_2 (1-\xi^{1+1/\alpha})}{\rho_1 \xi^{1+1/\alpha}}, \tag{4}$$

$$\frac{u_1}{u_2} = \Gamma \cdot \sqrt{\frac{\xi}{1-\xi}}. \tag{5}$$

Contributed by the Fluids Engineering Division for publication in the JOURNAL OF FLUIDS ENGINEERING. Manuscript received by the Fluids Engineering Division November 13, 2002; revised manuscript received September 30, 2003. Associate Editor: M.V. Ötügen.

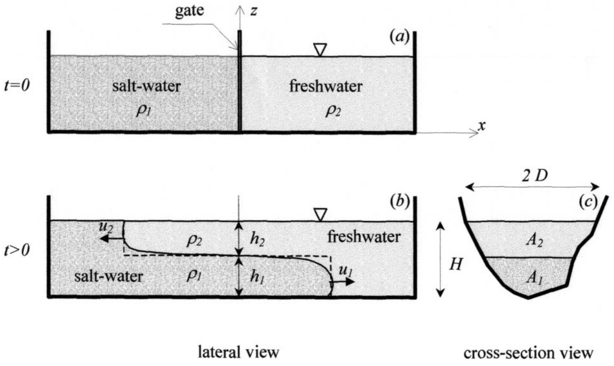

Fig. 1 Sketches of an arbitrary cross-section channel showing (a) the lateral view of the initial configuration, (b) the exchange flows lateral view as seen some time after withdrawing the gate, and profiles suggested by the *box-model* (dashed lines), and (c) a cross-section view

The parameter β that gives the relationship between the horizontal and vertical scales is not present in these equations. Combining Eqs. (4) and (5), an algebraic equation to determine ξ as a function of Γ, α and ρ_2/ρ_1 is obtained

$$\frac{\rho_2}{\rho_1}\frac{(1-\xi^{1+1/\alpha})}{\xi^{1+1/\alpha}}-\Gamma\cdot\sqrt{\frac{\xi}{1-\xi}}=0 \tag{6}$$

The solution of Eq. (6) is a smooth function varying between $\xi=1$ for $\alpha=0$ and $\xi=1/(1+\Gamma^{2/3})\approx 0.5$ for $\alpha=\infty$ (Fig. 3(*a*)). The corresponding evolution of the front velocity ratio is depicted in Fig. 3b for three values of Γ. The open diamond resumes the experiments reported below, which agrees well with the experimental value obtained by Simpson [8] (circle inside the diamond) for a right-angled triangular cross-section. This may be taken as a confirmation that the front velocity ratio does not depend on this angle (or, on parameter β in the general case), as anticipated by the model. Figure 3b also includes the value corresponding to an open circular tube filled to a quarter depth ($u_1/u_2=1.33$) reported by Simpson [8], whose associated value of $\alpha=2.55$ was obtained by means of a best fit process using Eq. (3) for the wet cross-section contour. The few available experimental results suggest that the assumptions are valid at least for $1\leqslant\alpha<\infty$, i.e. for cross-section shapes ranged between triangular ($\alpha=1$) and rectangular ($\alpha=\infty$). More experiments using more complex cross-sections shapes, in particular for $\alpha<1$, are required to check thoroughly the model.

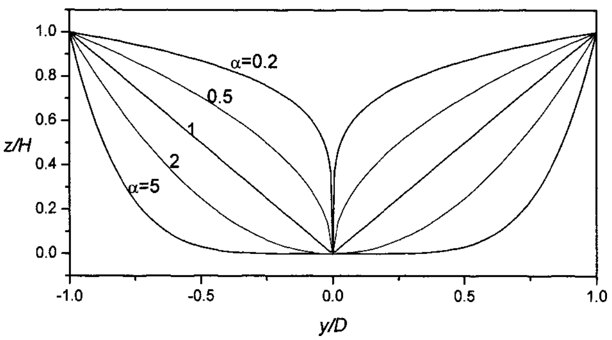

Fig. 2 Channel cross-section shapes suggested by Eq. (3) for different values of the parameter α with $\beta=1$

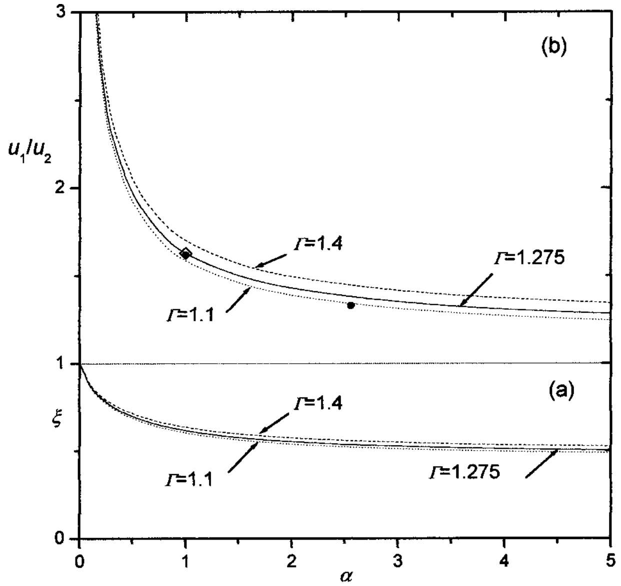

Fig. 3 Fractional depth (a) and front velocity ratio (b) of the bottom current for $\rho_2/\rho_1\approx 1$

Figure 3 indicates that the cross-section shape may affect the velocity ratio for small α, suggesting for example a fast saltwater flow and an almost quiet buoyant plume for cross-sections with a pronounced central depression.

Experimental Validation

A series of lock-exchange experiments were performed in a right-angled triangular cross-section channel with transparent Perspex sidewalls, varying the initial value of g' [9].

Figure 4 is a log-log representation of the front velocities of the lighter fluid current running along the water surface and the dense current moving over the bottom. A best-fit process using a function that is proportional to $\sqrt{g'}$ (see Eq. (2)) gives the straight lines whose ratio $u_1/u_2=1.62$ agrees well with that reported by Simp-

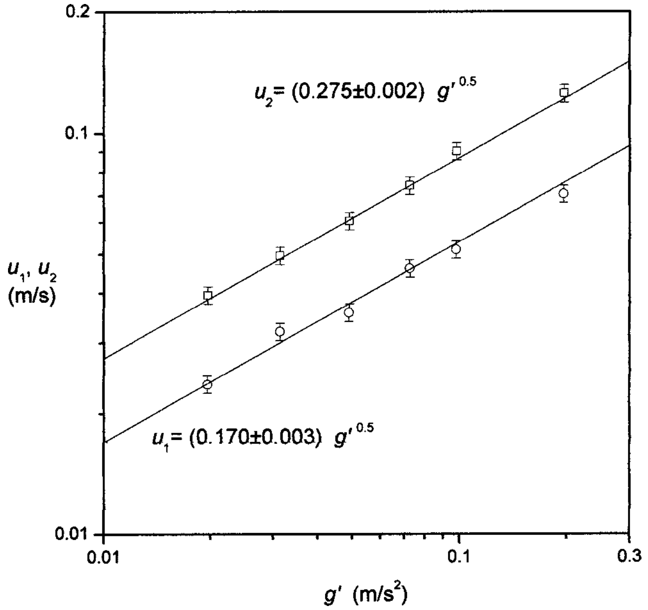

Fig. 4 Velocities of the fronts of the gravity currents running over the bottom (circles) and below the free surface (squares) for different values of g′

son [8]. The related Froude numbers are $F_1=0.75$ and $F_2=0.6$, similar to those obtained for lock-exchange flows generated in open rectangular cross-section channels, and then $\Gamma=1.275$ that is employed as a reference value.

The in-line average lateral density distribution is also measured from the digitised images registered by a video-camera placed at a fixed lateral position 6.00 m away from the tank. The fractional depth associated with the contour $0.5\Delta\rho/\rho_2$ at $x=0$ is $\xi=0.63$ that is very close to the value foreseen by the model (i.e., $\xi=0.62$). A careful examination of the lateral views shows that the *whole* dense current appears elevated almost 0.005 m with respect to the bottom of the tank, spreading over a very thin layer of freshwater that remains fastened during the passage of the gravity current. This feature is absent in gravity currents performed in rectangular cross-section channels and was confirmed by a visual inspection during the experiments. The layer resembles a boundary layer in which the effect of viscosity is important however high the Reynolds number of the flow bulk is. Eventually, the dense fluid replaces the freshwater of the layer after an interval that is longer than the time in which the experiment is completed.

Conclusions

A new simple model based on the global mass balance and the front Froude number suggests the front velocity evolution of lock-exchange flows driven by density difference in non-rectangular cross-section channels. It is found that the front velocity ratio does not depend upon the ratio between the vertical and transversal scales. New experimental results concerning gravity currents running along a triangular cross-section tank complement the scarce laboratory results in the literature, and indicate new features of the currents involved which may affect the erosion and particle deposition processes that occur in sedimentary flows of rivers, estuaries and hydraulic engineering structures.

Nomenclature

A_i = cross-section area of the current i
D = semi-width of the channel
$F_i=u_1/(g'\cdot h_i)^{1/2}$ = Froude number of current i
g = gravity acceleration
$g'-g(\rho_1-\rho_2)/\rho_2$ = reduced gravity, $g'\ll g$
h_i = height of current i
$H=h_1+h_2$ = maximum fluid depth
u_i = front velocity of current i
x, y, z = longitudinal, transversal, and vertical coordinates
α, β = constants associated with the shape of the channel contour
ρ_i = density of fluid i
$\Delta\rho=\rho_1-\rho_2>0$ = density difference
$\Gamma=F_1/F_2$ = Froude numbers ratio
$\xi=h_1/H$ = fractional depth of the dense current

Subscripts:

i = 1, for dense fluid (saltwater)
i = 2, for light fluid (freshwater)

References

[1] Pritchard, D. W., 1956, ''The Dynamic Structure of Coastal Plain Estuary,'' J. Mar. Res., **15**, pp. 33–42.

[2] Hansen, D. V., and Rattray, M., 1965, ''Gravitational Circulation in Straits and Estuaries,'' J. Mar. Res., **23**, pp. 104–122.

[3] O'Donnell, J., 1993, ''Surface Fronts in Estuaries: A Review,'' Estuaries, **16**, pp. 12–39.

[4] Simpson, J. H., and Nunes, R. A., 1981, ''The Tidal Intrusion Front—An Estuarine Convergence Zone,'' Estuarine Coastal and Shelf Science, **13**, pp. 257–266.

[5] Wong, K. C., 1994, ''On the Nature of Transverse Variability in a Coastal Plain Estuary,'' J. Geophys. Res., **99**, pp. 209–222.

[6] Wong, K. C., and Munchow, A., 1995, ''Buoyancy Forced Interaction Between Estuary and Inner Sheft—Observation,'' Cont. Shelf Res., **15**, pp. 59–88.

[7] Valle-Levinson, A., and Lwiza, K. M. M., 1995, ''The Effects of Channels and Shoals on Exchange Between the Chesapeake Bay and the Adjacent Ocean,'' J. Geophys. Res., **100**, pp. 18551–18563.

[8] Simpson, J. E., 1997, Gravity Currents in the Environment and the Laboratory, Cambridge University Press, Cambridge, U.K.

[9] Thomas, L. P., Marino, B. M., and Dalziel, S. B., 2003, ''Measurement of Density Distribution in a Fluid Layer by Laser-Induced Fluorescence in Non-Rectangular Cross-Section Channels,'' Int. J. Heat Technol., **21**, pp. 143–147.

Journal of Fluids Engineering

Book Review

Low-Speed Aerodynamics, Second Edition, by Joseph Katz and Allen Plotkin. Cambridge Aerospace Series, 2001; 613 pages.

REVIEWED BY A. T. CONLISK[1]

This is truly a unique and comprehensive book designed for a one year course in low Mach number aerodynamics. Perhaps because I am not an aeronautical engineer I appreciate the comprehensive nature of the book in which the subject matter ranges from a basic discussion of high Reynolds number fluid mechanics to a comprehensive discussion of three dimensional flow past relatively complex aerodynamic bodies.

The authors have made a conscious decision to restrict themselves to the limit of low Mach number, unlike more conventional aerodynamics books such as the book by Bertin, *Aerodynamics for Engineers*, *Fourth Edition* (2002) which devotes a considerable amount of space to compressible and even hypersonic flow. In my view, this is not a weakness of the book; the fundamentals of aerodynamics are presented in great detail and the inclusion of detailed computer programs, at the time of its first publication was relatively rare. There is a healthy mix of theory and analytical methods owing to the years of experience of Professor Plotkin and computational methods primarily provided by the years of experience of Professor Katz.

The text is a second edition and is over 600 pages in length; not only is it useful as a textbook, but it also serves as a ready reference book for incompressible aerodynamics. Graduate students find it easy to read and comprehensive enough so that they can initiate a research effort essentially independently. At the same time, the text provides fundamental insights into basic incompressible fluid mechanics with aerodynamic applications. In particular, I have not seen the extensive discussion of 3-D panel methods discussed in such detail anywhere else. At the same time a chapter on the fundamental theory of the laminar boundary layer has been added in this, the second edition, a unique feature in a book tailored to aeronautical engineers. In addition, complete computer programs written in Fortran for two and 3-D panel methods are provided in an appendix allowing the easy development of special purpose computer programs by the reader.

In my view, the book may be divided into four parts. Chapters 1–3 present the basics of incompressible fluid mechanics. Much of this material appears in undergraduate textbooks a fact which adds to the book's completeness. Chapters 4–8 describe the basic theory of linearized potential theory while Chapters 9–13 describe the numerical implementation of the basic theory. Chapters 14 and 15 while not necessary for completeness of the text add to its usefulness by presenting the basics of viscous flow theory and full 3-D implementation of the methods described in the previous chapters.

Chapters 1–3 provide a basic introduction to the fundamentals of fluid dynamics. Chapter 1 begins with a discussion of the notion of flow lines which and dimensional analysis and the presentation of the governing equations which often appears in undergraduate texts in fluid dynamics. Chapter 2 introduces the concept of vorticity and circulation in incompressible flow with a short derivation of Bernoulli's equation. Much of the material in this chapter appears in undergraduate texts and their presence in this text reinforces the theme of a self-contained presentation which permeates the entire text. An exception to this is the discussion of the Biot-Savart Law, the basic building block of 3-D aerodynamics. Chapter 3 provides an introduction to potential theory leading into Chapters 4 and 5 which discuss the flow over three-dimensional wings and 2-D airfoils respectively. Chapter 6 describes 2-D potential flow analysis using complex variables; this classical analysis is supplemented by a detailed discussion of the force on the airfoil obtained both by the Kutta-Joukowski law and by an integration of the pressure distribution. Airfoils with finite trailing edges are also considered.

Chapters 1–6 comprise what may be stated as the fundamental portion of the text except for Chapter 14, which discusses boundary layer theory, a chapter which was added in the 2nd edition. Chapters 7–12 present solution methods for the basic problems in two and 3-D aerodynamics.

Chapter 7 introduces the concept of 2-D thin aerofoil theory which leads into singular perturbation theory. This treatment is somewhat unusual in classical aerodynamic texts yet the discussion of thin aerofoil theory in terms of singular perturbations is extremely enlightening. Following the theme of Chapter 7, the 3-D, slender wing is presented. Here the fundamental notion of a lifting-line is introduced and the formulas for the loads on the airfoil are also calculated.

Chapters 9–12 provide a lucid introduction to the classical numerical analysis appropriate to thin airfoils in both two and three dimensions. First, 2-D panel methods are described in Chapter 9 where the airfoil is described by a lumped vortex element. In Chapter 10, the various kinds of singularities which may be used to represent airfoils, including source, doublet and vortex distributions. Along with the basic theory of singularity elements, the various methods of approximation of the strength of the elements is discussed.

Chapter 11 presents several examples of the numerical solution of the 2-D theory first introduced in Chapter 9. Here specific examples of a flat plate and cambered airfoils are solved numerically. Both Dirichlet and Neumann boundary conditions are treated. A minor note: Fig. 11–36 is considerably out of date and should be redone.

Building on the basic numerical methods in two dimensions, 3-D methods are described in Chapter 12. Significant attention is paid to the horseshoe vortex and vortex ring models for flow past a 3-D fixed wing.

In a rather lengthy chapter, Chapter 13 several examples of unsteady problems are presented. It is shown that the methods described previously for the steady problem may be readily extended to the unsteady problem. The sudden acceleration of a 2-D flat plate and a pitching wing are considered explicitly. The 2-D thin airfoil theory presented in Chapter 5 is completely redone for unsteady flow.

A unique feature of this book is the discussion of boundary

---

[1] Professor, Department of Mechanical Engineering, The Ohio State University, 206 W. 18th Avenue, Columbus, Ohio 43210

layer theory in Chapter 14. The boundary layer on a curved surface is discussed first; this problem corresponds to the viscous flow near the leading edge of an airfoil. Next the basic theory of similarity solutions is presented corresponding to the viscous flow on the airfoil away from the leading and trailing edges. The von Karman integral approach is also presented and the first order interaction between the boundary layer and the outer inviscid is described.

The book concludes with a Chapter on applications, including a basic discussion of separated flow and high angle of attack aerodynamics. Problems ranging from 2-D unsteady flow past a 2-D flat plate airfoil to the 3-D flow past an entire aircraft are presented. An extensive set of references follows the chapter so that the reader may look up the original references.

This book is a significant contribution to the aerodynamic literature. Several of my students have been able to begin their research careers in aerodynamics by reading and digesting this book. It is certainly a significant contribution to modern aerodynamic theory and numerical computation of aerodynamic flows over both simple 2-D and complex 3-D shapes.